SAND88-8004

Sandia Combustion Research

Annual Report

1987

Printed in the United States of America
Available from
National Technical Information Service
5285 Port Royal Road
Springfield, VA 22161

NTIS price codes
Printed copy: A11
Microfiche copy: A01

SAND88-8004
UC-96

Sandia Combustion Research Program

Annual Report

1987

Prepared by Sandia National Laboratories, Livermore, California 94551-0969
for the U. S. Department of Energy under Contract DE-AC04-76DP00789

Sandia Combustion Research Program
Annual Report
1987

Director: P. L. Mattern

Department Managers: J. S. Binkley
W. J. McLean

Technical Editors: R. E. Palmer
B. R. Sanders

Production Editor: C. A. Ivanetich
Art: J. H. Bishop
Production Assistants: D. L. Atwood
S. K. Brown
P. K. Bullock
C. A. Flores

To give comments or request more information, please contact:

Dr. Peter L. Mattern, Director
Combustion and Applied Research
Sandia National Laboratory
Livermore, California 94551-0969
(415) 294-2520

Contents

Section 3. Combustion Chemistry

Section 4. Reacting Flows

Section 5. Combustion Modeling

Section 6. High-Temperature Material Reactions

Section 7. Combustion in Engines and Furnaces

Section 8. Coal Combustion

Section 9. Energetic Materials

Section 10. Technology Exchange

COMBUSTION RESEARCH AT SANDIA

Peter L. Mattern, Director

More than a decade ago, in response to a national energy crisis, Sandia proposed to the U.S. Department of Energy a new, ambitious program in combustion research. Our strategy was to apply the rapidly increasing capabilities in lasers and computers to combustion science and technology. Shortly thereafter, the Combustion Research Facility (CRF) was established at Sandia's Livermore location. Designated a "User Facility," the charter of the CRF was to develop and maintain special-purpose resources to support a nationwide initiative—involving U.S. universities, industry, and national laboratories—to improve our understanding and control of combustion.

Today, the Combustion Research Facility occupies a unique niche among Department of Energy "User Facilities." Our resources are diverse, and include specialized lasers, computers, and more than two dozen laboratories optimized for the study of combustion-related processes. One of our strongest assets is our highly trained resident technical staff, with backgrounds and skills covering a broad spectrum of disciplines in the combustion sciences.

The Office of Basic Energy Sciences within the U.S. Department of Energy (DOE) provides support for the operation of the facility, for individual and collaborative visits by Users, and for fundamental research by Sandia staff in combustion-related chemistry, reacting flows, and advanced diagnostic methods. These basic studies are complemented by applied research programs supported by DOE's Offices of Conservation and Fossil Energy. We also have taken on work for several offices of the Department of Defense, NASA, and the NRC when the specialized resources of the CRF are required.

Our mission emphasizes the meaningful involvement of industry and universities. The Visiting Scientist Program reflects our commitment to this goal. As is evident in Figure 1 of Section 10, more than 800 scientists came to the CRF in 1987 for short visits, typically to exchange ideas and information on combustion-related research and technology. Figure 2 shows the continued increase in long-term collaborative and independent research at the CRF: in 1987, 69 scientists were in residence for two weeks or more. Recognizing that there are some 40 professionals associated with our Combustion Program, this monotonically increasing trend must saturate soon. In addition, we continue to strengthen our ties with local universities, and seek to expand a highly successful post-doctoral research program. This year, we saw the initiation of a post-doctoral position supported by the Gas Research Institute.

"Industrial competitiveness" and "technology transfer" have become increasingly familiar phrases in the national laboratory community. Working Groups (see Section 10), organized through CRF programs and comprised of key staff from industry, academia, and national laboratories, are a decade-old concept here at the CRF, and continue to provide a valuable forum for the meaningful exchange of problems, ideas, and information. Based on a perception of success, we have expanded the number and scope of these groups in the past year, and believe even more strongly that they represent an important model for meaningful and effective exchange of technology with industry. This report includes descriptions of several research projects which have been stimulated by Working Groups and involve the on-site participation of industry scientists. DOE's Industry Technology Fellowship Program has been instrumental in the success of some of these joint efforts.

The remainder of this report presents research results of calendar year 1987, separated thematically into nine categories. Refereed journal articles appearing in print during 1987, along with selected other publications, are included at the end of Section 10. In addition to our "traditional" research —chemistry, reacting flow, diagnostics, engine combustion, and coal combustion—you will note continued progress in somewhat recent themes: pulse combustion, high temperature materials, and energetic materials, for example. Moreover, we have just started a small, new effort to understand combustion-related issues in the management of toxic and hazardous materials.

New capabilities were made available to the combustion community during the past year. A large (for us), flexible-purpose, multi-fuel combustor was installed, enhancing our ability to deal with fossil fuel-related issues of interest to U.S. industry. In response to a need for better understanding of liquid-fuel combustion, a new facility dedicated to spray combustion was designed and constructed. To aid in the control of materials-related nucleation and deposition phenomena, we have commissioned a new laboratory for laser-based studies of ceramic powder synthesis. Finally, we have fully consolidated our centralized computing resources, and

have made Cray-level supercomputing available to on-site Visiting Scientists. These new capabilities significantly increase the breadth and depth of resources available at the CRF for combustion-related science.

What does the future hold for the Combustion Research Facility? In FY1987 & 1988, the U.S. Congress appropriated more than $4M towards the start of the CRF-II Construction Project. The major intent of this project is to double the amount of laboratory space readily accessible to Users, complete the office building, and add next-generation laser and computer technology. Current plans for new equipment include a femtosecond laser source for chemistry studies, a pulse-burst laser for high-speed imaging and spectroscopy, and access to a Class VI scientific supercomputer. Overall, our intent is to achieve balance between two opposing objectives, both in support of Users: to provide opportunities for new science, and to make existing capabilities more accessible to Visiting Scientists. An additional $15M in the "out" years will be required to finish the job. We have sought and received peer-response to the proposed new facility and equipment, and have modified our plans accordingly. An updated Visiting Scientist booklet, as well as new brochures describing the proposed new laser and computer resources are now available to prospective visitors.

Our research will strive to take maximum advantage of the new capabilities coming on line, and will seek to provide an overlap with the wide interests of new Visiting Scientists. Control of toxics, pollutants, and other deleterious by-products of energy use will continue to motivate our mainstream program. We are broadening the charter of our energy conservation research into continuous combustion, and are seeking the establishment of a research program to develop the technology base still needed for the clean combustion of coal beyond the year 2000. As before, we will continue to invest a small fraction of our effort in new, forward-looking activities.

I trust you will be intrigued by some of the research you encounter as you browse through this report, and will want to know more. Give me a call—I look forward to hearing from you.

The structure of a "steady" spray flame is characterized by large spatial variations and rapid temporal fluctuations. This photograph of a kerosene flame was taken in our new spray combustion facility and represents an expanded direction for the DOE Energy Conversion and Utilization Technologies program.

Facilities and Special Equipment

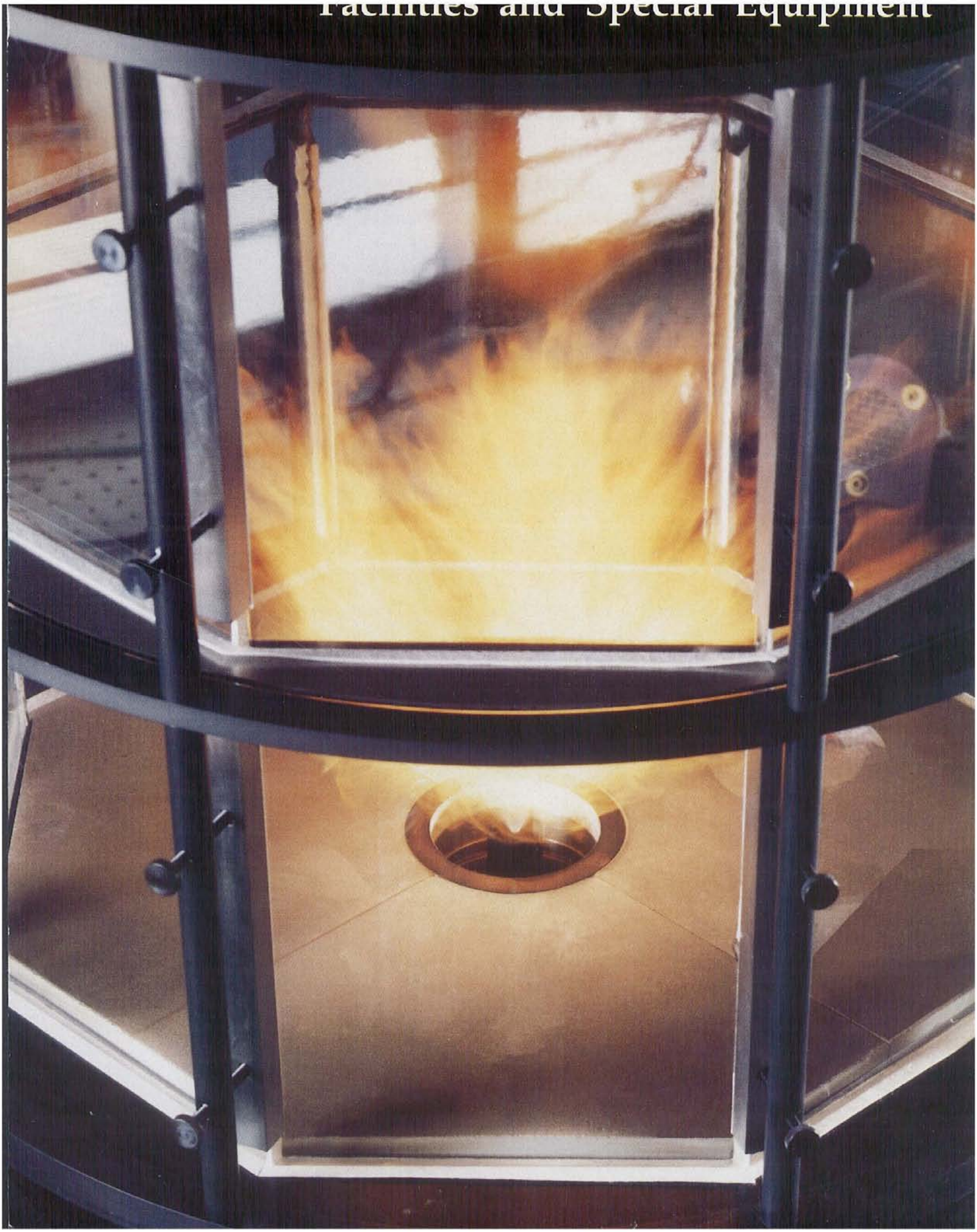

We have recently completed the development and initial testing of an optically accessible research furnace to investigate the group combustion processes in steady spray flames. The coupling of processes, including injection, vaporization, mixing and combustion affect overall system efficiency and heat transfer characteristics as well as the emission of pollutants such as soot and nitrogen oxides. The facility has been designed to allow separate control of the key experimental parameters to allow systematic variation from a regime characterized by a gas-phase flame sheath to the other extreme characterized by individual droplet burning. Combined laser-induced fluorescence and Mie-scattering, two-dimensional imaging techniques are being implemented to reveal the spatial locations and temporal variation of droplets, combustion regions and soot particulates.

The results of these studies are closely coupled to the development of multidimensional spray combustion models. The CRF is applying the Los Alamos-developed KIVA model to this realistic, confined flow furnace. Submodels that describe the nature of the fluid mechanics, combustion, and emission processes are being refined and validated. The systematic variation of parameters coupled with extensive *in situ* measurements will provide the essential insight to build more physically-based accurate submodels.

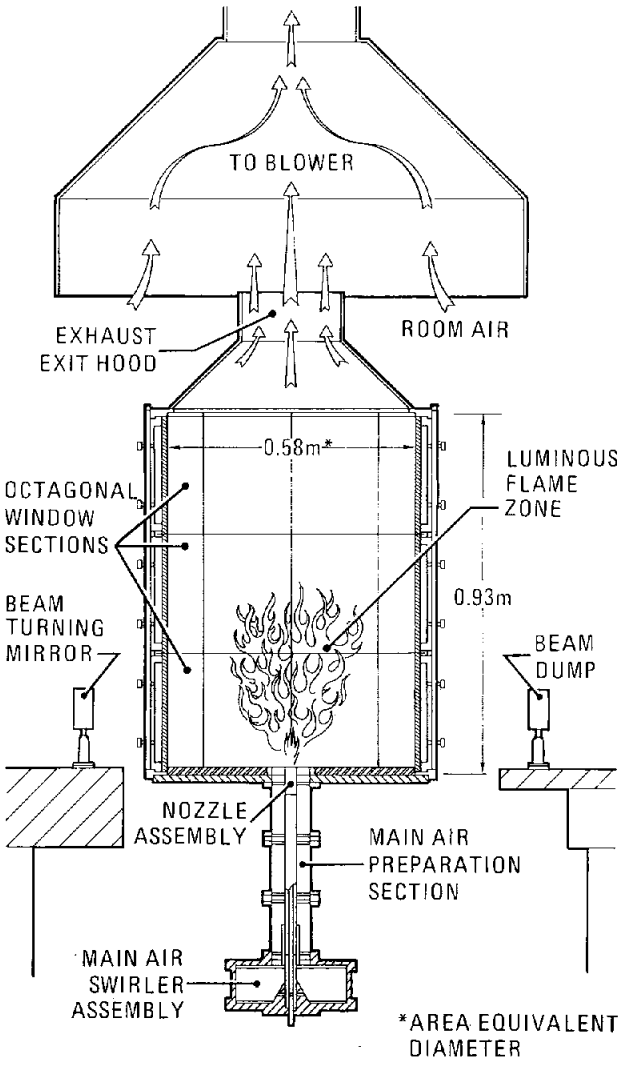

Section 1
Facilities and Special Equipment

The Combustion Research Facility is a 51,500 square-foot, four building complex located on the east side of Sandia National Laboratories Livermore. The Facility, which includes an office building, laboratory, auditorium, and mechanical equipment building, provides a highly sophisticated research environment for the resident staff and visiting researchers. It is located outside the Sandia security area to permit easy access for visitors.

A number of unique features have been incorporated in the facilty: three central facility laser systems that provide state-of-the-art diagnostics, access to a broad range of computers ranging from minis and superminis to 2-million-word Cray systems, and a sophisticated, microprocessor-controlled laboratory safety system.

A high temperature, multifuel flow reactor and a large spray flame facility, both fully optically accessible, provide specialized multiphase combustion environments.

The Facility Laser System

The Facility Laser System consists of three centrally located lasers and a facility beam distribution (periscope) system. The three facility lasers are: Diana, a flashlamp-pumped dye laser; Sirius, a single-frequency Nd:YAG laser and dye laser system; and Dye Blaster, a general-purpose Nd:YAG laser. These lasers may be transmitted to any of the laboratories in the CRF using the facility periscope system.

R. L. Schmitt

The following are examples of the use of the Combustion Research Facility (CRF) laser systems:

Diana

Diana is a flashlamp-pumped dye laser system designed for single-shot temperature and species concentration measurements in turbulent environments. This laser delivers the high pulse energy required for single-shot spontaneous Raman scattering measurements in a relatively long pulse (~2 μs) that prevents dielectric breakdown in the focused beam. Diana consists of a prism-tuned oscillator followed by three amplifiers, and produces 500 mJ to 5 J per pulse depending on the dye used. Diana may be tuned from 400 nm to 600 nm using a variety of dyes.

Professor Marshall Long and graduate student Brandon Yip of Yale University used Diana for instantaneous three-dimensional imaging measurements in turbulent jets. In their experiment, the beam from Diana was formed into a thin sheet using cylindrical lenses, and this sheet was translated through the measurement volume by a high-speed scanning mirror. A high-speed framing camera (up to 20 frames/μs) synchronized to the laser pulse captured a series of two-dimensional images during the laser pulse. Each frame was spatially separated from the previous frame by ~0.2 mm. The series of frames was then digitized and stored in computer memory. The frames will be used to construct three-dimensional images needed to study flame structure.

Mehdi Namazian (Altex Technologies) and Robert Schefer have used Diana and a Raman imaging system to measure methane concentration in nonpremixed jet and bluff-body flow and flames. For these experiments, Diana was tuned to 444 nm (using Coumarin 440), and two-dimensional images of Raman-scattered light were recorded using two cameras. (Using two cameras extended the dynamic range of the data by a factor of ten over a single-camera system.) The measurements were used to derive the scalar dissipation for jet flows. The results will be used to test the validity of common flame modeling assumptions.

Bob and Mehdi also used Diana for simultaneous two-dimensional mapping of CH and CH_4 concentration in nonpremixed jet and bluff-body stabilized flames. For these experiments, the cavity of the laser was modified to operate with two rear mirrors and thus produce two independently tunable wavelengths (431.5 and 444 nm). The shorter wavelength was used to excite fluorescence from CH and the other was used for spontaneous Raman scattering measurements of CH_4. Together, these images provided important information on the interrelationship between fuel-air mixing and subsequent combustion.

Professor Larry Talbot (University of California at Berkeley), Ian Sheperd (Lawrence Berkeley Laboratories), Mehdi, and Bob used Diana and the Raman imaging system to measure CH concentration in v-shaped turbulent ethylene flames. For these experiments, Diana was tuned to 431.5 nm (using Coumarin 440) to excite fluorescence from CH. The CH concentration profiles will be used to study the interaction between flame propagation and turbulence in premixed combustion.

Robert Dibble and Mohey Monsour (University of Sydney) used Diana to make spontaneous Raman scattering measurements of major species in a turbulent premixed methane flame. The experiments were designed to study chemical kinetic effects in turbulent flames at high mixing rates, as well as supplying a data base for testing and developing theoretical models. The steep gradients associated with the the flame zones challenged the resolution limits of the spontaneous Raman system. Another study showed that the resolution was adequate for first and second moments of species concentration and temperature.

Sirius

Sirius is a multi-purpose laser system for nonlinear optical techniques such as CARS (coherent anti-Stokes Raman spectroscopy) and IRS (inverse Raman spectroscopy). The Sirius laser system consists of a Q-switched frequency-doubled Nd:YAG laser system, a narrow-band tunable dye laser and a broadband dye laser. The Nd:YAG laser is a Molectron MY-34 which has been modified for single-frequency operation. We have installed a diode-laser-pumped injection seeding system[1] to ensure reliable single-frequency operation, and we have modified the laser cavity to a self-filtering unstable resonator (SFUR)[2] to improve the spatial beam quality. In this configuration, the laser produces 10-ns pulses with pulse energies up to 100 mJ at 532 nm. Since many experiments require more than 100 mJ at 532 nm, we plan to install another Nd:YAG amplifier to the laser.

Roger Farrow and David Chandler used Sirius and another single-frequency Nd:YAG laser to measure state-to-state energy transfer rates of H_2. A single-frequency Nd:YAG laser and a pulse-amplified ring-dye laser were used to populate the v =1 state of a single rotational level of H_2 via stimulated Raman pumping. Then, after a suitable delay to allow collision-induced population transfer, the Sirius laser and a pulsed dye laser were used to probe the v =1 populations using scanning CARS. The data were used to determine the rotational relaxation rates for the v =1 state of H_2.

Dye Blaster

The Dye Blaster is Q-switched, frequency-doubled Nd:YAG laser that provides additional capability to pump dye lasers located in remote user laboratories. This laser has been useful both for users who lack an Nd:YAG laser and for users with experiments that require several lasers. The Dye Blaster is a Quanta-Ray DCR-2 that produces up to 350 mJ at 532 nm in ~7-ns pulses. It can be synchronized with other lasers or experimental apparatus as required.

Mark Maris (an Industrial Fellow from Computer Genetics) used Dye Blaster to pump a broadband dye laser for broadband N_2 CARS measurements in a tube furnace. These experiments tested a prototype lens system that allows translation of the CARS probe volume. Ultimately, this lens system will be used by Computer Genetics to perform spatially-resolved CARS measurements in an industrial coal furnace.

Robert Schefer used the Dye Blaster to perform instantaneous spatially-resolved measurements of the OH concentration in turbulent nonpremixed flames. For these experiments, the 532-nm beam from the Dye Blaster was used to pump a tunable dye laser. The output of the tunable dye laser was frequency-doubled to 284 nm and used for fluorescence excitation of the OH molecule. In addition to single-point measurements, a cylindrical lens was used to form the laser into a sheet for two-dimensional imaging of the OH concentration distribution.

References:

1. R. L. Schmitt and L. A. Rahn, Appl. Opt. **25**, 629 (1986).

2. P. G. Gobbi, S. Morosi, G. C. Reali, and S. Zarkasi, Appl. Opt. **24**, 26 (1985).

Multifuels Combustor

The Multifuels Combustor considerably expands the capabilities at the Combustion Research Facility to conduct fundamental studies of the combustion of condensed phase fuels such as pulverized coal and coal/water slurries. Special features allow study of postcombustion phenomena such as the transport and deposition of inorganic mineral species on temperature-controlled surfaces.

D. R. Hardesty and T. T. Bramlette

An important new capability has been added to the Combustion Research Facility (CRF) during the past year. After a three-year planning, design, and development effort, the Multifuels Combustor now occupies a major part of the large high-bay laboratory at the south end of the CRF. Shown in the figure, the Combustor is essentially a long-residence-time, high-temperature, turbulent-flow reactor. While any test fuel can be used, the Combustor is specifically designed to address fundamental issues related to pulverized coal combustion, including the transport and deposition of inorganic mineral species. Researchers can take advantage of the CRF's central facility lasers. As shown in the figure, multiple beams from these lasers are routed through special inter-laboratory ducting and are introduced to the Combustor's open test section via a vertical periscope.

The Combustor is a completely automated, computer-controlled device consisting of 13 integrated subsystems. These include the following:

- main combustor
- multi-sectioned turbulent flow reactor column (up to seven sections are provided)
- open test section
- combustor air supply system
- combustor fuel supply system
- electrical guard heater system
- gas, liquid and solid test-fuel feed systems
- chemical additive injection system
- inert gas or dilution air injection system
- cooling water system for the injectors
- product exhaust and cleanup system
- minicomputer control, monitoring and data-logging system
- integrated safety control system.

The most important new design features are as follows:

(1) A supply of clean vitiated air is provided by the main combustor at peak temperatures of 700 K to 1800 K, velocities of 0.5 to 3 m/s for products of combustion of H_2 or CH_4 and air or oxygen-enriched air. The nominal firing rate of the main combustor is 0.5×10^6 Btu/hr.

(2) Multiple injection points for coal, coal-water slurry, fuel oil (#2 oil, or heat-traced lines for #6 oil), inert particulates, diluents or volatile or condensed-phase additives are located along the reactor. This permits variable residence time as well as variable temperature profiles (by dilution) from the point of reactant injection to the bench-top measurement location on the ground floor. Both coarse and fine-scale resolution on residence time are available.

(3) Complete thermal shielding is achieved by virtue of ceramic insulation and electrical guard heaters along the reactor. The reactor is designed in seven individually controlled and assembled sections (any number can be removed by virtue of the flexible supply lines shown in the figure). Each section contains an internal ceramic tube (15-cm-diameter, 1-m-length). Each section is equipped with access ports for addition of reactant test fuel (or combustion additive or sorbent), inert gas, or secondary air. Each section contains individual silicon-carbide, electrical-guard heaters.

(4) The reactor operates with flat radial profiles of temperature, velocity and dispersed fuels (or additives) which permits sampling of *both solid and gas phase species* at the measurement point. The flat profiles eliminate the gas and solid phase radial transport limitation of our existing laminar flow reactors.

(5) There is open access at table-top level on the ground floor for optical or physical sampling systems and for insertion of temperature-controlled deposit substrates for deposition, corrosion or erosion studies in coal combustion product streams. The figure shows a typical experiment in the open test section using the CRF's central lasers for measurement of surface and entrained flow properties.

(6) Vertical down-flow geometry minimizes buoyancy effects and loss of solid material due to wall deposition.

By way of comparison, the bench-scale, laminar-flow reactors presently used in the Char Combustion and Coal Devolatilization Laboratories at the CRF simulate the key features of the

early devolatilization and char oxidation regimes of pulverized coal combustion. The new Combustor extends the range of residence times from a few hundred milliseconds to several seconds. Access to the "burnout" phase of pulverized coal combustion, without resorting to high excess oxygen concentrations, is afforded. Research capabilities for mineral matter studies are greatly enhanced by virtue of several different operating modes. The Combustor can, for example:

- Simulate an entire time-temperature profile of an industrial combustor. This is achieved by introducing the test fuel (e.g., pulverized coal) near the inlet to the reactor column and by programming the downstream temperature profile using diluent addition and adjusting the guard heater currents appropriately, or,
- Allow access to any point on the time-temperature (t-T) profile. This is done by moving the pulverized coal injection point closer to the reactor exit and readjusting the location and balance of dilution air and guard heater current to produce the same (t-T) profile downstream. Since the location of the diagnostics test section is fixed in laboratory space, the residence time between the fuel injection point and the measurement point decreases accordingly.
- Operate in an isothermal mode, similar to the existing bench-scale reactors. Any residence time at constant temperature can be achieved by independently varying the coal injection point, the total flow rate of gaseous fuel and air to the main combustor (hence the mean velocity in the plug flow column), and the guard heater currents.

The system entered the final shake-down phase of development in September 1987. These tests should be complete about mid-year. Planning and design of the combustion experiments and the associated diagnostics for the open-access test section are underway.

Development of this facility was sponsored by the DOE Offices of Fossil Energy and Conservation.

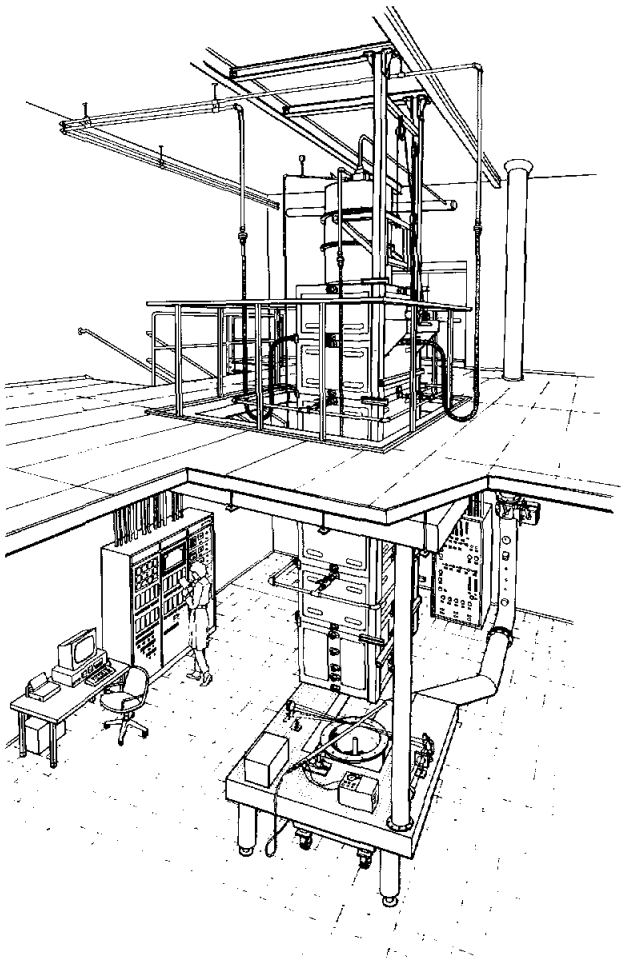

Figure 1. Schematic of the Multifuels Combustor showing controls on the first floor and the cylindrical gas combustor and flexible test-fuel feed lines on the second floor. Also shown is a typical experimental arrangement on the optical table. The table surrounds the open test section and permits multiple laser access to the flow from the combustor. A periscope is shown on the near side of the table which is being used to introduce a facility laser into the test section. In the configuration shown, a temperature-controlled deposition surface is being monitored using the facility lasers.

The Sandia Spray Combustion Facility

We have developd a spray combustion facility to study the critical processes of group combustion in steady spray flames. Facility design has incorporated laser imaging techniques that may be brought to bear on the problem.

C. F. Edwards, R. M. McConkie, and N. R. Fornaciari*

Even after the energy crisis of the early 1970s, the United States remains a petroleum-dependent society. Calendar year 1986 saw the U. S. consume more than 5.8 billion barrels of crude petroleum with more than 37% imported from foreign sources.[1] Of that total, in excess of 2.3 billion barrels (40%) were used in liquid spray combustion devices—furnaces/boilers, gas turbines, diesels—making this class of combustor the largest consumer of petroleum in the United States.[2]

Surprising as it may be, and despite the apparent economic and political incentives, little is known about the fundamental physics of liquid spray combustion in these devices. Recent years have seen major advances in the study and characterization of the fuel spray and combustor fluid mechanics, but as yet little is known of the detailed structure of the reaction zone within the spray flame. Analytical and modeling attempts to engage this problem have highlighted both the difficulty and importance of understanding the structure of the spray flame, but have had to work largely in the dark—there being little experimental data with which to make comparison.

Fortunately, we are now in a position to provide experimental insight into the spray combustion flame through recent advances in laser diagnostics. Using planar, laser-induced fluorescence in combination with Mie scattering and image processing, a thin slice of the flame may be extracted and analyzed by computer to determine the statistics of the flame/spray interaction. The result of this analysis—the group combustion number—not only provides modelers with the experimental grounding needed to further their analysis, but will also provide a direct indication of the propensity of a combustion device to provide clean, efficient fuel usage.

*Chabot College, Hayward, CA.

Figure 1 illustrates the Sandia Spray Combustion Experiment, developed with DOE Energy Conversion and Utilization Technologies program funding to address the group combustion problem. Fuel and air are supplied to the furnace housing through the burner assembly shown at bottom center. Flame stabilization can be achieved either through use of a bluff body or aerodynamically (by using swirl), as illustrated. Reactant entry conditions, both thermodynamic and fluid mechanic, are carefully controlled and tailored to provide suitable conditions for modeling, while the upper furnace housing is of octagonal cross-section to provide an approximation of axis-symmetry but with planar surfaces for optical access. Each of the 24 furnace surfaces is of fused silica, giving complete optical access and near symmetry in thermal boundary conditions. These surfaces may be selectively replaced with other materials of known radiative and conductive properties in order to examine the effect of heat transfer on flame structure.

Figure 2 is a photograph of the flame luminosity for a moderate-intensity, kerosene spray

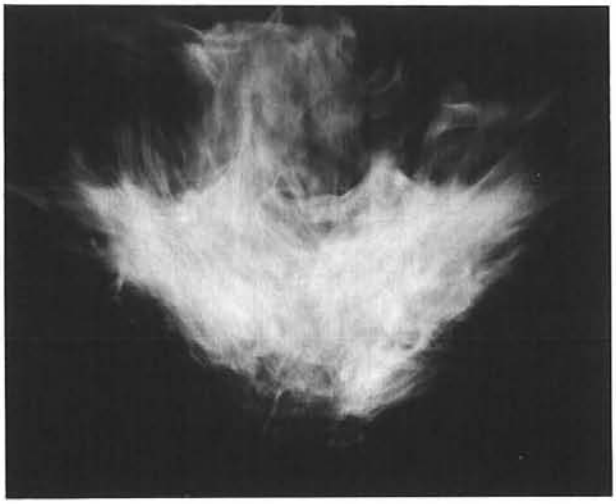

Figure 1. Illustration of the spray combustion equipment that was developed expressly for this experiment.

flame with aerodynamic stabilization. This photograph illustrates the highly variable, inhomogeneous nature of these "steady" spray flames.

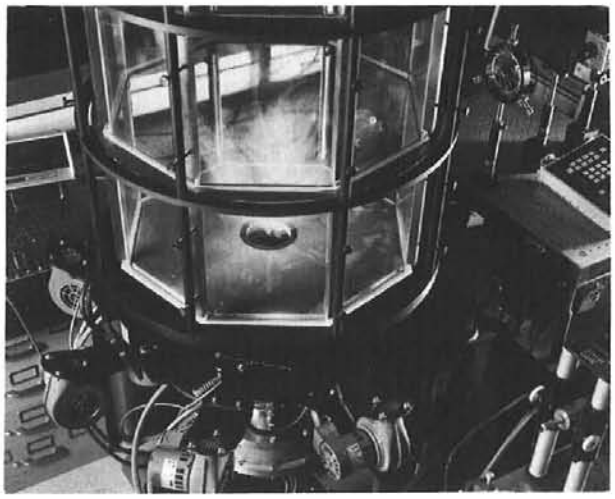

Figure 2. Flame luminosity illustrates the transient, inhomogeneous nature of "steady" spray flames.

Diagnosis of the structure of steady spray flames by high-speed-laser/image-processing techniques provides information that can be used to improve fuel efficiency, performance, and emissions of this important class of combustion systems. Diagnostic design and analysis is currently underway at the Combustion Research Facility.

References:

1. *Annual Energy Review*, DOE/EIA-0384 (1986).

2. *Annual Energy Outlook*, DOE/EIA-0383 (1984).

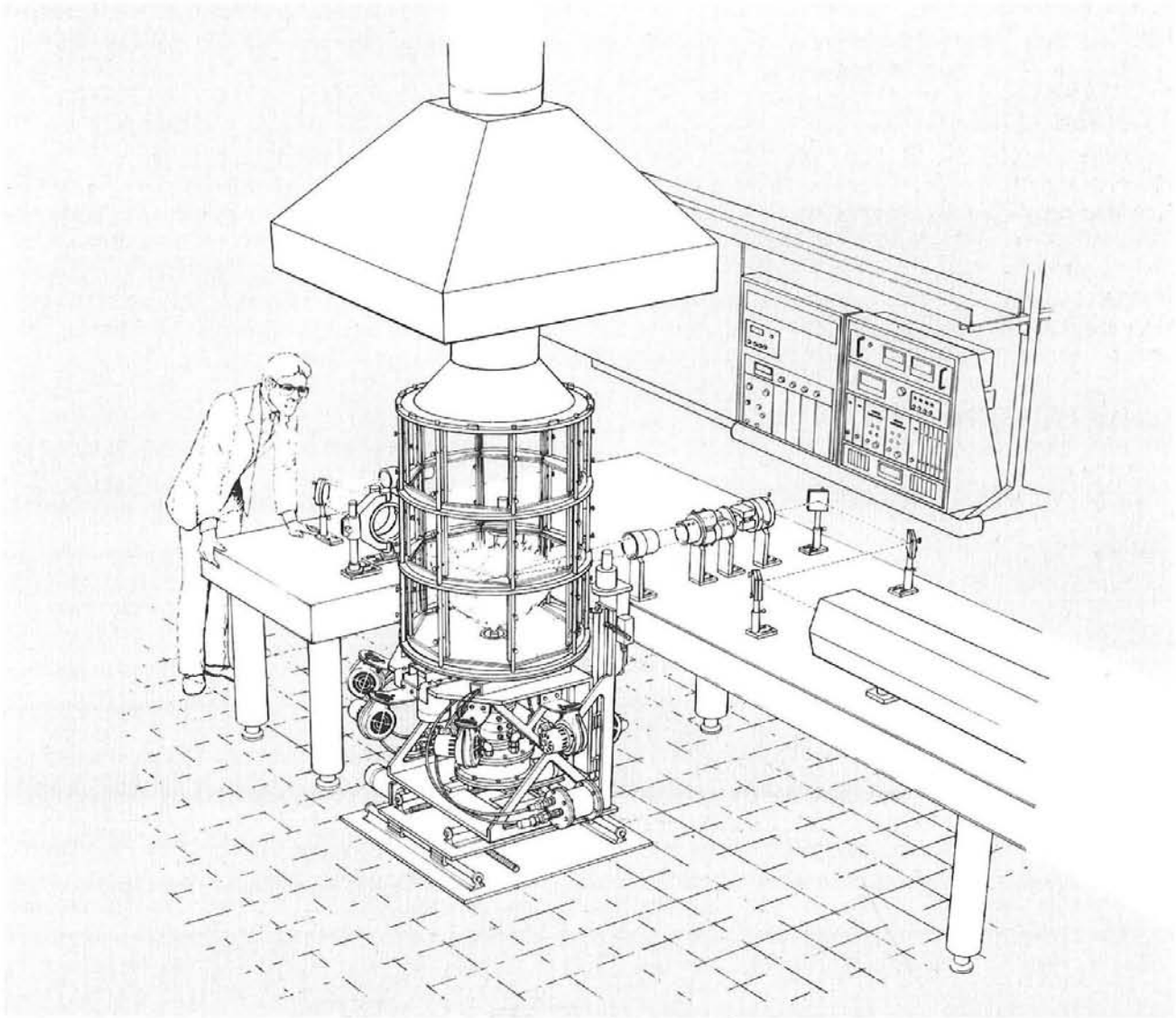

The Facility Computers

Computing capabilities at the Combustion Research Facility have been further enhanced this year. We have added new Central Processing Units, including a Cray 1S, plus additional disk drives, printers, and software.

D. E. Benthusen

Several additions have been made to the computing capability at the Combustion Research Facility this year. The most important addition has been a Cray 1S, which is available through Sandia's Restricted Access network. In addition to the Cray, another VAX 11/780 has been added to serve as a backup terminal concentrator for the Cray. Our VAX 8600 was upgraded to a VAX 8650, giving it six times the CPU speed of a VAX 11/780. Additional disks have been added, making a total of nearly 14 gigabytes of rotating storage on the VAX computers. There is an additional ten gigabytes of disk storage on the Cray. We have also added two new high-performance magnetic-tape drives to service the increase in tape requests caused by the presence of the Cray. Our network currently includes two VAX 11/780 computers in the CRF computer center, two additional VAX computers and the Cray 1S in Sandia's Central Computing Facility, and 14 microVAX computers used to support individual experiments with experiment control, data reduction, or theoretical modeling services. In addition to these 18 CPUs, we have attached 16 DECservers (terminal servers) to the network. They provide 128 terminals with terminal access to any of the CPUs on the network, and they have some very useful features, such as multiple concurrent sessions on the same or different computers. The final piece of hardware to be added this year was an LPS40 PrintServer. The LPS40 is a high-performance laser printer (40 pages/minute) that attaches to the Ethernet and can accept jobs from any CPU on the network. It is a PostScript printer, which makes it useful for integrating text and graphics.

The Cray 1S runs the CTSS (Cray Time Sharing System) operating system, and the VAX computers are running either VMS V4.4 or Ultrix, which is DEC's version of Unix. A FORTRAN 77-compatible compiler is available both on the VAX computers and on the Cray. Other DEC software on the VAX systems includes PASCAL, C, LISP, DECALC, All-in-One, FMS, Datatrieve, and the Common Data Dictionary. The DRS database manager, and three commonly used math program libraries are also available, and the WordMarc Composer word-processing software runs on the Word Processing (WP) VAX 11/780. The TEX typesetting software continues to be widely used, although a larger portion of our word processing and typesetting work is now done on personal computers, such as the Macintosh.

The major graphics system on the Cray is ISSCO's DISSPLA package. DISSPLA can be used to produce graphics on a variety of output devices, such as Tektronix 4014 terminals, Talaris and Printronix printer-plotters, and LN03+ laser printers. TELL-A-GRAF and CUECHART, both from ISSCO, are also available on the VAX computers. These programs are graphics systems that accept plain English commands and can display input data in the form of a plot, a bar-chart, or a pie-chart. In addition, Sandia-designed programs TEXT and NEWPLOT are heavily used for making high-quality presentation aids. All of these systems are now capable of producing color graphics when used in conjunction with the proper output device. The above-mentioned products can make use of a Sandia-designed software system called the Virtual Graphics Device (VGD). The VGD allows powerful graphics editing and the ability to write files that can be processed directly on one of the Dicomed Computer Output Microfilm systems to produce journal-quality output in either black-and-white or color.

Overall demand for CPU cycles on CRF computers continues to increase steadily. Usage averages about 40-45 interactive users on the scientific machines and another 25-30 on the WP VAX. This is a substantial increase in scientific usage, but use of the WP VAX seems to have leveled off, mostly attributable to word processing on personal computers. Meanwhile, because of the increasingly heavy use of the scientific machines, we are supplying more CPU cycles than ever before; however, the addition of a VAX 11/780 and a Cray 1S to our network, and the upgrading of our 8600, has allowed us to meet the demand for the near term. If the computational demands at the Combustion Research Facility continue to increase at the present rate, the CPU power we have in place will probably

probably be adequate to meet our needs until mid-1989. Beyond this time frame, it is our plan to take advantage of the latest generations of Cray, VAX, and other computer systems.

Another avenue for achieving a greater level of performance from computers is the utilization of work stations, which are powerful enough to do many simultaneous computing jobs locally. Networking protocols for work stations are very efficient, and it is reasonable to think in terms of running an application on a bigger VAX or on the Cray, and "exporting" the output for real-time display on the work station. Users need not concern themselves with the compatibility between the work stations and the larger computers, all of which may in fact be running different operating systems. Standard communication protocols between computing environments allow users to control applications transparently through windows, icons, and similar easy-to-use human interfaces. The high-performance processors in today's work stations—with greatly improved performance tomorrow—will dramatically enhance the computing capabilities at the CRF in the future.

Laser sources with high spectral resolution are important for developing state-of-the-art combustion diagnostics. The pulsed dye laser amplifier shown in the figure allows a computer-controlled, single-frequency cw dye laser to be amplified to peak powers of greater than 1 MW for coherent anti-Stokes Raman spectroscopy experiments.

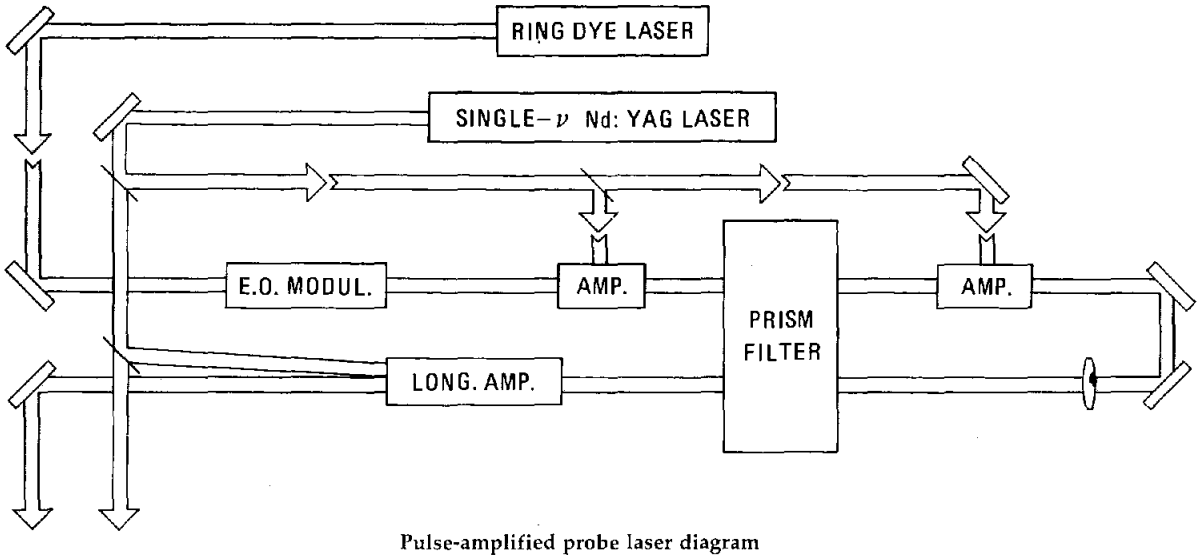

Pulse-amplified probe laser diagram

Modern combustion diagnostics rely heavily on the availability of high-resolution tunable lasers, both to generate a reliable spectroscopic data base and to perform accurate measurements in combustion environments. Continuous-wave (cw) ring dye lasers offer high resolution with wide tunability, but their output powers are too low for most types of nonlinear spectroscopy. Therefore, pulsed dye amplifiers are frequently used to increase the instantaneous power from ring dye lasers. For example, coherent anti-Stokes Raman spectroscopy (CARS) is a combustion diagnostic that uses pulsed dye amplifiers for high-resolution applications. The pulsed dye amplifier system for our high-resolution CARS experiment is shown in the diagram above. A single-mode, feedback-stabilized cw ring dye laser produces tunable laser radiation with a 1-MHz bandwidth. The ring dye laser beam is amplified to a peak power of ~1 MW in three amplifier stages that are pumped by the frequency-doubled output of an injection-seeded, single-mode Nd:YAG laser operating at 10 Hz. The spectral profile and frequency shift from a similar amplifier is shown in the figure to the right. The spectral profile is determined from the transmission of the pulsed beam through a confocal etalon with a free spectral range of 749 MHz, and is compared in the figure to that of the cw ring laser output. In this case, the 22-ns amplified pulse has a spectral width (FWHM) of ~45 MHz (0.0015 cm^{-1}) and a first moment that is blue shifted by <10 MHz from the cw ring laser frequency. The amplified dye laser pulse, used in conjunction with the frequency-doubled, single-mode Nd:YAG laser as the pump beam, yields high-resolution CARS spectra such as that of carbon monoxide in a flame. The net spectral resolution in these measurements is ~90 MHz (0.003 cm^{-1}), which is sufficient for fully resolving the Raman line shape.

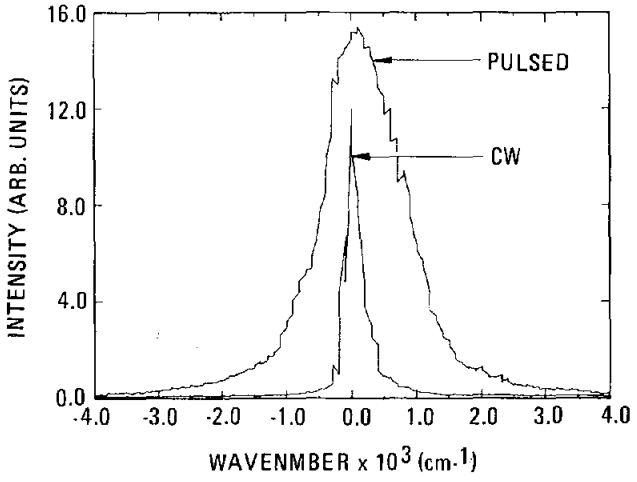

Combustion Diagnostics

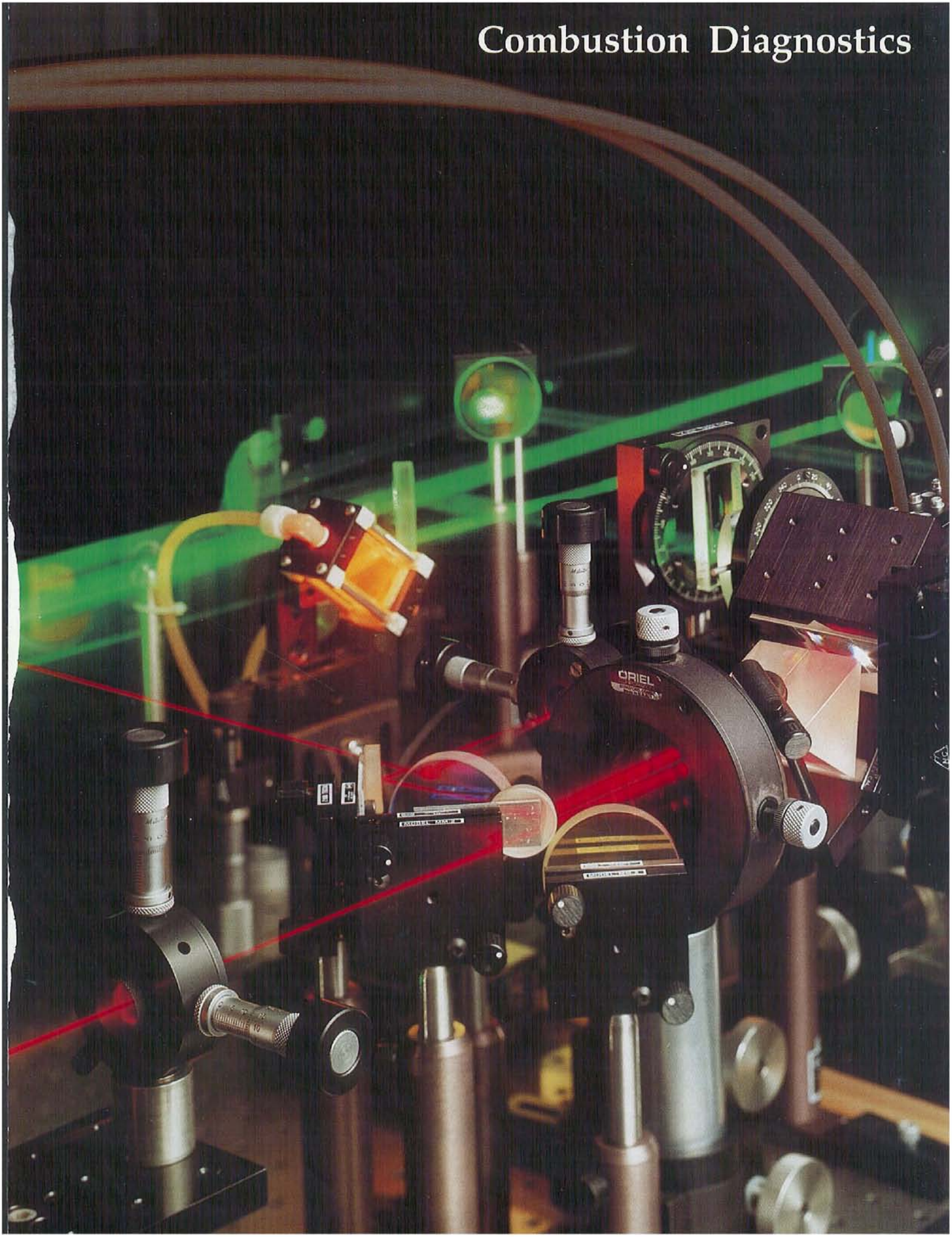

Photochemical Effects in Two-Photon-Excited Fluorescence Detection of Atomic Oxygen in Flames[†]

This article describes photochemical effects observed using 226-nm two-photon-excited fluorescence detection to measure the atomic oxygen concentration in hydrogen-oxygen flames. In particular, we demonstrate that excess atomic oxygen concentrations can be produced by single-photon excitation of the Schumann-Runge bands of vibrationally-excited oxygen molecules present in the flame.

J. E. M. Goldsmith

Much of the recent attention on developing techniques for measuring radical concentrations in flames, and for atoms in particular, has focused on the use of multiphoton excitation schemes. There has been relatively little attention, however, paid to the possible role of perturbations introduced into the measurements due to photochemical production (by the intense laser pulses used for multiphoton excitation) of the species being measured. Using two-photon-excited fluorescence detection of atomic hydrogen in flames, we discovered that the 205-nm laser beam created significant quantities of hydrogen atoms by single-photon photolysis of vibrationally excited water produced in the flame, leading to erroneous concentration profile measurements.

In this article, we describe photochemical production of significant quantities of atomic oxygen during two-photon-excited fluorescence detection of oxygen atoms in flames, and demonstrate that excess atomic oxygen concentrations can be produced by single-photon excitation of the Schumann-Runge bands of vibrationally-excited oxygen molecules present in the flame.

Most of our efforts in this study were directed towards studying a lean (equivalence ratio 0.8), atmospheric-pressure hydrogen-oxygen flame that we have used for making other measurements of flame radicals. A series of atomic oxygen concentration profiles measured in this flame is shown in Figure 1. The absolute scale along the vertical axis refers to the profile indicated by the solid curve. This profile was determined by measuring the absolute OH concentration in the flame with laser absorption spectroscopy and using partial equilibrium calculations to infer the absolute atomic oxygen concentration profile. This profile is in excellent agreement with a relative profile (solid circles) measured at low excitation intensities using resonant multiphoton optogalvanic spectroscopy. This agreement gives us confidence that the profile represented by the solid curve is fairly close to the true profile.

The four relative profiles represented by the open symbols were measured under various excitation intensities using two-photon-excited fluorescence detection. Because these are relative profiles, it was necessary to choose scaling factors to compare them with each other and with the previous measurements. These factors were chosen such that the profiles agreed near the burner surface, where the natural concentration of atomic oxygen is highest and perturbation of this concentration by photochemical effects should be least significant. The profile represented by the squares was recorded using the lowest excitation intensity and is also in excellent agreement with the solid curve, further supporting our confidence in that measurement. The profiles represented by the other open symbols were recorded using higher excitation intensities from other pulse-energy, focal-length combinations. Increasing discrepancies are evident between these profiles and the profile represented by the solid curve.

The profiles in Figure 1 become nearly flat as a function of height above the burner as the excitation intensity is increased. This suggests that a stable post-flame species is the source of the extra atomic oxygen, since radical concentrations drop off rapidly as a function of height above the burner. The only candidates in a lean hydrogen-oxygen flame are molecular oxygen and water vapor. When we made the flame leaner by decreasing the hydrogen flow rate, the "created" atomic oxygen signal increased approximately twofold, suggesting that molecular oxygen (which increased in relative concentration) was the cause of the signal, rather than water vapor (which decreased in relative concentration).

The molecular-oxygen Schumann-Runge bands have strong absorption features in the far uv (200-250 nm) arising from thermally excited vibrational levels in the ground electronic state (v">0), and in particular the (0,3) and (2,4) rovibronic bands have

[†]Applied Optics **26**, 3566 (1987).

Section 2
Combustion Diagnostics

One of the primary thrusts of the combustion research program at Sandia National Laboratories is the development of diagnostic techniques that take advantage of the latest advances in modern technology. This development effort has three objectives: innovative methods for measurements in combustion systems, a quantitative understanding of the usefulness and limitations of these methods, and the transfer of technology from research to application environments.

Because of their nonintrusive nature and great versatility, laser-based optical techniques—both point-resolved and two-dimensional imaging—receive the strongest emphasis. Laser-induced fluorescence, spontaneous and coherent Raman spectroscopy, laser Doppler velocimetry, and multiphoton optogalvanic spectroscopy are but a few of the diagnostic methods that are being developed to measure temperature, species concentrations, velocity flow fields, and other parameters of key importance to the understanding of combustion phenomena. The capabilities of such techniques depend directly on the availability of laser sources with unique spatial, temporal, and spectral properties; thus, an important feature of the combustion diagnostics program is the development of high-performance lasers that meet the requirements of specialized situations. In addition to laser-based optical probes, modern intrusive probes are also being developed and evaluated.

Sandia's efforts to develop advanced combustion diagnostics, especially advanced laser-based optical probes, are supported primarily by the Chemical Sciences Division of the Department of Energy's Office of Basic Energy Sciences. Work in this program is complemented by work in the applied research programs to develop diagnostic techniques for specific combustion applications.

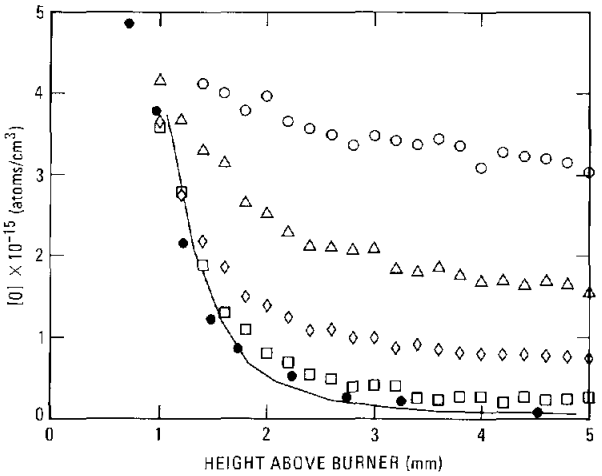

Figure 1. Atomic oxygen concentration profiles in a lean (equivalence ratio 0.8), atmospheric-pressure hydrogen-oxygen flame. Solid curve: absolute profile calculated from measured OH concentration. Solid circles: relative profile measured at low excitation intensity using optogalvanic detection. Open squares, diamonds, triangles, and circles: relative profiles measured using fluorescence detection and listed in order of increasing excitation intensity. The observed profile changes as the excitation intensity is increased because excess atomic oxygen is produced, and subsequently detected, by the laser pulses.

features nearly coincident with the three resolved fine-structure transitions in the atomic oxygen two-photon-excitation spectrum. To investigate the possibility that rapid predissociation of the excited molecular oxygen electronic state could lead to excess atomic oxygen concentrations in flames, we used a second laser system to provide relatively low-energy 226-nm pulses for use as a probe beam. The higher-energy output of the first laser system, used as a pump beam, was then scanned across several molecular oxygen resonances in the region 220.8-221.6 nm, and the atomic oxygen fluorescence induced by the probe beam was monitored.

The top part of Figure 2 shows the resulting signal as the pump beam was scanned, indicating not only that the pump beam created atomic-oxygen concentrations at least ten times in excess of that naturally present in the flame, but that the enhancement has strong resonances in wavelength. The bottom part of Figure 2 was recorded by replacing the interference filter used for O-atom detection with a uv-transmitting filter, so that molecular-oxygen fluorescence induced by the pump beam could be observed directly; we have identified the rovibronic structure as being from overlapping transitions in the (1,3), (2,3), and (3,4) bands. The top and bottom resonances are clearly the same, demonstrating that Schumann-Runge band excitation, followed (presumably) by rapid predissociation, can

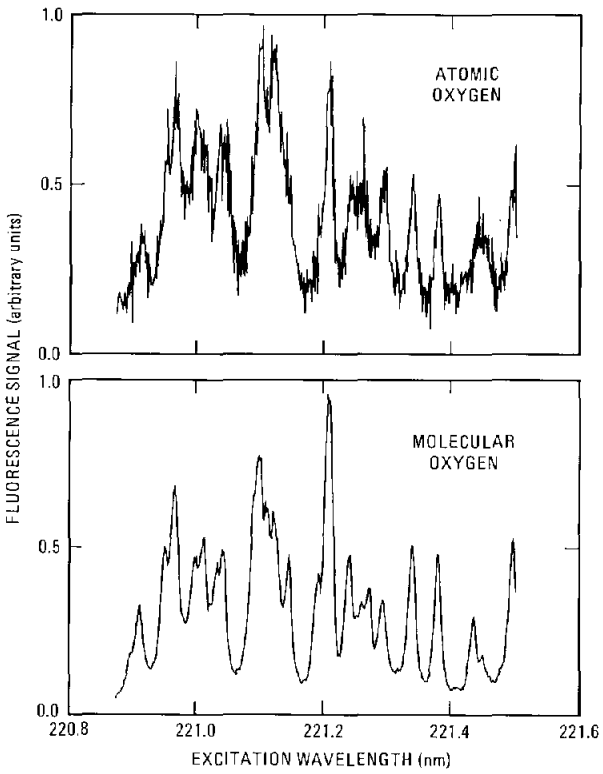

Figure 2. Molecular oxygen Schumann-Runge bands observed in a very lean (equivalence ratio 0.25) hydrogen-oxygen flame 6 mm above the burner surface by monitoring atomic oxygen produced in the flame (top) and by monitoring the molecular-oxygen fluorescence signal directly (bottom). The appearance of the same resonances in the two spectra indicate that excess atomic-oxygen concentrations can be produced by excitation of these (single-photon) molecular-oxygen bands, followed by rapid predissociation to produce oxygen atoms.

lead directly to enhanced atomic oxygen concentration in flames. We do not yet have sufficient evidence, however, to demonstrate that Schumann-Runge band excitation is the dominant, much less the only, process leading to the artificially high atomic-oxygen concentration profiles shown in Figure 1.

The significance of these and other photochemical effects depends strongly on the details of the flame conditions at the point being probed (i.e., temperature and species concentrations). Determination of detection limits cannot be based solely on signal-to-noise considerations, but must also take into account the degree to which the species being measured may be produced by the laser pulse. It is clear from our study of this flame (using relatively modest excitation conditions) that great caution must be exercised in making relative atomic-oxygen concentration measurements with this method, even in post-flame gases, where variations in quenching rates are not a major issue.

Higher-Order Collision-Enhanced Wave Mixing in a Sodium-Seeded Flame†

We observe subharmonics of the hyperfine splitting of sodium in a hydrogen-air flame. These nonlinear-optical effects represent the first observation of higher-order, collision-enhanced wave mixing.

R. Trebino and L. A. Rahn

The study of collisions is essential for many features of combustion. One area that may contribute to our understanding of this process is that of collision-enhanced resonances. This type of resonance is either weak or not present in the absence of collisions, but in the presence of collisions, it can be seen, having strength proportional to the square of the collision rate.

We have been studying two types of collision-enhanced resonances, those known as Zeeman and hyperfine resonances. These are, respectively, resonances between Zeeman and hyperfine levels in $2\omega_1-\omega_2$ four-wave-mixing experiments. Ordinarily, these resonances cannot be seen because the two processes that simultaneously give rise to these effects cancel out. (One process is proportional to the population density in one Zeeman or hyperfine level, while the other is proportional to the negative of the population density of the other level, and the two levels are equally populated.) Collisions, however, introduce non-cancelling components in each process that allow these resonances to be observed in an environment such as a sodium-seeded, atmospheric-pressure, hydrogen-air flame.

Figure 1a shows a collision-enhanced, four-wave-mixing spectrum with a Zeeman resonance at $\delta \equiv \omega_1 - \omega_2 = 0$ and hyperfine resonances at $\delta \cong \pm 0.06\ cm^{-1} \cong \pm\omega_{hfs}$. In Figure 1b, the intensity is higher, and we see significant saturation-broadening of the four-wave-mixing spectrum. In addition, new spectral features are present at frequencies of about one-half of the hyperfine resonance frequencies. These "subharmonic resonances" are due to collision-enhanced, higher-order wave mixing.

It is easy to see that higher-order processes yield subharmonics. Adding and subtracting an input frequency from the signal-frequency expression of a four-wave process, and adding and subtracting the corresponding k-vector from the signal k-vector expression easily creates a phase-matched, six-wave-mixing process. Adding and subtracting additional input frequencies and k-vectors can create arbitrarily high-order processes. For example, in the $2\omega_1-\omega_2$ four-wave-mixing geometry, the six-wave-mixing $[2(\omega_1-\omega_2)]+\omega_2$ and the eight-wave-mixing $[2(\omega_1-\omega_2)]+\omega_2-\omega_1+\omega_1$ processes can occur. Both of these higher-order processes have resonances at $2(\omega_1-\omega_2) = \pm\omega_{hfs}$, i.e., $\omega_1-\omega_2 = \pm\omega_{hfs}/2$. Even higher-order processes, having subharmonic resonances at $\pm\omega_{hfs}/m$, where m = 3, 4, ... , are also possible.

Testing this hypothesis by using higher intensities, where higher-order wave mixing might be expected to increase further in strength relative to four-wave mixing, fails, however, because the broadening increases also, smearing out the entire

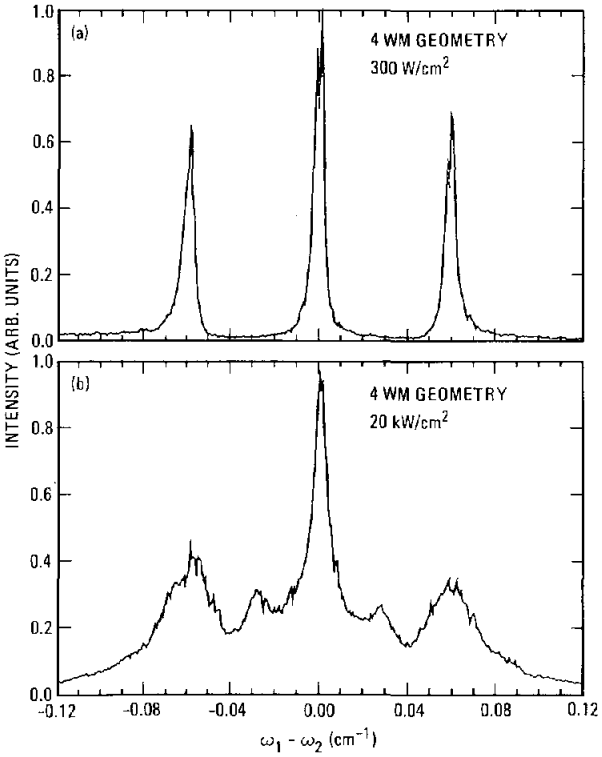

Figure 1. (a) Four-wave-mixing spectrum of collision-enhanced Zeeman ($\omega_1 - \omega_2 = 0$) and hyperfine ($\omega_1 - \omega_2 = \pm\omega_{hfs} = \pm 0.06\ cm^{-1}$) resonances in sodium in a flame at low laser intensity. (b) Same as (a) except that much higher intensities illuminate the flame. Observe the additional "subharmonic" spectral components at $\pm 0.03\ cm^{-1} = \pm\omega_{hfs}/2$.

†Optics Letters **12**, 912 (1987).

spectrum. Instead, we use a six-wave-mixing geometry, which eliminates—by phase-matching—all four-wave-mixing contributions to the spectrum. Figure 2 shows such a geometry. While it is phase-matched for six-wave processes of the form $3\omega_1$-$2\omega_2$, rather than $[2(\omega_1-\omega_2)]+\omega_2$, it has similar difference-frequency resonances to the latter process (see Figure 3) and also the eight-wave-mixing process $[2(\omega_1-\omega_2)]+\omega_2-\omega_1+\omega_1$. Both of these higher-order processes are automatically phase-matched in $2\omega_1$-ω_2 four-wave-mixing experiments. On the other hand, the six-wave-mixing geometry is not phase-matched for four-wave-mixing processes; thus it allows us to observe higher-order wave-mixing effects that appear in four-wave-mixing spectra, unobscured by the generally stronger four-wave-mixing effects.

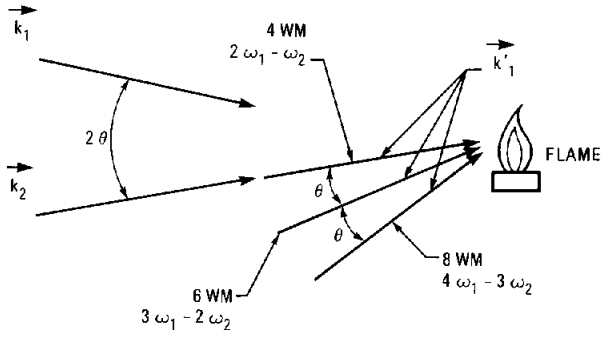

Figure 2. Six-wave-mixing and eight-wave-mixing beam geometries using small-angle, planar phase matching. A planar four-wave-mixing geometry is also shown for reference. These higher-order geometries exclude lower-order, wave-mixing signals.

Figure 4a shows a typical experimental spectrum using the six-wave-mixing geometry with the Zeeman resonance at $\delta = 0$, the hyperfine resonance at $\delta = \pm\omega_{hfs}$ and subharmonics at $\delta = \pm\omega_{hfs}/2$ and at $\pm\omega_{hfs}/3$ (in the form of *dips*). Figure 4b shows a typical spectrum using the eight-wave-mixing geometry. This spectrum reveals a weak hyperfine resonance at $\delta = \pm\omega_{hfs}$ and several subharmonics: $\delta = \pm\omega_{hfs}/2$, $\pm\omega_{hfs}/3$, $\pm\omega_{hfs}/4$, and $\pm\omega_{hfs}/5$. While eight-wave-mixing processes can accommodate $\pm\omega_{hfs}/2$ and $\pm\omega_{hfs}/3$ subharmonics, at least ten-wave mixing is required for the $\pm\omega_{hfs}/4$ subharmonic, and *fourteen*-wave-mixing is the minimum-wave process that can yield $\pm\omega_{hfs}/5$ subharmonics.

Even higher-order processes should be easily observed using higher-order geometries. Significantly, only slightly higher intensities should be necessary for these observations because these processes are nearly resonant. In addition, a magnetic field can split the Zeeman resonance allowing higher-order, collision-enhanced Zeeman resonances to be identified. The ease with which these effects can be observed indicates that these higher-order effects offer a whole new class of nonlinear-optical effects for potential gas-phase diagnostics.

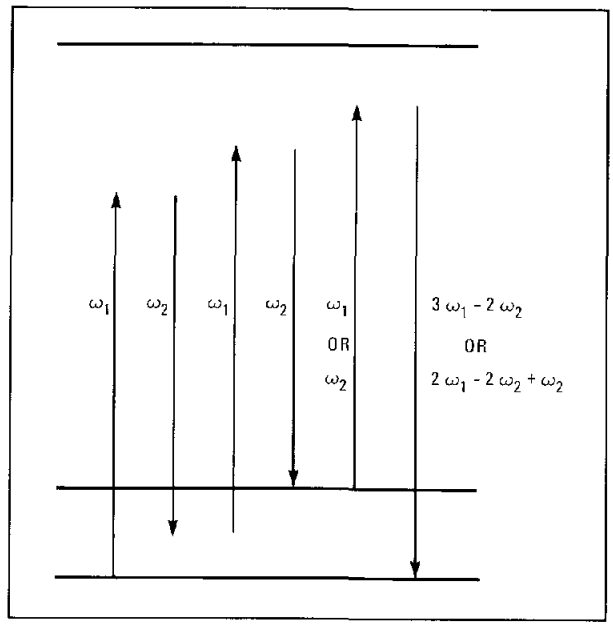

Figure 3. Energy level diagram for six-wave-mixing showing a four-photon $(2(\omega_1 - \omega_2))$ subharmonic resonance. The $3\omega_1 - 2\omega_2$ process requires a six-wave-mixing geometry, while the $2\omega_1 - 2\omega_2 + \omega_2$ process is phase-matched in four-wave-mixing geometries.

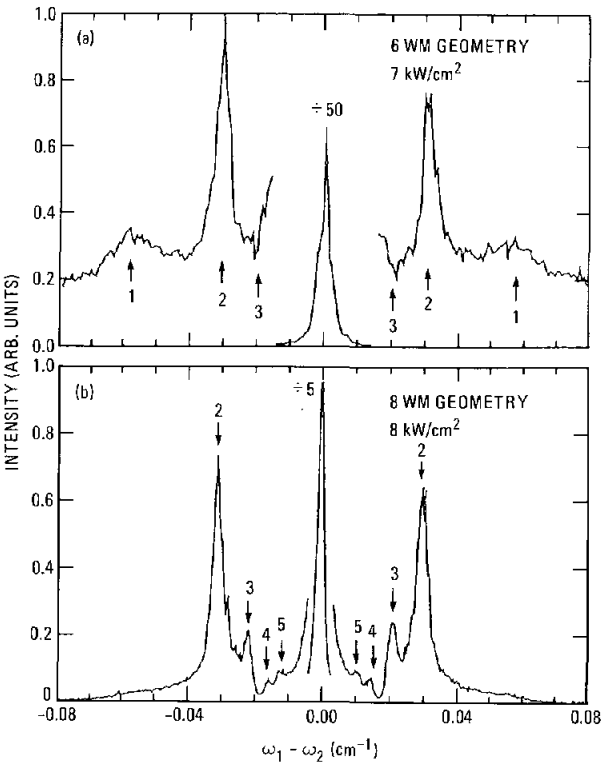

Figure 4. (a) Spectrum of collision-enhanced resonances in a sodium-seeded flame obtained using a six-wave-mixing geometry ($3\omega_1 - 2\omega_2$, in the lowest order). (b) Spectrum obtained using an eight-wave-mixing geometry ($4\omega_1 - 3\omega_2$). Observe the subharmonics at ± 1/2, ± 1/3, ± 1/4, and ± 1/5 of the hyperfine splitting (labeled 2, 3, 4, and 5, respectively).

A New Nonlinear-Optical Expansion and Diagrammatic Approach: Higher-Order Collision-Induced Effects[†]

We introduce a new nonlinear-optical perturbation expansion and diagrammatic approach that yields collision-induced effects without the need for large amounts of algebraic manipulation.

R. Trebino

Nonlinear-optical methods are playing an increasingly important role in combustion diagnostics. Techniques such as coherent anti-Stokes Raman spectroscopy (CARS), inverse Raman scattering (IRS), and, more recently, four-wave mixing (4WM) yield useful diagnostic information often unobtainable in other ways. Another nonlinear-optical phenomenon that has been receiving much attention lately is collision-induced wave-mixing, in which the presence of collisions allows nonlinear-optical resonances that are ordinarily prohibited, to be seen. These resonances promise to yield interesting information on the collision process, which is important for understanding the details of combustion chemistry, for example.

Like CARS, IRS, and 4WM, collision-induced phenomena require for their theoretical description careful examination of complex expressions obtained from quantum-mechanical perturbation theory. Because these expressions are complex, a diagrammatic approach for writing them has helped in theoretical work involving them. Diagrams represent terms in the perturbation expansion, and, once rules are memorized for interpreting them, it is much easier to calculate with diagrams than with the terms themselves. Calculations of expressions for collision-induced phenomena have not benefitted as much from the diagrammatic approach, however, because many terms (or diagrams) must be summed to yield each term corresponding to a collision-induced effect. Because of the potentially very large number of terms ($5 \bullet 10^{13}$ for thirteenth order, for example), this problem can be a significant barrier.

In order to perform calculations for collision-induced effects, we have developed a new nonlinear-optical perturbation expansion, mathematically equivalent to the currently used expansion, but which immediately yields expressions for collision-induced phenomena. We also define new diagrams to describe the terms in this new expansion.

To see how this new approach works, note that the third order of the currently used expansion, which contains the terms responsible for CARS, IRS, 4WM, and several collision-induced effects, has 48 terms. Figure 1 shows three of these third-order terms and their corresponding diagrams. Collision-induced phenomena result from manipulating 36 of these terms, three at a time, to yield 36 new terms, 24 of which are proportional to three-term sums of dephasing rates, $\Gamma_{ij} + \Gamma_{jk} - \Gamma_{ik'}$ where Γ_{ab} is the dephasing rate between states a and b. Figures 2 and 3 show the three terms that result from this manipulation of the terms in Figure 1. The latter 24 terms (e.g., those in Figure 3) are the collision-induced terms because the three-term sum of dephasing rates vanishes (or becomes small) in the absence of collisions. When collisions are present, it is approximately proportional to the collision rate.

This rearrangement of the third-order terms is quite advantageous: in it, the form of the collision-induced terms is immediately apparent. The question that immediately arises is whether such an algebraic rearrangement of terms is possible for other orders. The answer is yes. We have been able to prove that all orders of the nonlinear-optical expansion can be written as the sum of two types of terms: terms such as those of Figure 2 and collision-induced terms such as those of Figure 3. We have also developed a diagrammatic approach for writing these terms (See Figures 2 and 3). These figures reveal the main advantage of the new approach: collision-induced terms emerge immediately from the diagrams, with no algebra necessary.

In addition to this advantage, however, several important results also can be seen easily with the new expansion and diagrams. The most important result is that collision-induced phenomena exist in all orders of perturbation theory, not just the third. In addition, interestingly, all collision-induced terms are proportional to factors of the form, $\Gamma_{ij} + \Gamma_{jk} - \Gamma_{ik}$. Another result that follows easily from the new approach involves an interesting type of effect: resonances between unpopulated states. With the new approach, it is easy to show that, in all orders, these resonances are collision-induced.

[†]Physical Review A, submitted (1987).

Finally, an additional benefit of this expansion and its diagrammatic approach is that they provide some physical insight into the complex mathematics involved in the perturbation theory.

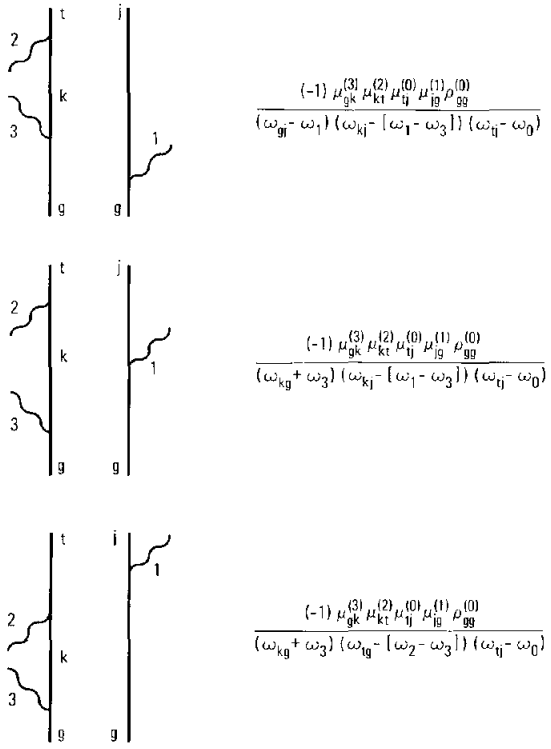

$$\frac{(-1)\,\mu_{gk}^{(3)}\mu_{kt}^{(2)}\mu_{tj}^{(0)}\mu_{jg}^{(1)}\rho_{gg}^{(0)}}{(\omega_{gj}-\omega_1)\,(\omega_{kj}-[\omega_1-\omega_3])\,(\omega_{tj}-\omega_0)}$$

$$\frac{(-1)\,\mu_{gk}^{(3)}\mu_{kt}^{(2)}\mu_{tj}^{(0)}\mu_{jg}^{(1)}\rho_{gg}^{(0)}}{(\omega_{kg}+\omega_3)\,(\omega_{kj}-[\omega_1-\omega_3])\,(\omega_{tj}-\omega_0)}$$

$$\frac{(-1)\,\mu_{gk}^{(3)}\mu_{kt}^{(2)}\mu_{tj}^{(0)}\mu_{jg}^{(1)}\rho_{gg}^{(0)}}{(\omega_{kg}+\omega_3)\,(\omega_{tg}-[\omega_2-\omega_3])\,(\omega_{tj}-\omega_0)}$$

Figure 1. Three double-sided diagrams and the terms obtained from them for the third-order nonlinear-optical process, $\omega_0 = \omega_1 + \omega_2 - \omega_3$. The states are labeled g, k, t, and j; $\mu_{\alpha\beta}^{(q)}$ is the dipole-moment matrix element between states α and β for the polarization of the beam with frequency ω_q; and $\rho gg^{(0)}$ is the initial ground-state population density.

$$\frac{(-1)\,\mu_{gk}^{(3)}\mu_{kt}^{(2)}\mu_{tj}^{(0)}\mu_{jg}^{(1)}\rho_{gg}^{(0)}}{(\omega_{kg}+\omega_3)\,(\omega_{tg}-[\omega_2-\omega_3])\,(\omega_{gj}-\omega_1)}$$

Figure 2. A single-sided diagram for the third-order nonlinear-optical process, $\omega_0 = \omega_1 + \omega_2 - \omega_3$. This term corresponds to a process that is not collision-induced.

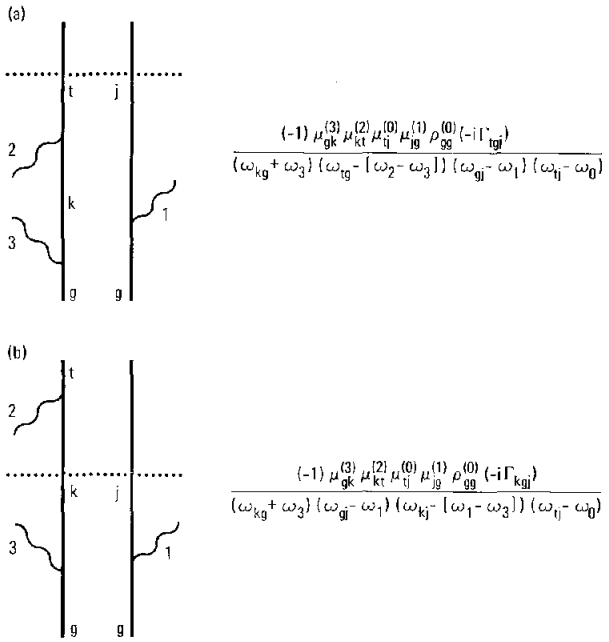

$$\frac{(-1)\,\mu_{gk}^{(3)}\mu_{kt}^{(2)}\mu_{tj}^{(0)}\mu_{jg}^{(1)}\rho_{gg}^{(0)}(-i\Gamma_{tgj})}{(\omega_{kg}+\omega_3)\,(\omega_{tg}-[\omega_2-\omega_3])\,(\omega_{gj}-\omega_1)\,(\omega_{tj}-\omega_0)}$$

$$\frac{(-1)\,\mu_{gk}^{(3)}\mu_{kt}^{(2)}\mu_{tj}^{(0)}\mu_{jg}^{(1)}\rho_{gg}^{(0)}(-i\Gamma_{kgj})}{(\omega_{kg}+\omega_3)\,(\omega_{gj}-\omega_1)\,(\omega_{kj}-[\omega_1-\omega_3])\,(\omega_{tj}-\omega_0)}$$

Figure 3. Collision-induced diagrams and their corresponding terms for the third-order nonlinear-optical process, $\omega_0 = \omega_1 + \omega_2 - \omega_3$. In these expressions, $\Gamma_{ijk} \equiv \Gamma_{ij} + \Gamma_{jk} - \Gamma_{ik}$.

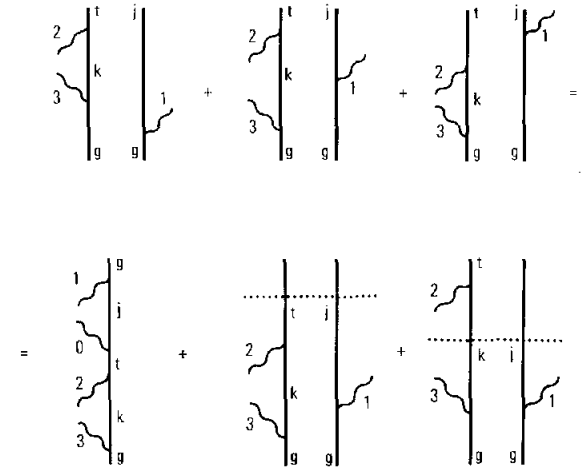

Figure 4. Diagrammatic sum showing that the three terms corresponding to the three double-sided diagrams of Figure 1 sum to yield the term corresponding to the single-sided diagram of Figure 2 plus the two terms corresponding to the two collision-induced diagrams of Figure 3. This type of algebraic expression is typical of the terms in all orders of the expansion.

Collisional Broadening and Doppler Effects on ac-Stark Splitting†

The resolution of the ac-Stark doublet, observed in the two-color, three-photon 1s → 3p excitation spectra of atomic hydrogen produced in hydrogen-air atmospheric pressure flames, is greatly improved by eliminating the Doppler contribution of the 1s → 2s two-photon transition. As pressure increases, the peak asymmetry parameter of the doublet decreases, and, at high enough pressure (several atmospheres), the doublet becomes one broad resonance.

A. M. F. Lau

In earlier experiments[1,2] to detect atomic hydrogen produced in H_2/air diffusion flames, the 3p level of hydrogen was excited by absorption of two 243-nm photons and a 656-nm photon via the 2s resonant intermediate level (see Figure 1). For a given detuning Δ_b of the 656-nm laser, the 3p → 2s fluorescence was collected as a function of the 243-nm laser detuning Δ_a from the 1s-2s two-photon resonance. The flame temperature was around 2500 K, and the pressure was 1 atmosphere. Both the experimental[2] and calculated[3] spectra did not reveal any ac-Stark splitting for the smaller detunings $|\Delta_b| \leq 2.3$ cm^{-1}, whereas for larger detunings, the ac-Stark doublets were well resolved. Rough estimates showed that these spectra contained a significant Doppler effect since the lasers were propagated in the same direction. This finding prompted us to investigate ways to eliminate the Doppler effect to improve the resolution. Since the system is in the high-pressure regime, we also studied how the ac-Stark doublet spectrum and its peak asymmetry changed with pressure.

The theoretical spectra are calculated using the density matrix equations of motion describing a three-level system in single- or multi-photon resonant interaction with two finite-bandwidth lasers and subject to high pressure. We consider first counter-propagating the 656-nm laser beam and the 243-nm laser beam. The Doppler-averaged spectra are shown in column (b) of Figure 2, next to those for the case of co-propagation in column (a). We see that there is only a slight improvement in resolution of the doublet.

Next, we consider splitting the 243-nm laser beam and counter-propagating the resulting beams so that the 1s - 2s two-photon absorption would be Doppler-free. Since this is an S-to-S transition ($\Delta m = 0$), it is possible to eliminate the "pedestal" (in the Doppler-free spectral line) due to absorption of two photons from the same beam by having both counter-propagating beams circularly polarized in the same sense with respect to the direction of propagation (and hence of opposite helicities with respect to the laboratory frame). In this beam geometry, the 656-nm laser beam can propagate in any direction. The results are shown in column (c). There is a dramatic improvement in the resolution. Furthermore, we found quite surprisingly that *these spectra are indistinguishable from the corresponding spectra without any Doppler averaging.* This result occurs because the contribution (≈ 0.5 cm^{-1}) of the 656-nm 2s-3p transition to the overall Doppler effect is insignificant due to the larger collisional relaxation rates (≥ 1 cm^{-1}) of the two-photon 1s-2s transition, which accounts for almost all of the Doppler effect. This last beam geometry, to be called "quasi-Doppler-free," improves the detection sensitivity of various features of ac-Stark splitting.

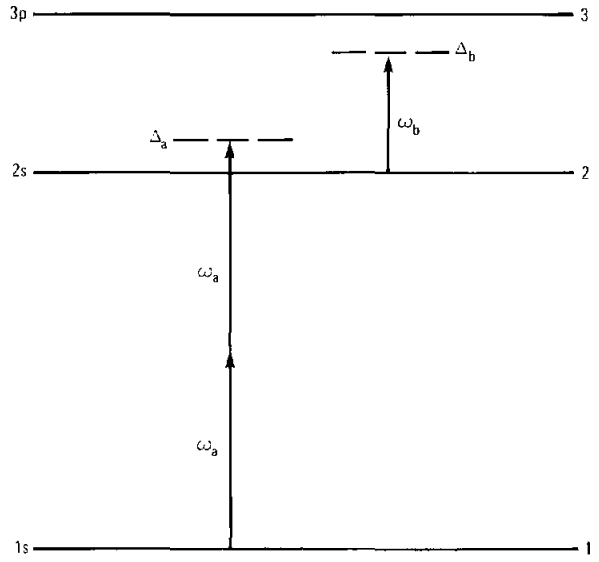

Figure 1. Schematic energy diagram of hydrogen showing the three-photon excitation of the 3p level by uv (λ_a = 243 nm) and visible (λ_b = 656 nm) laser radiation.

†Optics Communications **64**, 144 (1987).

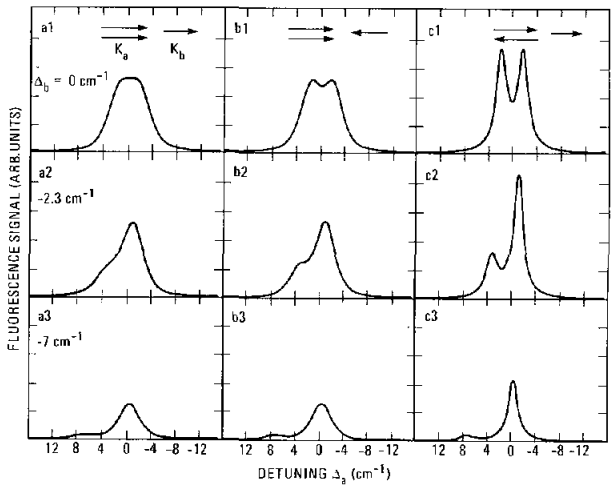

Figure 2. Improved resolution of the ac-Stark doublet in H-atom detection in flames due to reduction of the Doppler effect. Column (a) shows the specra at three different detunings Δ_b for co-propagating the 243-nm and the 656-nm laser beams. Column (b) shows the corresponding spectra by counterpropagating the two beams. Column (c) shows the results of splitting the 243-nm laser beam into two counter-propagating beams and for any direction of the 656-nm laser beam (the "quasi-Doppler-free" beam geometry). These spectra are indistinguishable from those without any Doppler averaging. The pump beam intensity I_b is 4.4 MW/cm^2.

With the quasi-Doppler-free geometry, we study the effect of pressure variation on the resolution of the ac-Stark doublet and its peak asymmetry. The results presented in Figure 3 for the pump-laser intensity $I_b = 4.4\ MW/cm^2$ and detuning $\Delta_b = -2.3\ cm^{-1}$ show that as the pressure is increased, the overall signal decreases as expected from larger collisional quenching. Since collisional broadening causes abnormal peak asymmetry in the ac-Stark doublet,[3] one might think that higher pressure would accentuate the asymmetry. However, we find that the asymmetry parameter $A \equiv (h_- - h_+)/(h_- + h_+)$ decreases from 0.52 at 0.1 atm to 0.34 at 2 atm. For pressures > 2 atm, collisional broadening dominates over the Rabi frequency so that the doublet becomes one broad peak.

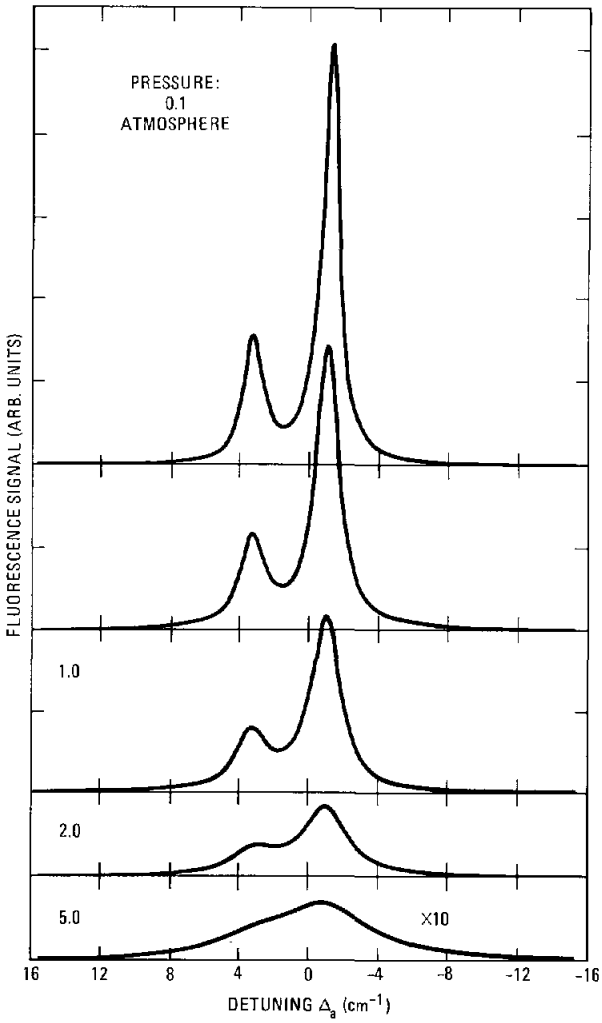

Figure 3. Pressure dependence in the peak asymmetry and the resolution of the quasi-Doppler-free ac-Stark doublet for Δ_b = -2.3 cm^{-1} and I_b = 4.4 MW/cm^2.

References:

1. J. E. M. Goldsmith, Opt. Lett. **10**, 116 (1985).

2. J. E. M. Goldsmith, *Laser Spectroscopy VII*, T. W. Hansch and Y. R. Shen, eds. (Springer, New York, NY, 1985), p. 410.

3. A. M. F. Lau, Phys. Rev. A **33**, 3602 (1986).

Comparison of Motionally Narrowed CARS Line Shapes of H_2 with Hard- and Soft-Collision Models†

We have compared high-resolution CARS measurements of the Q(1) transition of H_2 with hard- and soft-collision line-shape theories accounting for Doppler effects, including motional narrowing. The soft-collision model was found to be in better agreement with the data.

R. L. Farrow and R. E. Palmer

Raman line widths of the *Q*-branch transitions of H_2 exhibit a well-known contraction with increasing pressure (up to approximately two and one-half atmospheres) according to an effect first analyzed by Dicke. Often termed "Dicke" or "motional" narrowing, the effect is due to a reduction of the Doppler contribution to the total line broadening with increasing collision frequency. The decrease in Doppler broadening results from a coherent averaging of frequencies within the normal Doppler line profile, induced by velocity-changing collisions that conserve vibrational phase. Narrowing is significant when the path length for velocity-changing collisions is comparable to the transition wavelength. If the frequency of velocity-changing collisions is greater than that of dephasing collisions, sub-Doppler total line widths can result.

There have been relatively few considerations of Doppler broadening in coherent anti-Stokes Raman spectroscopy (CARS) line shapes, with the bulk of existing results contained in the doctoral thesis of M. A. Henesian. Until now, modeling has been limited to the use of Lorentzian and Voigt-type expressions. The additional effects of motional narrowing have typically been treated using the augmented-Lorentzian model of Dicke. This model is limited to application at high pressures; e. g., H_2-line shapes are well-described only for pressures above ~200 torr.

In this paper, we present a comparison of high-resolution CARS measurements of the H_2 $Q(1)$ transition with two line shape models that include fundamental descriptions of motional narrowing. Both models are intended to apply over wide ranges of pressure, spanning the regimes of Doppler, motionally narrowed, and homogeneous broadening. The soft-collision model first proposed by Galatry and the hard-collision model considered by Rautian and Sobel'man and others differ in their treatment of velocity-changing collisions. The former model assumes that a typical single collision perturbs the velocity only slightly and that the velocity correlation function decays according to the diffusion approximation; the latter model assumes that the velocity probability distribution is thermalized by a single collision, i.e., that the final velocity after a collision is uncorrelated to the initial velocity.

We used a high-resolution scanning CARS system to obtain spectra of the $Q(1)$ transition of H_2 in a static cell. A single-frequency Nd:YAG laser produced a smooth, nearly Gaussian second-harmonic pulse with a duration of 18 ns and a FWHM linewidth <45 MHz. A pulse-amplified ring dye laser was used for the Stokes beam. All laser polarizations were parallel and vertically oriented. The relative beam angles were sufficiently small, <1.5°, that essentially forward-scattering Raman line shapes were measured.

In the results described below, the observed line shapes were compared to predictions of the hard- and soft-collision models. Dephasing collisions were included in both models by assuming that dephasing (broadening) and velocity-changing (narrowing) collisions are statistically independent. With the additional assumption of velocity-independent dephasing, the observed line profile is equivalent to a Doppler-induced line shape convolved with a dephasing-induced Lorentzian line shape. For the dephasing line width, we used an average of the $Q(1)$ measurements of Owyoung and of Bischel and Dyer: $8.63 \pm 0.10 \times 10^{-4}$ cm^{-1}/amagat (HWHM). The necessary complex line-shape functions were calculated with the aid of computer routines developed by Varghese, Herbert, and Humlicek.

We evaluated the two models by fitting each to experimental spectra measured at pressures between 50 and 3047 torr. The motional narrowing coefficient, the transition frequency, and an intensity scaling factor were varied for best agreement at each pressure. Figure 1 shows a comparison between the soft-collision model (solid lines) and experiment (data points) for several observations. The combined pump and Stokes laser width is indicated in the figure; it is ~ 4 times smaller than the

†Optic Letters **12**, 984 (1987).

Raman linewidths observed and was accounted for by a convolution with the computed intensity profile. As seen in Figure 1, the agreement between theory and experiment is very good; no systematic deviations larger than 3-4% of peak magnitude were observed.

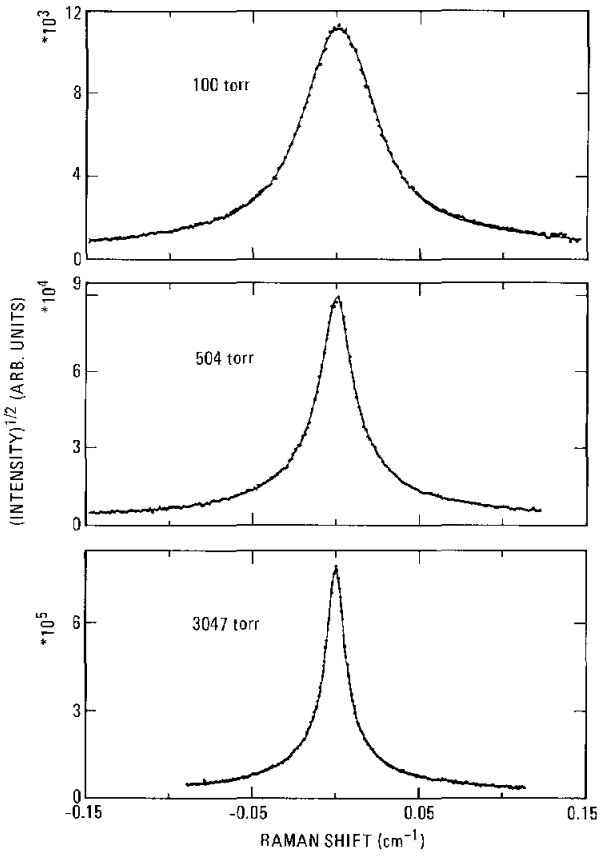

Figure 1. Experimental spectra (data points) of the $Q(1)$ transition of H_2 at 295 K and various pressures. The curves are theoretical calculations using the soft-collision model with the motional-narrowing coefficient least-squares fitted for best agreement at each pressure. The square root of I_{CARS} is plotted to display the agreement in the wings of the line shapes.

In addition to describing individual line shapes well, a further criterion for the validity of motional narrowing models is that the narrowing coefficient be independent of pressure. The best-fit values for the narrowing coefficient of the soft-collision model are shown in Figure 2a. The solid line results from a linear regression analysis of the data. According to fit-sensitivity and regression-error limits, the slope of the line is statistically insignificant. We conclude that our data are consistent with a pressure-independent narrowing coefficient, β_G (effective frequency of velocity-changing collisions per unit pressure) having a value of 0.047 ± 0.004 cm^{-1}/amagat. From the relation $\beta_G = kT/2\pi cmD$, this value corresponds to an optical self-diffusion coefficient, D, of 1.36 ± 0.12 cm^2-amagat/s. This diffusion coefficient is also used by the simple Dicke model to predict augmented-Lorentzian linewidths. By so fitting $Q(1)$ Raman line widths measured at densities above ~1 amagat, Owyoung obtained 1.39 ± 0.04 cm^2-amagat/s for D, and Bischel and Dyer obtained 1.42 cm^2-amagat/s.

When we compared the hard-collision model to our data, somewhat better line shape fits were obtained for pressures of 50-500 torr. The slightly improved line shape agreement of the hard-collision model is belied, however, by a significant pressure-dependence in the best-fit narrowing co-efficient for this model. As seen in Figure 2b, β_H slopes sharply upward with pressure, with a lower slope above 380 torr.

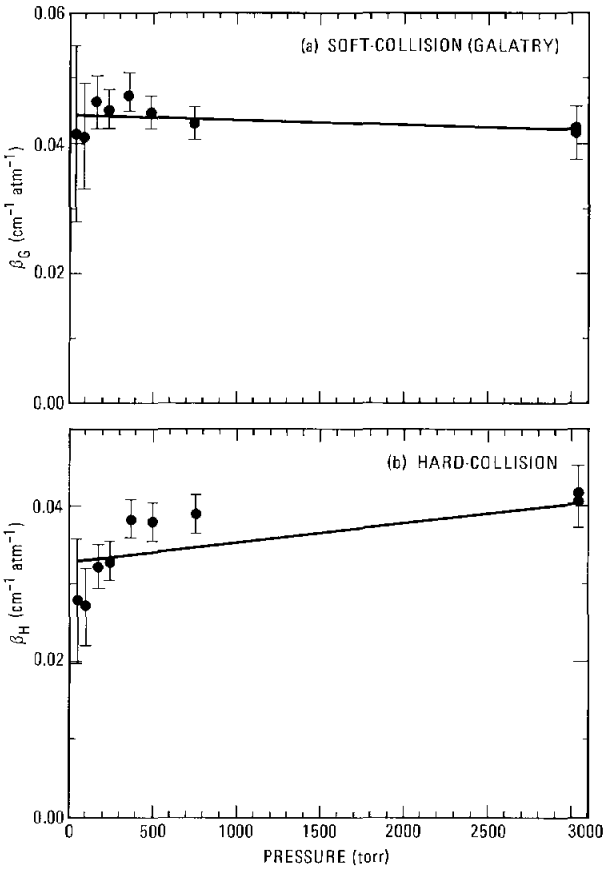

Figure 2. Best-fit values for the motional-narrowing coefficient of the soft-collision model (β_G) and the hard-collision model (β_H) vs pressure. The error bars are based on the sensitivity of fitting residuals to variation in β_G; the limits indicate a 20% increase in each residual, which resulted in a noticeably poorer fit. The solid line results from a linear regression analysis of the data.

Based on these observations, we conclude that the soft-collision model is in better agreement with our data. Measured spectral profiles are well described using a pressure-independent narrowing parameter, a failing of the hard-collision model. The narrowing parameter is also consistent with the known mass diffusion constant within our uncertainties.

Measurements of Nitrogen *Q*-Branch, Foreign Gas-Broadening Coefficients Relevant to Flames†

We have measured foreign gas-broadening coefficients of the Q-branch spectrum of nitrogen by gaseous water, n-butane, and propane using high-resolution, inverse Raman spectroscopy.

L. A. Rahn and R. L. Farrow

Coherent anti-Stokes Raman spectroscopy (CARS) has proven to be one of a few optical techniques capable of measurements in highly-sooting or particulate-laden combustion gases. Nitrogen (N_2), as a major component in air-fed combustion gases and the species usually chosen for thermometry, has received much theoretical and experimental spectroscopic study in this respect. However, most investigations have dealt with the pure gas, and, except for a comparison of flame linewidths with self-broadened linewidths by inverse Raman spectroscopy (IRS),[1] little consideration has been given to the effects of foreign-gas environments on N_2 spectra.

In this paper, we report a study of the effects of gaseous H_2O, n-butane (C_4H_{10}), and propane (C_3H_8) on the *Q*-branch spectrum of N_2, using high-resolution IRS. We present broadening coefficients for N_2 transitions broadened by H_2O at 1570 K and by the two fuel gases at room temperature. These results form a preliminary basis for modeling CARS spectra of N_2 in n-C_4H_{10} and C_3H_{10} flames.

The experimental technique applied to the measurement of the N_2 *Q*-branch linewidths is quasi-cw inverse-Raman spectroscopy. The apparatus used in this experiment is described in detail in Reference 1 and only aspects specific to this study will be described here.

The room-temperature sample cell used in these studies was made of stainless steel with 12-mm-thick, 50-mm-diameter windows fitted on either end. Pressure was measured with a calibrated capacitance gauge with an estimated uncertainty of ± 0.002 atm (1 atm = 101.3 kPa). Two gas mixtures were used in these experiments. The N_2 in n-C_4H_{10} mixture was a commercial product containing 25 ± 1% N_2 (mole fraction, prepared by weighing). The N_2 in C_3H_8 mixture was made from a commercial 5% N_2 in C_3H_8 mixture to which we added pure N_2, resulting in an N_2 concentration of 25 ± 1%.

Nitrogen broadening by H_2O vapor was measured in an atmospheric-pressure $H_2/O_2/N_2$ flame, using a sintered-bronze, porous-plug burner. Input flows of 6.0±0.3, 3.0±0.15, and 3.0±0.15 SLPM of H_2, O_2, and N_2, respectively, produced post-flame gases containing mole fractions of 0.67 ± 0.05 for H_2O and 0.33 ± 0.03 of N_2. These post-flame concentrations were calculated using DEQUIL,[2] a computer code based on the assumption of thermal equilibrium chemistry, a good approximation for this stochiometric flame. An argon co-flow of 25 SLPM was used in all cases. All measurements were performed 0.6 cm above the burner surface, where CARS scans of the ground and first excited states of the N_2 *Q*-branch indicated a temperature of 1570 ± 40 K.

Spectra were measured for the N_2 *Q*(*J*) fundamental ($v = 0$ to $v = 1$) transitions from $J = 0$ to 18 in C_3H_8 and up to $J = 20$ in n-C_4H_{10}. The fuel-gas broadened spectra were recorded at pressures of 0.2, 0.67, 1.8, and 2.0 atm at 296 K.

We have used a Voigt profile to account for the small Doppler effect at 0.2 atm, and a Lorentzian profile to fit the spectra taken at higher pressures. In the latter spectra, the Doppler effect is negligible compared to the experimental uncertainties in the linewidths. The theoretical Raman frequency, the collisional broadening coefficient, and a vertical scaling factor were varied for best fit to each *Q*-branch transition.

Rotational collapse of the *Q*-branch spectrum can be an important perturbation to the fuel-broadened spectra, especially at the highest pressures and for low-*J* transitions. While the spectra can be fit using perturbation approximations or by diagonalization of the collision matrix, we have chosen to use the isolated-line approximation at reduced pressures for the lower-*J* transitions. Thus, we have only used data from $J > 7$ at 0.67 atm and $J > 13$ at 2 atm for linewidth analysis. The resulting linewidths were corrected for self-broadening using the coefficients reported by Rosasco, *et al.*[3] The non-ideal gas behavior of the fuel gases has been taken into account, and the resulting fuel-gas-broadening coefficients are compared with the self-

†Twenty-Second Symposium (International) on Combustion, accepted (1988).

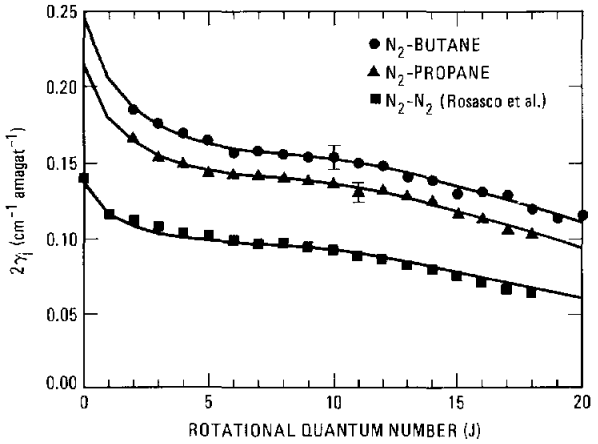

Figure 1. Experimental line-broadening coefficients (symbols) for Q-branch transitions of N_2 in fuel gases, measured at 296 K. The solid lines indicate predictions of a modified exponential energy-gap (MEG) model based on three fitting parameters.

broadening coefficients of N_2 in Figure 1. The uncertainty in the fuel gas-broadening coefficients is estimated to be ± 0.01 cm^{-1}.

Spectra were measured in the post-flame gases of an $H_2/O_2/N_2$ flame for the N_2 $Q(J)$ fundamental ($v = 0$ to $v = 1$) transitions from $J = 0$ to 18. The spectra were measured at room pressure (745 torr) at 1570 K. The effects of collisional collapse of the Q-branch were not observable in these spectra; thus, the isolated-line approximation was used for line broadening analysis. Collisional-broadening coefficients were derived from the data by least-squares fitting each rotational-state transition to a Galatry lineshape model. The optical diffusion coefficient was assumed equal to the mass diffusion coefficient of N_2 in H_2O (7.5 cm^2s^{-1} at 1570 K) calculated from molecular potential parameters. The resulting broadening coefficients for the N_2 Q-branch are shown in Figure 2 as filled circles. The open circles, shown for comparison, are self-broadening coefficients determined[1] from MEG model calculations at 1570 K. The estimated error for the flame coefficients is ±10%. The average increase of the H_2O-broadening coefficients for N_2 over those for self-broadening is ~ 45%.

Our results show that linewidths of N_2 in combustion gases can be expected to be significantly larger than those of pure N_2; the fuel gas- or H_2O-vapor-broadening coefficients for dilute N_2 were typically ~ 45% larger. In addition, these broadening measurements have recently proven useful in CARS measurements of the H_2O, n-C_4H_{10}, and C_3H_8 nonresonant susceptibilities. Future applications include accounting for the increased H_2O-vapor broadening of N_2 CARS spectra in post-flame gases, and modeling N_2 in fuel-rich regions of flames or internal combustion engines utilizing n-C_4H_{10} or C_3H_8. For applications in conditions not reported here, moderate extrapolations to other temperatures, pressures, and rotation quantum numbers can be achieved via the MEG model. Other supporting measurements are in progress and are expected to contribute to the formulation of a comprehensive model for the N_2 Raman spectrum in combustion environments.

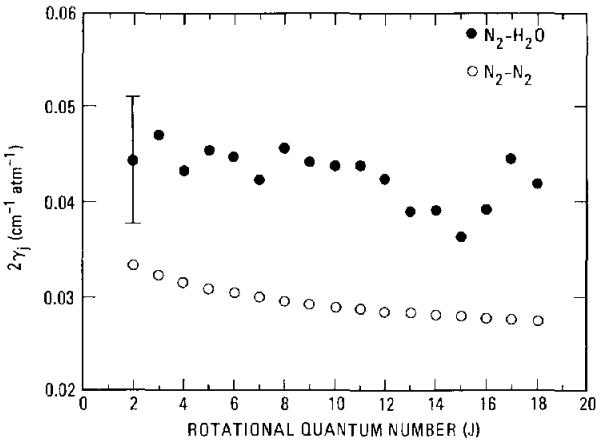

Figure 2. Experimental line-broadening coefficients (symbols) for Q-branch transitions of N_2 in H_2O vapor, measured at 1570 K. The open circles are coefficients for pure N_2 from MEG model calculations at 1570 K.

References:

1. L. A. Rahn and R. E. Palmer, J. Opt. Soc. Am. B **3**, 1164 (1986).

2. The DEQUIL computer program was modified by R. J. Kee from the program STANJAN, developed by W. C. Reynolds, Stanford University, Stanford, CA.

3. G. J. Rosasco, W. Lempert, W. S. Hurst, and A. Fein, Chem. Phys. Lett. **97**, 435 (1983).

Measurement and Prediction of Raman *Q*-Branch Line-Broadening Coefficients for Carbon Monoxide From 295 to 1500 K†

High-resolution inverse-Raman measurements of the J- and temperature-dependent broadening coefficients for the Q-branch of pure carbon monoxide are reported for Q(J) transitions from J=0 to 38 and for temperatures in the range 295 to 1500 K. It is shown that a fitting law, based on a modified exponential energy gap model for the rates of state-to-state, rotationally-inelastic collisions, can account for the observed J-dependence.

G. J. Rosasco,* L. A. Rahn, W. S. Hurst,* R. E. Palmer, and S. M. Dohne*

Coherent anti-Stokes Raman spectroscopy (CARS) of vibrational *Q*-branch spectra has become an important diagnostic probe in many combustion processes. The sensitivity of the CARS spectra to linewidths, line shapes and line positions has resulted in a need for accurate predictions of spectral profiles over the wide ranges of pressure, temperature, and composition found in combustion environments.

In this paper, we report high resolution inverse Raman measurements of the J- and temperature-dependent, line-broadening coefficients for the *Q*-branch of pure CO for Q(J) transitions with J = 0 to 38 and for temperatures in the range 295 to 1500 K. The Q(15) v = 1 to v = 2 hot-band transition was also measured at 1000 and 1500 K. All spectra were recorded at 1 atm except the 295 K spectrum, which was measured at 2.8 atm. It is shown that a fitting law,[1] based on a modified exponential energy-gap (MEG) model for the rates of state-to-state, rotationally-inelastic collisions, can account for the observed J-dependence. This rate law model, used in conjunction with a relaxation matrix description of the *Q*-branch spectrum, is shown to give good agreement with the observed, partially collapsed spectra.

The experimental technique applied to the measurement of the CO *Q*-branch linewidths is quasi-cw-inverse Raman spectroscopy (IRS). The apparatus has been described in detail previously[1] and will not be discussed further here.

The fitting of the elevated temperature spectra to extract collisional-broadening coefficients requires careful consideration of Doppler broadening, Dicke narrowing, and line interference effects. We have found that, in the case of CO *Q*-branch transitions, all of these effects can be treated as perturbations to the collisionally-broadened, Lorentzian line shape for spectra measured at 1 atm. At this pressure, the primary corrections are due to the Doppler effect at the highest temperatures, while the line-interference effects are most important for low-J transitions and at the lower temperatures. Collisional-broadening coefficients are extracted from the data by first fitting the spectra using a lineshape function that accounts for the collisional mixing of Lorentzian lines by perturbation theory[2] to first order in density. The resulting widths are then corrected for the effects of Doppler broadening to yield pressure-broadening coefficients.

The pressure-broadening coefficients are plotted in Figure 1 as a function of rotational quantum number. Fits to the hot-band spectra gave results for ν_{offset} and line-broadening coefficients which, within the statistical uncertainty, were indistinguishable from those for $Q_1(15)$. Thus, we find no evidence for a vibrational state dependence in the linewidth.

In the course of the analysis, we have determined the parameter s of the MEG law by a best fit to the J dependence of the line broadening coefficients at each temperature. The MEG law, which describes the rate of transitions from J to J′ with J′>J, i.e., the upward rate, is given by[1]

$$W_{J'J} = P\,\alpha(T)\left(\frac{1 + AE(J)/kTd}{1 + AE(J)/kT}\right)^2 \exp(-bE_{J'J}/kT) \qquad (1)$$

with P the pressure, $E_{J'J} = |E(J')-E(J)|$ the energy gap, and d, b, A constants (T independent) specific to the molecular system. The rate for the inverse transition is found from detailed balance. The constant A is a measure of the duration of a collision. The precise value of this constant is not critical to the ability of the

†Journal of Chemical Physics, submitted (1988).

*U. S. National Bureau of Standards, Gaithersburg, MD.

MEG law to represent the data. We use A = 2 based on an estimation of the collision length by the distance of closest approach for CO at 295 K. The MEG law is fit to the set of experimental line-broadening coefficients at each temperature by means of a linearized least-squares adjustment of the parameters $\alpha(T)$, d, and b. The constants d and b are found to be very nearly temperature independent. In fact, the use of the average values at each temperature results in MEG law predictions that vary from the best-fit predictions by considerably less than the experimental precision of the data. We take the "best-fit" MEG law to be defined by the average values given by d = 1.246 and b = 1.462. Using these values, the scaling of the MEG law with temperature (the $\alpha(T)$) is fit very well by the formula

$$\alpha(T) = \alpha(T_0)\,\frac{1-\exp(-m)}{1-\exp(-mT_0)}\,(T/T_0)^{0.5} \qquad (2)$$

with $\alpha(T_0) = 0.01334$ cm^{-1}/atm, m = 0.19 and T_0 = 295 K. Thus, with Equations (1) and (2) and the parameters above, we have completely specified the best-fit MEG law. The predictions of this MEG law are shown as the lines in Figure 1. This MEG law predicts the observed line-broadening coefficients with an RMS error of 2.8% from 295 to 701 K, and RMS errors of 4.5 and 3.7% at 1000 and 1500 K respectively. These errors are typically of the order of ± 0.001 cm^{-1}/atm, or less, over the entire temperature range.

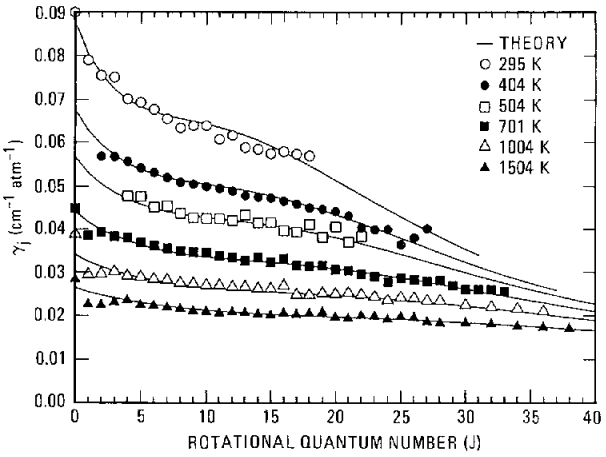

Figure 1. Pressure-broadening coefficients as a function of rotational quantum number J at each of the measurement temperatures. The symbols are the best set of pressure-broadening coefficients. The curves exhibit the pressure-broadening coefficients derived from the MEG law with b=1.462, d=1.246, m=0.19, and $\alpha(T)$=0.01334 cm^{-1}/atm, where T_0=295 K.

The MEG law is very useful in that it provides a simple, unified, and accurate representation of both the J and temperature dependence of the *Q*-branch line broadening for the CO-CO system. More importantly, however, this MEG law should allow us to completely specify the entire relaxation matrix as a function of temperature. As discussed previously, this is necessary to describe accurately the *Q*-branch spectrum as a function of temperature and pressure. Figure 2 presents the prediction of the best-fit MEG law for the *Q*-branch spectrum at room temperature and a pressure of 2.8 atm. This partially collapsed *Q*-branch is well represented by this best-fit MEG law.

Of course, there is a great deal more information implicit in the MEG law description, which is yet to be verified by a study of collisional collapse at high temperatures and pressures. The success[1] of the MEG law for the case of N_2-N_2 suggests the strong possibility of similar success for the case of CO-CO. The relative importance of the smaller energy gaps and the dipole-dipole interaction in the CO system as they affect the J and T dependence of the state-to-state rates is not understood at this time. Foreign gas-broadening studies should be helpful in understanding both the N_2 and CO systems.

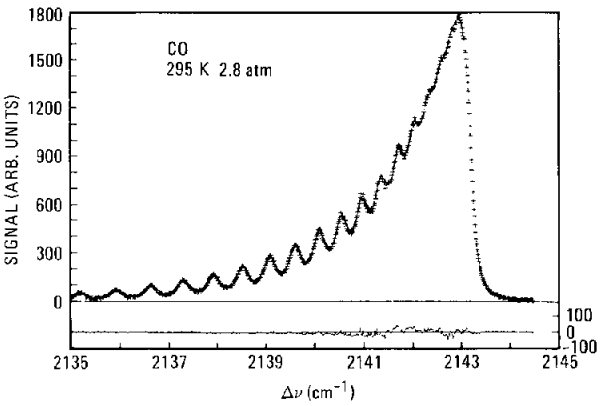

Figure 2. Q-branch spectrum (J=0 to 21) for CO at 295 K and 2.8 atm, exhibiting partial collapse. The experimental data points are given by the crosses and the solid curve gives the prediction of the MEG law that employs the best-fit constants given in the text. Displayed beneath the spectrum is the residual given by the difference between data and theory.

References:

1. L. A. Rahn and R. E. Palmer, J. Opt. Soc. Am. B **3**, 1164 (1986).

2. G. J. Rosasco, W. Lempert, W. S. Hurst, and A. Fein, Chem. Phys. Lett. **97**, 435 (1983).

Calculation of Saturation Line Shapes and Intensities in Coherent Anti-Stokes Raman Scattering Spectra of Nitrogen†

The density matrix equations for the coherent Raman interaction are numerically integrated to give saturation line shapes and intensities for Q-branch lines of nitrogen.

R. P. Lucht and R. L. Farrow

The usefulness of coherent anti-Stokes Raman scattering (CARS) as a technique for gas-phase temperature and species-concentration measurements has been demonstrated in numerous experiments. At low laser powers, CARS line shapes and spectral profiles are independent of the intensities of the pump and Stokes laser beams. As laser intensities increase, however, CARS spectra are perturbed by Stark effects and by saturation of the Raman transitions. Saturation effects become more important in perturbing line shapes compared to Stark effects as laser line widths decrease or as the pressure of the medium being probed decreases. Thus, when narrow line-width lasers are used, or low-pressure media such as plasmas or supersonic jets are probed, saturation becomes the main factor limiting laser intensity.

We previously reported[1] experimental measurements of saturation line shapes and intensities for nitrogen CARS using high-resolution, nearly Fourier-transform-limited pump and Stokes lasers, which have electric fields that are well-characterized functions of time. Here, we perform numerical calculations of saturation lineshapes and intensities for CARS spectra of the Q(12) line in the nitrogen (0,1) vibrational Raman manifold. The density-matrix equations for the CARS interaction are numerically integrated using the measured pump and Stokes laser pulse shapes. The anti-Stokes electric field amplitude is calculated as a function of time and of frequency detuning to determine the homogeneous response of the medium. Stark-shifting of the nitrogen *Q*-branch is included in the homogeneous calculations.

Doppler effects are then included in the calculations by summing CARS amplitudes from different velocity groups at each time step during the numerical integration. It was necessary to treat Doppler broadening at this fundamental level, rather than by performing a frequency convolution, because of the complicated dependence of the CARS amplitude on time and detuning. The electric field amplitude caused by the interaction of the pump and Stokes field with the nonresonant susceptibility of the medium is then added to the CARS amplitude at each time step.

Comparison between theory and experiment is shown in Figure 1 for a highly saturated

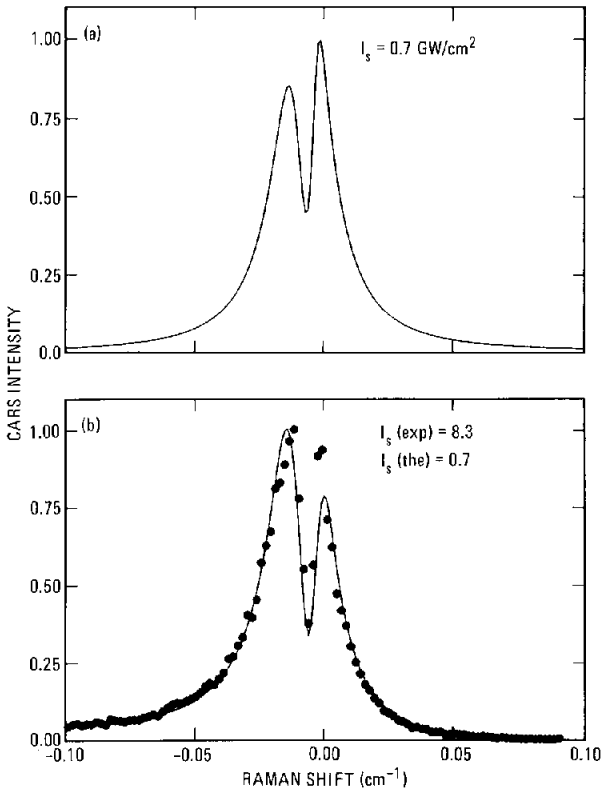

Figure 1. Saturated CARS line shape of the Q(12) line of nitrogen at 25 torr: the solid lines are theoretical calculations of (a) the homogeneous line shape, and (b) the line shape including Doppler effects and the nonresonant background. Experimental data in (b) are indicated by solid circles. The peak intensity of the Stokes laser was 8.3 (experimental) and 0.7 (theoretical) GW/cm^2. The peak intensities of the pump laser beams were 37 GW/cm^2, both experimentally and theoretically. The nonresonant background susceptibility was $1.2 \cdot 10^{-18}$ cm^3/erg at line center with a slope of $\pm 2.8 \cdot 10^{-18}$ cm^3/erg/cm^{-1} at line center. The Stark shifting coefficient K_{Stark} was equal to $-0.6 \cdot 10^{-13}$ cm^{-1}/W.

†Journal of Optical Society American B, accepted (1988).

nitrogen line. Saturation is clearly indicated by the presence of the saturation dip and by the broadening of the line. The calculated homogeneous line shape, shown in Figure 1(a), exhibits a deep dip near line center and significant asymmetry due to Stark shifting. The peak on the high-frequency side of the dip is narrower and more intense for the homogeneous line shape. Inclusion of the nonresonant background shifts peak intensities, so that in Figure 1(b) the peak on the low-frequency side is higher. Note that the Doppler effect does not eliminate the saturation dip, as might be expected, because the calculated Doppler width (FWHM) is 0.0054 cm^{-1}.

Agreement between the theoretical spectrum (after inclusion of the Doppler effect and nonresonant background) and the experimental spectrum is very good. The intensity ratio between the peaks on either side of the saturation dip is slightly different in the theoretical and experimental spectra, but agreement is excellent in terms of the depth of the dip, the overall width of the line, and the relative widths of the spectral features on each side of the dip. The experimental and theoretical Stokes laser intensities differ by a factor of ten, which we attribute to the effects of the spatial profiles of the laser beams.

The temporal histories of the resonant and nonresonant CARS intensities, and the excited-state population are shown in Figure 2 for different values of the laser detuning. The nonresonant response of the medium is extremely fast, and the nonresonant CARS intensity is proportional to the instantaneous product of the Stokes intensity and the square of the pump laser intensity. The resonant CARS intensity peaks nearly 10 ns before the peak of the nonresonant intensity. The excited state population n exceeds 0.5 for brief periods. Furthermore, when n is 0.5 at t = 12 ns, the resonant CARS intensity is just past its peak. At steady state, the resonant CARS intensity is zero when n = 0.5. Clearly, in this intensity regime and at this pressure, the steady-state solution would be inaccurate. Damping of the Rabi oscillations as the laser pulse proceeds indicates that a fully transient, collisionless solution would not apply in this case either. As detuning increases, the pumping of the excited state becomes less efficient, and the resonant-intensity profile shifts closer to the nonresonant-intensity profile. Note that even at a detuning of -0.004 cm^{-1}, which is three times the homogeneous HWHM (0.00135 cm^{-1}), nearly 35% of the ground-state population is pumped to the excited state.

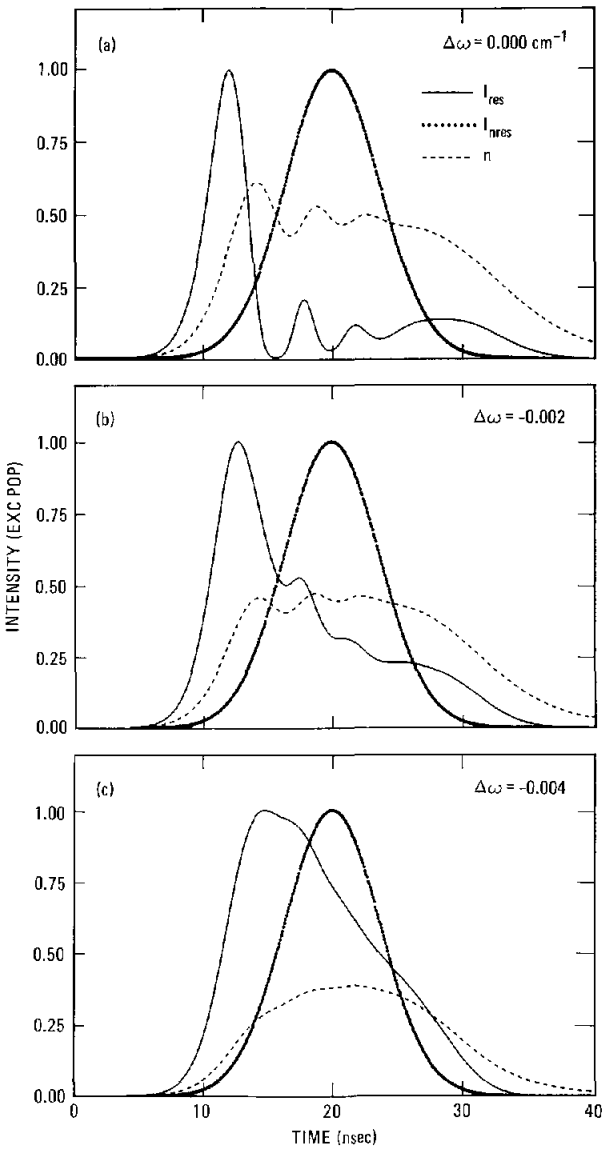

Figure 2. Resonant CARS intensity as a function of time for the homogeneous line, nonresonant intensity, and the excited-state-population fraction at homogeneous detunings Δω of (a) 0.000, (b) -0.002, and (c) -0.004 cm^{-1}. The ratio of the detuning to the Raman line width (HWHM), 2Δω/Γ, is (a) 0.0, (b) 1.48, and (c) 2.96. The parameters used in the calculation are identical to those of Figure 1, except that Stark shifting is neglected.

Reference:

1. R. L. Farrow and R. P. Lucht, Opt. Lett. **11**, 374 (1986).

Laser-Enhanced Flame Ionization Detector[†]

This article discusses the concept of a laser-enhanced flame ionization detector (FID), and describes a preliminary demonstration of such a device using a conventional flame ionization detector placed inside the cavity of a cw dye-laser system. Suggested improvements may ultimately result in a lowering of the present FID-detection limits for hydrocarbons by factors of 10-100.

T. A. Cool* and J. E. M. Goldsmith

The response of the conventional flame ionization detector (FID), used for the universal detection of hydrocarbons in gas chromatography, is limited by the rate of the chemi-ionization reaction between $CH(X^2\Pi)$ radicals and O atoms present within the flame zone, $CH + O \rightarrow HCO^+ + e^-$. Recent experiments have demonstrated that the chemi-ionization reactions between laser-excited $CH(A^2\Delta)$ and $CH(B^2\Sigma)$ radicals and O atoms are a thousandfold faster than the $CH(X^2\Pi)/O$ reaction.[1] This suggests the possibility of using a laser system to saturate a CH electronic transition, leading to very substantial molecular populations in the excited state, which would, in turn, lead to a greatly enhanced rate of chemi-ionization in the flame. Such a laser-enhanced flame ionization detector can, in principle, lead to a device with a sensitivity 10-100 times greater than currently available with conventional FIDs. This article describes experiments that demonstrate laser enhancement of the response of a commercially-available FID.

The apparatus used for this demonstration experiment is shown in Figure 1. A state-of-the-art commercial gas chromatograph (Varian model 3300) was modified slightly by drilling two small holes on opposite sides of the tower that surrounds the flame zone to provide optical access, and by tapering the base of the flame tip to provide a smaller diameter flame zone. These modifications made no measurable changes in the operating characteristics of the FID. The entire gas chromatograph and a mechanical chopper were placed inside the extended cavity of a Stilbene 420-cw dye laser that was tuned to individual rovibronic transitions of the CH $A^2\Delta \leftarrow X^2\Pi$ (0,0) band near 431 nm.

We studied the laser-induced enhancement in the FID signal in two ways. In the first method, the current of the FID in the presence and in the absence of the laser beam was measured with the standard detector electronics of the gas chromograph. As shown in Figure 2, the additional dc current attributable to laser enhancement is 6% of the conventional response. In the second method, the lock-in amplifier was used to measure the modulation in the steady ionization current produced by the chopped dye-laser beam. The noise in the observed signal was due entirely to the Johnson noise of the resistor in the measurement circuit and was not noticeably affected by the laser operation or the flame characteristics. This latter method provides a way of using sensitive ac detection techniques to monitor the FID current, with possible subsequent improvements over the dc electronics in conventional gas chromatographs.

These preliminary experiments, while providing a successful demonstration of laser enhancement in the ionization rate of a state-of-the-art flame ionization detector, also demonstrate the substantial improvement required to provide reductions in the detection limits already available with the conventional FID. The experiments were limited by the available laser intensities, which were ~300 times less than the estimated saturation intensity. Moreover, the flame ionization zone was poorly illuminated by the small laser beam; we estimate that only 10-15% of the flame ionization zone was illuminated by the laser. Given these factors, and taking the chemi-ionization rate from the laser-excited state to be 2000 times faster than from the ground state, we expect an enhancement in the ionization rate by a factor of ~1.4, compared to the measured value of ~1.1.

Performance improvements can be expected if conditions closer to laser saturation can be achieved, if the flame ionization zone can be more completely illuminated, and if the device can be operated in conditions where the inherent noise limits are imposed by the flame or the laser rather than the measurement electronics itself. Operation at a lower pressure, the use of a slot-burner configuration, or the use of a multiple-pass configuration may provide large increases (100-1000) in the laser-enhanced reponse. Such improvements, combined with reductions in the noise level of the electronics, may ultimately result in a lowering of the present

[†]Applied Optics **26**, 3542 (1987).

*Cornell University, Ithaca, NY.

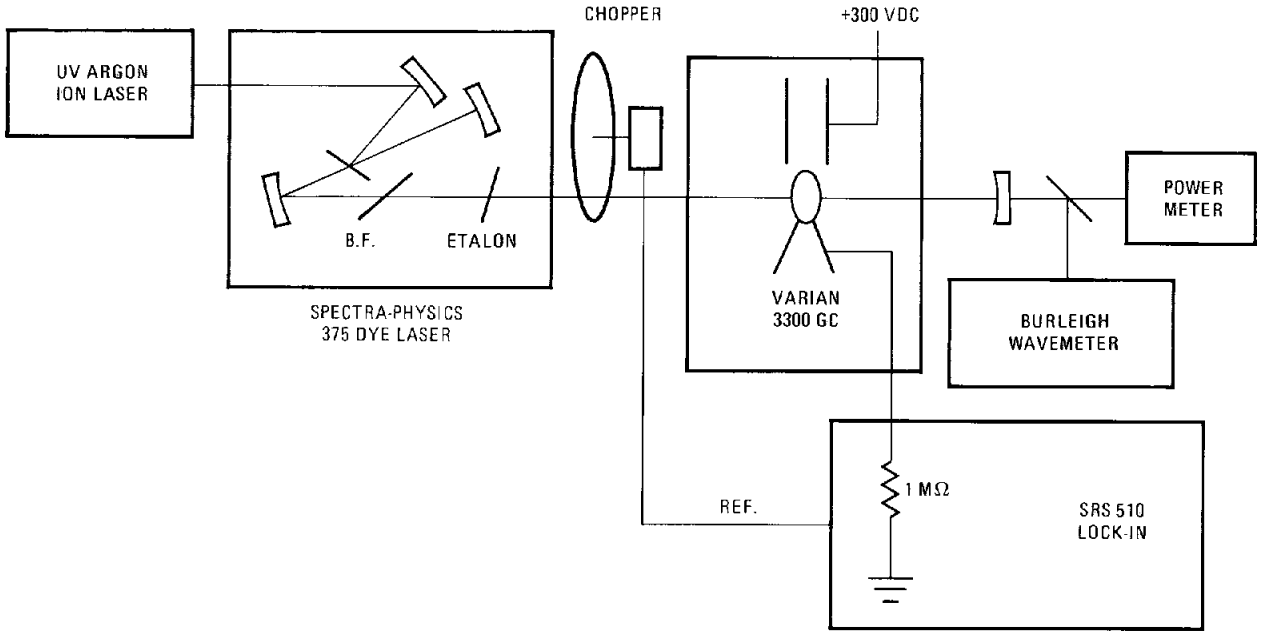

Figure 1. Experimental apparatus used to demonstrate the laser-enhanced flame ionization detector. The flame ionization detector of the gas chromograph was operated inside the extended cavity of the Stilbene 420-cw dye laser.

FID detection limits for hydrocarbons by factors of 10-100. Additional studies are needed to ascertain whether these possible increases in sensitivity are accompanied by corresponding increases in linear dynamic range and to establish the degree to which the equal-per-carbon response of the FID is retained with laser enhancement.

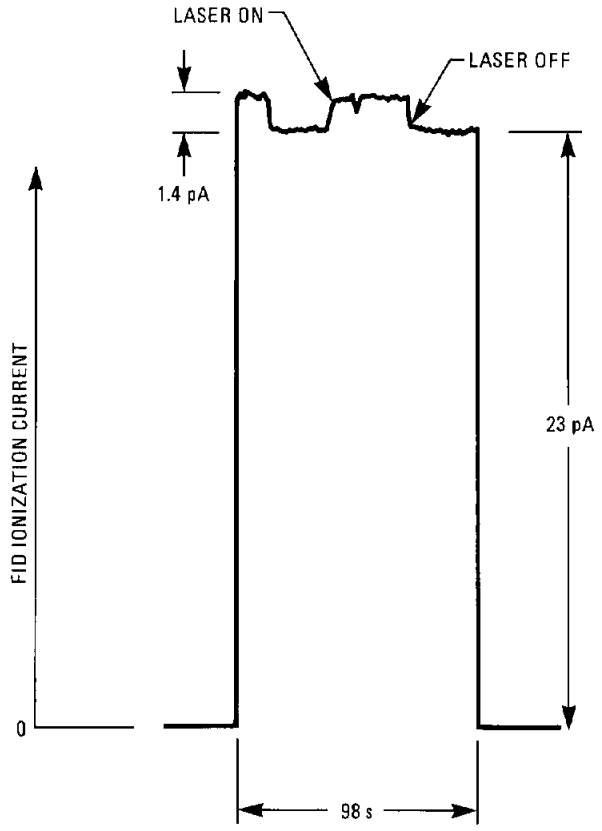

Figure 2. Laser-induced modulation of the output current of the flame ionization detector in the presence and absence of the intracavity laser beam. An optimized system would result in a much larger increase in current in the presence of the laser.

Reference:

1. T. A. Cool and P. J. H. Tjossem, Chem. Phys. Lett. **111**, 82 (1984).

Resonantly Enhanced Multiphoton Ionization of Jet-Cooled Dichlorobenzenes

Resonantly enhanced multiphoton ionization spectroscopy, in conjunction with high resolution time-of-flight mass spectrometry, is applied to the dichlorobenzene isomers in a cold molecular beam as part of a program to develop selective trace detection schemes for chlorinated aromatics.

E. A. Rohlfing and G. A. Fisk

There is a clear need for techniques that provide trace detection of chlorinated aromatics in the exhaust streams of incinerators. The requirements of such gas-phase detection techniques are: (1) ultrahigh sensitivity (at least part-per-billion in molecular concentration), (2) isomeric selectivity, and (3) real-time or quasi-real-time applicability. Here, we describe the recent results of our continuing investigations into several laser-based spectroscopic techniques that may satisfy these requirements, and we discuss experiments in which resonantly enhanced multiphoton ionization (REMPI) spectroscopy has been used in conjunction with reflectron time-of-flight mass spectrometry (TOF MS) to study the dichlorobenzenes (DCBs). These experiments are performed in a cold molecular beam in order to eliminate spectral congestion and thermal broadening.

Our apparatus consists of two vacuum chambers: a chamber for generating the pulsed molecular beam and one for the reflectron TOF MS. A pulsed valve is used to produce a free-jet expansion of the sample diluted in helium (typically at 2-3 atm) through a nozzle orifice of 0.3 mm diameter. The free-jet expansion is collimated by two 1-mm-diameter skimmers at 8 cm downstream and 21 cm downstream of the nozzle before entering the ionization region of the TOF MS. Ions are created via the 1+1 REMPI process through the S_1-S_0 transition by a frequency-doubled dye laser operating in the 271 - 281-nm region. We have also performed two-color REMPI experiments in which the tunable uv laser excites the molecule and the fourth harmonic of the Nd:YAG laser at 266 nm ionizes the excited molecule.

The photoions are mass analyzed in the reflectron TOF MS that can be operated in two modes. In the first mode the TOF MS is operated "normally;" that is, the ions are extracted toward the ion detector that they strike after drifting 40 cm in a field-free region. In the "reflectron" mode of operation, the ions are initially extracted away from the detector, drift in a 10-cm field-free region, and then enter a reflecting field. This reflector decelerates the ions, brings them to a complete stop, and then accelerates them back onto the ion detector. Signals from the ion detector are amplified and processed with boxcar averagers (spectral scans) or a digital oscilliscope (mass spectra); both are interfaced to a laboratory computer for data acquisition.

Figure 1 shows representative mass spectra of jet-cooled 1,4 DCB taken with the TOF MS operated in the normal and reflectron modes. The mass spectrum is dominated by the cluster of parent ions corresponding to the naturally-occurring isotopes of dichlorobenzene in the 146-150 amu region. The spectra in Figure 1 are taken at ~3.0 mJ/pulse, a sufficiently high intensity to cause substantial ion fragmentation. The greatly improved mass resolution provided by the reflectron can be clearly seen in Figure 1. The reflectron improves mass resolution because it compensates for the initial spread in ion energies by bringing the ions to a temporal focus at the detector. This compensation is clearly observed for daughter ions that have a large energy spread from the kinetic energy released upon fragmentation. We find that the fragmentation pattern of 1,4 DCB is strongly influenced by the intensity of the uv laser. Also, the loss of a single Cl to give a fragment ion near 111 amu can be greatly enhanced by the addition of the dye laser fundamental at 548 nm; this fragmentation process is observed only weakly with just the uv laser (see Figure 1). The fragment ions can all be assigned to hydrocarbon or chlorinated hydrocarbon species.

In Figure 2, we exhibit three examples of 1+1 REMPI spectra taken for 1,4 DCB. The top and central panels compare one-color ($\lambda_1+\lambda_1$) REMPI spectra taken at room temperature (298 K) and under jet-cooled, molecular beam conditions. The room temperature spectrum displays many vibronic lines due to sequence congestion and each line is rotationally broadened. As can be seen in the central panel, the effect of jet-cooling on the REMPI spectrum is dramatic. The sequence congestion due to hot bands is virtually eliminated and each vibronic band sharpens due to the extremely cold rotational temperature in the beam (~10 K). We know

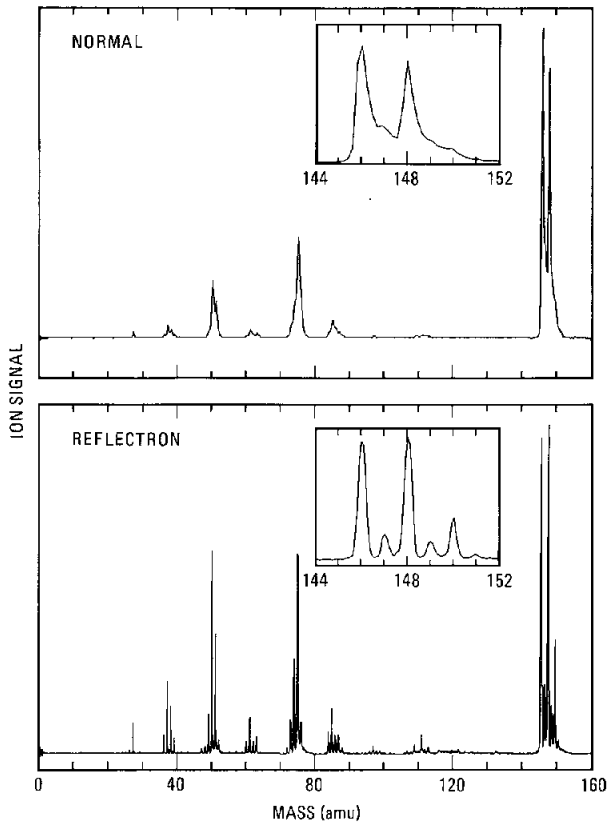

Figure 1. Molecular beam TOF mass spectra of jet-cooled 1,4 dichlorobenzene (DCB) taken with the normal TOF (upper panel) and the reflectron TOF (lower panel). Ionization is by 1+1 REMPI through the 274.10-nm band with ~ 3 mJ pulse energy.

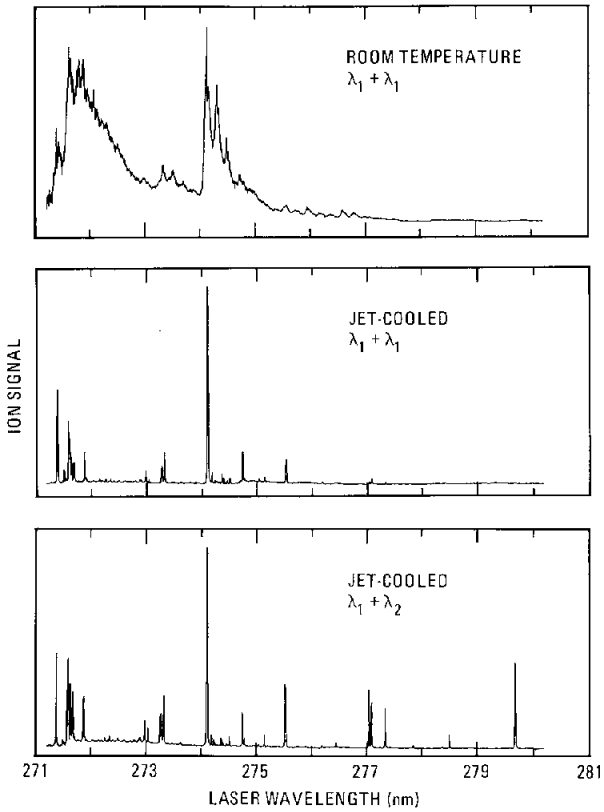

Figure 2. REMPI spectra of 1,4 DCB as a function of laser wavelength under several conditions. Top panel: one-color REMPI of a room-temperature sample (~ $4x10^{-6}$ torr); central panel: one-color REMPI of a jet-cooled sample; bottom panel: two-color REMPI of a jet-cooled sample where λ_2 is the fourth harmonic of the Nd:YAG laser at 266 nm. Only the parent ion, $^{12}C_6H_4{}^{35}Cl_2^+$, is monitored with the TOF MS in the normal mode.

from previous room temperature absorption spectra of 1,4 DCB that there are strong S_1-S_0 absorption bands, including the origin, to the red of 276 nm where the one-color REMPI spectra ends. These bands are absent from the one-color REMPI spectra in the top two panels of Figure 2 because the uv photon that excites the S_1-S_0 transition has insufficient energy to ionize the excited molecule via absorption of one photon.

The origin region of the spectrum can be observed using two-color (λ_1+λ_2) REMPI spectroscopy. Such a spectrum is shown in the bottom panel of Figure 2 in which the fourth harmonic of the Nd:YAG laser at 266 nm has been used for λ_2. We now can see clearly the origin transition at 279.67 nm and other red bands that were unobservable in one-color REMPI. Two-color REMPI has another advantage in that the second laser can be made intense enough to ionize essentially all of the excited molecules produced by the first laser.

We have also performed a similar set of REMPI/TOF MS experiments on the 1,2 DCB isomer and find that isotopic selectivity is easily obtained under jet-cooled conditions. Similar selectivity has been obtained for a series of dichloronaphthalene isomers.[1] We estimate a detection sensitivity of ~10 ppb for 1,4 DCB; this estimate is based on a molecular concentration ratio referenced to atmospheric pressure behind the nozzle and thus represents a valid detection limit for an incinerator exhaust stream. It should be possible to implement REMPI on other toxic species such as the chlorinated dioxins and furans. The difficulty with these molecules is the rapid intersystem crossing from the S_1 excited state to the triplet manifold. This process makes the quantum yield of fluorescence negligible and may limit the applicablility of REMPI if the crossing is fast enough to compete with ionization out of S_1. Even in this case REMPI can work if an appropriate scheme for ionizing triplet molecules can be found. Finally it seems feasible to implement jet-cooled REMPI/TOF MS in quasi-real-time in an incinerator-effluent stream, although it may be necessary to include additional preliminary separation techniques such as gas chromatography.

Reference:

1. E. A. Rohlfing, D. W. Chandler, and G. A. Fisk, "Laser-Based Techniques for the Detection of Chlorinated Aromatic Hydrocarbons," Sandia Report *SAND87-8787* (Sandia National Laboratories, Livermore, CA, 1987).

This figure represents a two-dimensional projection of the spatial product distribution resulting from the photodissociation of methyl iodide. It was obtained using photofragment imaging, a technique recently developed at the CRF that is well suited to investigating the detailed dynamics of elementary chemical and physical processes. Here, color specifies intensity, and the initial symmetry axis of the molecule lies on a vertical line through the centers of the two lobes. The shape of the distribution reveals immediately that dissociation occurs rapidly as a result of a parallel-type electronic transition. Quantitative analysis of the intensities reveals much more about the dissociation dynamics.

Combustion Chemistry

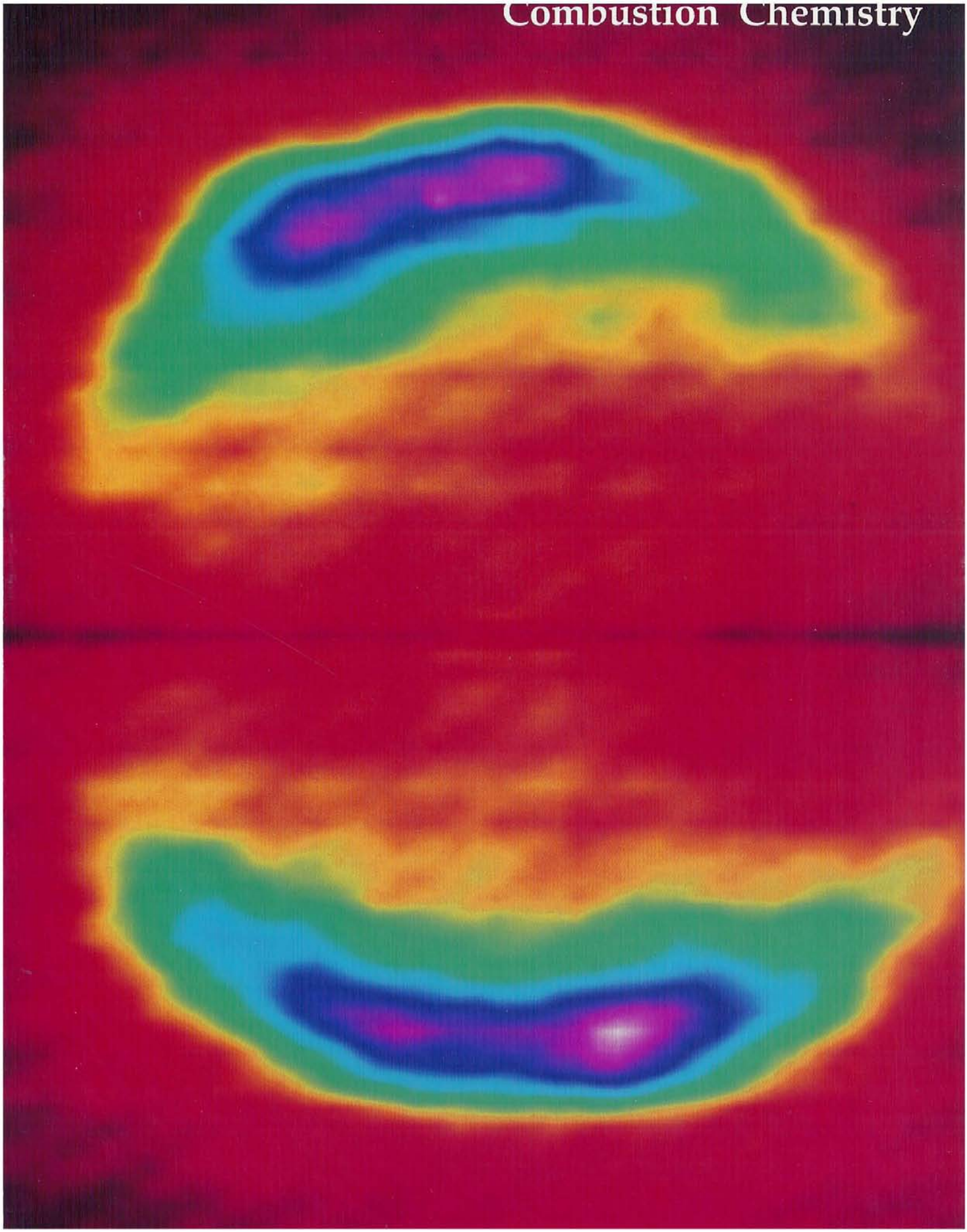

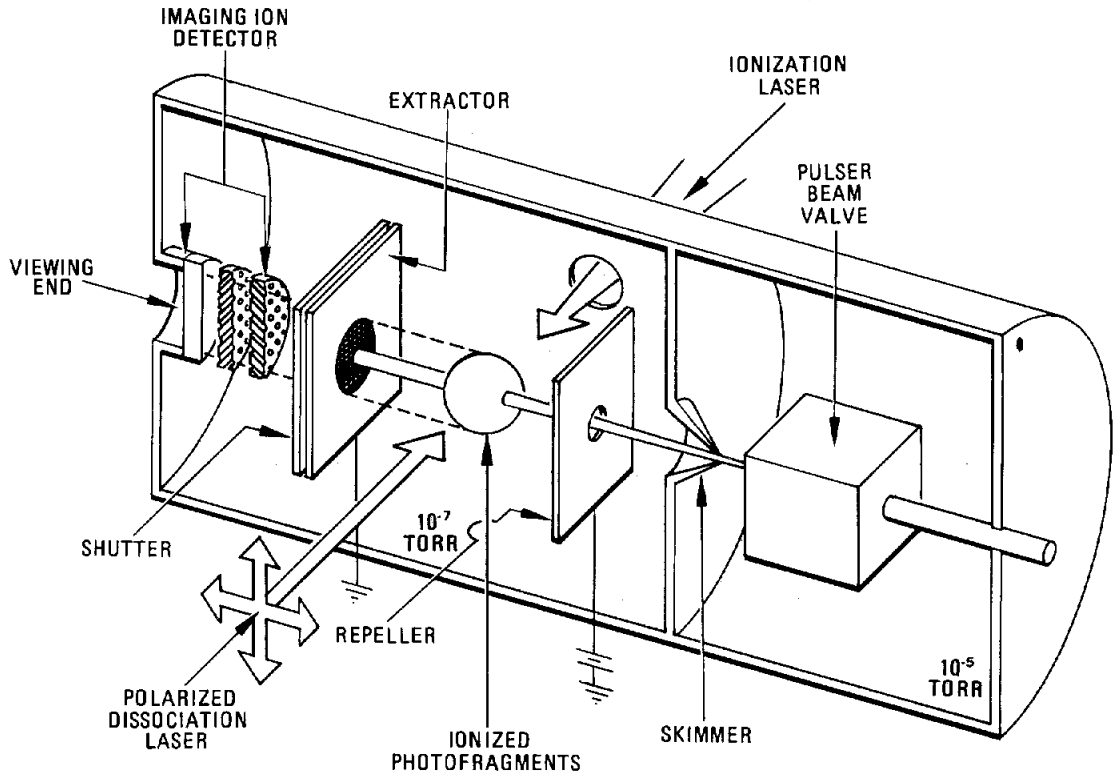

Ion imaging is a versatile technique illustrated here for the specific case of photodissociation. The pulsed valve shown at the right of the diagram generates a supersonic molecular beam containing the molecules to be investigated. A portion of the beam enters a high-vacuum chamber in which a small fraction is dissociated by the output of a polarized laser. A pulse from a second laser state-selectively ionizes the resulting fragments, which continue to drift with the velocities they had before ionization. After a predetermined time delay, the ions are accelerated onto a position-sensitive detector, and their spatial distribution is recorded. The intrinsic symmetry of the problem allows reconstruction of the original three-dimensional fragment distribution from the recorded image.

The three-dimensional distribution of product velocities contains a wealth of information about the dissociation process. The shape of the distribution for a particular quantum state reveals the nature of the electronic transition responsible for the dissociation and the time scale on which dissociation occurs. From conservation of energy, the speed distribution for one fragment defines the distribution of internal energy in the other fragment. For example, in methyl iodide, the branching ratio for dissociation to ground- or excited-state iodine atoms is easily obtained from the speed distribution of the methyl fragment. Correlations between velocity and angular momentum in the products reveal subtle details about the forces that act during dissociation. These correlations are studied by varying the relative polarizations of the beams from the dissociation and ionization and lasers.

Research on methyl iodide and on hydrogen sulfide clearly shows that photofragment imaging is a valuable tool for studying the dynamics of intramolecular processes. Work is presently underway to extend the technique to investigations of intermolecular phenomena.

Section 3
Combustion Chemistry

Under the sponsorship of the Department of Energy's Office of Basic Energy Sciences, Sandia National Laboratories undertakes fundamental experimental and computational research in combustion chemistry. This work provides information needed to understand the complex chemical processes involved when fuels are burned. The program emphasizes measurements of reaction rates using state-of-the-art diagnostics and stresses the close coupling of experiment, theory, and modeling.

Staff and visitors investigate elementary reactions important to the burning of fuels or the production of pollutants. Typical experiments utilize slow-flow reactors together with such techniques as laser photolysis and laser-induced fluorescence (LIF) to generate and detect, respectively, reactive species. Using mass spectrometry and LIF as diagnostic tools for experiments conducted in low-pressure flames, researchers study the kinetic mechanism involved in prototypical combustion systems. Other experiments and related theoretical efforts address fundamental questions of molecular dynamics—questions that must be addressed to develop adequate models of kinetic processes.

Theoretical calculations of potential energy surfaces enable predictions of the product distributions that result when reactive species interact. These calculations are useful in extrapolating measured reaction rates. Computer modeling of the complete kinetics for combusting systems defines the dominant reaction pathways.

The experimental, theoretical, and modeling programs are focused on topics of importance to energy-producing technology. Themes of current emphasis include the formation and destruction of nitrogen-containing pollutants and the oxidation of hydrocarbons.

Two-Dimensional Imaging of State-Selected Photodissociation Products Detected by Multiphoton Ionization

A new technique is presented that makes it possible, with a single laser pulse, to determine the three-dimensional spatial distribution of state-selected photoproducts. The technique is illustrated by recording the spatial distribution of methyl fragments produced in their vibrational ground state by the 266-nm photodissociation of CH_3I and CD_3I. From this study, it is determined that the branching ratio for different vibrational states of the $CH_3(CD_3)$ fragment into the $I(^2P_{1/2})$ excited state and $I(^2P_{3/2})$ ground state decreases with increasing vibrational excitation.

D. W. Chandler, P. L. Houston,* D. H. Parker,** and M. Jannsen***

Many problems in molecular dynamics demand the simultaneous measurement of internal energy and velocity. Consider the case of a photodissociation that produces two fragments, AB and CD. Even if the internal energy distributions of the AB and CD fragments were each measured separately, it would still be necessary to obtain information on the recoil speed in order to determine which levels of the AB fragment were generated in coincidence with given states of the CD fragment. The recoil angle with respect to the polarization vector of the dissociating light gives additional information about the transition moment in the parent molecule and the time scale of dissociation. Although the earliest photofragment spectrometers measured either the recoil velocity distribution or the internal energy of the fragments, it has only been recently that a Doppler technique has been developed to obtain the correlation between these properties. In this paper, we present a technique in which the three-dimensional spatial distribution of a photofragment, measured at a set time after photodissociation, is projected onto a two-dimensional surface. The method is applied here to the photodissociation of CH_3I and CD_3I. CH_3I dissociates into two channels leading to either methyl radical plus electronically-excited iodine, $I(^2P_{1/2})$ + CH_3, or methyl radical plus ground-state iodine, $I(^2P_{3/2})$ + CH_3. For dissociation at 266 nm, the fraction leading to $I(^2P_{1/2})$ is about 0.75. The ground state CH_3 fragment generated in coincidence with the ground state $I(^2P_{3/2})$ channel has approximately 1.3 times the velocity as the ground state CH_3 generated in coincidence with $I(^2P_{1/2})$.

We form a molecular beam[1] of CD_3I/He by flowing He at 25 psi over CD_3I at 0°C and then flowing the mixture through a pulsed nozzle. Most of our experiments are performed on CD_3I because ionization detection of CD_3 is much cleaner than CH_3 due to less predissociation of the resonant intermediate states. The pulsed beam is skimmed and directed into the imaging ion detector through a hole in a repeller plate. An unfocused, quadrupled Nd:YAG-laser beam (266 nm) intersects the molecular beam at right angles and dissociates the CD_3I. A focused (12-cm f/1 lens), counterpropagating, doubled-dye-laser beam (wavelength near 330 nm) intersects the fragments 10 ns later and ionized CD_3 via 2+1 multiphoton ionization on the 0-0 band of the $3P_z(^2A_2'') \leftarrow 2P(^2A_2'')$ transition. The state-selected ions are created between the repeller (0-200 V) and a pair of grounded grids mounted in front of the imaging detector and separated from the repeller by 7.5 cm. Another screen, which is used as an ion shutter, is located between the grounded screens and the ion detector. This screen remains at ground potential until the CD_3^+ passes, and it is then switched positive (250 V) to repel any CD_3I^+ ions or high-molecular-weight background ions. The position of each ion is recorded with a combination micro-channel plate/phosphor-screen detector. The images are recorded by a CCD electronic camera or by a photomultiplier tube. By using the photomultiplier tube (1P28) to detect the ions, we determine the arrival time of the CD_3^+, thereby allowing us to set the timing of the voltage pulse to the ion shutter.

*Cornell University, Ithaca, NY.
**University of California at Santa Cruz.
***Katholic University, Nijmegen, The Netherlands.

Figure 1 shows the apparatus and an image of the $CD_3(v=3)$ fragments after dissociation for alignment of the polarizatrion of the dissociation laser beam parallel to the detector face. We know that the fragments are from v=3 because we are ionizing the CD_3 fragment via resonantly-enhanced, multi-photon ionization through the 2_1^3 band. From inspection of the image, the nature of the dissociation can be seen directly. The $\cos^2$ dependence in the intensity pattern indicates a parallel transition accompanied by prompt dissociation. We obtain the distribution of photofragments, at a fixed time delay after dissociation, by reconstructing the three-dimensional "ion cloud" that gave rise to the two-dimensional image.

The problem of reconstructing a three-dimensional function from a two-dimensional projection has been considered extensively. When the 3D object is cylindrically symmetric, one 2D projection taken parallel to the polarization axis is sufficient for complete determination of the 3D function. A double ring is obtained in both the observed image and the reconstruction. The relative intensities indicate that less than 50% of the $CD_3(v=3)$ fragments are formed in coincidence with $I(^2P_{1/2})$. This is in contrast to the percentage (75%) found when the measurement is made over the average of all the vibational states of the CD_3.

It should be emphasized that the imaging technique described above is applicable to a wide range of chemical problems. This technique is easily generalizable to the detection of products in crossed molecular beams, where acceleration to the state-selected fragment ions in any direction perpendicular to the relative velocity vector will provide a projection from which the full three-dimensional velocity distribution can be reconstructed.

In conclusion, we have shown that it is possible to record, at one time, the entire spatial distribution of a state-selected, photofragment in such a manner that both its angular and speed distributions are determined. This technique gives us direct information on the dynamics and time scale of the photodissociation event. Additionally, by studying the effect of the polarization of the ionization laser relative to the polarization vector of the dissociation laser, information of the internal alignment is obtained.

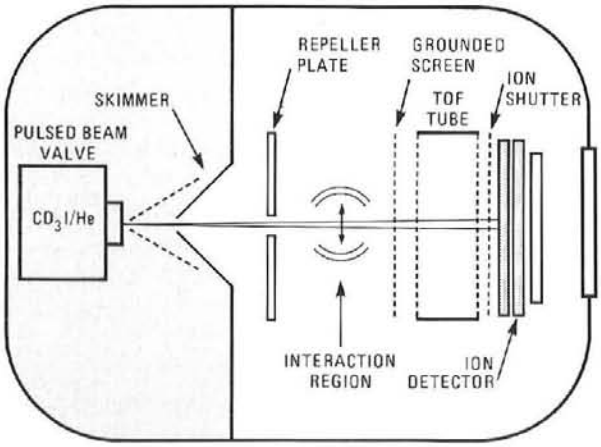

Figure 1. Schematic of the apparatus showing the geometry of the skimmed molecular beam to the imaging ion detector. Also shown is an image of $CD_3(v=3)$ obtained after the dissociation of CD_3I with a vertically polarized laser beam at 266 nm. From inspection of the image, two rings are clearly seen. These represent CD_3 fragments born in coincidence with either ground state (outer ring) or electronically-excited state (inner ring) iodine.

Reference:

1. D. W. Chandler and P. L. Houston, J. Chem. Phys. **87**, 1445 (1987).

Proton Production in Two-Color Laser Ionization Dissociation of Molecular Hydrogen†

We have investigated the mechanisms for the production of H^+ during the multiphoton ionization of the H_2 molecule. Three distinct mechanisms have been observed and explained.

J. D. Buck,* D. H. Parker,* and D. W. Chandler

Proton production has been observed in recent resonance enhanced multiphoton ionization (REMPI) studies of molecular hydrogen.[1] In this study, we report REMPI studies of H_2 that lead to the production of H^+ in multicolor, multi-resonant MPI experiments. Using time-delayed, two-laser REMPI where the initial electronic-excitation step to the E,F state is separated by 50 ns from the ionization steps, we identify three separate processes leading to H^+.

In order to perform laser ionization detection of H_2 quantifiably, the competing processes of ionization and dissociation must be understood. Traditionally, electron impact, and to a smaller extent absorption of single high-energy photons, have been employed in studies of dissociation of ground-state H_2 into H^+ and H. The short average internuclear distance of the ground state requires, via the Franck-Condon principle, that the excited-state, potential-energy curves are accessed only in the 0.6 - 0.9-Å range. Since this bond distance corresponds to points high on the repulsive wall for most states that can yield protons, the observed thresholds for proton production have typically been considerably above the asymptotic energies of the responsible states. When the E,F states are used as intermediate levels, the observed thresholds fall surprisingly close (within a few tens of wave numbers) to the asymptotic limits.

The following kinetic scheme lists several possible H_2 REMPI-dissociation processes leading to H^+ for two-color experiments.

[1] $H_2(X\,^1\Sigma_g^+) \xrightarrow{n h\nu} H_2^*$ n-photon resonant excitation

[2] $H_2^* \xrightarrow{h\nu} e^- + H_2^+ \xrightarrow{h\nu} H + H^+ + e^-$
direct or autoionization/molecular ion photodissociation

[3] $H_2^* \xrightarrow{h\nu} H + e^- + H^+$ dissociative ionization

[4] $H_2^* \xrightarrow{h\nu} H(1s) + H(nl) \xrightarrow{h\nu} H(1s) + e^- + H^+$
dissociation/ionization of excited fragments

[5] $H_2^* \xrightarrow{h\nu} H^- + H^+ \xrightarrow{h\nu} H + e^- + H^+$
ions pair formation/photodetachment of H^-

The initial n-photon excitation, step [1], to an excited electronic state is assumed separable from any subsequent ionization mechanism steps [2, 3, 4, or 5]. Some of these subsequent photoprocesses, such as [2], are well-characterized by classical spectroscopy and some, such as [5], have been studied only recently by laser techniques. Figure 1 schematically shows the energy requirements of steps [2-5] and potential energy curves for the relevant lower-singlet, excited-electronic states of H_2.

The apparatus consists of a time-of-flight mass spectrometer separated from the gas-laser interaction region by a biased slit that also serves as the ion extractor. The laser beam(s) intersect an effusive flow of hydrogen from a thin quartz nozzle 2 mm in front of the extractor.[1] Typical operating pressures are 0.005 torr in the ionization region and 5×10^{-7} torr in the time-of-flight chamber. The light necessary to cause optical excitation to the E,F levels by two-photon absorption was generated as the fourth anti-stokes Raman order of the frequency-doubled output from a Nd:YAG-pumped rhodamine-dye laser. A 10-cm lens focuses the uv beam (30-80 mj/pulse) on the mass spectrometer axis and the resulting ions are extracted by a field of several hundred V/cm. *Q*-branch transitions are used to populate the v = 0, 5, 6, 7, and 8 rovibrational levels of the E,F electronic state (also designated as the E0, F3, E2, F4, and E3 vibrational levels, respectively).

A second counterpropagating Nd:YAG-pumped dye-laser beam (750-640 nm, typically 1 MW/cm^2, unfocused) is directed into the chamber about 50 ns after the uv excitation pulse. The ions resulting from absorption of photons from the second laser beam appear as separate peaks, delayed 50 ns in the time-of-flight signal with respect to the ions generated by the first laser. The two delayed signals, from protons and molecular-hydrogen ions, are simultaneously recorded as the wavelength of the total energy attained by absorption of one photon out of a given E,F intermediate level was near the H(n=1) + H(n=2) dissociation limit (118,475 cm^{-1}).

†Journal of Physical Chemistry **91**, 2035 (1987).
*University of California at Santa Cruz.

The mass-selected species generated by the second laser, a tunable dye laser, are independently monitored as the dye-laser wavelength is scanned. We usually employ excited-state resonances slightly below the second dissociation limit ($H_2 \rightarrow H(1s) + H(2s,p)$) as the first step in a multistep process. From the E,F state, the threshold for molecular ion formation is reached by absorption of at least two red photons, whereas three red photons are required to produce protons. At the relatively low power densities used (unfocused laser), it is somewhat surprising to see a three-step process occur when a two-step channel is available. Such behavior underscores the importance of dissociative channels available to excited states of molecular hydrogen.

The first pattern of proton production, illustrated in Figure 1, is observed by scanning the ionization laser wavelength througfh 656.4 nm, the Balmer α wavelength for the H(n=3) $\leftarrow$ H(n=2) atomic transition. A strong, broad (FWHM 16 cm^{-1}) peak is seen in the proton channel when exciting from the E,F v=5 and v=6 states, but not from v=4. Formation of H(n=2) atoms depends on reaching the second dissociation threshold (18,475 cm^{-1}) with one photon from the selected E,F level. This is the case for E,F ($v \geq 5$) but not for the lower lying v=4 state excited by 656.4 nm light. Protons are generated by (1 + 1) REMPI of H(n=2) through the H(n=3) level. H(n=2) is produced by one-photon absorption from the E,F level to the dissociation continuum. Here, the resonant step is the second step in a three-photon process.

A second mechanism for double-resonance proton production is evident when exciting from the E,F(v=5) level. The probe laser is tuned to be one-photon resonant with a discrete state (most of these are B' levels) slightly below the second dissociation limit at 118,475 cm^{-1}. When the total energy reached by one more red photon at this resonant frequency exceeds by even a few tens of wave numbers, the asymptotic H(n=1) + H(n=3) dissociation threshold (133,712 cm^{-1}), protons are observed. Here, proton production occurs via nonresonant ionization of H(n=3). As soon as the n=3 channel is reached by absorption of two red photons, the signal switches almost completely from H_2^+ to H^+, a rather surprising behavior. Our results parallel the finding by others using single-laser, three-photon-resonant REMPI studies that above the third dissociation threshold, H(n=3) production and concommitant ionization of the fragment is the dominant ionization channel.

A third mechansim for proton production is observed when the E,F v=6, J=1 level is populated and the red probe beam is tuned to either the C $^1\Pi_u$ v=13, J=1 or J=2 levels at 118,351 and 118,379 cm^{-1}, respectively. Absorption of one more red photon from these two states gives total energies of 133,090 and 133,150 cm^{-1}, which are both below the 133,710-cm^{-1} threshold for n=3 dissociation. Approximately equal signals of H^+ and H_2^+ are detected for these resonances. Protons are not observed when B'-state resonances at similar energies (~ 118,350 cm^{-1}) are selected. We tentatively propose a mechanism of proton production based on the shape of the C state potential curve. The C and B' states both dissociate to H(n=1) + H(n=2), but the B' curve approaches the asymptote much more sharply. It seems feasible to make an optical transition from a vibrational level of the Cl Π electronic state into the dipole-dipole resonance-attraction well of a $^1\Pi_g$ repulsive state that dissociates to H(n=1) + H(n=3).

In conclusion, proton formation in laser excitation of prepared E,F states is shown to occur by dissociation of electronically-excited H_2, either by ionization of excited fragment, or by dissociative ionization, depending on the energy of the dissociation-causing photon.

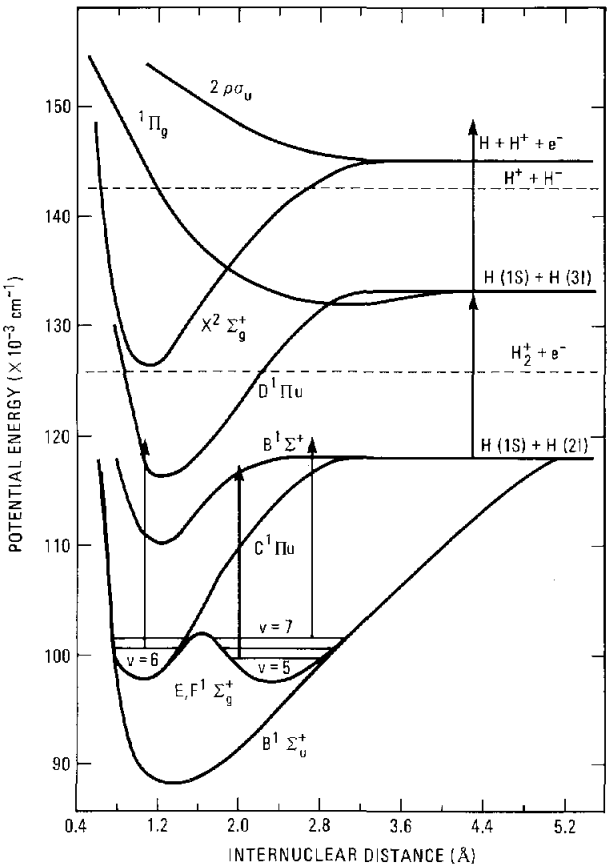

Figure 1. Schematic representation of the mechanism responsible for the H^+ production in laser ionization of H_2 via resonant enhancement through the n=2 to n=3 Balmer α resonance.

Reference:

1. D. H. Parker, J. D. Buck, and D. W. Chandler, J. Phys. Chem. **91**, 2035 (1987).

Measurement of Transition Moments Between Molecular Excited Electronic States Using the Autler-Townes Effect†

Autler-Townes splitting observed in the two-color four-photon ionization of hydrogen molecules is in good agreement with theory. From theoretical fits to the spectral profiles, the value of the electric dipole transition moment between the excited vibronic states E,F $^1\Sigma_g^+$ v=6, and D $^1\Pi_u$ v'=2, is determined to be 2.0 ± 0.5 a.u.

A. M. F. Lau, D. W. Chandler, M. A. Quesada,* and D. H. Parker*

Analogous to the splitting of two degenerate molecular levels by a dc Stark field, the Autler-Townes effect (also known as ac, optical, or dynamical Stark splitting) is the splitting of two (nearly) resonant levels by a strong high-frequency field. When this energy level structure is probed by a second weaker laser, the spectrum reveals a doublet, from whose peak separation one may deduce the transition moment between the two levels coupled by the strong laser. We shall discuss the advantages of this method of measuring molecular transition moments over the traditional methods.

Figure 1 shows the multiphoton ionization scheme of the hydrogen molecule. The ions were collected as a function of detuning Δ_a of the ultraviolet (λ_a=193 nm) laser around the two-photon X-E,F resonance, while the detuning Δ_b of the infrared (λ_b=726 nm) laser was kept fixed.

In the experiments, two counterpropagating lasers, coincident in time, intersect in the ionization region of a time-of-flight mass spectrometer. One laser, acting as the probe laser, operates near 193 nm. The light is generated by Raman shifting the output of a frequency-doubled dye laser in a high-pressure gas cell of hydrogen. In this manner, we are able to generate 80 microjoules of light (5-ns pulse at 10 Hz). This laser is used to probe the ac-Stark splitting induced in the molecule by the second laser. The second laser, tuned to be in near-resonance between the E,F v=6, J=1 state and the D v=2, J=2 state, is a dye laser (10-ns pulse width at 10 Hz) operating near 726.8 nm (LDS 750 laser dye). As the frequency of the ultraviolet laser is scanned through the Stark-split levels, H_2^+ ions are formed in the sample (3-microbar pressure) and extracted into the time-of-flight mass spectrometer with fields of around 200 volts per cm. The infrared beam is expanded and the center section is passed through a diaphragm of 4.0±0.4 mm diameter. Corning 754 filters were used to attenuate the beam. The films have a transmission of 0.44 at 726 nm. The overlap of the beams was optimized by maximizing the signal at the wavelength of the small peak. This gave reproducible results over the time period of a few weeks that the data was taken. The ionization spectra at different infrared intensities I_b for a given detuning Δ_b are shown on the left column of Figure 2.

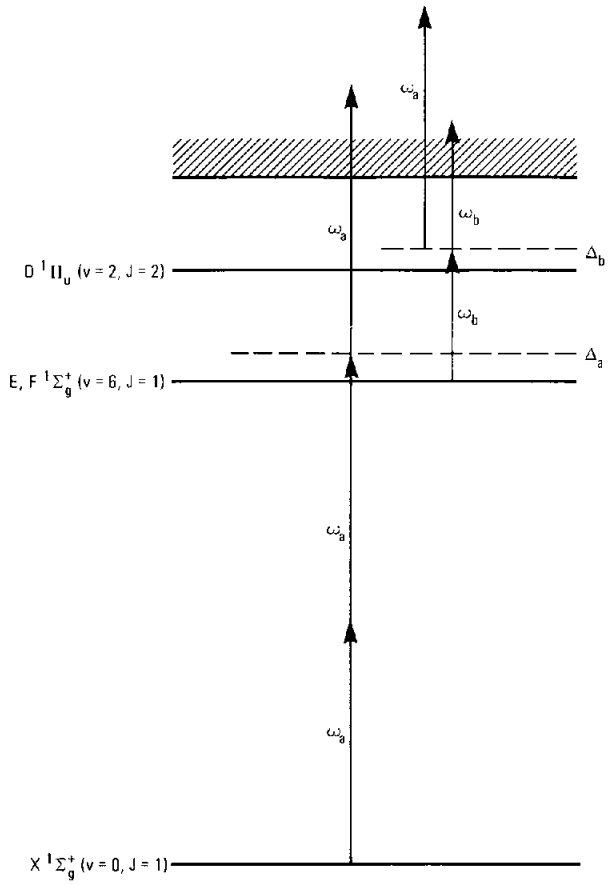

Figure 1. Schematic H_2 energy-level diagram showing multiphoton ionization with uv(ω_a) and ir(ω_b) lasers.

†Physical Review A **35**, 4107 (1987).
*University of California at Santa Cruz.

To calculate the corresponding spectral profiles, we solve the density matrix equations describing the three-level molecular system interaction with the laser fields. The longitudinal and transverse relaxations of the molecule due to radiative decays, photoionization, and the laser bandwidths are taken into account in the theoretical model. The solutions we obtain numerically are in the nonsteady-state regime, since multiphoton ionization continuously depletes the molecular population in the bound levels. The theoretical fits to the observed spectra are shown on the right-hand column of Figure 2. They yield a value for the vibronic transition moment between E,F v=6 and D v'=2 of 2.0 ± 0.5 a.u., where the estimated errors are largely due to the uncertainty in the measured average infrared intensity. This is in good agreement with the *ab initio* value 1.97 a.u. calculated by Huo and Jaffe.[1]

We note that in the above method, the determination of the peak separation of the Autler-Townes doublet is a frequency measurement, which can usually be done with high accuracy. Another advantage of the method is that in the strong saturation regime, the accuracy of the determined transition moment does not depend critically on precise knowledge of the molecular relaxation rates, the photoionization rates, or the laser bandwidths. In order to obtain absolute values of the transition moments, conventional methods generally require absolute measurements of populations, fluorescence intensities, or lifetimes of radiative decay to numerous lower states, whereas the method here is pair-wise state-selective, is independent of absolute population, and requires only the measurement of laser intensity and frequency detuning. These features make it particularly advantageous for measuring transition moments between excited electron states.

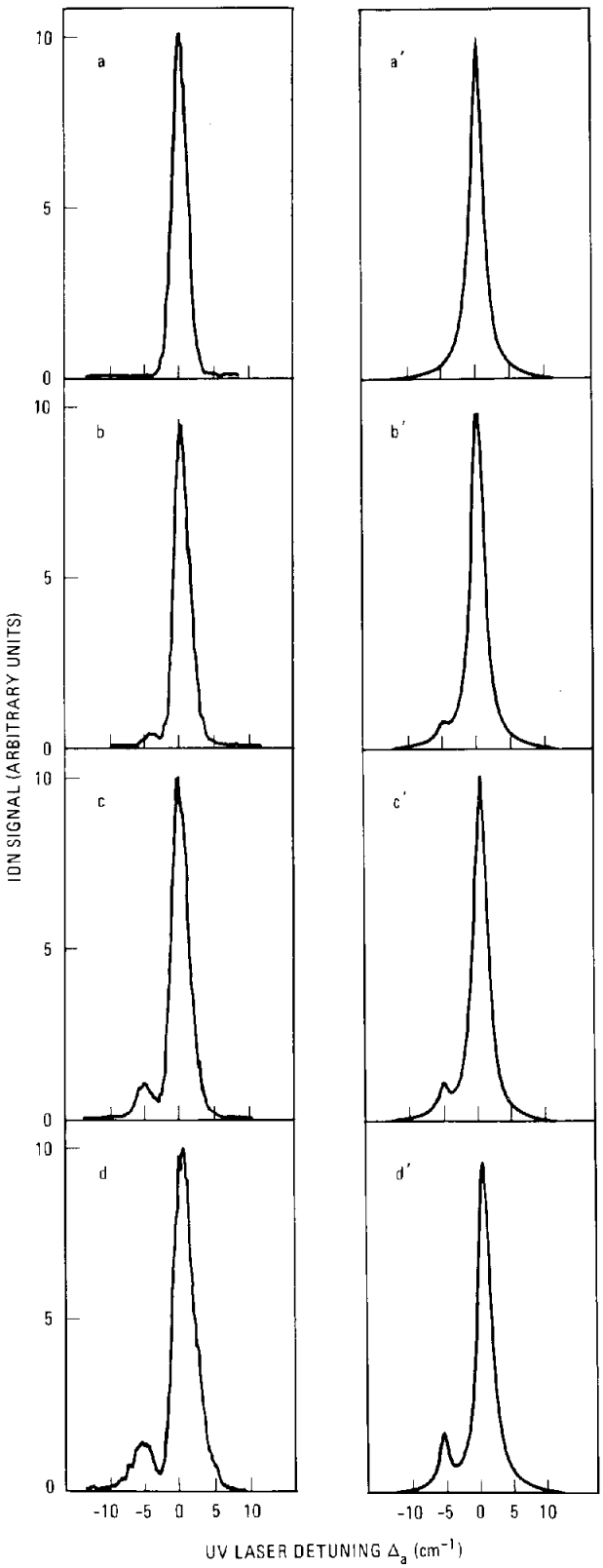

Figure 2. Comparison of the calculated multiphoton H_2^+-ion spectra (a'-d') with the corresponding observed spectra (a-d) at ir laser-pulse energies: (a) 0 mJ; (b) 1.9 mJ; (c) 4.4 mJ; and (d) 10 mJ. The ir laser detuning Δ_b is 4.8 cm^{-1}. Splitting of the transition by the Autler-Townes effect can be used to determine the molecular dipole moment.

Reference:

1. W. M. Huo and R. L. Jaffe, Chem. Phys. Lett. **101**, 463 (1983).

Measurements of State-to-State Energy Transfer Rates in the v = 1 State of H_2

We have measured state-resolved, rotation energy-transfer rates in $H_2(v = 1)$ - H_2 $(v = 0)$ collisions using optical pump-probe techniques. A single rotation level was populated using stimulated Raman pumping, and the degree of collision-induced population transfer was monitored using either coherent anti-Stokes Raman spectroscopy (CARS) or multiphoton ionization spectroscopy (MPI). The results are in good agreement.

R. L. Farrow and D. W. Chandler

State-to-state energy transfer rates can play an important role in influencing basic chemical combustion reactions and in determining relaxation rates affecting combustion-related spectroscopy. Several forms of nonlinear spectroscopy, including coherent anti-Stokes Raman spectroscopy (CARS) and saturated laser-induced fluorescence (LIF), are critically dependent on bimolecular rotational relaxation rates. Such relaxation rates control saturation thresholds and can thus dictate laser-power levels and sensitivity limits. A number of theoretical models exist for predicting these rates, but direct, state-resolved measurements are limited.

We have measured rotationally-resolved, energy-transfer rates in H_2-H_2 collisions, using optical pump/probe techniques. A single-rotational level is excited to the v = 1 state via stimulated Raman pumping, and after a suitable delay to allow collision-induced population transfer, the v = 1 level populations are probed using CARS or multiphoton ionization (MPI) spectroscopy. The rotational transfer rates are analyzed from the data using a least-squares fitting program that calculates all relevant populations for a given delay time, according to a rate matrix which is varied for best fit. We have previously measured transfer rates in HD using MPI to detect the excited-state populations.[1] For H_2, CARS was employed additionally as a probe in order to examine its applicability in these experiments and to compare with the MPI results.

The MPI experiment is similar to that described previously.[1] A separate CARS-based experiment is shown schematically in Figure 1. Single-mode Nd:YAG and pulse-amplified dye lasers were used for the Raman pumping to achieve maximum reproducibility in the population excited by each laser pulse. Due to the narrow combined bandwidth of these lasers [80 MHz full width at half maximum (FWHM)] compared to the Raman-Doppler widths involved (~ 1300 MHz), less than 5% of the ground-state population of a given transition was excited to v = 1. Thus, our results represent collisions of v = 1 molecules with nearly thermal v = 0 molecules. After time delays of 85-500 ns at pressures of 15 and 30 torr, populations were probed with scanning CARS, using a separate frequency-doubled, single-mode Nd:YAG laser and pulsed dye laser. The laser pulses had durations of ~ 10 ns (FWHM). All measurements were performed at room temperature.

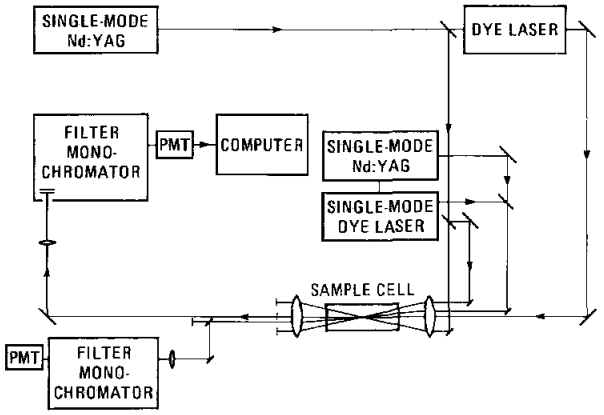

Figure 1. Experimental layout of H_2 energy-transfer experiment using stimulated Raman pumping and CARS probing of v = 1 populations.

Each of the four *Q*-branch transitions with significant population at room temperature (j = 0-3) was excited by the Raman-pumping lasers. When an even j level was pumped, we observed measurable population transfer only to the other even level, and similarly for an odd level. (At pressures of 200 torr and with much larger delays, this rule was not obeyed, which we attribute to resonant v-v exchange processes.) Thus, the energy transfer dynamics are, to a large degree, controlled by two rates: $k_{1,2}$ and $k_{1,3}$, with the reverse rates determined by detailed balance. For convenience, we fitted the data to a rate matrix based on a simple two-parameter exponential gap model.[1]

An example of the time-dependent CARS spectra obtained after various time delays is shown

in Figure 2 (indicated by data points). Here, the J = 3 level in v = 1 is initially populated, and population transfer is to J = 1. The spectra were measured with increasing delay between pump and probe pulses. The top spectrum is furtherest from rotational equilibrium with the 295-K translational temperature, which is calculated to have a J = 1 to J = 3 (v = 1) population ratio of 6.5 to 1. The bottom spectrum is within 35% of equilibrium. (Though not shown, spectra with longer delays were observed to reach equilibrium.) The solid lines are theoretical spectra computed using the experimental delay times and a best-fit transfer rate $k_{1,3} = 4.4 \times 10^6$ s^{-1} amagat^{-1}.

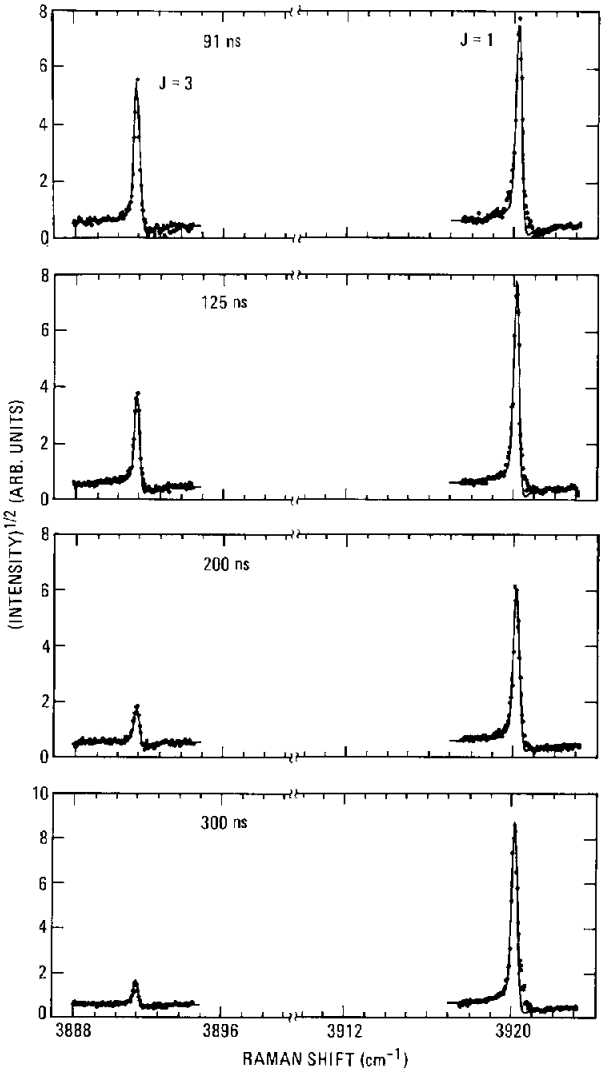

Figure 2. Time-dependent CARS spectra of the J = 1 and J = 3 transitions of H_2(v = 1 → 2) at 295 K, measured with various time delays following excitation of the J = 3 (v = 1) level. The square root of intensity is plotted so that the peak heights are approximately indicative of population.

The measured best-fit rates for $k_{1,2}$ and $k_{1,3}$ from the CARS experiments are given in Table I. Within the experimental uncertainties of ± 15% (due to noise in the data, the finite laser pulse widths, and uncertainties in the delay time), the results are in good agreement. Also shown is a measurement by Meier, *et al.*[2] for $k_{1,3}$, who used Raman pumping followed by LIF probing. Their result is somewhat higher than ours, but still agrees within the uncertainties. Finally, theoretical rates, calculated for v = 0 by Zarur and Rabitz[3] are found to be significantly lower than the experimental results. We believe the disagreement results from the omission of cross-sections for resonant *r-r* exchange collisions in the calculation of the rates.[2] These collisions do not result in energy exchange between vibrational and translational degrees of freedom, and thus are not detected in the v-*t* type experiments for which the cross-section calculations were performed. Our experiments do detect resonant-exchange processes due to vibrational labeling of the perturbed molecule and indicate that these collisions occur relatively frequently for H_2.

Table I

Comparison of rotational energy transfer rates for H_2 (v = 1) at 295 K, given in units of 10^6 S^{-1} amagat^{-1}.

Source	Experiment	$k_{1,2}$	$k_{1,3}$
This work	CARS detection	180 ± 27	44 ± 7
This work	MPI detection	180 ± 27	56 ± 8
Meier *et al.*	LIF detection	-	61 ± 12

References:

1. D. W. Chandler and R. L. Farrow, J. Chem. Phys. **85**, 810 (1986).

2. W. Meier, G. Ahlers, and H. Zacharias, J. Chem. Phys. **85**, 2599 (1986).

3. G. Zarur and H. Rabitz, J. Chem. Phys. **60**, 2057 (1974).

Rotational Energy Transfer in HCl (v=1)

The rotational energy transfer of $H^{35}Cl$ (v=1) in collisions with thermal Hydrogen Chloride (HCl) at 298 K is investigated using stimulated Raman pumping to excite a specific rotational level in v=1 and 2+1 resonantly-enhanced multiphoton-ionization to detect the time-dependent rotational populations. Multiquanta transitions account for ~ 30% of the total population loss from a given rotational level.

E. A. Rohlfing, D. W. Chandler, and D. H. Parker*

Rotationally inelastic collisions have served for years as one of the simplest examples of inelastic scattering, therefore providing a popular research area for both experimentalists and theoreticians. Recent experimental approaches have focused on the use of infrared-infrared laser double-resonance techniques. While these techniques provide an important source of experimental data on rotational relaxation, the interpretation of this data in terms of state-to-state rate constants typically requires the use of a simplifying model to reduce the number of independent-rate parameters to a manageable level. This article describes experiments from which we determine the rotationally inelastic-rate constants for $H^{35}Cl$ (v=1) in collisions with thermal HCl *directly* from the data, without the use of a simplifying model for the rate constant matrix. Our experimental approach makes use of a combination of stimulated Raman pumping to achieve rotationally-selective excitation of v=1 and mass-selective, resonantly-enhanced multiphoton ionization (REMPI) to detect the rotational levels that are subsequently populated by energy transfer. A non-mass-selective version of this technique has been previously applied in this laboratory to the study of rotational energy transfer in HD (v=1) and in H_2 (v=1).

The apparatus consists of two independent Nd:YAG/dye-laser systems and a two-section vacuum chamber. One section contains the source region of a simple time-of-flight mass spectrometer (TOF MS) into which HCl (1-30 mtorr) is admitted. This section is separated from the other section of the chamber by a metallic collimated-hole structure that maintains a large pressure differential while serving as a grounded extraction grid for the TOF MS. The rest of the ion-source region is defined by a stainless steel repeller plate that is 2 cm from the collimated hole structure and is typically held at +1000 V. Ions formed in the extraction region accelerate, pass through the hole structure, and then drift in a 40-cm-long field-free region in the high vacuum section before striking a dual-microchannel-plate ion detector. Stimulated Raman pumping of HCl v=1 is accomplished with the 532-nm Nd:YAG second harmonic and the dye-laser output (627-629 nm) from the first of the two laser systems. HCl parent and fragment ions are formed via 2+1 REMPI of HCl through the $E\,^1\Sigma^+ - X\,^1\Sigma^+$ 0-1 band *Q*-branch at 247-248 nm, and this radiation is generated with the second Nd:YAG/dye laser system by Raman shifting the doubled dye-laser output in hydrogen and taking the first anti-Stokes shift. The focused Raman-pumping laser beams are spatially overlapped with the focused ultraviolet REMPI laser beam at a point ~ 0.3 cm in front of the collimated hole structure. The REMPI laser beam is temporally delayed from those of the Raman pump lasers by a combination of digital-delay generator and coaxial-delay line.

A typical set of data for pumping J=4 in $H^{35}Cl$ is shown in Figure 1 where we display three REMPI scans of the E-X 0-1 transition as a function of the pressure-time delay product, $p\tau$. It is clear from the increasing population in the adjacent rotational states that the extent of rotational relaxation increases as $p\tau$ increases. Furthermore, the sensitivity of the REMPI process allows us to observe relaxation on extremely short collisional time scales. The largest $p\tau$ shown in Figure 1, 4.6-ns-torr, represents only 0.03-hard-sphere collisions for HCl. We have taken data similar to that shown in Figure 1 for pumping of J=1-6 of $H^{35}Cl$(v=1) and have calibrated the REMPI process against known Boltzmann populations in v=1 in order to determine empirical factors that allow us to convert REMPI line intensities into relative rotational populations.[1]

The rotational populations are governed by the coupled differential equations that describe rotational relaxation and are conveniently cast in the usual matrix formulation, $d\mathbf{N}/dt = \mathbf{N}\mathbf{K}\rho_0$, where the time rate of change of the populations is given in terms of an n-dimensional row vector of populations, **N**, the n by n-rate constant matrix, **K**, and the density of the collision partner, ρ_0. The elements of the rate constant matrix are the rate constants

*University of California at Santa Cruz.

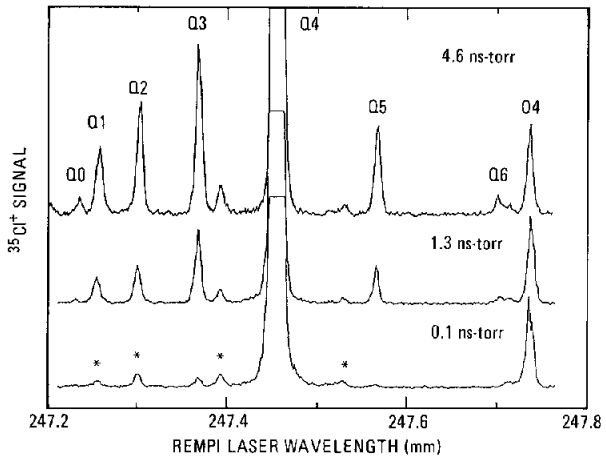

Figure 1. The 2 + 1 REMPI spectra of E $^1\Sigma^+$ - X $^1\Sigma^+$ 0-1 band taken after stimulated Raman pumping of v=1, J=4 for three different pressure time-delay products. Only the $^{35}Cl^+$ signal is monitored, and the spectra have been normalized to the Q(4) line. The asterisks in the lowest trace label the Q(0)-Q(3) lines of the V $^1\Sigma^+$ - X $^1\Sigma^+$ 6-0 band.

that describe energy transfer from J to J′-excited molecule, k(J→J′), and are sums and Boltzmann averages over the state-to-state rate constants for molecule-molecule collisions. This sum includes all rotation-translation (R-T) processes and rotation-rotation (R-R) processes. The solution to the relaxation equations is $\mathbf{N}(t) = \mathbf{N}(0)\exp(\mathbf{D}t)$, where **D** is a diagonal matrix containing the eigenvalues of $\mathbf{K}\rho_0$ and **N**(0) is the vector of initial populations. In practice, we assume that at time zero all the population resides in the pumped rotational level and then calculate the populations for each $p\tau$ (or equivalently $\rho_0\tau$) by diagonalizing $\mathbf{K}\rho_0$ to obtain **D**.

As the data in Figure 1 demonstrate, we observe a large number of rotational populations (typically up to $|\Delta J| = 3$) on very short collisional time scales. This allows us to fit our data to the rate-constant matrix directly, without the use of a model, because each population is almost entirely determined by a single element of the rate-constant matrix (i.e., one rate constant). We fit our complete data set using a nonlinear-least-squares algorithm in which the upward rate constants (J<J′) are variable parameters while the downward rate constants (J>J′) are determined by detailed balance. A representative comparison of the fit to the data for a series of J=2 experiments is shown in Figure 2. The fit to the data is good, with the final residuals typically being within the estimated experimental error. The poorest agreement between data and fit occurs for the smallest $p\tau$ value, 1.3 ns-torr, where our assumption of instantaneous pump and probe lasers may be invalid. The rate constants obtained from the fit to the complete data set are given in Reference 1.

We have compared our rate constants to previous measurements for HCl (v=1)[2] and HF(v=2)[3]. The previous study of HCl rotational relaxation seriously underestimates the importance

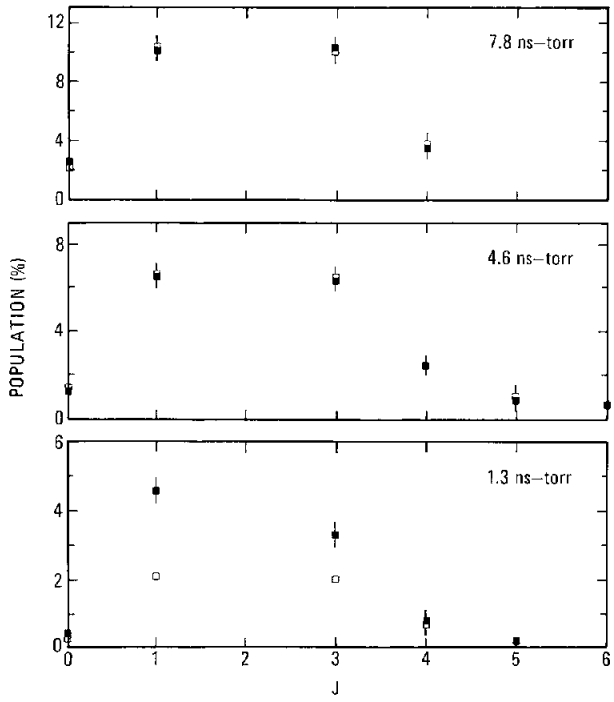

Figure 2. Comparison of the observed (filled squares with vertical error bars) and calculated (open squares) rotational populations (given as percentage of the total population) for the rotational relaxation of $H^{35}Cl$ initially pumped into v=1,J=2 at three different pressure time-delay products ($p\tau$). At each $p\tau$, the J=2 population is off scale; these values are 94.4%, 81.8%, and 71.6% for 1.3, 4.6, and 7.8 ns-torr, respectively.

of multiquanta transitions, producing rate constants that decrease far too quickly with increasing $|\Delta J|$. Also, the $H^{35}Cl$ (v=1) and HF (v=2) systems are remarkably similar. In both of these systems, rotational energy transfer is extremely facile with typical transfer rates that correspond to about five times the hard-sphere collision rate. In both systems, multiquanta transitions are very important, accounting for ~ 30% of the total depopulation rate. The relative largeness of rate constants for $|\Delta J| > 1$ transitions is undoubtedly due to the contributions of near-resonant multiquanta R-R processes.

Our $H^{35}Cl$ (v=1) rate constants cannot be reasonably described by models based solely on the energy gaps in the excited molecule, i.e., exponential gap or power law models. This is also true for HF(v=2)[3] and it appears that both HCl and HF are examples of polar molecule-polar molecule systems where rotational energy transfer cannot be described by a simple model based solely on energy defects. This is in stark contrast to the hydrogenic systems (HD and H_2) in which the exponential gap law does extremely well in describing the rotational energy transfer rates.

References:

1. E. A. Rohlfing, D. W. Chandler, and D. H. Parker, J. Chem. Phys. **87**, 5229 (1987).

2. F. Menard-Bourcin, T. Delaporte, and J. Menard, J. Chem. Phys. **84**, 201 (1986).

Translational Spectroscopy of Isocyanic Acid Photodissociation

In order to determine whether there is a barrier to dissociation in the photodissociation of the HNCO molecule, the velocity of the CO fragment was measured. This measurement confirmed that the appearance potential of NH + CO is indeed the dissociation threshold to within a few hundred wave numbers.

T. A. Spiglanin* and D. W. Chandler

We have recently measured the distribution of energy in rotation and vibration of the NH($a\,^1\Delta$) and CO($X\,^1\Sigma$) fragments produced by photodissociation of the HNCO molecule.[1-2] The rotational-state distributions of the fragments show that energy is not partitioned among the fragments statistically, but instead distributed by the impulsive nature of the dissociation. Analysis of the internal state distributions is based upon knowing the energy available to the fragments. For HNCO (isocyanic acid), we measured the threshold energy for forming NH($a\,^1\Delta$) from HNCO to be 41530 cm^{-1}, and, after determining that the NH($a\,^1\Delta$) contains little internal excitation near the photodissociation threshold, we concluded that this threshold is the dissociation energy.[1] It is possible that a barrier to dissociation exists, leading to a dissociation energy below the observed threshold energy. Because this would require dissociation dynamics that funnel virtually all of the energy available to the dissociation into translation, it seems unlikely. Nevertheless, this hypothesis needs to be investigated experimentally. We describe here our measurement of the kinetic energy released by photodissociation of HNCO.

In order to determine whether there is a barrier to dissociation, we measure the velocity of CO ejected by HNCO photodissociation using a form of multiphoton-ionization translational spectroscopy. This technique tags the CO fragment of HNCO dissociation by laser ionization immediately after photolysis. Because CO does not appreciably change mass when losing an electron, CO^+ travels the same path in a field-free region as the neutral would have. By looking at ions, we can detect fragments that arrive at a point in our apparatus with higher sensitivity than is possible for neutrals. We ionize CO state-selectively by using resonantly enhanced multiphoton ionization. The wavelength of the ionization laser specifies the internal energy of the CO photofragment that is ionized. We determine the kinetic energy of the CO($X\,^1\Sigma$) (and the total kinetic energy released in the dissociation) by measuring the time required for the photoproduced CO^+ to travel a fixed path-length in known potential fields.

Figure 1 shows time-of-flight spectra that result from several time delays following photodissociation of HNCO at 43460 cm^{-1} (230.1 nm) with detection of vibrationless CO in rotational states J = 0-5. Two distinct peaks appear in the spectra, and the separation between them increases as the delay between the photolysis-laser pulse and the extraction-voltage pulse increases. One of these peaks results from CO ions that travel initially toward the extractor and the other results from ions that travel initially away from the extractor. For delays of less than 2 μs, the separation between the two peaks is not resolved, but the overall width of the ion packet narrows as expected. Neither the shapes of these curves nor their absolute intensities depend strongly on the orientation of the electric vector of the linearly-polarized photolysis laser.

To interpret the results, we need to develop an algorithm to calculate arrival times for ions based on their initial positions and velocities and on the geometry of the apparatus. For these spectra, CO^+ results from the selective ionization of vibrationless CO in J = 0-5, corresponding to an average rotational energy of less than 30 cm^{-1}. Because the internal energy[2] of the NH($a\,^1\Delta$) is approximately 70 cm^{-1} following photodissociation at 43460 cm^{-1}, almost all of the energy in excess of the dissociation energy must reside in translation of the CO and NH fragments. We therefore assume that single-translational energy accounts for the data of Figure 1. Due to the thermal velocity spread of the room-temperature NHCO, any small velocity distribution corresponding to different internal states of the products is lost. We fit the data to a single kinetic energy. If our measured threshold energy[2] for dissociation (41530 cm^{-1}) is the dissociation energy, then the energy available to the photofragments is 1930 cm^{-1}. We would therefore expect a kinetic energy release of 1830 cm^{-1} to account for the data. If the

*Now with Aerospace Corporation, Los Angeles, CA.

threshold energy includes the effect of a barrier to dissociation, the kinetic energy release would exceed 1830 cm^{-1} by the height of the barrier to association. The smooth curves through the data of Figure 1 show the results of these calculations. By adjusting the assumed value of the kinetic energy released by the photodissociation in the calculations, we find the kinetic energy that best describes all of the observed spectra to be 1800 ± 200 cm^{-1}. This value agrees well with that calculated above from our measured threshold energy for the dissociation. We therefore conclude that the threshold energy for the dissociation equals the dissociation energy, within the uncertainty of our measurements.

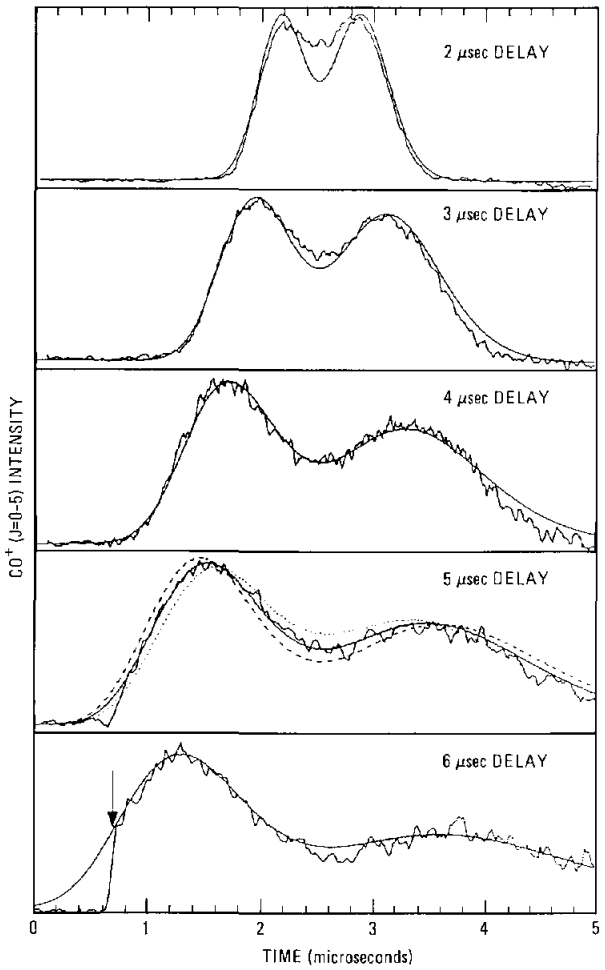

Figure 1. Translational spectra of CO (v=0, J=0-5) produced by photodissociation of HNCO at 43460 cm^{-1} for several delays between laser pulse and extraction-voltage pulse. The smooth curves through the data are calculated spectra based on a total kinetic-energy release of 1800 cm^{-1}. Agreement of this value with the previously measured threshold dissociation energy indicates that a barrier to dissociation probably does not exist. The dotted and dashed curves in the frame that displays the 5-μs data show the effect of decreasing and increasing (respectively) the value of the kinetic energy in the calculations by 300 cm^{-1}. The arrow in the bottom frame points to the minimum ion-arrival time imposed by the position of the repeller.

The agreement between the calculations with a total kinetic energy of 1800 cm^{-1} and the data of Figure 1 is quite good, the most obvious deviations occurring for the 2-μs delay. Based on the 1800-cm^{-1} energy, CO moves at an average speed of $7.3 \bullet 10^4$ cm/s away from the laser photolysis region. At a delay of 2 μs, the ion cloud has not expanded enough to make neglect of molecules moving away from the spectrometer axis a good assumption. These molecules contribute significantly to the ion signal and, because they have less kinetic energy along the spectrometer's axis, cause the separation between the two peaks to appear narrower than in the calculations. When the delay between photolysis and extraction is greater than 4 μs, neglecting fragments that move away from the spectrometer axis results in good agreement between the calculations and the data. The estimate of the kinetic energy of 1800 cm^{-1} results from the three calculations for 4-, 5-, and 6-μs delays and is fixed for the 2- and 3-μs calculations.

The curve for 6-μs delay exhibits a much sharper rise in ion intensity at short time (indicated by the arrow in Figure 1) than does any of the other curves. This behavior is not accounted for by the calculations. We can easily understand this effect by considering the origin of the ion signals. Fragments that initially move toward the extractor plate prior to the extraction-voltage pulse are accelerated by the potential field for a relatively short time prior to reaching the extractor. Ions that move in the opposite direction experience acceleration due to the extraction potential for longer times and achieve higher final velocities than do the other ions. These faster ions overtake the slower ions in the field-free drift region. Thus, ions that initially move away from the aperture arrive at the detector before ions that initially travel toward the aperture. The sharp rise in the 6-μs data of Figure 1 results from ions that move away from the extractor with sufficient velocity to impact the repeller plate before the extraction potential pulse occurs.

References:

1. T. A. Spiglanin, R. A. Perry, and D. W. Chandler, J. Chem. Phys. **87**, 1577 (1987); J. Chem Phys. **87**, 1568 (1987).

2. T. A. Spiglanin, R. A. Perry, and D. W. Chandler, J. Phys. Chem. **90**, 6184 (1986).

Hydrolysis and Hydrogen Isotopic Exchange Kinetics of Isocyanic Acid

The rate constants for the loss of (1) HNCO from the gas phase and the reactions of (2) HNCO + H_2O and (3) HNCO + D_2O were studied. The rate for (1) is second order with respect to HNCO, with a rate constant of 222 cm^3 mol^{-1} s^{-1}. The mechanism probably involves surface dimerization as the rate-limiting step. The rate constant for (2) is very small, but it is very large for (3), 2.0 x 10^4 cm^3 mol^{-1} s^{-1}.

L. R. Thorne, F. P. Tully, and A. E. Lutz

Isocyanic acid, HNCO, has been identified as an important chemical species in several combustion processes, and it is present in most combustion systems that contain H, N, O and C. Furthermore, HNCO is an important intermediate for the combustion of energetic nitramines such as RDX and HMX. Isocyanic acid also plays an important role in the production of NO during combustion,[1] and it has been added to engine exhaust streams to reduce NOx emission via the RAPRENOx process.[2] Because of its importance in combustion, a study has been initiated to elucidate the reactivity of HNCO toward other combustion species such as $O(^3P)$ and OH.[3] In that study, isotopically-labeled HNCO, i.e., DNCO (deuterated isocyanic acid), was used to determine that hydrogen abstraction is the dominant mechanism in the OH + HNCO reaction at elevated temperatures.

The present study was undertaken to estimate the lifetime of HNCO and DNCO in ongoing kinetics[3] and spectroscopic studies. Three reactions are important in the depletion of gaseous HNCO and DNCO: (1) condensation to a low-vapor pressure product (e.g., polymerization), (2) hydrolysis (HNCO + H_2O → products), and (3) isotopic exchange, in the case of DNCO.

In studies involving isotopically-labeled reactants to determine reaction mechanisms, it is imperative to know the initial concentration of the isotopically labeled species. In the case of DNCO, this may be a problem if the isotopic exchange with H_2O is rapid, because adsorbed water is notoriously difficult to remove entirely from most experimental apparata. Water may cause problems in another way if hydrolysis is rapid. Most combustion systems of practical importance contain water in high concentrations, and rapid hydrolysis could significantly deplete HNCO. In addition, hydrolysis may be important in the application of the RAPRENOx process in terms of delivering controllable quantities of HNCO and the fate of HNCO in the environment.

Isocyanic acid used in this study was prepared by the pyrolysis of cyanuric acid, $(HOCN)_3$, in a two-stage heater. Cyanuric acid was sublimed at 325°C in the first stage and cracked to HNCO at 450°C in the second stage. The pyrolysis products were trapped at 77 K and purified by trap-to-trap distillation. Deuterated isocyanic acid was prepared in the same fashion, but starting with $(DOCN)_3$ that was prepared from isotopic exchange with D_2O. Although the solubility of cyanuric acid is low in D_2O, exchange is quite facile because of its acidic hydrogens.

A BOMEM DA3.002 infrared spectrometer was used to measure the gas-phase concentrations of the various species of interest in this study. The sample cell consisted of a 2.8-cm-I.D., 10.5-cm-long Pyrex tube fitted with BaF_2 infrared transmitting windows. The cell was fitted with two greaseless (Teflon core) stopcocks that facilitated loading the sample. To one of the stopcocks was attached a small Pyrex neck which was loaded with water vapor for the hydrolysis and exchange experiments. Concentrations were determined from infrared absorbance spectra using spectral stripping whereby the absorbance of a sample is compared to that of a standard sample of known concentration. In this analysis, Beer's Law was assumed to hold, i.e., concentration is proportional to absorbance.

The hydrolysis and isotopic exchange kinetics of HNCO were studied in three experiments. In the first, the infrared cell was filled to 5 torr with HNCO, and the loss of HNCO was monitored for 8000 s by monitoring the absorbance of the ν_1 band near 3530 cm^{-1}. In the second experiment, the infrared cell was filled to 5 torr with HNCO, and after the first spectrum was acquired, H_2O vapor was admitted to the cell by opening the stopcock leading to the small neck containing the water vapor. The HNCO concentration was monitored for 3500 s. The third experiment was similar to the first, but D_2O was used in place of H_2O and the concentrations were monitored for 7000 s. The concentration

of DNCO was monitored by the absorbance of the ν_1 band near 2635 cm^{-1}.

The loss of HNCO as a function of time for the first experiment was fit to the second-order, integrated-rate law $1/[HNCO]_t - 1/[HNCO]_{t=0}$ using a nonlinear least-squares procedure. The rate constant and the initial concentration were used as adjustable parameters. The fit of the data to the second-order rate law is good, as indicated by the straight line in Figure 1. This implies that the gross kinetics follow the reaction 2HNCO → products. The slope of the line in Figure 1 is two times the reaction rate. Thus, the rate is 222(3) $cm^3\ mole^{-1}\ s^{-1}$, where the uncertainty is given in parentheses and refers to the last digit. Although the slope has an uncertainty of only 2%, the uncertainty of the reaction rate is more realistically 10 or 15% due to measurement errors in the pressure, unknown surface effects, etc. That the reaction is not third order in HNCO is confirmed by plotting $(1/[HNCO]_t)^2 - (1/[HNCO]_{t=0})^2$ *vs* time, which should give a straight line if the reaction is third order. The observed data fall on a curved line. These measurements confirm Perry's observation[4] that without an inert buffer gas, HNCO samples at pressures greater than 15 torr are rapidly depleted in HNCO. Dimerization would explain the observed second-order rate law, but three-body collisions would be necessary for gas-phase dimerization, and this would likely give a third-order rate law. Thus, the probable HNCO loss mechanism is surface polymerization of HNCO in which the reaction of two molecules of HNCO is the rate-limiting step.

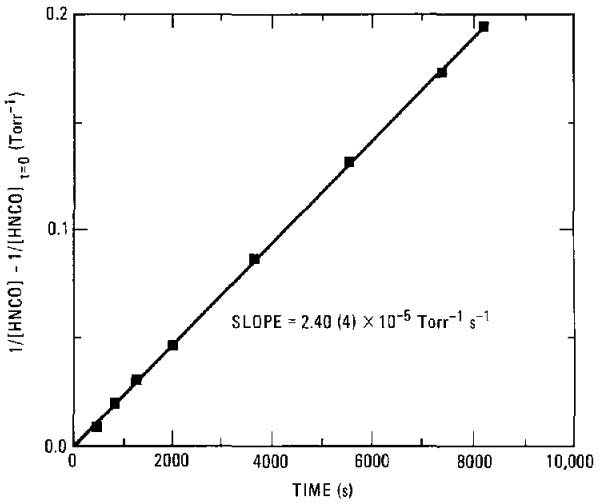

Figure 1. Reaction rate for HNCO → products. The reaction follows second-order kinetics as demonstrated by the close fit of the data (symbols) to a straight line. The slope of the line is 2.40×10^{-5} $torr^{-1}\ s^{-1}$, which is two times the reaction rate for the reaction 2HNCO → products. The rate for the reactions is 222 $cm^3\ mole^{-1}\ s^{-1}$.

Adding H_2O to the system reduces the HNCO loss rate. Extracting the second-order rate constant as before gives a value that is slower by a factor that is close to the mole fraction of HNCO in the HNCO-H_2O mixture (X_{HNCO} = 0.76, ratio of rates = 0.78). In light of the results of the previous experiment, this suggests that H_2O is displacing HNCO from the surface sites necessary for the dimerization.

When D_2O is added to the system, the loss of HNCO is more rapid because isotope exchange occurs in addition to the second-order loss of HNCO by polymerization. However, the sum of the HNCO and DNCO partial pressures follow a second-order rate law. The rate constant is close to the second-order rate for HNCO alone, but as with H_2O, it is reduced by a factor equal to the initial mole fraction of HNCO. The observed data were modeled using a kinetic reaction scheme that included second-order HNCO loss, DNCO production and loss, and (D,H)NCO and $(D,H)_2O$ isotope exchange. We obtain a rate from this analysis of 2×10^4 $cm^3\ mole^{-1}\ s^{-1}$ for the isotopic exchange reaction HNCO + D_2O → DNCO + HDO.

This study suggests that the surface-to-volume ratio should be minimized in any HNCO delivery system, and gaseous HNCO should be stored either at low pressure or with a buffer gas. Since the hydrolysis of HNCO is slow, delivering significant quantities to exhaust streams may not be a problem. However, because the isotopic exchange of hydrogen between water and HNCO is very fast, great care must be taken in studies involving DNCO so that it is not unknowingly depleted.

References:

1. R. A. Perry, J. Chem. Phys. **82**, 5485 (1985).

2. R. A. Perry and D. L. Siebers, Nature **324**, 657 (1986).

3. F. P. Tully, R. A. Perry, L. R. Thorne, and M. D. Allendorf, "Free Radical Oxidation of Isocyanic Acid," Twenty-Second Symposium (International) on Combustion (The Combustion Institute), submitted (1988).

4. R. A. Perry, private communication.

Free-Radical Oxidation of Isocyanic Acid

Laser-based kinetic studies of the reactions $O(^3P)$ + HNCO → Products (1) and OH + HNCO → Products (2) are described. The mechanistic implications of these results on the RAPRENOx process are discussed.

R. A. Perry,* F. P. Tully, and M. D. Allendorf

Isocyanic acid, HNCO, plays a role in nitric oxide (NO) formation during combustion[1] and facilitates NO removal from exhaust gas streams (RAPRENOx process).[2] Although we have proposed a reaction mechanism to explain NO reduction upon addition of HNCO to exhaust gases,[2] questions concerning the potential involvement of various oxidative processes remain. Specifically, detailed kinetic data on the reactions of $O(^3P)$ and OH with HNCO have been unavailable; these reactions may affect nitrous oxide formation during combustion and exhaust gas treatment via the radical intermediates NH and NCO. This study provides kinetic information needed in detailed modeling of nitrogen chemistry.

In order to evaluate the role that oxygen atoms will assume in the production or reduction of NO, we measured the absolute rate coefficient (k_1) for the reaction of $O(^3P)$ with HNCO as a function of temperature and pressure using a laser photolysis/NO_2 chemiluminescence technique. Three reactive channels are possible:

$$O(^3P) + HNCO \rightarrow NH + CO_2 \quad \Delta H = -43 \text{ kcal mol}^{-1} \quad (1a)$$

$$O(^3P) + HNCO \rightarrow HNO + CO \quad \Delta H = -38 \text{ kcal mol}^{-1} \quad (1b)$$

$$O(^3P) + HNCO \rightarrow OH + NCO \quad \Delta H = +7 \text{ kcal mol}^{-1} \quad (1c)$$

Reactions (1a) and (1c) are potential sources of N_2O due to the reactions of NH and NCO with NO, while reaction (1b) would lead to NO production.

We also measured the absolute rate coefficient (k_2) for the reaction of OH with HNCO as a function of temperature and pressure using the laser photolysis/laser-induced fluorescence technique. The potential importance of two reaction channels

$$OH + HNCO \rightarrow H_2O + NCO \quad \Delta H = -10 \text{ kcal mol}^{-1} \quad (2a)$$

$$OH + HNCO \rightarrow NH_2 + CO_2 \quad \Delta H = -32 \text{ kcal mol}^{-1} \quad (2b)$$

is addressed. Reaction (2a) could result in N_2O formation, and reaction (2b) would lead to more efficient NO removal through the NH_2 + NO reaction.

Pseudo-first-order rate coefficients, k', obtained in studies of reaction (1) at two temperatures are plotted in Figure 1. At 741 K, the argon pressure was varied by a factor of four and no change in the kinetics was observed. The bimolecular rate coefficients, k_1, determined from the slopes of the ([HNCO],k') data points are listed, along with their estimated overall uncertainties, in Table I. From these data we may generate the Arrhenius equation $k_1(T) = 5.4 \times 10^{-12} \exp(-10.3 \text{ kcal mol}^{-1}/RT)$ cm^3 molecule^{-1} s^{-1}. This expression should be used for semi-quantitative estimates only, since we measured k_1 at only two temperatures

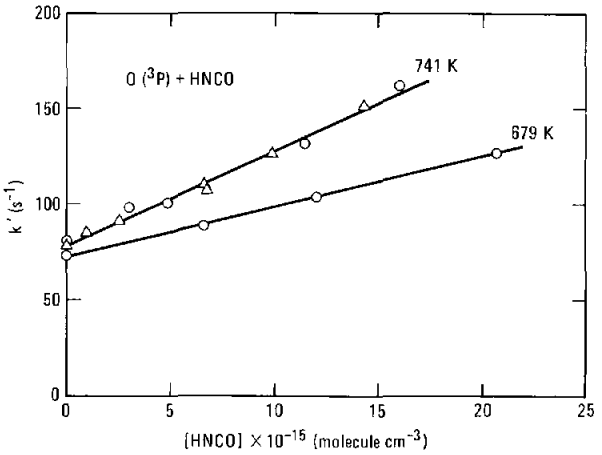

Figure 1. Pseudo-first-order rate coefficients k' measured at two temperatures in studies of the reaction $O(^3P)$ + HNCO → Products. ○, 200 torr argon; △, 50 torr argon.

Table I
k_1 as a function of temperature

Temperature (K)	k_1 (cm^3 molecule^{-1} s^{-1})
679	$(2.6 \pm 0.8) \times 10^{-15}$
741	$(4.9 \pm 1.5) \times 10^{-15}$

*Technor, Inc., 2374 Research Drive, Livermore, CA 94550

Figure 2 displays ([HNCO], k') data obtained at five temperatures in our kinetic study of reaction (2). Data for $k_2(T)$ obtained from best fits of the ([HNCO],k') data points are listed, along with their estimated overall uncertainties, in Table II. At one temperature, we made rate-coefficient measurements at two pressures, and within experimental error, we observed no change in k_2. We utilized all six data points to derive the Arrhenius expression $k_2(T) = (4.4 \pm 0.9) \times 10^{-12} \exp[-(5.54 \pm .28) \text{ kcal mol}^{-1}/RT] \text{ cm}^3 \text{ molecule}^{-1} \text{ s}^{-1}$. The data for $k_2(T)$ and the above Arrhenius representation are displayed in Figure 3.

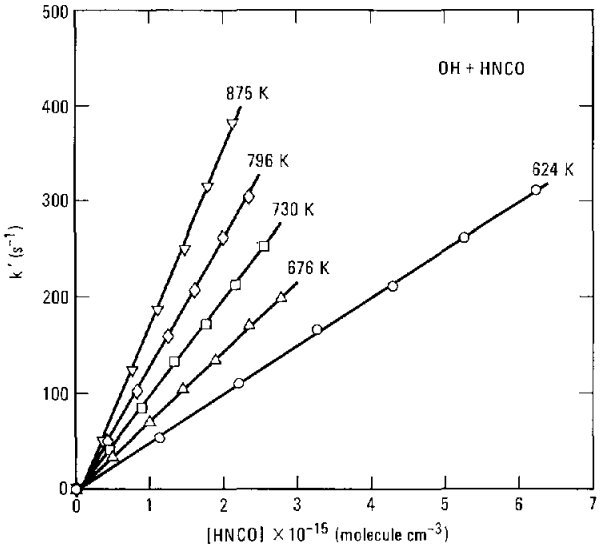

Figure 2. Pseudo-first-order rate coefficients, k', determined for the reaction OH + HNCO → Products. The diffusion contribution to the [OH] decays has been subtracted out from each reactive decay in accordance with previously described procedures.[3]

Table II
k_2 as a function of temperature and pressure

Temp. (K)	He press. (torr)	k_2 (cm^3 molecule^{-1} s^{-1})
624	750	$(5.02 \pm 0.33) \times 10^{-14}$
676	750	$(7.23 \pm 0.48) \times 10^{-14}$
730	750	$(1.00 \pm 0.07) \times 10^{-13}$
731	200	$(9.42 \pm 0.75) \times 10^{-14}$
796	870	$(1.33 \pm 0.10) \times 10^{-13}$
875	750	$(1.82 \pm 0.15) \times 10^{-13}$

In deriving a mechanism for the consumption of HNCO and NO using the RAPRENOx process,[2] reactions (1) and (2) were neglected relative to the reaction

$$H + HNCO \rightarrow NH_2 + CO \qquad \Delta H = -10 \text{ kcal mol}^{-1}. \qquad (3)$$

In view of the kinetics experiments described above, this assumption appears justified for reaction (1) but, in excess oxygen, it is inappropriate for reaction (2). In our experiments, we measured the rates of reactant disappearance but not those for product formation. The reaction of OH with HNCO could occur via either pathway (2a) or (2b). Unfortunately, theoretical calculations do not point conclusively to one channel or the other. If electrophilic addition is the dominant reactive channel, 1,3-hydrogen-atom migration must be fast relative to thermal decomposition of the HNC(OH)O adduct. If direct hydrogen-atom abstraction is most important, we would expect measurable quantities of N_2O to be formed in RAPRENOx experiments. Extensions of the present experiments aimed at definitively identifying the products of reaction (2) are in progress.

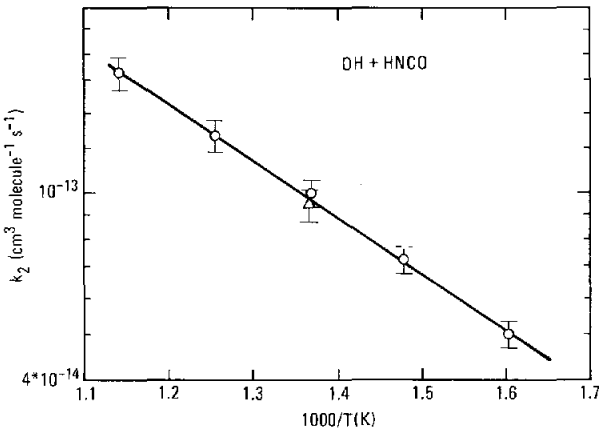

Figure 3. Absolute rate coefficients, k_2, determined for the reaction OH + HNCO → Products. ○, 750 torr He; Δ, 200 torr He.

References:

1. R. A. Perry, J. Chem. Phys. **82**, 5485 (1985).

2. R. A. Perry and D. L. Siebers, Nature **324, 657** (1986).

3. F. P. Tully, A. T. Droege, M. L. Koszykowski, and C. F. Melius, J. Phys. Chem. **90**, 691 (1986).

Study of Cyanogen-Radical Kinetics

A new apparatus has been constructed for the study of cyanogen-radical kinetics. Preliminary results demonstrate that the laser-photolysis/laser-excited-fluorescence technique used will produce highly-precise rate coefficients.

J. L. Durant and F. P. Tully

Chemical reactions of the cyanogen radical (CN) are important in a wide variety of combustion environments. In rich flames, large amounts of CN are produced by C + NO → CN + O, and CN is linked to HCN by the partial equilibration, H_2 + CN ↔ HCN + H. CN reactions provide a path for the conversion of fuel nitrogen to NOx. Additionally, CN is of considerable importance in understanding the chemistry of nitramines, an important class of energetic materials.

Despite their importance, there is a decided lack of kinetic data on CN-radical reactions, especially as functions of temperature and pressure. Perhaps the most important CN reaction is that with O_2. However, there is an almost complete lack of temperature-dependent data on this reaction; indeed, recent determinations of this rate coefficient at room temperature are scattered over a factor of 4. CN reactions with alkanes are reported to be very fast with negative temperature dependences near room temperature. It would be of great interest to characterize these reactions over a much broader temperature range. Also of combustion interest are the reactions of CN with H_2, O, NO, NO_2, N_2O and CO_2.

We have, therefore, undertaken the development of a laser-photolysis/laser-excited fluorescence (LEF) apparatus to study CN reactions. Building on earlier, highly successful studies of OH kinetics, this apparatus combines an excimer laser as a pulsed, photolytic radical source with an argon-ion laser-pumped cw dye laser for CN detection. Use of a cw laser for radical detection allows probing of the entire radical decay profile on each photolysis pulse. This greatly improves the duty cycle of the experiment, allowing routine collection of decays that are essentially noise-free.

We produce CN by laser flash photolysis, using an ArF excimer laser at 193 nm to dissociate C_2N_2. This provides a clean photolytic source of CN. We are able to operate comfortably with C_2N_2 pressures < 10 μ, where the reaction CN + C_2N_2 has a pseudo first-order rate coefficient, k', of less than 1 s^{-1}, while our reactions of interest have k' > 100 s^{-1}.

To monitor CN, we have chosen to use the B - X (0,0) transition, located at 25797 cm^{-1} (387.5 nm). The choice of the B - X system over the optically more accessible A - X system is necessitated by the 7 μs radiative lifetime of the A state, which would result in almost complete quenching of our LEF signal. The B state's shorter radiative lifetime of 61 ns ensures that the LEF signal is largely unattenuated by collisional quenching. However, the B - X (0,0) band is in a spectral region not conveniently accessed by cw laser sources. To remedy this situation, we are optimizing a standing-wave dye laser for use with the dye Polyphenyl 1, which has a reported lasing range of 362 - 412 nm.

Figure 1 shows a CN spectrum obtained by scanning the probe laser. The P and R branches of the (0,0) band can be seen extending to the red and blue of the band origin at 387.5 nm. Also clearly visible is the (1,1) band, which appears as the less intense lines within the (0,0) R-branch envelope.

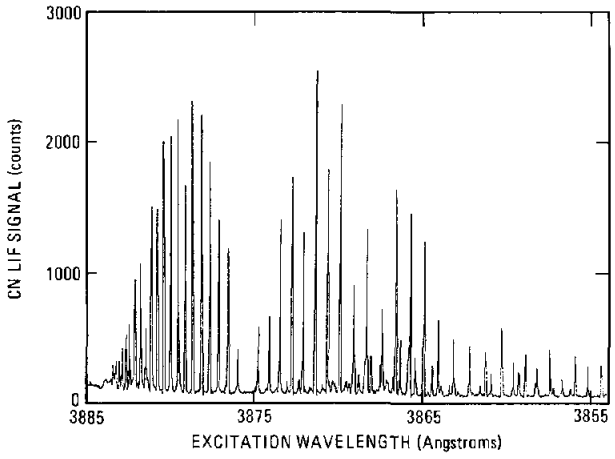

Figure 1. CN (B-X) transition at 387.5 nm probed using our cw Polyphenyl 1 dye laser.

Figure 2 shows a typical CN decay. The decay is well fit to a single exponential, and the extremely low levels of scattered light observed allow us to follow the decay for several 1/e lifetimes, making our rate determinations extremely precise. Application of this new, laser-based experimental configuration to CN-radical kinetic studies is under way.

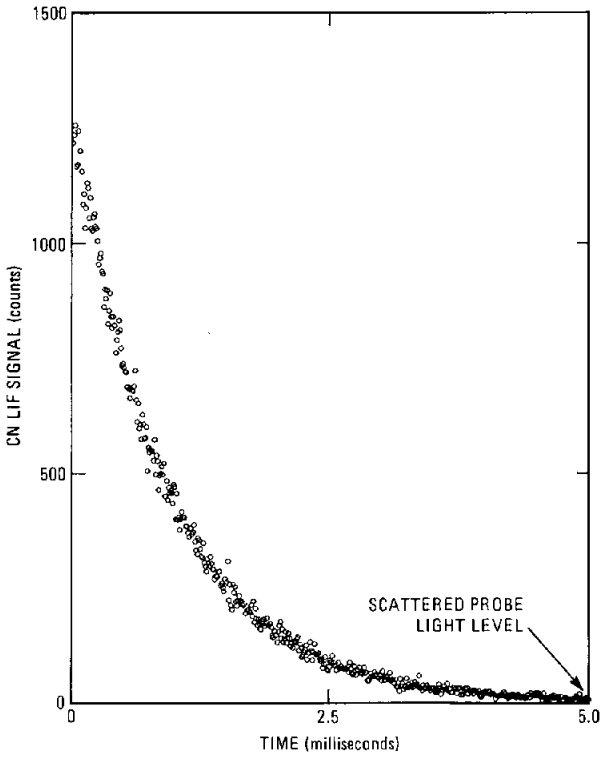

Figure 2. Typical CN decay curve observed following pulsed photolysis of $(CN)_2$ precursor. The decay is well fit by a single exponential and displays our extremely low scattered-light levels.

Hydrogen-Atom Abstraction by Hydroxyl-Radical From Ethene and 1-Butene†

Rate coefficients and kinetic isotope effects for hydrogen-atom abstraction reactions from ethene and 1-butene by hydroxyl radical are reported

F. P. Tully

Hydroxyl-radical reactions with unsaturated hydrocarbons are critically important in combustion and atmospheric chemistry. In previous work on the reactions OH + ethene and OH + propene, we showed that the reaction mechanisms change markedly with temperature. At T ≤ 500 K, electrophilic addition of OH to the alkene double bond, reaction (A),

$$OH + C_nH_{2n} \rightarrow HO \bullet C_nH_{2n} \qquad (A)$$

$$HO{\cdot}C_nH_{2n} \rightarrow OH + C_nH_{2n} \qquad (-A)$$

$$HO{\cdot}C_nH_{2n} \rightarrow \text{products} \qquad (B)$$

$$OH + C_nH_{2n} \rightarrow H_2O + C_nH_{2n-1} \qquad (C)$$

dominates the reaction mechanism. Both OH + ethene and OH + propene are pressure-dependent reactions at these temperatures because energized $HO \bullet C_nH_{2n}$ is stabilized by collisions with buffer gas. At temperatures between 500 and 650 K, the recombination/dissociation reactions (A,-A) approach chemical equilibrium on the millisecond time scale of the experiments, and the phenomenological OH disappearance rate decreases by a factor of 3-15 as the temperature is raised. This dimunition of net reactivity demonstrates that $HO \bullet C_nH_{2n}$ decomposes predominately via reaction (-A), but does not exclude a small contribution by channel (B). At T ≥ 650 K, rate coefficients increase as T is raised, because hydrogen-atom abstraction reactions (C) dominate the chemistry.

In this study, we report measurements of the absolute rate coefficients, k_1 to k_4, for the reactions

$$OH + C_2H_4 \xrightarrow{k_1} \text{products} \qquad (1)$$

$$OH + C_2D_4 \xrightarrow{k_2} \text{products} \qquad (2)$$

$$OH + 1\text{-}C_4H_8 \xrightarrow{k_3} \text{products} \qquad (3)$$

$$OH + 1\text{-}C_4D_8 \xrightarrow{k_4} \text{products} \qquad (4)$$

over the temperature range 650 - 901 K. These measurements represent only a portion of ongoing, exhaustive studies on reactions (1) - (4) that focus on quantifying the kinetics of the recombination/dissociation reactions (A,-A). Here we demonstrate that reactions (1) - (4) are dominated by H- and D-atom transfer processes [(C) and its deuterated analog] above T = 650 K. We compare our data with the high-temperature results of analogous reactions and we discuss the measured kinetic isotope effects k_1/k_2 and k_3/k_4.

We performed all experiments using the laser photolysis/laser-induced fluorescence experimental technique. Photodissociation of an OH precursor initiates chemical reaction in a heated quartz cell; laser-induced fluorescence quantifies the evolution of the reaction in time.

The absolute rate coefficients measured in this work are displayed as log $k_i(T)$ versus 1000/T in Figure 1. Over the temperature range of the experiments reported here, there is no evidence for the existence of curvature in the Arrhenius plots. Therefore, we performed nonlinear, least-squares fits of our kinetic data (weighted as $w_k = 1/\sigma_k^2$) to the two-parameter expression $k_i(T) = A_i \exp -(E_i/RT)$. The resulting best-fit expressions, represented by the solid lines in Figure 1, are, in the units cm^3 $molecule^{-1}$ s^{-1}, $k_1(T) = (3.36 \pm 0.64) \times 10^{-11} \exp -[(5955 \pm 287)$ cal mol^{-1} /RT], $k_2(T) = (5.85 \pm 1.54) \times 10^{-11} \exp -[(7816 \pm 407)$ cal mol^{-1} /RT], $k_3(T) = (3.74 \pm 0.63) \times 10^{-11} \exp -[(2217 \pm 243)$ cal mol^{-1} /RT], and $k_4(T) = (3.56 \pm 0.25) \times 10^{-11} \exp -[(2730 \pm 98)$ cal mol^{-1} /RT], where the stated error limits are 2σ values.

Although we did not monitor reaction products directly in this study, we offer the following strong evidence that the reported k_1 through k_4 describe the kinetics for H- and D-atom transfer reactions to OH. First, k_1 and k_3 were studied as functions of collisional environment between 650 and 900 K; diluent-gas identity (k_1 only) and pressure (k_1 and k_3) had no effect on the measured kinetics. Second, our ongoing studies of the kinetics of the recombination/dissociation equilibria prove that addition mechanisms will be largely unimportant above 650 K on the millisecond time scale of the

†Chemical Physics Letters **143**, 510 (1988).

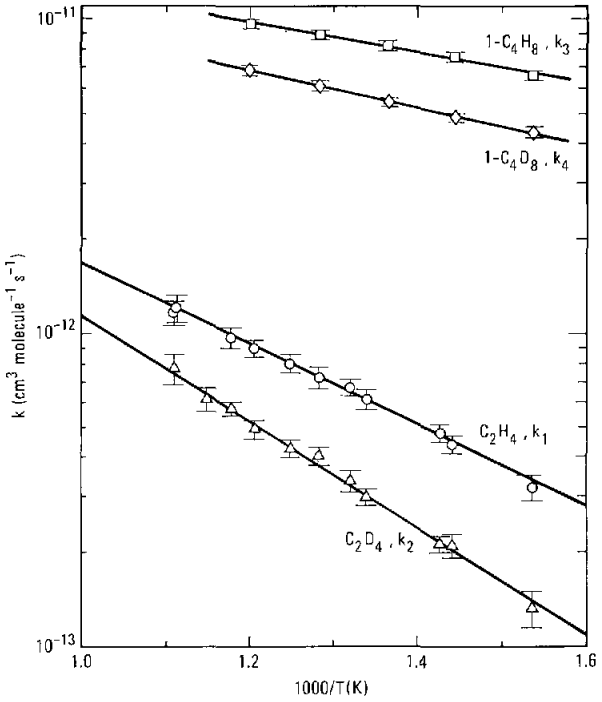

Figure 1. Arrhenius plot of kinetic data for reactions (1) - (4). The error limits represent ± 2σ estimates of the total experimental uncertainty.

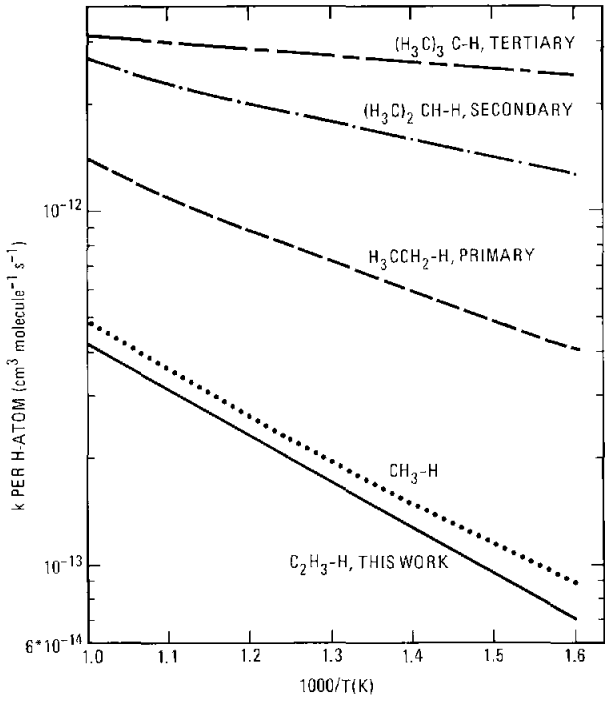

Figure 2. Absolute rate coefficient *per hydrogen atom* for abstraction of hydrogen atoms from hydrocarbons by OH. C-H bond strengths are given for each molecule. C_2H_3-H, 106 kcal mol^{-1}; CH_3-H, 105 kcal mol^{-1}; H_3CCH_2-H, 98 kcal mol^{-1}; $(H_3C)_2$CH-H, 95 kcal mol^{-1}; $(H_3C)_3$C-H, 93 kcal mol^{-1}.

present experiments. Third, as shown in Figure 2, the magnitude and slope of $k_1(T)$ *per hydrogen atom* are entirely consistent with corresponding site-specific, "abstraction only" rate coefficients determined previously in our OH-alkane kinetic studies. Finally, as displayed in Figure 3, the magnitudes of the kinetic isotope effects, $k_1/k_2(T)$ and $k_3/k_4(T)$, follow the emerging trend of larger k_H/k_D with increasing C-H(D) bond strength.

Several prior studies of reactions (1) and (3) have been published. While our measurements of $k_3(T)$ agree well with and extend previous determinations, our $k_1(T)$ values are *much lower* than those recommended in numerous reviews. For the experimental conditions of this study, abstraction reactions dominate the chemistry above 650 K, and new, chemically-sensible expressions for the kinetics are obtained. It would appear prudent to re-evaluate combustion models that include ethene production and consumption as reactive steps.

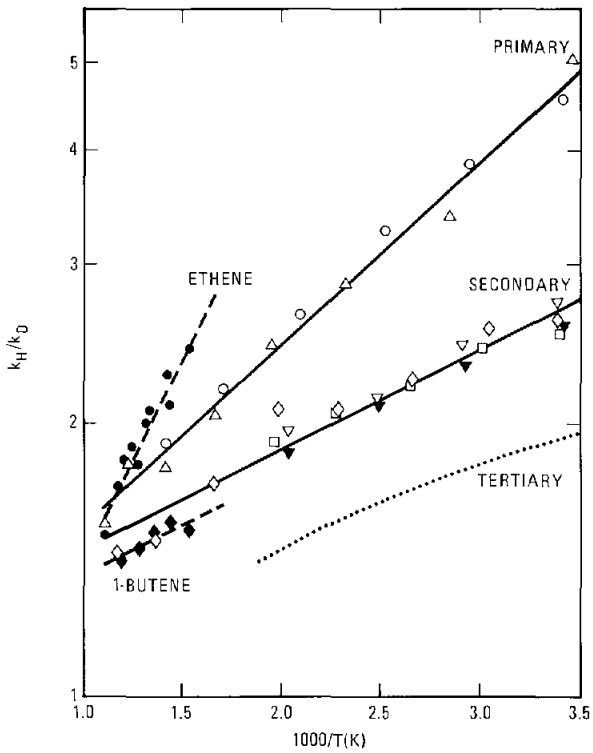

Figure 3. Kinetic isotope effect versus temperature for abstraction by OH from different types of C-H(D) bonds: ○, ethane; △, neopentane; ◊, propane; o, n-butane; ▽, cyclopentane; ▼, cyclohexane; ..., isobutane; ◆, 1-butene, this work. Bond strengths for primary, secondary, and tertiary C-H sites may be grouped at 98, 95, and 93 kcal mol^{-1}, respectively.

A Theoretical Analysis of the Reaction Between Hydroxyl and Acetylene

A detailed theoretical analysis, based on quantum-chemical and statistical-mechanical calculations, is given for an important combustion reaction.

J. A. Miller and C. F. Melius

The reaction between hydroxyl and acetylene is problematic in combustion modeling. No consistent set of rate coefficients, or even a clear determination of the dominant product channel, has emerged from experiments at temperatures of direct interest in combustion. Almost all high-temperature determinations are indirect, involving a complex analysis of flame or shock tube data. Only recently have limited data been obtained directly for T > 1000 K. Low-temperature measurements are dominated by the pressure-dependent addition reaction, which is insignificant under most combustion conditions. Various sets of products have been proposed for the high-temperature reaction, although CH_2CO (ketene) + H and $C_2H + H_2O$ are most prevalent. The product distribution is potentially important in determining the rate of growth of higher hydrocarbons in rich flames.

In the present investigation, we have used potential-surface parameters based on BAC-MP4 calculations and statistical-theoretical methods to calculate rate coefficients for the following reactions:

(a) $OH + C_2H_2 \xrightarrow{k_a} C_2H + H_2O$

(b) $OH + C_2H_2 \xrightarrow{k_b} HOC_2H + H$

(c) $OH + C_2H_2 \xrightarrow{k_c} CH_2CO + H$

(d) $OH + C_2H_2 \xrightarrow{k_d} CH_3 + CO$

and the high-pressure limit of the addition reaction,

$$OH + C_2H_2 \xrightarrow{k_\infty} C_2H_2OH.$$

Three levels of approximation are used in the statistical-theoretical treatment:

i) canonical theory, CT, (no energy or angular momentum conservation and no tunneling);

ii) microcanonical/J-conservative theory, μJT, (conserves both energy and angular momentum); and

iii) microcanonical/J-conservative theory with one-dimensional tunneling, μJT-T.

Our calculations show that, in the absence of collisional stabilization, the ketene channel (c), considerably enhanced by tunneling through the barrier to the 1,3 hydrogen transfer, is dominant at low temperature, whereas the abstraction (a) and the exchange reaction (b) dominate at high temperature. However, at 500 K, $k_t < 10^{-3} k_\infty$ where $k_t = k_b + k_c + k_d$ (k_a is negligible at 500 K). This result agrees with the conclusion of Perry and Williamson that there is no significant "zero-pressure intercept" at low temperature.

In Figure 1, we compare our calculations for k_a and k_t with several experimental results. All the experimental rate coefficients in Figure 1 can be identified with either k_a or k_T, where $k_T = k_a + k_t$ ($k_T \approx k_a$ at temperatures of interest in Figure 1). The agreement between theory and experiment is very good, particularly considering the disparity among the experiments themselves. We find particularly good agreement of the theory with the experiments of Fenimore and Jones (FJ), and Smith, Fairchild, and Crosley (SFC).

In Figure 2, we compare our theoretical predictions for k_b and k_t with several experimental rate coefficients that are not k_a, identified by the experimenters as probably k_c. We get good agreement with the experiments of Bittner and Howard (BH); in fact, the agreement can be made almost perfect with a very modest adjustment to the potential-energy barrier governing k_b. Our principal products, however, are different from those suggested by Bittner and Howard. The discrepancy of the theory with the other experiments in Figure 2 is far beyond what we would expect from errors in the theory.

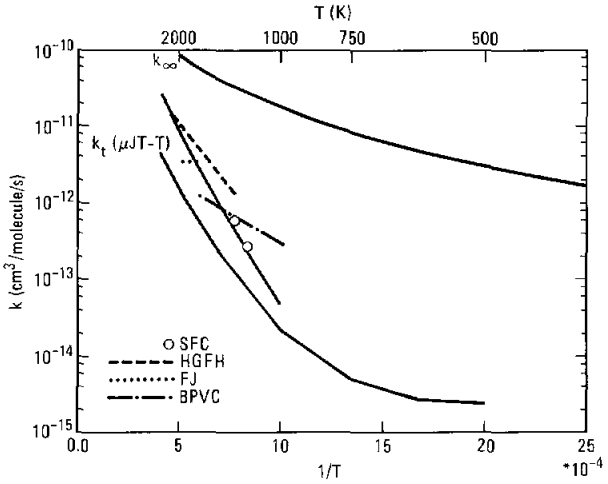

Figure 1. Comparison of theoretical and experimental results for the reaction OH + C_2H_2. All the experimental results are for k_a or k_T, where $k_T = k_a + k_b + k_c + k_d$.

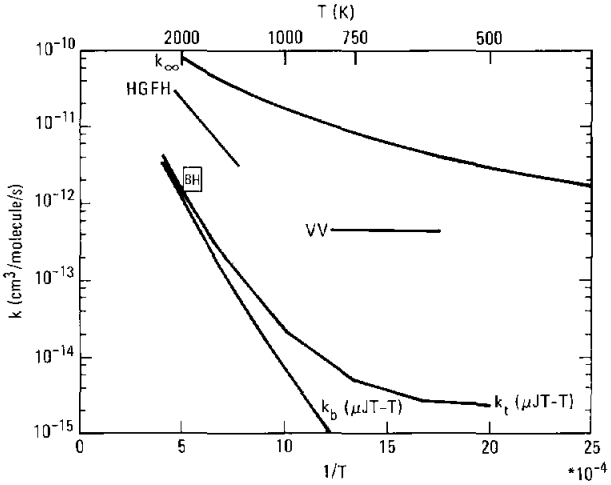

Figure 2. Comparison of theoretical and experimental results for the reaction OH + C_2H_2. All the experimental results were attributed by the experimenters to k_c, the CH_2CO + H channel.

Semiclassical Calculation of Vibrational Spectra Using *Ab Initio* Electronic Structure Energies†

A new method, coupling semiclassical dynamics and quantum chemistry, has been developed for the study of vibrational spectra, and it has been applied to ozone.

M. L. Koszykowski and C. M. Rohlfing

We report the application of a new method in semiclassical dynamics to a grid of accurate *ab initio* potential energy points. This technique uses the points directly and involves no empirical fitting in order to extract the dynamics results. We also investigate the semiclassical correspondence to chaos by demonstrating that previous results showing chaotic motion near the bottom of the ozone (O_3) well are incorrect. For the first time, we have a reliable method for analyzing initial and final conditions in polyatomic scattering calculations.

We have previously[1] developed and tested a method for obtaining dynamical information directly from discrete points on a potential energy surface. The method uses a spline under tension to locally develop an analytical representation of the surface which is smooth and has continuous derivatives. The use of tension eliminates problems with ringing that have plagued other attempts to use points directly and many analytic fits. For a multidimensional Morse oscillator, the method produces results accurate to 0.0001%. The method is then a useful tool for testing the quality of electronic structure calculations since there is no artistic alteration of the points, which is present in every fit surface. This study employs the tense spline method, combined with our well-known spectral analysis method,[1] to examine the stretching vibrations of O_3 on two different potential energy surfaces.

The surfaces for O_3 were obtained as follows: First, a grid of points corresponding to O-O bond lengths in the range of 1.21 - 1.39 Å was chosen. The bond angle was fixed at 116.5°. Second, a standard double-zeta-plus-polarization basis set was employed to calculate *ab initio* energies for each geometry. Third, two quantum chemical techniques that account for electron correlation were selected for evaluating the total energy. The first is Møller-Plesset perturbation theory through fourth order (MP4), and is based on a single reference, the self-consistent-field (SCF) wavefunction. The second method is a type of multi-configurational SCF known as complete-active-space (CAS) SCF. Ozone is a molecule for which the single reference approximation is inadequate because there are two dominant configurations necessary to properly describe the bonding. Thus it is expected that the surface generated by the MP4 method will be inferior.

Classical trajectories were run on these grids of points corresponding to initial conditions of $n_1 = 1/2$, $n_2 = 0$ and $n_1 = 0$, $n_2 = 1/2$. These trajectories are the classical correspondence rule analogues to the (0,0)-(1,0) and (0,0)-(0,1) transitions in spectroscopy. The transition frequencies are obtained by calculating the relevant correlation function and from linear-response theory; the Fourier transform of the time correlation function is the spectrum. A sample trajectory is shown in Figure 1. This is clearly a quasi-periodic trajectory at these low

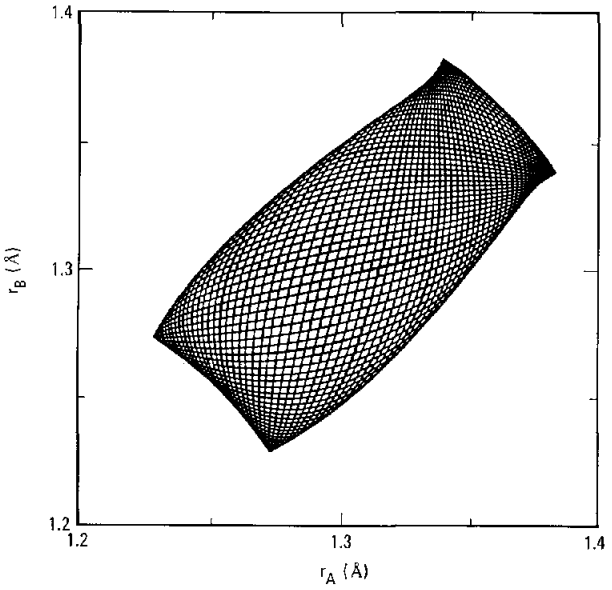

Figure 1. A trajectory for the symmetric stretch of O_3 (where r_A and r_B are the two oxygen-oxygen bond distances), based on the CAS surface. The trajectory is quasi-periodic and was used to obtained the semi-classical vibrational spectra.

†Chemical Physics Letters **142**, 67 (1987).

energies, as expected. It is interesting to note that the method used here does not give rise to chaos near the bottom of the well, a problem present in every previous polynomial fit to a vibrational surface.

The frequencies are listed in Table I. It is evident that the MP4 results are in much worse agreement with experiment than the CAS results, as expected. It would be interesting to use points generated from a calculation including electron correlation beyond the CAS level. However, this is not computationally feasible at present for O_3, so we have begun a similar and more extensive study on H_2O.

Table I
Theoretical and Experimental Stretching Frequencies for O_3

Transition	MP4	CAS	Expt.
1,0	985	1020	1042
0,1	1340	1060	1103

Reference:

1. M. L. Koszykowski, G. A. Pfeffer, and D. W. Noid, *Chaotic Phenomena in Physics and Astrophysics* (Academy of Science, New York, NY, 1987), p. 173.

Rich Acetylene Flame Chemistry

Experimental observations of progressively richer acetylene-oxygen flames are providing insight into the mechanisms of formation of soot precursors.

J. V. Volponi, J. L. Durant, and G. A. Fisk

Understanding soot formation is of great technological importance. Obviously, combustion processes should be tailored to prevent the release of soot into the environment. Less obvious, however, are the benefits of soot formation within a flame. Incandescence from soot particles provides most of the light associated with flames; the presence of soot also strongly enhances heat-transfer rates in many combustion systems. The problem is to understand soot sufficiently well that we can use it to our advantage without being harmed by it.

The formation of small, unsaturated hydrocarbons is important in the formation and growth of soot. Soot formation is posited to begin with the attack of the C_2H radical on acetylene to form diacetylene. Further additions of C_2H and C_2H_2 form progressively higher-molecular-weight hydrocarbons, eventually leading to soot. Detailed knowledge of the formation mechanism is the focus of investigations now underway in our flame-chemistry laboratory. Working with a series of progressively richer acetylene-oxygen flames, we are measuring concentration profiles of stable flame products and of intermediates such as diacetylene and several radicals. These measurements, coupled with parallel computational modeling, are shedding light on the kinetics of formation of soot precursors.

The low-pressure flame apparatus we use consists of a 9.7-cm-diameter, premixed, flat-flame burner housed in a vacuum chamber maintained at 25 torr. Stable gas species are sampled through a quartz microprobe attached to a differentially-pumped quadrupole mass spectrometer operating in a chopped-beam mode. Concentration profiles are obtained by translating the burner vertically relative to the microprobe. We use the deuterium scavenging technique developed in this laboratory to measure radical species profiles (H, OH, O, C_2H, and CHO). Laser-excitation spectroscopy (LES), using a frequency-doubled, excimer-pumped dye laser, is employed to measure OH and CH concentration profiles. We also use the LES spectra to determine the flame temperatures, because thermocouples are not suitable for use at the high temperatures and radical concentrations encountered in this work.

Figure 1 shows the concentration profiles obtained with the mass spectrometer for selected species found in three acetylene-oxygen-argon flames of equivalence ratios 1.0, 1.66, and 2.0. Figure 2 shows the profiles obtained by LES for the radical species CH and OH in the same flames. As the equivalence ratio increases (i.e., the flames become richer), the concentration profiles of the products change systematically. Specifically, the CO concentration increases as the flames become richer due to the decrease in OH concentration and the resulting slowing of the reaction of OH with CO to form CO_2. Also, more CH and C_2H are seen over a wider range of flame positions as the flames become richer. The diacetylene concentration profiles show the expected increase in maximum concentration as the flames approach the sooting limit.

Comparison of our experimental concentration profiles with those from a parallel program to model these flames is enhancing our understanding of soot formation. We are now ascertaining the reactions responsible for the formation and destruction of diacetylene. Our next goal is to determine how aromatic rings are formed.

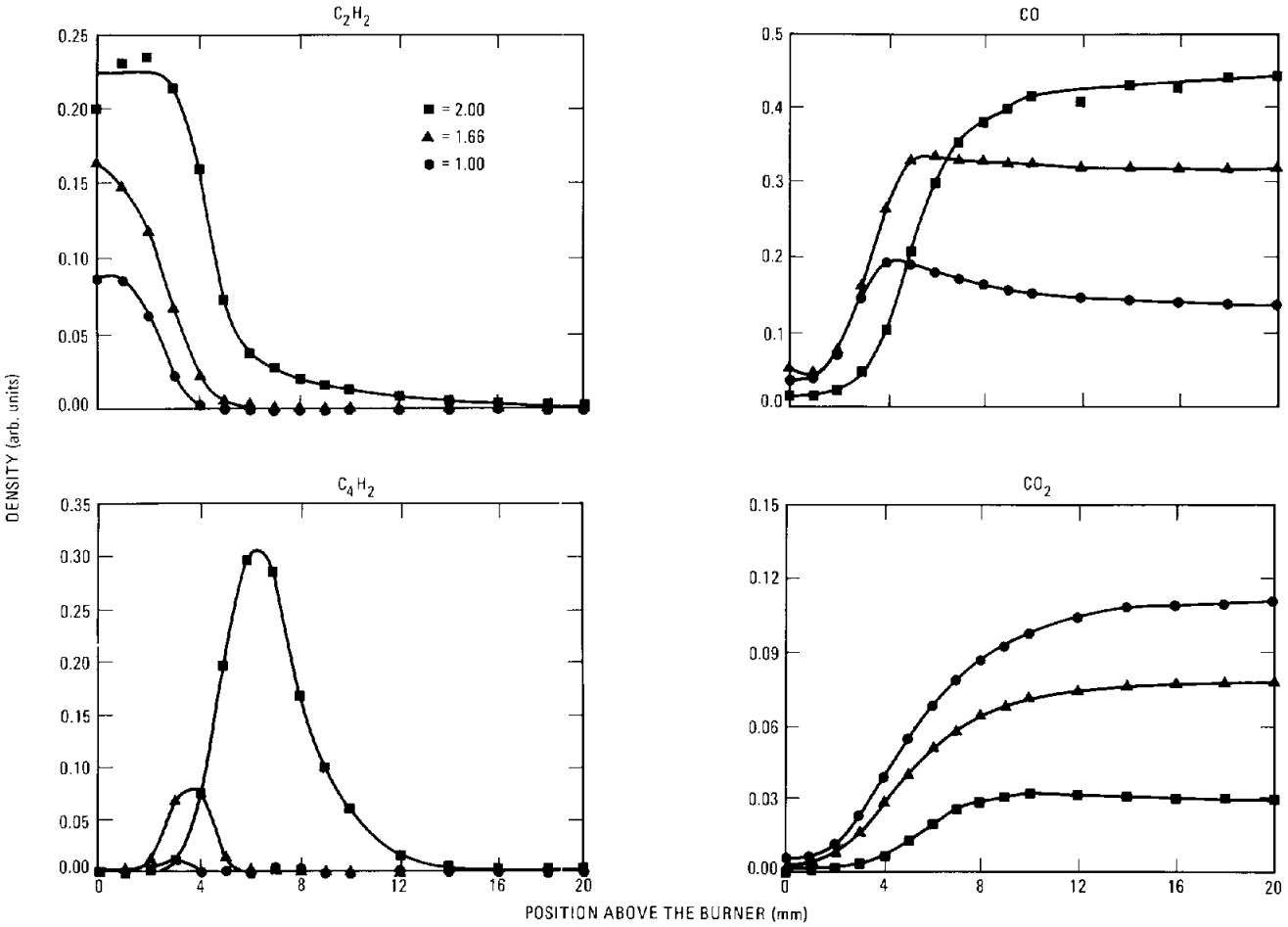

Figure 1. Concentration profiles for C_2H_2, CO, C_4H_2, and CO_2 found in three C_2H_2-O_2/argon flames of equivalence rations 1.0, 1.66, and 2.00. These species profiles are determined by mass spectrometric analysis.

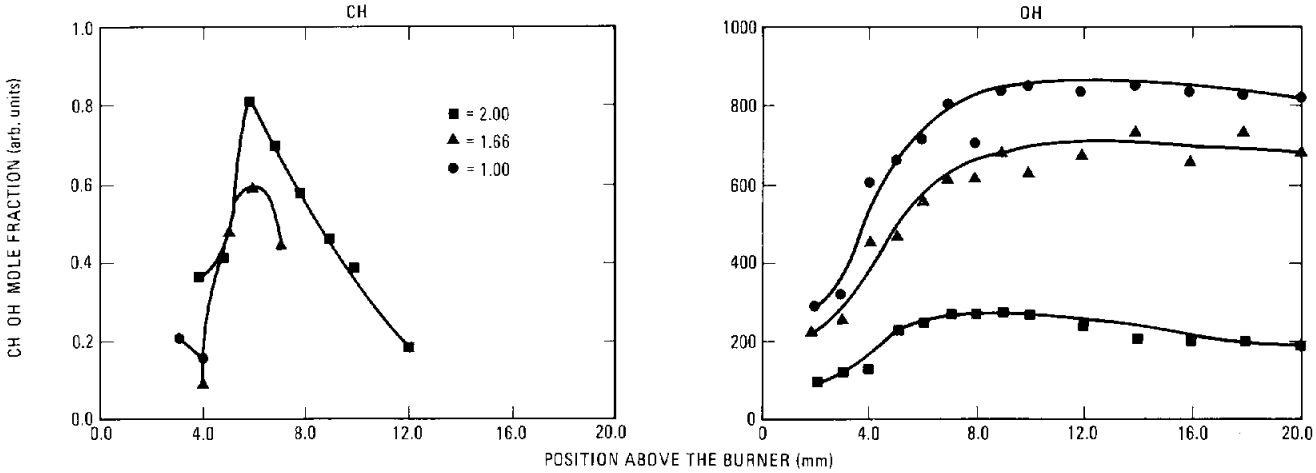

Figure 2. Concentration profiles for CH and OH found in three C_2H_2-O_2/argon flames of equivalence ratios 1.00, 1.66, and 2.00. These radical species profiles are determined by LES analysis.

Theoretical Characterization of the Minimum Energy Path for the Reaction $H + O_2 \rightarrow HO_2^* \rightarrow HO + O$[†]

The minimum energy path for the reaction $H + O_2 \rightarrow HO_2^* \rightarrow HO + O$ has been accurately characterized using state-of-the-art quantum chemical techniques.

C. M. Rohlfing, S. P. Walch,* C. F. Melius, and C. W. Bauschlicher, Jr.*

The potential energy surface for the important combustion reaction

$$H + O_2 \rightarrow HO_2^* \rightarrow HO + O$$

has been characterized in the vicinity of the minimum energy path using highly correlated *ab initio* quantum chemical calculations. Previous theoretical treatments of lesser accuracy have predicted a small barrier for H atom addition, and no study has yet examined the HO + O portion of the potential energy surface.

Atomic natural orbital basis sets are employed in the present work. Such a basis is optimal for describing atomic electron correlation and is quite flexible for molecular calculations. The O and H basis sets are (13s8p6d4f)/[4s3p2d1f] and (8s6p4d)/[3s2p1d], respectively. For the reaction surface, the electron correlation treatment requires an extension beyond a single reference such as the self-consistent-field (SCF) wave function. In a localized orbital description, it is obvious that several references are needed to adequately describe reactants, transition state, and products. The approach used here is a type of multi-configurational SCF known as complete-active-space (CAS) SCF, which can smoothly describe orbitals over the course of the reaction. The final wave function consisted of a contracted configuration interaction (CCI) treatment based on a 240-configuration CAS reference.

Properties of the potential energy surface are listed in Table I, and the agreement with experiment is excellent. A very small barrier (0.4 kcal/mol) for H atom addition to O_2 is found. The recombination of OH and O is complicated by the long-range interaction between the OH dipole moment and the O atom quadrupole moment. This electrostatic interaction dominates at O-O separations greater than 6.0 a_0, while formation of an O-O chemical bond dominates at shorter O-O separations due to a surface crossing. A shallow well (1.0 kcal/mol) at $r_{OO} = 6.0\ a_0$ and a small barrier (0.5 kcal/mol) at $r_{OO} = 5.5\ a_0$ are found.

Along the CCI minimum energy path, multi-reference configuration interaction calculations were performed in the same basis in order to further refine the energetics. These computations show essentially no barrier (0.1 kcal/mol) for the addition of an H atom to O_2. The calculated energies are increased to 53.9 and 11.2 kcal/mol for Δ_e (H-O_2) and $\Delta E_{reaction}$, respectively, in better agreement with experiment.

Table I
Potential Energy Surface Properties for the Reaction $H + O_2 \rightarrow HO_2^* \rightarrow HO + O$[a]

Property	Calc.	Expt.
$\Delta E_{barrier}$ 0.4	<0.2	
De(H-O_2)	53.1	54.6 ± 0.6
$r_{OH}(HO_2)$	1.840	1.846
$r_{OO}(HO_2)$	2.520	2.523
$\measuredangle(HO_2)$	104.4	104.1
ω_1	3508	3414
ω_2	1557	1389
ω_3	1111	1101
D_e(HO-O)	63.2	68.3 ± 0.6
$\Delta E_{reaction}$ 10.1	13.6	

[a]Energies in kcal/mol, bond lengths in a_0, angles in degrees, and frequencies in cm^{-1}.

[†]Journal of Chemical Physics (1988), in press.

*NASA Ames Research Center, Moffett Field, CA.

Simultaneous measurements of major species concentrations using Raman scattering and OH radical concentration with laser-induced fluorescence are performed in the Turbulent Diffusion Flame Facility. The Diana flashlamp-pumped dye laser (green beam) is used for the Raman scattering measurements, and a frequency-doubled, Nd:YAG-pumped dye laser (red beam fundamental) is used for the fluorescence measurements.

Reacting Flows

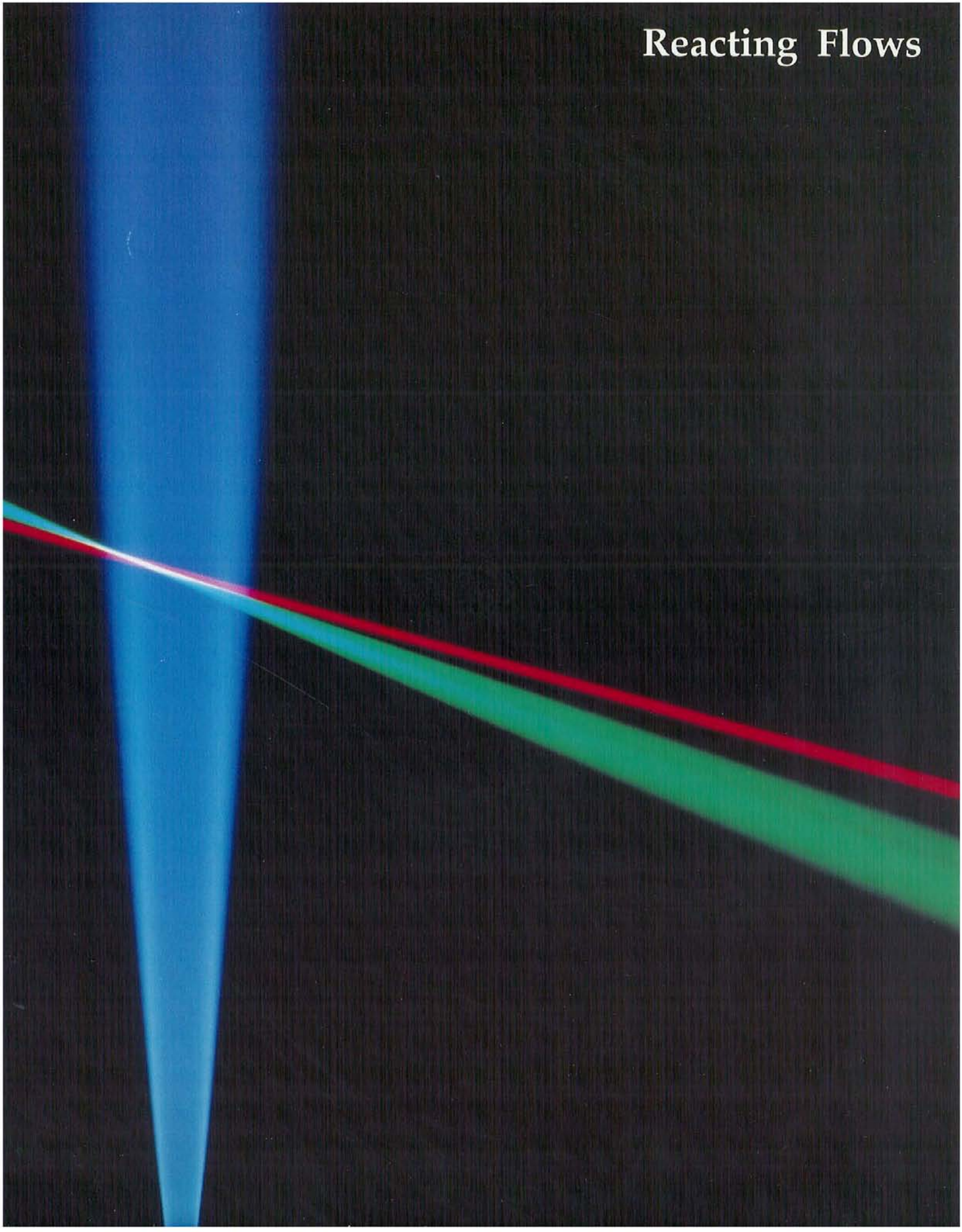

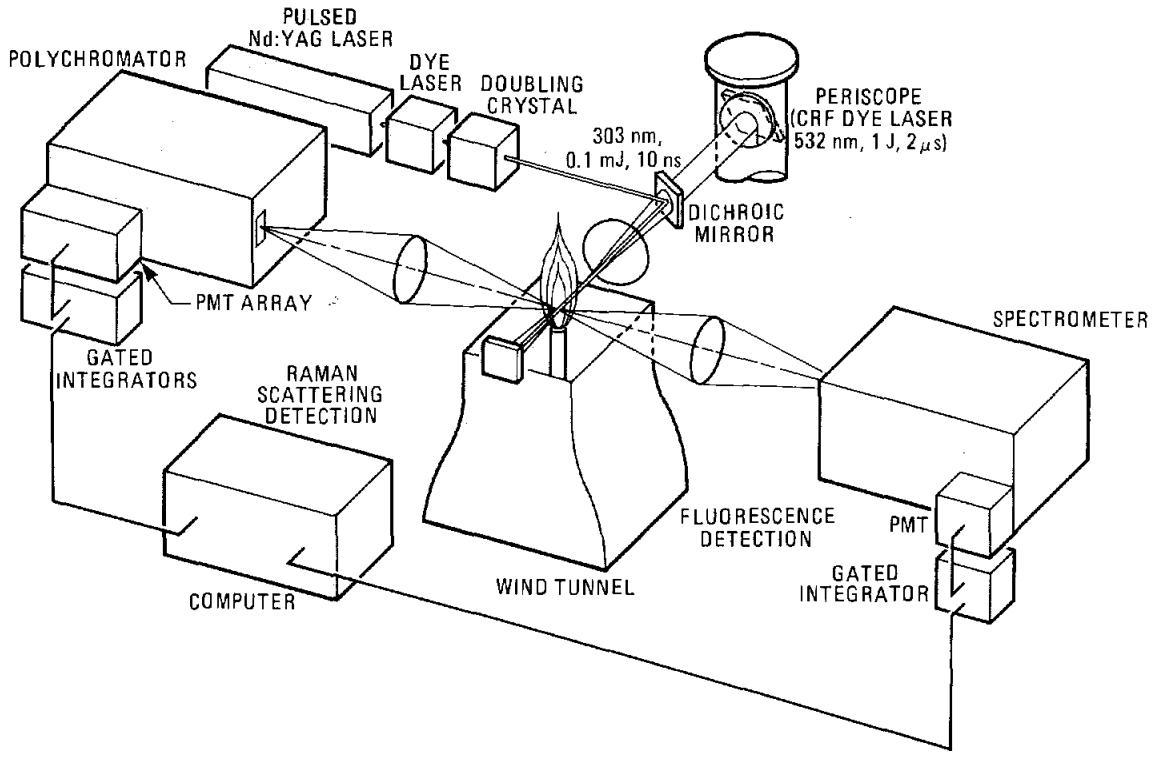

The experimental apparatus for simultaneous acquisition of spontaneous Raman scattering and laser-induced fluorescence (LIF) data is depicted schematically. Collinear laser beams from the Diana facility dye laser and a Nd:YAG-pumped, frequency-doubled dye laser are propagated through a turbulent diffusion flame. Raman scattering from the Diana beam is collected using a spectrometer and an array of photomultiplier tubes; flame temperature and major species concentrations are calculated from the observed signals. The frequency-doubled dye laser is tuned to an OH resonance, and the resulting fluorescence signal is collected by a separate spectrometer and photomultiplier system. OH concentrations are calculated after the fluorescence data are corrected for quenching; quenching rates are calculated from the Raman scattering data.

Section 4
Reacting Flows

A multidisciplinary program in reacting flows establishes an important link between fundamental studies of combustion chemistry and the "real" world of practical combustion. The objective of the program, which is sponsored by the Division of Chemical Sciences in the Department of Energy's Office of Basic Energy Sciences, is to use experimentation and computer modeling to increase our understanding of the fundamental interactions between chemistry and fluid dynamics in chemically reacting flows. Research results will be used to improve predictive capabilities for turbulent combustion of hydrocarbon fuels. Experimental studies include flows involving complex fluid mechanics but simplified chemistry; these flows are used to probe primary turbulent transport mechanisms. Studies of flows with complex chemistry but simplified fluid mechanics help identify combustion mechanisms responsible for the formation and growth of soot. Concomitant modeling studies employ stochastic approaches to predict turbulent flow quantities and deterministic approaches to predict unsteady flame structure and effects of flow fields on soot growth and transport.

An important element of the experimental program is the development of new laser diagnostic techniques capable of imaging portions of the flow field in a temporally-resolved manner. These diagnostics make it possible to obtain two-dimensional measurements of major and minor chemical species and velocity during time scales that are short compared with the characteristic chemical or fluid dynamical time scales involved in combustion. Obtaining such measurements at high frequency makes it possible to follow the temporal development of unsteady reacting flows.

Regular workshops are held with scientists from universities and industry who are involved in the fundamental aspects of reacting flow research. These meetings provide a forum for information discussion of new developments and research opportunities in the field.

Scalar Dissipation Measurements in the Developing Region of a Jet†

Scalar dissipation (square of the scalar gradient) was derived from the methane mass fraction (scalar) images taken in the developing region of an isothermal jet. These results were used to test some common stable- and lifted-flame modeling assumptions such as isotropy and lognormality of the scalar dissipation, and statistical independence of the scalar and scalar dissipation.

M. Namazian,* R. W. Schefer, and J. Kelly*

Scalar dissipation (χ) is an important parameter in turbulent combustion modeling. In Bilger's[1] conserved scalar formulation of nonpremixed flames, scalar dissipation is a multiplying factor on the diffusion term. In Peters'[2] flamelet model, scalar dissipation enhances diffusion and determines the rate of the stretch of the laminar flames imbedded in the turbulent flow. In these and other models, some common modeling assumptions are utilized that are untested. In developing a model for lifted diffusion flames, Peters and Williams[3] assumed statistical independence between the scalar and χ, and employed a lognormal conditional pdf (probability density function) for χ at the stoichiometric surface. Their predicted burner liftoff heights are sensitive to the assumed functional form of the scalar and χ pdfs and their correlation. There is insufficient data to properly define these forms, especially near the jet exit where liftoff occurs.

In an attempt to provide data and test these common modeling assumptions, the instantaneous planar images of CH_4 mass fraction in the developing region of an isothermal jet flow were used to obtain instantaneous, mean, standard deviation, pdf, and correlations for χ and the scalar. The lognormality of the scalar dissipation pdf is tested for unconditioned χ and also for χ at the stoichiometric surface where the reaction occurs. The concentration images were obtained by simultaneously collecting Raman-scattered light with two cameras oriented perpendicular to a thin sheet of laser light passed through the axis of the jet. Using two cameras enhanced the dynamic range by a factor of ten over a single-camera system and allowed concentration measurements down to a mass fraction of 0.003. The jet issued into still air at room temperature from a long tube of inner diameter d=5.4 mm. The jet velocity was 21.0 m/s, corresponding to a Reynolds number of 7,000.

Figure 1 compares the axial, χ_x (open symbols) and radial, χ_y (solid symbols) contributions to the mean scalar dissipation at x/d=5. The peak of the axial component is located at the centerline, but the peaks of the radial component are located in the shear layer. These results point out the nonisotropy of the radial and axial components of χ in the shear layer of a developing jet. This nonisotropy persisted up to x/d=13. It should be noted that, at all axial locations, χ_x and χ_y are equal on the centerline.

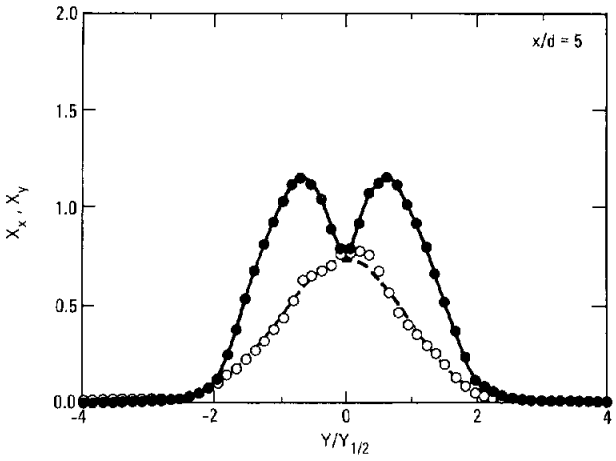

Figure 1. Axial (open symbols) and radial (solid symbols) mean scalar dissipation in an isothermal CH_4 jet.

Figure 2 shows the scalar-dissipation correlation coefficient between the scalar and χ at x/d=9. These results indicate that the scalar and χ are uncorrelated on the centerline where the correlation coefficient is low, but correlated in the outer region of the shear layer with a peak correlation coefficient of 0.6. Other results[4] show that the value of the correlation coefficient peak drops from 0.9 at x/d=5 to 0.3 at x/d=17.

†Combustion and Flame, accepted (1987).

*Altex Technologies Corporation, Los Gatos, CA.

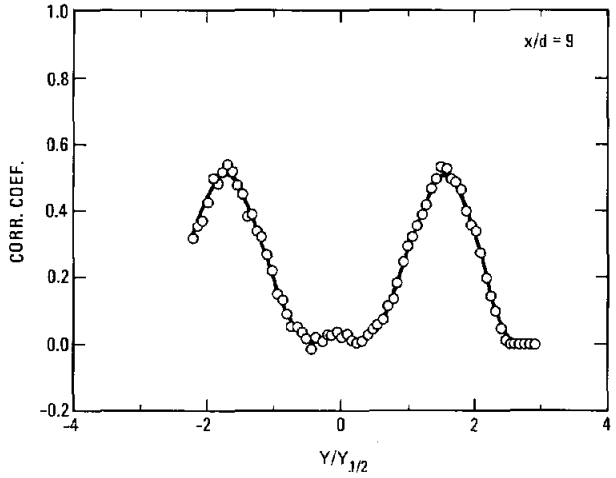

Figure 2. Correlation coefficient between scalar and scalar dissipation in an isothermal CH_4 jet.

The high degree of correlation in the outer region of the shear layer is explained by the presence of relatively sharp instantaneous jet boundaries.[4] These results indicate that the commonly assumed independence between the scalar and χ needs to be re-evaluated, particularly for flame liftoff analyses, which focus on the developing shear region of the jet.

The sharp space- and time-varying gradients, associated with the jet boundary, produce scalar dissipation levels with significant fluctuations around the mean. The extent of the fluctuations in χ at the center of the shear region can be observed in the scalar dissipation pdf, P_χ, plot of Figure 3a. One striking aspect of all pdfs is that they have a long tail toward high χ levels. For example, the tail of the pdf at x/d=5, which has a mean value of 2.0 s^{-1}, extends to values as large as 7.5 s^{-1}. The large levels of instantaneous scalar dissipation could stretch the flamelets to extinction even though mean values are small.

The pdf data of Figure 3a were transformed to pdf of $\ln\chi$, $P_{\ln\chi}$, using $P_{\ln\chi} = \chi P_\chi$, and the results are plotted in Figure 3b. The parameters μ and σ are the mean and rms of $P_{\ln\chi}$. The solid line represents a normal distribution. All of the data collapse to a nearly normal distribution, indicating that P_χ is lognormally distributed. The data are perfectly lognormal at x/d=13 and 17. At x/d=5 and 9, some—but not significant—deviation of the distribution from lognormality is observed at very large values of the scalar dissipation. Similar lognormal distribution results were found for many other locations. Therefore, throughout the measured region, the pdfs of χ can be defined by two parameters μ and σ. The pdf of χ at the instantaneous stoichiometric condition was also found to be lognormal. The mean μ and standard deviation σ of the lognormal pdfs are reported in Reference 4.

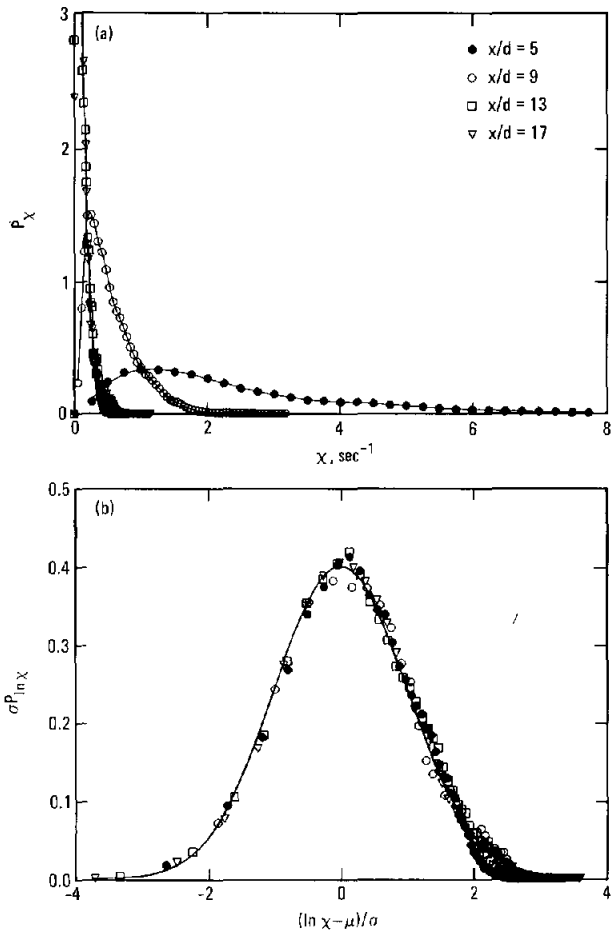

Figure 3. Pdf of scalar dissipation (a) and pdf of the log of scalar dissipation (b).

The scalar dissipation levels at the stoichiometric condition and at the expected jet flame liftoff height of x/d=5 were also measured and found to be around 4.5 s^{-1}. This value is comparable to the stoichiometric extinction values of 5 derived[2,3] from the extrapolation of opposed jet diffusion flame data. Therefore, the present results are consistent with the hypothesis that lifted flames are caused by excessively stretched flames.[2,3]

References:

1. R. W. Bilger, Comb. Sci. Tech. **19**, 89 (1979).

2. N. Peters, Prog. Energy Comb. Sci. **10**, 319 (1984).

3. N. Peters and F. A. Williams, AIAA J. **21**, 423 (1983).

4. M. Namazian, R. W. Schefer, and J. Kelly, Comb. Flame, accepted (1987).

Velocity Discrimination Technique for Two-Phase Measurements in Dense Particle-Laden Flows

Particle and gas-phase velocities have been measured in dense, two-phase jets using a laser-Doppler technique that combines amplitude discrimination with velocity pdf filtering. The resulting data base will be used for development of models for dense, particle-laden flows.

R. S. Barlow and C. Q. Morrison*

The injection and effective dispersion of heavily-loaded, two-phase mixtures is an important concern in the design of entrained-flow coal gasifiers, furnaces, and toxic waste incinerators. However, experimental data needed to validate models for such flows have been unavailable, due to the difficulty in measuring gas-phase velocities in densely-loaded flows. (The initial mass-flow-rate ratio, ϕ_0, is below 1.0 for most available data sets for round jets.) The objectives of this study were to develop a laser-based technique for the measurement of particle- and gas-phase velocities in heavily-loaded flows and to provide a data base for a dense flow of simple geometry. This article describes the measurement technique and presents representative data from round jets of glass beads in air to illustrate some of the major effects of dense particle loading on the flow field.

The flow facility (Figure 1) consists of a conical hopper for the glass beads, an air-injection and flow-conditioning section, and a 1-cm-diameter injector tube that exhausts vertically downward into quiescent air. The flow rate of the spherical glass beads (density = 2825 kg/m^3, mean diameter = 163 μm) is controlled by a metering orifice at the base of the hopper. The air flow rate was maintained at 5.84 standard liters per minute, which corresponds to a bulk velocity at the injector exit of about 1.2 m/s. Velocities were measured using a two-color (488 nm and 514.5 nm), frequency-shifted laser-Doppler velocimetry (LDV) system. Number densities were obtained through a combination laser particle counting and probe sampling.

Measurements of gas velocities in dilute flows have generally been made by seeding the gas with micron or submicron particles and applying some form of amplitude discrimination to reject LDV signals from the large particles of the dispersed phase. However, methods based on amplitude discrimination alone are not appropriate for very dense flows. Consequently, we have used a combination of amplitude discrimination and discrimination based on velocity probability density functions (pdf's) to separate data for the two phases.

To implement the velocity-discrimination technique, two sets of LDV measurements were made at each location. First, axial and radial velocities of the particles were measured with no seeding of the gas phase. Then the measurements were repeated with seeding and with amplitude discrimination being used to reduce the number of LDV validations from the large particles. In the more dilute regions of the flow, the axial velocity pdf's for the two phases are well separated, so particle data can be removed from the gas-phase record by applying a simple velocity cutoff filter. As the local density of the jet increases, the fraction of misidentified

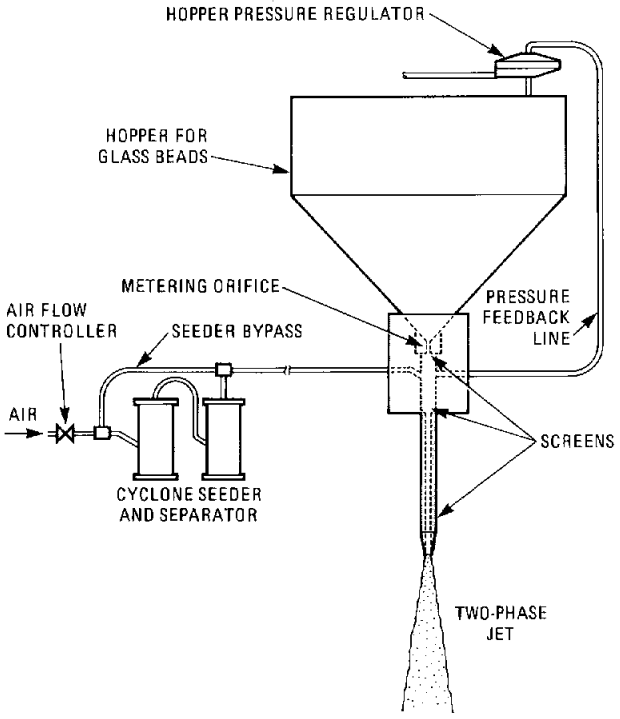

Figure 1. Schematic of the flow facility for velocity measurements in dense particle-laden jets.

†Experiments in Fluids, submitted (1987).

*Science Applications International Corp., Chatsworth, CA.

particles in the seed-plus-particle data record increases. At the same time, the mean slip velocity between phases decreases, causing the pdf's for seeds and particles to overlap, as shown in Figure 2a. A cutoff velocity U_p is defined, and the conditional probability that velocity is greater than U_p is calculated for the seed-plus-particle pdf and for the particle-only pdf (Figure 2b). The particle-only pdf is then scaled by the ratio of these conditional probabilities and subtracted from the seed-plus-particle pdf to produce the velocity pdf for the gas phase alone.

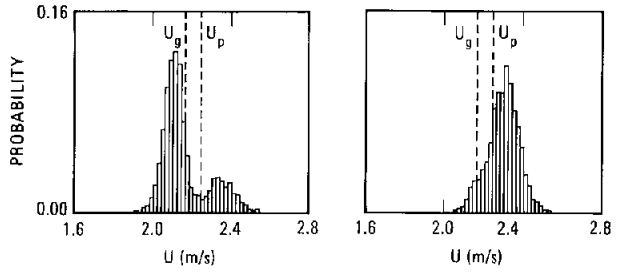

Figure 2. Axial velocity pdf's at x/d_0 = 20, r/d_0 =20, r/d = 0.4 in the ϕ_0=54 jet for: (a) seeds and particles, and (b) particles only.

Mean velocity profiles for round jets with mass loadings of ϕ_0 = 6.5 and ϕ_0 = 54 are shown in Figure 3, to illustrate some of the differences between a relatively dilute jet and a dense jet. The Reynolds number based on the bulk air velocity and the injector diameter was only 780 in both cases. Consequently, the dominant driving mechanism is the gravitational acceleration of the particles. In the dilute case and at the outer edges of the dense jet, there is little or no direct interaction between particles. Therefore, particle velocities are determined primarily by simple aerodynamic response to the gas-phase flow field. The slip velocity of each particle approaches the terminal velocity it would achieve in still air, and the mean slip velocity approaches the number-averaged terminal velocity for the distribution of particles. In the center of the dense jet, the mean slip velocity is only a fraction of this terminal velocity because the momentum of the dispersed phase is far greater than the momentum of the gas phase. The centerline gas-phase velocity is higher in the dense case than in the dilute case, and the radial gradient of gas velocity ($\partial U/\partial r$) is steeper.

The dependence of slip velocity on local mass loading (or number density) is shown in Figure 4. For the particles used in the present study, slip velocity is found to be independent of local loading for $\phi \leq 0.3$ (number densities below roughly 100 cm^{-3}). Modaress, *et al.*[1] found the mean slip velocity (measured at $x/d_0 = 20$ in a round jet of 50 μm glass spheres) to be independent of *initial* mass loading up to ϕ_0 = 0.85. This independence is characteristic of dilute flows. Figure 4 shows that our "dilute" case (ϕ_0 = 6.5) departs from this behavior near the center of the jet at x/d_0 = 20 and begins to exhibit the effects of dense particle loading. The slip velocity is reduced by half at $\phi \approx 2$ and continues to decrease toward zero as local loading increases.

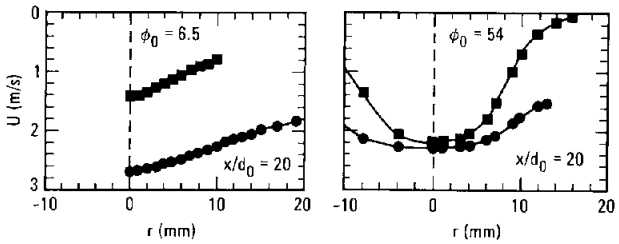

Figure 3. Profiles of mean axial velocity at x/d_0 = 20 in (a) a dilute jet (ϕ_0=6.5), and (b) a dense jet (ϕ_0=54) show that dense loading reduces the slip velocity between phases. ●, particles; ■, gas phase.

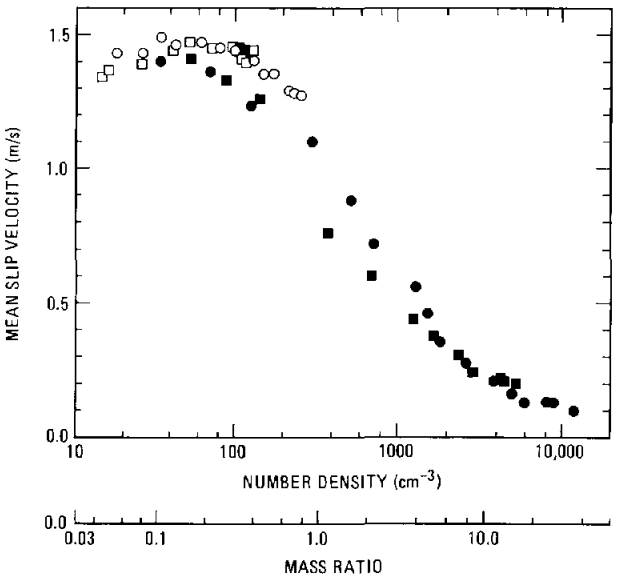

Figure 4. The mean slip velocity between phases in these particle-laden jets is roughly constant for dilute regions but decreases with increasing local particle-mass ratio, ϕ: ○, ϕ_0=6.5, x/d_0=20; ❑, ϕ_0 =6.5, x/d_0 =40; ●, ϕ_0 =54, x/d_0=20; ■,ϕ_0=54, x/d_0 =40.

In summary, a laser-based technique has been developed that allows measurement of gas-phase velocities, as well as particle velocities, in heavily loaded two-phase flows. Measurements in a round jet have shown that dense-particle loading causes reduction in the interphase slip velocity, in velocity fluctuations, and in the spreading rate of the jet. These data will be useful for model development and validation.

Reference:

1. D. Modaress, H. Tan, and S. Elghobashi, AIA J. **22**, 624 (1984).

Methane Concentration Imaging in Bluff-Body-Stabilized Flames

An enhanced dynamic range, two-camera Raman-imaging system was used to obtain instantaneous planar images of the CH_4 concentration in nonpremixed-jet and bluff-body-stabilized flames. The instantaneous images were averaged to obtain mean and fluctuating statistics and probability distributions of the CH_4 concentration. The instantaneous planar images reveal flow and mixing structure information that is lost when time-averaged and instantaneous point-measurement techniques are used.

R. W. Schefer, M. Namazian,* and J. Kelly*

The importance of large-scale organized structure in turbulent shear flows has long been recognized. Recently developed two-dimensional-imaging techniques are well suited for the study of turbulent-flow structure, since they provide simultaneous multipoint data that are necessary to identify and characterize the large-scale structures in turbulent flows.[1] A two-dimensional Raman-imaging system for measuring methane (CH_4) concentration has been used to investigate the flow structure in two combusting flows of current interest: a CH_4 turbulent nonpremixed-jet flame into still air and a bluff-body-stabilized CH_4 flame.[2]

A novel feature of the Raman-scattering imaging system was the use of two cameras. Such an arrangement provided an enhanced dynamic range that allowed methane concentrations to be resolved with good accuracy down to 0.5 mole percent. One camera was used to obtain data from the high-methane concentration in the central flow region. The second more sensitive camera was used to obtain data from the low-methane concentration regions adjacent to the main fuel jet. The images from the two cameras covered a 4-mm x 40-mm-total field of view. For the measurements, the Sandia facility flash-lamp-pumped dye laser was used to produce a 444.0-nm beam. At this wavelength, the laser provided 0.5 J of energy in a 1.8-μs pulse. The beam was formed into a 0.2-mm-thick sheet of light by a multipass light cell consisting of two cylindrical mirrors. The sheet of laser light passed through the axis of the burner. The Raman-scattered light from the sheet was collected by two identical 24-mm-focal-length f/1.4 camera lenses, located on each side of the light sheet, and focused onto intensified Vidicon detectors that recorded the scattered light intensity. With this optical system, the 100 x 100-pixel format of the camera detector provided a spatial resolution of 400 μm x 400 μm. The scattered light was transmitted through 10-nm-bandwidth interference filters centered at 510 nm, which passed only the Raman CH_4 signal to the image-intensifier tubes. The two detectors were controlled synchronously by an LSI 11/23 micro-computer, which triggered the laser and image intensifiers, and collected the data from both cameras.

The burner consisted of an axisymmetric bluff-body (50 mm diameter) with methane fuel supplied through a centrally located 5.4-mm-diameter tube.[3] The fuel-jet velocity was 21 m/s, corresponding to a fuel-jet Reynolds number of 7,000. For the bluff-body flow, air was supplied through a coaxial jet surrounding the bluff-body at a velocity of 25 m/s. Measurements in the nonpremixed jet were made in the same burner with no coaxial air flow.

Axial and radial profiles of the normalized mean and fluctuating CH_4 concentration were obtained by statistically averaging 900 instantaneous images at selected locations. Shown in Figure 1 are radial profiles of the mean and fluctuating (rms) CH_4 concentration in the bluff-body flame at an axial distance, x, of 50 mm from the central jet exit. The CH_4 concentration data are normalized by the CH_4 number density for 100 percent CH_4 at STP conditions (2.5×10^{19} molecules/cm^3). The mean concentration profile clearly shows a region near the centerline corresponding to the central-fuel jet and an outer region in which a significant, but lower, CH_4 concentration extends out to the annular-air boundary. Velocity measurements show that this region is a recirculating flow zone.[4]

Two well-defined maxima exist in the fluctuations, one at the centerline and the other at a radial distance of 10 mm. The outer maximum corresponds to the shear layer located between the recirculation zone and the annular-air flow. The high fluctuation level at the centerline is related to large-scale oscilla-

*Altex Technologies Corporation, Los Gatos, CA.

tions in the axial location of the centerline stagnation zone. These axial oscillations result in a situation where a fixed measurement location alternately contains reverse-flowing air and downstream-flowing jet fluid.

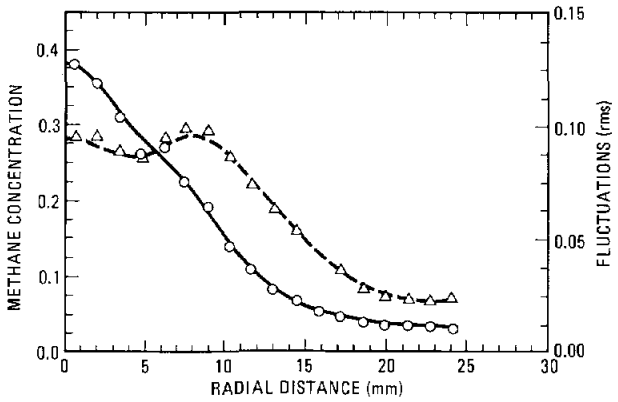

Figure 1. Time-averaged radial profiles of the mean (solid line) and fluctuating (dashed line) CH_4 concentration in a bluff-body-stabilized flame. Profiles are at an axial distance of 50 mm from the burner inlet.

Shown in Figure 2 are two of the instantaneous radial concentration profiles from which the statistically averaged profiles of Figure 1 were calculated. The two profiles shown (indicated by solid and dashed lines) correspond to different laser shots. The steep gradients along the boundaries of the central-fuel jet are indicative of the narrow interfacial regions separating high CH_4 concentration jet fluid from the lower CH_4 concentration-recirculation zone gases. Superimposed on this larger-scale structure are small-scale spatial variations in the CH_4 concentration, which correspond to small-scale turbulent eddies. These instantaneous profiles are considerably different from the time-averaged mean profiles of Figure 1.

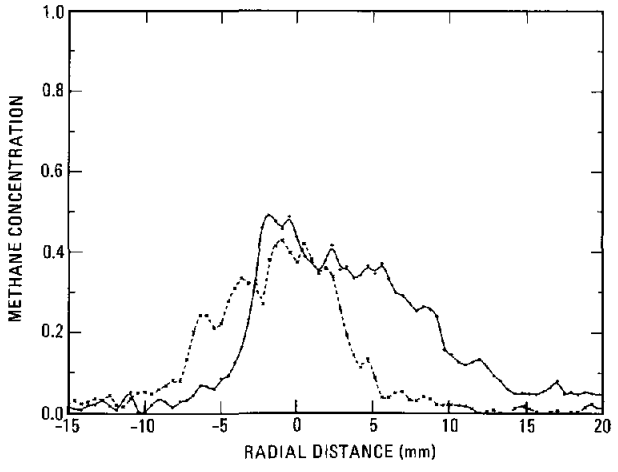

Figure 2. Instantaneous radial profiles of CH_4 concentration in a bluff-body-stabilized flame. The two curves correspond to instantaneous profiles obtained from different laser shots. The axial distance is 50 mm from the burner inlet.

The high fluctuations in the mixing region an be attributed to the movement of these sharp instantaneous boundaries separating high- and low-CH_4-concentration regions across the measurement location. The extent of this movement is shown statistically in Figure 3, where the probability distribution of the instantaneous jet boundary location is shown at x = 50 mm. The jet boundary is defined here as the radial location where the instantaneous CH_4 concentration has decreased to half the maximum value.

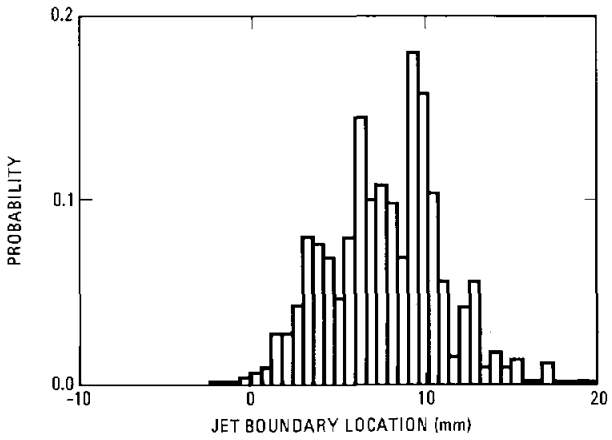

Figure 3. Probability density distribution of instantaneous jet boundary location in a bluff-body-stabilized flame. The axial distance is 50 mm from the burner inlet.

A similar large-scale-interface interpretation of the high-concentration fluctuations in the mixing region of a nonpremixed-jet flame can be made based on imaging measurements and is presented in Reference 2. These results illustrate the usefulness of imaging techniques to provide a more physically-realistic interpretation of traditional time-averaged data in turbulent flows. In addition, by statistically averaging a sufficient number of images, quantitative measurements of turbulence quantities at points within the flow can be obtained. It is only through such measurements that the accuracy of numerical-model predictions can be assessed and model assumptions validated.

References:

1. M. Namazian, R. W. Schefer, and J. Kelly, "Scalar Dissipation Measurements in the Developing Region of a Jet," Comb. Flame, accepted (1987).

2. R. W. Schefer, M. Namazian, and J. Kelly, "CH_4 Concentration Imaging in Nonpremixed-Jet and Bluff-Body Flows," Comb. Sci. Tech., submitted (1987).

3. M. Namazian, J. Kelly, R. W. Schefer, S. C. Johnston, and M. B. Long, "Nonpremixed Bluff-Body Flow and Flame-Imaging Study," Exper. Fluids, submitted (1987).

4. R. W. Schefer, M. Namazian, and J. Kelly, Comb. Sci. Tech. **56**, 101 (1987).

Diluted Nonpremixed Flamelet Modeling

Bluff-body-burner flames can be significantly diluted by recirculating combustion products. Flamelet-model predictions show that cold- and hot-gas dilution significantly alter the resistance of flamelets to extinction.

J. Kelly,* M. Namazian,* and R. W. Schefer

Bluff-body burner flows are characterized by high levels of turbulent entrainment and large-scale recirculation of combustion products. Fuel and air are initially separated by recirculation-zone combustion products and are likely to be diluted with combustion products prior to reaction. Flow, mixing, and combustion in these flames have been studied using direct-flame photography, planar flow visualization, concentration imaging and laser-Doppler velocimetry techniques. In particular, simultaneous CH (a flame tracer) and CH_4 (fuel) imaging has shown that bluff-body-burner flames (as traced by CH) consist of narrow envelopes that form in the vicinity of fuel/air mixing structures. Simple-jet, CH-flame envelope locations and shapes relative to fuel/air interfaces have been found to be similar to bluff-body results. In addition, CH_4 concentration distributions within the flames (i.e., CH_4 conditioned on peak CH) are similar between bluff-body and simple-jet flames, and relatively independent of location. These similarities suggest that the structure of flames for these two burner types are similar. This is not totally expected, since bluff-body burner fuel and air are more likely to be diluted by combustion products than simple-jet cases. To assess the importance of dilution on flames and to help interpret the experimental results, a flame structure model has been developed and applied in this experimental study.

For cases where the laminar flame thickness is smaller than the scale of turbulence, nonpremixed turbulent combustion can be considered as an ensemble of stretched laminar flamelets located in the vicinity of fuel/air interfaces.[1] The steady-state and unity Lewis-number form of the low Mach number conservation equations are utilized as a basis for the flamelet equations. Consistent with the approach of Peters,[1] a Crocco-type transformation is used to convert from physical coordinates to a conserved scalar coordinate, Z, which is fixed to the stoichiometric surface in the flow field. The conserved scalar varies from 0 to 1 in going from the oxidizer to fuel boundaries. Since the flamelet is thin, terms associated with gradients perpendicular to the surface are retained and higher-order nonperpendicular gradient terms are discarded. The flamelets are assumed to be separated in space, and unreacted or diluted fuel and air are used as the two boundary conditions. The flamelet equations are solved by a Newton-Raphson iterative technique.[2] A proven 28-species, 122-elementary-chemical-reaction model is used to predict the effect of turbulence-induced stretch and dilution on flamelet structure.

In the flamelet formulation, the effect of turbulence-induced flame stretch on coupled diffusion and reaction is contained in a single parameter, X, the scalar dissipation. Transport to and from the interface is enhanced by increases in scalar dissipation. For large values of scalar dissipation, flamelet peak temperature is reduced; for very large values, flamelet reactions can be extinguished. Experimental results have shown that both bluff-body and simple-jet[3] scalar dissipation is largest near fuel/air mixing boundaries, where flames are expected to reside.

Flamelet calculations have been made for scalar dissipation levels between $0.1s^{-1}$ and the level needed to extinguish flamelets. Values of $0.1s^{-1}$ represent essentially unstretched or laminar-type flames. Undiluted, cold-gas diluted, and hot-gas diluted cases are predicted. The undiluted case represents a reference and is most like conditions near the exit of a simple-jet flame where reaction is just being initiated. The cold-gas dilution case represents the conditions near the cooled bluff-body burner face, where recirculated combustion products have been cooled prior to entrainment into the reaction zone. The hot-gas diluted case corresponds to the internal recirculation in the bluff-body flow where hot products have not had time to radiatively cool or contact cool heat-transfer surfaces.

Figure 1 presents CH_4, O_2, CO_2, and H_2O mole-fraction profiles in undiluted flamelets. At low stretch ($X=0.1s^{-1}$), the reactants rapidly decrease as the stoichiometric surface ($Z=0.055$) is approached. The water vapor (H_2O) concentration profile peaks near the stoichiometric surface,

*Altex Technologies Corporation, Los Gatos, CA.

whereas the CO_2 profile peaks on the air side of the flame. For this unstretched flame, very little overlap of reactants is observed in the flame zone ($0.04 < Z < 0.08$). When the flame becomes highly stretched ($X=10.0s^{-1}$), the reaction zone moves toward the fuel-rich zone, reactants overlap in the flame zone, and product concentration peaks are reduced. Flame temperature profiles in Figure 2 show that, at low stretch, the flame temperature is sharply peaked near the stoichiometric condition. Stretch is seen to reduce the peak temperature and shift the temperature peak towards the fuel-rich side of the flame.

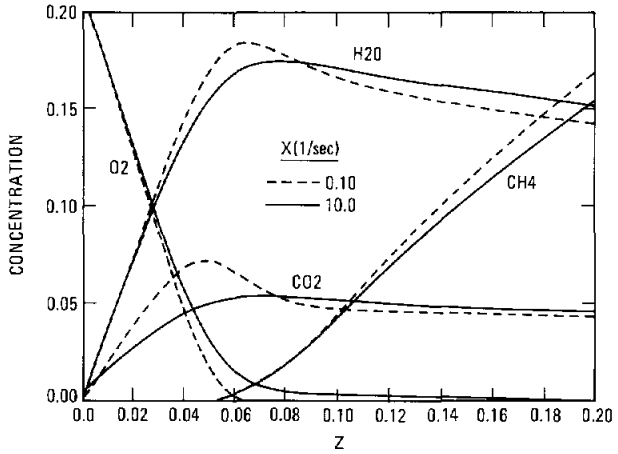

Figure 1. Predicted O_2, CH_4, CO_2, and H_2O mole-fraction distributions through flamelets, showing signifiant overlap of reactants, and reduction in produce peaks for highly stretched case.

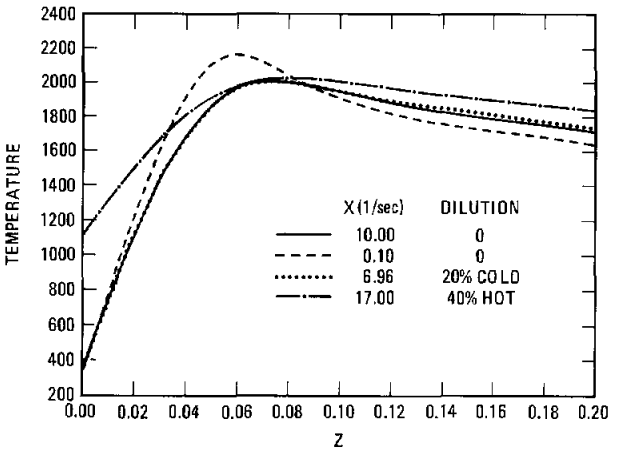

Figure 2. Predicted temperature distributions through unstretched- and stretched-undiluted, cold-gas-diluted, and hot-gas-diluted flamelets, showing similarity of reaction zone temperature near extinction.

From detailed output not presented here, changes in flamelet characteristics near extinction are brought about by the following events. Under low stretch, the CO and H_2 formed on the fuel-rich side of the flame diffuses to the lean side, rapidly converts to products, and releases heat. Under highly stretched conditions, the rate of conversion of CO and H_2 to products on the fuel-lean side cannot keep up with the increased rate of diffusion. Reduced conversion of CO and H_2 to products decreases heat release and temperature. The ratio of the temperature-sensitive chain-branching reaction rate to chain-terminating reaction rate then decreases and the flame extinguishes. These results show that the extinction mechanism is strongly related to temperature.

Cold-gas dilution, which reduces peak temperature, significantly impacts flamelet extinction. Predictions show that a 20% dilution of fuel and air by cold combustion products reduces the X at extinction by 30%. At this reduced level of stretch ($X=6.96s^{-1}$), the peak values of temperature are very similar to the nondiluted results (see Figure 2). The detailed output shows that the extinction mechanism highlighted above is operable for cold-gas-diluted flamelets. Apparently, temperature in the reaction zone is a key parameter and dilution of the reactants by relatively nonreactive combustion products is a secondary effect.

Hot-gas dilution does not change the peak temperature. However, by increasing the initial temperature of the reactants, flame-zone heat loss is reduced and the flames should be more resistant to stretch. Figure 2 shows that for the 40% hot-gas dilution case, the temperature profile in the reaction zone is similar to both the cold-gas diluted and undiluted cases. Detailed output shows that the extinction mechanism highlighted above is operable for hot-gas dilution. However, the level of stretch at extinction ($X=17.0s^{-1}$) is increased by 70% over the undiluted case due to the reduced heat loss at the boundaries for hot-gas dilution.

These results show that dilution significantly impacts the level of stretch needed to extinguish flamelets. For cold- and hot-gas dilution, less and more turbulence-induced stretch are needed to extinguish flamelets, respectively. In all cases, the extinction occurs at comparable flame zone temperatures via the same extinction mechanism.

References:

1. N. A. Peters, Progress in Energy and Comb. Sci. **10**, 319 (1984).

2. R. M. Kendall and J. T. Kelly, "Premixed One-Dimensional Flame Code User's Manual," *Acurex Final Report 78-278* (Acurex, Mountain View, CA, 1976).

3. M. Namazian, R. W. Schefer, and J. Kelly, "Scalar Dissipation Measurements in the Developing Region of a Jet," Comb. Flame, accepted (1987).

Instantaneous Three-Dimensional Concentration Measurements in Turbulent Jets and Flames†

We describe a method for obtaining instantaneous three-dimensional concentration measurements in turbulent flows. Each three-dimensional image is constructed from a series of two-dimensional images, all recorded during a single 1.4-microsecond-long laser pulse. The three-dimensional images provide valuable information on structures in turbulent flows.

B. F. Yip,* R. L. Schmitt, and M. B. Long*

Laser-imaging techniques have proved to be useful for studying large-scale structures in turbulent reacting and nonreacting flows. By simultaneously gathering data from a large number of points, we have obtained insight into the spatial characteristics of the flow. To date, however, most of the techniques used have provided data in one or two dimensions only. Turbulent flow is necessarily a three-dimensional phenomenon and further insight might be gained if three-dimensional data were available. In particular, information on the topology of the structures such as surface-to-volume ratios, connectedness, and possible fractal dimensions could be investigated by analysis of volumetric data.

The goal of the present experiment is to measure the instantaneous three-dimensional gas concentration distribution in high-speed turbulent gas jets and flames by detecting molecular scattering. A rapidly scanning mirror is used to sweep a pulsed sheet of laser light through the volume of a gas jet or flame. As the sheet passes through the flow, an electronic framing camera images light scattered by the gas molecules at 90°, so that up to twelve distinct planes of the flow are recorded as the laser sheet traverses the flow region. The phosphor-output screen of the framing camera is imaged directly onto a two-dimensional CCD (charge-coupled device) array camera that records the images.

The experimental setup is shown schematically in Figure 1. The laser used for this experiment was Diana, the Combustion Research Facility flashlamp-pumped dye laser. This laser has a pulse length of 1.4 μs (short enough to "freeze" the turbulent fluid motion) and a pulse energy of up to 550 mJ at 440 nm (enough energy for single-shot measurements). The laser beam was formed into a 250-μm-thick, 3-cm-tall sheet by a spherical focusing lens and a vertically-oriented cylindrical beam expander. This sheet was scanned through the flow region with a 3.97-kHz resonant scanner. The moving laser sheet (which has a velocity at the nozzle of ~ 4.9 km/s) traversed a substantial fraction of the flow volume during the 1.4-μs laser pulse.

A high speed electronic framing camera (Hadland Photonics Imacon 790) captured up to twelve two-dimensional images during each 1.4-μs laser pulse. Each exposure was 1- ns long, and each

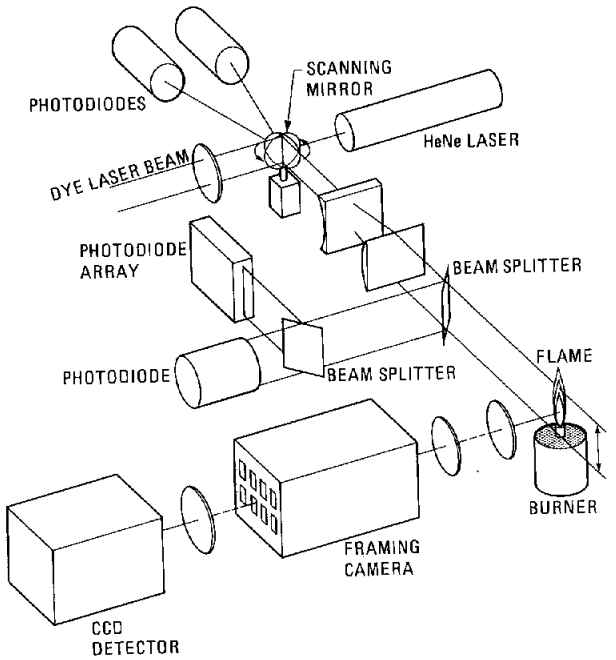

Figure 1. Experimental setup for measuring the instantaneous three-dimensional gas-concentration field in a turbulent jet or flame. A flashlamp-pumped dye-laser beam is reflected from a rapidly scanning mirror, and lenses form this beam into a thin illumination sheet that sweeps through the flow volume. As the sheet sweeps through the flow, a high-speed framing camera records up to 12 distinct images during a single 1.4-μs laser pulse. This series of two-dimensional images can be reconstructed to obtain a three-dimensional concentration map of the scattering species.

†Optics Letters **13**, 96 (1988).

*Yale University, New Haven, CT.

frame was separated in time by 50 ns. Combined with the speed of the moving laser sheet, the interframe period resulted in a 250-μm separation between the consecutive flow planes imaged by the camera, approximately the thickness of the laser sheet. The phosphor-output plane of the framing camera was demagnified and imaged onto a 584 x 390-pixel CCD array camera that recorded the data. Each of the twelve imaged planes of the flow occupied 58 x 120 pixels, corresponding to 6 mm x 12 mm in real space. Therefore, the volume elements resolved in the measurement were 94 μm x 94 μm x 300 μm.

The data were corrected for the CCD array's nonuniform pixel bias and sensitivity and the temporal and spatial response of the laser and framing camera. As each three-dimensional measurement was performed, the temporal intensity profile of the particular laser shot was monitored by a fast photodiode connected to a high-speed digitizer. In addition, a linear-photodiode array mounted parallel to the vertical laser sheet monitored the spatial intensity distribution in the laser pulse. The output of this array was recorded by another digitizer. These temporal- and spatial-intensity profiles provided the information required to correct for the nonuniformities in the illumination sheet used to measure the sequence of flow planes.

Figure 2 shows a three-dimensional surface of constant gas concentration in a room-temperature Freon-12 jet, measured by imaging Rayleigh scattering. The surface corresponds to a concentration of 73% of the maximum in this region, and has been reconstructed from the measured data and displayed with computer graphics. A pixel-binning operation was performed on the digitized data set (before displaying it) to increase the signal-to-noise ratio and to reduce the number of nodes created by our surface-generation algorithm. The resulting resolution volume in the displayed surface is 376 μm x 376 μm x 300 μm.

Stronger light-scattering mechanisms were used to increase the signal-to-noise ratio of the images. Mie scattering from soot particles marking the flame front in low-speed nonpremixed flames gave high signal levels, as did Mie scattering from submicron-sized aerosols seeded in both reacting and nonreacting flows. However, aerosol seed particles are much more massive than the molecules of the gas flow; hence, their ability to follow the fluid motion is limited. Biacetyl vapor used as a fluorescent marker of the flow produced signals with a noise level of 10%. Figure 3 shows a constant fuel-concentration surface in a premixed methane-air-biacetyl flame, measured by imaging the intensity distribution of biacetyl fluorescence through the flow volume after excitation by a 440-nm laser pulse. This surface corresponds to a concentration of 64% of the maximum in this region.

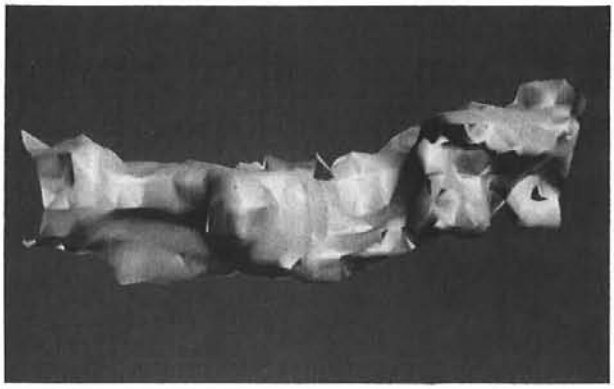

Figure 2. Instantaneous constant gas concentration surface in a turbulent jet (Reynolds number 13,800) measured by imaging Rayleigh scattering from the Freon-12 nozzle gas. The surface corresponds to a concentration of 73% of the maximum in this region, which is 3.4 x 1.7 x 0.7 nozzle diameters (d =3.5 mm) in dimension and centered 6.90 diameters downstream of the nozzle. The flow direction is from left to right.

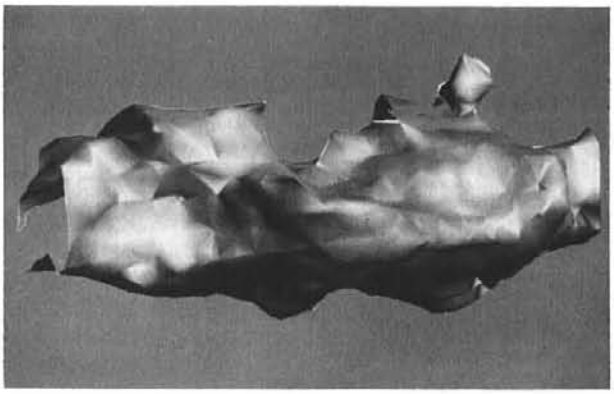

Figure 3. Instantaneous constant fuel gas concentration surface in a turbulent premixed flame. The surface corresponds to a concentration of 64% of the maximum in this region and has been generated from experimental data by use of computer graphics. The flame was a stoichiometric methane-air mixture seeded with biacetyl vapor as a fluorescent marker, with a jet exit velocity of 19.5 m/sec. The imaged region is 2 x 1 x 0.5 nozzle diameters (d=6 mm) in dimension, centered 5 diameters downstream of the burner. The flow direction is from left to right.

In summary, we have successfully demonstrated the ability to make time-resolved measurements of the three-dimensional gas distribution in turbulent reacting and nonreacting flows by imaging molecular and particulate scattering. The data obtained from this technique are unique and should prove to be an asset in the study of combustion and the process of turbulent mixing.

Turbulent Nonpremixed Flames of Methane Near Extinction: Conditional Probability Density Functions†

Spontaneous Raman-Rayleigh measurements of temperature and species concentrations have been made in turbulent nonpremixed flames of methane close to extinction. It is found that for mixture fraction ranges lying below the rich reaction limit, combustion is generally bimodal, and fluid samples are either burnt or unburnt. For ranges above the rich limit, the majority are partially reacted; the correlation between the various conditional pdfs indicate that more than a single-step reaction mechanism is required to adequately describe the chemistry.

A. R. Masri, R. W. Bilger, and R. W. Dibble

There is great need in combustion research for understanding the local instantaneous structure of turbulent flames of hydrocarbon fuels. Such fuels are widely used in industry and have chemical kinetics that are inherently different from those of fuels such as H_2 and CO. Close to extinction, the local flame structure and overall combustion efficiency are influenced by chemistry as well as by turbulence. Theoretical models that predict these flames must account, therefore, for finite-rate kinetic effects and must be capable of predicting flame blow-off. Various concepts have been developed to describe the local instantaneous structure in turbulent flames, but their relevance to turbulent nonpremixed flames of hydrocarbon fuels has never been tested. A number of existing theoretical models can account in various ways for finite-rate kinetic effects, but the chemical aspects of these models have not been tested. This is because of the lack of experimental data, which are very difficult to collect in the hostile flame environment. The purpose of this paper, and others already reported,[1] is to present space- and time-resolved data taken in regions of nonpremixed flames of methane where the interactions between turbulence and chemistry are strong. The data give new insights into the structure of turbulent nonpremixed flames of methane and a new understanding of the phenomenon of flame extinction.

Space- and time-resolved measurements of temperature and species concentrations have been made in the blue (visibly soot free) regions of methane flames using the pulsed spontaneous Raman-scattering technique. These measurements were performed in the Turbulent Diffusion Flame Facility. A large base of data has been collected at various axial locations in flames ranging from slowly mixing flames to ones close to extinction. At each laser shot, the Raman and Rayleigh scattering for CH_4, O_2, H_2O, H_2, CO, CO_2, and N_2 were collected simultaneously.

Reactedness from species i, b_i, is defined as

$$b_i = \frac{P_i - P_{m,i}}{P_{a,i} - P_{m,i}}$$

where P_i is the measured scalar used, and $P_{m,i}$ is the frozen value of the scalar at the measured mixture fraction ($P_{m,i} = 0$ for H_2O and CO_2 and $P_{m,i} = 295$ for temperature). From the calculations of Miller, *et al.*[2] for the laminar diffusion flame of methane, $P_{a,i}$ is the calculated, fully burnt value of the scalar at the measured mixture fraction, ξ, for the flame with $a = 1\ s^{-1}$ (where a is a stretch parameter, and flame extinction occurs at $a \cong 320\ s^{-1}$). The fully burnt values are different from the equilibrium calculations, particularly on the rich side of stoichiometric. The values of b_i vary between zero for frozen and one for fully burnt mixtures. Each laser shot produces a value of b_i.

Figure 1a shows the conditional joint probability distributions (*cjpdf*s) in the lean reactive range; b_T vs b_{O_2} are shown for flame *B* (low fuel velocity). The correlation in this range is excellent and holds for other *cjpdf*s and other flame locations not presented here. The bimodality is most distinct and the probability of encountering partially reacted samples is almost negligible. In a higher velocity flame, which is close to extinction, the probability for fully burnt pockets of fluid remains high and is about an order of magnitude lower than that for fully unburnt ones.

In the rich reactive range, the various *cjpdf*s shown in Figure 1b are partially bimodal. The correlation is excellent in this range and holds for all values of b_i. The spread in the data around the diagonal is minimal, considering that the false color

†Combustion and Flame, accepted (1987).

*University of Sydney, New South Wales, Australia.

change on the plots is based on a near logarithmic scale. This correlation deteriorates badly for richer mixtures not shown. In these rich ranges (Y and Z), temperature and fuel show more progress than O_2 and H_2O. The broadening around the diagonal is only partly due to experimental error and implies that multistep reactions are taking place. It is worth noting the centered distribution of the *cjpdfs* in the rich ranges in contrast with the bimodal ones in fuel-lean ranges (i.e., Figure 1a).

The comparison of the various values of $< b_i >$, as well as the variations in the correlations shown in the *cjpdfs*, implies clearly that more than a single-step reaction is needed to model the chemistry in these flames. The following two-step reaction scheme may be adequate:

$$CH_4 + O_2 \rightarrow CO + H_2O + H_2,$$

$$CO + O_2 + H_2 \rightarrow CO_2 + H_2O.$$

Two other candidates have been proposed; these mechanisms are systematically reduced, from the full kinetic scheme of Miller, *et al.*[2] for methane, to three or four reactions. More accurate measurements of CO and CO_2 are needed, however, to determine the most appropriate reaction scheme for these flames. The use of reduced reaction schemes is a major and necessary simplification both for distributed reaction zone models and for laminar flamelet models, particularly if a four-variable formulation is used to build the library of laminar flamelets. A comparison between turbulence microscales and appropriate reaction zone scales is needed to determine whether the reaction zone is thin and laminar or broad and distributed with turbulence within it.

The prediction of full flame blow-off is imperative in any worthwhile model of turbulent combustion. All the conditional *pdfs* presented in this paper are consistent in showing that, near extinction, the flame is maintained alight by fully burnt pockets that appear to be responsible for the re-ignition of the flame farther downstream when the chemical kinetics are fast enough compared with the decreasing mixing rates. The probability of these pockets peak in the lean reactive range. The whole flame will be extinguished when the frequency of occurrence of these burnt pockets decreases below a certain limit.

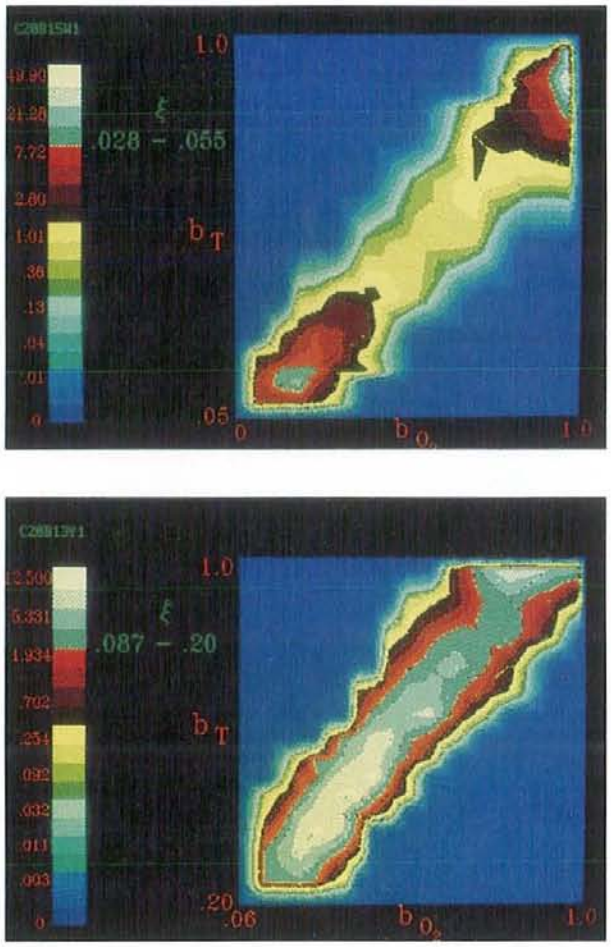

Figure 1. (a) The conditional joint probability distributions (*cjpdfs*) in the lean reactive range; (b) the various *cjpdfs* are partially bimodal in the rich reactive range.

References:

1. A. R. Masri, R. W. Bilger, and R. W. Dibble, "Turbulent Non-Premixed Flames of Methane Near Extinction: Probability Density Functions," Comb. Flame, accepted (1987).

2. J. A. Miller, R. J. Kee, M. D. Smooke, and J. R. Grcar, *Western States Section* (The Combustion Institute, Pittsburgh, PA, 1984), Paper No. WSS/C184-10.

Modeling Turbulent Nonpremixed Flames with a Composite PDF

A second-order conditional model for turbulent, nonpremixed flames with a composite probability density function (pdf) has been developed to simulate the existence of a superlayer between the turbulent and nonturbulent parts of the flow. Comparisons of model predictions with experimental data suggest that an accurate representation of the pdf shape, such as the one studied here, may be essential to the predictions of NO and other minor chemical species.

J.-Y. Chen

An assumed shape for the probability density function (pdf) of the mixture fraction is often used in modeling turbulent nonpremixed flames. In most moment closure methods, only the first two moments of the mixture fraction are calculated; therefore, they allow only two free parameters in the pdf. This restricts the possible pdf shape to limited categories. Previous studies indicated that the predicted mean properties are not sensitive to the assumed shape. However, this may not be true for minor chemical species. An example is the thermal formation of nitric oxide, which strongly depends on the pdf values around the stoichiometric of the fuel mixture. Moreover, some recent turbulence models[1] have been proposed to include the effects of heat release on turbulence. The pdf of the mixture fraction is required in these new models so that the delicate interactions between turbulence and combustion can be properly simulated. Therefore, the role of the mixture fraction pdf in modeling turbulent reacting flows becomes more important as more advanced models are developed.

A second-order conditional model for turbulent nonpremixed flames with a composite pdf has been developed to better represent the pdf shape.[2] The composite pdf formula consists of three parts of the scalar field: a fully turbulent part, a surrounding nonturbulent part, and a superlayer part. The conditional moment equations are derived using Favre averaging (density weighting) with the interfacial interaction terms appearing in explicitly separate groups. These equations are closed by a second-order scheme and models for the interfacial terms. Nitric oxide formation is computed by a model including the effects of intermittency and nonequilibrium oxygen-atom concentration.

The performance of the proposed model, referred to here as Model IV, is evaluated by comparisons of model predictions with three different sets of experimental data for turbulent nonreacting and reacting jets. Also included in the comparisons are the results obtained with an unconditional model using two different pdf shapes (Model I and Model II) and a conditional model with an assumed beta function for the pdf in the turbulent zone (Model III). The first two models represent more or less the traditional scheme for turbulent flows, but with a second-order closure. These models solve unconditional moment equations with an assumed function for the mixture fraction pdf. The most widely used pdf shapes have been considered; namely, the beta function (Model I) and the clipped Gaussian function (Model II). Although the beta function is more convenient than clipped Gaussian function for numerical calculations, it has the disadvantage that it cannot account for the intermittency spikes. The clipped Gaussian function, however, provides spikes at the mixture fraction values at zero and one but requires tedious numerical computations. The third model incorporates directly the effects of intermittency into the scheme by solving modeled transport equations for the conditional statistics. In the turbulent part of the flow, the pdf is a combination of a beta function and an intermittency spike. The fourth model is similar to the third but with a composite pdf formula.

Figure 1 presents a comparison of model predictions with experimental data in the regions of high intermittency. As seen from the measurements, there are smooth transient regions between the air spike and the broader distribution. These smooth regions are attributed to the presence of a superlayer between the turbulent and nonturbulent parts of the flow. Comparison of the details of the pdf profiles reveals that this salient feature is captured only by the composite formulation, although

[†]Combustion and Flame **69**, 1 (1987).

all the model predictions are within the experimental accuracy. Figure 2 shows various model predictions of the centerline density profile for an H_2-air non-premixed jet flame.[3] The predictions have been improved by incorporating intermittency and a composite pdf. The sensitivity of model predictions of nitric oxide formation to the pdf shape is illustrated in Figure 3. The experimental data are included here for a reference purpose only since there are serious doubts about the accuracy of the probe measurements. The influence of the pdf shape on the formation of nitric oxide is evidently seen from this comparison. Different shapes can cause a 25% difference in the predicted peak values, suggesting a realistic pdf presentation, such as the one studied here, is essential to the predictions of minor chemical species.

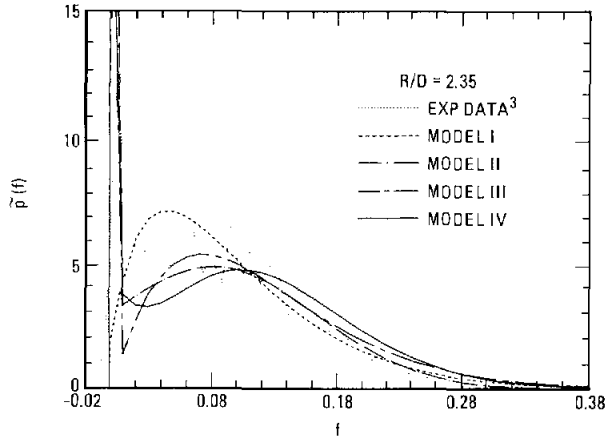

Figure 1. Pdf distributions of the mixture fraction at 30 diameters downstream for a turbulent C_3H_8-air isothermal jet. The data show that the air spike at f=0 and the broader turbulent distribution are connected by a smooth transient region, which is due to the existence of a super-layer between the turbulent and nonturbulent parts of the flow. This salient feature is captured only by the composite pdf model (IV).

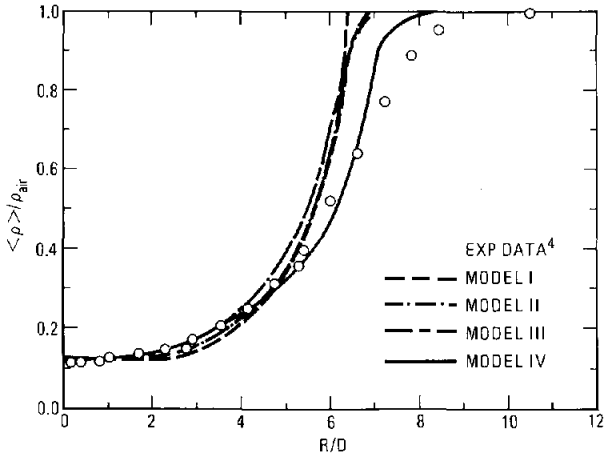

Figure 2. Axial centerline variations of the mean density for a 22% Ar-H_2-air nonpremixed turbulent jet flame. Model predictions are improved with the composite pdf formulation (IV).

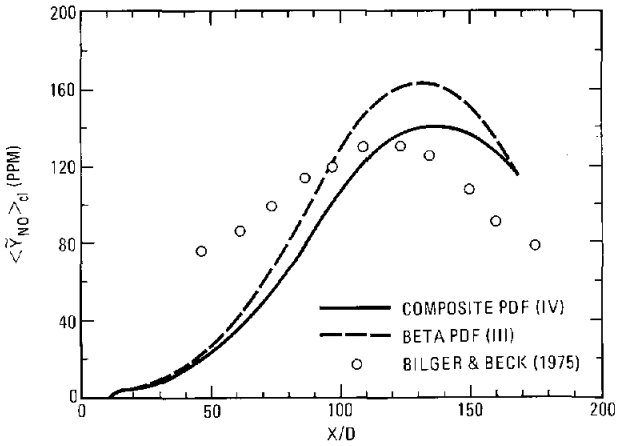

Figure 3. Centerline variations of nitric oxide concentration for a H_2-air nonpremixed turbulent jet flame. Experimental data are included for reference only due to the inaccuracy in probe measurements. The predictions of the formation of nitric oxide are seen to be very sensitive to the pdf shape, which could result in a 25% difference in the peak value.

References:

1. E. Effelsberg and N. Peters, Comb. Flame **50**, 351 (1983).

2. R. W. Schefer and R. W. Dibble, "Rayleigh Scattering Measurements of Mixture Fraction in a Turbulent Nonreacting Propane Jet," presented at the 24th Aerospace Science Meeting (AIAA, Washington, DC, 1986).

3. R. W. Dibble, R. W. Schefer, J.-Y. Chen, V. Hartmann, and W. Kollmann, *Western States Section* (The Combustion Institute, Pittsburgh, PA, 1986), Paper No. WSS/CI 86-85.

4. R. W. Bilger and R. E. Beck, *Fifteenth Symposium (International) on Combustion* (The Combustion Institute, Pittsburgh, PA, 1975), p. 541.

Soot Particle Temperatures in Axisymmetric Laminar Ethylene-Air Diffusion Flames at Pressures up to Seven Atmospheres

Average soot-particle temperatures have been determined as a function of axial position in axisymmetric laminar diffusion flames at pressures up to 0.7 MPa. At late times, the cooling rate for heavily sooting flames at pressures of 0.2 MPa and above was about -22 K/ms, independent of either fuel flow rate or pressure.

W. L. Flower

The formation of soot in axisymmetric laminar diffusion flames of ethylene and air at pressures up to 1.0 MPa has been examined previously.[1] In that study, the axial variation of the integral of the soot volume fraction f_v across the flame diameter ($\int_{-\infty}^{+\infty} f_v \, dr$) was determined from measurements of the attenuation of laser light across the flame. The measurements show a region early in the flames where the integrated soot volume fraction increases with axial position, indicating a zone of soot formation. This is followed by a region in which ($\int_{-\infty}^{+\infty} f_v \, dr$) either remains constant or decays back toward zero. The latter case indicates the influence of oxidative processes in removing soot late in the flame. The peak integrated soot volume that is formed increases with pressure to a power of about 1.2, and the extent of soot oxidation decreases as pressure is increased.

Because of the important effect of temperature on soot formation and oxidation processes, a knowledge of the temperature history in sooting flames is useful to help characterize these processes. However, the presence of soot particles can hinder the measurement of flame temperatures using some of the more common diagnostic techniques. Here, we report temperature measurements based on line-of-sight measurements of the emission and absorption of near-infrared radiation by soot particles. Average soot particle temperatures have been determined as a function of axial position in axisymmetric laminar diffusion flames at pressures up to 0.7 MPa.

The radiation emitted at wavelength λ by a nonblackbody at temperature T is given by $I_\lambda = \varepsilon_\lambda I_{b\lambda}(T)$, where ε_λ is the spectral emissivity of the radiator and $I_{b\lambda}(T)$ is the Planck function. The effective spectral emissivity of an equilibrium distribution of particles in a given direction is related to the transmissivity in the same direction by $\varepsilon_\lambda = 1 - \tau_\lambda$, where we have neglected scattering of light by the particles. If both the absolute intensity of light emitted by a cloud of soot particles and the transmission coefficient of those particles are measured at a given wavelength, these relations may be used to determine the particle temperature, assuming that temperature is uniform along the optical path.

Measurements of soot emission and absorption were made along horizontal paths passing through the centerline of flames identical to those of Reference 1. Temperatures determined in this way represent averages across the diameter of the flame weighted toward the regions of highest soot loading. Average temperatures determined in this way are reasonably representative of the temperature in the soot-laden region, since previous measurements in axisymmetric and two-dimensional diffusion flames have shown that temperature does not vary greatly (less than about 100 K) across the region where most of the soot is located.

The 1.27-cm-diameter vertical burner tube from which the gaseous fuel flows is surrounded by a co-flowing air stream and is enclosed in a pressure vessel. Experiments were performed at a sequence of pressures from 0.1 to 0.7 MPa using ethylene as the fuel.

A calibrated tungsten-filament standard lamp served as a source of continuum radiation (Figure 1). The lamp filament was imaged at the center of the flame and was then reimaged on a variable slit. Light passing through the slit was split by a cube beamsplitter. The intensity of each of the split beams was measured using a silicon photodiode preceded by a bandpass filter defining the detection wavelength.

Displayed in Figure 1 are temperature measurements for flames at pressures up to 0.7 MPa. The flow time t was determined by integrating the reciprocal of the axial velocity, which in coflowing laminar diffusion flames is approximated quite well by the expression $v = (2az)^{1/2}$, with $a = 3100 \text{cm/s}^2$.[2] For these flames, the soot temperature decays with increasing axial position in the flame, and, for a

fixed fuel flow rate, the temperature is lower at a given vertical position in flames at higher pressures, for which the soot volume fractions are greater. At atmospheric pressure, the particle temperature initially increases before leveling off and then gradually decreasing at later times. At higher pressures, the temperature variations in the region nearest the burner rim are not so great, temperature remaining relatively constant until decreasing at later times. At each pressure, temperature has declined from the early plateau value before the location of the peak soot volume fraction, which is marked by an arrow in Figure 1. The decrease in temperature before this point is greatest at the highest pressure, ranging from about 65 K at 0.1 MPa to 90 K at 0.7 MPa. At late times, the cooling rate for heavily sooting flames at pressures of 0.2 MPA and above was about -22 K/ms, independent of either fuel flow rate or pressure. However, for a fixed fuel flow rate, the onset of cooling occurs earlier for flames at higher pressures, for which the soot volume fractions are greater.

The complete set of measurements of soot volume fraction, temperature, and gas velocity suggests the following description: the quantity of soot that is formed increases as pressure is increased, which results in greater radiative energy losses from the flames at higher pressures. These increased radiative losses cause the soot temperature to drop sooner in flames at higher pressures, effectively quenching the oxidation of soot that takes place at late times in soot-laden flames. The amount of soot that is ultimately emitted by these flames, therefore, increases with pressure both because a greater quantity of soot is formed as pressure increases, and because a smaller portion of the soot that is originally formed is later removed by soot oxidation.

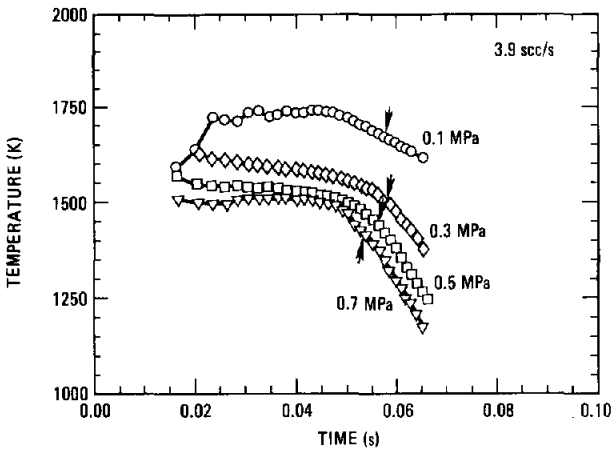

Figure 1. Average particle temperatures on the flame diameter as a function of residence time. Shown are measurements obtained for 3.9 scc/s fuel-flow rate at pressures up to 0.7 MPa. For each pressure, an arrow indicates the time at which the peak soot-volume fraction is first attained.

References:

1. W. L. Flower and C. T. Bowman, *Twenty-First Symposium (International) on Combustion* (The Combustion Institute, Pittsburgh, PA, 1988), p. 115.

2. W. L. Flower, Comb. Sci. Tech. **48**, 31 (1986).

Fuel Concentration Effects on Soot Formation in a Diffusion Flame

The isolated effects of fuel concentration and flame temperature variation on soot formation when an inert gas is added to the fuel have been investigated experimentally for counterflow diffusion flames. The results show that both temperature and concentration contribute to a reduction in soot volume fraction, and concentration accounts for a substantial amount of this reduction.

R. L. Axelbaum,* W. L. Flower, and C. K. Law*

Inert addition has often been employed as a useful technique for studying soot formation in diffusion flames. The addition of an inert to either or both of the reactant streams modifies not only the flame temperature, but also the reactive-species concentration of the respective stream. Also, kinetic considerations require that the soot formation process depends on both temperature and concentration. Thus, it is of fundamental interest to attempt to isolate the influence and thereby assess the relative importance of these two parameters.

The significance of this issue was first addressed by Glassman and Yaccarino,[1] who suggested that the effect of fuel partial pressure is secondary to that of temperature. A subsequent study by Kent and Wagner[2] indicated that the amount of soot reduction through fuel dilution is more than can be explained by the reduction in flame temperature and that fuel concentration could be a significant factor in influencing the soot production rate. It was further emphasized that fuel dilution cannot be relied on to obtain simple temperature relations. Mechanistically, it may be expected that, although inert addition decreases the flame temperature, it also reduces the fuel concentration and, consequently, the soot inception and surface growth rates.

In view of the above considerations, it is clear that, to identify the separate effects of flame temperature and fuel concentration, experiments need to be conducted in such a manner that these two parameters can be independently varied. To this end, we propose herein an alternate flame temperature adjustment technique that allows for such independent variations.

The counterflow diffusion flame established in the forward stagnation region of a porous cylinder is used in this study. Measurements are taken along the forward stagnation streamline where, due to symmetry, the flame is essentially one-dimensional. The burner consists of a porous cylinder mounted horizontally in a vertically-oriented wind tunnel. The oxidizer gases are supplied by the wind tunnel, while the fuel gases (ethylene and nitrogen) are ejected from the porous cylinder.

Temperature measurements are obtained with a silica-coated thermocouple, and soot measurements are obtained by using standard light scattering and extinction techniques. The velocity component along the forward stagnation streamline is obtained using a single-component, laser-Doppler velocimetry system.

The conditions of this study require that the fuel flow rate be varied. Since the fuel flow rate is an important parameter in coflow flames, we have investigated how the flow rate of pure fuel influences soot formation in the present flame. We found that, unlike in the coflow flame, soot formation in the counterflow diffusion flame is almost independent of fuel flow rate in our range of interest.

These results are not surprising if we consider the characteristics of this flame. Diffusion controls the transport of fuel across the stagnation point, while the flame location is governed by stoichiometry, making the distance from the flame to the stagnation point not strongly dependent on the fuel flow rate. The flow field on the oxidizer side of the stagnation point is then not as strong a function of the fuel flow rate and thus, unlike the coflow flame, the residence time of soot in the counterflow flame is little affected by the fuel flow rate.

To isolate the effect of dilution and temperature in a systematic way, we employ a temperature adjustment technique that allows the maximum flame temperature to be increased without affecting the concentrations of the reactive species. The technique involves replacing part of the nitrogen on the oxidizer side by an equal amount of argon; the extent of substitution depends on the extent of flame temperature adjustment desired. The procedure is as follows: the undiluted fuel is burned in air and the maximum flame temperature is measured. This fuel is then diluted with a given amount of nitrogen and its flame temperature in air is again measured.

*University of California at Davis.

Finally, the diluted fuel is burned in an oxidizer of 21% oxygen and an argon/nitrogen mixture such that the maximum temperature of this flame equals the temperature of the undiluted fuel burned in air. With these three flames, temperature and concentration effects can be assessed separately since we have: (a) two flames with different maximum temperatures but the same fuel concentration, and (b) two flames with different fuel concentrations but the same maximum temperature.

Spatial temperature measurements reveal that when the maximum temperatures of the diluted flames are adjusted to be identical to that of the undiluted flame, the temperature distributions in the soot region are also almost identical. Furthermore, since the pyrolysis reactions and the early particle life are critical to soot formation, it is reasonable to expect that the proposed temperature-adjustment methodology will allow temperature and dilution effects to be studied independently.

In Figure 1, the soot volume fraction ϕ is plotted as a function of time from the flame front. Filled symbols show the reduction of soot due to the combined thermal and dilution effects of inert addition, while the open symbols show the corresponding reduction mainly due to dilution. If we take the case of the 50% fuel dilution as an illustration, the maximum soot volume fraction decreases by 64% and 55% when the maximum flame temperature is allowed to vary and held fixed, respectively. Thus, as rough indications, one can attribute a 55% reduction in soot to the dilution effect and the remaining 9% to temperature reduction.

The volumetric soot production rate ($d\phi/dt$) is readily obtained from the slope of the curves in Figure 1. The roughly linear behavior of the maximum soot-volume fraction with concentration suggests that the soot production rate scales with the initial mole fraction of the fuel $X_{F,0}$. Plotting $(1/X_{F,0})\ d\phi/dt$ versus time for different concentrations but for the same maximum flame temperature (Figure 2), we find that the curves for different concentrations collapse into a single band, indicating that the soot production rate varies linearly with initial fuel concentration; that is, $d\phi/dt \sim X_{F,0}$.

The specific surface growth rate σ is defined as the soot production rate per unit surface area, $(d\phi/dt)/S$, where $S = N\pi D^2$ is the total available surface area per unit volume, N the number density, and D the nominal diameter. A plot of σ versus time reveals that σ is independent of the initial fuel concentration $X_{F,0}$. Since $d\phi/dt$ varies linearly with $X_{F,0}$, one may then expect from the definition of σ that S should also vary linearly with $X_{F,0}$. Indeed, the history of $S/X_{F,0}$ is not sensitive to $X_{F,0}$. The above results suggest that the change in fuel concentration due to dilution affects soot formation by changing

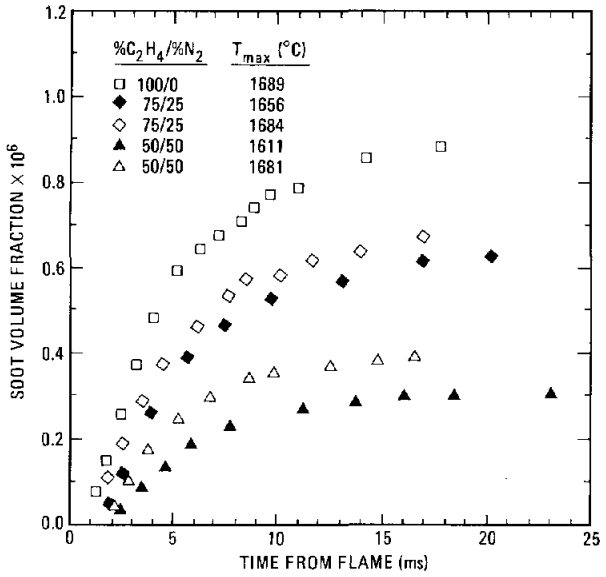

Figure 1. Soot volume fraction as a function of time from the flame front. Filled symbols show the reduction of soot due to the combined thermal and dilution effects, while open symbols show the corresponding reduction that is mainly due to dilution.

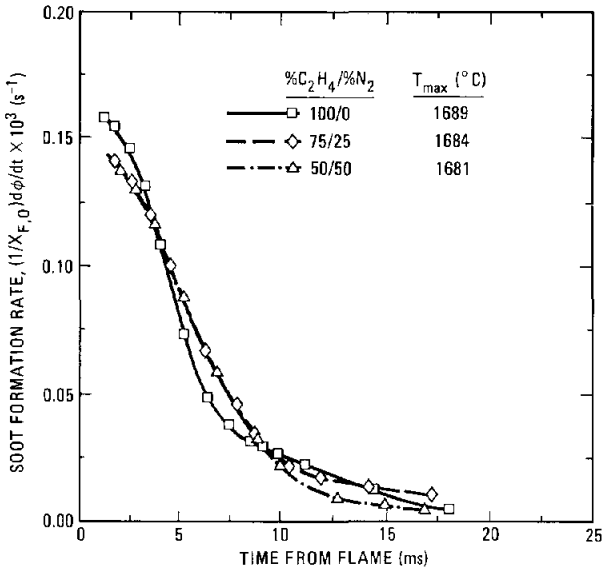

Figure 2. Soot production rate scaled by the initial mole fraction of the fuel as a function of time from the flame front. The results indicate that the soot production rate varies linearly with initial fuel concentration.

the available surface area for growth and not by changing the surface growth reaction rates.

References:

1. I. Glassman and P. Yaccarino, *Eighteenth Symposium (International) on Combustion* (The Combustion Institute, Pittsburgh, PA, 1981), p. 1175.

2. J. H. Kent and H. G. Wagner, *Twentieth Symposium (International) on Combustion* (The Combustion Institute,. Pittsburgh, PA, 1984), p. 1007.

Chemical Effects of Plasma Gases on Flame Kernel Development†

A study of the plasma jet ignition of lean methane-air mixtures was conducted to determine the effect of different plasma gases on flame-kernel development. Measurements of the two-dimensional distribution of OH concentration by laser-induced fluorescence in a diametral plane above the igniter yielded information on the ignition process.

S. R. Vosen, R. J. Cattolica, and F. J. Weinberg*

The use of plasmas to ignite combustible mixtures has been shown to be effective in promoting the combustion of both quiescent premixed gas mixtures and turbulent gas mixtures and in improving the performance of internal combustion engines.[1] It has also been observed that flame propagation occurs with Plasma Jet Ignition (PJI) of mixtures that are below the lean flammability limit when appropriate plasma gases are injected. This ability to increase the rate of combustion and to extend the flammability limits has been attributed to complex interactions of thermal energy deposition, radical deposition, and turbulent mixing.

The chemical effects of plasma gases on lean methane-air mixtures were studied from measurements of the hydroxyl radical concentration. The hydroxyl radical is a good indicator of chemical activity in premixed, methane-air flames. The technique of hydroxyl radical mapping by laser-induced fluorescence produces good quantitative data for nonsteady propagating methane-air flames[2] and has been useful in determining qualitatively the effect of fluid dynamics on flame structure.[3] In the present work, the technique has been used to map regions of chemical activity for a variety of plasma sources capable of producing OH on their own or by reacting with surrounding gases.

The ignition of premixed gases was studied in a constant volume combustion chamber using plasma jet ignition. The chamber had a volume of two liters with four quartz windows (100 mm diameter) providing access for schlieren observations and for spectroscopic imaging measurements. The plasma jet igniter used in this study was constructed to provide the flexibility needed to conduct a parametric study of the plasma prechamber geometry and of the feed gases. The plasma prechamber was cylindrical with an orifice restricting the flow of plasma gases into the combustion chamber. The diameter and height of the cylindrical prechamber were 3.0 mm each for this study, giving a volume of 22.2 mm.[3] The orifice used was 2.0 mm in diameter. A plasma was created by an electric discharge between a cathode centered at the closed end of the cylindrical volume and an anode formed by the orifice plate at the other end of the chamber. A shutter was used to isolate the gases in the plasma igniter from the gases in the combustion gases prior to ignition. The plasma gas mixture was controlled by purging the gas in the cavity through two gas lines which entered near the cathode.

The OH concentration distribution was measured in a plane through an axial section of the jet by laser-induced fluorescence (LIF) imaging. The laser beam from a Nd:YAG pumped-dye laser tuned to excite the OH molecule was expanded into a sheet 0.5 mm thick and 50 mm high. The fluorescence image from a 50-mm section of the laser sheet was focused onto a gated ISIT vidicon camera, resolving the fluorescence from a cubic volume 0.5 mm on a side. The fluorescence signal was collected perpendicular to the laser sheet by lenses that focused the emitted light onto a two-dimensional detector array. The fluorescence signal follows temporally the 5-ns laser pulse used for excitation. Since this time interval is much faster than the time scale of the flow in the combustion chamber, the resulting planar image is an instantaneous picture of the OH distribution in the combustion chamber.

The effect of OH produced by the plasma was studied by varying both the gas in the plasma cavity (the plasma mixture) and the gas into which the plasma was injected (the chamber mixture). The results presented here are for $2H_2+O_2$ plasma discharge into N_2, $2H_2+O_2$ plasma discharge into air, $2H_2+O_2$ plasma discharge into $\phi = 0.50$ CH_4/air, and $2H_2+O_2$ plasma discharge into $\phi = 0.65$ CH_4/air.

Stills from a schlieren movie (Figure 1) show the development of a $2H_2+O_2$ plasma injected into $\phi = 0.50$ CH_4/air. The jet advances rapidly into the combustion for 2 ms, with high contrast indicative of large temperature gradients. After 2 ms, the

†Royal Society of London, accepted (1988).

*Imperial College of Science and Technology, London, England.

penetration of the jet into the combustion chamber slows, and the contrast (and thus the temperature gradients) lessen. Schlieren images for this case do not look very different from those taken of plasma jets injected into inert gases, making it difficult to determine the extent of combustion.

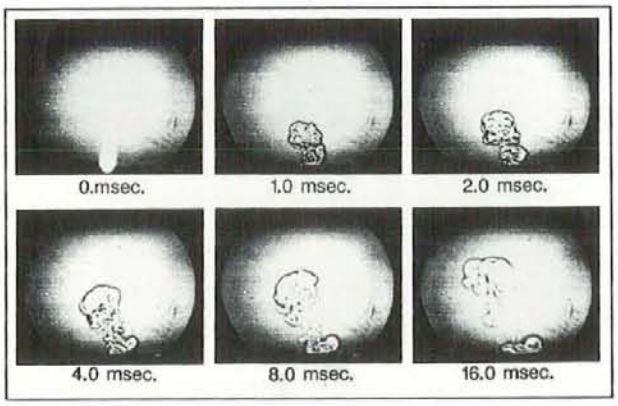

Figure 1. Schlieren images of a $2H_2+O_2$ plasma injected into a ϕ=0.50 methane/air mixture.

The effect of plasmas on flammability can be studied by injecting the same plasma mixture ($2H_2+O_2$) into various chamber gas mixtures. Figure 2 shows the OH concentration in a plane above a plasma igniter 0.50 ms after discharging a $2H_2+O_2$ mixture into N_2, air, ϕ = 0.50 CH_4/air, and ϕ = 0.65 CH_4/air mixtures.

As the reactivity of the combustion chamber gas is increased in progression from N_2, to air, to ϕ = 0.50 CH_4/air, to ϕ = 0.65 CH_4/air, the high concentrations of OH are seen to last for progressively longer times. The OH produced from the plasma and from plasma/air reactions alone were found to disappear by 1.00 msec; the increased levels of OH in the ϕ = 0.50 CH_4/air mixture are therefore due to reactions with the entrained methane/air mixture. H, O, and OH from the plasma react with the methane and enhance the chain branching reactions of methane combustion. The plasma is effective in promoting combustion, as the mass of gas burned for the ϕ = 0.50 CH_4/air case is over 100,000 times the mass of the gases originally contained in the plasma igniter as determined from pressure measurements in the combustion chamber, with an energy of 300 J.

In conclusion, plasma-jet ignition and flame-kernel development were studied by mapping the OH distribution above a plasma igniter filled with a variety of plasma media injected into various inert and reacting gases. Results show sporadic, small, chemically active regions, generally off-axis and often associated with vortex-like structures. These flame kernels grow, under conditions of increasing reactivity, leading to propagating flames. For the combustion of mixtures that can readily be ignited by a conventional spark discharge, the main effect of PJI is in enhancing turbulence in the growing flame kernel. For up to two ms after injection, schlieren photographs of all plasma mixtures injected into either N_2, air, or ϕ = 0.50 CH_4/air, reveal similar plasma plumes. An examination of the development of the OH distribution shows that important differences exist as early as 0.50 ms after injection. OH produced in the plasma mixture alone persists for approximately 0.50 ms, and reactions with the oxygen in the entrained air persist for 1.00 ms. For ϕ = 0.50 mixtures, flame propagation was maintained for up to 35 ms with PJI.

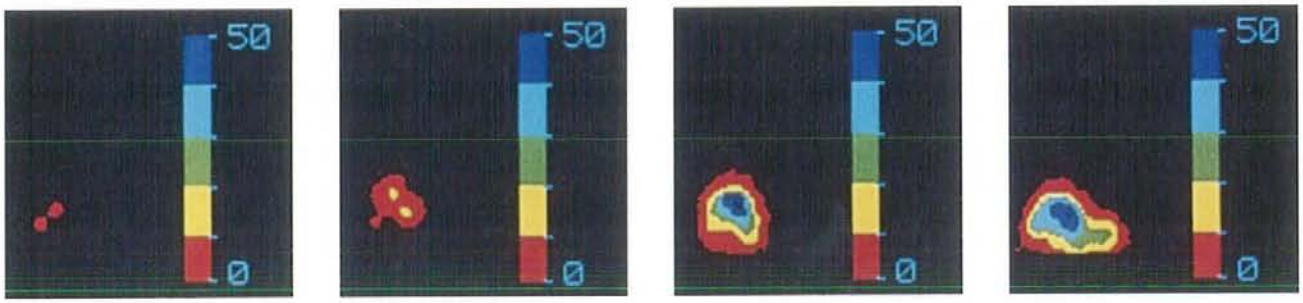

Figure 2. OH maps during plasma injection 0.50 ms after discharge in a plane perpendicular to the plasma igniter. The conditions are the discharge of a $2H_2+O_2$ plasma into (a) N_2, (b) air, (c) ϕ=0.50 CH_4-Air, and (d) ϕ=0.65 CH_4-Air. The concentration scale is 100=10^{15}/cc.

References:

1. F. J. Weinberg, *Advanced Combustion Methods* (Academic Press, London, England, 1986), Ch. 5.

2. R. J. Cattolica and S. R. Vosen, *Twentieth Symposium (International) on Combustion* (The Combustion Institute, Pittsburgh, PA, 1984), p. 1273.

3. R. J. Cattolica and S. R. Vosen, Comb. Sci. Tech. **48**, 77 (1986).

Propagation of a Premixed Flame in a Divided-Chamber Combustor†

Experimental observations of the propagation of premixed ethylene-air flames in a divided-chamber combustor have been compared with a numerical simulation based on a flame-sheet/vortex-dynamics model over a range of Reynolds numbers. The predicted prechamber flame propagation rates and the calculated spatial and temporal development for the lowest Reynolds-number flame agree with the experiments. At higher Reynolds-number conditions, the model predicts slower flame propagation without the experimental observed shear layer instabilities.

R. J. Cattolica, P. K. Barr, and N. N. Mansour*

The propagation of lean premixed ethylene-air flames in a divided-chamber combustor has been investigated both experimentally and numerically. A comparison shows excellent agreement of the measured and predicted interactions of the flame with the vortex ring.

In both the experiment and the simulation, the combustion vessel is divided by a small cylindrical prechamber, with a spark electrode located near the closed end and a circular orifice leading to the main combustion chamber at the other end. The entire combustion vessel is filled with premixed combustible gas, and the ignition by the spark in the prechamber causes the expanding flame to push gas out through the orifice into the main chamber. This flow through the orifice causes a vortex ring to grow behind the downstream side of the orifice plate. When the flame burns past the orifice, it encounters the toroidal region of vorticity and the flame distorts, taking on a "mushroom-like" shape.

The combustion vessel was fitted with four orthogonal windows to allow optical access in the experiment. The propagation of the flame in the main combustion chamber was observed with a laser-schlieren videography system. The cw laser light was formed into a series of 0.5 μs pulses synchronized with the framing rate (2000 frames per second) of a high speed video camera. The Reynolds number was varied between runs by changing the equivalence ratio of the combustible mixture. For the ethylene-air mixtures used in the paper, the flame speed was changed by a factor of 2.4, while the density ratio varied by a factor of 1.2. Individual frames taken from the video recording of the spatial development of the propagating flame are presented in Figure 1 for the leanest equivalence ratio condition. The time given with each frame was referenced to the spark discharge time.

The axisymmetric numerical simulation combines a wrinkled laminar flame sheet model with the discrete-vortex method. The flame-interface algorithm requires a fixed numerical mesh to determine both the flame position and the combustion-generated flow field. The growth of the vorticity region that is produced in the main chamber by the gas flowing through the prechamber orifice is simulated by introducing individual vortex rings at the orifice edge and tracking them as they interact with each other and with the combustion-generated flow field. In the numerical results, the effects of the combustible mixture are accounted for by the flame speed and the density ratio.

The flame shapes that were predicted by the simulation are also shown in Figure 1 for the same conditions as in the experiment. Both the experimental and numerical results are shown at the same time intervals. As can be seen from the figure, both results show that the flame propagates through the center of the toroidal distribution of vorticity and is pulled around the core and spirals into its center. The combustion process continues to reduce the amount of unburned gas within the toroid, until it is consumed. As shown in Figure 1, the numerically predicted time development for this lowest Reynolds number laminar flame condition agrees well with the experimental results.

As the fuel-air equivalence ratio was increased in the experiment, the increased velocities and Reynolds numbers characterizing the flame propagation began to exceed some of the idealized assumptions used in the numerical simulation. At higher equivalence ratios, which produced higher flow velocities, the temporal agreement between the experimental and computational results diverged.

†Combustion and Flame, accepted (1988).

*NASA Ames Research Center, Moffett Field, CA.

This may be the result of the variation of the flame speed caused by flame stretch, an effect not included in the model. Kelvin-Helmholtz instabilities were also observed in the experimental results at the highest equivalence ratios. The fact that the numerical results did not predict these instabilities indicates that a more sophisticated model of the behavior of the vortex elements is needed to capture the physical phenomena that occur at higher Reynolds number conditions.

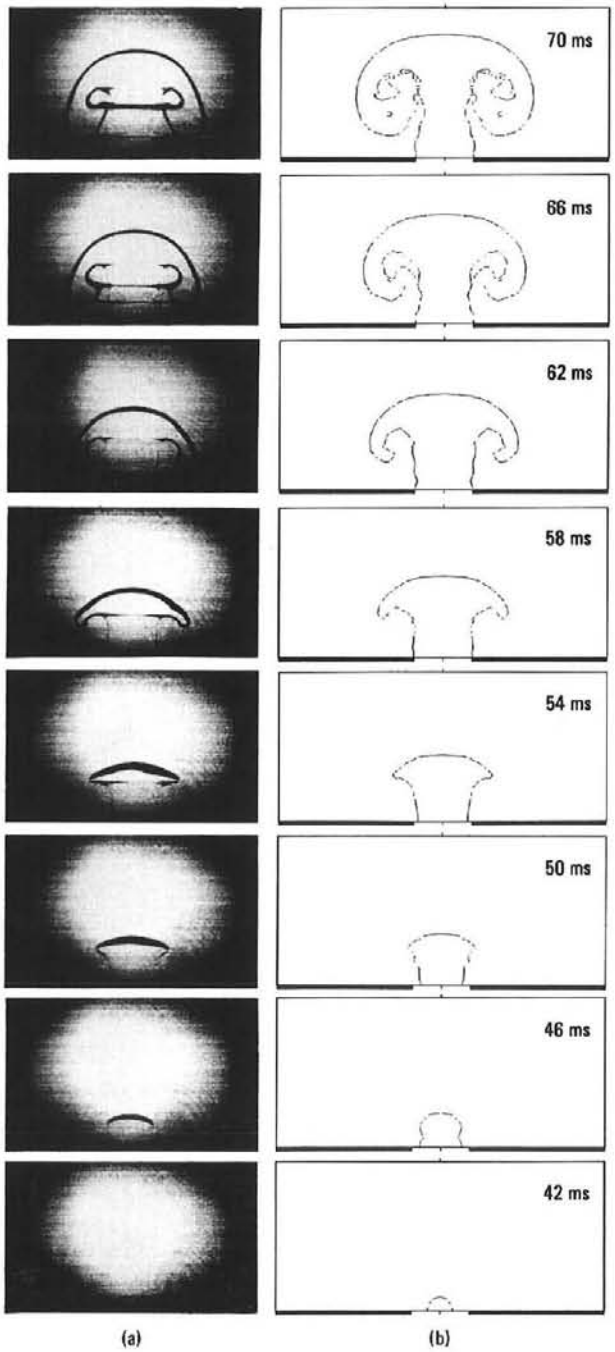

Figure 1. Flame development in the main combustion chamber for ϕ=0.5. Time from spark discharge is as shown. (a) Laser-schlieren visualization; (b) numerical simulation.

Numerical calculation of the transport and chemical reaction of debris during a simulated core-melt nuclear reactor accident.

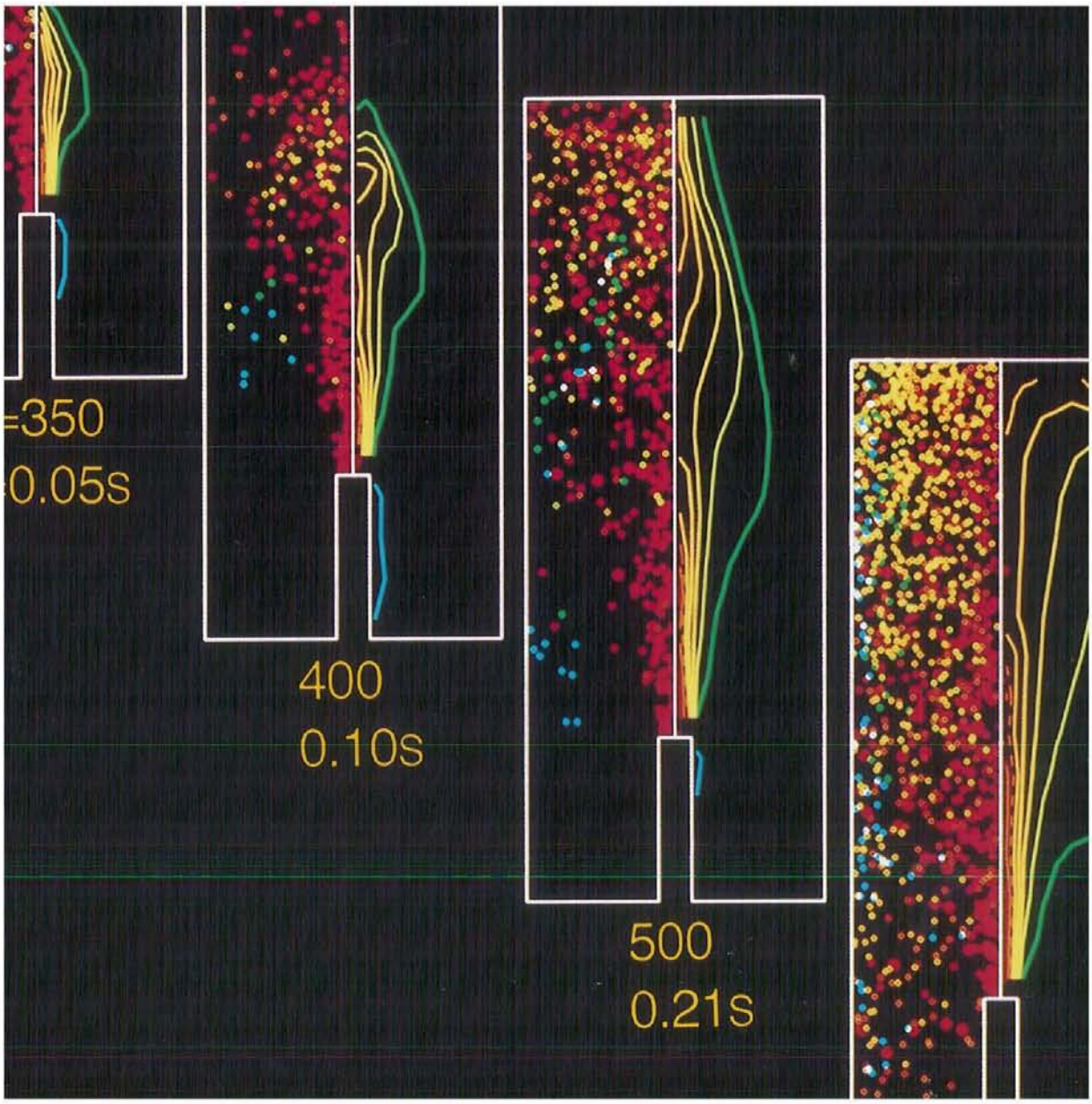
=350
0.05s
400
0.10s
500
0.21s

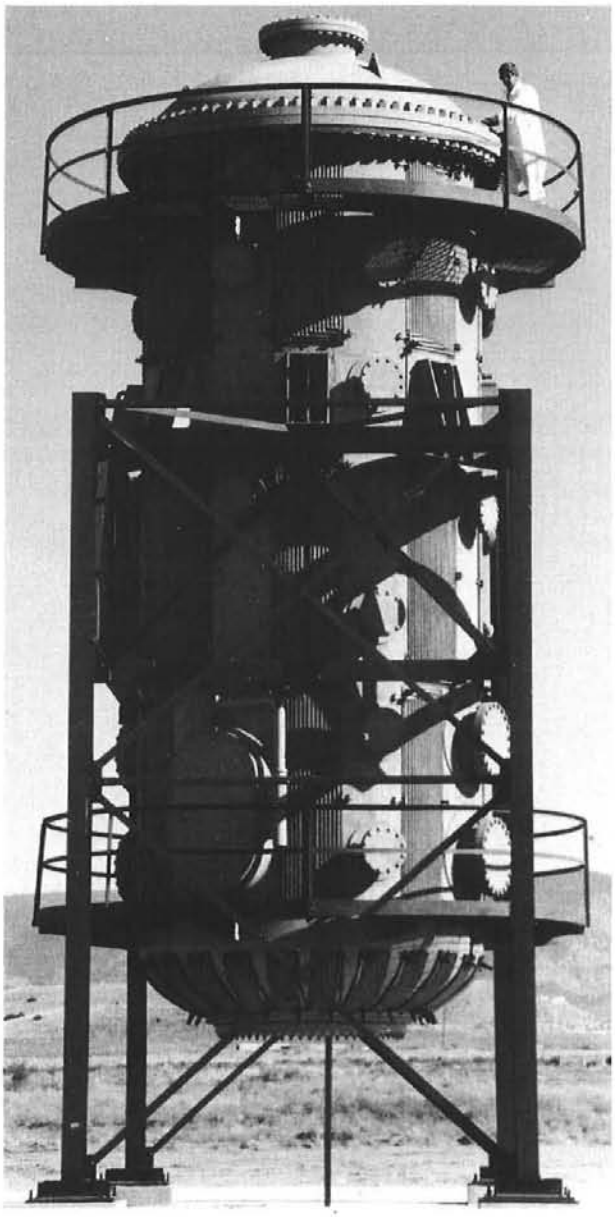

Surtsey Test Facility was developed to study loads placed on nuclear reactor containment buildings during severe accidents.

The sequence of plots on the previous page illustrate results from a computer simulation of debris transport and chemical reaction in the Surtsey Direct Heating Test Facility. This facility (see photo this page) is being used to determine the effects of injection of molten debris into nuclear reactor containment buildings. The plots on the previous page show isotherms (right) and the positions of typical debris particles (left) at various times during injection of debris from a chute at the bottom of the facility. The color code indicates a range of temperatures from 300 K (blue) to 2300 K (red). The figure below shows how the computed pressure history compares with that obtained experimentally. The pressure computed with and without chemical reactions are given to indicate the effect of oxidation of the debris.

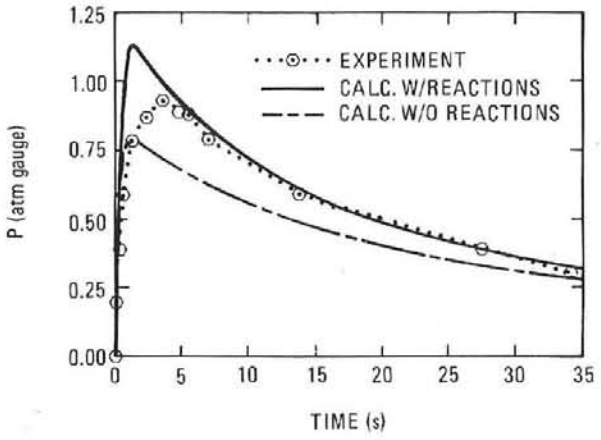

Section 5
Combustion Modeling

The combustion modeling programs at Sandia National Laboratories emphasize the application of innovative mathematical and numerical approaches to predict the mutual influences of reactions and fluid transport mechanisms. Most combustion applications include, in addition to chemical kinetics, complex fluid dynamics associated with a combination of multidimensional geometries, unsteady conditions, moving boundaries, and two-phase transport. Our current modeling research programs attempt to provide a fundamental understanding of these subprocesses so that future simulations will contain more realistic chemical and physical descriptions of combustion phenomena. The areas selected for study are strongly influenced by ongoing experimental research activities, in which direct comparison with data from well-characterized experiments verify and extend our combustion models.

A strong emphasis of the modeling programs supported by the DOE Office of Basic Energy Sciences is the numerical simulation of combustion processes. Since current computational limitations prevent a detailed analysis of both fluid mechanics and chemistry, the research projects tend to focus on one of these aspects. Reacting turbulent and two-phase flows emphasize the complex nature of fluids transport with simple-heat release, while the CHEMKIN family of codes provides users with comprehensive chemical kinetics and molecular transport capabilities.

Field Equation Formulation of Turbulent Premixed Flame Propagation†

Formulation of the process of turbulent, premixed flame propagation as an initial value problem for a scalar field yields a computationally efficient algorithm for computing the turbulent burning velocity in simulated homogeneous turbulence.

A. R. Kerstein, W. T. Ashurst, and F. A. Williams*

A fundamental problem in combustion theory is the determination of the burning velocity of turbulent, premixed flames in the laminar-flamelet regime, in which burned and unburned regions are separated by a thin, wrinkled surface. This surface is convected by the unsteady flowfield and propagates toward the unburned region at a normal velocity u_F which depends on the local curvature of the surface as well as the local strain field. Furthermore, volumetric expansion due to heat release at the surface induces global as well as local distortions of the strain field.

As a paradigm of this and other processes involving the passage of a chemical reaction front through a stirred medium, the following simplified problem may be considered. A surface, initially planar, is convected by an unsteady homogeneous flowfield, and the surface propagates relative to the flowfield at a constant normal velocity u_F. This propagation mechanism is assumed to be passive in that it does not affect the fluid velocity field $\mathbf{v}(\mathbf{x},t)$. This velocity field may be regarded as a realization of Navier-Stokes turbulence.

Several fundamental issues concerning this, as well as the more complicated processes of practical interest, are as yet unresolved. Foremost among these is the issue of the existence of a steady-state turbulent burning velocity. The turbulent burning velocity u_T is defined in this context as the volume flux through the evolving surface per unit cross-sectional (projected) area in the direction of propagation. It has not been established that, for a statistically steady flowfield, the ensemble-average value of u_T eventually converges to a constant. Furthermore, the dependence of u_T on the root-mean-square (rms) velocity fluctuation u' (a measure of turbulence intensity) and on Reynolds number is uncertain.

Resolution of these issues for the propagation of a passive surface may provide insights relevant to the more complicated processes of practical interest. To investigate the simplified problem, it is useful to formulate the interface propagation problem as an initial value problem for a scalar field $G(\mathbf{x}, t)$ whose level surfaces (loci of constant G) represent interfaces. Steps in this direction have been taken previously, but in previous formulations, the turbulent burning velocity was expressed as a function of a particular level surface, e.g., $G = 0$. In contrast, we have formulated an initial value problem which yields a valid realization of the propagation process for every level surface $G = c$, allowing u_T to be expressed as a functional of the entire scalar field. This formulation is advantageous for both computational and analytical study of the propagation process.

The field equation which we adopt is

$$\frac{\partial G}{\partial t} + v \bullet \nabla G = u_F |\nabla G|, \qquad (1)$$

where $\mathbf{v}(\mathbf{x},t)$ is a given flowfield. The left-hand side of Equation (1) is the convective derivative DG/Dt. It is easily seen that the source term on the right-hand side causes any level surface to propagate with a normal velocity u_F relative to a local fluid element. For instance, consider some point $\mathbf{x}_o$ on any level surface $G = c$ at time t_o. In some neighborhood of $(\mathbf{x}_o, t_o)$, G can be approximated by the lowest-order terms in a Taylor expansion, namely

$$G(\mathbf{x},t) = G(\mathbf{x}_o,t_o) + (\mathbf{x} - \mathbf{x}_o) \bullet \nabla G(\mathbf{x}_o,t_o) + (t - t_o)\frac{\partial G(\mathbf{x}_o,t_o)}{\partial t}. \qquad (2)$$

In the limit $t \to t_o$, the point $\mathbf{x}(t)$ specified by

$$\frac{\mathbf{x}(t) - \mathbf{x}_o}{t - t_o} = \mathbf{v}(\mathbf{x}_o,t_o) - u_F \frac{\nabla G_o}{|\nabla G_o|}, \qquad (3)$$

where $G_o \equiv G(\mathbf{x}_o, t_o)$, is on the level surface $G = c$ at time t. This follows from the definitions of $\mathbf{v}$ and u_F. Namely, a fluid element at point $\mathbf{x}_o$ is convected by the local fluid velocity $\mathbf{v}$, and the level surface propagates relative to the fluid with velocity $u_F\mathbf{n}$, where $\mathbf{n} = -\nabla G_o / |\nabla G_o|$ is the unit vector normal to the level surface. (The convention is adopted that propa-

†Physical Review A **37**, 2728 (1988).

*Princeton University, Princeton, NJ.

gation is in the direction of decreasing G.) Therefore, the right-hand side of Equation (3) is the velocity of the level surface at $(\mathbf{x}_o, t_o)$, so $G(\mathbf{x},t) = G(\mathbf{x}_o, t_o)$ to first order in $t - t_o$ for the above choice of $\mathbf{x}(t)$, as claimed. For this choice of $\mathbf{x}(t)$, Equation (2) thus reduces to

$$\frac{\partial G_o}{\partial t} = -\frac{\mathbf{x}(t) - \mathbf{x}_0}{t - t_0} \bullet \nabla G_o . \qquad (4)$$

Substitution of Equation (3) into Equation (4) yields Equation (1).

Although we have specified that u_F is constant, this derivation is valid if u_F is taken to be any function of $G(\mathbf{x},t)$, $\mathbf{v}(\mathbf{x},t)$, and their derivatives. In particular, the aforementioned strain and curvature effects can be incorporated, as demonstrated below.

In order to derive a convenient expression for u_T, we have analyzed the time evolution of $G(\mathbf{x},t)$ viewed as an initial value problem, based on Equation (1) and the initial condition $G(\mathbf{x},0) = \mathbf{x}$, where the position vector $\mathbf{x}$ is expressed as $\mathbf{x} = (x, y, z)$. Since the field equation is nonlinear, the choice of initial condition is nontrivial. For this initial value problem, we have derived the following expression for u_T as defined above:

$$u_T = \langle u_F \, | \nabla G \, | \rangle \qquad (5)$$

where the brackets denote a volume average.

For purposes of numerical simulation, a practical advantage of the field formation with Equation (5) for u_T is that the entire computational domain contributes to the estimate of u_T at any epoch, in contrast to formulations in which a single interface within an Eulerian computational domain is simulated.

To investigate computationally the issue of the convergence of u_T, we have numerically solved the initial value problem for G in a forced Navier-Stokes flow on a 32^3 grid. In this calculation, u_F was taken to be dependent on the local strain field and the local curvature of the level surface as prescribed by laminar flame theory, namely

$$u_F = u_L (1 - l_M k), \qquad (6)$$

where u_L represents the laminar flamespeed in the absence of strain or curvature effects. The flame stretch k is given by

$$k = - b + \nabla \bullet \mathbf{n},$$

where $\mathbf{n} = - \nabla G / |\nabla G|$, $b = \mathbf{n} \bullet \mathbf{e} \bullet \mathbf{n}$, and $\mathbf{e}$ is the strain-rate tensor. The Markstein length l_M, whose value depends on flame chemistry, was taken to be $0.0125\ l_C$, where l_C is the edge length of the computational domain. This choice of l_M was based primarily on numerical stability considerations, but it also corresponds to a physically interesting case.

Figure 1 shows a simulated time history of u_T, computed from the numerical solution for G and the flowfield. The transition from an initial rise to fluctuations about a steady value is indicative of convergence to a constant ensemble-average value of u_T in this case. For this realization, $u' = 1.2\ u_L$ and the integral length scale estimated from the transverse velocity correlation is $l_l \approx 0.1\ l_C$. Therefore, the characteristic time for large eddy turnover is $\tau = l_l / u' \approx 0.1\ l_C / u_L$. This is consistent with the time scales for transient relaxation and subsequent fluctuations of u_T, as evident in Figure 1.

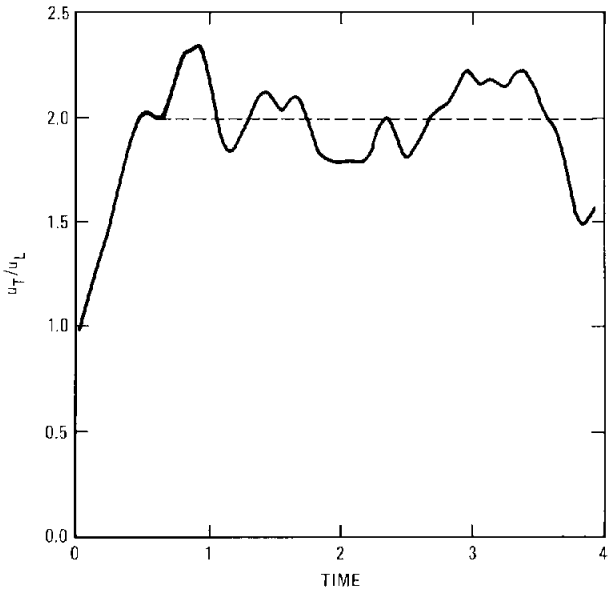

Figure 1. Normalized volume flux u_T/u_L through a level surface, estimated from a simulated realization of the field G, as a function of time expressed as a multiple of l_l/u_L. (l_l is the turbulence integral scale and u_L is the propagation velocity in the absence of strain or surface curvature.) G was convected by a homogeneous Navier-Stokes velocity field with turbulence intensity $u' = 1.2u_L$. The propagation velocity u_F depends on strain and curvature effects as expressed by Equations (6) and (7). A time average over the period indicated by the dashed line yields $u_T/u_L = 1.99$.

Block-Inversion Model of Turbulent Scalar Transport and Mixing†

A one-dimensional representation of turbulent scalar transport and mixing is implemented as a Monte Carlo simulation. Key features of scalar mixing measured in grid turbulence are reproduced.

A. R. Kerstein

A significant limitation of most existing approaches for modeling turbulent transport and mixing is their inability to treat distinctly the effects of molecular diffusion and fine scale convection. On length scales smaller than the computational mesh spacing, these two effects are generally subsumed into a phenomenological sub-grid-scale model. One consequence of this approach is that dependences on the Peclet number $Pe = D_T/D_M$ (the ratio of turbulent to molecular diffusivity) are not incorporated in a physically sound manner. Such models cannot predict experimentally observed Peclet-number effects in combusting shear layers and other configurations.

To rectify this shortcoming, a novel approach has been adopted in this work. The strategy is to incorporate all relevant length scales by refining the mesh. To keep the computation affordable at Peclet numbers of practical interest, the computational domain is restricted to one dimension, representing a transverse coordinate in a flow which is homogeneous along the other transverse coordinate. (Planar shear layers, for instance, obey this property.) Simulated time evolution along the transverse coordinate corresponds to the streamwise evolution of a spatially-developing flow.

Since all relevant length scales are resolved, molecular processes can be incorporated in a physically sound manner by introducing Fickian diffusion of the scalar field. Continuous fluid motions cannot be achieved in one dimension (except for the uninteresting case of spatially-constant velocity), so convective effects are represented by discrete events which introduce discontinuous fluid motions. In the present formulation, these events are block inversions.

Block inversion consists of the random selection of an interval

$$(y_0 - \frac{1}{2}, y_0 + \frac{1}{2})$$

of the line, where l represents the turbulent integral scale, and replacement of the scalar field $q(y)$ within that interval by $q(2y_0 - y)$. In effect, the scalar field is spatially inverted within the interval, but unchanged elsewhere.

This formulation is simple in both concept and implementation, involving a single input parameter, the Peclet number. (The model analog of the turbulent diffusivity D_T is the diffusivity of a marker particle induced by successive block inversions.) This parameter is proportional to the frequency of block-inversion events.

The block-inversion model can be implemented either computationally or analytically to predict the evolution of the scalar field from a given source configuration, which may be localized or distributed. In computer simulations, the source configuration determines the initial and boundary conditions, but the algorithm is otherwise unaffected. Although the model is formulated as spatially continuous, it is implemented computationally on a line discretized into cells of equal size. The cell size is set small enough to resolve all relevant length scales of the scalar field. Adequacy of the spatial resolution has been verified by comparison of computed results to analytical results based on the continuum formulation.

An initial application of the model involves the simulation of the spatial development of the thermal plume downstream of a line source in homogeneous turbulence. (The line source is transverse to the mean flow.) The computations are event-oriented Monte Carlo simulations. The initial condition is a vector of scalar values, all set to zero except for a single entry, representing the source, which is equated to the source temperature T_o. Molecular diffusion is implemented by regularly updating the scalar field using a finite-difference formulation of Fick's law. At randomly selected times, block-inversion events occur, involving the random selection of the block location and rearrangement of the scalar field accordingly. Scalar statistics are gathered as a function of spatial location y, representing transverse displacement relative to a streamwise

†Combustion Science and Technology, submitted (1988).

coordinate intersecting the line source, and time t. Time t is interpreted as streamwise location x based on $x = Ut$, where U is the mean streamwise flow velocity. Typically, hundreds of realizations are simulated in order to accumulate scalar fluctuation statistics for a given configuration.

Computed results have been compared in detail to thermal plume measurements downstream of a heated wire in grid turbulence.[1] A key comparison is shown in Figure 1. As one would expect, the transverse profile of mean temperature decreases monotonically away from the centerline and the profile width increases with time. However, the measured, as well as the computed, transverse profile of the rms temperature fluctuation develops an off-centerline peak.

Analysis of the model reveals the origin of this behavior. At early times, the block-inversion process, representing convective stirring, subdivides the plume into independently wandering "blobs." The rms fluctuation is determined by the probability of encountering a blob at a given transverse location. This probability decreases monotonically with increasing transverse displacement. As the blobs accumulate and spread due to molecular diffusion, they eventually overlap and thereby suppress scalar fluctuations. This suppression occurs first near the centerline. This sequence of events, predicted by the block-inversion model, constitutes the first mechanistic explanation of the experimental observations.

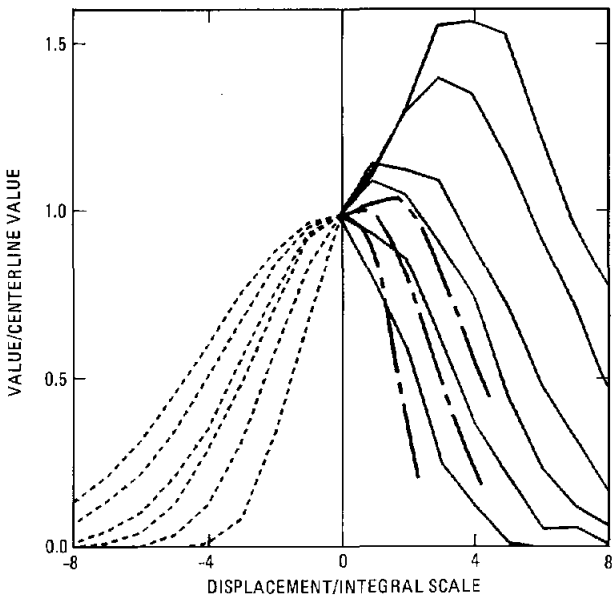

Figure 1. Transverse profiles, in terms of scaled displacement from the centerline, of mean temperature (dashed; plotted left of centerline) and rms temperature fluctuation (solid; plotted right of centerline), computed for the thermal plume downstream of a heated wire using the block-inversion model. These curves correspond, lowest to highest, to scaled plume-development times t/t_L = 1, 2, 3, 4, 6, and 8, respectively, where t_L is the Lagrangian eddy-turnover time. Measured[2] rms temperature profiles (chain-dashed) correspond, lowest to highest, to scaled times t/t_L = 1.4, 2.6, and 3.4, respectively. Computations and measurements were performed at a Peclet number of 100.

References:

1. A. R. Kerstein, "A. Linear-Eddy Model of Turbulent Scalar Transport and Mixing," Comb. Sci. Tech., submitted (1988).

2. Z. Warhaft, J. Fluid Mech. **144**, 363 (1984).

The Alignment of Vorticity, Scalar Gradient, and Pressure Gradient with Strain Rate in Navier-Stokes Turbulence

From single spatial point analysis of computed turbulence, we infer that a stretching vortex flow pattern is the generic structure for the most dissipative regions. This flow pattern creates gradients in a scalar quantity by differential rotation about the vortex axis.

W. T. Ashurst, A. R. Kerstein, R. M. Kerr,* C. H. Gibson,** J.-Y. Chen, and M. M. Rogers***

From direct numerical simulations of Navier-Stokes turbulence, we have determined the probability of alignment with the strain-rate eigenvectors for the following quantities: vorticity, gradient of a passive scalar, and pressure gradient. From this analysis, we infer that conservation of angular momentum determines the evolution of the local turbulence and determines a unique shape for the strain-rate tensor at large strain rate. The details of our single, spatial-point analysis are given in References 1 and 2. Our results show that vorticity has the largest probability to align with the intermediate strain direction, and while this strain rate is more likely to be positive (extensional), its magnitude is relatively small compared to the other strain rates. Figure 1 presents the probability distribution for the shape of the strain-rate tensor in the limit of large strain rate. The peak corresponds to strain-rate ratios of 3 : 1 : -4 (they sum to zero for incompressible flow). In the small strain-rate limit, the distribution has a symmetric triangular shape. The strain rate dependence for the transition between these two distributions appears to be invariant to the large scale flow conditions. The probability that vorticity aligns with the largest extensional strain rate is small, which might seem odd in that a logical guess would be for vorticity to be pulled out in the direction of the largest positive strain. However, conservation of angular momentum appears to dictate that a self-stretching vortex flow pattern develop, and this developing flow yields the largest magnitude strain rates in the plane normal to the vortex axis. A restricted Euler model by Vieillefosse[3] shows that given arbitrary strain rates and vorticity in an isolated volume of fluid, then in a time that we found to be short compared with the large-scale eddy turnover time, the dynamical coupling between strain and rotation will re-orient the vorticity so that it moves into the intermediate strain-rate direction and that this strain will be positive. The underlying cause is that in three dimensions, when two components of angular momentum are constant, then so must be the third. Examination of a stretching vortex flow with uniform axial strain reveals that two components of angular momentum are indeed constant by symmetry. This flow is a steady-state solution when viscosity is included, since the diffusion of vorticity away from the axis of rotation is balanced by the radial inward flow induced by the axial stretching. The vorticity has an exponential distribution with the large strain-rate region in a halo around the vortex core. Vieillefosse did not include viscosity in his model, but if we use his equations to calculate the energy dissipation (square of strain rate) we find that the dissipation of energy increases as the fluid volume develops into a self-stretching vortex. Thus, the lifetime of this stetching vortex will be finite. Of course, interaction with neighboring volumes which are undergoing the same dynamics may cause major deviations from this picture for a particular volume. It is worth noting that this stretching vortex is the main ingredient in Lundgren's model[4] which exhibits an energy spectrum with a -5/3 power law range. Lundgren assumes that a strong vortex will be maintained by some out-of-plane strain (which may be the self-stretch effect to conserve angular momentum) and this strong vortex will wrap other weaker vorticity into a spiral around the vortex core. If this spiral region is not axisymmetric, then a 5/3 exponent is found from the Fourier description of sheets of vorticity in the spiral.

*National Center for Atmospheric Research, Boulder, CO.
**University of California at San Diego.
***NASA-Ames Research Center, Moffett Field, CA.

We have also found that a passive, diffusive scalar in these Navier-Stokes simulations shows increased probabililty for alignment of scalar gradient in the direction of the most compressive strain rate. Gibson[1] wrote an equation for the isoscalar velocity which shows that in regions of large scalar gradient the diffusing scalar will act more like a nondiffusive scalar. Given a constant strain rate, the gradient of a nondiffusive scalar grows exponentially in time. Thus, the differential rotation about a stretching vortex core can rapidly increase the gradient of a diffusing scalar and make the gradient direction be normal to the vortex direction.

In a homogeneous shear flow simulation, we have found that the pressure gradient given by the velocity fluctuations has the same alignment behavior as the passive, diffusive scalar, but the pressure gradient related to the mean velocity gradient shows no alignment features.

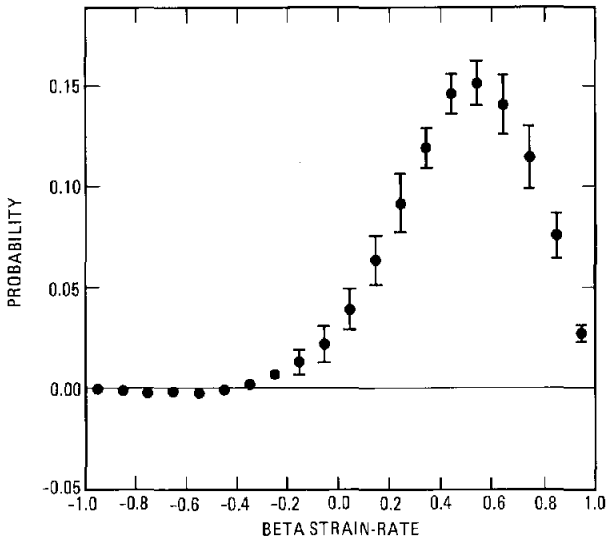

Figure 1. Probability distribution for the shape of the strain-rate tensor in the limit of large strain rate as determined from Navier-Stokes simulations. The intermediate strain rate, β, has been normalized so that β of -1 is the case of two equal compressive strain rates, and β of +1 is the situation of two equal extensional strain rates.

References:

1. W. T. Ashurst, A. R. Kerstein, R. M. Kerr, and C. H. Gibson, Phys. Fluids **30,** 2343 (1987).

2. W. T. Ashurst, J.-Y. Chen, and M. M. Rogers, Phys. Fluids **30**, 3293 (1987).

3. P. Vieillefosse, J. Phys. (France) **43**, 837 (1982).

4. T. S. Lundgren, Phys. Fluids **25**, 2193 (1982).

A Computational Model of the Structure and Extinction of Strained, Opposed-Flow, Premixed Methane-Air Flames

We use numerical methods, including arc-length continuation, to simulate the complex chemical kinetics behavior in strained premixed methane-air flames that are stabilized between two opposed-flow burners. We predict both the detailed structure and the extinction limits for these flames over a range of fuel-air mixtures.

R. J. Kee, J. A. Miller, and G. Dixon-Lewis*

Understanding the structure and extinction of well-controlled stretched flames is critically important to the development and application of laminar flamelet concepts to turbulent flame propagation. The opposed-flow flame, shown schematically in Figure 1, is an excellent configuration in which to study stretch effects in premixed flames. Furthermore, by invoking boundary-layer assumptions, a one-dimensional mathematical model can be constructed that permits efficient computational solution, even when complex chemical kinetic and molecular transport models are included. Here we use computational methods to study premixed, methane-air, opposed-flow laminar flames that were investigated experimentally by Law, *et al.*[1] who measured extinction limits as a function of the fuel-air mixture. In addition to determining the extinction limits, we use sensitivity analysis to provide insight into the complex chemical kinetic behavior.

This flame configuration can be modeled using the stagnation-point, boundary-layer assumptions, which result in a significant mathematical simplification of the governing equations. The underlying assumption is that strain field can be characterized by the classic inviscid potential flow in the vicinity of a stagnation point, i.e., $u_e = ax$ and $v_e = -ay$, where the velocity gradient a is called the strain rate in the laminar-flamelet context. The system of equations and boundary conditions is a two-point, boundary-value problem, which we solve by a hybrid Newton/timestep method that we have developed to compute the structure of premixed flames.[2] The method is computationally efficient, and the adaptive meshing features provide high accuracy. In addition to computing flame structure, we are especially concerned here with the prediction of extinction limits. This task is facilitated by the application of arc-length continuation methods.[3] Continuation methods are useful in situations where the solution to a system depends on a parameter, and where one seeks a sequence of solutions for a range of parameter values. In the work presented here, the parameter is the strain rate (velocity gradient) a.

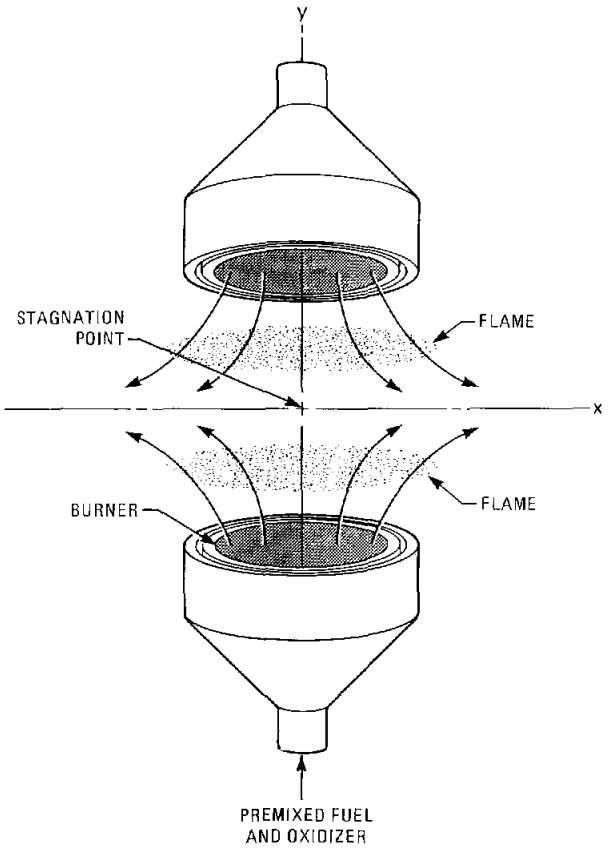

Figure 1. Schematic representation of the strained, opposed-flow, premixed flame configuration.

We determined the structure and extinction limits for flames involving five methane-air mixtures ranging from lean to rich (7, 8, 9, 10, and 11 percent methane) and for a range of strain rates. Figure 2 compares our extinction strain rate, a_{ex}, predictions with the experimental determinations of Law, *et al.*[1] and the computational simulations of Stahl, *et al.*[4] Both sets of simulations are higher than the data, with Stahl being about a factor of two

*University of Leeds, Yorkshire, England.

higher and ours about 50 percent higher. Also, the peak in both simulations occurs at about the stoichiometric point (9.5 percent methane), whereas the experiment shows a peak slightly on the lean side. What are the possible explanations of these disagreements?

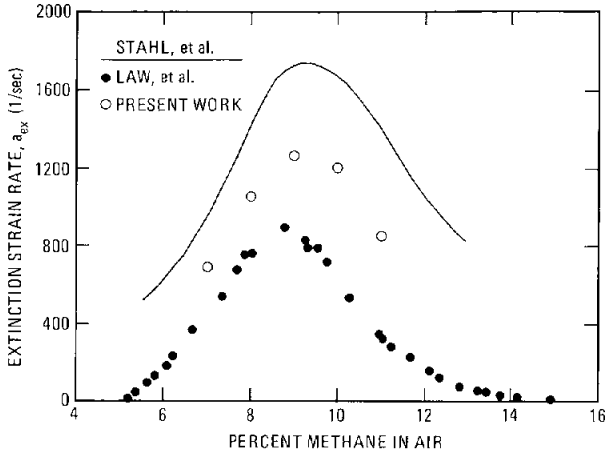

Figure 2. Extinction limit comparison with the Law, *et al.* data and the Stahl, *et al.* computation.

The governing equations in both models are nearly identical. We have used a more accurate multi-component transport formulation, but this only accounts for a small change in extinction point. In all important respects, our reaction mechanism is comparable to that of Stahl, *et al.* and we are confident of the reaction mechanism because it has been applied successfully over a wide range of flame and flow situations. Thus, the differences between the two simulations cannot be explained on the basis of the reaction mechanism. Furthermore, the disagreement with the data is difficult to explain based on the reaction mechanism. This view is further reinforced by a detailed sensitivity analysis, which shows that the system is sensitive only to reactions whose rates are well known. The most likely cause for discrepency with the data is an inherent limitation of the boundary layer approximations or unaccounted heat losses in the experiments.

Despite some quantitative discrepancies with the extinction data, the simulations are able to provide important new insight about flame behavior near extinction. Because they are at atmospheric pressure, these flames are very thin, on the order of 0.5 mm. As the strain rate increases, the flame thickness decreases only slightly and its position moves toward the centerline, but the flame structure remains remarkably similar in both flames, as can be seen in Figures 3 and 4. Note that even the peak concentrations of active intermediates, such as H atoms, remain about the same right up to the extinction point. Insofar as the flame structure is concerned, it appears that the extinction process is very abrupt—either the flame burns or it does not. This is an important observation to the laminar flamelet applications.

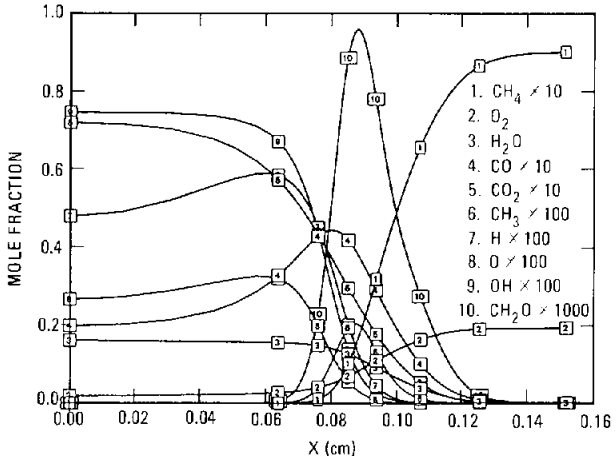

Figure 3. Selected species mole fractions showing the structure of a stoichiometric flame at a = 600/s, which is far from the extinction limit.

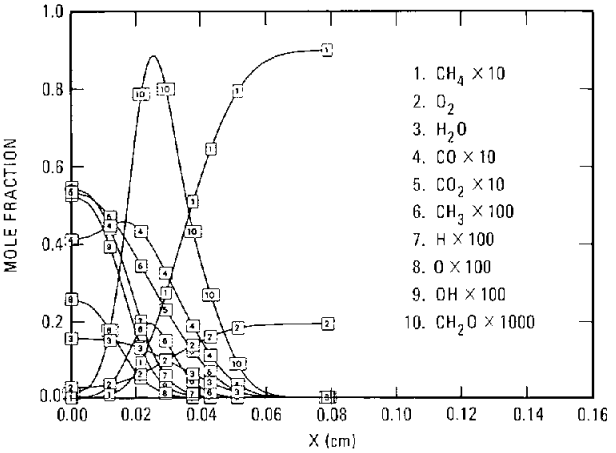

Figure 4. Selected species mole fractions showing the structure of a stoichiometric flame at a = 1260/s, which is quite near the extinction limit.

References:

1. C. K. Law, D. L. Zhu, and G. Yu, *Twenty-First Symposium (International) on Combustion* (The Combustion Institute, Pittsburgh, PA, 1987), p. 1419.

2. J. F. Grcar, R. J. Kee, M. D. Smooke, and J. A. Miller, *Twenty-First Symposium (International) on Combustion* (The Combustion Institute, Pittsburgh, PA, 1987), p. 1773.

3. H. B. Keller, "Numerical Solution of Bifurcation and Nonlinear Eigenvalue Problems," *Applications of Bifurcation Theory*, P. Rabinowitz, ed. (Academic Press, New York, NY, 1977).

4. G. Stahl, B. Rogg, and J. Warnatz, "Simulation of Stretched Premixed CH_4 and C_3H_8 Flames with Detailed Chemistry," *Eleventh ICDERS Conference* (Warsaw, Poland, 1987).

New Sensitivity Analysis Capability for Homogeneous Chemical Kinetics Models

We have developed a computer program to model a variety of homogeneous chemical kinetics problems with sensitivity analysis. Program SENKIN predicts the time evolution of the temperature and composition of a mixture, and computes first-order sensitivity coefficients with respect to the elementary reaction rates.

A. E. Lutz, R. J. Kee, J. A. Miller

A new computer program has been developed to predict the time-dependent chemical kinetics behavior of a homogeneous gas mixture in a closed system. In addition to computing the species and temperature histories, program SENKIN[1] can also compute the first-order sensitivity coefficients with respect to the elementary reaction rate parameters. This program now supersedes our previous sensitivity analysis programs,[2,3] because it provides an improved sensitivity analysis capability.

The solution to the model depends on both the initial conditions and the parameters that define the reaction rates. Because there is often uncertainty in the values of some of the parameters, it is helpful to know how sensitive the solution is to these parameters. Sensitivity analysis is a formal procedure to determine quantitatively how the solution to a model depends on certain parameters in the formulation. Thus, sensitivity analysis allows one to understand how the model will respond to changes in the rate parameters, without solving the problem repetitively with different values for the rate constants. It also provides insight into the relative importance of different reaction pathways.

The local sensitivity analysis is much more efficient than repetitive running of the model—especially when the number of parameters is large. The reason for the computational efficiency lies in the fact that the equations for the sensitivity coefficients are linear, regardless of the nonlinearities in the model itself. Furthermore, the model is solved by an implicit multistep method, so that the solution of the sensitivity equations can use the same Jacobian matrix that is formed during the solution of the model.

The program is designed to model a variety of practical applications that place different thermodynamic constraints on the system. Five general problem types are considered: (A) an adiabatic system with constant pressure, (B) an adiabatic system with constant volume, (C) an adiabatic system with the volume a specified function of time, (D) a system where the pressure and temperature are constant, and (E) a system where the pressure is constant and the temperature is a specified function of time. Options A through C generally apply to spontaneous ignition problems and may find use for modeling combustion bombs, rapid compression machines, and perhaps reflected-wave shock tubes. Another general type of homogeneous kinetics problem is considered by problem types D and E. In these problems, heat release is not important, because either the chemistry is not strongly exothermic or the mixture is extremely dilute. In these cases, the assumption of adiabaticity is replaced by the condition that the temperature is known. Case E is useful for modeling situations such as a plug flow reactor, where the temperature history can be measured.

The program uses the DASAC software[4] to solve both the nonlinear ordinary differential equations that describe the temperature and species mass fractions and the set of linear differential equations that describe the first-order sensitivity coefficients. This program is a modification and extension of Petzold's differential/algebraic equation solver called DASSL.[5] The numerical method is based on the backward differentiation formulas, which are especially well suited for solving the stiff equations that are common in chemical kinetics applications. The program runs in conjunction with the CHEMKIN package,[6] which handles the chemical reaction mechanism.

As a demonstration of program SENKIN, we present a computation of the autoignition of a stoichiometric, hydrogen-oxygen mixture at constant pressure. The temperature and species mole fractions are presented in Figure 1, with the minor

species being magnified to appear on the same scale. Figure 2 shows the normalized sensitivity coefficient of temperature with respect to the two most important reactions in the ignition process. The sensitivity is largest near the time of ignition, but because the temperature is changing rapidly. Under these conditions, the temperature depends on the competition for H atoms between the chain branching and three-body-recombination reactions. However, at higher temperatures, the chain branching reaction dominates and the ignition occurs much earlier in time.

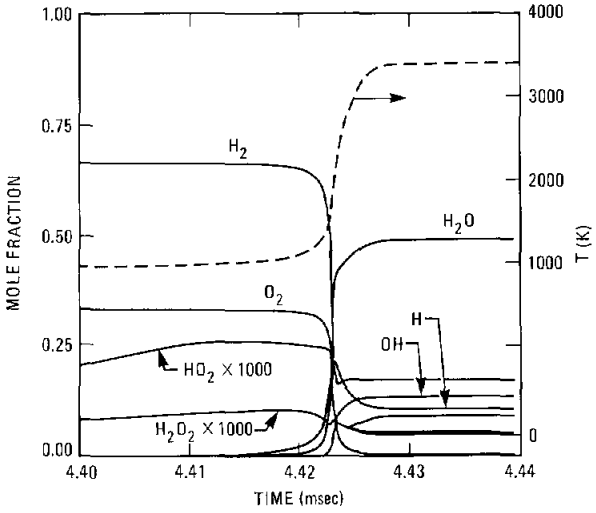

Figure 1. Species mole fractions and temperature (dashed curve) of a stoichiometric, hydrogen-oxygen mixture during autoignition. Initial conditions are 950 K and 1 atm.

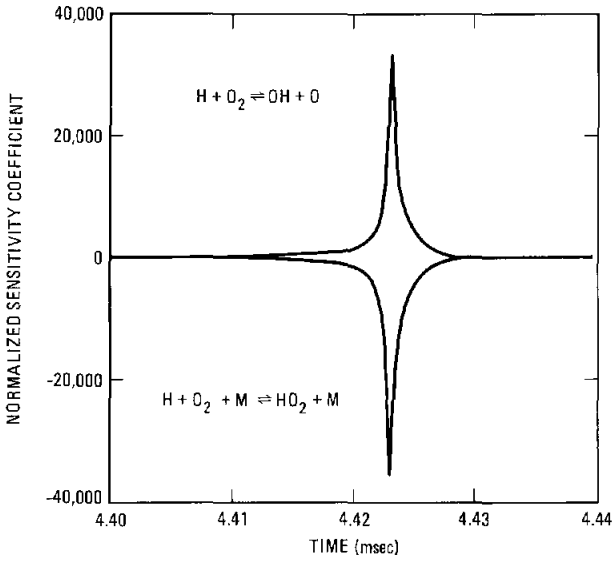

Figure 2. Normalized sensitivity coefficients for temperature with respect to the reaction rates controlling the species profiles shown in Figure 1.

References:

1. A. E. Lutz, R. J. Kee, and J. A. Miller, Sandia Report *SAND87-8248* (Sandia National Laboratories, Livermore, CA,1987).

2. M. A. Kramer, R. J. Kee, and H. Rabitz, Sandia Report *SAND82-8230* (Sandia National Laboratories, Livermore, CA, 1982).

3. M. A. Kramer, J. M. Calo, H. Rabitz, and J. J. Kee, Sandia Report *SAND82-8231* (Sandia National Laboratories, Livermore, CA, 1982).

4. M. Caracotsios and W. E. Stewart, Computers and Chem. Engineering **9**, 359 (1985).

5. L. R. Petzold, Sandia Report *SAND82-8637* (Sandia National Laboratories, Livermore, CA, 1982).

6. R. J. Kee, J. A. Miller, and T. H. Jefferson, Sandia Report *SAND80-8003* (Sandia National Laboratories, Livermore, CA, 1980).

Modeling Autoignition Centers in Hydrogen and $C_{1,2}$-Hydrocarbon Mixtures†

We compute local autoignition at exothermic centers within a combustible mixture using a chemical kinetics model for several hydrocarbon fuels. We predict chemical induction and energy release times and the magnitude of the induced pressure pulse in the center.

A. E. Lutz, R. J. Kee, J. A. Miller, H. A. Dwyer,* and A. K. Oppenheim**

A chemical kinetics model is being used to investigate autoignition at small centers within a hot, combustible gas mixture. Under practical conditions, a mixture that is rapidly heated or compressed is not homogeneous, so that autoignition first occurs at individual hot spots, or *exothermic centers*. The hot spots have been observed in rapid compression machines and shock-tube experiments under a variety of conditions.[1] Their behavior is interesting because they serve as precursors to the combustion of the bulk mixture.

The ignition of an exothermic center does two things: it establishes a large temperature jump across the boundary, and it drives a compression wave into the surrounding mixture. The temperature gradient may lead to flame propagation later in the combustion process. However, the compression wave rapidly transfers energy to the mixture surrounding the center, which may significantly reduce the overall induction time of the bulk. This effect is especially important when the chemical induction time is sensitive to temperature.[2,3]

We picture the exothermic center as a hot kernel of combustible mixture surrounded by an inert mixture with the same properties and initial state. The geometry of the kernel can be planar, cylindrical, or spherical. Diffusional processes are neglected, as are spatial gradients inside the kernel. The kernel undergoes an adiabatic process, while the compression process in the gas immediately outside the kernel is isentropic. The model combines the equation of motion for the boundary of the kernel with energy and species equations for the reacting mixture inside, so that chemical- and gas-dynamic behavior are combined in a model that remains zero-dimensional. The velocity of the kernel boundary comes from the compatibility equation across a characteristic at the interface,[4]

$$u = \frac{2a_o}{\gamma - 1}\left[\left(\frac{p}{p_o}\right)^{\alpha} - 1\right], \quad \alpha = (\gamma - 1)/2\gamma$$

where u is the velocity, p the pressure, a the sound speed, γ is the ratio of specific heats, and the subscript "o" refers to the initial state. This relation constrains the gas-dynamic expansion of the kernel, without including spatial conservation equations for the surroundings. The combination of this constraint and the comprehensive chemical kinetics make this model a unique extension of previous efforts.[5-7]

Autoignition of a typical exothermic center in planar geometry is shown in Figure 1 for a stoichiometric hydrogen-air mixture, initially at 1000 K and 5 atm. After an induction period, t_i, the exothermic reactions begin to deposit energy in the kernel. The pressure in the kernel rises during the excitation time, t_e, which is the duration of the rise of the chemical power pulse shown in frame (d). The pressure in the kernel causes it to expand; this expansion is shown on an x-t diagram in frame (a). As the power pulse decays and the center continues to expand, the pressure relaxes to its initial value. The magnitude of the maximum pressure depends on the race between the chemical energy release and gas-dynamic expansion, the latter being limited by the sound speed in the surrounding gas. In this example, the maximum pressure is 1.56 times the initial value. The exothermic chemical energy is divided between internal heating of the gas in the kernel and expansion work done on the surroundings. Of the total chemical energy produced, about 23 percent is transferred to the surrounding gas as expansion work; the chemical energy and pdV-work are compared in frame (c).

An important effect of the ignition of an exothermic center is the compression wave that is generated in the mixture surrounding the center. Figure 2 shows the maximum pressure in the kernel for stoichiometric mixtures of the $C_{1,2}$-hydrocarbon fuels with air. The pressure pulse varies significantly over a range of initial pressure from

†Twenty-Second Symposium (International) on Combustion, accepted (1988).

*University of California at Davis.
**University of California at Berkeley.

1 to 10 atm. The fact that the pressure typically reaches 1.5 times its initial value indicates that the compression wave driven into the surrounding mixture may heat it enough to accelerate the ignition process.

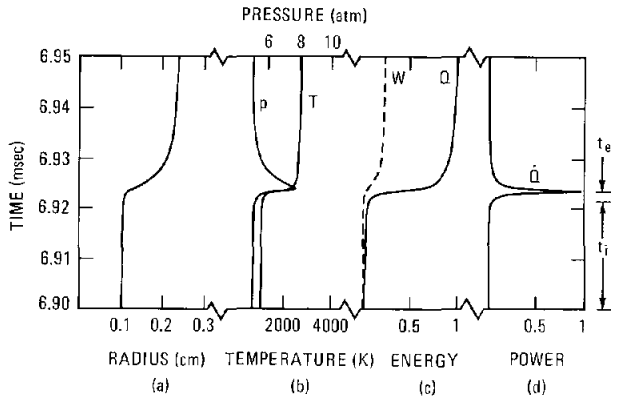

Figure 1. Autoignition of an exothermic center in a stoichiometric hydrogen-air mixture. Initial conditions are T = 1000 K, p = 5 atm, and r = 1 mm. Geometry is planar. Frames are: (a) the position of the kernel interface in time, (b) the temperature and pressure in the kernel, (c) the exothermic energy produced by the chemical reactions (solid line) and work done by the expansion of the kernel (dashed line), (d) the power pulse of the chemical reactions. The exothermic energy is $Q = \int \dot{Q} dt$, where $\dot{Q}$ is the chemical power; the work is $W = \int p dv$. The power and energy are normalized by their maximum values, 2×10^9 W/gm and 3×10^3 J/gm. The induction time, t_i, is 6.922 ms; the excitation time, t_e, is 1.66 μs.

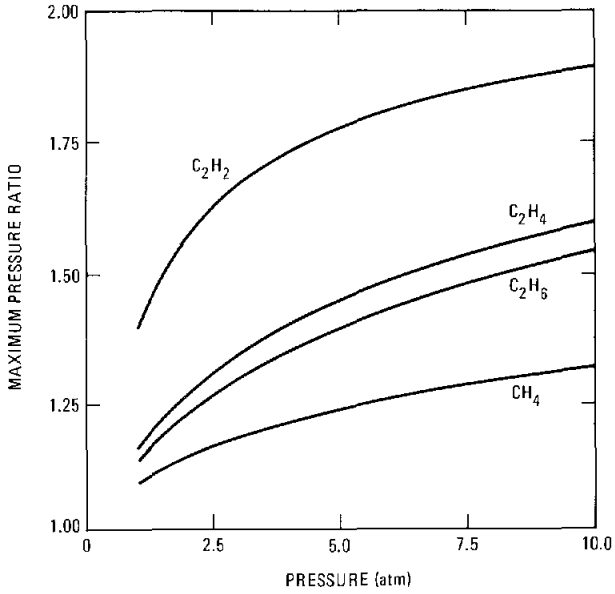

Figure 2. Maximum pressure ratio in the exothermic center divided by the initial pressure for stoichiometric methane, acetylene, ethylene, and ethane mixtures with air (a) over a range of temperature at p = 1 atm, and (b) over a range of pressure at T = 1500 K. Initial radius of the center is 1 mm and geometry is planar.

References:

1. J. W. Meyer and A. K. Oppenheim, *Thirteenth Symposium (International) on Combustion* (The Combustion Institute, Pittsburgh, PA, 1971), p. 1153.

2. E. S. Oran and J. P. Boris, Comb. Flame **48**, 149 (1982).

3. A. E. Lutz, R. J. Kee, and J. A. Miller, Western States Section/ Japanese Section Joint Technical Meeting, Honolulu, HI (The Combustion Institute, 1987).

4. A. K. Oppenheim, Phil. Trans. Royal Soc. London A, **315**, 471 (1985).

5. L. J. Zajac and A. K. Oppenheim, AIAA J. **9**, 545 (1971).

6. L. M. Cohen, J. M. Short, and A. K. Oppenheim, Comb. Flame **24**, 319 (1975).

7. J. W. Meyer and A. K. Oppenheim, AIAA J. **10**, 1509 (1972).

Simulation of the Transport and Chemical Reaction of Molten Debris†

A computer model for the transport and oxidation of molten debris has been developed. It is being used to simulate experiments pertinent to the direct heating of nuclear reactor containment buildings.

K. D. Marx

The transport and chemical reaction of molten debris is a problem of current interest in the study of certain nuclear reactor accident scenarios.[1,2] In some situations, debris from the core of a reactor could be expelled into the atmosphere inside a reactor-containment building. The debris would then heat the gas, resulting in an increase in the pressure in the containment. Furthermore, the exothermic reaction of the debris with the oxygen in the air would cause additional heating of the atmosphere. The present work is part of a study being carried out to determine whether this heating will be sufficient to place the integrity of the containment building at risk due to overpressurization. We have developed methods for computer simulation of some of the physical processes involved in such direct containment heating scenarios. These numerical algorithms have been used to model experiments pertinent to the reactor debris dispersal problem.

The computer code which is used as a basis for the calculations is the KIVA code developed at Los Alamos National Laboratory.[3] This code was written for the simulation of internal combustion engines. It includes models for the transport, evaporation, and combustion of a liquid fuel spray. The behavior of the spray is coupled to the flow of the gas into which it is introduced. Hence, the code provides a good framework for the simulation of debris transport through the atmosphere.

A number of modifications have been made to KIVA to adapt it to the debris simulation problem. These include the following: (1) The characteristics of the liquid droplets were changed from a single species of evaporating liquid fuel to a multispecies distribution of nonevaporating metal particles. The particles are typically in the liquid state at injection, and are allowed to solidify by implicitly including the heats of fusion in the enthalpy tables. (2) The algorithm for injecting the fuel droplets into the gas was modified to accommodate the specification of the species concentrations within the debris particles and the distributions of particle sizes and injection velocities. (3) A method for allowing the bouncing and trapping of particles at walls was introduced. (4) Algorithms were provided to account for radiative heat transfer and for that component of convective heat transfer which occurs at length scales too small to be resolved on the finite-difference grid. (5) Allowance was made for chemical reactions between some of the chemical species in the particles and the oxygen in the atmosphere.

The resulting modified version of KIVA has been applied to the simulation of experiments performed in the Surtsey[4] facility at Sandia National Laboratories in Albuquerque, New Mexico. This facility consists of a container 10-m-high by 3.6 m in diameter. Debris formed by igniting a thermite powder is ejected from a chute at the bottom of the container with a predominantly upward velocity. The facility is equipped with pressure and temperature transducers and various instruments for gas and debris analysis.

Results of a simulation performed with the code are shown in Figures 1 and 2. In this experiment, 9.47 kg of debris was injected at a temperature of 2500K. The thermite powder which formed the debris consisted of 53% iron and 47% alumina. It was injected over a period of 0.64 seconds with a velocity distribution which had a mean value of 72 m/s. Figure 1 shows isotherms and the locations of representative debris particles at three different times in the calculation. The first plot indicates the configuration just after injection has started. Most of the particles have an upward trajectory and only the very smallest particles have frozen, i.e., cooled below the melting point of iron. In the second plot, injection is half over; many of the particles are falling and have cooled significantly. Only a few particles have been trapped on the walls of the container. (When this happens, the debris is taken out of the calculation; it no longer oxidizes or gives up heat to the atmosphere. It is assumed that trapped debris transfers all of its heat to the cool walls of the container.) In the third plot, injection has ended and the debris has cooled significantly. The particles are

†Nuclear Science and Technology, submitted (1988).

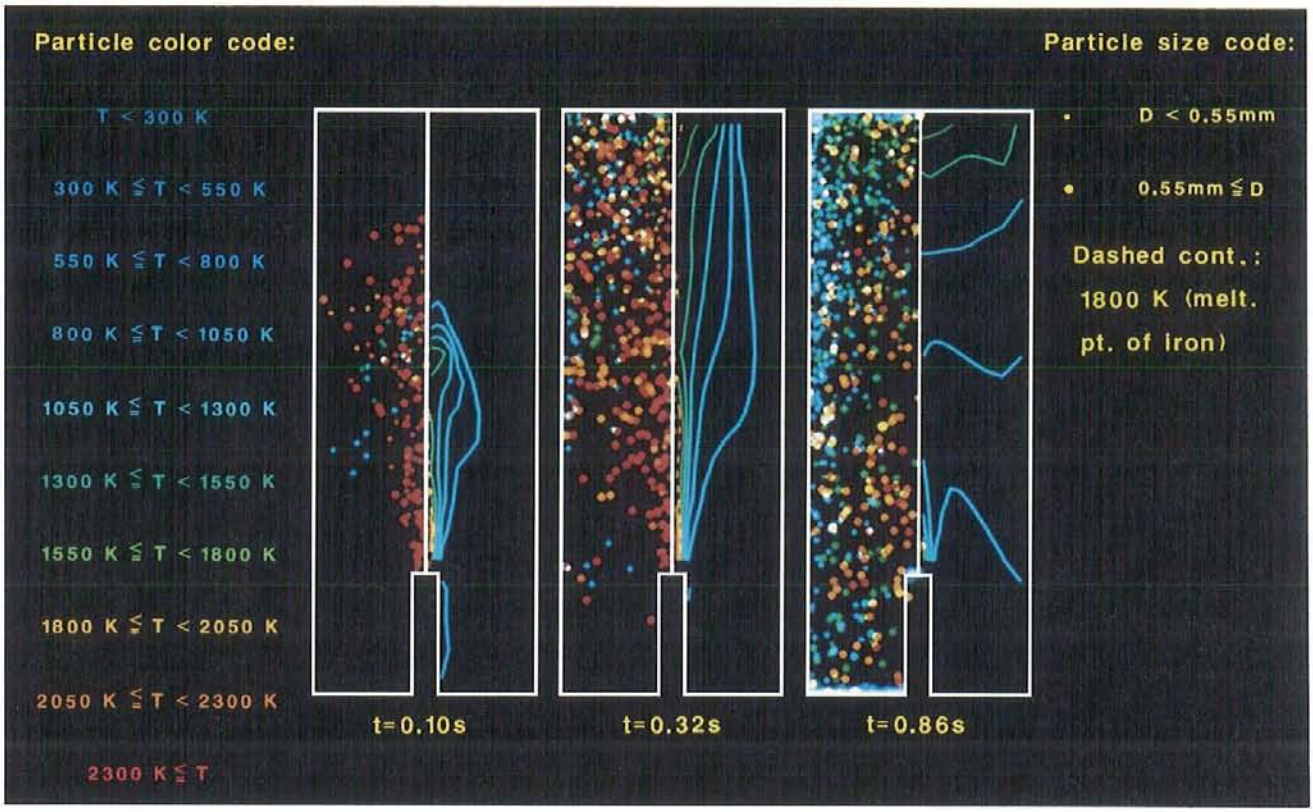

Figure 1. Sequence of plots showing isotherms and the distribution of representative debris particles.

either trapped on the walls or floor, or are falling toward the floor.

Figure 2 gives a comparison of the computed and experimental pressures. The agreement is seen to be quite good.

Simulation of experiments with greater amounts of debris is more difficult. In such cases, the agglomeration of debris particles through collisions becomes more important. Furthermore, since the debris cloud is more dense, it tends to retain its heat longer; this means that the interaction of the debris with the walls of the container becomes more important in determining the amount of heat transfer to the gas. Future research will concentrate on accounting for these factors.

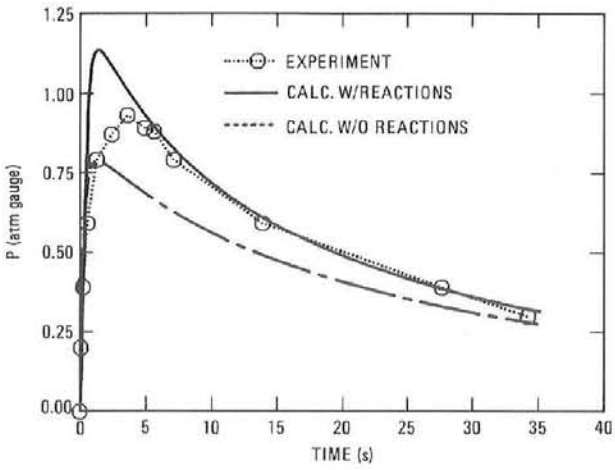

Figure 2. Comparison of experimental pressures and calculations with and without chemical reactions.

References:

1. D. C. Williams, K. D. Bergeron, D. E. Carroll, R. D. Gasser, J. L. Tills, and K. E. Washington, "Containment Loads Due to Direct Containment Heating and Associated Hydrogen Behavior," *Sandia Report NUREG/CR-4896, SAND87-0633* (Sandia National Laboratories, Livermore, CA, 1987).

2. D. C. Williams, K. D. Bergeron, D. E. Carroll, and J. L. Tills, "Impact of Chemical Phenomena in Direct Containment Heating," Severe Accident Chemistry Symposium, Anaheim, CA, (American Chemical Society,1986).

3. A. A. Amsden, J. D. Ramshaw, P. J. O'Rourke, and J. K. Dukowicz, "KIVA: A Computer Program for Two- and Three-Dimensional Fluid Flows with Chemical Reactions and Fuel Sprays," *Los Alamos Report LA-10245-MS* (Los Alamos National Laboratory, Los Alamos, NM, 1985).

4. W. W. Tarbell, J. E. Brockman, M. Pilch, J. W. Ross, M. S. Oliver, D. A. Lucero, T. E. Kerley, F. E. Arellano, and R. D. Gomez, "Results from the DCH-1 Experiment," *Sandia Report NUREG/CR-4871, SAND86-2483* (Sandia National Laboratories, Livermore, CA, 1987).

A Newton's Method Scheme for Solving Free-Surface Flow Problems

A scheme for employing Newton's method in conjunction with finite differences for the study of nonlinear problems arising in fluid mechanics is presented. The scheme is stable and achieves the well-known quadratic convergence associated with Newton's method.

D. S. Dandy and L. G. Leal*

To date, much of the numerical work done in the general area of intermediate Reynolds-number, free-surface flows has centered on the use of finite-element techniques. Finite elements gained an early foothold in the intermediate Reynolds number category because of the difficulties encountered in finding suitable coordinate geometries for use with finite-difference techniques. Early attempts at using finite differences were restricted to problems with domain boundaries coinciding with analytical coordinate lines, or else resorted to describing the boundaries and accompanying boundary conditions by interpolation between nodal points on the pre-assigned finite-difference grid. However, finite-difference techniques are slowly growing in popularity due to the advent of boundary-fitted, grid-generation techniques,[1] but the growth has been slow.[2-4] The general numerical technique used in all three of these studies was successive approximations with the calculation of the interface shape decoupled from the flow variables.

Because of the quadratic nonlinearities present in the Navier-Stokes equations, successive approximation methods can be very slow to converge (that is, many iterations are needed), particularly when extreme under-relaxation is required. Further, in gas- and liquid-phase combustion problems currently under study, the highly nonlinear Arrhenius terms present in the conservation equations for mass and energy can have significant effect on convergence properties. An alternative to successive approximations is to simultaneously iterate on all of the unknown variables (flow field and shape). Equally important, we are trying to solve a set of coupled, nonlinear partial-differential equations and boundary conditions, for which no theory exists on solution existence, uniqueness, or boundedness. Consequently, it is of extreme interest to know the dependence of the solution on the dimensionless parameters of the problem, and Newton's method provides us with powerful techniques for computer-aided study of this dependence, along with the ability to examine multiplicity.[5]

As an illustrative example of using the method, we will solve the Navier-Stokes equations and boundary conditions for the shape and flow-field for a buoyant deformable bubble, using a solution of Laplace's equation to describe an orthogonal boundary-fitted coordinate grid and finite-difference approximations for all equations and boundary conditions. To implement Newton's method for this problem, it is necessary to include as unknowns not only the shape and flow variables, but also the mapping variables. We demonstrate that Newton's method is indeed a viable means of solving problems of this type.

Assuming that the bubble follows a rectilinear trajectory, the problem is reduced from one of three dimensions to two. Due to the axisymmetry of the problem, it is convenient to cast the flow equations in terms of the streamfunction ψ and vorticity ω rather than the primitive variables $\mathbf{u}, p$. First, the steady Navier-Stokes and continuity equations are nondimensionalized. The resulting equations contain the Reynolds number R, which is defined as $R = 2\rho a U_\infty / \mu$. The curl of the dimensionless Navier-Stokes equations is taken and we obtain an equation in terms of the vorticity and velocity. We then define the components of the velocities in the general (ξ, η) coordinate system using the streamfunction and substitute these into the velocity-vorticity equations.

The governing equations for the flow and mapping, and their associated boundary conditions, are approximated using second-order centered finite differences. The result is a set of coupled, nonlinear algebraic equations which are solved using Newton's method. If the vector set of equations is

*California Institute of Technology, Pasadena, CA.

symbolically represented as $\mathbf{G}(\mathbf{x}) = 0$, where $\mathbf{x}$ is the vector set of unknowns, then starting with some initial guess $\mathbf{x}^{(o)}$, the approximation to the solution at the (n + 1) step is $\mathbf{x}^{(n+1)} = \mathbf{x}^{(n)} - (\mathbf{A}^{(n)})^{-1}\,\mathbf{G}^{(n)}$.

The matrix $\mathbf{A}$ is the Jacobian matrix defined by $\partial\mathbf{G}/\partial\mathbf{x}$. The Jacobian matrix generated in this type of problem is sparse and, in general, large. For the discretization used in this work—61 x 61—the matrix is over 14,000 by 14,000. Because of the size of the linear system, it is necessary to use the Cray X-MP with its associated Solid-State Storage Device.

A number of runs were done at a variety of different Reynolds and Weber numbers. One set of these results is shown in Figure 1, where a sequence of runs was done for fixed R and $4 < W < 8$. The flow is viewed left-to-right, with the upper half-plane of each shape corresponding to streamlines and the lower half to vorticity lines. The drag coefficient C_D is also displayed. Note that when the bubble becomes sufficiently deformed, an attached recirculating wake forms on the downstream side.

Through this result and others, we have seen that Newton's method is a viable means of solving the nonlinear problems that arise in fluid mechanics. The next step in utilizing the method is to consider systems of greater interest, i.e., ones where chemical reaction and heat transfer are present. The process is conceptually no more difficult than the one considered here. The number of unknowns will increase, but the next-generation supercomputers will have no problems with the increased problem size.

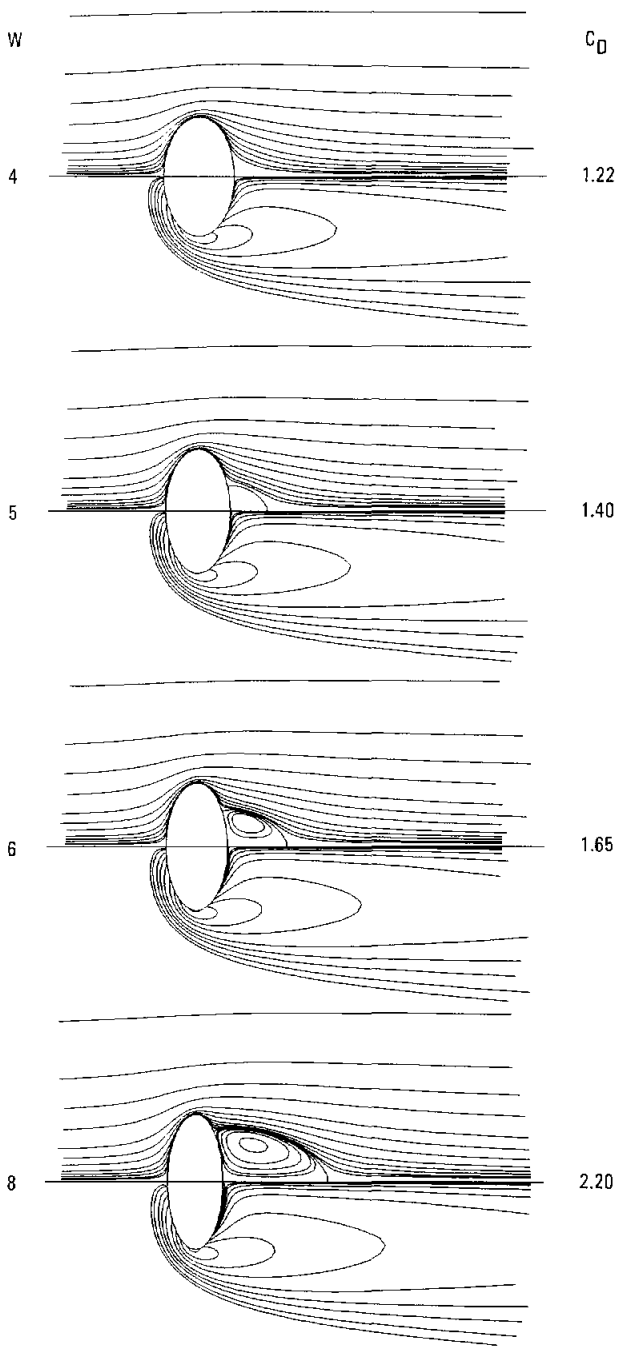

Figure 1. Flow fields and shapes for R=50 and W=4, 5, 6, and 8.

References:

1. J. F. Thompson, Z. U. A. Warsi, and C. W. Mastin, *Numerical Grid Generation: Foundations and Applications, (Elsevier, New York, NY, 1985).*

2. C. I. Christov and P. K. Volkov, J. Fluid Mech. **158**, 341 (1985).

3. G. Ryskin and L. G. Leal, J. Fluid Mech. **148**, 1 (1984).

4. D. S. Dandy and L. G. Leal, J. Fluid Mech., submitted (1987).

5. R. A. Brown, L. E. Scriven, and W. J. Silliman, *New Approaches in Nonlinear Dynamics,* (SIAM, Philadelphia, PA, 1980).

Unsteady Processes in Droplet Combustion: Applications to Hazardous Waste Incineration

In this study we use numerical models to simulate combustion processes in multicomponent liquid hazardous waste droplets. Our numerical predictions are compared with experimental data.

N. E. Bergan, E. K. Flatbush, and H. A. Dwyer*

Individual droplet processes play an important role in liquid hazardous waste incineration. In spray-fired incinerators, liquid wastes are chemically decomposed by exposing them to high temperature oxidizing environments for a specified time. Destruction efficiencies can be seriously degraded by individual burning droplets at the edge of sprays or by oversize droplets which penetrate the flame zone. Therefore, it is precisely the non-average or individual droplet behavior which must be considered to ensure destruction requirements as high as 99.9999%

In this study, we apply our understanding of droplet combustion processes to problems in hazardous waste incineration. We use numerical simulations of droplets to predict ignition, burning rates, droplet trajectories, and extinction. Our numerical predictions are compared with experimental data.

We are studying a particular class of liquid hydrocarbons: chlorinated hydrocarbon wastes. These wastes, commonly found in dry cleaning fluids, paint solvents, and other industrial processes,[1] do not readily ignite and burn by themselves. Recent research[2] indicates that blending with hydrocarbon fuels may enhance combustion, and therefore thermal destruction, by providing an ignition source, increasing the burning rate, and possibly delaying extinction of the waste droplets. The blended droplet in these studies is composed of 35% nonane and 65% tetrachloroethane, by volume. We choose to study this particular combination of waste and fuel because the components have approximately the same boiling temperature. Therefore, no preferential volatility effects are present, making other combustion mechanisms easier to distinguish.

Two different numerical simulations are performed. The first is a one-dimensional solution of the unsteady Navier-Stokes equations for multicomponent, spherically-symmetric droplet combustion. This multicomponent model calculates temperature and concentration profiles to study the ignition, burning rate, and extinction of multicomponent droplets.

Since a droplet must vaporize before it can be destroyed, we are interested in understanding the mechanism which controls gasification in these droplets. The gasification rates predicted by this model agree with experimental trends, but predict burning rates conservatively low, due to the absence of convection in the model (the experimental data are for Reynolds number on the order of one). Actual droplets will burn faster than our predictions and thereby achieve a higher destruction efficiency. The concentration and temperature profiles inside the droplet give us information about the rate-controlling step for gasification. Early theories[3] suggested a diffusion-controlled process for high-liquid-Lewis-number droplets (where Lewis number is defined to be the ratio of thermal to mass diffusion), and a distillation-controlled process for low-Lewis-number droplets. However, more recent results show that the Peclet number (defined to be the ratio of gasification rate to species diffusion) may be a more appropriate parameter. Our objective is to extend this research using our full Navier-Stokes solution to simulate combustion processes in multicomponent hazardous waste droplets.

Figure 1 shows results from our multicomponent model for a burning droplet (burning rate approximately 0.5 mm^2/sec). For Lewis number 30, the predictions resemble a diffusion-controlled process, where the mass fraction of nonane is essentially constant as a function of time. However, when the Lewis number is lowered, the predictions do not behave like a distillation-controlled process, in which equal-volatility components would be expected to vaporize at the same rate. Our model shows that a preferential vapor-concentration gradient is created by the flame surrounding the droplet, causing one component to be depleted from the droplet more rapidly than the other. The characteristics of the flame (in particular, the submodel used to simulate that flame) influence the vapor concentration profiles of each component, thereby controlling the

*University of California at Davis.

vaporization process within the droplet. This is an important consideration for hazardous waste incineration, since rapid depletion of the blended hydrocarbon could signal the onset of premature extinction and therefore inefficient waste destruction. Preliminary experimental data[2] show that droplet concentration remains approximately constant throughout the droplet lifetime.

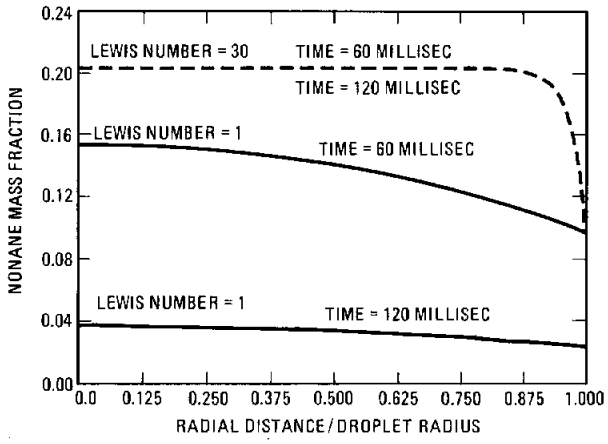

Figure 1. Mass fraction of nonane inside blended droplet as a function of droplet radius at times 60 ms and 120 ms. By changing the Lewis number, we see the effect of species diffusion within the droplet. Le=30 is species-diffusion limited. Le=1 is equal species and thermal diffusion. Initial droplet radius, 250 μm.

The second model is a one-dimensional Lagrangian model of droplet motion to study the sensitivity of droplet trajectory to combustion parameters. This model calculates the penetration distance of a single droplet. We use gasification rates from the above detailed models and experiments, and drag correlations recommended for vaporizing droplets in References 4 and 5. Our objective is to perform a sensitivity analysis on both burning rates and drag to quantify the effect of uncertainty in each.

Two droplet trajectories are calculated for a pure nonane droplet: one for the burning rate of pure nonane predicted by our multicomponent model (no convection), $K_c = 0.73$ mm^2/sec; and one for a measured[2] burning rate of 0.93 mm^2/sec. The calculated burning rate results in a droplet trajectory 35% longer than that for the measured burning rate. When designing for complete destruction of hazardous wastes, 35% conservatism will be tripled or quadrupled with factors of safety, adding unnecessary costs and size to the incinerator.

Figure 2 shows the droplet penetration distance as a function of time for a vaporizing and a burning droplet, calculated using two different drag correlations. The total distances predicted for each droplet are compared, and differences are noted as ΔY.

Results from Figure 2 show that the two correlations produce results which agree within 10% for a vaporizing droplet (vaporization rate, $K_v = 0.3$, mass transfer number, B =1), but as the gasification rate increases (burning rate, $K_c = 0.95$, mass transfer number, B = 8), the difference becomes significant, ΔY = 90%. The primary difference between these correlations is the definition of the Reynolds number. These results help us quantify the sensitivity of droplet trajectory to drag-force correlations and burning rate.

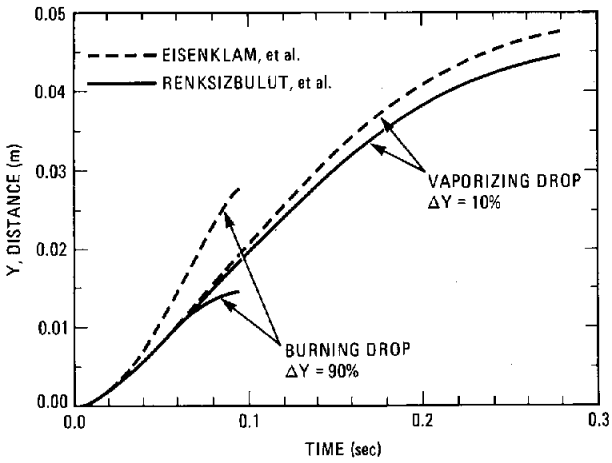

Figure 2. Droplet penetration distance calculated using two different drag correlations for both a vaporizing and a burning droplet.

References:

1. M. Sittig, *Handbook of Toxic and Hazardous Chemicals* (Noyes Pub., New York, NY, 1985), p. 841.

2. R. R. Steeper, N. W. Sorbo, D. P. Chang, and C. K. Law, "Incineration of Liquid Hazardous Wastes: Vaporization and Combustion of Droplets of Chlorinated Hydrocarbons," *International Symposium on the Incineration of Hazardous, Municipal, and Other Wastes*, Palm Springs, CA (AFRC, 1987).

3. C. K. Law, AIChE J. **24**, 626 (1978).

4. P. Eisenklam, S. Arunachalam, and J. Weston, *Eleventh Symposium (International) on Combustion*, (The Combustion Institute, Pittsburgh, PA, 1967), p. 715.

5. M. Renksizbulut and M. Yuen, J. Heat Transfer **105**, 389 (1983).

New Modes of Quasi-Periodic Combustion†

Steady, planar propagation of a condensed phase reaction front is unstable to disturbances corresponding to pulsating and spinning waves for sufficiently large values of the activation energy. We consider the nonlinear evolution equations for the amplitudes of the pulsating and spinning-waves to describe closed branches of solutions which represent new quasi-periodic modes of combustion.

S. B. Margolis and B. J. Matkowsky*

In the combustion synthesis of refractory materials, steady planar reaction fronts are known from both experimental and theoretical investigations to be unstable under a variety of circumstances. In a cylindrical geometry, the combustion front $x_3 = \Phi(r, \psi, t)$, where x_3 is the coordinate normal to the planar front, r and ψ are the radial and angular transverse coordinates, and t is time, then propagates in one of a variety of ways. Based on experimental observations,[1,2] these have been classified as self-oscillatory, spinning, and standing (multiple-point) combustion waves. In the spinning mode of propagation, a spiraling motion of a nonuniform front occurs, and one or more luminous points are observed to move in a helical fashion along the surface of the cylindrical sample. The self-oscillatory mode is a special case of spin combustion in which a front with no angular dependence propagates in a pulsating manner. Finally, in multiple-point combustion, one or more luminous spots are observed to appear, disappear, and reappear on the sample surface.

The mathematical model that we employ to investigate these phenomena contains three parameters: namely, a parameter Δ which is proportional to the activation energy of the reaction, a melting parameter M, $0 < M < 1$, which is related to the temperature at which melting of one of the reactants occurs, and the radius R of the cylindrical sample. A linear stability analysis[3] then gives the pulsating neutral stability boundary depicted in Figure 1, where k is the transverse radial wave number of the disturbance and Ξ is the ratio of Δ to $2(1 - M)$. Since the radius of the sample is finite, only discrete values $k = k_{n,m}$ are admissible and are determined by the condition $J'_n(k_{n,m}R) = 0$, where n is the angular wave number of the disturbance and J_n is the Bessel function of order n. Thus, as R varies, so do the locations of the discrete wave numbers on the neutral stability boundary. Thus, there exist critical values $R = R_c$ such that the value $\Xi = \Xi_c$ at which stability of the steady, planar solution is lost coincides with disturbances of two discrete wave numbers k_1 and k_2, and corresponding frequencies ω_1 and ω_2. This is the case illustrated by the square markers in Figure 1. When R is perturbed from this critical value, the double eigenvalue Ξ_c is split into two simple, but closely spaced, eigenvalues, as illustrated by the circular markers in Figure 1.

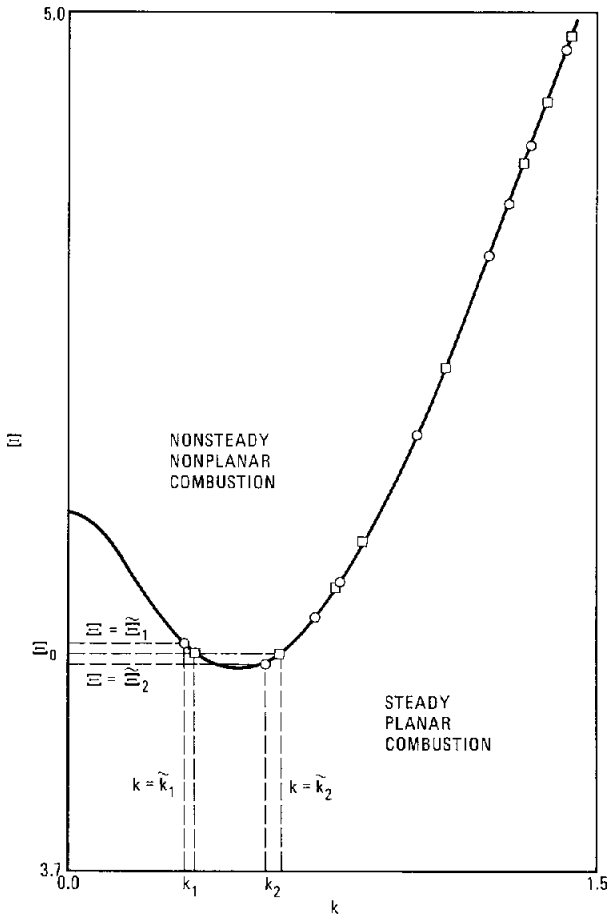

Figure 1. The neutral stability boundary.

†SIAM Journal of Applied Mathematics, accepted (1988).

*Northwestern University, Evanston, IL.

In a recent study,[4] the behavior of the solution in the neighborhood of a double eigenvalue of the linear stability problem was investigated and led to a representation of the solution in the form

$$\Phi(r,\psi,t) \sim -t-\varepsilon^2 b_1(|A_{1,1}|^2+|A_{1,2}|^2)-\varepsilon^2 b_2(|A_{2,1}|^2+|A_{2,2}|^2)t$$
$$+\varepsilon\left[|A_{1,1}|e^{i(\omega_1 t+\varepsilon^2\varphi_{1,1}t+n_1\varphi)}+|A_{1,2}|e^{i(\omega_1 t+\varepsilon^2\varphi_{1,2}t-n_1\psi)}\right]J_{n_1}(k_{n_1,m_1}r)+\text{c.c.}$$
$$+\varepsilon\left[|A_{2,1}|e^{i(\omega_2 t+\varepsilon^2\varphi_{2,1}t+n_2\varphi)}+|A_{2,2}|e^{i(\omega_2 t+\varepsilon^2\varphi_{2,2}t-n_2\psi)}\right]J_{n_2}(k_{n_2,m_2}r)+\text{c.c.}$$

where "c.c." denotes the complex conjugate and the small "splitting" parameter ε is proportional to $|R-R_0|^{1/2}$.

The first term in Equation (1) corresponds to the solution for steady, planar burning, in which the planar front moves normal to itself with unit velocity. The complex amplitudes $A_{i,j}$ for i,j = 1,2, correspond to the amplitude of (counter) clockwise disturbances associated with the wave number k_i and frequency ω_i, are determined from coupled amplitude equations, which are nonlinear, ordinary differential equations with respect to the slow time $\tau = \varepsilon^2 t$. These equations thus determine the number and stability of the bifurcation branches in the neighborhood of the double eigenvalue Ξ_o and depend on the values of the bifurcation parameter Δ and the auxiliary parameter M.

Steady solutions of the amplitude equations, corresponding to various periodic and quasi-periodic (since ω_1 and ω_2 are in general incommensurate) modes of burning were obtained.[4] A typical bifurcation diagram, indicating the loss of stability of the basic solution and the secondary and higher-order transitions to various nonsteady, nonplanar modes of burning, is shown in Figure 2, in which the scaled bifurcation parameter σ is proportional to $\Delta - \Delta_o$, where $\Delta_o(M) = 2\Xi_o(1 - M)$. In that figure, solutions Ia, b, c, d have one nonzero amplitude, solutions IIa, b, c, d, e, f have two nonzero amplitudes, solutions IIIa, b, c, d have three nonzero amplitudes, and solution IV has all four amplitudes nonzero. We remark that the type I solutions represent time-periodic spinning modes of combustion, whereas solutions IIa ($|A_{1,1}| = |A_{1,2}| \neq 0$) and IIb ($|A_{2,1}| = |A_{2,2}| \neq 0$) represent time-periodic standing (pulsating) modes. The remaining solutions represent various quasi-periodic modes of propagation. We also note that the phases $\varphi_{i,j}$ are perturbations of the spinning or pulsation frequency ω_i through the slow time $\varepsilon^2 t$.

In the present work,[5] we have obtained new solutions for the amplitudes which are nonsteady solutions to the amplitude equations. In particular, since the amplitude equations are differential equations with respect to the slow time τ, there exist time-periodic solutions in addition to the steady solutions discussed above. These additional solutions, which, from Equation (1), represent new modes of quasi-periodic combustion, appear as closed, stable branches when the melting parameter M is above a critical value M_c. This is shown by the dotted curves in Figure 2, which was obtained for a value of M greater than M_c. As M approaches M_c from above, the two (Hopf) bifurcation points on solutions IIIc and IIId, between which these solutions are unstable, coalesce into a single degenerate point. For M in a neighborhood of M_c, we employ a perturbation method to show that these new solution branches appear as elipses on IIIc and IIId. Alternatively, we may determine these branches from a numerical integration of the amplitude equations for an arbitrary value of $M > M_c$.

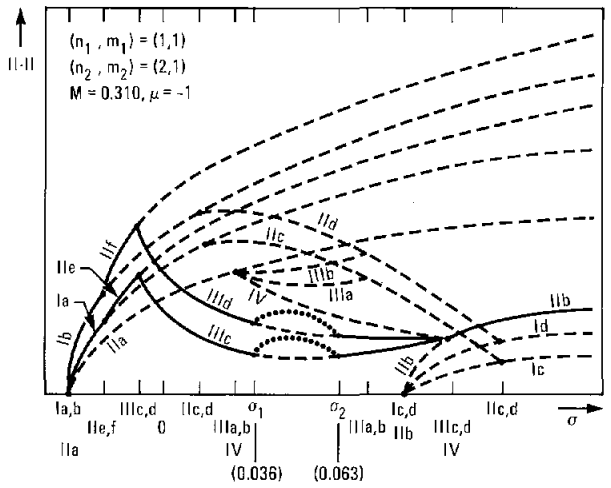

Figure 2. Bifurcation diagram near a double eigenvalue for a given pair of mode interactions and a value of the melting parameter $M > M_c$. Solid (dashed) curves denote stable (unstable) solutions.

References:

1. A. G. Merzhanov, A. K. Filonenko, and I. P. Borovinskaya, Dokl. Phys. Chem. **208**, 122 (1973).

2. A. V. Dvoryankin, A. G. Strunina, and A. G. Merzhanov, Explosion and Shock Waves **18**, 134 (1982).

3. S. B. Margolis, SIAM J. Appl. Math. **43**, 351 (1983).

4. M. R. Booty, S. B. Margolis, and B. J. Matkowsky, SIAM J. Appl. Math. **46**, 801 (1986).

5. S. B. Margolis and B. J. Matkowsky, SIAM J. Appl. Math., accepted (1988).

The enlarged photograph shows the "hot stage" of a Raman microprobe apparatus—capable of acquiring chemical information characteristic of the material under study at elevated temperatures and at spatial resolutions limited only by the laser beam and instrument optics. The inset photograph is an optical micrograph of the surface studied with the Raman microprobe, an Fe-13Cr alloy surface after 105 minutes of oxidation in 10^{-24} atmospheres partial pressure of O_2 at 700°C. Raman microprobe analysis allows phase identification of oxides over grain boundaries and over the adjacent grain material, as shown in the work presented on pages 6-4 and 6-5. The chromia-rich regions above the grain boundaries are characteristically a few μm across.

High-Temperature Materials

In order to orient the reader to the similarities and differences between Raman scattering and optical second harmonic generation (SHG)—the major diagnostic probes used in the work reported in this section—we examine their origins from the interactions, on a microscopic level, of a laser beam and the material upon which it is incident.

The oscillating electric field of the laser beam exerts a force on the charge distribution (electrons and nuclei) of the atoms composing the material, thereby causing these distributions to oscillate about their equilibrium positions. Thus, the material is said to be polarized. This oscillatory polarization, in turn, results in optical emission at frequencies determined by the spectrum of the induced charge polarization. In the case of a low-intensity incident laser beam, the degree of polarization is directly proportional to the incident electric field strength, i.e., the material responds linearly with the incident field strength, and the intensity of the light emitted by the material is proportional to the first power of the incident laser intensity. Rayleigh and spontaneous Raman scattering result from a linear material response.

As the intensity of the incident laser beam is increased, the material will be driven past its limit of linear response and it will begin to respond in a nonlinear fashion, i.e., the polarization will be a nonlinear function of the electric field strength, which can give rise to the emission of light for which the frequency is a multiple of the incident laser frequencies and the intensity of which is proportional to second or higher powers of the incident laser intensities. Thus, the second order term describes the emission of second harmonic light (frequency equals two times the incident beam's frequency), the intensity of which varies as the square of the incident laser intensity, or of sum or difference frequency mixing (as, for example, by mixing visible and infrared radiation to produce a shifted visible beam). The third order term describes coherent anti-Stokes Raman scattering (CARS), discussed elsewhere in this report.

The specific nonlinear response of a given material depends on the composition and structure of the material and is reflected in the form of the nonlinear susceptibilities, the coefficients of an expansion of the polarization in powers of electric field strength. For the field-squared term, the susceptibility is identically zero (in the dipole approximation) in bulk materials having centrosymmetric structures (e.g., the gas phase and nearly all metals), due to their symmetry. *However, at the interface between two centrosymmetric materials, the inversion symmetry is broken and nonlinear generation can occur.* It is this behavior which produces the intrinsic interface sensitivity of SHG.

The following table summarizes the complementarity of Raman scattering and surface SHG:

Raman Scattering	**SHG**
• Volume specific	• Surface specific
• Signal depends on average laser power	• Signal depends on average squared intensity
• Probes vibrational structure	• Probes electronic and atomic structure
• Spontaneous, incoherent process	• Produces stimulated coherent beam

Section 6
High-Temperature Materials

Research in high-temperature material reactions at Sandia National Laboratories is sponsored by the Materials Sciences Division of the Department of Energy's Office of Basic Energy Sciences, as well as by Sandia Internal Research and Development discretionary internal funds. Emphasis is on the use of laser-based techniques—primarily Raman scattering, nonlinear optical spectroscopies, and other supporting analytical methods—to study systems *in situ* and in real time. This effort focuses on the interface between the material surface and its gaseous environment and can include research in the formation of thin films or particles; adsorption and segregation studies; flame-generated species, including deposition onto immersed materials, with concomitant gas/surface and deposit/substrate reactions; and the development of advanced diagnostic methods for application to these and other multiphase studies. The work is necessarily interdisciplinary in character, involving the chemistry, physics, and fluid mechanics of the systems studied using nonperturbing probes and modern computational techniques.

Work described here utilizes Raman scattering to understand material reactions in systems ranging from alloy surfaces under processing conditions to flames used for material synthesis (including silica-particle-laden flame diagnostics) and has even permitted the observation of alloy grain boundary effects using the spatial resolution offered by Raman microprobe techniques. Through the use of new optical second harmonic generation techniques—capable of providing real time, *in situ* interface information at the atomistic level from UHV to actual pressure conditions—results are shown that describe hydrogen adsorption on a nickel crystal surface at monolayer coverage.

Real-Time Studies of the Oxidation of Undoped and Y-Doped Chromium-Content Alloys

The mechanism of oxidation of Fe-13Cr and Fe-24Cr alloys undoped and doped with 0.3% yttrium has been studied in real time by Raman spectroscopy. The evolution of the oxide phases formed during heating at 700°C in both low (10^{-24} atm) and high (10^{-1} atm) oxygen partial pressure environments was determined. During the oxidations, transient oxide phases were observed. Upon quenching the alloys to room temperature in these environments, substantial phase changes occurred. Only small differences in the evolution of oxide phases with time were observed between the yttrium-doped and undoped alloys.

K. F. McCarty, J. C. Hamilton, and W. E. King*

The initial stages of oxidation have been identified as being critical in determining the long-term oxidation resistance of high-temperature alloys.[1] This study determined the phase compositions during the transient stages of oxide film growth using Raman spectroscopy. Both low chromium-content alloys (Fe-13Cr) and high chromium-content alloys (Fe-24Cr) undoped and doped with 0.3% yttrium were studied. Alloy coupons were oxidized at 700°C in both low (10^{-24} atm) and high (10^{-1} atm) oxygen partial pressure environments. The yttrium-doped alloys provide an example of the "reactive element" effect, a well-documented but poorly understood effect in which improvements in the oxidation resistance of alloys are achieved by additions of rare-earth elements or other reactive metals.

The oxidation studies were performed at atmospheric pressure in a flowing-gas furnace equipped with optical access for an incident laser beam and Raman-scattered radiation.[2] Well-polished coupons were oxidized in either a 10^{-24}-atm oxygen environment (generated by saturating a hydrogen flow with water vapor) or a 10^{-1}-atm oxygen environment (generated by a flow of 7% O_2 in Ar). The furnace was heated to 700°C over the course of about 8 minutes and held at 700°C for 80 minutes. After this exposure, the furnace was shut off and the composition of the oxide film was reexamined after the sample had cooled overnight. The Raman-scattered radiation, excited by a 514.5-nm, 300-mW, argon-ion laser, was collected with an f/2.2 lens system and dispersed by a Spex Triplemate monochromator onto a multichannel diode array detector. Spectra were obtained using 30-second integration times. The thickness of the oxide films was determined by optical interferometry using a photodiode to monitor the intensity of the reflected laser beam.

Figure 1 illustrates the evolution of oxide phases for an Fe-13Cr (low Cr) alloy oxidized at low oxygen partial pressure. After about one minute at 700°C (9 minutes of heating, including the temperature ramp), bands at 550 cm^{-1} and 665 cm^{-1} were present in the Raman spectrum, corresponding to chromia (Cr_2O_3) and spinel ($Fe_{3-x}Cr_xO_4$), respectively. Thus, initially both chromia and spinel are formed. With time, the spinel began to transform to chromia and after about 90 minutes, the transformation was completed. Figure 2 illustrates the dramatic changes which occur in the oxide upon cooling the sample to room temperature in the low-oxygen partial-pres-

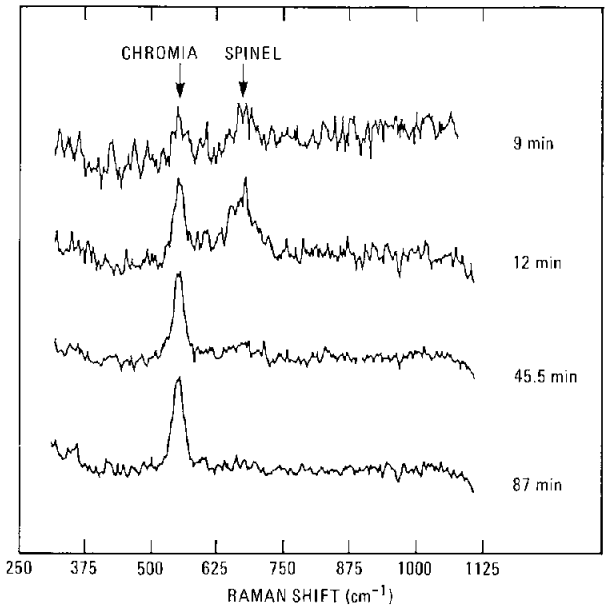

Figure 1. Evolution of oxide phases during the oxidation of undoped Fe-13Cr coupon in 10^{-24}-atm oxygen at 700°C. Transformation of an oxide film initially contining both chromia (Cr_2O_3) and spinel ($Fe_{3-x}Cr_xO_4$) to a film containing only chromia is illustrated.

*Lawrence Livermore National Laboratory, Livermore, CA.

sure environment. The Raman band at 665 cm^{-1} reappears, indicating that spinel reforms in the oxide film as it is cooled to room temperature. This major phase change upon cooling has not been observed previously and has important consequences regarding the accepted mechanisms of oxidation which are based on post-exposure analysis. The identification of the transient spinel phase during the film growth and its reappearance upon cooling highlights the necessity of conducting *in situ*, real-time measurements in order to properly understand corrosion mechanisms.

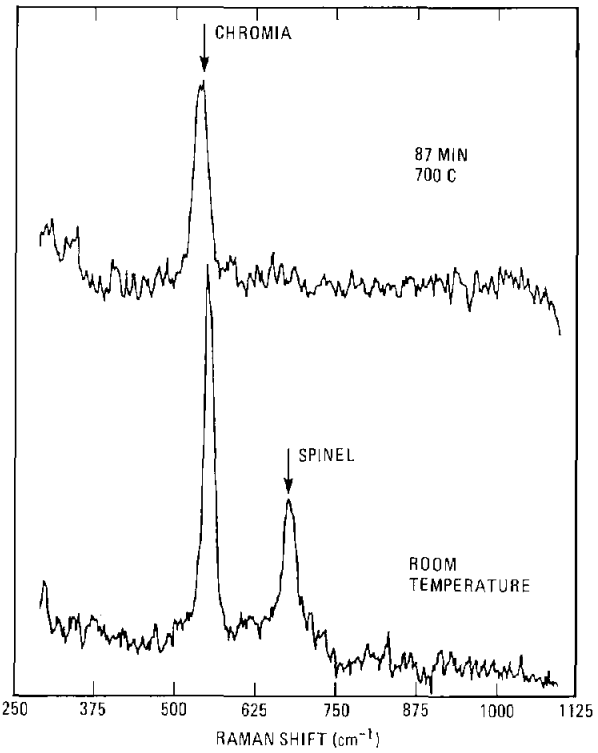

Figure 2. Formation of spinel ($Fe_{3-x}Cr_xO_4$) upon cooling to room temperature the oxide film grown on an undoped Fe-13Cr alloy at 700°C in 10^{-24} atm oxygen (see Figure 1). At 700°C, the oxide film was almost exclusively chromia (Cr_2O_3).

The oxide film growth on a high chromium content alloy (Fe-24Cr) oxidized in a 10^{-24}-atm oxygen environment is quite different (Figure 3) from the low chromium results (Figure 1). Here, only chromia was formed, even in the initial stages of oxidation. In addition, no phase changes occurred upon cooling the sample to room temperature. The difference between Fe-24Cr and Fe-13Cr is to be expected. Higher chromium contents favor the formation of chromia, and indeed, the Fe-13Cr alloy is marginal for the formation of chromia at all. That is, below about 13% Cr, Fe-Cr alloys do not form chromia.

The oxide-phase evolution was markedly different for oxidations in the high oxygen environment. For both Fe-13Cr and Fe-24Cr, α-Fe_2O_3 formed

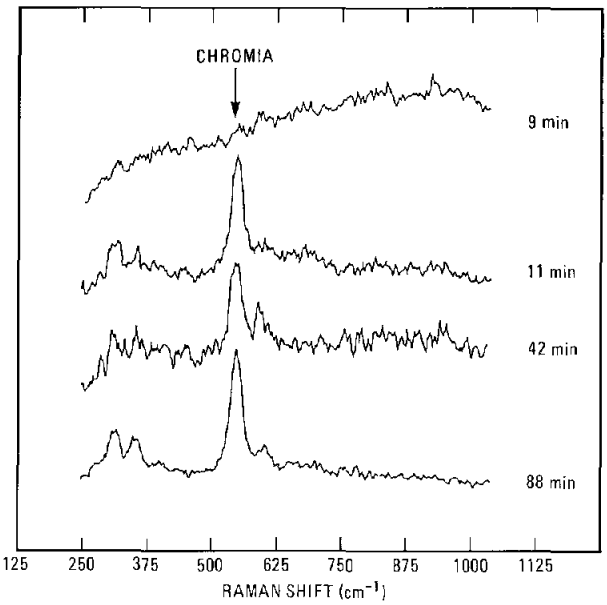

Figure 3. Growth of oxide film during the oxidation of undoped Fe-24Cr coupon in 10^{-24}-atm oxygen at 700°C. This high chromium-content alloy, in contrast to the low chromium alloy (Figure 1), produces only chromia during all stages of oxidation.

during the temperature ramp to 700°C. Upon reaching 700°C, Cr_2O_3 began to form, resulting in the formation of Cr_2O_3-Fe_2O_3 solid solutions. With increasing oxidation time, the solid solutions become increasingly rich in Cr_2O_3.

For the conditions employed in this study, only minor differences in the evolution of oxide phases with time were observed by Raman spectroscopy between the yttrium doped and undoped alloys. That is, yttrium doping had little effect here in enhancing the early formation of a protective chromia layer. The only dramatic effect was morphological in nature —nodules were formed on the oxide film of the Fe-13Cr/0.3Y alloys oxidized in both low and high oxygen environments. These nodules were of the order of a few microns across and a few microns high and result from very rapid oxide growth in localized regions. Post-exposure analysis, by SIMS and by Rutherford backscattering, established that the nodules grew over regions of the alloy containing yttrium. A Raman microprobe analysis of the nodules produced in oxidation at high oxygen partial pressures established that the nodules consisted of an Fe_2O_3-Cr_2O_3 solid solution which was considerably more Fe_2O_3-rich than the adjacent, smooth regions of the oxide film.

References:

1. D. P. Whittle and J. Stringer, Phil. Trans. R. Soc. Lond. A **295**, 309 (1980).

2. K. F. McCarty, J. C. Hamilton, D. R. Boehme, and A. S. Nagelberg, J. Electrochem. Soc., accepted (1987).

Role of Alloy Grain Boundaries on the Growth of Oxide Films: A Raman Microprobe Study

The role of alloy grain boundaries in oxidation mechanisms has been investigated using a Raman microprobe. Chromia (Cr_2O_3) was observed to preferentially form over the alloy grain boundaries of an Fe-13Cr alloy oxidized at 700°C while spinel ($Fe_{3-x}Cr_xO_4$) forms over the bulk of the grain. These differences in composition are in agreement with other results in the literature, suggesting that alloy grain boundaries provide rapid paths for the diffusion of chromium.

K. F. McCarty

The determination of phase composition with high spatial resolution is greatly desirable in a number of applications. One such application occurs in high-temperature, alloy-oxidation studies. It has been suggested in the literature that the mechanism of oxide formation near alloy grain boundaries is different from that over the bulk of the alloy grains. More specifically, in Fe-Cr alloys, the grain boundaries have been proposed to be paths along which chromium atoms can rapidly diffuse from the bulk of the alloy to the growing oxide film. The rapid diffusion of chromium is critical to the formation of adherent and protective chromia (Cr_2O_3) films on the alloys. If an insufficient amount of chromium is available at the oxide interface, iron-containing oxides such as spinel ($Fe_{3-x}Cr_xO_4$) form. Spinel is poorly adherent and thus a nonprotective oxide. Changes in the grain size can lead to large differences in the composition of the oxide that forms. For example, the time necessary to form a protective chromia film has been reduced significantly by producing alloys with small grain sizes.

We have performed a Raman microprobe study to address the role of alloy-grain boundaries in high temperature oxidation. Raman microscopy offers several important advantages as an analytic technique. First, chemical phases can be identified with about 1-μm resolution. This is in contrast to some techniques, such as SEM/EDAX, that provide a microscopic analysis of the elements present, but no information about the phase. While transmission electron-microscopy techniques can provide structural information, expensive sectioning and thinning techniques are required. In contrast, Raman microscopy requires little, if any, sample preparation. The second major advantage of the Raman microprobe is the ability to perform *in situ* measurements. Phase determinations can be made rapidly, with about 1-minute-time resolution, at atmospheric pressures, and at temperatures approaching 1000°C. Most analytical techniques require high vacuum and/or low temperatures which preclude *in situ* measurements.

Here, we discuss results of an Fe-13Cr alloy oxidized for 105 minutes in 10^{-24} atm oxygen partial pressure at 700°C. Differences in the spatial distribution of the oxide film composition allow the alloy grains to be distinguished. Figure 1 shows the Raman spectra obtained by scanning an approximately 1-μm-diameter laser beam from the interior of one grain across the grain boundary region and into the interior of the adjacent grain. Two different Raman peaks are observed. The 545-cm^{-1} peak arises from chromia while the 675-cm^{-1} peak arises from spinel. These assignments are based on an extensive series of spinel solid solutions ($Fe_{3-x}Cr_xO_4$, $0 \le x \le 2$) that were synthesized and analyzed by x-ray diffraction and Raman spectroscopy.

Figure 2 illustrates the ratio of chromia to spinel as a function of distance from the grain boundary. It is clearly seen that chromia dominates the oxide film over the grain boundary, while spinel dominates the oxide over the bulk of the grain. These differences in composition are in agreement with other results in the literature suggesting that alloy grain boundaries provide rapid paths for the diffusion of chromium. The results here show directly the dramatic differences in oxide phase composition resulting from the different diffusion paths.

Presently, *in situ* alloy oxidation measurements are being made using a microscope hot stage in which the gaseous environment can be carefully controlled. This apparatus will allow the evolution of the oxide phases to be determined as functions of time and proximity to grain boundaries.

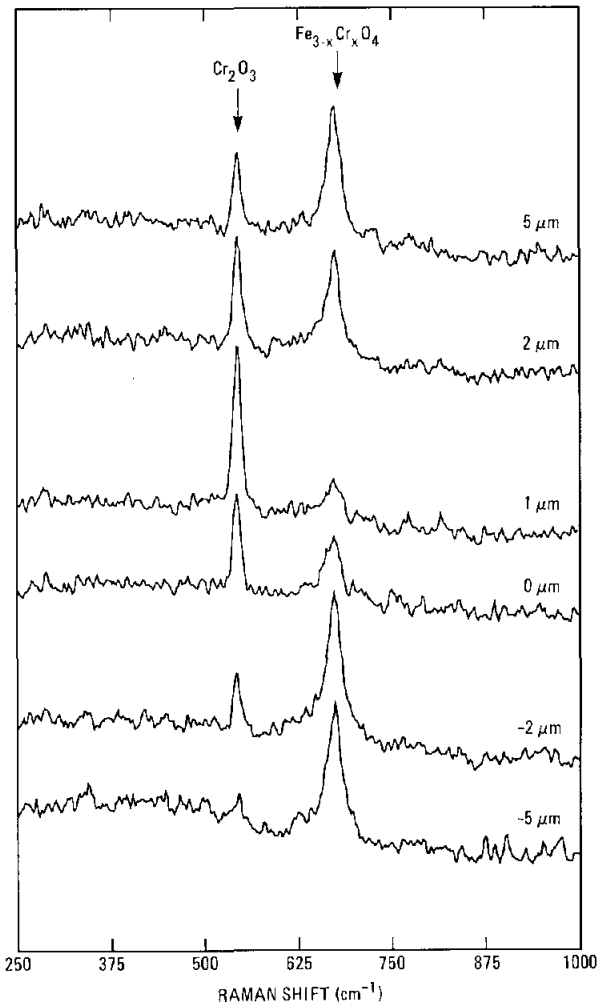

Figure 1. Raman spectra obtained at room temperature as a function of distance from the alloy grain boundary for an Fe-13Cr alloy oxidized for 105 minutes in 10^{-24} atm oxygen partial pressure at 700°C.

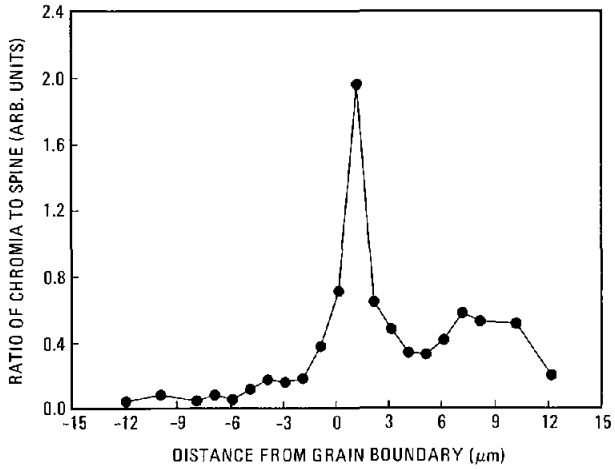

Figure 2. Ratio of the chromia to spinel intensity as a function of distance from the grain boundary. The formation of chromia is greatly enhanced over the grain boundary, while spinel forms over the bulk of the grain.

Azimuthally Resolved Optical Second-Harmonic Generation From Hydrogen on Nickel (111)†

A nonlinear optical probe is specific to surface conditions of both adsorbate coverage and site symmetry.

R. J. M. Anderson and J. C. Hamilton

The behavior of materials in combustion systems presents a wide range of technological problems. Structural members weakened by corrosion fail, deposit-laden structures inhibit heat flow, and poisoned catalysts lose their chemical activity. In each case, the change in the material is initiated at the surface, and, even if thicker layers form eventually, the driving reaction proceeds at the substrate-adsorbate interface or at the gas-deposit interface. To probe processes at interfaces—at the monolayer level—we must have diagnostic tools that are sensitive to the electronic and vibrational structures of a monolayer surface. A promising laser-based technique for such analysis is surface nonlinear optical spectroscopy.[1]

We have utilized the simplest manifestation of this phenomenon, surface second-harmonic (SH) generation, to probe the structure of material surfaces. The sample acts, essentially, as a nonlinear mirror. A single-pulsed laser beam, incident on an interface, generates an oscillating dipole at the surface at twice the frequency of the incident light. Light emitted by this dipole is a coherent beam that propagates along with the reflected fundamental and can be filtered and detected. The intensity of the second harmonic is a function of the electronic structure and physical symmetry of the reflecting interface; thus, the technique is sensitive to surface structure as well as adsorbate coverage.

Hydrogen adsorbed on Ni(111) is an important model system for the study of heterogeneous catalysis and the effects of hydrogen on metals, such as embrittlement. It is a relatively simple system showing two distinct thermal desorption peaks corresponding to β_1 and β_2 adsorption states of hydrogen. A half-monolayer of hydrogen in the β_2 state is observed to undergo an order-disorder transformation at about 270 K. Multiple-scattering calculations show that hydrogen is adsorbed in the threefold hollow sites and that below 270 K, a graphite-like array of hydrogen exists on the surface.[2]

We have measured the SH intensity as a function of both azimuthal orientation (rotation about the surface normal) and surface hydrogen coverage, from which we have inferred the changes in the isotropic and anisotropic components of the second-order susceptibility associated with both the β_1 and β_2 states of hydrogen. We find that the 3 m symmetry of the Ni(111) surface is manifest by a three-fold symmetry in the SH intensity, which persists at coverages and temperatures at which the low-energy electron diffraction (LEED) pattern shows both ordered and disordered hydrogen overlayers. This demonstrates that SHG probes local symmetry, not long-range ordering. The changes of both the isotropic and anisotropic contributions to the net susceptibility, due to occupation of β_2, are about twice those caused by filling β_1. We find that second-harmonic generation is dramatically reduced by hydrogen adsorption, almost disappearing at saturation coverage. This indicates that the major contribution to the second-order susceptibility comes from the surface, suggesting that resonances with electronic transitions between surface states are responsible for the large SH intensity from clean Ni(111).

For p-polarized excitation and detection, the intensity of the second harmonic generated from a surface of 3 m symmetry can be written

$$I(2\omega) \propto |\chi^{(2)}|^2 I^2(\omega) = |A + B\cos(3\psi)|^2 I^2(\omega). \qquad (1)$$

Here, $\chi^{(2)}$ is the second-order susceptibility, A and B are linear combinations of the susceptibility components, and ψ is the orientation of the plane of incidence measured relative to the surface vector <211>. It is generally not possible to separate surface and bulk contributions to the susceptibility for a clean surface. However, it is possible to study relative contributions from surface and bulk by chemical means, since the bulk contribution will not be affected by adsorption of gases or other surface chemical changes.

At azimuthal angles $\psi = 0°, 30°, 60°$, and $90°$, we have measured SH intensity from Ni(111) during adsorption and thermal desorption of hydrogen.

†Physical Review Letters, submitted (1987).

The data (shown in Figure 1) are analyzed using a model involving linear changes with H_2 coverage in the isotropic and anisotropic components of the susceptibility.[1] We generalize Equation (1) for two non-equivalent states,

$$\chi^2 \propto A\,(1 - C_{1A}\theta_1/\theta_{1s} - C_{2A}\theta_2/\theta_{2s}) + B\cos(3\psi\,(1 - C_{1B}\theta_1/\theta_{1s} - C_{2B}\theta_2/\theta_{2s}), \quad (2)$$

where θ_1 and θ_2 are the absolute coverages in the β_1 and β_2 states, and θ_{1s} and θ_{2s} are the saturation coverages for the β_1 and β_2 states. The C_{ij} are constants giving the linear decrease in the components of the second-order susceptibility caused by hydrogen adsorbed in the β_i state. We assume that hydrogen adsorption does not alter the 3 m point group symmetry of the Ni(111) surface. This is consistent with hydrogen adsorption at the three-fold hollow site as determined by low-energy electron diffraction,[2] as well as the data of this study.

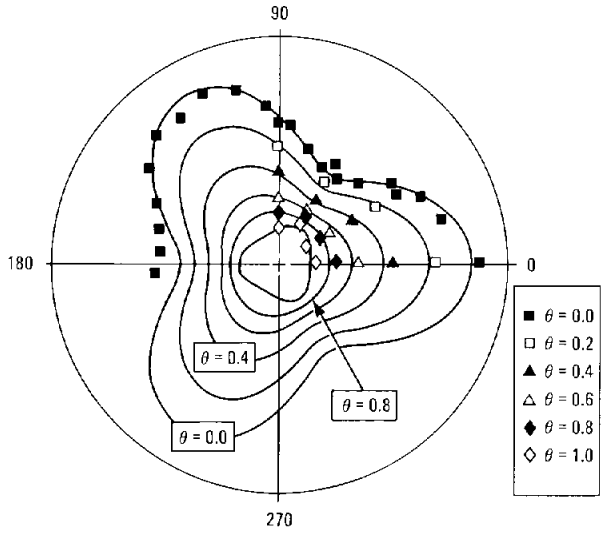

Figure 1. Continuous curves show the calculated square root of the SH intensity (proportional to $\chi^{(2)}$) as a function of azimuthal angle, ψ, for hydrogen coverages, θ = 0.0, 0.2, 0.4, 0.6, 0.8, and 1.0. Discrete data points are shown for the clean surface (outer curve), and at inferred coverages from the adsorption/desorption data.

The fractional coverage of hydrogen in each state during adsorption was calculated using one-site Langmuirian kinetics. That is,

$$d\theta_i/d\varepsilon = 2S_i^{O}(1 - \theta_i/\theta_{is}) \quad (3)$$

where S_i^{O} is the sticking coefficient for a hydrogen molecule in an empty β_i site and ε is the hydrogen exposure. The evolution of second-harmonic intensity during thermal desorption was modeled using the Polanyi-Wigner differential equation. For a state i on the surface, the rate of desorption is

$$d\theta_i/d\varepsilon = \upsilon_i\theta_i^{n_i} \exp(-E_i/RT), \quad (4)$$

where υ_i is a frequency factor, n_i is the reaction order for desorption from the ith state and E_i is the desorption activation energy. For hydrogen on nickel, second-order desorption kinetics for both states has been demonstrated previously. The adsorption and desorption data at all four azimuths were fit collectively by varying A/B, S_1^{O}, S_2^{O}, E_1, E_2, C_{1A}, C_{2A}, C_{1B}, and C_{2B} of equations 2, 3, and 4, using a least-squares fitting routine.

The good agreement between these results obtained with SHG and results using traditional techniques demonstrates the validity of this model and of the inferred dependences of $\chi^{(2)}$ on the hydrogen coverage. The azimuthal dependence of $\chi^{(2)}$ was calculated as a function of total fractional coverage, $\theta = (\theta_1 + \theta_2)/(\theta_{1s} + \theta_{2s})$, using insusceptibility coefficients C_{ij} from the least-squares fit and Equation (2) and is shown in Figure 1. Data points representing $\sqrt{I(2\omega)}$ at appropriate coverages from averaged adsorption/desorption data are also plotted along with additional measurements taken for the clean surface at 10° azimuthal increments. The isotropic component of the susceptibility is considerably greater than the anisotropic component at all hydrogen coverages. The change in the susceptibility associated with adsorption of a half-monolayer into the β_2 state is about twice the change in susceptibility associated with subsequent adsorption of a half-monolayer into the β_1 state. Furthermore, the anisotropic portion of the susceptibility decreases more rapidly than the isotropic portion as hydrogen is adsorbed, passing through zero at total fractional coverage 0.84 and reversing the sign of the contribution at full coverage. The calculated angular patterns and discrete data points combine to show graphically the progressive reduction of the total susceptibility and the sign-reversal of the anisotropic component. Based on the quality of the fits, we believe that this model gives an accurate representation of the effects of hydrogen adsorption on the isotropic and anisotropic components of the second-order susceptibility.

This study demonstrates forcefully the capability of surface nonlinear optical techniques to probe the energetics and dynamics of interface phenomena.

References:

1. Y. R. Shen, *The Principles of Nonlinear Optics* (Wiley, New York, NY, 1984), Ch. 25.

2. K. Christmann, R. J. Behm, G. Ertl, M. A. Van Hove, and W. H. Weinberg, J. Chem. Phys. **70**, 4168 (1979).

Temperature Measurements in Flames Containing Silica Particles by Spontaneous Raman Scattering from Oxygen

Spontaneous Raman spectra of oxygen were recorded in the post-flame gases of a lean methane/oxygen flame containing up to 10^{11} particles/cm^3. These non-absorbing particles appear to have no effect upon the measurement and demonstrate the usefulness of this technique for probing high-temperature material synthesis processes.

M. D. Allendorf and I. Souche*

Optical fiber for use in the communications industry is currently manufactured by a variety of processes, all of which begin with the pyrolysis of a gas-phase silicon compound (usually $SiCl_4$) to form silica (SiO_2) particles. In the Vapor Phase Axial Deposition (VAD) process, for example, $SiCl_4$ is decomposed in a lean hydrogen/oxygen flame, forming silica particles which grow primarily by agglomeration before being deposited on a rotating boule. Impurities in the silica, such as water and transition metals, are minimized in these high-temperature processes, an advantage which is critical to the production of low-light-loss fiber.

Improvements in the efficiency of silica production during the last ten years have come in the absence of fundamental studies, and further increases in production rates require a more detailed understanding of the dynamics of particle formation and growth in these systems. One important parameter in the characterization of high-temperature flows is the gas temperature; this can also be interpreted as the particle temperature, if the particles are assumed to be in thermal equilibrium with the gas. Gas temperatures are required if nonintrusive light-scattering methods are to be used to determine particle size; they are also critical for the evaluation of particle-growth models, in which the viscosity of silica is an important and highly temperature-dependent parameter. Temperature measurements in these flows are particularly difficult, however. Thermocouples, for example, are quickly coated with silica, yielding unreliable readings. Laser-based techniques do not disturb the gas flow, but the presence of high-number densities of particles (up to 10^{11}/cm^3) results in a large amount of scattered light. Particles also reduce the threshold power density for laser-induced breakdown, limiting the energy from pulsed lasers which can be used in the flame.

*National Center of Scientific Research (CNRS), Poitiers, France.

Spontaneous Raman spectroscopy has been shown to be an effective method for measuring temperatures in clean flames[1] and other high temperature systems, such as CVD reactors.[2] In the presence of carbon soot particles, spontaneous Raman measurements are difficult, if not impossible, to make due to high background luminosity (at average laser powers in excess of ~ 75 watts) absorption of the laser beam by the soot particles, causing them to radiate at a high black-body temperature. Silica particles, however, are gray bodies and do not absorb visible light, so the major source of noise (other than shot noise) is Mie-scattered light, which can be eliminated with a monochrometer and/or appropriate filters. Thus, Raman measurements of temperature should be feasible in flames or other high-temperature flows containing large concentrations of silica particles. In the study reported here, we have evaluated spontaneous Raman spectroscopy as a technique for making temperature measurements in flames containing silica particles.

A water-cooled porous plug burner was used for all experiments. Methane and oxygen were fed to the burner using mass-flow controllers and were premixed. For the spectra shown here, the flow rates were 1.2 liters/min CH_4 and 10 liters/min O_2 (0.24 equivalence ratio). To minimize flame disturbances caused by room air currents, a shroud flow of room-temperature nitrogen, moving at the velocity of the cold premixed gas, was employed. Silica was formed from hexamethyldisiloxane (HMDS) vapor, carried into the burner by bubbling argon through HMDS liquid. Approximately 0.17 g/min of silica soot was deposited in the flame. This is comparable to some industrial CVD burners, which typically deposit ~ 0.7 g/min.

An argon-ion laser producing 10.5 watts of power at 5145 Å generated Stokes scattering from oxygen in the post-flame gases. We chose to use a cw rather than a pulsed laser because the lower average power density does not induce gas breakdown. The laser beam was focused to a beam waist of 75 μm using a 212-mm focal-length lens.

Raman signals were collected at 90° and focused after image rotation on the slits of a double spectrometer. Signals were detected by a Princeton Instruments linear diode array and stored on an IBM PC-AT computer. The Sandia CARS code,[3] modified for spontaneous Raman scattering, was used to analyze the data.

The lean mixtures used for these experiments produced very thin flames situated nearly on the burner surface. The post-flame gases in which the measurements were made were not luminous, so the amount of noise present in the spectrum at room temperature did not increase in the presence of the flame. A typical oxygen Raman spectrum taken in the absence of particles is shown in Figure 1. Background signals were collected with the laser off for an equivalent amount of time before the spectrum was taken. The burner was allowed to stabilize thermally before any measurements were made and our spectra showed no evidence for long-term temperature drift. The 0-1, 1-2, and 2-3 vibrational *Q*-branches are apparent in the spectrum, and a good fit to a temperature of 1507 K was obtained.

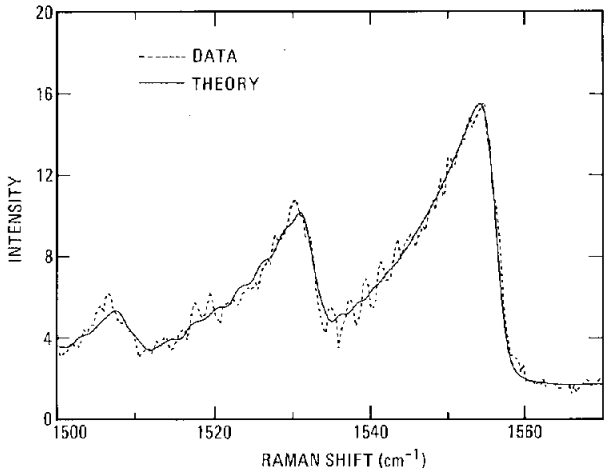

Figure 1. A typical oxygen Raman spectrum taken in the absence of particles.

The introduction of silica particles to the flame produced no increased luminosity at these flame temperatures, even at the highest silica production rate. A fine stream of white soot could be observed above the burner, however, and the laser beam was clearly visible in the post-flame gases due to light scattered by the particles. An oxygen Raman spectrum taken at the same flame location as that shown in Figure 1, but with the highest silica particle concentration is presented in Figure 2. The signal/noise ratio is similar to that seen in the absence of particles, and a theoretical fit to the data shows that the temperature (1500 K) changes very little when particles are present. Based on diffusion-broadening measurements of particle size in a similar flame,[4] the density of particles can be calculated. Assuming monodisperse particles with an equivalent sphere diameter of 200 nm (based on extrapolation of the data in Reference 4 to positions higher in the post-flame gases), a particle-number density of 10^{11} particles/cm^3 is obtained. Number densities of this magnitude are typical of systems used in the manufacture of optical fiber. The quality of the spectra obtained under these conditions indicates that Raman spectroscopy can be an effective technique for measuring temperatures in gas flows containing high concentrations of silica particles. We are currently applying the technique to other flames, including ones which are richer and thus more luminous, in order to fully determine the limitations of the technique.

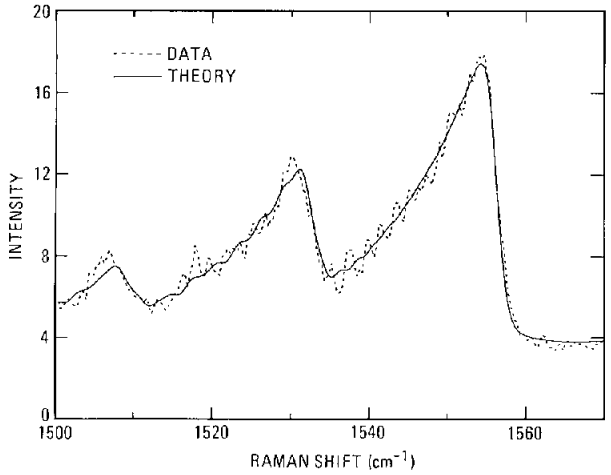

Figure 2. An oxygen Raman spectrum taken at the same flame location as that shown in Figure 1, but with the highest silica-particle concentration.

References:

1. M. Lapp, L. M. Goldman, and C. M. Penney, Science **175**, 1112 (1972).

2. W. G. Breiland and M. J. Kushner, App. Phys. Lett. **42**, 395 (1983).

3. R. L. Farrow, R. P. Lucht, G. L. Clark, and R. E. Palmer, Appl. Opt. **24**, 2241 (1985).

4. W. L. Flower and A. J. Hurd, Appl. Opt. **26**, 2236 (1987).

A New Experimental Facility for Laser Diagnostic Studies of Gas-Phase Ceramic Powder Synthesis

Development of experimental facilities for the study of ceramic powders formed in high-temperature gas flows has been completed. The incorporation of laser-based diagnostics permits a detailed study of the dynamics of gas-phase particle formation.

M. D. Allendorf and D. R. Hardesty

The production of solid materials from gas-phase reactants via flames is one of the oldest synthetic techniques in existence. Today, combustion processes are used to manufacture a variety of products, including carbon black (used in ink, paint, and as polymer reinforcement), titanium dioxide (used in paint), and silicon dioxide (silicone products and optical fiber). These materials account for millions of tons of production each year. Gas-phase-synthesis techniques are now being applied in the laboratory to synthesize more specialized materials such as ceramic powders. Ceramic components produced from powders such as silicon nitride and silicon carbide are extremely resistant to thermal stress and corrosion, making them excellent candidates for application to heat exchangers, turbines, and automobile engines. Unlike metals, ceramics fail catastrophically, which has limited their usefulness. This has often been attributed to agglomerates, impurities, and inadequate control over particle size during powder synthesis.

Gas-phase techniques have the potential to improve powder characteristics and increase the utility of ceramics by exerting much greater control over powder synthesis conditions than was formerly possible. This has led us to initiate a program to study the dynamics of high-temperature refractory particle formation. Our research in this field was begun in 1986 when, in collaboration with AT&T, we applied CARS, diffusion-broadening spectroscopy, and spontaneous-Raman spectroscopy to flames containing high concentrations of silica particles. This technology is being transferred to AT&T.

During the past year, we have completed construction of an experimental facility which will permit a detailed study of the physics and elementary-reaction chemistry of gas-phase particle formation. The goal of this research is the development of an engineering model capable of predicting the properties of powders synthesized in the gas phase. Application of this model to specific synthesis techniques will provide a new degree of control over powder characteristics.

Figure 1 illustrates the complexity of the gas-phase, particle-synthesis process. Reactants, such as silane and ammonia, must mix and be heated before reaction takes place. Following the generation of reactive species, primary particles form; in the case of extended molecular solids, such as silicon nitride (Si_3N_4 does not exist as a gas), the nucleating molecule is unknown. Depending on particle concentration, temperature, and flow rate, primary particles can grow by condensation of gas-phase species, coalescence, or agglomeration. Since most of these effects are present to some degree in all gas-phase-synthesis techniques, we have designed a laboratory reactor which incorporates as few system-specific elements as possible. This should permit the widest possible application of the computational model. We therefore chose not to use lasers or plasmas, for example, as heat sources, as these have unique problems which are not found in other techniques.

A schematic of our reactor is shown in Figure 2. A quartz tube, 120-cm long, is surrounded by a furnace, allowing gases flowing through the tube to be heated as high as 1350 K. Gases enter the reactor from the left and are pumped through it by a vacuum pump (operating pressures are 1-600 torr). Flow rates are controlled using electronic mass-flow controllers. Four ports with purged-quartz windows at the downstream end yield optical access for spontaneous Raman, laser-induced fluorescence, and light-scattering spectroscopies. Thus, major and minor species as well as particle size may be monitored. Time resolution is achieved with a movable stainless steel injector (as is found in discharge-flow reactors used to study elementary chemical reactions), and residence times as long as several seconds can be achieved. The injector is cooled (water or air) to prevent thermally-unstable reactants (like silane) from decomposing. Powders may be sampled using an isokinetic sampler at the downstream end of the tube.

To facilitate computational modeling, we choose reactor conditions which simplify calculations. Pressures $\leq$ 10 torr promote rapid mixing; calculations (using a flame code developed by R.

Mitchell) indicate that mixing is sufficiently rapid at these pressures to be considered instantaneous. Low pressures also favor the detection of some important reactive species, such as SiH_2, whose fluorescence is quenched at higher pressures. Reactant concentrations are kept low so that the heat released by reactions can be neglected; fluid flow can then be calculated separately, with detailed chemical mechanisms and aerosol dynamics added afterward.

Our initial investigations are focusing on the decomposition of silane to form silicon particles for several reasons. First, a detailed chemical reaction mechanism exists for the pyrolysis of silane.[1] Second, the chemical species which can nucleate to form particles is clear (*viz.*, silicon atoms or clusters can condense). Finally, investigations of this process by other investigators[2] have laid some groundwork for the application of aerosol physics to the problem. Later experiments will examine both silicon nitride and silicon carbide formation.

References:

1. M. E. Coltrin, R. J. Kee, and J. A. Miller, J. Electrochem. Soc. **133**, 1206, (1986).

2. M. K. Alam and R. C. Flagan, Aerosol Sci. Tech. **5**, 237 (1986).

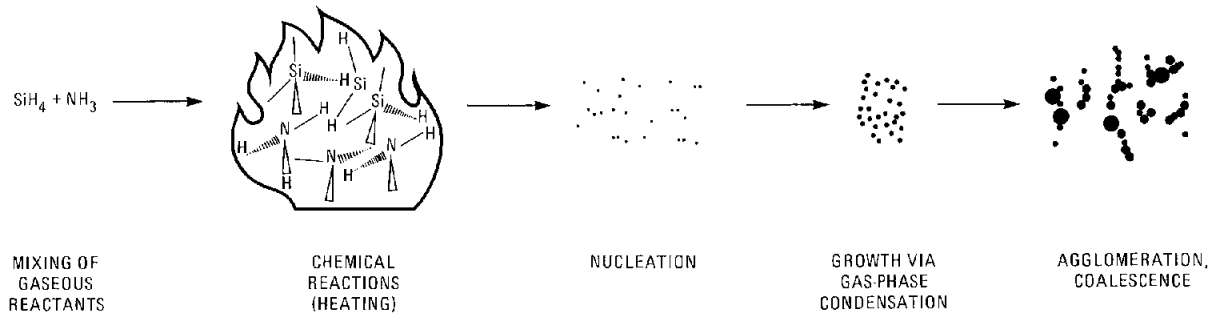

Figure 1. Physical and chemical processes present during the gas-phase synthesis of ceramic powders.

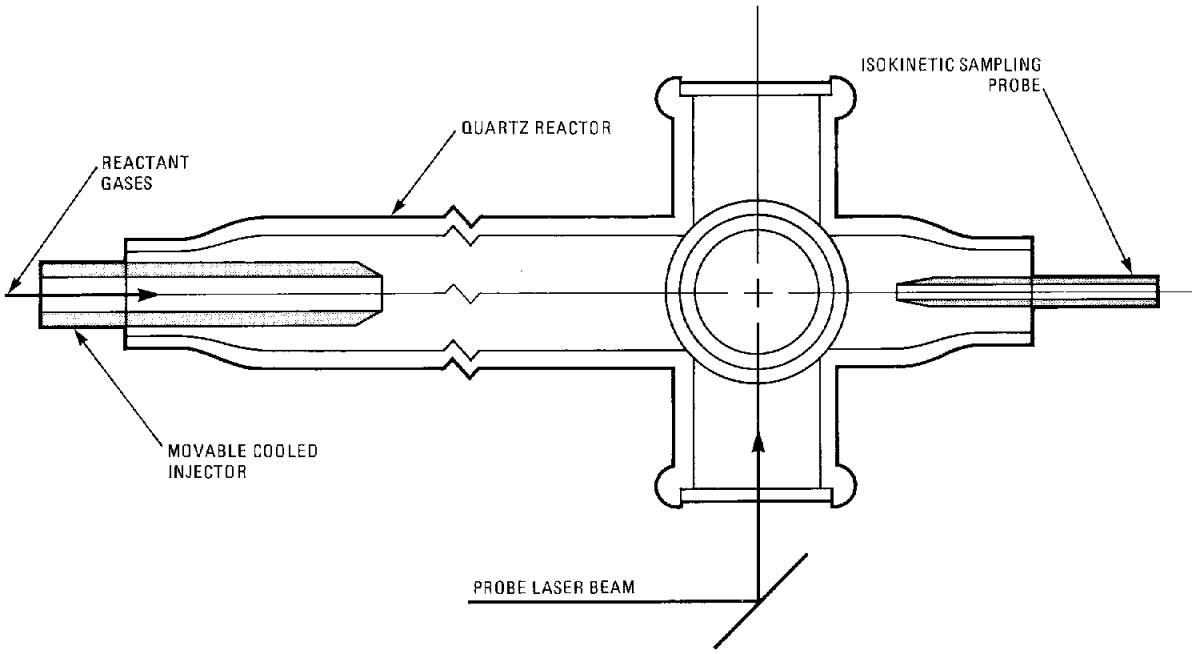

Figure 2. Schematic of quartz reactor used for particulate dynamics studies. The length of tube left of the optical ports (~ 100-cm long) is enclosed in a furnace.

The double-walled quartz exhaust pipe section for our pulse combustion furnace has allowed extensive real-time measurements of instantaneous velocities (laser velocimetry pictured at left), turbulence, temperature and wall heat flux. Altogether, these measurements form a definitive data set to provide key insight into the processes controlling heat transfer and convective transport in the acoustically-driven turbulent exhaust pipe flow.

Combustion in Engines and Furnaces

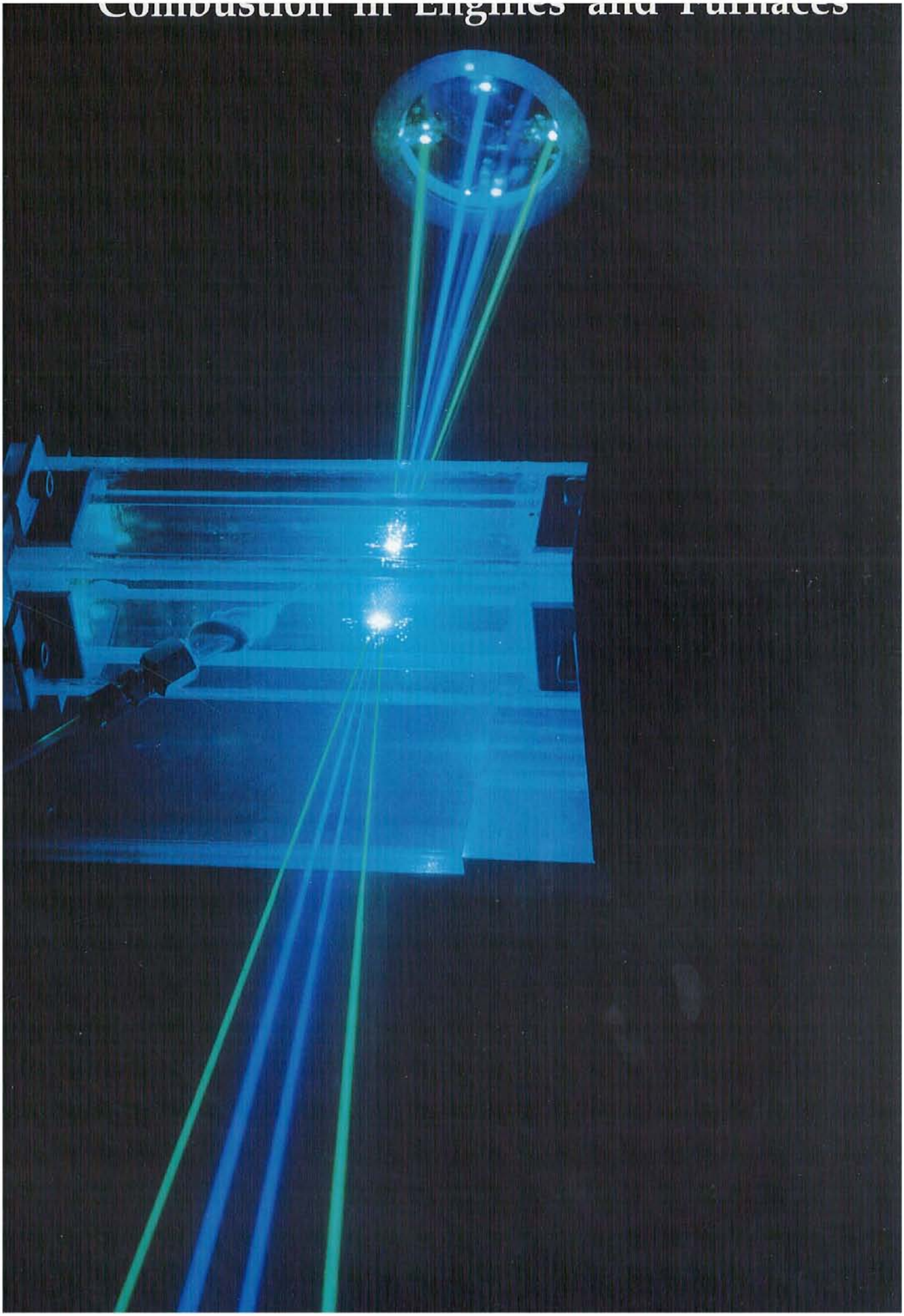

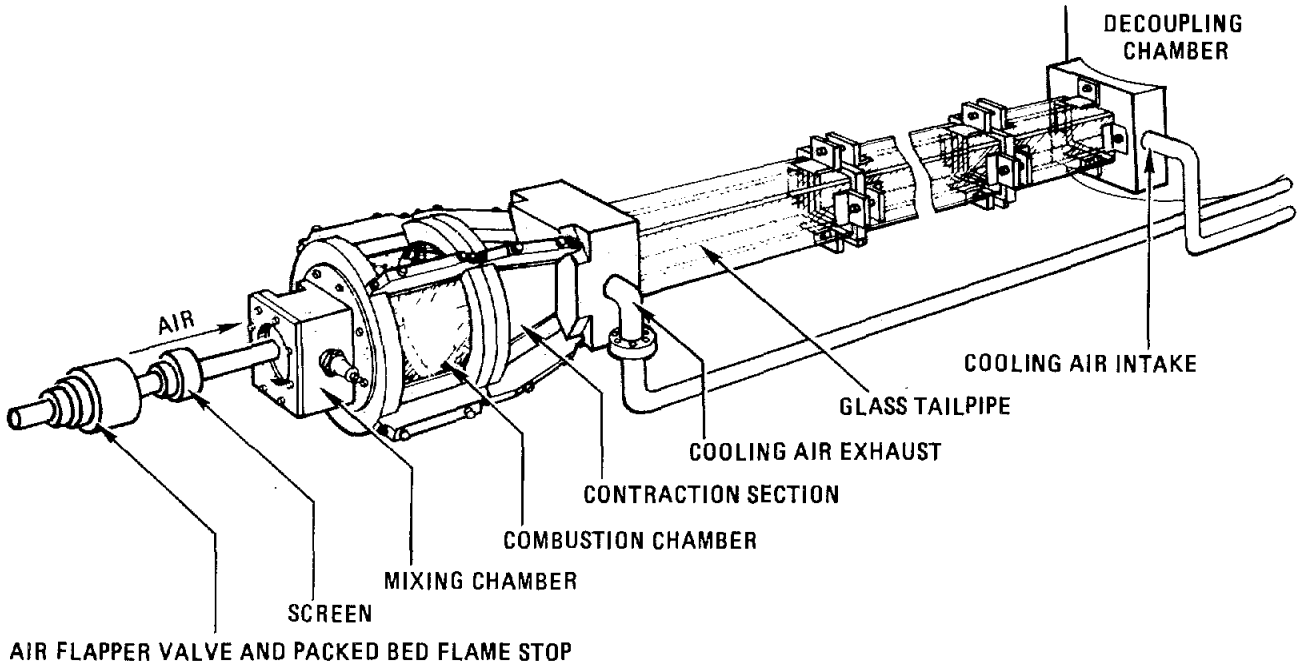

DOE's Energy Conversion and Utilization Technologies (ECUT) Program is investigating the combustion processes that occur in pulse combustion furnaces. These units offer tremendous technical potential including thermal efficiencies near 95% compared with conventional furnace efficiencies of 70%. Pulse furnaces also have a three-fold improvement in heat transfer rate, a three-fold improvement in NOx emissions and a better than ten-fold improvement in combustion intensity.

Along with these positive attributes come an important liability, that is, designs typically require months, and even years, of painstaking empirical experimentation. Critical issues limiting their widespread introduction are the lack of understanding of the complex acoustically-coupled processes controlling the operating stability, multifuel characteristics, noise levels, and scalability. Sandia National Laboratories is addressing these issues in the combustor shown schematically above. Closely simulating the geometry and operational characteristics of commercial units, it offers complete optical access for extensive laser diagnostic investigations.

During the past year, the understanding of the fundamental processes controlling the operating of a pulse combustor has increased significantly. The concept of characteristic times for the coupled competing processes has been established both experimentally and theoretically. It has been shown that the fluid dynamic mixing time is the dominant time affecting the proper phasing of energy release, and that minor variations in fuel properties are also important because of their effect on the chemical ignition delay time. A simple model for combining these two effects was developed and has been incorporated into the one-dimensional, nonlinear pulse combustor model. This pulse combustor model can now be used to accelerate the design and development of prototype pulse combustors with the incorporation of realistic valving dynamics, wall heat transfer estimates, and inlet and exhaust decouplers.

New applications of this powerful technology for both domestic and industrial heating are still being discovered. Research is poised at the leading edge of huge technical advances that signal new competitive opportunities for U.S. industry.

Section 7
Combustion in Engines and Furnaces

Under the sponsorship of DOE's Energy Conversion and Utilization Technologies (ECUT) Program, Sandia National Laboratories is pursuing a broad program of research on the combustion processes in internal combustion engines. The program focuses on the application of advanced laser diagnostics to provide insight into critical problems impeding the development of improved engine concepts. The problem areas under investigation include: the interaction between precombustion fluid mechanics and combustion, end-gas autoignition leading to engine knock, and the autoignition and combustion properties of alternative fuel sprays for diesel applications. Research involves the development of nonperturbing, laser-based methods that provide time- and space-resolved measurements inside combustion engines. A new focus this year is toward the application of these diagnostics toward more practical engine configurations.

A relatively new activity that focuses broadly on continuous combustion systems for furnace and boiler applications has begun to produce interesting new results. The program focuses on improved furnace concepts. The initial emphasis of this program is to perform an experimental and theoretical investigation of the pulse combustion process. The goal of this experimental and theoretical program is to develop a fundamental understanding of the physics governing a gas-fired pulse combustor. The experimental work involves the use of nonperturbing laser diagnostics to provide time- and space-resolved measurements of the fluid dynamic and chemical processes controlling the combustion process. The experimental work is closely tied to the development of a one-dimensional, nonlinear numerical model.

Several cooperative research groups have been established with industry partners to ensure that this research is relevant to the practical needs of industry and that the resulting technology is transferred quickly to the production sector.

The Autoignition of Isobutane in a Knocking Spark-Ignition Engine

The chemical aspects of the autoignition of isobutane were studied experimentally in a spark-ignition engine. The results of these studies show that under certain conditions, even with the relatively knock-resistant fuel, isobutane, there is still a significant amount of fuel breakdown in the end gas, with a resulting heat release and temperature increase.

R. M. Green and C. D. Parker*

In the last 10 to 15 years, engine designers have been able to build fuel-efficient engines that are reasonably nonpolluting while burning the fuels currently available. Engine knock will limit spark-ignition engines, and we will need advancements in current engine designs that will extend their effectiveness in the short term and provide the time needed for the development of new engine concepts. These advancements might include better combustion chamber designs and improved engine control strategies, in conjunction with the modification of the chemical make-up of fuels.

The goal of our ongoing research is to improve our understanding of the low temperature chemistry occurring in the compressively-heated end gas prior to autoignition and knock in a spark-ignition engine.[1] Using a thermodynamic heat-release analysis, we can determine the end-gas temperature history from the measured combustion chamber pressure history. In addition, we obtain time-resolved samples of end gas prior to the autoignition and analyze them to determine the concentration histories of the stable species.

We have recently studied the autoignition behavior of isobutane.[2] Previous work[1] has indicated that n-butane, a lower octane fuel, exhibited a considerable degree of heat release in the end gas prior to autoignition. This effect reduces the accuracy of our end-gas temperature predictions; thus our ability to study the chemical kinetic behavior is impaired. Preliminary studies using isobutane illustrated that under most operating conditions, heat release in the end gas is much less significant.

Table I summarizes the experimental operating conditions we used in this study. Also included are the averaged values of the measured autoignition times and the calculated end-gas temperatures at the time of autoignition. The pressure histories measured near the time of autoignition and the temperature histories calculated using the thermodynamic model are illustrated in Figure 1. The effect of engine speed on the autoignition process can be observed in Table I and Figure 1. These data indicate that the calculated end-gas temperature during the latter stages of compression and heat release, as well as at the knock point, increase with engine speed. Unfortunately, during flame propagation and including the knock point, the effect of heat release in the end gas may become sufficiently important that the thermodynamic model might be underpredicting the temperature. Notice that between 300 and 600 rpm, the autoignition temperature increases nearly 120 K, but from 600 to 900 rpm, it increases only about 30 K. It is difficult to attach a great deal of significance to a 30-K difference in these temperature predictions. Therefore, it is probably safe to presume that the difference in the calculated knock-point temperatures for the 600- and 900-rpm cases is negligible; however, the difference between this temperature and that for the 300-rpm case is significant.

It appears likely that in the case of the 300-rpm data, heat release in the end gas is leading to a higher end-gas temperature at the time of autoignition than was calculated. At 600 and 900 rpm, our interpretation of the results indicates that end-gas heating is primarily due to compressive work, while at 300 rpm, the greater time available during compression leads to significantly more chemical activity and heat release. This statement is supported by the observation that the estimated end-

*Jackson State University, Jackson, MS.

gas temperatures at the time of autoignition were nearly independent of manifold temperature, as indicated in Table I.

A broad view of the experimental results of this investigation reveals a general agreement with observations from engine knock studies that have been published over the last 30 to 40 years.[3] However, the contribution of the present work is manifested primarily in the interpretation of the experimental results using a detailed chemical-kinetic model. This interpretation strongly suggests that end-gas heat release is the important clue needed to understand autoignition and knock in an engine.

There has been considerable discussion about the role of low temperature reactions, or cool flames, in the engine knock phenomenon. One point of view is that the production of reactive intermediate chemical species (i.e., a presensitization of the fuel-air mixture) is the most important result of low-temperature-oxidation kinetics. In contrast, this work suggests that the most important product of low-temperature oxidation processes is energy release. Although relatively small, this energy release results in a more rapid attainment of high-temperature ignition.

Table I
Operating Conditions and Autoignition Data

Engine Speed (rpm)	Spark Timing (CAD)	Manifold Temp. (K)	Manifold Press. (bars)	Equiv. Ratio	Autoignition Time (ms*)	Autoignition Temp. (K)
300	352	492	1.78	1.0	-1.25	968
600	352	490	1.78	1.0	1.65	1088
900	352	492	1.78	1.0	1.91	1121
600	352	467	1.78	1.0	1.72	1078
600	352	443	1.78	1.0	1.92	1048
600	352	430	1.78	1.0	2.26	1048

*Referenced to TDC

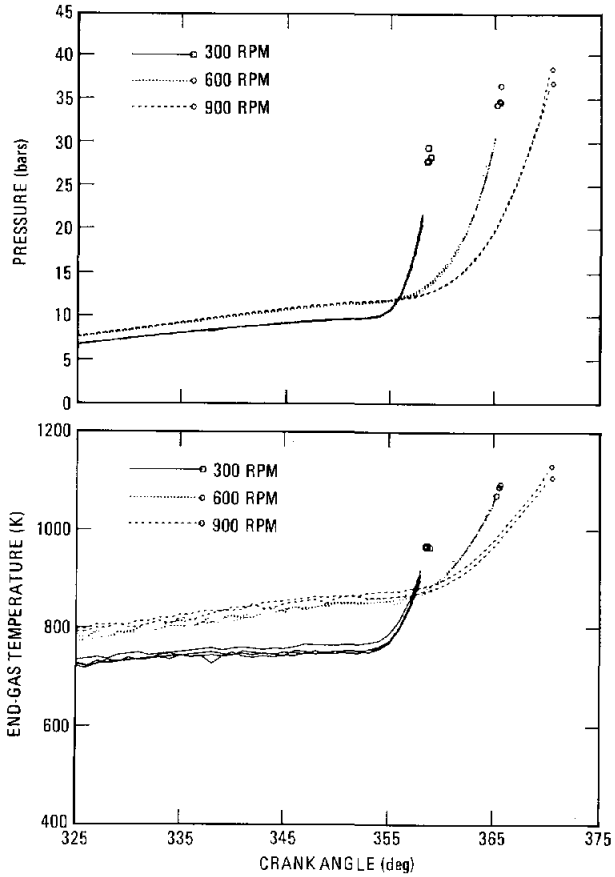

Figure 1. Measured end-gas pressure and estimated end-gas temperature histories as functions of engine speed. Engine operating conditions: equivalence ratio, 1.0; manifold temperature, 493K; manifold pressure, 1.78 bars; spark ignition at 352 CAD.

References:

1. J. R. Smith, R. M. Green, C. K. Westbrook, and W. J. Pitz, *Twentieth Symposium (International) on Combustion* (The Combustion Institute, Pittsburgh, PA, 1984), p. 91.

2. R. M. Green, C. D. Parker, W. J. Pitz, and C. K. Westbrook, *SAE Paper No. 870169* (1987).

3. M. E. Gluckstein, and C.Walcutt, SAE Transactions **69**, 529 (1961).

The Role of Low Temperature Chemistry in the Autoignition of N-Butane

We have studied the chemical aspects of the compression ignition of n-butane in a spark-ignition engine. The results of these studies demonstrate the effects of initial-charge composition and chemical preconditioning on the autoignition process.

R. M. Green and N. P. Cernansky*

Over the years, studies of knock in spark-ignition engines have included nearly all aspects of engine combustion.[1-3] Investigations involving experiments and/or modeling have probed the chemical, thermodynamic, and mechanical details of the processes involved and have resulted in significant advances in our understanding of the phenomena. Unfortunately, there are still many facets of the problem that need to be unraveled in order to control engine knock.

In the current experiments,[4] the engine control strategy consisted of a three-cycle sequence in which the first cycle was a fired cycle wherein a propagating flame, initiated by a conventional spark, led to end-gas autoignition and knock. This was followed by a skip cycle where the intake charge was compressed and expanded with neither spark ignition nor autoignition. Finally, in the last cycle of the sequence, the charge autoignited by compression ignition. Since the normal scavenging efficiency of the engine is roughly 80%, these cycles contained 80% fresh charge and either 20% recycled products of combustion (in the case of a prior spark- or compression-ignition cycle) or 20% partially-oxidized reactants (in the case of a prior skip cycle).

The basic behavior observed in these experiments is illustrated in Figure 1, which shows single-cycle pressure histories for the three cycles in the control sequence. In the fired cycle, one can observe the discontinuity in the rate of heat release that occurs at the time of autoignition and the characteristic pressure oscillations that accompany knocking operation. In the next cycle, there is barely perceptible heat release prior to TDC (Top Dead Center) due to pre-ignition reactions, but there is no hot ignition. On the other hand, the third cycle shows a noticeable degree of pre-ignition-reaction heat release before TDC and has a clearly defined autoignition event well after TDC.

*Drexel University, Philadelphia, PA.

Cycle-averaged sampling and gas chromations (which include residual products of combustion since they both follow a hot-ignition event) show nearly identical reaction histories up to the point of spark ignition and flame propagation in the fired cycles. At that point, the preignition reactions in the fired cycles accelerate due to the rapidly rising pressure and temperature, but are prevented from proceeding too far by the autoignition event. The compression-ignition cycles show markedly different behavior. They start out with initial intermediate-species concentrations that are characteristic of the partially oxidized residual from the prior skip cycle. Subsequently, the preignition reactions commence earlier in the cycle and proceed much farther. The most striking characteristic of the compression-ignition process is that, under the operating conditions that we observed, compression ignition occurs only on a skip cycle that follows another skip cycle. This seems to indicate that the residual products of hot combustion or recycled intermediates resulting from partial oxidation of the fuel carried over from the previous cycle and mixed with the fresh incoming fuel-air charge have important effects on the chemistry preceding the autoignition.

In previous investigations of the autoignition behavior of different hydrocarbon fuels, it has been proposed that the role of preflame chemistry in the autoignition process is primarily to provide heat release to raise the end-gas temperature to a level where the reactions of hot ignition will proceed. The end-gas sampling measurements reported in the present work provide strong evidence supporting this contention. If we compare the intermediate-species concentrations (measured just before autoignition on the fired cycle) with those of the compression-ignition cycle, we see a significant difference in the concentration levels. Indeed, the concentrations are a factor of 3-to-4 less on the firing cycle. This large disparity in the intermediate concentration levels just prior to autoignition leads

us to speculate that the chemical extent (and perhaps even the nature) of the preflame reactions is important to the autoignition process only insofar as it affects the end-gas temperature.

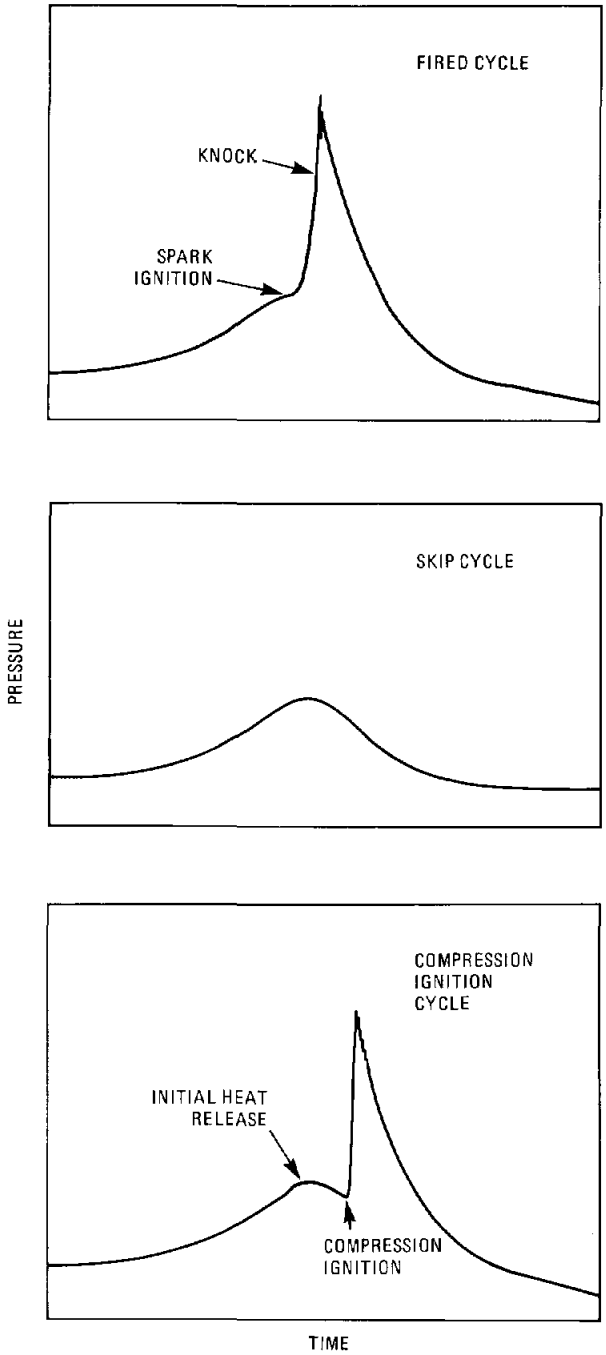

Figure 1. Typical pressure histories illustrating the compression and expansion strokes of the fired-, skip-, and compression-ignition cycles for an engine speed of 600 rpm. Notice that the heat release near TDC in the compression-ignition cycle is not present in the fired cycle and is only barely perceptible in the skip cycle.

The results of this study have provided some exciting new insights into our study of autoignition and knock in spark-ignition engines through observations of the process of compression ignition. This work has strengthened the hypothesis that the role of the low-temperature end-gas chemistry is to provide enough heat release that the end-gas temperature increases to a level where hot ignition can occur. Furthermore, this work has pointed out that the recycled residual products of combustion have a significant influence on the end-gas reactions.

References:

1. A. Egerton, F. L. Smith, and A. R. Ubbelohde, Phil. Trans. of the Royal Soc. of London A **744**, 433 (1935).

2. D. Downs, A. D. Walsh, and R. W. Wheeler, Phil. Trans. of the Royal Soc. of London A **242**, 462 (1951).

3. J. R. Smith, R. M. Green, C. K. Westbrook, and W. J. Pitz, *Twentieth Symposium (International) on Combustion* (The Combustion Institute, Pittsburgh, PA, 1984), p. 91.

4. R. M. Green, N. P. Cernansky, W. J. Pitz, and C. K. Westbrook, "The Role of Low Temperature Chemistry in the Autoignition of N-Butane," International Fuels and Lubricants Meeting and Exposition, Toronto, Ontario, Canada (SAE, 1987), Paper No. 872108.

Two-Component Laser Velocimeter Measurements in a Spark-Ignition Engine†

Simultaneous measurements of two components of velocity have been obtained during premixed charge combustion in a spark-ignition engine.

D. E. Foster* and P. O. Witze

The simultaneous measurement of two velocity components in a plane permits direct calculation of two of the three normal stress components acting on a fluid element, as well as one shear stress component. Schock, *et al.*[1] have demonstrated the simultaneous measurement of two velocity components in a motored engine, but did not report measurements of the turbulence shear stress. The purpose of our study was to measure two components of velocity and the corresponding turbulence stresses as combustion takes place.

Because the velocity changes rapidly in the vicinity of the flame surface, cyclic variations in the combustion rate cause smearing of an ensemble-averaged, mean-velocity profile and broadening of ensemble velocity distributions that result in artificially high turbulence intensities. We used a conditional sampling procedure to reduce these problems.

The simultaneous two-component LDV measurements were made in the forward scatter mode. All measurements were made at one location in the center of the disc-shaped clearance volume, with the spark plug located 90-degrees from the optical axis of the LDV system. Dual Bragg cells were used to frequency shift both velocity components. Zirconium fluoride particles, approximately 0.3 microns in diameter, were used as the seeding material. The engine was operated on a stoichiometric propane-air mixture at speeds of 300, 600, and 1200 rpm. Ignition timing was set to give average peak pressure at about 10 crank-angle degrees after top-dead-center.

Figure 1 illustrates our experimental setup. The conditional sampling on flame-arrival time was done using one of the spent LDV beams for the velocity component normal to the piston surface. This beam was directed onto a photodiode, such that when the flame crosses the beam, the gradients in the index of refraction deflect the beam off the photodiode, producing a distinct signal.

Figure 2 summarizes the flame-arrival-time sampling conditions used for this study. The full histograms for each engine speed show the distribution of flame arrivals for all engine cycles. As expected, cyclic variation in the combustion rate increased with engine speed. The darkened regions in the center of each histogram indicate those engine cycles that were used to compute the ensemble-averaged quantities.

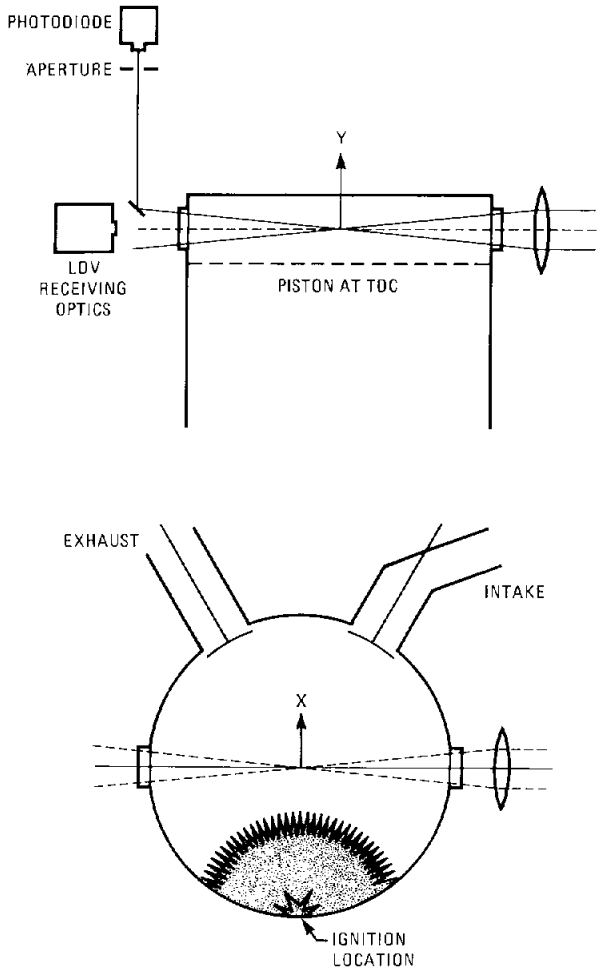

Figure 1. Schematic of experimental setup, showing the forward-scatter LDV optics and the laser-beam-refraction flame arrival detector.

†Combustion Science and Technology **59**, 85 (1988).
*University of Wisconsin at Madison.

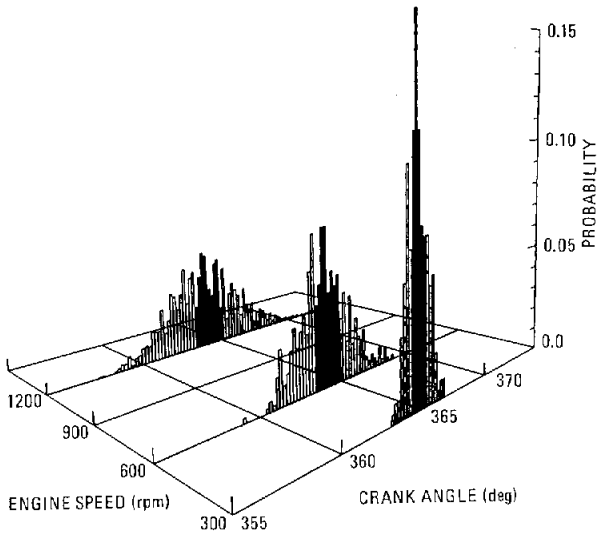

Figure 2. Histograms of flame arrival measurements, normalized to have unit areas. The solid bands indicate the conditions selected for the LDV measurements.

The ensemble-averaged turbulence stresses are given in Figure 3. Also shown in the figure as lighter weight lines are curve fits to motored data. The cross-hatched regions indicate the flame arrival windows used for the conditional sampling, and the bar-shaded areas represent low data rate intervals immediately behind the flame. Too little data were obtained in these regions to provide meaningful statistics.

Analysis of the data indicates that the flow field goes through a transition as the engine speed is increased. At 300 rpm, the turbulence is isotropic and it does not scale, relative to the higher speeds, with the mean piston speed. There also appears to be an enhancement of the turbulence by the flame that is not present at the higher engine speeds. At both 600 and 1200 rpm, the turbulence is highly anisotropic, the turbulence stresses scale with the mean piston speed, and combustion does not have an appreciable effect on the preflame and postflame gases. In fact, at 1200 rpm, it appears that the flame actually attenuates the turbulence slightly. In contrast, the behavior of the shear stress during combustion is very different in that, for the two higher engine speeds, the approaching flame clearly destroys the correlation of the velocity fluctuations at the LDV probe volume. Whether this is a change in turbulence structure or a reorientation of the relevant coordinate system due to flame tilt is not understood at this time.

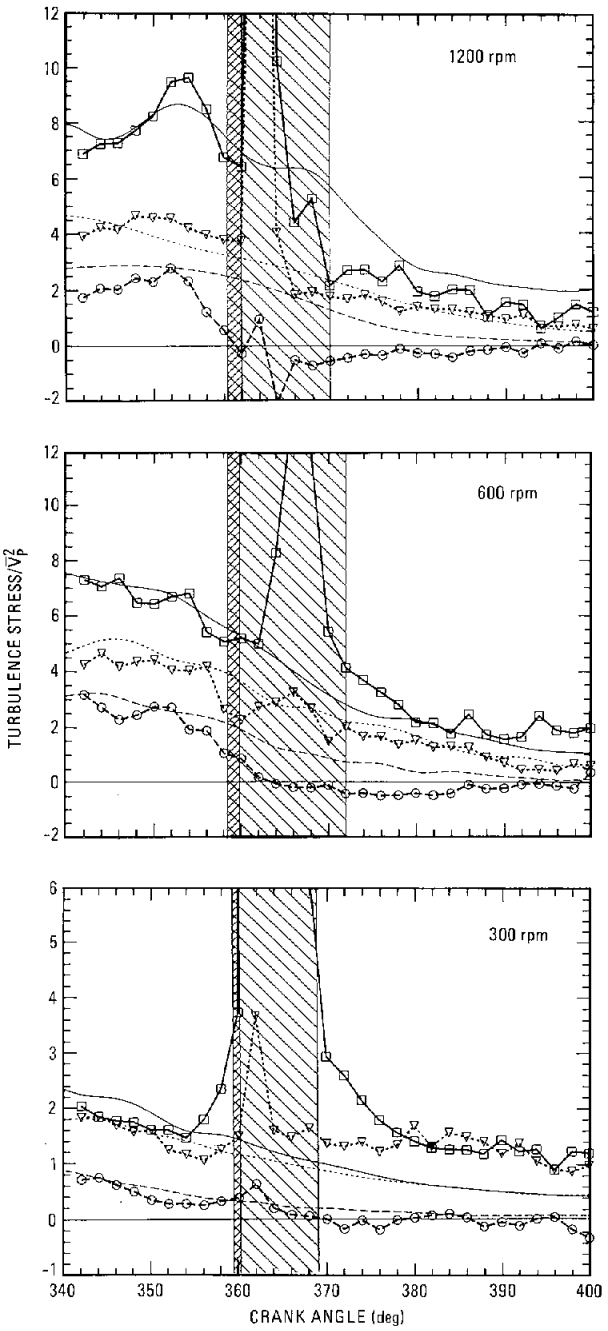

Figure 3. Ensemble-averaged turbulence stress results, normalized by the mean piston speed $\bar{V}_p$: (❑ ❑ ❑) normal stress parallel to flame propagation direction; (▽ ▽ ▽) normal stress perpendicular to flame propagation direction; (○ ○ ○) shear stress. The corresponding lines without symbols are motored results.

Reference:

1. H. J. Schock, C. A. Regan, W. J. Rice, and R. A. Chlebecek, TSI Quarterly **IX-4**, 3 (1983).

Velocity Measurements in the Wall Boundary Layer of a Spark-Ignited Research Engine†

Laser-Doppler velocimetry has been used to measure the velocity boundary layer in a spark-ignition engine. Data obtained to within 0.06 mm of the wall reveal a boundary-layer thickness less than 1.0 mm with low swirl and 0.2 mm with high swirl.

D. E. Foster* and P. O. Witze

An understanding of heat transfer from the combustion gases to the walls of a reciprocating engine is critical to the design and ultimate performance of the engine, yet very little is actually known about the details of the process. Recently, Lucht and Maris[1] used the coherent anti-Stokes Raman scattering (CARS) technique to measure burned gas temperatures to within 25 microns of the wall in a spark-ignited engine. The head of the engine was shaped as a convex dome that allowed skimming the CARS laser beams close to the surface with minimum interference from the wall. We have used the Lucht/Maris idea of tailoring the wall surface to enable us to measure the velocity and turbulence boundary layer profiles in an engine using laser-Doppler velocimetry (LDV).

In order to establish a flow field that would be amenable to analytic and numerical analysis, we used an axisymmetric swirling flow and made measurements away from the centerline of the cylinder. Because it was important for the wall surface to be convex at the measurement location, a head having a toroidal shape with the apex at the half-radius of the cylinder was designed, as illustrated in Figure 1. Two different swirl levels were generated by varying the size and orientation of a shroud on the intake valve. All of the measurements were obtained at 300 rpm for a stoichiometric propane-air mixture, with ignition at the center of the head. Two diametrically-opposed fused-silica windows were used to make forward scatter LDV measurements, as illustrated in Figure 1.

A summary of the character of the high swirl boundary layer profiles is shown in Figure 2, where data are presented to within 70 microns of the wall. The motored mean velocity results suggest a boundary layer thickness of less than 200 microns, but the profile is not resolved. With combustion, the higher postcombustion temperatures increase the thickness of the velocity boundary layer considerably. The motored turbulence intensity data show a large increase near the wall, indicative of a turbulent wall boundary layer. With combustion, the free-stream turbulence is nearly doubled, but it is difficult to draw conclusions about the data near the wall because combustion-induced beam-steering effects influence the measurements.

A summary of the character of the low swirl boundary layer profiles is given in Figure 3. The mean velocity profiles for motored and fired operation of the engine are both clearly resolved and appear to be similar in shape but shifted by about 0.8 m/s. The motored turbulence intensity profile is quite flat, without the large increase near the wall that was seen in the high swirl profile given in Figure 2. With combustion, the turbulence intensity profile is similar in shape to the corresponding mean velocity profile.

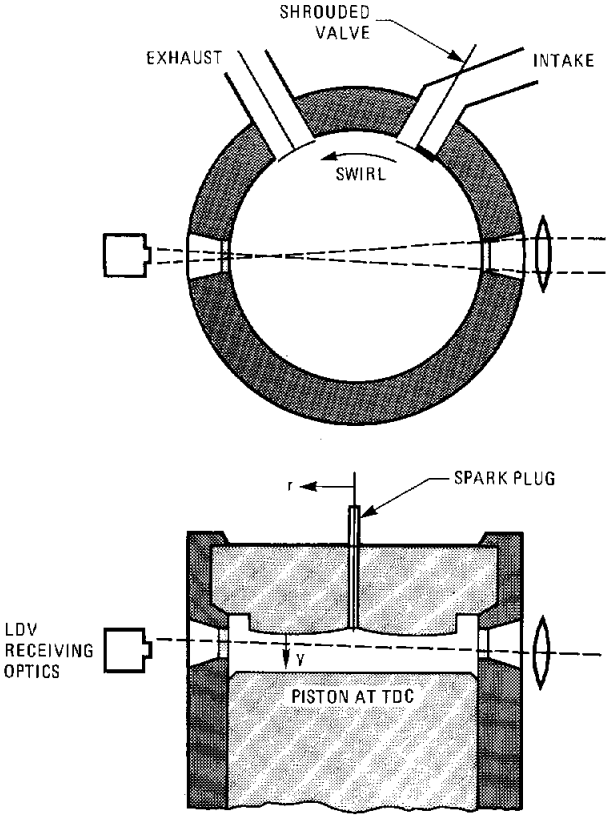

Figure 1. Schematic of the engine combustion chamber, showing the optical configuration for the forward scatter LDV system.

†SAE Paper No. 872105 (1987).
*University of Wisconsin at Madison.

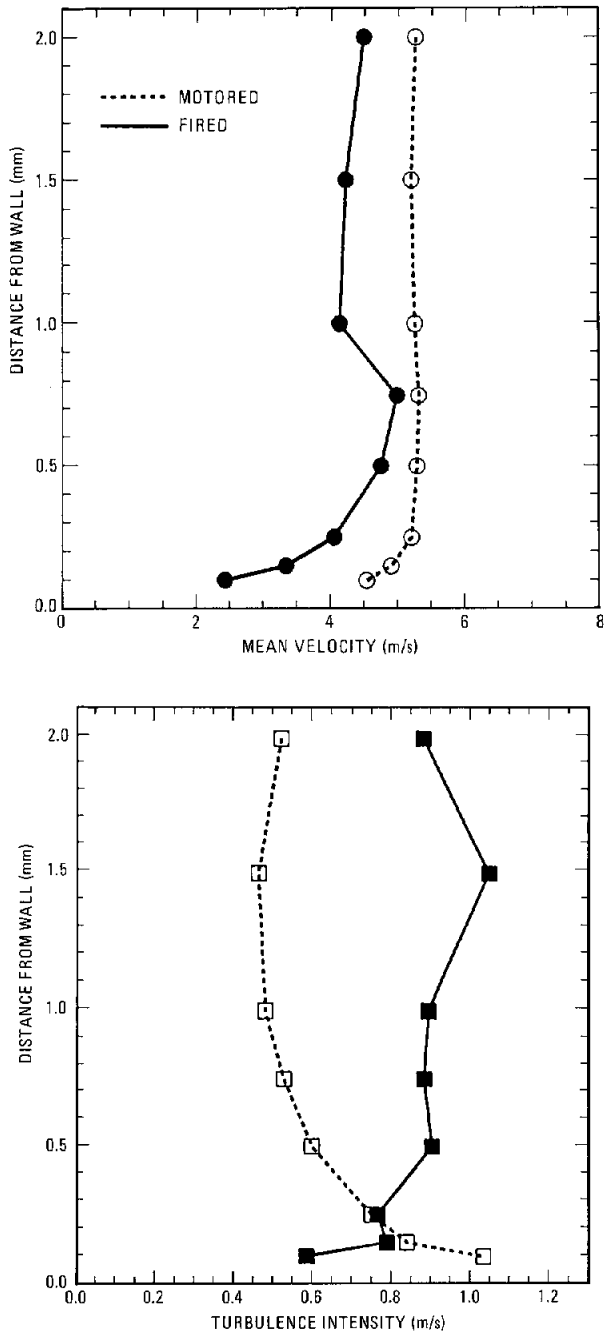

Figure 2. Summary comparison of the measured profiles for the high swirl case.

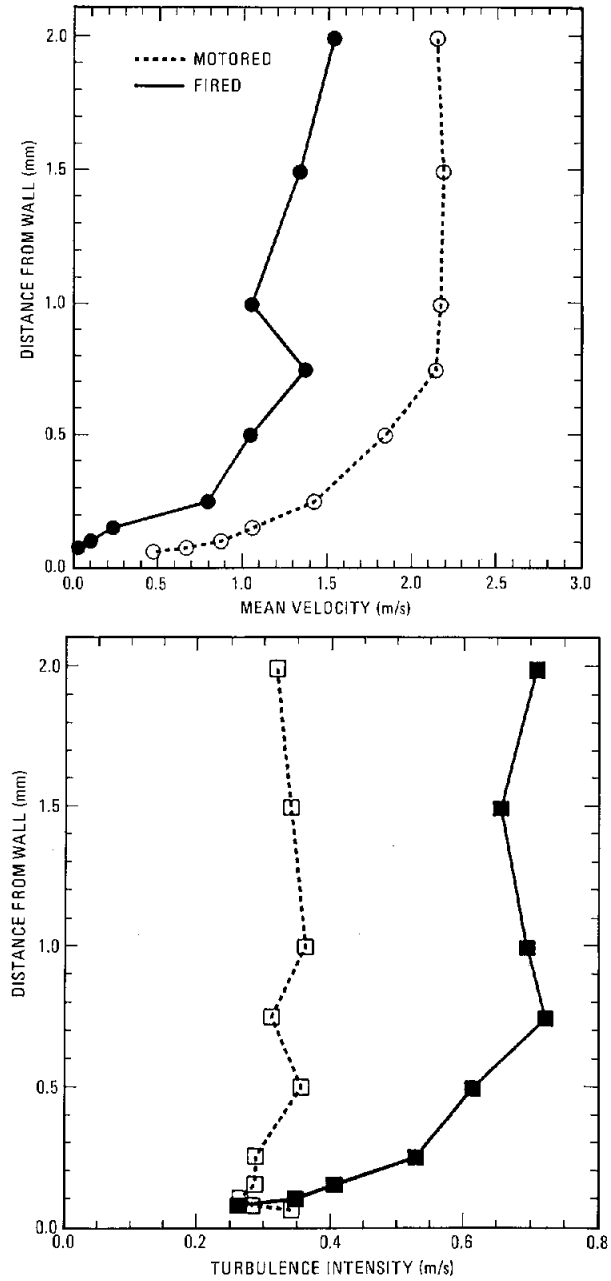

Figure 3. Summary comparison of the measured profiles for the low swirl case.

Figure 4 shows the low-swirl mean velocity profile compared with a laminar Blasius profile and a turbulent 1/7th power law profile. The close similarity of the data with the laminar profile is consistent with the absence of a turbulence intensity increase near the wall, which is characteristic of a turbulent boundary layer. We believe that the large freestream turbulence in this case is responsible for the thickening of the boundary layer at the outer edge.

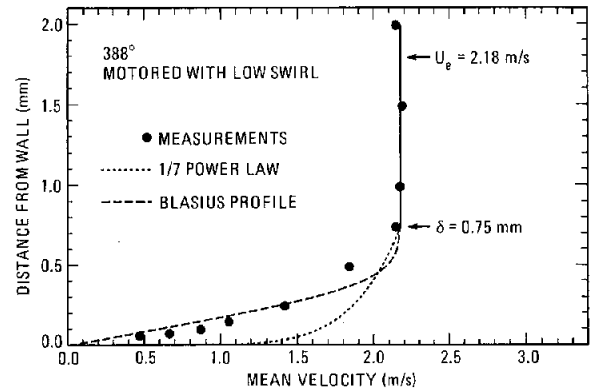

Figure 4. Comparison of boundary layer velocity measurements with a Blasius profile (laminar) and a 1/7th-power law (turbulent).

Reference:

1. R. P. Lucht and M. A. Maris, SAE Paper No. 870459 (1987).

A Comparison of Flame Detection Techniques for Premixed-Charge Combustion in Spark-Ignition Engines†

Ionization probe, laser-beam refraction, and visible luminosity techniques for detecting flame location in a spark-ignition engine are compared.

D. E. Foster* and P. O. Witze

The purpose of this study is to critically evaluate techniques that are currently being used to detect flame arrival at a specified location in space. The standard instrument for detecting the reaction zone is the ionization probe. Its major advantage over the line-of-sight techniques to be discussed is that it responds to the arrival of the flame at a single point. The major disadvantage of the ionization probe is that it can measurably perturb the flowfield in an engine. Evidence of this is shown in Figure 1, where two-component LDV measurements from an engine motored at 1200 rpm are compared for tests made with and without the presence of an ionization probe. The measurements were made in the center of a disc-shaped chamber with the ionization probe protruding a full radius, as indicated in Figure 2. Even though there is no forced swirl in this engine, there is enough inherent fluid motion for significant perturbations to be introduced by the ionization probe.

Laser-beam refraction is a nonintrusive flame-detection technique that relies on the deflection of a laser beam by the refractive index gradients within the flame. Our implementation of the method is shown in Figure 2, where one of the spent LDV beams for the axial velocity component is used. The beam is directed through an iris diaphragm and onto a photodiode. When the flame intersects the beam, refractive index gradients deflect the beam off the aperture. Because this is a line-of-sight measurement, the accuracy of the system is compromised for highly irregular flame shapes. In the past, we have minimized this problem by bringing a laser beam in through a top window, reflecting it off a mirror bonded to the piston surface, and then directing the return beam onto a detector.

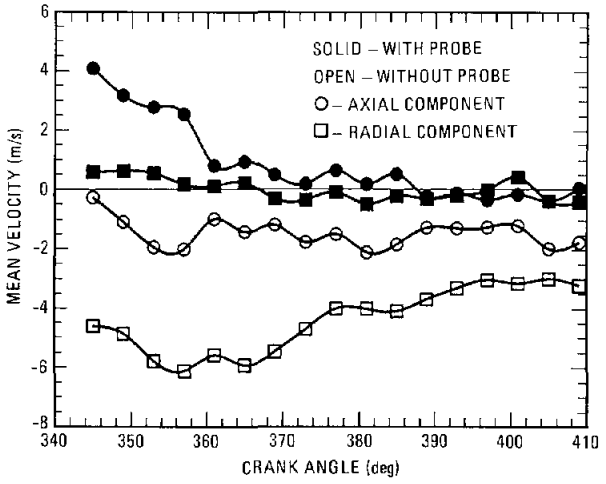

Figure 1. Motored mean velocities at the center of the combustion chamber comparing operation with and without the ionization probe. 360 CAD corresponds to top-dead-center of the compression-expansion strokes.

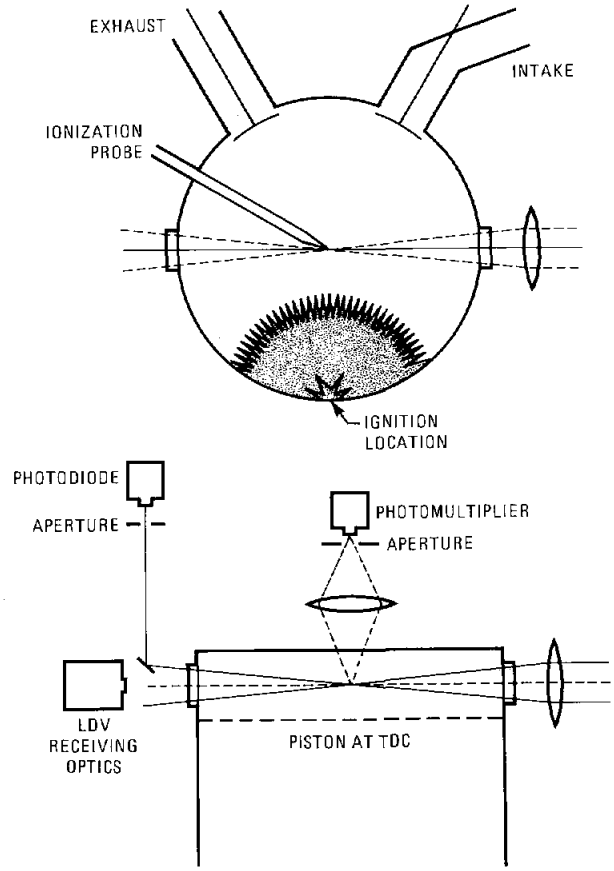

Figure 2. Schematic of the engine combustion chamber, showing the two-component LDV optics and the laser beam refraction, visible luminosity and ionization probe flame arrival detectors.

†Experiments in Fluids 6, 283 (1988).

*University of Wisconsin at Madison.

Because there are problems and limitations associated with attaching a mirror to the piston crown, we recently have been experimenting with a technique that uses the natural emissions of the flame if the viewing position is from above the piston. The visible luminosity detector shown in Figure 2 limits line-of-sight errors to flame irregularities across the clearance height. A large lens collects the emitted light and creates a real image of the flame at the aperture plane. The aperture is positioned to pass to the photodetector only the light radiated from the field of view of a 1-mm-diameter probe volume located between the ionization probe electrodes.

Each of the techniques described generates a sudden change in an analog signal when the flame is detected. For the ionization probe, this change is well defined by the ionized gases in the reaction zone, and we believe that this signal can be monitored with better than 10-microsecond accuracy. This is not the case for the other two techniques, where the change in the signal can be less distinct.

The experimental procedure used was to make simultaneous measurements with the ionization probe and either laser-beam refraction or visible luminosity. The two optical techniques are shown compared with the ionization probe in Figure 3, where the abscissa is the crank-angle difference between the optical measurements and the ionization probe. Thus, positive values indicate that the ionization probe detected the flame first. Normalized (unit area) histograms of the flame arrival differences were calculated using 0.2 crank-angle-degree (CAD) intervals, which correspond to 28 microseconds at 1200 rpm.

At 300 rpm, the two line-of-sight measurements show comparable results, but as the engine speed, and thus turbulence, is increased, the spread in the laser beam refraction measurements becomes increasingly larger than the results by visible luminosity. Somewhat unexpected is the increased probability with increased turbulence that laser-beam refraction detects the flame later than the ionization probe. Earlier detections will occur when the flame is distorted in the plane of the piston, since any intersection of the beam with the flame across the entire diameter of the cylinder will trigger detection. However, late detections by the beam method can only be explained by decreased sensitivity of the technique with increased turbulence.

We do not believe that ionization probe errors are responsible for this late detection problem, because similar behavior is not seen with the visible luminosity data. For the two higher engine speeds, there is an increased probability at 0.2 CAD that ionization probe detection will occur before the luminosity technique, but this also represents the resolution of the measurement. The broadened probability (that with increased speed the visible light will be detected first) can be explained by either a tilted flame with the leading surface above or below the ionization probe or increased radiation ahead of the flame due to the thicker turbulent flame.

In conclusion, these results indicate that the line-of-sight measurement made from above the piston is far preferable to the longer path-length measurement made across the combustion chamber. Under conditions where pertubations of the flow-field by an ionization probe can be tolerated, this would seem to be the preferred technique.

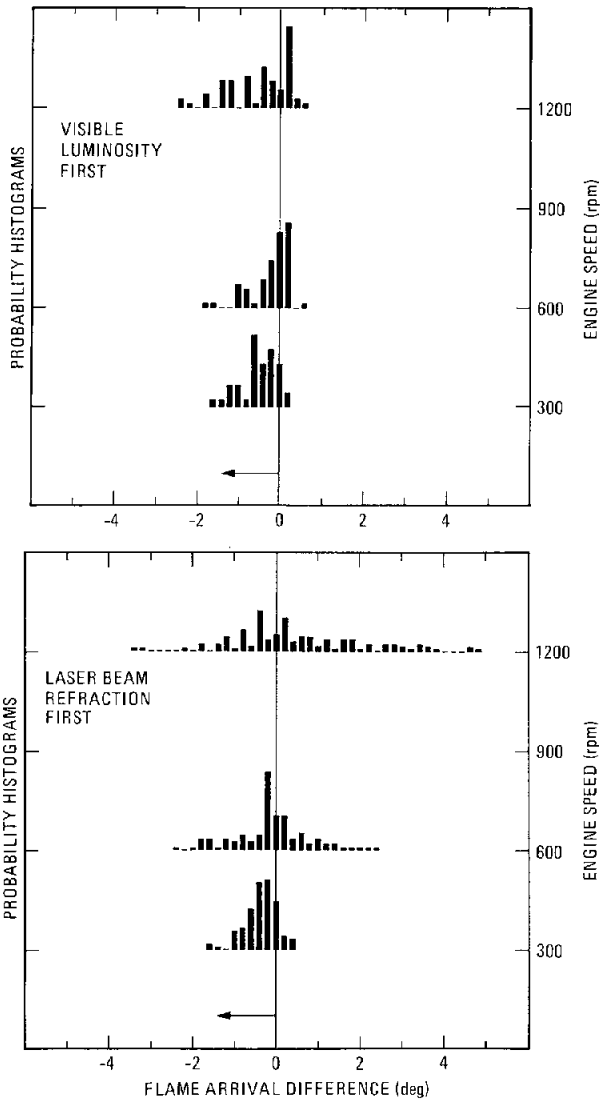

Figure 3. Comparison of flame-arrival-time measurement techniques, presented as normalized histograms of the crank-angle difference from simultaneous ionization probe measurements. Positive values mean that the ionization probe detected the flame earlier than the line-of-sight measurement.

Particulate Formation/Oxidation in a Diesel Engine

A study of particulate formation/oxidation in a realistic diesel engine has been initiated. The work is being conducted in collaboration with Cummins Engine Company under the DOE Industrial Fellow Program. Both single-point time histories of soot and two-dimensional images of the spatial distribution of soot in a diesel engine are planned.

D. L. Siebers, A. zur Loye,* and H. K. Ng*

A new research program to study particulate formation/oxidation in diesel engines with optical diagnostics has been initiated at the Combustion Research Facility (CRF) in collaboration with Cummins Engine Company. This program is motivated, in part, by the need to meet new engine emissions regulations mandated for diesels. A better understanding of particulate formation/oxidation processes would significantly aid the effort to meet these regulations. In addition, the program, sponsored by the Department of Energy's Industrial Fellow Program, DOE Conservation, and Cummins, was specifically set up to encourage efficient and timely transfer of technology from government-sponsored research programs to industry. The close collaboration between national laboratories and industry researchers established on this program will help assure this latter goal. Achieving more efficient technology transfer can have a significant impact on the international competitiveness of U. S. industry.

The contributions of Cummins to this program include two staff members based at the CRF who will participate in the research (one part-time and one full-time), an optically-accessible diesel engine and auxiliary equipment, expertise on diesel engine emissions, and expertise on diesel engine operation. Sandia's contributions to the program include staff and technical support, expertise in advanced laser-based diagnostics for engines, laboratory facilities, lasers and instrumentation, expertise on soot formation/oxidation and DOE/ECUT (Department of Energy/Energy Conversion Utilization Technology) support.

The problem of particulate emissions is a critical one for the diesel engine industry because of the new emissions regulations that are being phased in between now and 1994. The new regulations call for significantly-reduced emission of several exhaust-gas species, one of them being particulates. (See Table I for new particulates and NOx standards.) The new particulates standards are proving difficult to meet because of the trade-off that exists between nitrogen oxides (NOx) and particulates formed during combustion. Efforts to reduce the emission of particulates from diesels typically lead to increased emission of NOx or vice versa. To meet the new 1994 standards for particulates, and at the same time meet the NOx standard and maintain engine efficiency, a more detailed understanding of the particulate formation and oxidation processes in diesel engines is needed.

Since the combustion processes, and therefore the particulate formation/oxidation processes, are strongly affected by interactions between the complex turbulent flow field in an engine, the spray, and the fuel chemistry, the research will be conducted in a diesel engine which resembles as closely as possible a production engine. Modifications for optical access have been kept to a minimum. The engine used is a single-cylinder version of a Cummins NH series diesel engine. This engine mirrors the multicylinder, turbocharged, direct-injection, four-valve, four-stroke NH series engine. The compression ratio of the engine is 14.5:1. The bore and stroke are 14.0 cm and 15.2 cm, respectively, giving a 2.33-liter displacement. The speed and power rating of the single-cylinder engine are 1800 rpm and 56 kW, respectively.

The main features of the experimental facility located at the CRF are the diesel engine, a dynamometer to control engine speed, laser diagnostics which include an LDV system for flow field measurements, and an Nd:YAG-pumped, dye-laser system for planned imaging work, an IBM/AT-based computer-data acquisition and engine-control system, an intake air system that provides compressed, dried and temperature-controlled air, and temperature-controlled water and oil-recirculation systems. The intake air can be compressed to pressures as high as 375 kPa and heated to temperatures as high as 150°C to simulate turbocharging.

*Cummins Engine Company, Columbus, IN.

To gain optical access to the engine, a spacer plate containing two pairs of opposing windows has been added between the head and the block. The spacer plate is shown schematically in Figure 1. These windows give optical access in two directions across the cylinder. A special head used in combination with the spacer plate, which has one of the two exhaust valves removed and a window inserted in its place, provides optical access from above. This exhaust port window is located directly over one of the optical paths across the cylinder, as shown in Figure 1. The compression ratio of the engine with the spacer plate is maintained by extending the piston. Window fouling by oil is minimized by using bronze-impregnated Teflon piston rings and by operating the cylinder without oil. This optical access, although not ideal, allows the engine combustion processes in a near-production engine configuration with regard to cylinder shape, cylinder flow field, and cylinder thermodynamic conditions to be probed by optical methods.

The planned measurements include two-dimensional imaging and line-of-sight time-histories of soot, as well as flow field velocity measurements. The first goal is to acquire velocity measurements in the engine to better define the flow field in the NH series engine, in particular at the time of injection. These velocity measurements will also be compared with multidimensional flow field calculations that are being performed at Cummins using the DOE-developed KIVA computer model from Los Alamos.

This industry-national laboratory exchange has generated considerable interest and serves as an excellent example of the strong collaboration between industry and national laboratories that is being sought in the DOE Industrial Fellow Program. The program couples the experience of Cummins with diesel engines and the experience of Sandia with optical diagnostics on a critical problem of national interest.

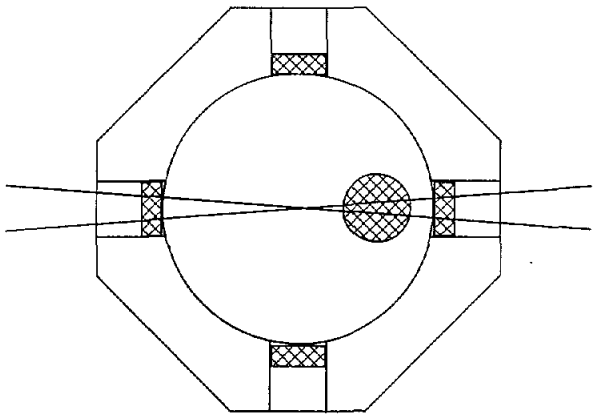

Figure 1. A schematic of the spacer place and optical access into the diesel engine. Depicted is the LDV setup.

Table I
The new on-highway particulate and NOx emissions standards for 1988, 1991, and 1994.

Year	1988	1991	1994
Particulates (g/Bhp•hr)	0.60	0.25	0.10
NOx (g/Bhp•hr)	6.0	5.0	5.0

Some Limitations to the Spherical Flame Assumption Used in Phenomenological Engine Models†

A two-dimensional axisymmetric numerical model is used to illustrate how the presence of walls can significantly influence the shape of a spark-ignited premixed gas flame, even when wall boundary layers are neglected. Comparisons made with a quasi-dimensional phenomenological model show that the assumption of a spherical flame surface held centered at the ignition location can lead to a large underprediction of the flame area.

P. K. Barr and P. O. Witze

Phenomenological models play a vital role in the analysis and design of reciprocating internal combustion engines. These models attempt to describe complex engine behavior in terms of separate, physically-based submodels of important identifiable phenomena. Typically, it is assumed that a thin spherical flame surface distinguishes two discrete zones of uniform composition, these being the unburned and burned gas regions. It is important to realize, however, that these models pay no explicit attention to the fluid mechanics of the combustion process, although it has been known for many years that premixed gas combustion is accompanied by strong gas motions.

In 1928, Ellis reported the results of several experiments on flame movement in gaseous explosive mixtures. Shown in Figure 1a is one of his multiple-exposure photographs of flame propagation from two ignition points within a closed tube.[1] The mixture was ignited simultaneously at one-quarter and one-half the tube length. Two very important features of confined combustion are illustrated in this figure. First, regarding the expanding flame on the left, it is evident that as the flame approaches the wall, the shape becomes nonspherical. This is because the flame propagation speed is greater along the axis of the tube; normal to the tube wall, the expansion velocity must go to zero at the wall. This results in an elongated flame with a surface-to-volume ratio far greater than that of a sphere. Second, regarding the flame on the right, it is seen that the fluid mechanics interaction between the two flames has a significant effect on the location of the flame centroid. In this case, the tendency is for the right-side flame to move towards a centered position in the right half of the tube.

Shown in Figure 1b are the results from our two-dimensional (2-D) numerical simulation of the Ellis experiment. This inviscid model is based on tracking the flame interface as it interacts with the combustion-generated flow field. Although it was necessary to empirically determine the flame propagation speed used in the model, it is clear that the numerical results reproduce the major features of the experiment. This is not the case for our phenomenological quasi-dimensional (Q-D) model[2] results shown in Figure 1c; here, the flames are assumed to burn as spheres centered at the ignition locations. Neither the elongated flame shapes nor the convection of the burned gas volumes on the right are simulated by the phenomenological model, because the fluid mechanics of the combustion process are neglected.

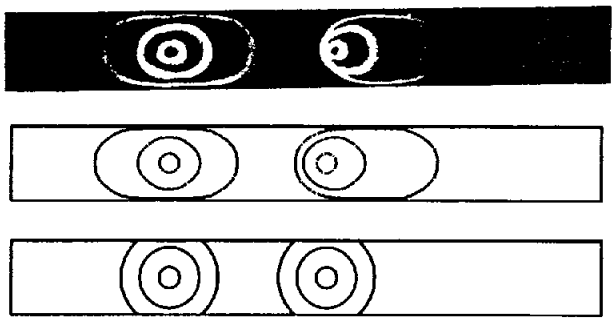

Figure 1. Laminar flame propagation in a closed tube for simultaneous point ignition at one-quarter and one-half the tube length. (a) Multiple exposure photograph; (b) Two-dimensional simulation; (c) Quasi-dimensional simulation.

This illustration of the limitations of assuming that the flame grows as a spherical surface held centered at the ignition location led us to investigate the errors incurred in the calculated flame surface area when phenomenological engine models are used.

The role of wall interactions with the velocity field created by combustion-generated volume expansion is illustrated in Figure 2, where we show the limiting cases for one-dimensional (flat flame) premixed gas combustion in a long tube open at one end. The shaded regions represent the burned gas. In the upper figure, the mixture was ignited along

†SAE Paper No. 880129 (1988).

a plane at the closed end of the tube, and from mass conservation the flame propagation speed is $U_f = S_L \rho_u/\rho_b$, where S_L is the laminar burning velocity and ρ_u/ρ_b is the unburned-to-burned gas density ratio. Just in front of the thin flame surface, the velocity of the unburned gas is $U_u = S_L (\rho_u/\rho_b - 1)$ and behind the flame in the burned gas region the velocity is $U_b = 0$.

Shown in the lower part of Figure 2 is the limiting case for ignition at the open end of the tube, for which it can be shown that $U_f = S_L$, $U_u = 0$, and $U_b = S_L(\rho_u/\rho_b - 1)$.

It is because the tube is open at one end and no compression of the burned or unburned gases occurs that these equations are exact for any axial location of the flame. Since the density change across a flame is considerably greater than unity, the difference between the propagation speeds of flames approaching and moving away from walls can be considerable. For one-dimensional geometries, this effect can be treated analytically because the combustion-generated flow field is also one-dimensional. However, for two- and three-dimensional geometries the flow field is complex and requires numerical solution of a multidimensional elliptic equation.

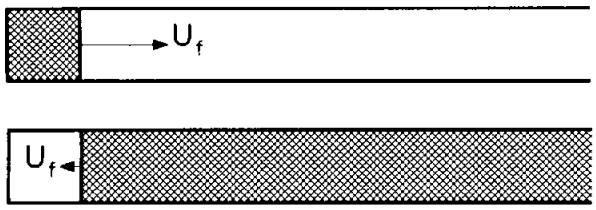

Figure 2. Limiting cases for one-dimensional flame propagation in a tube open at one end.

Figure 3 summarizes the calculations made for a disk-shaped combustion chamber with ignition on the axis of symmetry, flush with the top surface. A geometric comparison between the flame shapes for the Q-D and 2-D models is given in the upper portion of the figure, above quantitative comparisons of the (Q-D)/(2-D) ratios of the mass fraction burned X and the flame area A. It is seen that the Q-D and 2-D results are virtually identical until the Q-D flame contacts the opposite wall at 2.2 ms. From this, time on the spherical surface area of the Q-D flame is truncated by contact with the wall. In contrast, as the 2-D flame approaches the opposite wall, it flattens in a manner very similar to the photographs presented in Figure 1. This happens because the volume expansion contribution to the flame speed is being negated by the presence of the wall, as described earlier with Figure 2. This slowing of the propagation speed delays contact of the 2-D flame surface with the wall until 3.2 ms.

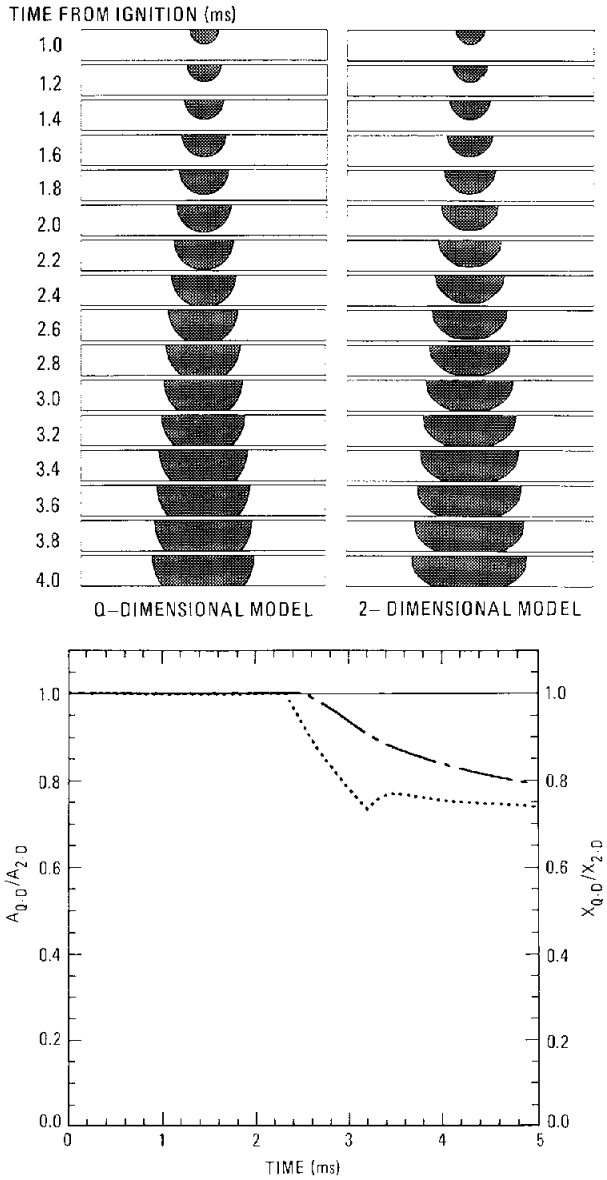

Figure 3. Comparison between Q-D and 2-D flame shapes for point ignition at the top center of a disk chamber.

Once both computed flames have contacted the opposite wall, their area ratio asymptotes to a value of 0.73 instead of 1.0. Although some of this difference is due to differences in the burn fraction, the continual decrease in the burn fraction ratio with time indicates that the 2-D flame is propagating faster than the Q-D flame. In the limit of large radius, the spherical Q-D flame approaches a nearly flat shape, while the 2-D flame remains highly curved, because the expansion velocity is preferentially retarded normal to the wall.

References:

1. O. C. de C. Ellis, Fuel in Science and Practice **7**, 526 (1928).

2. C. Borgnakke, G. C. Davis, and R. J. Tabaczynski, Trans. SAE **90**, 964 (1981).

Reduction of Nitric Oxide by the RAPRENOx Process†

The effects of temperature, cyanuric acid concentration, and carbon monoxide concentration on exhaust gas nitric oxide reduction with the RAPRENOx process have been investigated in a quartz flow reactor. All three are shown to have important effects on the process.

D. L. Siebers and J. A. Caton*

A new process for the **Rap**id **Re**moval of **N**itrogen **Ox**ides (RAPRENOx) from exhaust gas was discovered at the CRF.[1] Earlier work on RAPRENOx showed that this process was capable of significantly reducing nitric oxide (NO) levels in exhaust gas.[1] The RAPRENOx process works by adding gaseous isocyanic acid (HNCO) to an exhaust gas stream. HNCO drives a series of reactions which lead to the reduction of NO. HNCO is formed by heating cyanuric acid ($(HOCN)_3$) to 600 K or greater. At these elevated temperatures $(HOCN)_3$ sublimes and decomposes forming HNCO. A detailed reaction mechanism for NO reduction by HNCO has been proposed by Perry and Siebers.[1]

A number of questions still must be answered before the process is proven practical, however. Experiments are being conducted with the goal of determining (1) the residence time requirements, (2) the temperature requirements, (3) the efficiency of the process in terms of $(HOCN)_3$ use, (4) the effects of surfaces, as well as gas-phase species on the chemistry, and (5) the by-products of the process.

These experiments are being conducted in a quartz flow reactor to minimize surface effects. The quartz reactor and $(HOCN)_3$ feed system are shown schematically in Figure 1. There are three sections to the flow reactor: the exhaust preheater, the $(HNCO)_3$ vaporizer, and the reactor. Each section is electrically heated and has independent temperature control. All three sections are made from quartz tube with a 1.65-cm I.D. The exhaust preheat section is 30 cm long. In this section, a portion of the exhaust from a diesel engine is heated to a nominal temperature of 720 K.

The $(HNCO)_3$ vaporizer consists of a 24-cm-high vertical section and a 3.8-cm-long horizontal section. At the top of the vertical section, solid cyanuric acid particles (~100 μm in diameter) are fed into the $(HNCO)_3$ vaporizer with a gas-tight syringe-feed system along with a 0.20-slpm co-flow of dry air. The syringe is loaded with the $(HOCN)_3$ particles and the syringe plunger is advanced at a controlled rate with a variable speed DC motor. As the plunger advances, $(HOCN)_3$ particles fall into the heated vertical section and sublime. The vaporized $(HOCN)_3$ decomposes, forming HNCO. The co-flow of dry air is used as a carrier gas for flushing the vaporized $(HOCN)_3$ and its decomposition products into the reactor section. The temperature of the HNCO-carrier gas entering the reactor section is nominally 740 K.

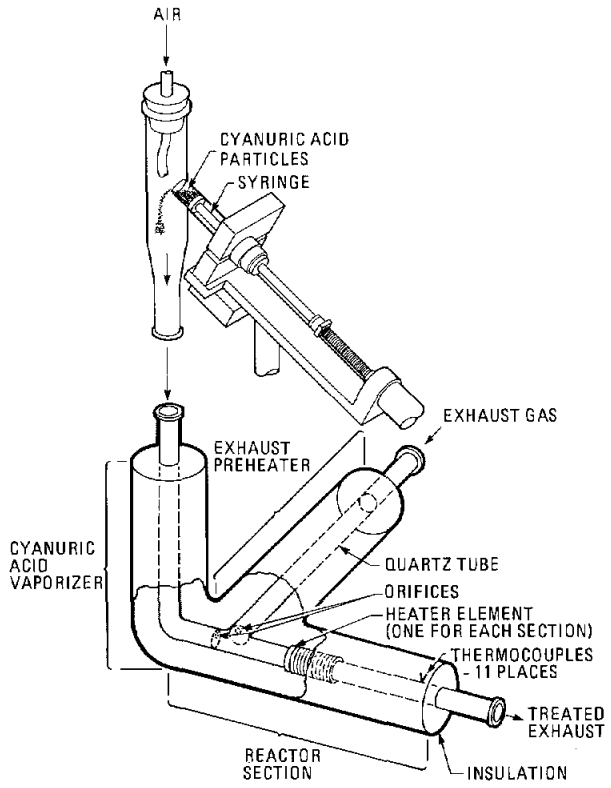

Figure 1. Flow reactor and cyanuric acid feed system.

The reactor section is 36.8 cm long. The temperature of the reactor section is uniform to ±4% over the last 80% of its length. This uniform temperature is the reported reactor temperature. The initial 20% of the reactor is considered a preheat section, since its temperature is low enough that little NO reduction occurs.

Figure 2 shows the NO reduction obtained in the flow reactor as a function $(HOCN)_3$ feed rate for three reactor temperatures. The figure is a plot

†SAND 88-8731 B

*Texas A&M University at College Station.

of the ratio of the reactor outlet-to-inlet NO concentration, in percent, versus the $(HOCN)_3$ concentration assuming no decomposition to HNCO. The data set for each temperature is connected by a dashed line. The engine exhaust flow and the HNCO source flow were 1.0 and 0.2 slpm, respectively, which resulted in a total reactor flow of 1.2 slpm. The diesel engine was operated with an overall equivalence ratio of 0.5. The molar concentrations of several species at the inlet of the reactor section after dilution of the engine exhaust gas by the HNCO carrier gas were: 12.3% O_2, 5.8% CO_2, 5.2% H_2O, 330 ppm NO, and 260 ppm CO.

Figure 2 shows that the maximum NO reduction is achieved for a $(HOCN)_3$ concentration of approximately 330 ppm or a $(HOCN)_3$/NO molar ratio of one. This concentration corresponds to a $(HOCN)_3$ feed rate of 2.3 mg/sec. Increasing the $(HOCN)_3$ feed rate above this level results in no additional reduction. The $(HOCN)_3$/NO molar ratio of one gives an HNCO/NO molar ratio of three, assuming a 100% conversion of $(HOCN)_3$ to HNCO. However, at this time the conversion efficiency of $(HOCN)_3$ to HNCO is not known and is the subject of current research.

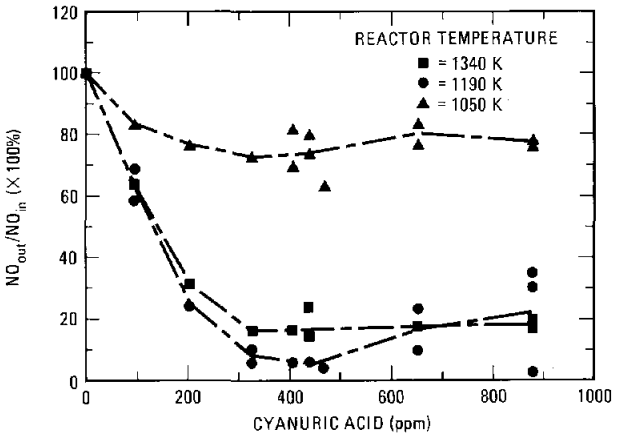

Figure 2. The effect of cyanuric acid ($(HOCN)_3$) concentration on NO reduction efficiency for three flow reactor temperatures.

Figure 3 demonstrates the temperature sensitivity of the process. It is a plot of the outlet-to-inlet NO ratio versus reactor temperature. All conditions are the same as for Figure 2 except that the $(HOCN)_3$ feed rate was fixed at 3.2 mg/sec. The cross-hatched region around the data set represents the spread in the data due to fluctuations of the diesel-exhaust NO concentration with time and the repeatability of the experiment. Figure 3 shows that NO reduction starts at a reactor temperature of 700 K. As the reactor temperature is increased, the reactor-outlet NO slowly decreases until a temperature of 1050 K. Above 1050 K, the reactor outlet NO decreases rapidly with increasing temperature,

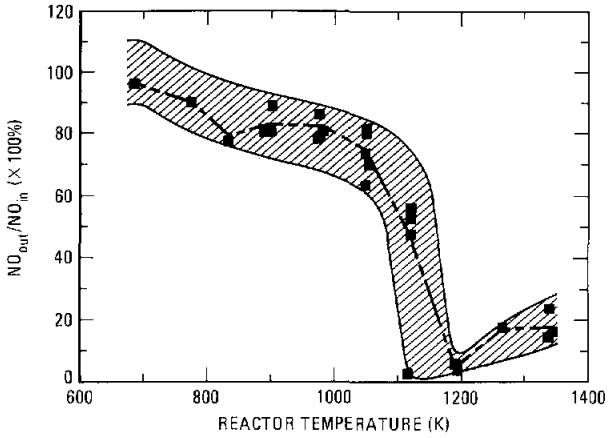

Figure 3. The effect of the flow reactor temperature on the NO reduction efficiency.

reaching a minimum at 1150 K. Beyond 1200 K, the outlet NO level slowly increases. The results illustrated in Figures 2 and 3 are corroborated by recent independent results of Perry,[2] even though the two experiments are different.

Figure 4 shows that CO has a dramatic effect on the NO reduction chemistry. The temperature for maximum NO reduction decreased from 1200 K to 970 K when an additional 7615 ppm of CO was mixed with the engine exhaust, which had a CO concentration of 260 ppm. A possible explanation of the effect of CO on the NO reduction chemistry is given in the reaction mechanism proposed by Perry and Siebers.[1] Carbon monoxide may be acting as an indirect source of hydrogen (H) atoms through the reaction, $OH + CO = H + CO_2$. Enhancing the concentration of H-atoms would enhance the reduction of NO, based on the proposed mechanism.[1]

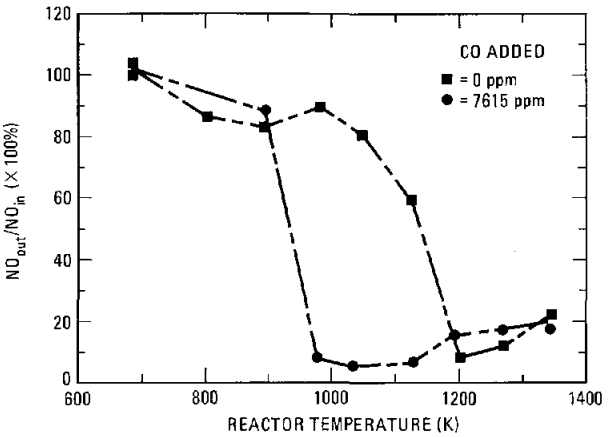

Figure 4. The effect of CO on the NO reduction efficiency as a function of flow reactor temperature.

References:

1. R. A. Perry and D. L. Siebers, Nature **324**, 657 (1986).
2. R. A. Perry, Personal Communication.

Pulse Combustion: The Quantification of Characteristic Times†

Individual characteristic delay times were calculated from a fluid dynamic mixing model and a chemical-kinetics model. These predicted times were then compared with experimentally measured mixing and delay variations.

J. O. Keller, T. T. Bramlette, C. K. Westbrook,* and J. E. Dec**

In an earlier work, Keller, *et al.*[1] established the concept of individual characteristic delay times, and that these times contribute nearly independently to a total ignition delay time. In this study, individual characteristic delay times were calculated from a fluid dynamic mixing model and a chemical kinetics model. These predicted times were then compared with experimentally measured variations in the total ignition delay time of a gas-fired pulse combustor for a wide range of fluid dynamic mixing times and homogeneous chemical ignition delay times.

The mixing model of Rife and Heywood[2] was extended and applied recently to the injection process that occurs in a pulse combustor.[3] Using this model, the rate at which the premixed reactants mix with hot combustion products from the previous pulse combustor cycle can be calculated. This model was used to estimate the fluid dynamic mixing times (τ_{mixing}) found in the pulse combustor.

Calculations were carried out to estimate the characteristic chemical-kinetic time scales in the pulse combustor. The computations use the HCT code[4] with a detailed reaction mechanism[5-7] which has been thoroughly tested for the fuel and conditions of this study. In the present work, this chemical kinetics model has been used to investigate the effect of homogeneous chemical ignition delay time ($\tau_{kinetic}$) on the magnitude of the total ignition delay time.

An externally valved, gas-fired, Helmholtz-type pulse combustor was used for this study. In this work, the combustor was operated in a premixed mode where the fuel and air were mixed upstream of the flapper valve. The total ignition delay time was inferred from ensemble-averaged measurements of OH* chemiluminescence (denoted by <OH*>). Measurements of OH* have been shown to be a good temporally-resolved indicator of the energy release rate.[8] The total ignition delay time was defined as the first point of inflection in the <OH*> chemiluminescence data ($\partial^2<OH^*>/\partial t^2 = 0$). Measurements of characteristic cycle time and combustion chamber pressure were also obtained.

The mixing and chemical kinetics models were calibrated against measured total ignition delay times for two independent studies; one in which the characteristic mixing time (τ_{mixing}) was varied, and one in which the homogeneous chemical kinetic ignition delay time ($\tau_{kinetic}$) was varied. The fluid dynamic and chemical processes leading to ignition are highly coupled and complex, and the functional form for combining these processes into a total ignition delay is not known. The simplest function, a linear sum of the two delay times, was used, although it will overestimate the influence of both delay times, since the two processes are actually occurring simultaneously. To minimize this potential error source, the mixing model calibration parameter was determined at a condition where $\tau_{kinetic} << \tau_{mixing}$. The chemical-kinetic model was calibrated by varying the diluent fraction while the mixing time was held constant. This reference value was then adjusted for other conditions in this study, accounting for variations in mass flux and combustor frequency.

Measured and calculated energy release curves for three values of the mean reactant mass flux are shown in Figure 1. These conditions were selected so that the homogeneous chemical ignition delay time could be assumed constant and small, making the measured <OH*> chemiluminescence a good approximation to the mixing rates in the combustor. In general, the predicted values agree well with those experimentally measured.

The ability of these models to accurately predict the total ignition delay time was also examined. Figure 2 shows a comparison between the calculated delay times from the two models (τ_{mixing} and $\tau_{kinetic}$) and the measured total ignition delay time. The relative contribution of the fluid dynamic mixing time and the chemical-kinetic time to the to-

---

†Combustion and Flame, submitted (1988).

*Lawrence Livermore National Laboratory, Livermore, CA.
**University of Michigan, Ann Arbor, MI.

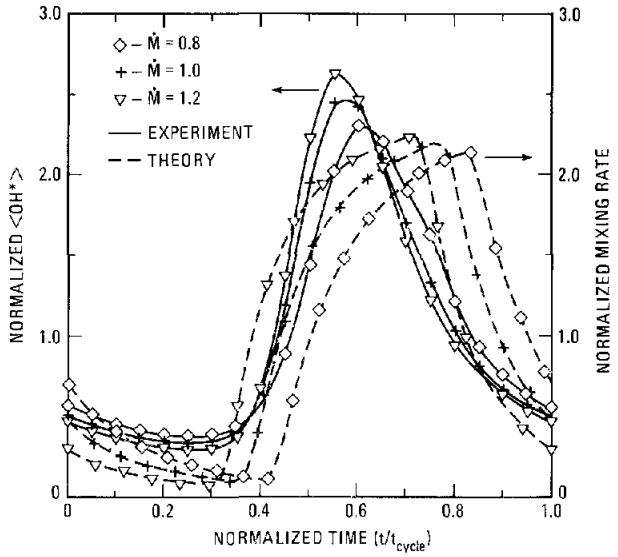

Figure 1. Comparison between the measured normalized <OH*> and the calculated fluid dynamic mixing rate for three different mass flux cases and constant N_2 diluent ($\psi = 0.10$) with different characteristic mixing times (τ_{mixing}).

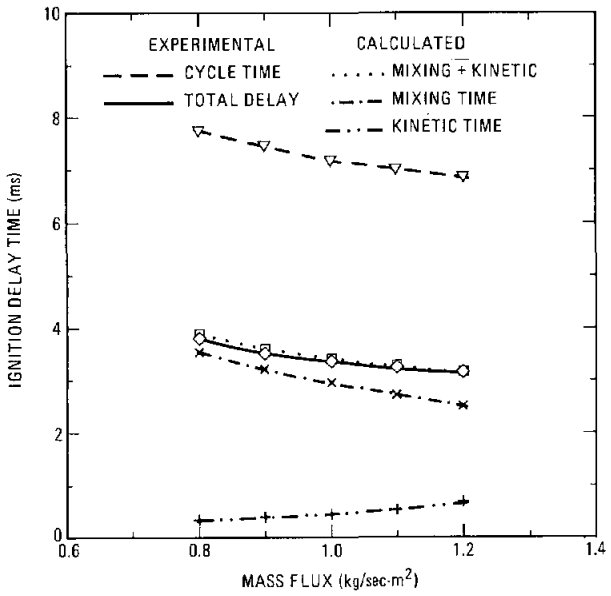

Figure 2. Shown are characteristic combustor times (normalized by the cycle time) as a function of mass flux and constant N_2 diluent mass fraction of $\psi = 0.10$. Presented are the calculated homogeneous chemical-kinetic ignition delay time, the calculated characteristic mixing time, the measured total ignition delay time, and the calculated total ignition delay time utilizing the linear assumption.

tal ignition delay time is shown in the figure. The calculated homogeneous chemical-kinetic delay time ranges from 5 percent to approximately 20 percent of the total cycle time, whereas the calculated mixing times range from 45 to 35 percent of the total cycle time. Since the measured total delay time is almost constant at approximately 50 percent of the cycle time, these results show that the fluid dynamic mixing is responsible for about 90 percent of the total ignition delay time, and the homogeneous chemical-kinetic processes only about 10 percent.

A systematic study has been performed in which magnitude of the total ignition delay time of a pulse combustor was measured and calculated for a wide range of operating conditions. A fluid dynamic mixing model and a homogeneous chemical-kinetic model, each with a single adjustable parameter, were utilized to calculate predicted characteristic mixing and chemical-kinetic times. The results of the models were compared with ensemble-averaged OH* chemiluminescence measurements from the laboratory combustor, which provide a measure of the total ignition delay time. The trends predicted by both the models closely resembled the trends found in the experiment.

Previous work had established that the characteristic times of interest contribute nearly independently to the total ignition delay time. Based on this, it was hypothesized that these times are not only independent, but they can be added together linearly to obtain the total ignition delay time. This concept was successfully tested by direct experimental verification at conditions of varying homogeneous chemical-kinetic ignition delay time and of varying fluid dynamic mixing time. Thus the models, while being simplifications of a very complex problem, have potential utility in the design and understanding of pulse combustion systems.

References:

1. J. O. Keller, J. E. Dec, C. K. Westbrook, and T. T. Bramlette, Sandia Report *SAND87-8783* (Sandia National Laboratories, Livermore, CA, 1987).

2. J. M. Rife and J. B. Heywood, SAE Transactions **83**, 2942 (1974).

3. T. T. Bramlette, Sandia Report *SAND87-8622* (Sandia National Laboratories, Livermore, CA, 1987). Also, Comb. Sci. Tech., submitted (1987).

4. C. M. Lund, Report *UCRL-52504* (University of California Lawrence Livermore Laboratory, Livermore, CA, 1978).

5. C. K. Westbrook, Comb. Sci. Tech. **20**, 5 (1979).

6. C. K. Westbrook and W. J. Pitz, Comb. Sci. Tech. **37**, 117 (1984).

7. W. J. Pitz, C. K. Westbrook, W. M. Proscia, and F. L. Dryer, *Twentieth Symposium (International) on Combustion* (The Combustion Institute, Pittsburgh, PA, 1985), p. 831.

8. J. O. Keller and C. K. Westbrook, Sandia Report *SAND86-8631* (Sandia National Laboratories, Livermore, CA, 1986).

Theoretical and Experimental Investigation of a New Pulse Combustor†

A new pulse combustor for drying applications has been invented. Experimental measurements in a bench-scale system agree well with theoretical predictions.

T. T. Bramlette and J. O. Keller

A new pulse combustor[1] for drying applications is shown conceptually in Figure 1. The main source of hot gases for drying is located in Decoupling Chamber 1. The decoupling chambers are large volumes that provide constant pressure boundary conditions at the ends of tubes 1_0,1_1, and 1_2. A secondary combustion source, located at 1_1, is used to set up an acoustic wave system in the vertical tube that induces oscillations in velocity and pressure that are responsible for significantly enhanced heat transfer to and mass transfer from the material to be dried (introduced at 1_3). These oscillations result from the acoustic coupling of the horizontal tube, 1_0, and the vertical tube, 1_1+1_2. A bench-scale version of this system has been investigated both theoretically and experimentally. The configuration considered differed from Figure 1 in that there was not a main combustion source and there were no decouplers.

The analysis was based upon the following assumptions: (1) the amplitudes of the acoustic waves are small, so that a linear analysis is valid, (2) the density and speed of sound in the jth section are constant, but may differ in each of the three sections, (3) the effects of buoyancy and damping are neglected, and (4) the transition at the junction of the three sections may be treated as "compact," i.e., the region in which the sound waves are not one-dimensional is small compared to the wave length of the acoustic waves. With these assumptions, one may show that the natural acoustic frequencies, ω, of the system may be determined from the roots of a complex transcendental equation, and that the pressure, as a function of space and time, is given by

$$P_j(x_j,t) = \frac{2A_0}{1+\psi^2(\omega)} [(\cos k_j x_j - \cot k_j l_j \sin k_j x_j) \cos \omega t + (\psi(\omega) \cot k_j l_j \sin k_j x_j - \psi(\omega) \cos k_j x_j) \sin \omega t],$$

for j = 1,2, where

$$A_0 = \frac{\omega^2 l_0^2 \rho_0}{(2)^{3/2}\pi} \frac{1+\psi^2(\omega)}{\sqrt{1+3\psi^2(\omega)}}, \qquad \psi(\omega) = \sum_{j=1}^{2} I_{0j} \cot k_j l_j.$$

I_{oj} is a ratio of acoustic impedances, and k_j is a wave number.

To test this theory, measurements of pressure, mean temperature, OH* chemiluminescence and frequency were made in the Sandia pulse combustion facility for a bench-scale version of the system that had the following geometry:

Branch Number, j	Length l_j(m)	Area S_j(m²)
0	0.11	0.0011
1	0.34	0.0045
2	0.75	0.0045

In these tests, the combustion source was a premixed propane flame that could be located at various positions in j = 0.

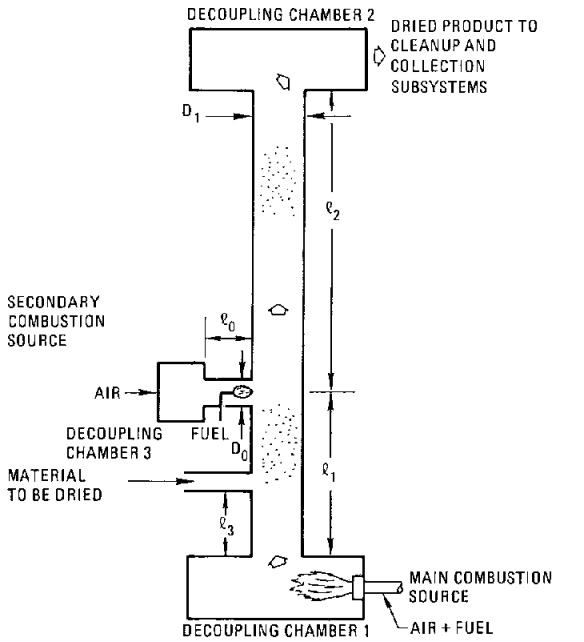

Figure 1. Schematic of a pulse combustor for enhanced drying applications.

†Sandia Report *SAND86-8050* (Sandia National Laboratories, Livermore, CA, 1987).

Figure 2 presents pressure versus location in the vertical section for several times in one cycle for the fundamental mode of the system. The agreement between theory and experiment is satisfactory.

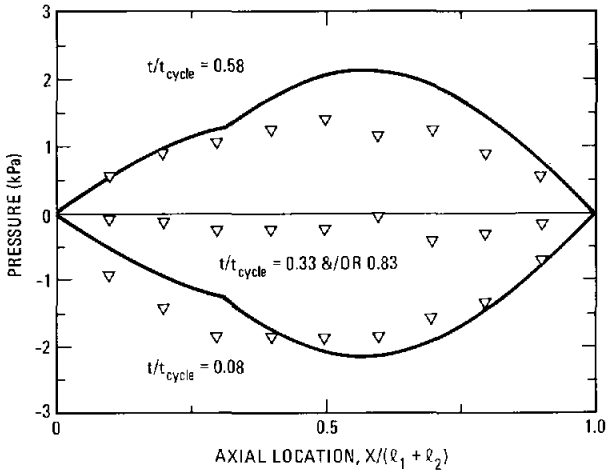

Figure 2. Pressure amplitude for three times in a cycle. This figure presents the pressure amplitude in the vertical section for three different times during a cycle: at the maximum and minimum amplitudes and at approximately zero amplitude. The solid lines are theoretical predictions. The discontinuity in slope is a consequence of the assumption of a "compact" transition. These results are for the fundamental acoustic mode of the system.

Figure 3 presents results for pressure versus time at a specific location within the vertical section. The time has been normalized by the experimental data and the theoretical prediction. The experimental frequency was 182 Hz, while the theoretical prediction was 204 Hz. The agreement between theory and experiment is again quite satisfactory. The present analysis neglects viscous losses. One would expect that viscous losses would decrease the amplitude of the velocity oscillations, and thus, the amplitude of the pressure oscillations. Such a trend is seen in the pressure data. It is believed that the disagreement between the experimental and theoretical frequencies is a consequence of the assumption of constant temperatures, and hence constant speeds of sound, in each of the three branches. From our more detailed anaysis,[2] and from experimental observations in a Helmholtz-type pulse combustor, it is known that heat transfer, and therefore the temperature distribution in a pulse combustor, is a critical factor in determining the frequency of operation.

Measurements were also made of OH* chemiluminescence, which has been shown to be an accurate marker of the temporal distribution of the energy release rate.[3] These data were very similar to

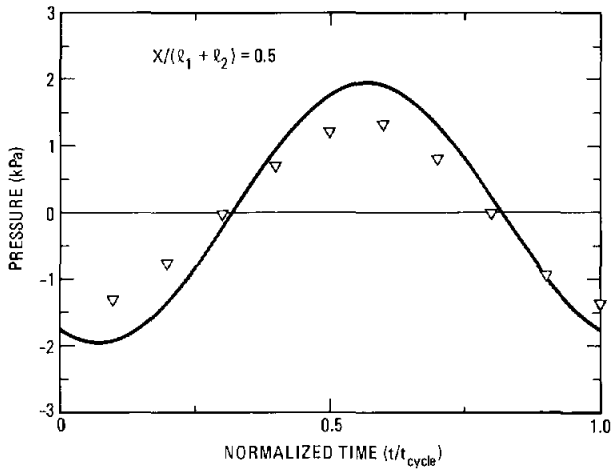

Figure 3. Pressure amplitude as a function of time. This figure presents the pressure amplitudes at a specific location within the vertical section. The solid line is the theoretical prediction. Time has been normalized by the cycle time (defined as 1/frequency).

those observed in other pulse combustors. By comparing the OH* chemiluminescence data with the pressure data in Figure 3, it was seen that the energy release rate and the pressure were in phase, thus ensuring that stable oscillations will occur.

The results obtained thus far are encouraging. Because only a small fraction of the total amount of fuel combusted in an actual application will be responsible for the acoustic oscillations, we believe the noise problem will be less severe than in the case of existing pulse combustion drying systems where the entire combustion process is modulated (experimentally, it is known that in other pulse combustors the sound pressure level depends upon the firing rate). The present system does not require valves, which will lead to mechanical simplicity. Many current, conventional drying systems contain cylindrical sections in which drying takes place. We believe there is potential for retrofitting these systems with the present concept.

References:

1. T. T. Bramlette and J. O. Keller, Sandia Report *SAND86-8050* (Sandia National Laboratories, Livermore, CA, 1987).

2. P. K. Barr, H. A. Dwyer, and T. T. Bramlette, Comb. Sci. Tech. **54**, 315 (1988).

3. J. O. Keller and K. Saito, Comb. Sci. Tech. **53**, 137 (1987).

Pulse Combustor Modeling

A pulse combustor model developed at Sandia has been used to assist several manufacturers in their design and development of commercially available pulse furnaces.

P. K. Barr

Pulse furnaces are attractive for many reasons, including high heat transfer and combustion intensity, low emissions of oxides of nitrogen, high thermal efficiencies, and self-aspiration. In such a device, steady pulsations occur when the periodic addition of energy is in phase with, and at the peak of, the resonant pressure oscillations. In spite of this seeming simplicity, the interactions among these processes are very complicated. As a result, the design and development of pulse combustors has proceeded largely by trial and error (or, appropriately, "cut-and-try"), a method that is time-consuming and costly, and one that does not guarantee an optimum design.

Our one-dimensional numerical model predicts the influences of the system geometry and operating parameters on the resulting wave structure within the combustor. Although many of the processes which take place in the pulse combustor are three-dimensional and are dominated by complex turbulent transport phenomena, the large length-to-diameter of these combustors allows the wave dynamics to be accurately described by a one-dimensional model. The model is based on the unsteady equations of continuity, momentum, and energy and is solved with variable-area geometry. Losses due to friction and heat transfer are also included. The numerical method used to solve the equations, MacCormack's explicit predictor-corrector algorithm, assures the propagation of nonlinear pressure waves at the correct amplitude and speed.

The model development has been guided by the experimental pulse combustor program at the CRF. However, commercially available pulse furnaces have a more complex geometry than our simplified laboratory system. Since both the sound level and thermal efficiency are of concern, in these commercially available systems the tail pipe exhausts into a large decoupler volume and then passes through a secondary heat exchanger before being exhausted to the atmosphere. In order to model one of these practical systems, we modified the geometry of the simulated pulse combustor to include a decoupler and vent pipe section. We also developed a dynamic injection algorithm to replace the dependence of flow rates on experimental measurement.

Lennox Industries is a leading U. S. manufacturer of pulse furnaces for domestic heating applications. Their currently available system has proven to be a very successful product. The engineers from Lennox are working on designing their next generation pulse furnace. One of their design goals for this system is a reduction in the sound emission. Because their current pulse furnace operates at moderate frequencies (between 50 and 60 Hz), the resulting noise is much more difficult to attenuate than if the combustor operated at higher frequencies.

The design engineers from Lennox spent several weeks at Sandia using the model to guide the design of their next generation pulse furnace. The collaboration with the engineers from Lennox utilizes their experience to evaluate the numerically-predicted performance of their pulse combustor under a variety of operating conditions, such as changing the equivalence ratio of the reactant, or throttling the inlet flow. The parameters in the model were calibrated by simulating the performance of an existing Lennox pulse furnace.

The engineers from Lennox Industries provided us with both the overall system dimensions and sets of performance data taken under several different operating conditions. Using these data sets we were able to tune our model to their system, including adjusting valve loss coefficients to match mean flow rates and pipe friction factors to match pressures. Once adjusted, we were able to reproduce the performance under the different operating conditions, including operating frequencies, reactant flow rates, temperatures, and pressures.

The Lennox engineers then systematically mapped out a range of design variations, such as changing the tail pipe length or diameter, or varying the volume of the combustion chamber or decoupler. The numerical predictions, which covered over 50 different conditions, were then combined to produce an initial design for the next generation pulse furnace.

Forbes Energy Engineering is working to provide large scale pulse furnaces for commercial use, as either boilers or water heaters, with inputs up to 2,000,000 Btu/hr. The engineers from Forbes were interested in understanding trends in their data obtained in a 150,000 Btu/hr system that was built for evaluation.

Because of the size of their systems, these pulse furnaces have multiple smaller diameter tail pipes, as opposed to a single large diameter tail pipe, to create additional surface area for increased heat transfer. Because these multiple tail pipes all have the same length and diameter, they were replaced in the model with a single tail pipe of the same cross sectional area. This is reasonable because the wave dynamics in each of the pipes should be the same if the gas temperatures at the tail pipe inlets, as well as all of the outlets, are the same. Other parameters were suitably adjusted to correct for the difference between the actual and the simulated surface areas.

In light of the fact that the model was developed to simulate small scale pulse furnaces, it produces reasonable predictions of the measured operating frequencies and strength of pulsation in these large systems. Because the simulations could not reproduce the fine differences occurring in the Forbes data, the comparisons also helped identify weak assumptions in the model. These include the predefined time distribution for the energy release profiles, heat transfer and friction coefficients, and the valve model.

Combustion of Chlorinated Hydrocarbon Droplets†

Experiments have been performed to characterize the combustion of mixtures of 1, 1, 2, 2-tetrachloroethane, a hazardous waste, with selected alkanes.

R. R. Steeper, N. W. Sorbo,* C. K. Law,* and D. P. Chang*

Sandia's Combustion Control of Hazardous Materials program was established in 1986 to answer an urgent need for advanced research into hazardous-waste disposal technologies. That same year, the program was broadened with the establishment of a collaborative agreement with Professors C. K. Law (Droplet Combustion) and D. P. Chang (Toxic Materials) of the University of California at Davis. Joint experiments that were begun under this collaborative agreement in 1986 have continued in 1987 and have produced significant results.

Chlorinated alkanes were chosen as the class of hazardous materials to be studied in the initial experiments for two reasons. First, the role of chlorine as a reaction-inhibiting radical scavenger is important in understanding waste incineration processes. Second, organo-chlorides make up a significant fraction of the 75 million tons of incinerable hazardous wastes generated each year in the United States. Because industrial wastes are usually blended to improve incinerability, we have emphasized the combustion of *mixtures* of chlorinated alkanes with regular hydrocarbon fuels in our tests.

In our experiments, monodisperse droplets of the test liquid are injected into the post-flame zone of a downflow reactor. The droplets ignite in the 1100-K environment and combust with an envelope flame as they traverse the reactor. A photomicrography system measures the droplet size history, and a sampling probe enables determination of liquid phase composition through the droplet's lifetime.

A series of experiments that yielded encouraging results this year looked at the combustion of 1,1,2,2-tetrachloroethane ($C_2H_2Cl_4$). Pure droplets of $C_2H_2Cl_4$ burn very weakly if at all, but addition of an alkane creates a mixture that burns well. Figure 1 presents the droplet size history of a mixture of 75% $C_2H_2Cl_4$ with 25% C_9H_{20} plotted as diameter squared (d^2) versus time. After initial preheating and ignition, the droplets enter a steady burning period that is characterized by a constant rate of decrease in d^2. This rate, defined by the classical d^2-Law, is termed the burning rate constant, K_c. At 70 ms, the curve undergoes an abrupt change in slope that marks the extinction of the droplet. The slope after extinction is labeled the vaporization rate constant, K_v, which is defined as the rate of decrease of d^2 in the absence of combustion.

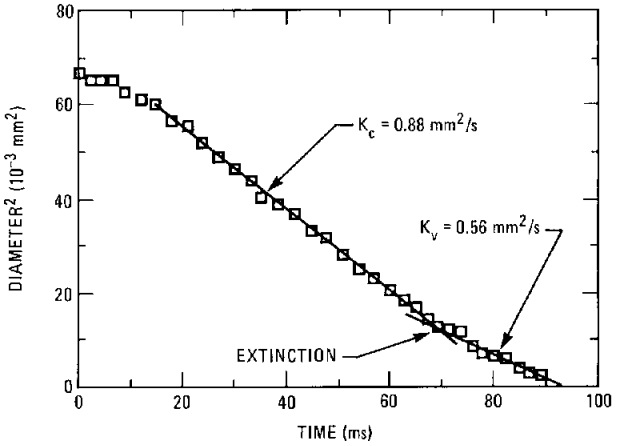

Figure 1. Droplet size history for a mixture of 75% $C_2H_2Cl_4$ with 25% C_9H_{20} by volume.

Figure 2 plots K_c and K_v for mixtures of $C_2H_2Cl_4$ and C_9H_{20}. Values of K_c are taken from data for droplets injected into an oxidizing environment (18% oxygen by volume), while the K_v values result from experiments performed in an inert environment. Note that at 100% $C_2H_2Cl_4$, the values of K_c and K_v are equal, indicating that pure $C_2H_2Cl_4$ does not burn at our temperatures and oxygen concentrations. The upper curve exhibits an unusual trend: the burning rate is relatively constant until $C_2H_2Cl_4$ concentration reaches 75%, and then falls off quickly to the level of the non-burning rate, K_v. The important conclusion is that the addition of only a small quantity of nonane (25%) causes $C_2H_2Cl_4$ to burn nearly as fast as pure nonane.

$C_2H_2Cl_4$ (boiling point = 146°C) and C_9H_{20} (boiling point = 151°C) have similar volatilities. In order to study the effects of volatility differentials on multicomponent droplet combustion, we measured burning rates for $C_2H_2Cl_4$ mixed with different

†J. Fluids Engineering, accepted (1988).

*University of California at Davis.

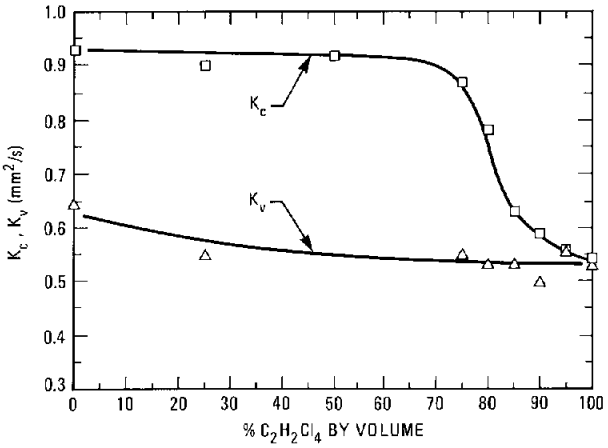

Figure 2. Gasification rate constants for mixtures of $C_2H_2Cl_4$ and C_9H_{20}.

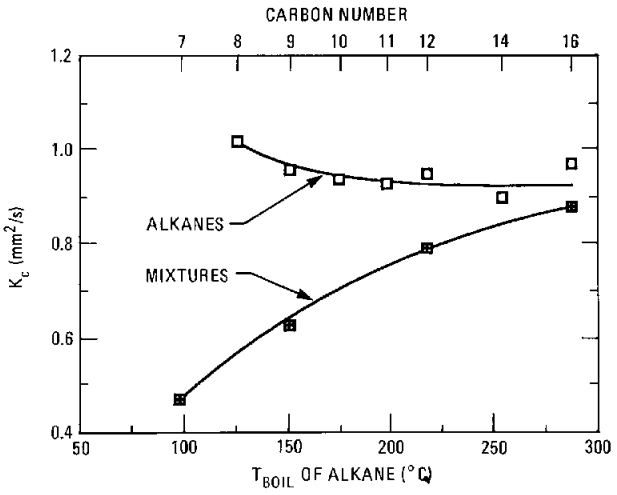

Figure 3. Burning rate constants of mixtures of 85% $C_2H_2Cl_4$ by volume with alkanes.

weight alkanes. Figure 3 presents values of K_c for these mixtures along with the K_c's of the alkane additives. The lower curve shows that the burning rate increases substantially with the carbon number of the alkane. The flatness of the upper curve indicates that this increase cannot simply be attributed to a trend in the K_c's of the additives. Rather, it is due to distillation. In the $C_2H_2Cl_4 - C_7H_{16}$ droplets, the lighter component, C_7H_{16}, is preferentially gasified leaving a droplet rich in $C_2H_2Cl_4$ that burns slowly or not at all. In the $C_2H_2Cl_4 - C_{16}H_{34}$ droplets, $C_2H_2Cl_4$ is the lighter component and its concentration drops enough to allow combustion. This result is potentially useful in devising blending strategies for incinerating chlorinated wastes.

This photograph shows two laser-based diagnostic techniques applied to the study of pulverized coal combustion in a laminar flow reactor as discussed on pages 8-14, 15. Multiple tracks of burning particles can be seen above the circular, blue flame front. Colinear He-Ne and Ar-ion cw laser beams (which appear pink) provide size and velocity information on individual single particles. A high energy pulsed Nd:YAG laser (green beam) is used to rapidly heat a single particle forming a laser "spark" (bright spot at the beam intersection). Light emitted from this hot plasma is used to determine the elemental constituents of the coal particle. With the size and velocity information for individual particles, the elemental mass flux may be calculated.

Coal Combustion

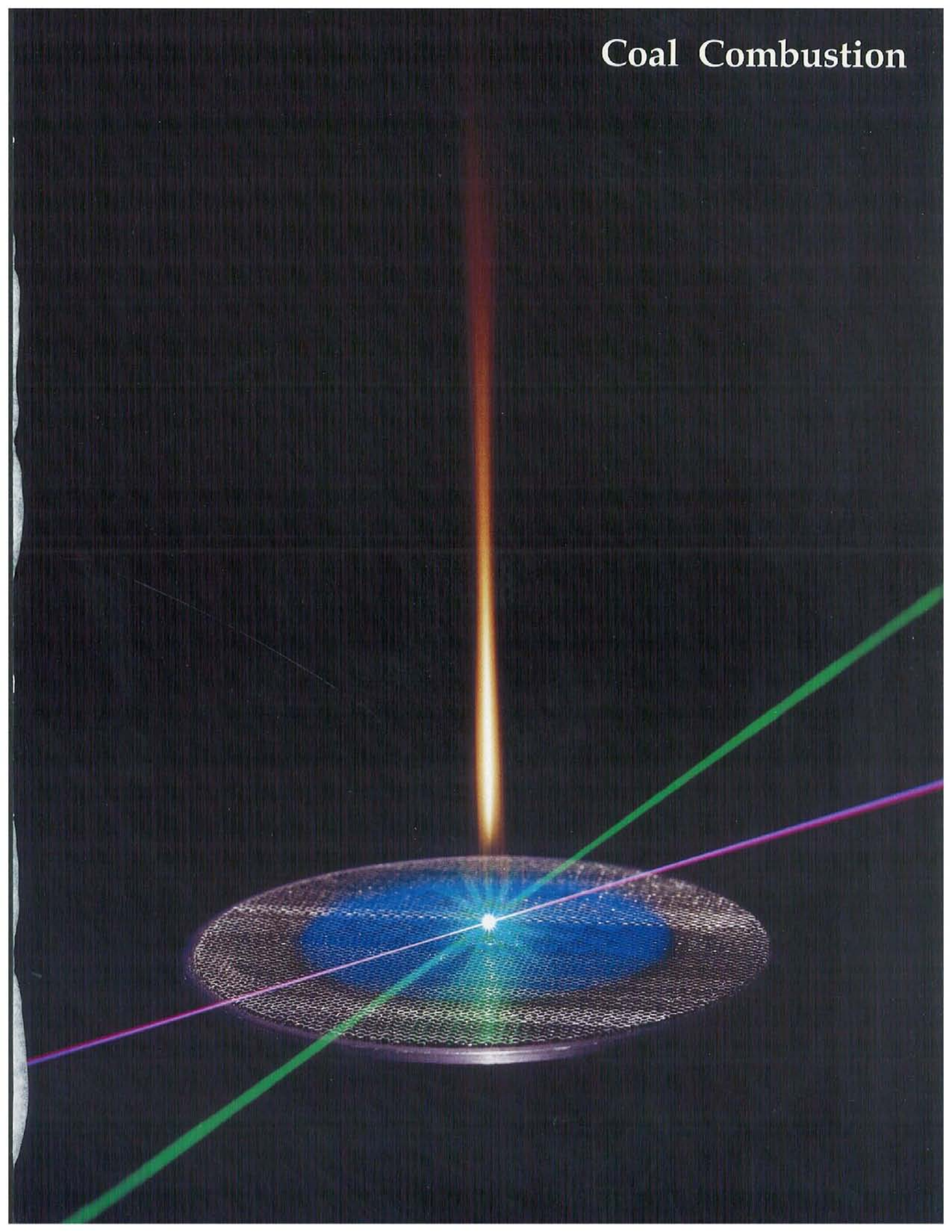

The study of chemical transformations occurring in solid materials during coal combustion has been a very difficult area for the application of modern optical diagnostics. The benefits of an *in situ* analytical technique would be of enormous value not only in expanding the basic knowledge of coal combustion, but also in developing real-time process control instrumentation for the monitoring of new fuel sources.

Laser spark spectroscopy (LASS) is an example of an optical technique which yields elemental chemical information specific to individual single particles. The process is diagrammed in Figure 1 illustrating the interaction of a coal particle with a high-energy pulsed laser beam. Extremely rapid heating of the solid produces a plasma (laser "spark"), and the spectral line emission can be analyzed using time-resolved spectroscopy to identify the elemental constituents of the individual particle. The high luminosity of these emissions allows this technique to be used *in situ* with minimal interference from the noisy combustion environment.

The combination of LASS with a colinear laser particle-sizing technique (as shown in Figure 2) thus provides both composition sensing and volume sensing for individual solid particles. If quantitative calibration standards are provided for the plasma emission lines, this hybrid optical method can be used to measure the elemental mass flux of solid particulates in a combustion environment.

The combination of such advanced optical diagnostics presents extremely complex problems in the development of an instrumentation system. This is illustrated by the timing diagram for the LASS-laser sizing experiment shown in Figure 3. Careful control is particularly critical for the measurement of a spark emission spectrum by the optical multichannel analyzer (OMA). The OMA signal delay and gate times are typically 1 to 2 μs in length, and must be uniformly maintained to ensure similar temperature conditions in successive laser-induced plasmas.

In addition, LASS, in combination with other optical methods such as Fourier transform infrared (FTIR) emission spectroscopy and spontaneous Raman scattering, can be used to investigate solid surfaces at elevated temperatures. These techniques offer the potential to develop powerful *in situ* probes to study the chemistry of deposition processes on structural substrates during fouling and slagging in coal combustion.

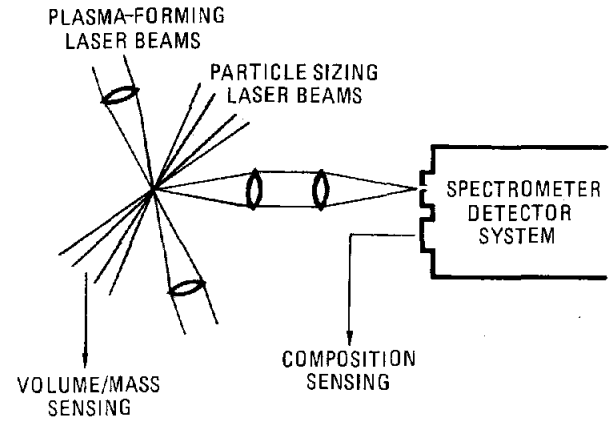

Figure 1

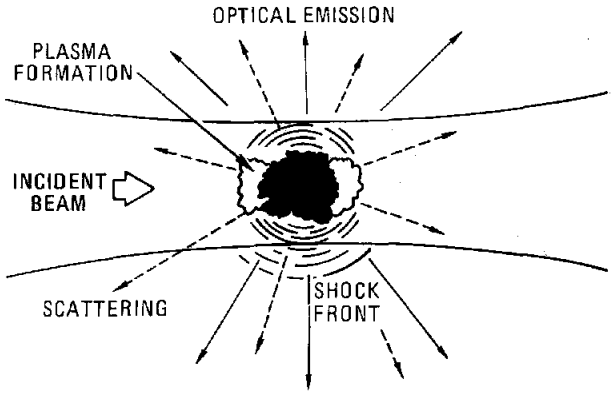

Figure 2

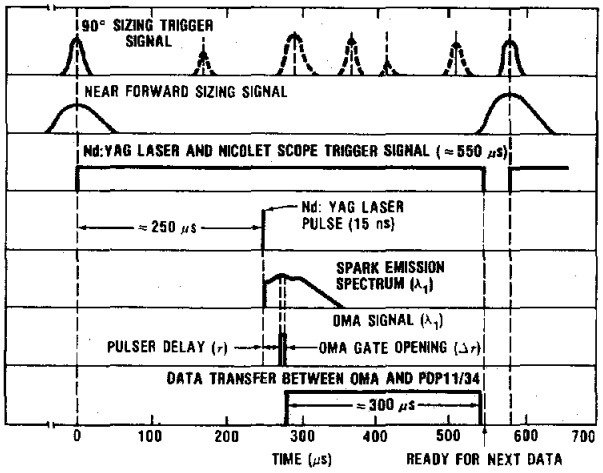

Figure 3

Section 8
Coal Combustion

Under the sponsorship of the Department of Energy's Office of Fossil Energy, a broad program of fundamental research on the combustion of pulverized coals has been developed at Sandia National Laboratories. These studies are aimed at predicting and measuring the rates and mechanisms of the devolatilization of coals and coal/liquid mixtures and of the subsequent oxidation of the residual chars. Special emphasis is given to determining the high temperature transformation and evolution of mineral species imbedded in the original coal. Experimental studies use well-controlled laboratory flow reactors to obtain spatially and temporally resolved information during the combustion of size-classified samples of well-characterized coal.

The reactors are instrumented with advanced optical detection systems, including a Sandia-patented, particle-sizing pyrometer, for *in situ* observation of particle size, temperature, and velocity, and with laser spectroscopic systems for detection of gas phase imbedded in the original coal.

Measurement of Coal Particle Temperatures During Devolatilization

An infrared-sizing pyrometer system has been developed to measure coal particle temperatures during devolatilization at rapid heating rates. Accurate determination of particle temperature is essential to the determination of kinetic parameters for coal devolatilization models.

T. H. Fletcher

Coal combustion has been studied for over forty years, yet current models of the devolatilization rate under rapid-heating conditions differ by five to seven orders of magnitude at any given temperature. Much of the controversy stems from difficulties in measuring particle temperatures as a function of time during rapid heating (10^3 to 10^6 K/s). A flameless, inert gas-flow reactor has been developed to provide maximum optical access for measuring simultaneously the size, temperature, and velocity of individual coal particles during devolatilization. The flow reactor is capable of providing a well-controlled laminar environment with gas temperatures as high as 1300 K. Optical access is provided by constructing the square reaction tower from transparent windows; quartz windows are used during solid sampling and high-speed cinematography studies, while sapphire windows are used during the particle temperature measurements.

An infrared-sizing pyrometer system, shown in Figure 1, has recently been developed which can measure particle temperatures as low as 900 K. Thermal emission from individual particles is collected using a reflecting microscope and imaged onto a coded aperture similar to that used by Tichenor.[1] Infrared wavelengths were chosen for this pyrometer system in order to (a) penetrate the tar cloud and (b) maximize the emission signal at low temperatures. Effective wavelengths of the pyrometer, as determined by tungsten lamp calibrations, are 1.36 and 2.2 μm. Emission intensities are measured by liquid nitrogen-cooled, indium-arsenide detectors. Detector signals pass through low-noise amplifiers and an electronic filter before being recorded on a digitizing oscilloscope and stored on the computer. Temperatures are determined using two-color pyrometry assuming graybody particle emission. Diameters are determined from the ratio of signals corresponding to the image of the particle as it passes through the two sizing slits on the coded aperture. Velocity is calculated from the image transit time across the large sizing aperture.

Light scattered off the particles by a helium-neon laser is used as a trigger to determine which particles are in the optical focal volume. The scat-

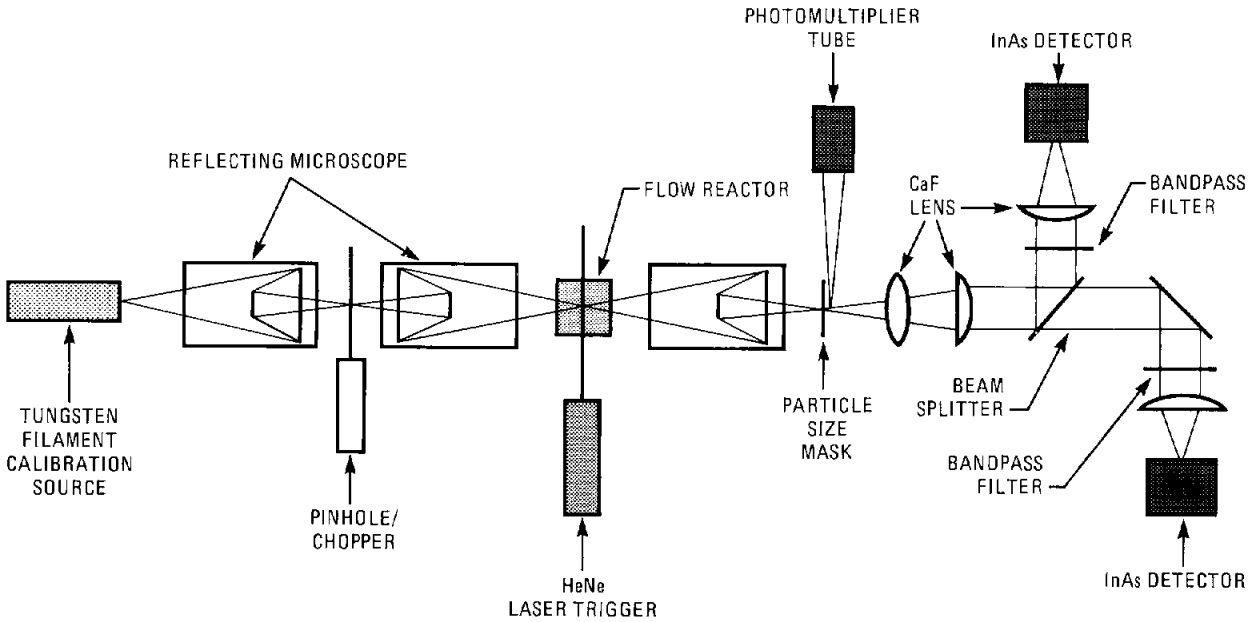

Figure 1. Schematic of the infrared-sizing pyrometer system.

tered light passes through the trigger slit in the sizing aperture, is reflected 45°, and passes through a narrow band-pass filter into a photomultiplier tube. Particle emissivities are calculated from the measured size, temperature, and emission intensity at the 2.2 μm wavelength. The emissivity calculation is used as a self-consistency check to eliminate erroneous signals which are principally due to multiple particle emission.

Tightly classified, nonfriable, pure carbon spheres (Spherocarb) are used in the flow reactor to calibrate the sizing-pyrometer system. Table I shows Spherocarb temperature and velocity measurements in an isothermal region of the flow reactor tabulated as a function of size. Standard deviations in the particle temperatures indicate the accuracy of the measurement technique. Particle temperatures decrease as a function of particle size due to radiative heat loss through the flow reactor windows.

Representative size and temperature measurements of a bituminous coal during devolatilization are given in Table II. The higher standard deviations in the coal particle temperatures are indicative of particle-to-particle variations in shape and composition. The coal particle temperature measurements seem to be unaffected by the presence of the surrounding tar cloud, which has an observed diameter ten times that of the particle. The coal particle sizes measured are too small to represent tar cloud sizes, indicating that the true particle temperature is being measured. Calculated coal particle emissivities are similar to the Spherocarb emissivities, which is further evidence that the tar cloud is not affecting the measurements. Coal particle velocities are lower than Spherocarb velocities, since the bulk density of the coal has decreased due to devolatilization.

A helium-quench probe is used to collect particles in the flow reactor as a function of residence time. The sampling system includes aerodynamic separation of char and tar. The inherent titanium in the coal is analyzed and used as a tracer to determine overall weight loss due to devolatilization. Measurements of bulk density, particle temperature, velocity, size, and weight loss are combined to yield devolatilization kinetics.

Reference:

1. D. A. Tichenor, R. E. Mitchell, K. R. Hencken, and S. Niksa, *Twentieth Symposium (International) on Combustion* (The Combustion Institute, Pittsburgh, PA, 1984), p. 1213.

Table I
Size, Temperature, and Velocity Measurements of Spherocarb Particles in the Flow Reactor

Size	#	T(K)	σ(T)	v_p	σ(v)	ε	σ(ε)
115	14	1026	4.5	0.77	0.03	0.81	0.08
125	24	1020	7.4	0.80	0.04	0.78	0.07
135	19	1019	5.3	0.81	0.02	0.71	0.06
145	17	1019	6.4	0.81	0.04	0.64	0.07
155	7	1016	3.5	0.81	0.01	0.57	0.03

Table II
Size, Temperature, and Velocity Measurements of PSOC 1451 Bituminous Coal Particles During Devolatilization

Size	#	T(K)	σ(T)	v_p	σ(v)	ε	σ(ε)
115	9	1094	24	0.78	0.11	0.48	0.05
125	14	1087	13	0.73	0.06	0.48	0.03
135	14	1088	20	0.73	0.04	0.45	0.02
145	11	1094	33	0.72	0.06	0.40	0.02
155	16	1104	22	0.70	0.01	0.40	0.02

Spectral Emittances of Size-Graded Coal Particles†

Spectral emittances of size-graded coal particles have been measured as a function of coal type and extent of pyrolysis. Parent coals exhibit significant nongrey behavior for particle sizes as large as 120 μm. Spectral features diminish as pyrolysis proceeds.

L. L. Baxter, T. H. Fletcher, and D. K. Ottesen

Spectral emittances of size-graded coal particles have been measured as a function of coal type, particle size, and extent of pyrolysis. These emittance measurements were performed to determine spectral regions where two-color pyrometric measurements of particle temperature during pyrolysis are applicable.

Estimation of particle temperatures using available heat capacity correlations has led to a wide discrepancy in reported kinetic expressions for the rate of pyrolysis.[1,2] Pyrometric temperature measurements during pyrolysis at high heating rates are necessary to obtain pyrolysis kinetics. Such temperature measurements are significantly affected by the spectral emission characteristics of pulverized coal particles.

The widely used KBr pellet technique for determination of spectral emittance is useful for identifying functional groups, but does not apply to larger particle sizes typical of pulverized coal applications (40 to 150 μm). Solomon and coworkers[3,4] have studied emission and transmission of reacting particle clouds entrained in hot gas and have reported spectral emittance data for a range of coal types, particle sizes, and temperatures. In contrast, we have studied stationary particles in order to identify wavelength regions where pyrometry measurements would be seriously affected by nongrey behavior.

A single layer of stationary, size-classified particles was placed on a heated NaCl window (see Figure 1) with temperatures ranging from 120 to 250°C. A layer of graphite particles of the same diameter as the coal particles was also placed on the window. The window was heated with an electric strip heater wrapped around an aluminum ring mount. Temperatures as high as 400°C were possible with this system, although coal degradation was observed at temperatures above 200°C. The heated sample, optics, interferometer, and detector were enclosed in a nitrogen-purged container. Particle temperatures reported here are actually readings from a thermocouple placed directly on the window near the samples.

Figure 2a shows the spectral emittance determined for a single layer of 140-μm diameter particles of a HVA bituminous coal (Pittsburgh #8, PSOC 1451). Peaks from various functional groups can be identified and agree with published spectra from many sources and techniques. The small peak at 1850 cm^{-1} has not yet been identified and may be a feature of larger coal particles. Detector noise is apparent at wavenumbers greater than 2700 cm^{-1} and below 550 cm^{-1}; signals beyond 4000 cm^{-1} were too noisy to yield meaningful information.

Figure 2b shows spectral emittances for 115-μm particles and can be compared with Figure 3a. Since the transmissivity is higher for smaller particles, spectral features for the smaller particle size are more pronounced than for the larger particle size. However, even in the larger particle size, the valley at 2000 cm^{-1} remains an important spectral feature.

Figure 3 shows spectral emittances of the Pittsburgh #8 bituminous coal that has undergone

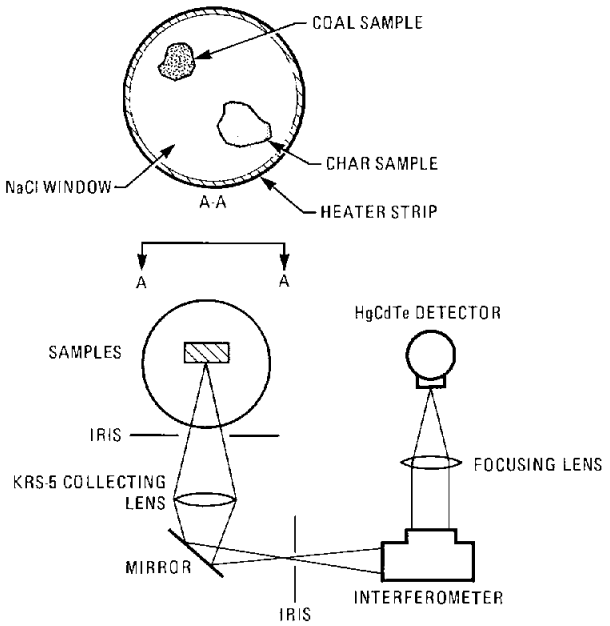

Figure 1. Schematic of experimental apparatus for measurements of the spectral emissivity of coal particles.

†Presented at the International Coal Science Meeting, Maastricht, The Netherlands (1987).

various extents of pyrolysis at rapid heating conditions (> 10^4 K/s) up to1300 K in an entrained flow reactor in 100% N_2. Weight loss was determined by measuring the titanium concentration in the collected samples and performing an elemental mass balance. Some of the spectral features of the raw coal have changed by the time 13% of the coal has been pyrolyzed. In particular, the spectral peaks between 2900 and 3800 cm^{-1}, as well as the peaks at 1300-1500 cm^{-1}, are not as pronounced for the partially reacted coal particles. However, the large valley at 2000 cm^{-1} remains even after 56% of the mass has been pyrolyzed. Spectral emittance measurements of partially oxidized char particles (which have completed pyrolysis) show the absence of spectral features, similar to that of pure carbon spheres (Spherocarb).

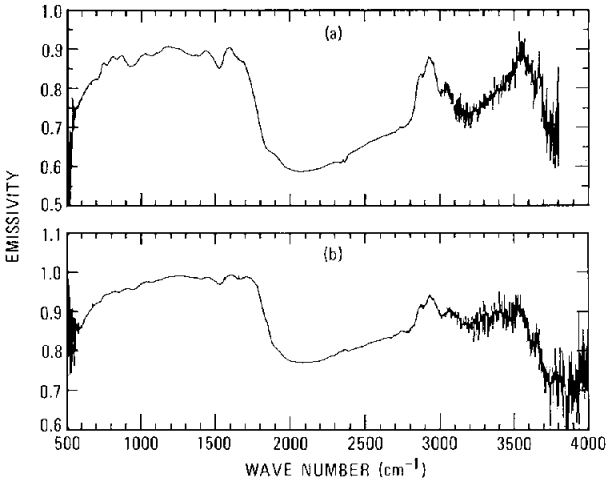

Figure 2. Spectral emissivity of (a) 55 μm bituminous coal particles (PSOC 1451d) at 171°C, and (b) 115 μm particles at 182°C.

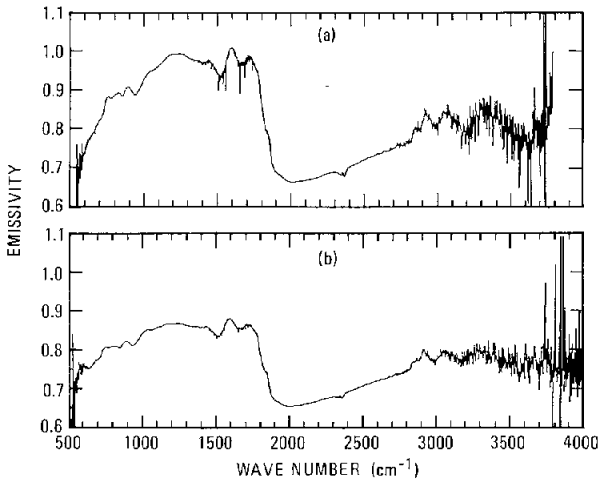

Figure 3. Spectral emissivity of partially pyrolyzed 115 μm bituminous coal particles (PSOC 1451d): (a) 13% weight loss and (b) 56% weight loss.

Spectral emittances of a New Mexico subbituminous coal (PSOC 1445d) and a North Dakota lignite (PSOC 1507d) have also been studied. The emittance of the lignite is slightly lower than in any of the other coals studied, which agrees with the trend reported by Solomon[3] that lower rank coals exhibit more nongrey behavior.

These spectral emittances are relatively noise free due to an innovative technique of relating the emission behavior to graphite samples at the same temperature. Although these measurements were obtained at low temperatures, spectral emission characteristics should be similar at high temperatures until thermal degradation and pyrolysis occur. As pyrolysis products leave the particle, the spectral emittance of the residual char becomes similar to a greybody.

When two-color emission measurements are made of individual coal particles for temperature determination, the spectral emittance of the particle over the wavelength bands of interest must either be known or constant. Generally, greybody behavior is assumed, which could result in temperature measurement errors of hundreds of degrees[5] during devolatilization if improper wavelengths are used. However, the spectra shown in this study indicate that there may be regions where spectral emittances are fairly uniform for 115-μm-diameter particles, especially at low wavelengths, and that some of the spectral features change early in the pyrolysis process.

References:

1. J. B. Howard, *Chemical Coal Utilization*, M.A. Elliott, ed. (Wiley & Sons, New York, NY, 1981), p. 665.

2. P. R. Solomon, M. A. Serio, R. M. Carangelo, and J. R. Markham, Fuel **65**, 182, (1986).

3. P. R. Solomon, P. E. Best, R. M. Carangelo, J. R. Markem, P. Chien, R. J. Santoro, and H. J. Semerjian, *Twenty-first Symposium (International) on Combustion* (The Combustion Institute, Pittsburgh, PA,1986), in press.

4. P. E. Best, R. M. Carangelo, J. R. Markham, and P. R. Solomon, Comb. Flame **66**, 47 (1986).

5. L. L. Baxter, D. K. Ottesen, and T. H. Fletcher, presented at Spring Meeting, Western States Section (The Combustion Institute, Pittsburgh, PA, 1987).

A Chemical Model of Coal Devolatilization Using Percolation Lattice Statistics

A chemical kinetic model of coal devolatilization has been developed that uses nuclear magnetic resonance characterization of the parent coal to describe product evolution rates and yields at rapid heating conditions. The model uses percolation statistics to describe bond-breaking processes during devolatilization.

D. M. Grant,* R. J. Pugmire,* T. H. Fletcher, and A. R. Kerstein

A chemical kinetic model of coal devolatilization has been developed that describes product evolution rates and yields at rapid heating conditions. Products are grouped into the broad categories of gas, tar, and char, based on molecular weight and reaction history. The behavior of different coal types is related to differences in the chemical structure of the parent coal.

Previous modeling efforts at Sandia National Laboratories described the coal molecule as a linear chain of nuclei connected by bridges.[1] A more detailed model of devolatilization, emphasizing the chemical content of pyrolysis gases, has recently been developed[2] which has been combined with a Monte Carlo description of the coal molecule to treat tar formation and release. Our new model is an attempt to describe the effect of coal type on pyrolysis behavior without the computational burden of Monte Carlo calculations.

The chemical percolation devolatilization (CPD) model treats coal as a macromolecular array of clusters representing the interconnections of aromatic ring structures of various sizes and types. These clusters are connected by a variety of chemical bridges of different bond strengths. Percolation statistics applicable to a Bethe lattice (a loopless tree structure) allow a mathematical description of the bridge-breaking process in closed form, providing an efficient alternative to Monte Carlo techniques.

Inputs to the CPD model include structural parameters based on solid-state NMR (nuclear magnetic resonance) analyses of the parent coal pertaining to the relative sizes and populations of aromatic clusters, peripheral groups, and stabilized char bridges.[3] Estimates for the degree of branching of the interconnections among aromatic clusters are also inferred from the NMR data. Kinetic parameters are assumed to be identical for coals of all types; differences in tar and gas yields for different coal types are explained by differences in the initial chemical structure. A global model for gas release is used, rather than models for individual species. The mean activation energy for the gas release was chosen to be an average of the 20 species treated in the gas release model of Solomon.[2] Activation energies are distributed in a manner corresponding to sequential release of gases as a function of molecular weight; the apparent activation energy changes according to a Gaussian distribution based on the fractional yield. Mass transfer effects on release of gas and tar are not yet treated in this model.

The reaction sequence proposed in this model is pictured below. A labile bridge L breaks to form a highly reactive intermediate L^* which is consumed by two competitive processes: (1) release of the bridge remnants as light gas g_2, with a rapid relinking of the two sites within the reaction cage to give a char bridge c, and (2) temporary stabilization of the remnants into side chains δ with the bridge remaining broken. The side chains are eventually converted into light gas fragments g_1 through a slower reaction step.

$$L \rightarrow L^*$$

$$L^* \rightarrow 2\delta$$

$$L^* \rightarrow c + 2g_2$$

$$\delta \rightarrow g_1$$

Figure 1 shows a comparison of CPD model calculations with devolatilization data for a Montana Rosebud coal obtained in an entrained flow reactor by Serio,[4] using kinetic parameters similar to those reported by Solomon for this set of data. The good agreement in both the time of gas and tar release and in the rates of release indicates the applicability of lattice statistics to the treatment of coal devolatilization. Good agreement has also been achieved with devolatilization data for Illinois #6 coal and Zap lignite in the same flow reactor without changing the kinetic parameters.

*University of Utah at Salt Lake City.

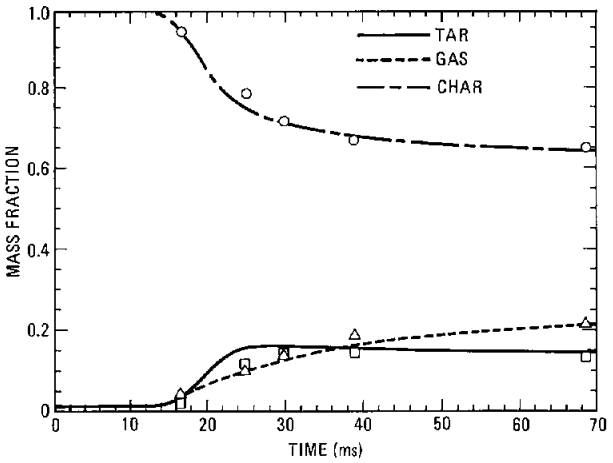

Figure 1. CPD model calculations compared with Solomon data for a Montana Rosebud coal heated to 1040 K in an entrained flow reactor.

References:

1. S. Niksa and A. R. Kerstein, Comb. Flame **66**, 95 (1986).

2. P. R. Solomon, D. G. Hamblen, R. M. Carangelo, M. A. Serio, and G. V. Desphande, ACS Div. of Fuel Chem. Preprints **33**, 83 (1987).

3. M. Solum, R. J. Pugmire, and D. M. Grant, ACS Div. of Fuel Chem. Preprints **34**, 273 (1987).

4. M. A. Serio, D. G. Hamblen, J. R. Markham, and P. R. Solomon, Energy and Fuel **1**, 138 (1987).

On the Product Split Between Carbon Monoxide and Carbon Dioxide at the Surfaces of Reacting Carbon and Coal Char Particles at High Temperature

In an investigation of combustion of char particles in hot oxidizing gaseous environments, it was determined that carbon dioxide is a primary product of the heterogeneous reaction occurring on the surfaces of particles. Size, temperature, velocity, and mass-loss measurements are combined to show that only when account is made for carbon monoxide formation can burning rate parameters be determined that balance both the mass and energy transport equations. For the bituminous coal investigated, 10 to 45% conversion of carbon to carbon dioxide (the remainder to carbon monoxide) is required in order to determine burning rates that satisfy both the particle mass and heat balance equations.

R. E. Mitchell

In developing models of the burning characteristics of pulverized-coal chars in gaseous environments typical of practical coal combustors, a critical issue concerns the products of the heterogeneous carbon oxidation reaction. Based largely on the results of Arthur,[1] it is generally assumed that the single film model[2] of a burning carbon sphere with CO as the sole reaction product applies to coal char particles burning under typical pulverized-coal combustor conditions. Recent studies, however, employing lignite[3] and graphite particles[4] indicate that CO_2 may be a primary heterogeneous reaction product as well. In this work, evidence is presented which suggests that in coal combustor environments, as much as 45% of the carbonaceous material of bituminous coal chars can be converted to CO_2 on the particle surface.

In the experiments, coal particles in the size-ranges 75 to 106 μm and 106 to 125 μm were injected into flow reactor environments having 6% and 12% oxygen in the temperature range 1550 to 1650 K. *In situ* measurements were made for the size, temperature, and velocity of individual particles using a particle-sizing pyrometer.[5] Samples of partially reacted coal chars were collected at selected residence times using an isokinetic solids sampling probe and analyzed for specific surface areas, apparent densities, and porosities. The fractional mass remaining, m/m_o, at each sampling height was determined from the weight of the collected sample and the weight of the coal fed to the reactor. The coal employed in the study was Pittsburgh #8, an HVA-bituminous coal.

In analyzing the data, the single film model of a burning carbon sphere is employed with allowance for a fraction ψ of the carbonaceous particle material to be converted to CO_2 at the particle surface and a fraction $(1-\psi)$, to CO. Allowance is made also for Stefan flow, the convective flow emanating from the particle surface when there is a change in the number of moles upon reaction. The approach of Frank-Kamenetskii[6] is taken in relating the overall particle burning rate per unit external surface area, q, to the gas temperature and oxygen partial pressure.

In this work, the overall particle burning rate is expressed in terms of an apparent chemical reaction rate coefficient, k_s, and an apparent reaction order, n, with respect to the oxygen partial pressure at the particle surface, P_s:

$$q = k_s P_s^n \qquad (1)$$

The temperature-dependent, apparent chemical reaction-rate coefficient includes the combined effects of pore diffusion and the intrinsic chemical reactivity of the particle material.

The intrinsic chemical reaction rate, q_i, is expressed in terms of an intrinsic chemical reaction rate constant, $k_{s,i}$, and a true reaction order, m, with respect to the oxygen concentration at the surface, C_s:

$$q_i = \eta\, k_{s,i}\, C_s^m \qquad (2)$$

where η is the effectiveness factor.[7] The intrinsic chemical reaction rate constant characterizes the true rate of the char-O_2 reaction. It is free of any effects associated with external mass transfer or internal pore diffusion. It is expressed in Arrhenius form.

The procedures used to determine the Arrhenius parameters A_a and E_a, and A_t and E_t, which

describe respectively the apparent chemical reaction-rate coefficients and the intrinsic reaction rate constants, are outlined in the papers by Mitchell.[8,9] Following the procedures, Arrhenius parameters for k_s and $k_{s,i}$ are derived for specified values of ψ. Table I shows the values determined. Note that the values determined for the true activation energy are relatively insensitive to the value specified for ψ. The set of rate parameters for each value specified for ψ yields calculated temperatures which agree (in the least-squares sense) with the measurements. Each set does not, however, yield calculated mass profiles which agree with the measurements.

Figure 1 shows calculated and experimentally determined values of m/m_o at the measurement heights for particles burning in 12-mole-% oxygen. The experimental values shown were obtained with coal particles in the 75- to 106-μm-size range and the calculations are for a 90-μm particle, the mean of the size-range used. Since the flow reactor code does not allow for the effects associated with coal devolatilization, in the calculations the measured values of m/m_o and the char density at a height of 6.35 cm in the reactor were used as starting values. A value of ψ in the range 0.3 to 0.45 agrees best with the data. Similar results are obtained for burning in 6-mole-% oxygen and for particles in the 106- to 125-μm-size range as well.

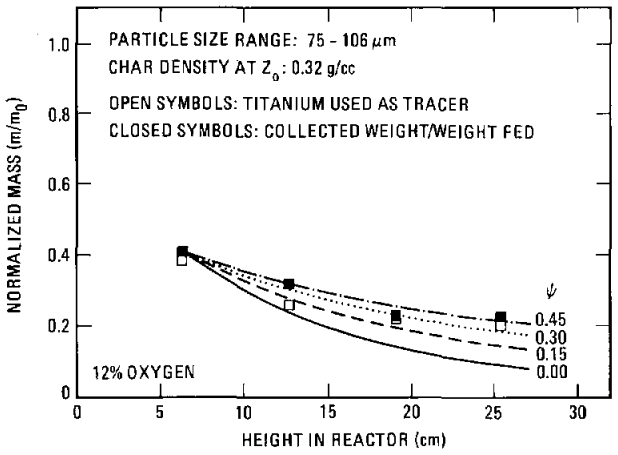

Figure 1. Calculated and experimentally determined normalized mass profiles in the flow reactor. Gas temperatures are in the range 1550 to 1650 K. Particle temperatures are in the range 1700 to 1800 K. The fraction of carbon converted to CO_2 at the particle surface is ψ.

Values of ψ in the same range were found to balance both the mass and energy conservation equations for graphite particles in the size range 100 to 150 μm burning in 12- to 36-mole-% oxygen and gas temperatures in the range 1300 to 1775 K.[4] Since the effect is observed with graphite particles, the CO_2 formation at the particle surface cannot be attributed to catalytic effects caused by the mineral matter in the coal as suggested by others.[3] This study underscores the importance of having to close both the mass and energy balance equations when determining kinetic rate parameters.

References:

1. J. R. Arthur,Transactions of the Faraday Society **47**, 164 (1951).

2. M A. Field, D. W. Gill, B. B. Morgan, and P. G. W. Hawksley, *Combustion of Pulverized Coal* (BCURA, Leatherhead, England, 1967), p. 186.

3. B. C. Young and S. Niksa, *Proceedings of the 1987 International Conference on Coal Science* (Maastricht, The Netherlands, 1987), p. 819.

4. B. J. Waters, R. E. Mitchell, R. G. Squires, and N. M. Laurendeau, "Evidence for Formation of CO_2 in the Vicinity of Burning Pulverized Carbon Particles," Comb. Flame, accepted (1987).

5. D. A. Tichenor, R. E. Mitchell, K. R. Hencken, and S. Niksa, *Twentieth Symposium (International) on Combustion* (The Combustion Institute, Pittsburgh, PA, 1984), p. 1213.

6. D. A. Frank-Kamenetskii, *Diffusion and Heat Transfer in Chemical Kinetics,* Trans. Ed. J. P. Appleton, (Plenum Press, New York, NY, 1969).

7. C. N. Satterfield, *Mass Transfer in Heterogeneous Catalysis,* (MIT Press, Cambridge, MA, 1970).

8. R. E. Mitchell, Comb. Sci.Tech. **53**, 165 (1987).

9. R. E. Mitchell, "Determination of the Intrinsic Reactivities of Pulverized-Coal Chars at High Temperature," Comb. Sci. Tech., submitted (1988).

Table I

Arrhenius parameters for the apparent chemical reaction rate coefficient and the intrinsic reaction rate constant for the char particles of Pittsburgh #8 coal: variations in ψ.

ψ	n	A_a (g/cm^2-s-atm^n)	E (cal/mole)	m	A_t (mole O_2/cm^2-s)	E_t (cal/mole)
0.0	0.35	5.13	19070	0.0	0.1330	34040
0.15	0.40	3.01	18000	0.0	0.0776	33860
0.30	0.45	1.95	16950	0.0	0.0596	33930
0.45	0.45	1.56	16920	0.0	0.0511	34070

Determination of the Intrinsic Reactivities of Pulverized-Coal Chars at High Temperature

A procedure is presented to determine the intrinsic chemical reactivities of pulverized coal chars using direct in situ *measurements of the size, temperature, and velocity of individual particles burning in a flow reactor and off-line measurements of the specific surface areas, apparent densities and porosities of partially reacted chars extracted from the reactor. The procedure is used to determine the kinetic parameters for an HVA-bituminous coal from Pittsburgh.*

R. E. Mitchell

The intrinsic chemical reactivities of pulverized coal chars are being determined using data obtained from laminar flow reactor experiments. These data include direct, *in situ* measurements of the size, temperature, and velocity of individual particles burning in the reactor[1] as well as off-line measurements of the specific surface areas, apparent densities, and porosities of partially reacted chars extracted from the reactor.

To derive intrinsic chemical reactivities from these experimental data, a model is employed which assumes that the porous char particles are spherical and isothermal; diffusion within the porous structure is represented by Fick's law assuming an overall invariant effective diffusion coefficient. The intrinsic chemical reaction rate, q_i is expressed as:

$$q_i = \eta\, k_{s,i}\, C^m \qquad (1)$$

where $k_{s,i}$ is the intrinsic chemical reaction rate constant, m is the true reaction order with respect to the oxygen concentration, C, and η is the effectiveness factor. The effectiveness factor is the ratio of the actual reaction rate to that which would occur if the entire particle were exposed to the oxygen concentration and temperature existing at the outer surface of the particle. The effectiveness factor concept is a simple means of accounting for the continuous changes in the local oxygen concentration and temperature inside the particle.

For a porous particle of diameter d_p, specific surface area S_g, apparent density ρ_p, and porosity θ, the Thiele modulus, ϕ, is defined as:[2]

$$\phi = 1/2\, d_p\, [\rho_p S_g k_{s,i} C_s^{(m-1)}/D_{eff}]^{1/2} \qquad (2)$$

where D_{eff} is the effective oxygen pore diffusion coefficient and C_s is the oxygen concentration at the outer surface. The Thiele modulus indicates the degree to which oxygen penetrates the particle's outer surface. For values of ϕ less than 3, oxygen almost completely penetrates the particle and reaction occurs throughout the particle at rates dependent upon the local oxygen concentration and temperature. The apparent density of the particle decreases with burnoff and its size remains somewhat constant. For values of ϕ greater than 10, the penetration depth of oxygen is low and only the periphery of the particle is involved in reaction. The particle burns essentially at constant apparent density with a decrease in size with burnoff. For intermediate values of ϕ, both the size and apparent density of the particle change with burnoff.

The relation between η and ϕ depends upon the true reaction order and can be determined from the oxygen concentration gradient at the outer surface of the particle and the definition of η as described, for example, by Satterfield,[3] for first-order reactions. Analytical solutions can be derived only for zeroth-, first-, and second-order kinetics; however, the results of Metha and Aris[4] indicate that the following expression (which is exact for first-order kinetics) yields approximate values of η for specified ϕ for all positive reaction orders:

$$\eta = 3/\phi_m\, (1/\tanh(\phi_m) - 1/\phi_m) \qquad (3)$$

where

$$\phi_m = \phi\, [(m+1)/2]^{1/2} \qquad (4)$$

For ν_0 moles of oxygen consumed per mole of carbon consumed, the following expression can be derived relating the overall particle burning rate per unit external surface area, q, and q_i:

$$q = [M_c/6\nu_o]\rho_p S_g d_p q_i \qquad (5)$$

where M_c is the molecular weight of carbon. Combining this equation with Equations (1) and (2) yields:

$$\phi^2\eta = 1.5\, \nu_o d_p q/(D_{eff} C_s M_c) \qquad (6)$$

This equation is used to determine the product $\phi^2\eta$ from the measurements. For each particle size, the overall particle burning rate, q, is determined from a particle heat balance equation.[5] The oxygen partial pressure at the particle surface, P_s, is determined by assuming that the single film model[6] of a burning carbon sphere applies with CO as the sole heterogeneous reaction product. The ideal gas law is used to calculate C_s from P_s.

The effective oxygen pore diffusion coefficient is calculated from the expressions given by Satterfield[3] using the measured values for the particle surface area, apparent density, and porosity. Allowances are made for both Knudsen and bulk diffusion in the particle pores. A tortuosity factor, τ, is used to allow for the fact that the pores are irregularly shaped, have varying cross-sections, and are randomly oriented. It also accounts for the various unknown degrees of anisotropy and inhomogeneity of the pore structure. Values of τ between 1 and 7 have been determined for diffusion and flow in a variety of finely porous media.[3]

For a specified reaction order, an iterative procedure is used to determine the values of ϕ and η which satisfy Equation (3) and which yield the product $\phi^2\eta$ as calculated via Equation (6). From the value of ϕ so determined, Equation (2) is used to determine $k_{s,i}$ for the true reaction order specified.

A value of $k_{s,i}$ is determined for each particle size and, hence, for each particle temperature. A nonlinear least-squares procedure is used to determine the parameters which correlate the values of the rate constant with temperature in the following Arrhenius form:

$$k_{s,i} = A_t \exp(-E_t/RT_p) \qquad (7)$$

where E_t is the true activation energy.

The results shown below are for Pittsburgh #8, an HVA-bituminous coal having approximately 33.6% volatile matter, 2.5% moisture, 13.3% ash, and 50.6% fixed carbon. Particles in the size range 106 to 125 μm are used. Reactor environments having 6 and 12% O_2 (by volume) are employed with gas temperatures ranging from 1550 to 1650 K. Figure 1 shows the values determined for the intrinsic reaction rate constants. The least-squares fit yields a value of 34 kcal/mole for the true activation energy. A true reaction order of zero was found to correlate the data the best.

A value of 3 was used for the tortuosity factor, τ. This assumes that oxygen diffusion is through a randomly oriented system of long cylindrical pores. The value determined for the true activation energy was found to be relatively insensitive to the value specified for τ.

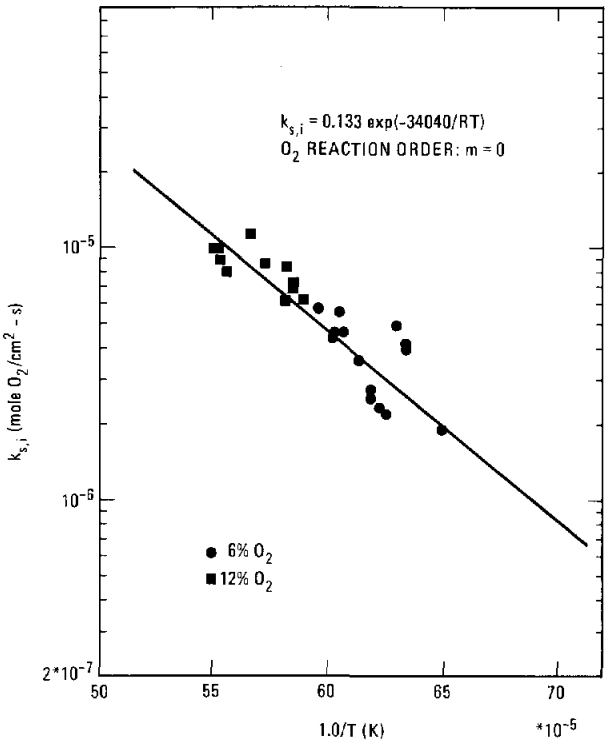

Figure 1. Intrinsic chemical reaction rate constants determined for the char particles of Pittsburgh #8 coal: CO as the reaction product.

The value determined for E_t is in the range expected for the burning of impure carbons. The value is nearly twice the value determined for the apparent activation energy (17-19 kcal) thereby supporting the hypothesis that under pulverized-coal combustor conditions, char particles burn in a regime in which their overall burning rates are limited by the combined effects of pore diffusion and the intrinsic chemical reactivity of the particle material.

References:

1. D. A. Tichenor, R. E. Mitchell, K. R. Hencken, and S. Niksa, *Twentieth Symposium (International) on Combustion* (The Combustion Institute, Pittsburgh, PA, 1984), p. 1213.

2. E. W. Thiele, Industrial and Engineering Chemistry **31**, 916, (1939).

3. C. N. Satterfield, *Mass Transfer in Heterogeneous Catalysis* (MIT Press, Cambridge, MA, 1970).

4. B. N. Metha, and R. Aris, Chem. Engineering Sci. **26**, 1699, (1971).

5. R. E. Mitchell, Com. Sci. Tech. **53**, 165, (1987).

6. M A. Field, D. W. Gill, B. B. Morgan, and P. G. W. Hawksley, *Combustion of Pulverized Coal* (BCURA, Leatherhead, England, 1967), p. 186.

Influence of Ash on Particle Size Distribution Evolution During Coal Combustion†

A population balance model of particle size distribution evolution during coal combustion is formulated which treats carbon and mineral matter distinctly. The model, which incorporates fragmentation effects, indicates that fly ash measurements during the combustion of a monodispersion would serve to discriminate between alternative fragmentation scenarios that have been proposed.

D. Dunn-Rankin* and A. R. Kerstein

There is substantial interest in using pulverized coal and coal/water slurry to fuel advanced heat engines, such as medium speed diesels and turbines. However, the ash formed from mineral matter during coal combustion causes serious erosion and corrosion problems in these engines. It is potentially useful, therefore, to understand the mechanisms involved in the evolution of the initial pulverized coal particle size distribution (PSD) to the final ash PSD. To this end, many experiments have been conducted that compare the initial coal PSD to the final ash PSD under typical combustion conditions. It is difficult, however, to interpret this experimental data without understanding the relationship between measured trends and the physical mechanisms involved. The present work is aimed at providing this understanding through numerical simulation.

The model generalizes our previous model of char PSD evolution[1] by including the influence of mineral matter. In the previous work, char particles were characterized by a single parameter—the particle size. In the present work, each particle is characterized by two parameters—the mass of mineral matter in the particle and the total mass of the particle (i.e., the mass of mineral matter plus the mass of carbon).

The model uses a discrete formulation so that two indices describe each particle type. Figure 1 is a three-dimensional particle-mass distribution showing how the total mass and the mineral mass indices define the bins of the distribution. The first index i represents the total mass of the particle and the second index j represents the mineral mass of the particle. Both the total mass bins and ash mass bins are logarithmically spaced in the simulation, and increasing indices represent decreasing mass. Figure 1 also shows the pure ash boundary, beyond which occurs the nonphysical condition of more mineral mass than total mass. The back wall of the three-dimensional plot indicates the number of particles in each total mass range irrespective of the mineral constituent of the particles. This integrated quantity is what is measured in experimental studies of PSD evolution.

Formally, a system of equations that balances the sources and sinks for each particle type (i.e., for each ij) governs the evolution of the particle-size distribution. Models of this type are often

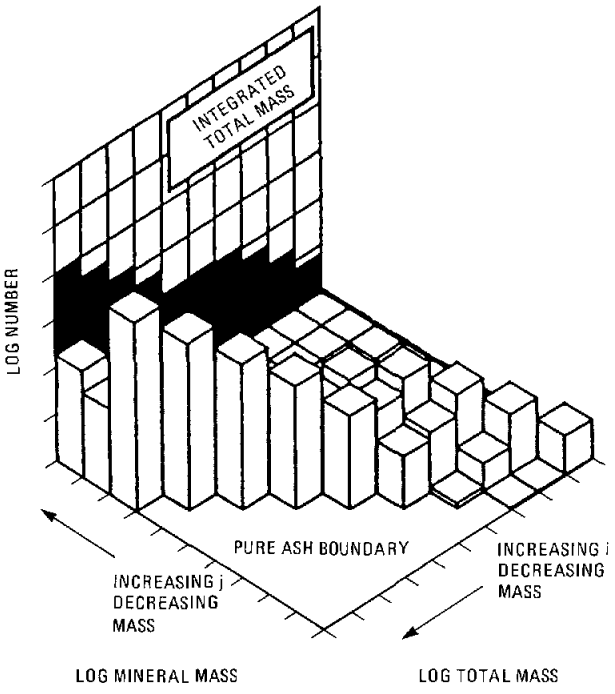

Figure 1. Three-dimensional size distribution showing the specification of discrete size bins by the two parameters, total mass and mineral mass. The figure also shows that increasing indices reflect decreasing mass. The back wall of the figure sums the number of particles, irrespective of their mineral mass, for a given total mass.

†Combustion and Flame, submitted (1987).

*University of California at Irvine.

described as population balances. The governing system of equations for population balance models of PSD evolution have appeared previously, but all of these models use a single parameter to characterize the particle type. In our two-parameter population-balance model the governing system of equations is:

$$\frac{dN_{ij}}{dt} = -C_{ij} N_{ij} + C_{i-1,j} N_{i-1,j} - S_{ij} N_{ij} + \sum_{\substack{k=1,i-1 \\ l=1,j}} b_{ijkl} S_{kl} N_{kl}$$

where N_{ij} represents the number of particles in the *ith* total mass bin and the *jth* mineral mass bin. The first pair of terms on the right-hand side of this expression are, respectively, the sink and source of N_{ij} due to burning. The C_{ij} are the elements of the burning-rate matrix. Each of these elements includes a burning-rate dependence on both total mass and mineral mass. The last pair of terms on the right side of this expression represent the influence of fragmentation. The elements of the fragmentation rate matrix S_{ij} are similar to the C_{ij} elements, with each S_{ij} including a fragmentation-rate dependence on total mass and mineral mass. The last summation is a source term that provides the contribution to N_{ij} from the fragmentation of all larger particles. The b_{ijkl} are the elements of a fragmentation-progeny matrix, with each element containing the number of type *ij* particles that are produced by the fragmentation of a single type *kl* particle. Because S_{kl} is the rate at which *kl* particles fragment, $b_{ijkl} S_{kl}$ is the rate at which particles enter the *ij* bin due to fragmentation in the *kl* bin.

In applications of this model, we examined two scenarios for fragmentation—breakage fragmentation and power-law fragmentation. Breakage fragmentation refers to the condition where fragments from the parent particle only enter the next smaller mass bin. Power-law fragmentation, on the other hand, contributes fragments to 10 mass bins smaller than the mass bin of the parent particle.

These scenarios, plus a control case involving burning but no fragmentation, have been simulated computationally based on the population balance equations with parametric inputs corresponding to combustion conditions of practical interest. Several alternative assumptions concerning the particle-size distribution of the feedstock were adopted. The feedstock was taken to be either monodisperse, power-law distributed, or a power law with a superimposed peak at large sizes. The latter distribution corresponds to size-graded feedstocks used in some experiments. These three feedstock assumptions, in conjunction with the three fragmentation scenarios, yielded a total of nine cases which were computed.

The results indicated only a weak sensitivity of the particle-size distribution evolution to the fragmentation scenario, except when the feedstock is monodisperse. This implied that measurements to date, involving feedstocks which are not highly monodisperse, do not decisively discriminate among the fragmentation scenarios. Experiments involving the combustion of a monodispersion of coal particles are needed to determine the dominant fragmentation mode. Although the particle-size distribution evolution of the polydisperse feedstocks used in practical applications appears to be insensitive to the fragmentation mode, fragmentation may nevertheless be important because fragments experience different time-temperature and fluid-mechanical time histories than fines present initially. Fragmentation may contribute disproportionately to the fly ash fines or to the unburned carbon fines which exit the combustor.

Reference:

1. D. Dunn-Rankin and A. R. Kerstein, Comb. Flame **69**, 193 (1986).

Laser Spark Spectroscopy for *In Situ* Analysis of Particles in Coal Combustion Flows†

We are developing optical laser-based instrumentation for in situ *measurements on particles in combustion environments. Laser-spark spectroscopy and near-forward Mie scattering are being used to determine particle composition, size, and velocity for pulverized coal in an entrained flow reactor.*

D. K. Ottesen

One of the most difficult challenges in developing diagnostic methods for coal combustion research is that of determining the composition of entrained coal, char, and mineral matter particles in the combustion zone. We are continuing to apply two laser-based optical techniques for the simultaneous measurement of the size, velocity, and elemental composition of particles in combustion flows. Our approach uses laser spark spectroscopy[1] to determine the elemental composition of coal particles, and various materials of uniform composition for calibration purposes.[2,3] Sizing measurements are done using a two-color, light-scattering technique described elsewhere.[4]

The two laser beams which are used to make sizing measurements are also used to trigger a high power Nd:YAG laser when a particle is centered in the confocal volume of the three beams. The laser energy deposited in the particle rapidly heats the material, forming a plasma. The hot elemental species contained in this "spark" produce a series of intense emission lines which are detected using a grating spectrometer with a diode array detector.

Optimum results are obtained by gating the detector array 2 μs after the initiation of the spark. This allows the very hot species in the plasma to decay into the neutral or singly ionized state with a considerable simplification in the number of emission lines and their interpretation. Our work has used a detection window of 2 μs. Species detected in coal by this method thus far include: C, H, O, N, Li, Na, K, Mg, Ca, Ba, Sr, Al, Si, Ti, Mn, and Fe.

A major advance in our experiments this past year has been the addition to our laboratory of a flat-flame burner which is used to generate a hot, combustion environment for the particle diagnostic measurements. Pulverized coal or other solids are entrained along the burner center line, and the residence time at the measurement position is varied by translating the burner assembly vertically with respect to the laser beams' confocal volume.

Preliminary experiments have been conducted on particles of several well-characterized coals entrained in a nitrogen flow using a $CH_4/N_2/O_2$ flame. The coals were obtained from the Penn State coal bank and were size classified with mean diameters of 45-63 μm.

Initial analyses indicate that the two-color, particle-sizing technique performs successfully at combustion temperatures. Measured particle sizes at short residence times corresponded very well with data taken at room temperature, and the distribution of mean particle diameters was not significantly different from the value at room temperature.

Excellent spark emission spectra were obtained for particle residence times of 5 to 40 ms. Good experimental signal/noise ratios were obtained and were comparable to previous measurements at room temperature. Spectra were obtained in the 250 - 500-nm-wavelength region and showed no significant interference from background species present in the hot environment.

Examples for two different particles at combustion temperature are shown in Figures 1a and b. These spectra (for a Pittsburgh HVAB coal) were acquired with a low dispersion grating. Major transitions are labeled for different atomic constituents for comparison.

Of particular interest is the large variation in intensity for the several observed species in these figures. The two spectra were chosen for their contrast and represent the extremes observed in single-particle spark-emission data for this coal type. The emission spectrum of the particle in Figure 1b indicates the presence of one or more large, Si-containing mineral inclusions.

Many of the overlapping lines in the previous figures can be resolved by using a higher dispersion grating. This is illustrated in Figure 2 for a spark emission spectrum of a single coal particle excited at room temperature in a nitrogen flow. Here, the unresolved Si(I) multiplet near 2520 Å is almost completely resolved, and Fe(I) lines which had masked a weak Al(I) doublet near 2570 Å are clearly separated. This considerably facilitates the

†Presented at the International Coal Science Meeting, Maastricht, The Netherlands (1987).

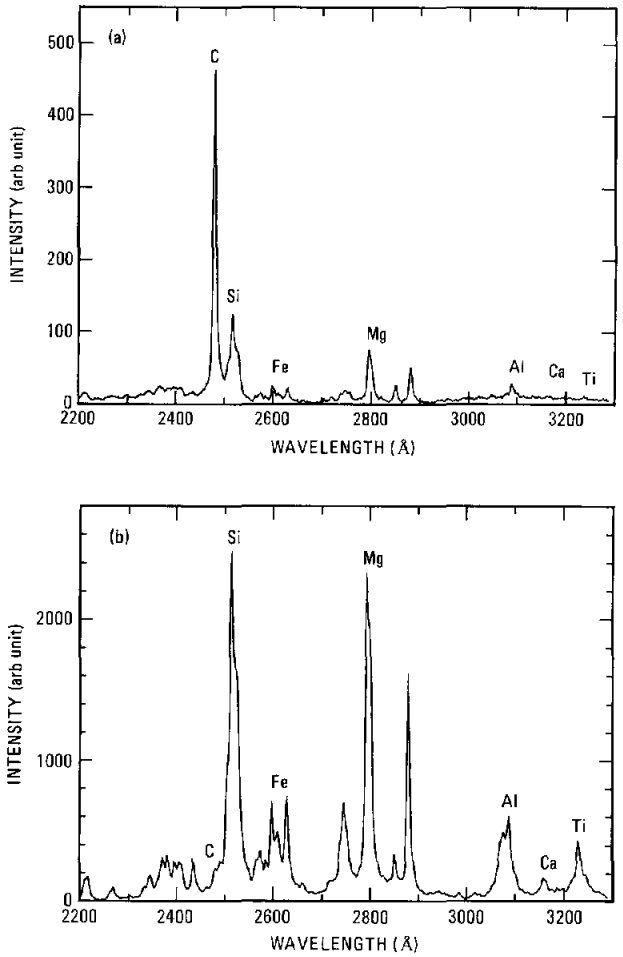

Figure 1. Representative spark emission spectra following laser breakdown of two single coal particles (PSOC 1451d) in a combustion environment.

quantitative analysis of the data in the determination of elemental composition.

An analytical computer code has been written to fit the observed data with reference lineshapes of given intensity and wavelength, and the results of a nonlinear least-squares fit is shown in Figure 2 as the dashed curve. Agreement for all observed species is quite good, and comparison on the individual line intensities within the Si(I) multiplet for a number of spectra indicates that self-absorption is not a problem for plasmas produced from particles in the present size range.

The extraction of quantitative elemental composition from the spark emission measurements is a central concern of our research. Previous results[2] on Na-containing water droplets of uniform size indicated that reproducible results were feasible by this technique for particles of constant size and composition. A further demonstration of this important aspect of our work was obtained this past year by studying the laser-spark spectra of sized ion-exchange resin particles.

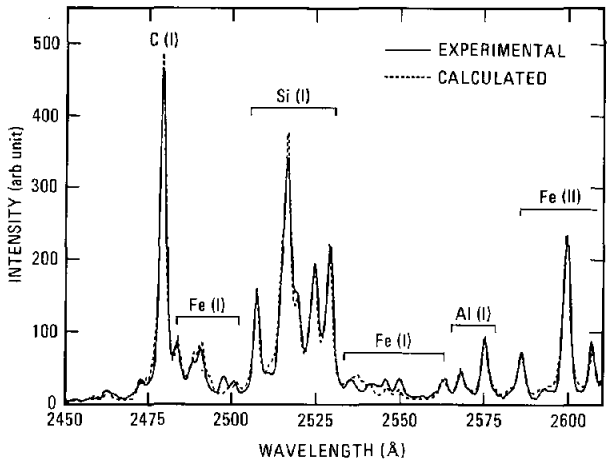

Figure 2. Experimental and calculated spark emission spectra for a single coal particle at higher spectral resolution.

Particles of amberlite (a carboxylic acid ion exchange resin) were loaded with 8-wt-% Ca, and were entrained in our flow reactor in nitrogen at room temperature. The resulting emission spectra were fit using a nonlinear, least-squares routine and reference transition-line intensities for calcium and carbon. The coefficients of the fit for C(I) and Ca(II) show a good correlation between the two species and depart from linearity only for the most intense sparks.

These results demonstrate the important fact that accurate, quantitative calibration standards for particulates can be determined with our technique. Future work will be concerned with the development of such homogenous reference materials based on impregnated chars and suitable for use at combustion temperatures.

At the present time, laser spark spectroscopy appears to be a promising method for on-line elemental analysis of particles in combustion flows. When these results are combined with the simultaneous particle size and velocity measurements, the resulting comprehensive statistical picture should be of particular importance in understanding the evolution and eventual fate of inorganic species such as ash and pollutants in pulverized coal combustion.

References:

1. R. W. Schmieder, Sandia Report *SAND83-8618* (Sandia National Laboratories, Livermore, CA, 1983).

2. D. K. Ottesen and J. C. F. Wang, ACS Div. of Fuel Chem. Preprints **31**, 13 (1986).

3. D. R. Hardesty and D. K. Ottesen, Energy **12**, 813 (1987).

4. J. C. F. Wang and K. R. Hencken, Sandia Report, *SAND85-8869*, (Sandia National Laboratories, Livermore, CA, 1985.)

Using Mie Scattering for Measuring Size Changes of Individual Particles†

An instrument has been developed to measure size changes of individual particles. Its accuracy in sizing both burning and nonburning droplets has been experimentally determined.

R. R. Steeper, P. A. Jensen,* and D. Dunn-Rankin**

In combustion research, it is often desirable to relate the rate of change in particle size, $\dot{d}$, to the size of the particle itself, d. An example is the measurement of the classical d^2 burning rate law for particles: $d(d^2)/dt = 2d\dot{d}$ = constant.

Typically, such information is obtained by comparing particle size distributions taken at different times in the combustion process. This method is accurate, however, only when the input particle stream is monodisperse. To avoid this restriction, we have designed an individual particle sizer (IPS) that measures the size of the *same* particle at two different locations. We built the prototype shown in Figure 1 to test the concept and used it to characterize the accuracy of the design in sizing both room temperature and burning droplets.

The IPS determines particle size by measuring scattered light as the particle traverses the narrow dimension of a collimated laser sheet. The sheet is formed to create a sample volume with a uniformly illuminated (within 7%), 3-mm x 3-mm cross-sectional area. These relatively large dimensions were chosen so that a particle stream will reliably pass through two such measurement volumes. The thickness of the laser sheet, 1.5 mm, was chosen to meet a uniform illumination criterion for our largest particles (400 μm), and to provide sufficient intensity for the smallest (50 μm). The experimental apparatus for testing the IPS consists of a piezoelectric droplet generator, a strobe synchronized to the droplet generator, and a microscope equipped with a 35-mm camera. Photographs taken as the droplets traverse the IPS sample volume provide accurate (± 7 μm), independent size measurements.

Figure 2 demonstrates the accuracy of the IPS by comparing photographic size measurements with IPS measurements for droplets of water and n-decane. The water drops were used to calibrate the system and the resulting maximum uncertainty is less than ± 4% (± 2 standard deviations) as shown

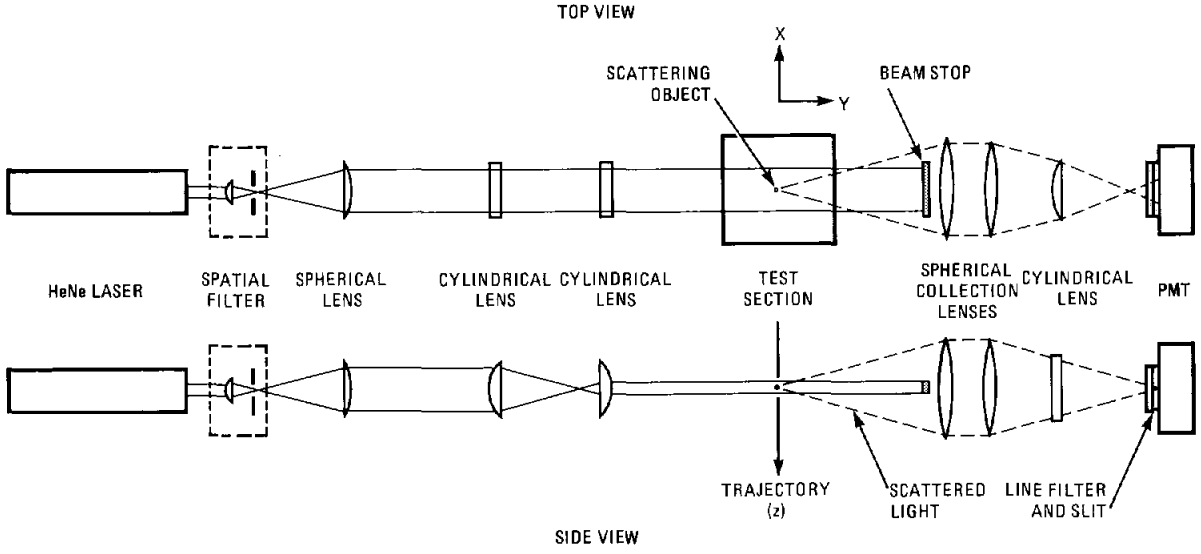

Figure 1. Schematic diagram of optical arrangement of the individual particle sizer (IPS). The top and side views show the two-dimensional nature of the laser sheet used in the IPS.

†Journal of Physics E: Scientific Instruments, accepted (1987).
*Energiteknikafdelingen, Risø, Denmark.
**University of California at Irvine.

by the vertical error bars. For n-decane, the uncertainty rises from 3% at the small particle end to 8% for the largest particles. This trend is due to an increasingly nonmonotonic Mie-scattering response of n-decane with increasing particle size.

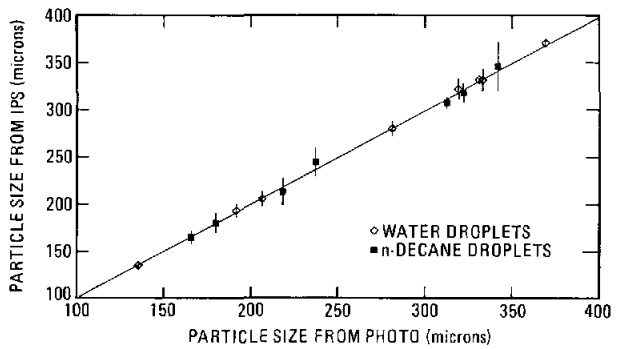

Figure 2. Direct comparison of particle size from photographs and particle size determined by the IPS. The error bars represent ± 2 standard deviations. Results for both water and nonburning n-decane droplets are shown.

To determine the effect of an envelope flame on the size measured by the IPS, Figure 3 compares the measured response of nonburning n-decane droplets with the measured response of burning n-decane droplets. Also included is the computed response of nonburning decane calculated with the Mie equations and calibrated with the water-droplet data. Data for the burning case indicates greater deviation from the computed response than for the nonburning case. The figure also shows a slight trend toward higher responses for the smaller burning droplets: the IPS "sees" these droplets as larger than their photographic images. Ray-tracing calculations indicate that a likely cause of this oversizing of burning droplets is beam steering by the envelope flame. Figure 4 shows that the flame-plus-vapor envelope surrounding a small droplet can refract the incident beam past the beam block into the collection lens, falsely raising the IPS response.

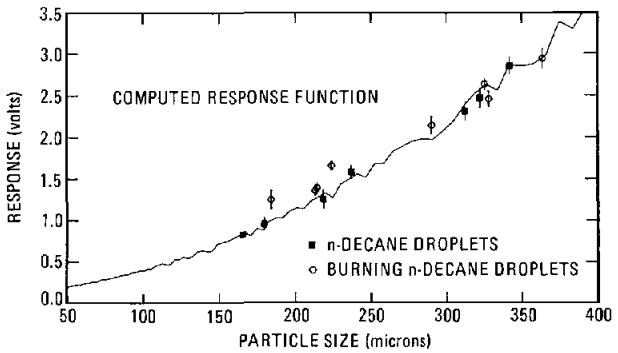

Figure 3. Comparison between measured size of burning and nonburning n-decane droplets. Error bars represent ± 2 standard deviations in measured response.

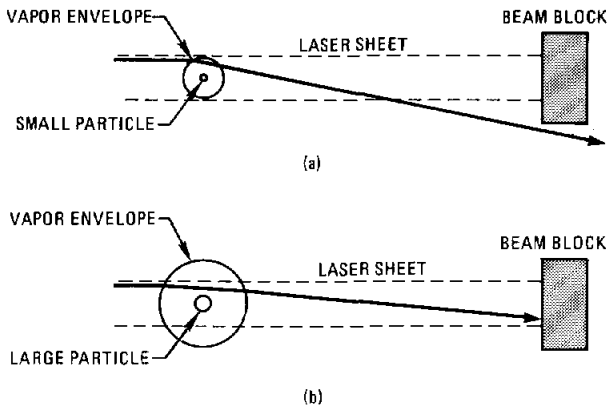

Figure 4. (a) Refraction of incident laser light past the beam block by a small vapor envelope. (b) Inconsequential refraction by a large vapor envelope.

This work demonstrates the capability of the IPS to measure the size of individual particles over a large sample volume cross section. Future experiments will combine two identical systems centered at different points on the particle trajectory to measure directly the change in size of individual particles. The well-characterized accuracy of the IPS makes it useful for further investigations of the effect of combustion on the sizing of droplets. In addition, the IPS is a nonimaging instrument that can be used to size smaller particles than can be accurately sized from photographs. Future work will extend the operating size range of the IPS by calibrating the system nonphotographically (for example, by means of calibrated microspheres).

The Role of Dispersant in Coal/Water Slurry Agglomerate Formation†

While agglomerate formation during coal/water slurry combustion is well documented, the force binding the agglomerates together is not. Our work examines the role that additives (specifically dispersant) to the slurry liquid could potentially play in the agglomeration process.

D. Dunn-Rankin* and D. R. Hardesty

One objective of our research is to determine combustion properties of coal/water slurry (cws) that will allow this fuel to replace the traditional gaseous and liquid fuels presently used by medium-speed diesels and gas turbines. Toward this end, our previous work examined the influence of the physical properties of the parent pulverized coal on cws combustion (e.g., the effect of beneficiation, the effect of micronizing, and the effect of coal rank). However, these previous studies suggest that the slurry liquid also contributes significantly to the cws combustion process. One example of this contribution involves the formation of large agglomerates during cws combustion. As the water evaporates from a slurry droplet, surface tension draws the coal particles in the droplet into contact. These particles often become bound into an agglomerate. Agglomerates pose a serious problem for advanced heat-engine applications of cws because they burn inefficiently, requiring a long residence time for complete burnout.

The principal component of cws liquid is water. However, pulverized coal in water does not form a stable slurry, and consequently, typical coal/water slurries also include a small quantity ($\approx 1\%$) of dispersant to improve the rheologic and stability properties of the slurry. Dispersants are surface-active agents that help disperse finely divided solids in a liquid medium. Despite the routine application of dispersants in cws fuel production, little is known about the influence of dispersants on the slurry droplets once the cws enters the high-temperature environment of a combustor. The present work examines this influence, with particular attention to the impact of dispersants on agglomerate formation during cws combustion.

The cws delivery system consists of a commercially available air-blast atomizer and a syringe pump. This delivery system supplies cws droplets at a volumetric rate of 2 cc/min. The droplets are introduced into a low-temperature environment (500 K, 21% O_2) for drying. Three hot-air driers, arranged symmetrically around the nozzle, produce this low-temperature drying environment. To examine the behavior of cws agglomerates, we use a scanning electron microscope (SEM). The SEM probes the morphology of individual agglomerates that are collected after being dried by the hot-air driers.

Amax Corporation provided the subbituminous coal, both as pulverized fuel and in slurry form, that is used for the experiments described here. The slurry contains 41.2% coal, 57.6% water, and 1.2% dispersant (percentages are by weight). The dispersant is anionic and is a commercially available ammonium napthalene sulfonate (Diamond Shamrock A-23).

We used two slurries in the spray-drying experiments. The first (Slurry A) was the commercial Amax slurry that contains dispersant. The second slurry (Slurry B) was a vigorously hand-mixed combination of dry pulverized subbituminous coal (25% by weight) and distilled water—no dispersant is used.

Figure 1 shows SEM photographs of two spray-dried cws agglomerates. Figure 1a is an agglomerate produced from Slurry A (contains dispersant); Figure 1b shows an agglomerate produced from Slurry B (no dispersant). The surface of the agglomerate in Figure 1a is smooth; in contrast, the agglomerate in Figure 1b is loosely packed, with no smooth surface. The individual particles making up the agglomerate are clearly distinguishable. It is evident from this contrast that dispersants contribute to the smooth, fused character of the agglomerate in Figure 1a.

Figure 2 shows the agglomerates of Figure 1 after they have been crushed with a glass microscope slide. Figure 2a indicates that the close-packed structure of the agglomerate with dispersant is confined to a relatively thin layer at the agglomerate surface. The interior of the agglomerate is more loosely packed, with the borders of individual particle clearly visible. The agglomerate

†Fuel, submitted (1987).

*University of California at Irvine.

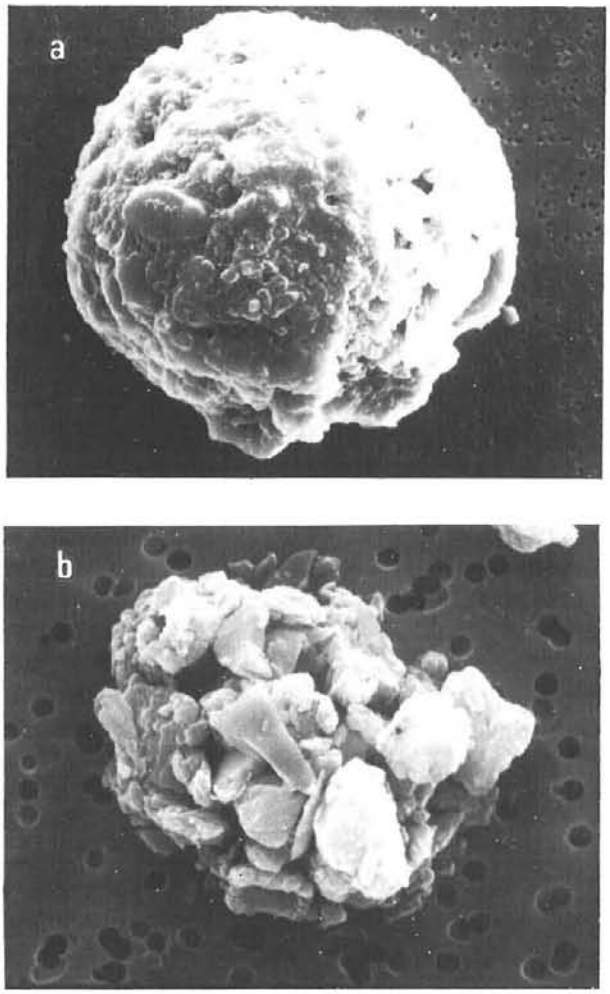

Figure 1. Scanning electron microscope photographs of subbituminous coal/water slurry agglomerates spray-dried at 600 K in air. (a) Slurry contained anionic dispersant; (b) slurry contained no dispersant.

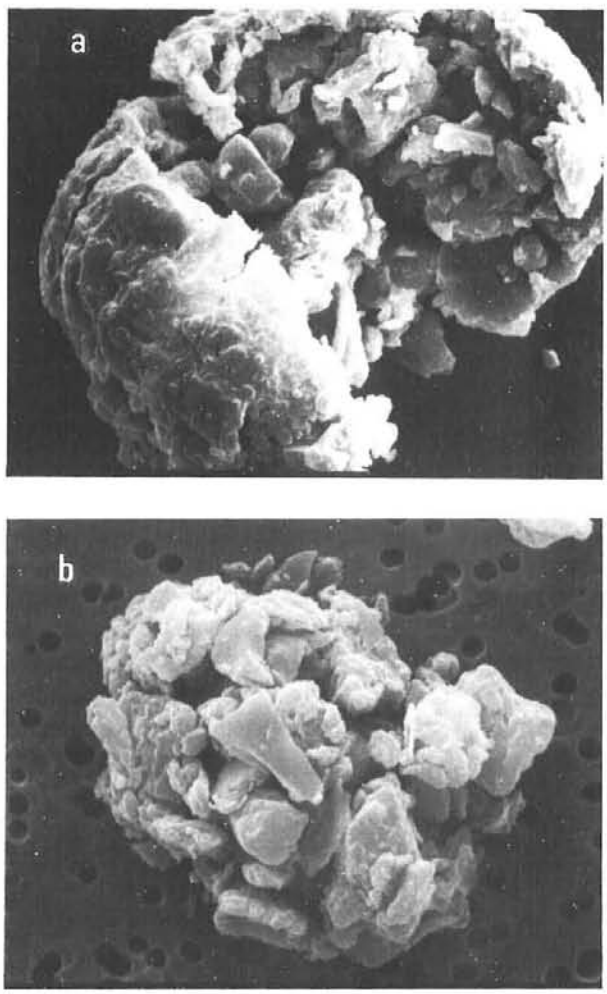

Figure 2. Scanning electron microscope photographs of cws agglomerates after being gently crushed. (a) Agglomerate of Figure 1a; (b) agglomerate of Figure 1b.

in Figure 2b shows little change after crushing. High-magnification SEM photographs of the surfaces of the crushed, fused shells obtained with Slurry A show cracks which do not follow any apparent particle surface. In contrast, Slurry B agglomerates clearly break up along particle surfaces.

The above results suggest that the dispersant migrates to the surface of the droplet as the water evaporates. With continued evaporation, the dispersant forms a continuous surface layer binding the agglomerate together.

The existence of a dense surface layer surrounding agglomerates has two potential consequences. First, the shell may produce a barrier to evaporation, which changes the thermal, and therefore chemical, response of the agglomerate. This change in physical response may substantially alter the results obtained from numerical simulations of cws combustion. Second, the shell might maintain contact between individual coal particles long enough for these particles to melt and fuse into a structurally integrated agglomerate.

The effect of dispersant during the oxidation phase of cws combustion is an area for further study. It is likely, however, that the often neglected contribution of additives in these slurries substantially affect the physical processes occurring during combustion.

Correlation of Rheology and Atomization of Coal/Water Mixtures†

Recent experiments at Sandia have compared the rheological properties of coal/water slurries under high-shear conditions with their combustion behavior. Correlations obtained with a novel high-shear rheometer were compared to observed combustion trends following high-shear atomization.

A. W. Lynch* and D. Dunn-Rankin**

Coal/water mixtures must remain stable with useful properties under widely varying conditions. The shear rates that the mixtures are subjected to range from ~ 1 s^{-1} during storage, to ~ 100 s^{-1} during pumping, to > 10,000 s^{-1} during atomization. A variety of tests, such as those which measure settling rates and intermediate shear viscosities, are used to determine slurry behavior during storage and pumping. Determining slurry behavior, under the high-shear regime typical of atomization, is much more difficult to accomplish.

Recently, a study was completed to determine whether a correlation exists between the rheology of the slurries and their atomization behavior. The project involved collaboration between staff at the rheology facility at Sandia Albuquerque (SNLA) and the Combustion Research Facility (CRF) in Livermore (SNLL). At SNLA, sample slurries were prepared and their rheological behavior was determined. This was accomplished using a high-shear helical-screw rheometer[1] which was designed to observe fluid behavior in the high shear range (10,000 s^{-1}) and to measure apparent high-shear viscosities. At the CRF, the atomization and combustion characteristics of the same slurries were examined in a laminar-flow reactor, using a particle-counter-sizer-velocimeter (PCSV). The PCSV measures the velocity and particle size distribution of particles in the 0.3 to 120 micron range.

Slurries made from Pittsburgh Seam and San Juan coals were chosen for these studies for several reasons: (1) their histories were well known;[2] (2) they differ in the rank of the coal used (bituminous vs subbituminous); (3) a body of information was developed on these two coals during a series of low shear experiments;[2] and (4) their particle size distributions, after grinding to ~ 200 mesh, were the same.

Figures 1 and 2 present typical results from the rotation rate and differential pressure measurements made in the high-shear rheometer. The data show the differences observed when slurries made from these two coals were subjected to high shear and then returned to low shear. Both slurries were prepared using lauryl sulfate as an anionic surface active agent. The curves show that as the Pittsburgh slurry (56% dry coal loading) was taken to high shear, the differential pressure increase was nonlinear, typical of pseudoplastic behavior. As the rotation rate was decreased, the curve became linear (approximating Newtonian behavior). The data for the San Juan slurry (46% dry coal loading) was different; as the shear rate increased, the slurry became slightly dilatent. The data became linear with a very slight yield stress as the shear rate was reduced.

The slurries described above were transported to the CRF and analyzed within 24 hours. The slurries were atomized and combusted in a laminar-flow reactor. A description of the reactor and PCSV instrument has appeared previously.[3,4] Particle-size distribution measurements were made approximately 20 mm above the burner surface, which corresponds to a particle residence time of approximately 10 ms. During this time the slurry liquor evaporates from droplets leaving behind a range of particle sizes from individual particles to large agglomerates. The data presented in Figures 3 and 4 are the particle size distributions obtained for the

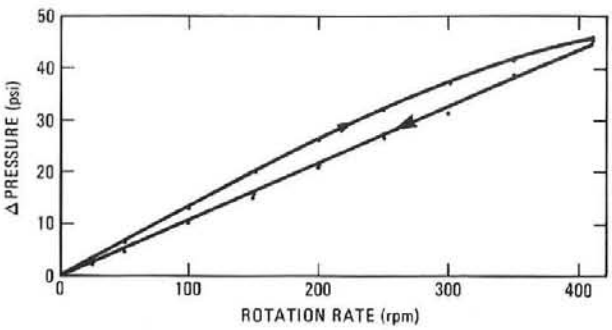

Figure 1. Rotation rate vs differential pressure data from slurry of Pittsburgh Seam coal (56%) with the surfactant lauryl sulfate.

†Sandia Report *SAND87-1971C* (Sandia National Laboratories, Albuquerque, NM, 1987).

*Sandia National Laboratories, Albuquerque, NM.
**University of California at Irvine

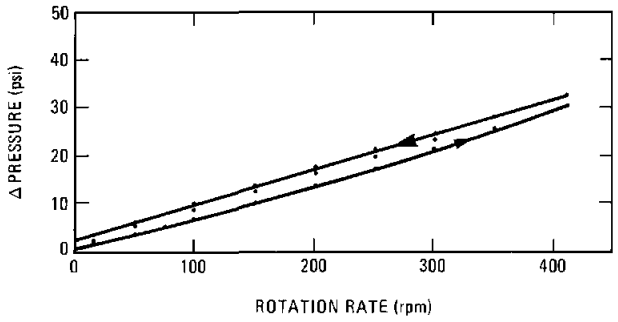

Figure 2. Rotation rate vs differential pressure data from slurry of San Juan coal (46%) with the surfactant lauryl sulfate.

Pittsburgh and San Juan slurries that had been subjected to high shear. They are typical of the measurements made on a number of slurries having various shear rate histories and coal loadings. The two sets of data are very similar and show that the highest particle number densities occur for particles less than 3 microns in size. There is also an indication that the largest particles are approximately the same size as the largest particles in the as-ground coal (~ 74 microns).

Recent evidence from high-speed films taken of slurries as they exit the atomizer nozzle, as well as films taken of particles combusting above the burner surface, indicates that large agglomerates (> 200 microns) exist in the spray. Even though the small particles are numerous and play an important role in combustion, the mechanism and completeness of combustion of the massive agglomerates could be important to the overall efficiency of the process. This is an area for further investigation.

While consistent differences in behavior between the two slurries were found during rheology measurements, only minor differences were found in their atomization and combustion behavior. It is possible that such a correlation may exist at shear rates greater than the maximum (10,000 s^{-1}) considered in this study.

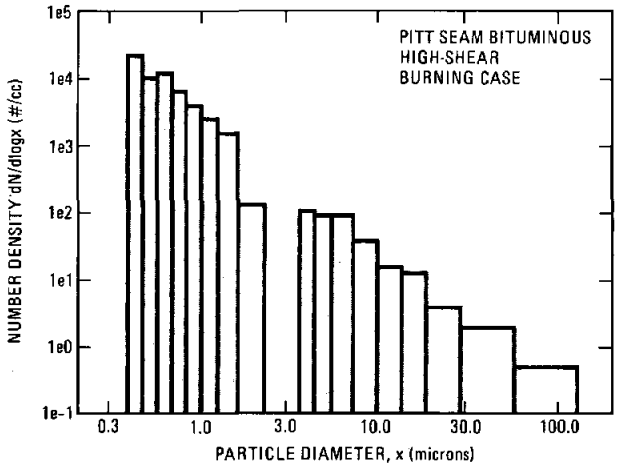

Figure 3. Particle size distribution of burning Pittsburgh Seam slurry.

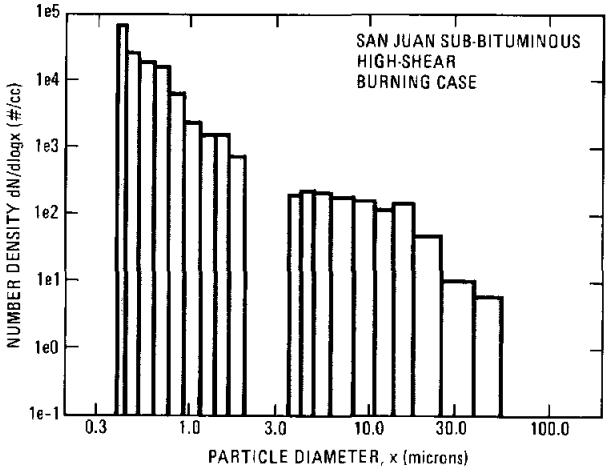

Figure 4. Particle size distribution of burning San Juan slurry.

References:

1. R. N. Chapman and A. W. Lynch, Sandia Report *SAND85-1276* (Sandia National Laboratories, Albuquerque, NM, 1985).

2. A. W. Lynch, *Proceedings* (AR&TD Direct Utilization Contractors Review Meeting, Warrendale, PA, 1986), p. 151.

3. D. J. Holve and K. D. Annen, Optical Engineering **23**, 591 (1984).

4. D. J. Holve and P. L. Meyer, Comb. Sci. Tech. **52**, 243 (1987).

Automated Image Analysis of Mineral Matter Species in Coal Particles Using a Scanning Electron Microscope†

Automated electron optical techniques are being applied to obtain statistical analyses of the joint distribution of the size and composition of mineral matter particles in coal samples. A comprehensive evaluation of the accuracy and precision of the method has been completed.

D. A. Nissen and F. A. Greulich

Industry requires the capability to predict the chemical transformations, release rates, and surface deposition of mineral species during coal combustion. This requires a considerable increase in the body of basic data on mineral species composition and evolution rates for a wide range of coals as a function of the combustion conditions. In order to accomplish this, more detailed and more extensive data are needed than can be provided by simple gross compositional analyses. Traditionally, the analysis of mineral matter in coal has involved destruction of the maceral matrix and determination of the mineral content by x-ray diffraction or wet chemical methods. The result is the gross chemical composition of the coal sample. While these data may be useful for some applications, a great deal of valuable information is irretrievably lost when these methods are employed. What is required is the actual size distribution and composition of the mineral particles in raw coal as well as the subsequent char. But because of its heterogenous nature, meaningful mineral analyses of coal can only be done by analyzing large numbers of particles. These data can be acquired by utilizing the automated scanning capability of the electron microscope coupled with analysis of characteristic x-rays emitted by mineral particles. We have completed a systematic study designed to define the limitations of this automated approach and to determine the accuracy and precision of the data.

In general, electron microscopy provides a powerful suite of tools that can be used to gather detailed information on the mineral matter in coal and chars. In our earlier work, we clearly demonstrated the ability of this technology to provide microanalytical and structural information on the composition and size distribution of mineral matter in coal.[1-4] Our results showed that the scanning electron microscope (SEM) or the electron probe microanalyzer (EPMA) can be used to determine the size distribution of discrete mineral particles larger than 0.25 μm in raw coal samples; similarly, STEM (Scanning Transmission Electron Microscope) was shown to be capable of analyzing mineral particles down to 20 nm in size; direct determination of the principal inorganic elements present in the organic matrix of the raw coal is also possible.

We have recently completed a comprehensive evaluation of the accuracy and precision of the statistical analysis of the joint particle size and compositional information generated by the Coal Mineral Analysis (CMA) program on our automated SEM and EPMA instruments. While quantitative identification of both the mineral species in coals and chars and their particle size and weight distributions is possible, there is no basis for *a priori* assessment of the relative errors, accuracy, or precision of the measurement of any of these parameters. These have been determined in the present work.

The samples used in this study were analyzed on a JEOL 733 Electron Probe Microanalyzer (EPMA), on which the Tracor Northern CMA program has been installed. The operating conditions that were used for these analyses were: CMA program edition, 1H; accelerating voltage, 20 kV; probe current, 1 namp; x-ray count-rate, < 5000 counts/sec; magnifications, 40/120/540 X; counting time for 600 particles, 140-150 min; maximum counting time, per particle, 15 sec. Chemical classification into one of 29 mineral species in a coal sample is based on the relative x-ray intensities of eleven different elements: Na, Mg, Al, Si, P, S, Cl, K, Ti, Fe, and Ca. Program output includes the mineral species present in a given sample, size distributions, weight distributions, and average composition for each classification. Briefly, mineral features are detected by a computer-controlled scanning of the sample by the electron beam of the microprobe, operating in the backscatter mode to highlight mineral matter, and comparing the digitized video signal with a predetermined threshold value.

Nine different samples of a standard reference coal, NBS 1632a, were prepared. By comparing the results from the different samples for a single

† *Proceedings of the First European Conference on The Influence of Inorganic Constituents on Coal Combustion* (The Institute of Energy, London, England, 1987).

mineral, an estimate of the precision of this technique could be made. NBS Standard Reference Coal 1632a contains 24.1 wt% ash (based on low temperature ashing), 0.23 wt % Ca, 1.1 wt % Fe, 0.42 wt % K, and 1.62 wt % S. The entire lot of coal was sieved and that fraction which was less than 70 μm was used to prepare samples for analysis. A minor, but important, added note is that in the course of this work, it was necessary to develop a new method of sample preparation in order to produce a better-quality sample for the SEM.

The mineral species present in NBS 1632a, as well as their respective concentrations, as determined by the CMA program, are given in Table I. Included for comparison are the results of a qualitative x-ray diffraction (XRD) analysis of a sample of the raw coal. All the mineral species detected by x-ray diffraction were quantitatively identified by the CMA program. The category "mixed silicates" results from mixed-layer clays of variable composition and/or physically associated silicates and in many instances comprises a significant fraction of the mineral matter.

With regard to the precision of the technique, Figure 1 summarizes the results of the analysis of nine separate samples of NBS 1632a. Statistical analysis of the data generated in this study shows that the concentration of any mineral species can be determined with a coefficient of variation of 12%.

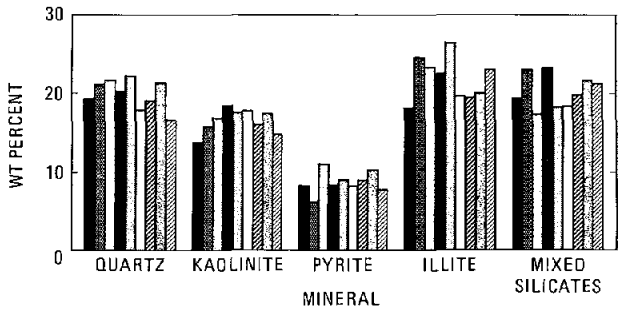

Figure 1. Results of the CMA analysis of nine samples of NBS 1632a.

In order to assess the accuracy of the CMA program as an analytical technique, the program was used to analyze samples of NBS 1632a to which were added varying concentrations of either quartz (SiO_2) or pyrite (FeS_2). By extrapolating the concentration of the added mineral species back to zero, the concentration of that species in the parent coal could be determined. The results are given in Table II and compared with those derived from LTA, NBS analysis, and CMA analysis of the parent coal. The agreement is excellent. It can be seen that the program was able to correctly identify the mineral species present in the sample and accurately determine their concentrations without the necessity of applying any correction factors.

Table I
Mineral Matter Analysis of NBS 1632a

CMA Program		X-ray Diffraction
Mineral	Wt %	Mineral
Quartz	20.0	Quartz
Pyrite	8.8	Pyrite
Calcite	2.2	Calcite*
		Clays
Kaolinite	16.6	Kaolinite
Illite	22.1	Illite
Montmorillonite	1.6	Montmorillonite*
Mixed Silicates	20.5	

*Minor phases

Table II
Results of Standard Addition Experiments

Species	Std. Add.*	CMA*	LTA*	NBS*
Pyrite	12.3	12.1	12.4	10
Quartz	18.3	16	19.8	---

*Wt. Percent

In summary, after evaluation of the method, we remain convinced that CMA is superior to all other approaches to coal minerals analysis. By operating on the raw coal, this technique eliminates problems inherent in the more conventional ashing methods, namely, transformation and reaction of mineral matter. Furthermore, this method of analysis does not depend on any calibration curves or reference data for comparison. And it is relatively rapid. We have found that this program works equally well on ash samples. The agreement between the CMA analysis of the mineral matter content of raw coal and the residue produced by low-temperature ashing is excellent.

References:

1. R. M. Allen and J. B. VanderSande, *Proceedings of the 1983 International Conference on Coal Science*, (International Energy Agency, Pittsburgh, PA, 1983), p. 361.

2. R. M. Allen and J. B. VanderSande, Fuel **63**, 24 (1984).

3. R. M. Allen, "Secondary Electron Imaging in the STEM," *Scanning Electron Microscopy*, O. Johari, ed., (SEM, Inc. Chicago, IL, 1985). Also, Sandia Report *SAND84-8682* (Sandia National Laboratories, Livermore, CA, 1984).

4. R. M. Allen, R. W. Carling, and J. B. VanderSande, Fuel **65**, 321 (1986). Also Sandia Report *SAND84-8713* (Sandia National Laboratories, Livermore, CA, 1984).

The Fate of Mineral Matter During Pulverized Coal Combustion I: High-Rank Bituminous Coal

Electron optical methods have been applied to examine the transformation of mineral species contained in partially-reacted samples of bituminous coal chars. SEM and STEM micrographs provide evidence for the accelerated oxidation of the carbonaceous char matrix due to the presence of mineral species such as apatite.

D. A. Nissen and D. R. Hardesty

One of the major problems resulting from the combustion of coal is the formation of mineral deposits on boiler walls and heat transfer surfaces. These deposits are caused by inorganic material that enters the furnace in association with the coal either as inherent or included mineral matter. Accumulation of these deposits on heat-transfer surfaces, the so-called processes of "fouling and slagging," leads to considerably reduced output and to a host of costly operational problems. On the other hand, it is quite possible that various mineral species in the coal matrix catalyze many of the organic transformations that take place during combustion.

One goal of our Coal Combustion Sciences program at the CRF is to relate the behavior of the inorganic constituents to the measured rates of devolatilization and char oxidation and to the evolution of the morphology of the organic matrix during combustion. This effort emphasizes the application of automated electron optical methods, in particular scanning electron microscopy (SEM), the electron probe microanalyzer (EPMA), and Auger electron spectroscopy (AES) to examine in detail both unreacted and quenched samples of partially devolatilized coals and chars obtained from the Coal Devolatilization and the Char Combustion laboratories at the CRF.

In one study,[1] the composition and the size distribution of the original mineral matter in narrow-size-fraction samples of several high-rank bituminous coals were determined. The coals employed in this work included an hvb-bituminous coal from Missouri (PSOC-287, 20 wt% ash, 5.4% sulfur), and a series of lvb-bituminous coals from the Smoky River Basin in Alberta, Canada. Partially reacted samples of these materials were examined to determine the evolution of the initial included mineral matter and the morphology of the resulting char during the combustion process. The samples were obtained at various residence times during combustion at well-controlled conditions of temperature (nominally 1550 K) and oxygen concentration (6 mole %) in the laminar flow reactor in the Char Combustion laboratory. An isokinetic helium quench probe was used to withdraw solid samples after different reactor residence times: 75, 100, and 125 ms for the nominally 100 μm particles in the raw coal feed.

For the high-volatile bituminous coal from Missouri, after 7- ms residence time in the flow reactor at the conditions described, the char particles exhibit a rounded, pock-marked appearance; apparently, the coal has softened and become very plastic, and volatiles formed in the interior of the particle have escaped. Our data indicate that this devolatilization process in bituminous coals is characterized by occasional formation of low density organic filaments which are ejected from the particle. Close examination of the ejecta shows that they are covered with a fine mineral-matter fuzz whose principal inorganic constitutents are Fe and S with minor amounts of Al and Si. As the volatile organic matter is ejected, minerals on the surface of the char particle adhere to its sticky exterior and are carried along with it. The very fine, lace-like structure of the mineral matter that can be seen on the surface may replicate the pore structure of the coal. The ratio of Fe:S in the mineral matter is < 1 which implies that, if the principal Fe/S species is FeS_2, it has either partially decomposed or oxidized. While the mineral species associated with the surface of the char retain some sulfur, those that have been ejected have completely lost sulfur. Analysis of the mineral matter on the surface of such particles shows only iron, from which we infer that the Fe/S species on the surface have been oxidized to iron oxide with the concurrent release of sulfur oxides.

After 100-ms residence time in the reactor, the char particles have a more rugged, pock-marked appearance than was seen at earlier times. Small, iron-rich spheres can be seen on the particle surfaces, evidence that the fine, lace-like mineral matter has begun to melt. There is also some indication of particle coalescence. The external appearance of the char particles is reflected in their internal structure. Back-scattered electron images of cross-sectional char particles show large internal voids in

those areas where volatile combustion products were produced. Their size may reflect a combination of deformation of the plastic matrix by internal pressure generated by volatile combustion products and oxidation by the combustion atmosphere. In the back-scatter mode, discrete mineral particles are seen as bright spots against the background organic material. Discrete mineral particles are visible in the interior. Energy Dispersive X-ray analysis shows that, in contrast to the mineral matter we found at the surface (composed principally of Fe and S), these are (a) SiO_2 and (b) what appears to be a partially iron-substituted illite.

With increasing residence time (up to 125 ms), the char samples are characterized by a much smoother external appearance; this reflects either oxidation of prominent surface features and/or the melting of surface mineral matter to produce a coating over the char particle. Cross-sections of these char particles show a very porous internal structure and very little evidence of surface or internal mineral matter. The quantity of small particles increases markedly; low-density organic streamers are observed, both free and attached to parent char particles. Mineral matter associated with the attached streamers retains some sulfur, while the iron in those which have become detached appears to have been oxidized to iron oxide.

Char samples obtained from the combustion of the low volatile Canadian bituminous coal were examined using the SEM. Probably the most interesting aspect of this investigation has to do with the presence of the mineral apatite, $Ca_5(PO_4)_3(OH)$, and its apparent influence on the combustion of coal particles. SEM micrographs of char samples obtained after a residence time of about 100 ms show that, in the immediate vicinity of apatite particles, the carbon matrix appears to have been extensively oxidized in contrast to the surrounding areas. That is, these mineral particles appear to be situated in holes in the char as shown in Figure 1. Typically, as a consequence of the general oxidation of the char, the more inert minerals are raised above the char matrix. Figures 1 and 2 indicate that these particles contain only Ca, P, and O. To determine the composition of these 2- to 5-μm particles, electron diffraction studies were done using the Scanning Transmission Electron Microscope (STEM). Semi-quantitative analysis of the electron diffraction patterns indicates that the mineral particles are most likely of the form $CaO \bullet Ca_3(PO_4)_2$. Independent experiments confirmed that very little transformation or volatilization of calcium phosphate occurs at temperatures up to 1500°C in either air or oxygen. Consequently, we believe that the pits in the carbon matrix are the result of accelerated oxidation of the matrix induced by apatite; there is definitive evidence for the influence of mineral matter on the oxidation process. The mechanism of the reaction and the degree to which such observations can be generalized to other coals and other mineral species remains to be determined.

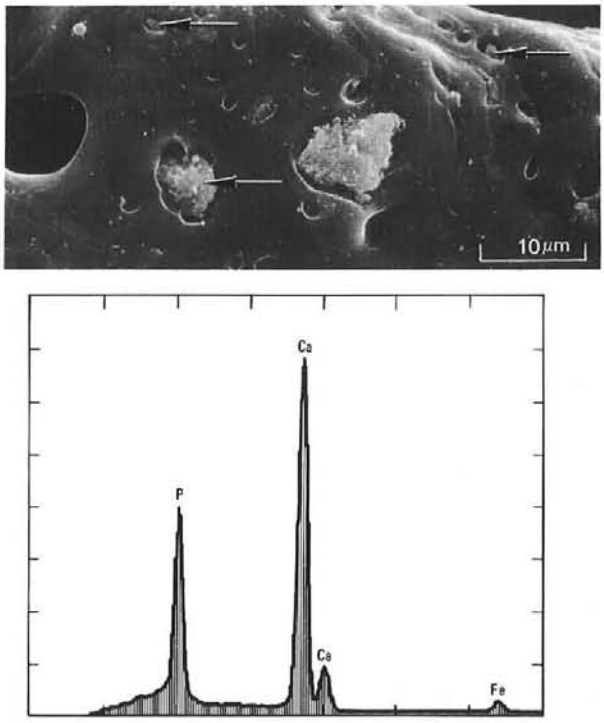

Figure 1. SEM image and X-ray spectrum of Smoky River char particle showing mineral species (arrows) situated in depressions in the char surface.

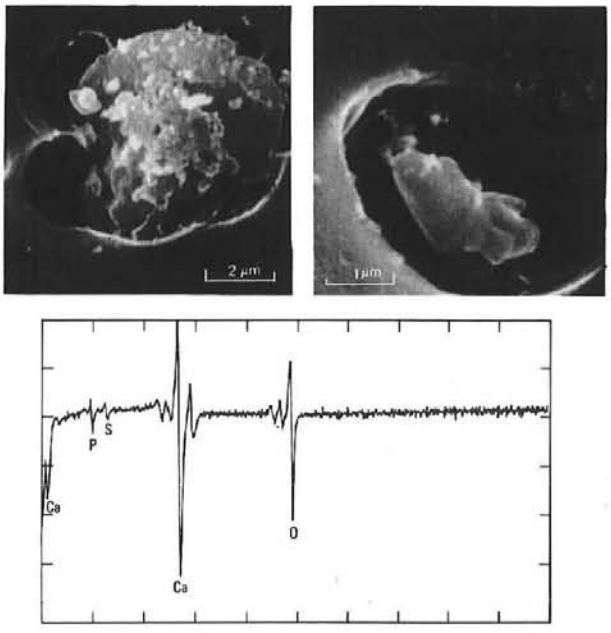

Figure 2. Magnified SEM image of two mineral particles along with their Auger spectrum, showing only Ca, P, O, and a trace of S.

Reference:

1. *Proceedings of the Conference on Effects of Coal Quality on Power Plants* (Electric Power Research Institute, Atlanta, GA, 1987).

The Fate of Mineral Matter During Pulverized Coal Combustion II: Low-Rank Lignites From the Western United States

The evolution of the morphology of lignite chars is in distinct contrast to that observed for bituminous coals. Electron microscopy reveals a lamellar char structure and the accretion of large quantities of calcium-containing droplets as a function of combustion residence time.

D. A. Nissen and D. R. Hardesty

Our study of the combustion evolution of the morphology of well-characterized samples of coal chars, and of the accompanying behavior of mineral matter during the combustion process, was completed with the examination of a lignite from North Dakota.[1] The coal examined was PSOC-86, obtained from the Penn State Coal Bank. This low-rank, North Dakota lignite contains 7.8 wt % ash and 0.8 % sulfur. The major mineral impurities include calcium, sulfur, and iron. Interest in such lignites stems from their importance as a low-sulfur fuel with unique "fouling and slagging" characteristics, which have been linked in practice to the high relative contents of sodium and calcium.

Samples of the lignite were treated in a similar fashion as the bituminous coals; discrete particle size fractions were prepared and reacted in the well-controlled conditions of the laminar flow reactor in the Char Combustion Laboratory. The same conditions in the laminar flow reactor were used as for the PSOC-287 coal; the reactor gas temperature was nominally 1550 K and the oxygen concentration was 6 mole %. Our studies indicate that both the evolution of char particle morphology as well as the distribution, composition, and structure of the mineral matter in the lignite char samples are in marked contrast to those observed for the hvb bituminous Missouri coal. As was the case for the bituminous coal study, the observations discussed here are representative of the whole sample population rather than of individual char particles. This is also true of the SEM micrographs used to illustrate various morphological or mineralogical features of the char samples.

After 75-ms residence time in the reactor, the lignite char particles do not show the extensive softening and plastic flow that characterized the bituminous char. Instead, volatiles generated in the interior of the particle appear to escape along planes in the coal matrix, forcing them apart. As a result, the lignite char is distinguished by a layer-like or lamellar morphology (Figure 1). Careful examination of the surfaces of these layers shows them to be covered with fine spherical droplets, shown in detail in Figure 2. From their discrete nature, as well as the fact that, in general, the droplet wetting angle is greater than 90°, it appears as though these droplets did not wet the surface of the char particle when they were molten. Their principal component is calcium; small amounts of sodium, magnesium, and aluminum are also present. These small droplets probably result from the melting of inorganic compounds which

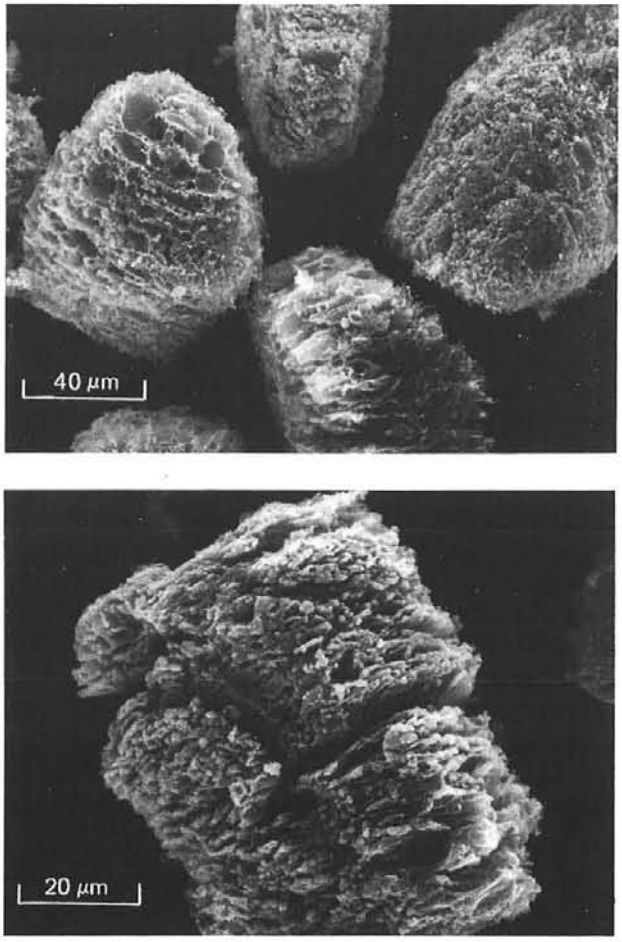

Figure 1. SEM images of lignite char particles sampled after 75-ms residence time at 1550 K and 6-mole-% O_2 showing their lamellar structure.

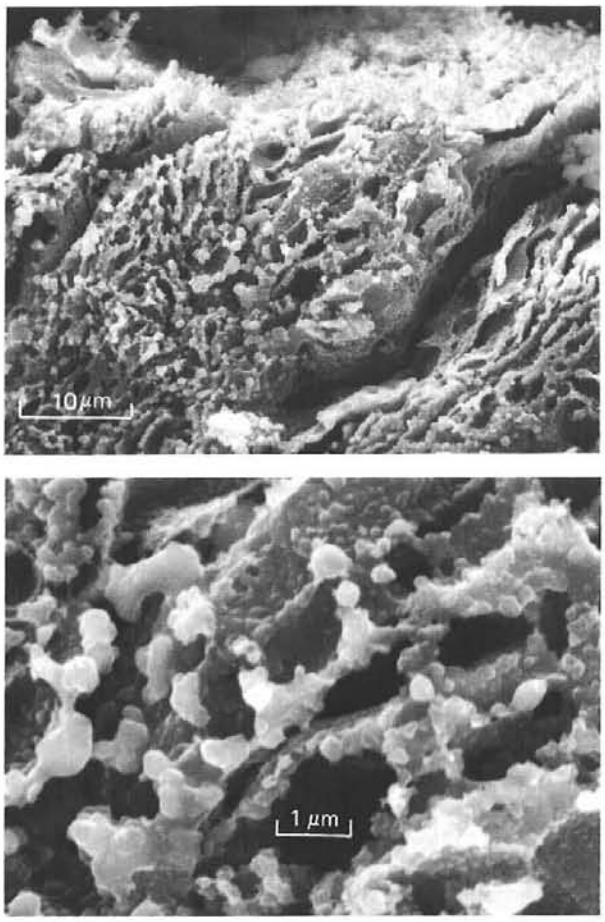

Figure 2. Surface of lignite char lamellae showing mineral droplet decoration and the discrete nature of the droplets.

were in intimate association with the original plant material. The borders of the lamellae are decorated with spherical mineral particles ~ 1 μm in diameter, which in many instances show evidence of coalescence. The spherical shape of these particles indicates that they were molten. The principal components of these solidified mineral droplets are aluminum, silicon, iron, and sulfur. Those particles which have coalesced also contain significant quantities of calcium.

At longer residence times, ~100 ms, the sampled char shows significant differences, both in the form and degree of surface coverage by solidified mineral particles, as well as in the particle morphologies. Spherical mineral matter particles, either free-standing or attached to small char particles, are apparent. At this stage, calcium is the dominant element in the surface mineral matter. Small amounts of sodium, magnesium, aluminum, silicon, and iron make up the remainder of the inorganic species.

At the longest residence times, ~125 ms, the layered structure which characterized earlier lignite char particles is not nearly so prominent either because of extensive surface oxidation and/or the formation of a thick mineral coating. Large, free-standing mineral particles (up to 20 μm) and minerals attached to char fragments are also present in this sample, Figure 3. The composition of these free-standing mineral particles appears to be dominated by calcium. Furthermore, their composition appears to be quite different from the mineral species which adhere to the char.

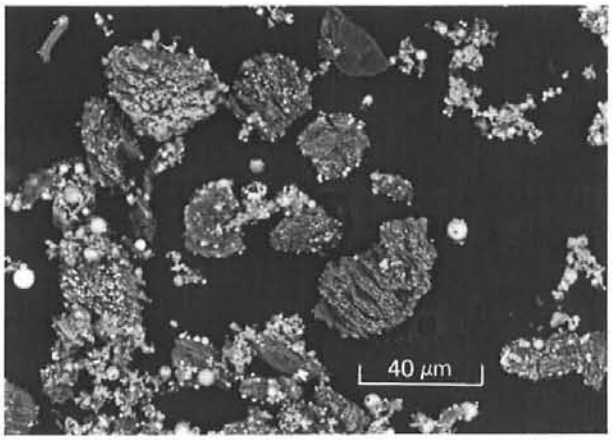

Figure 3. Backscatter SEM image of lignite char sample (125-ms residence time) showing large free-standing mineral clusters.

In summary, in contrast to the behavior during combustion of both the high and low volatile bituminous coals, in which volatiles escape by deforming the soft, plastic matrix, there is no evidence for extensive plastic deformation of the lignite matrix. Volatiles appear to escape from lignite particles by forcing apart the layered lignite structure. The extent of surface mineralization of the lignite char particles and the complex, heterogeneous nature of the minerals is very different from the bituminous chars. Extensive melting of the minerals was readily apparent in the 75-ms lignite sample, something that was not seen in the bituminous char until 100 ms, and then only on a sporadic basis. Even more striking is the quantity of visible mineral matter associated with the lignite chars as opposed to the bituminous chars, even though the ash content of the raw bituminous coal is significantly larger than that of the lignite coal (20.7 wt% ash vs 7.8 wt%). Undoubtedly, the small calcium-containing droplets which decorate the inner surfaces of the char particles are responsible for the majority of this external ash. As the char surface is oxidized away, more of these droplets are exposed. Furthermore, calcium may also depress the melting point of other mineral phases (e.g., silica, alumino-silicates) and act as a flux, lowering the surface tension and viscosity of the liquid phases and permitting them to flow and coalesce more readily.

Reference:

1. Proceedings of the Conference on Effects of Coal Quality on Power Plants (Electric Power Research Inst., Atlanta, GA, 1987).

Scanning Transmission Electron Microscopy of Coal: The Identification of Submicron Mineral Particles in a Bituminous Coal

Scanning transmission electron microscopy has been applied to identify the presence of submicron iron-oxide particles imbedded in the organic matrix of unreacted coal particles. In the past, the appearance of such species in partially-reacted char samples has been cited as evidence of a vaporization-condensation process involving iron-containing species. This new evidence indicates that recourse to such a mechanism may be unnecessary.

D. A. Nissen and F. A. Greulich

Measurements of the char matrix background x-ray spectrum during SEM studies of mineral-matter transformation have periodically shown a weak iron signal which could not be associated with any identifiable mineral matter. Recent laser-spark spectrographic data have been interpreted as indicating the presence of a highly dispersed, low level quantity of iron in a raw Kentucky coal (Kentucky #11, bituminous).[1] In an effort to identify the source of these data, a detailed investigation of a sample of raw Kentucky coal was done on the Scanning Transmission Electron Microscope (STEM). Samples were prepared by crushing coal particles between glass microscope slides and then lifting the fragments from the glass with acetone-softened nitrocellulose tape. The surface of the tape was dissolved in acetone leaving the coal fragments supported by the carbon film. We have found very small (~100 nm) crystals dispersed in the coal matrix. Elemental analysis, using a thin window detector, showed that the principal component of these crystals was iron. The presence of oxygen was also indicated, which leads to the conclusion that these small mineral crystals are probably iron oxides. In spite of the fact that automated image analysis of a sample of this coal showed that appreciable quantities of iron/sulfur compounds were present, principally as pyrite (46%) and iron sulfate (7.5%), there was no indication that sulfur was associated with these particles. Submicron particles (< 1 μm) have been detected before in coal by electron microscopy, principally calcite, pyrite, and various clays[2-5] but, as far as we know, this is the first report of submicron iron-oxide particles. These results seem to indicate that because submicron refractory metal oxide particles are present in the coal matrix initially, submicron ash particles can be formed directly without recourse to a vaporization-condensentation mechanism.

References:

1. D. K. Ottesen, "*In Situ* Real-Time Analysis of Particulates," *Quarterly Project Report* (Sandia National Laboratories, Livermore, CA, 1/1/87-3/1/87).

2. R. A. Strehlow, L. A. Harris, and C. S. Yust, Fuel **57**, 185 (1978).

3. K. C. Hseih and C. A. Wert, Materials Science and Eng. **50**, 117 (1981).

4. L. A. Harris, D. N. Braski,and C. S. Yust, "Electron Microscopy of Coal Constituents," *Microstructural Science, Vol. 5*, J. D. Braun, H. W. Arrowsmith, and J. L. McCall, eds. (Elsevier, New York, NY, 1977), p. 351.

5. J. S. Lin, R. W. Hendricks, L. A. Harris, and C. S. Yust, J. Appl. Cryst. **11**, 621 (1978).

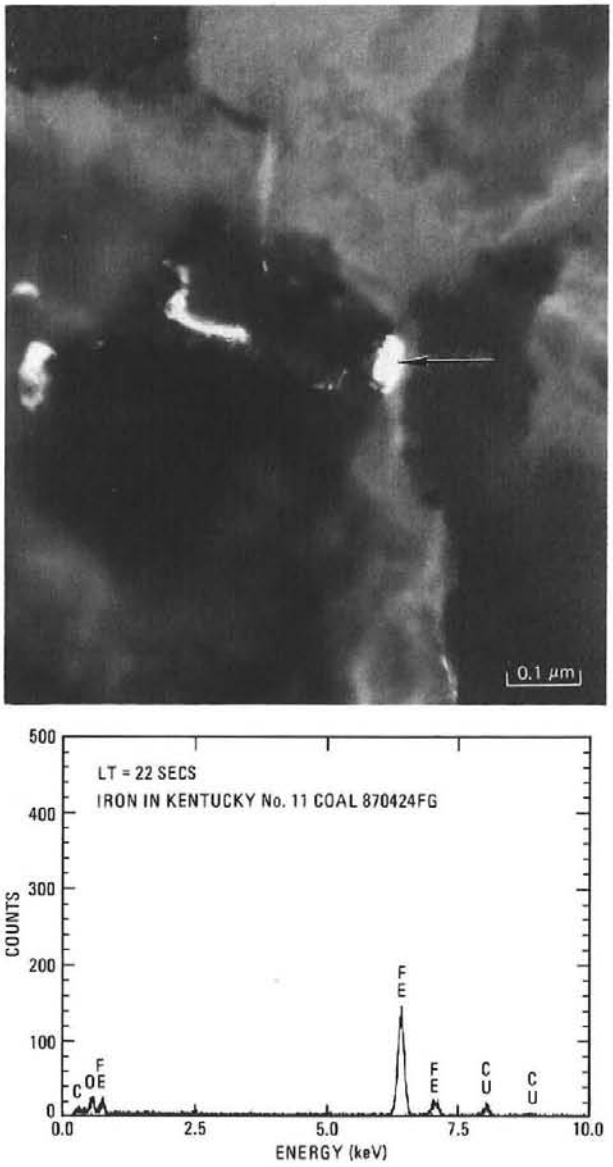

Figure 1. Transmission electron micrograph (dark field) and X-ray spectrum of an iron-oxide particle (arrow) embedded in coal.

Thermal decomposition measurements made on energetic materials (propellants and explosives) provide insight into the fundamental chemistry governing their sensitivity and performance. This photograph shows the interior of a high-vacuum system. The glowing furnace at the bottom of the photograph thermally decomposes energetic materials to create a molecular beam of molecular fragments. A beam flag (shown above the furnace) blocks the flow of molecules to provide a background reference. See related article on pages 9-2 through 9-5.

Energetic Materials

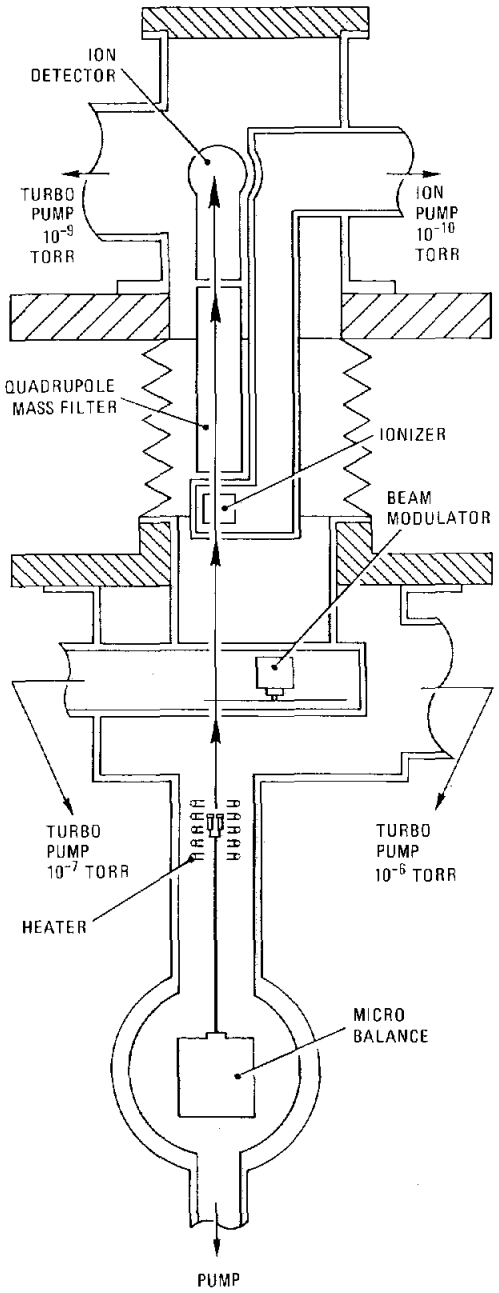

A schematic diagram of the simultaneous thermogravimetric modulated beam mass spectrometer (STMBMS) is shown at the left. In this instrument, small (10 mg) samples of propellant are placed in a reaction cell whose temperature can be accurately controlled. As the sample is heated and begins to decompose into gas phase products, the change in force due to the gas leaving the cell is determined by the microbalance. Once the gas molecules exit the reaction cell, they undergo no further collisions, due to the reduced background pressure created with the turbo pumps, and a fraction (indicated by the arrow) is detected with the mass spectrometer which consists of the ionizer, mass filter, and ion detector. The mass spectrometer helps determine the identity and amount of each type of gas decomposition product being formed in the reaction cell as a function of time during the decomposition. Using the beam modulator, only molecules from the reaction cell are detected. The instrument also allows the approximate molecular weight of the gas products to be determined by time-of-flight velocity spectra measurements.

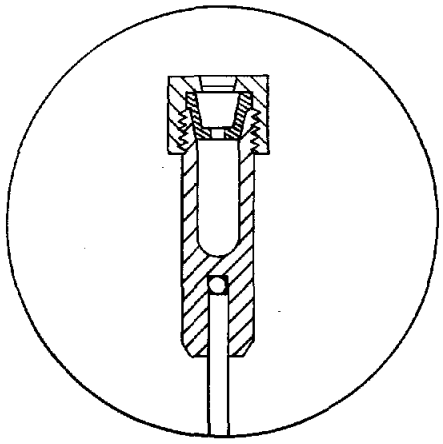

Cross section of the reaction cell showing the location of the thermocouple and exit orifice.

Section 9
Energetic Materials

A research program involving the combustion of energetic materials emphasizes studies of a fundamental nature that are directed towards understanding the combustion chemistry and physics of energetic solids and liquids. The objective of the research is to apply advanced laser diagnostics and computer modeling to propellant combustion with the ultimate goal of improving propellant performance and establishing an understanding that could lead to the development of new propellants for guns and rockets. Program sponsorship is derived primarily through a Memorandum of Understanding between the Department of Energy and the Department of the Army.

The experimental effort consists of solid-propellant thermal decomposition and deflagration studies as well as liquid mono-propellant ignition and combustion studies. Related gas-phase flame experiments at reduced pressure are designed to investigate the two-stage flame character exhibited by many solid propellants, including chain-branching chemistry and thermal diffusion effects. Thermal decomposition studies of solid propellants using a modulated molecular-beam mass spectrometer are carried out to determine quantitatively the molecular fragments and reaction products that result from the decomposition. Combustion experiments emphasizing deflagration of solid and liquid propellants under conditions of varying pressure and propellant composition are being performed using both spatially resolved and planar-imaging laser diagnostics.

A strong modeling program accompanies the experimental effort. Quantum chemistry calculations provide information about thermochemical heats of formation and possible reaction pathways for the decomposition of energetic molecules. Solid and liquid propellant deflagrations are being modeled analytically and through the use of multi-dimensional thermochemical codes. These studies include liquid mono-propellant droplet combustion calculations using a new code capability derived from hydrocarbon combustion work.

Thermal Decomposition Mechanisms of RDX†

The RDX pyrolysis products are formed via two reaction channels. The products from one channel are associated with N-N bond breaking and include H_2O, NO, NO_2, and hydroxy-s-triazine. The products from the other channel are associated with oxygen atom transfer from the NO_2 group to the carbon atom and include N_2O, H_2CO, H_2O, and 1-nitroso-3,5-dinitro-1,3,5-triazacyclohexane.

R. Behrens, Jr.

Information on the thermal decomposition mechanisms of RDX

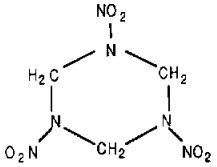

has been obtained by using deuterated and $^{15}NO_2$-labeled RDX analogues in the simultaneous thermogravimetric modulated beam mass spectrometry (STMBMS) and time-of-flight (TOF) velocity spectra experiments.

The experimental apparatus and analysis techniques have been described in detail previously.[1] Briefly, the pyrolysis products are measured with a quadrupole mass spectrometer, the TOF velocity spectra measurements help associate the ion signals measured with the mass spectrometer with the pyrolysis products formed in the reaction cell, and the STMBMS measurements provide quantitative data.

The results from the RDX decomposition are summarized in Table I. The molecular formulas of the ions formed from the different pyrolysis products along with the molecular weights of corresponding ion signals from the protonated, deuterated, and $^{15}NO_2$-labeled RDX are shown. The molecular weight of each pyrolysis product determined from the TOF velocity spectra is also shown in Table I. The combination of the ion formulas and the molecular weights of the pyrolysis products provide the formulas of the pyrolysis products shown in the last column of Table I. The partial pressure of RDX and each of its pyrolysis products generated during the decomposition of an 8-mg RDX sample are shown in Figure 1(a). The pyrolysis products can be divided into two temporally dependent groups. The products from the first group are shown in Figure 1(b), appear at 187°C, and gradually fall to

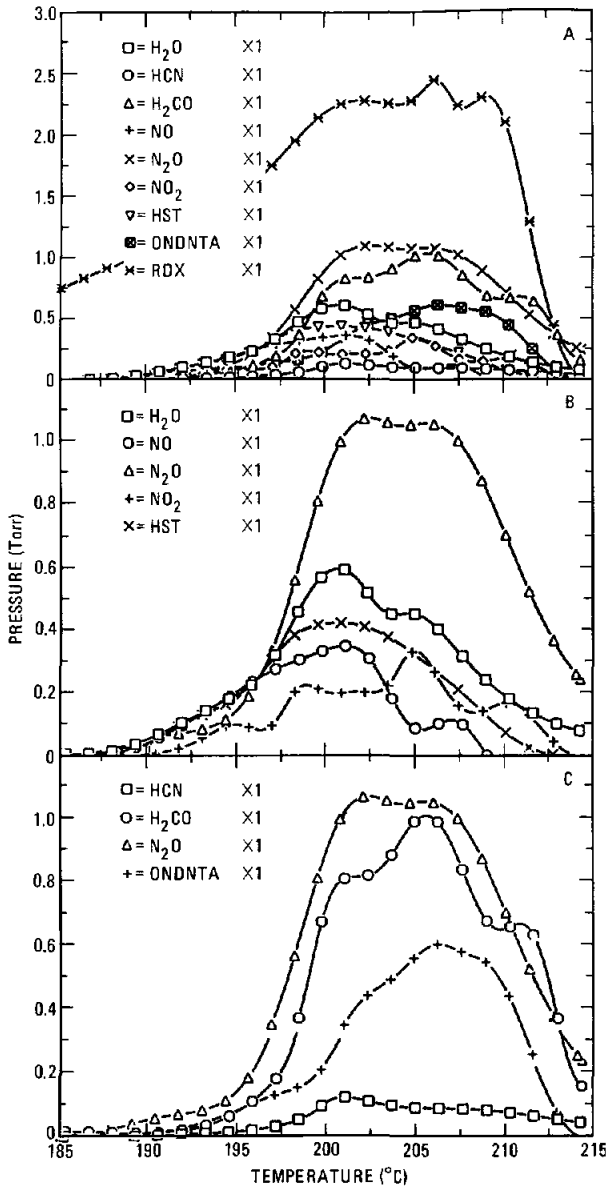

Figure 1. The partial pressures of RDX and the pyrolysis products from two different decomposition channels are shown. All of the products are shown in (a), the products associated with N-N bond fragmentation are shown in (b), and the products associated with oxygen atom transfer and ring fragmentation are shown in (c).

†*Proceedings of the 24th JANNAF Combustion Meeting* (CPIA, Baltimore, MD, 1987), p. 333.

Table I
RDX and RDX pyrolysis product molecular formulas, molecular weights and associated ion signal formulas and molecular weights from protonated, deuterated, and $^{15}NO_2$-labeled RDX

	Ion Properties			Pyrolysis Product Properties	
Formula*	Molecular Weight of Ion from Labeled Compounds			Molecular Weight	Formula
	RDX-h_6	RDX-d_6	RDX-$^{15}NO_2$		
H_2O	18	20	18	18	H_2O
HCO	29	30	29	30	H_2CO
NO	30	30	31	30	NO
N_2O	44	44	45	44	N_2O
NO_2	46	46	47	46	NO_2
HONO	47	48	48		
$H_2C_2N_2O$	70	72	70	97	$H_3C_3N_3O$
$N_3C_3N_3O$	97	100	97	97	$H_3C_3N_3O$
$H_4C_2N_4O_3$	132	136	134	206	$H_6C_3N_6O_5$
$H_4C_3N_4O_2$	128	132	129	222	RDX

*The stoichiometrics for the RDX pyrolysis products are substantiated by correlating ion signals from isotopically-labeled analogs.

zero as the sample is consumed. The product concentrations from the second group, shown in Figure 1(c), increase rapidly at 197°C and fall more rapidly than the first group as the sample is consumed. Nitrous oxide (N_2O) and water (H_2O) are common to both groups.

Each of these groups represents a different decomposition channel. The products of the first decomposition channel include NO, H_2O, NO_2, N_2O, and hydroxy-s-triazine (HST).

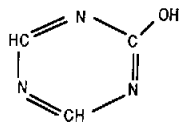

These are the first products to appear during the decomposition and fall off earlier than the products associated with the second decomposition channel. The products formed in the first decomposition channel are consistent with the RDX dissociating via N-N bonds. For example, the presence of HST indicates that the ring structure remains intact as the N-N bonds break to form NO_2 and N_2O, initially. Subsequent reactions produce the NO and H_2O.

The products associated with the second decomposition channel include H_2CO, N_2O, HCN, and 1-nitroso-3,5-dinitro-1,3,5-triazacyclohexane (ONDNTA).

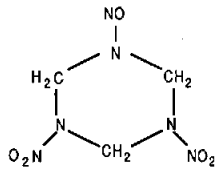

These products, especially H_2CO and N_2O, are consistent with RDX dissociating via oxygen-atom transfer from the NO_2 group to the carbon atom. The formation of ONDNTA and the delay between the release of N_2O and H_2CO is similar to the behavior of the HMX condensed-phase autocatalytic decomposition.

In summary, products associated with two different decomposition channels are observed in the RDX decomposition measurements. Products from one channel are associated with decomposition via rupture of the N-N bond, and the products from the other channel are associated with the oxygen-atom transfer to a carbon atom.

Reference:

1. R. Behrens, Jr., Rev. Sci. Instr. **58**, 451 (1987).

Thermal Decomposition Mechanisms of HMX†

The pyrolysis products formed during the thermal decomposition of HMX between 200°C and 260°C are characterized by oxygen-atom transfer from the NO_2 group to the carbon atom. The products are formed in an autocatalytic condensed-phase reaction. The major products include: H_2O, H_2CO, N_2O, NO, $H_6C_2N_2O$, and 1-nitroso-3,5,7-trinitro-1,3,5,7-tetraazacyclooctane.

R. Behrens, Jr.

Information on the thermal decomposition mechanisms of HMX

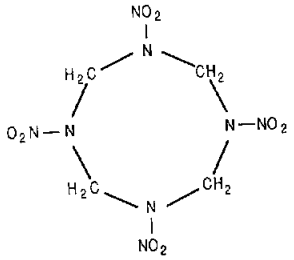

has been obtained by using deuterated and $^{15}NO_2$-labeled HMX analogues in the simultaneous thermogravimetric modulated-beam mass spectrometry (STMBMS) and time-of-flight (TOF) velocity spectra experiments.

The experimental apparatus and analysis techniques have been described in detail previously.[1] Briefly, the pyrolysis products are measured with a quadrupole mass spectrometer, the TOF velocity spectra measurements help associate the ion signals measured with the mass spectrometer with the pyrolysis products formed in the reaction cell, and the STMBMS measurements provide quantitative data.

The results from the HMX decomposition are summarized in Table I. The molecular formulas of the ions formed from the different pyrolysis products, along with the molecular weights of corresponding ion signals from the protonated, deuterated, and $^{15}NO_2$-labeled HMX, are shown. The molecular weight of each pyrolysis product determined from the TOF velocity spectra is also shown in Table I. The combination of the ion formulas and the molecular weights of the pyrolysis products provides the formulas of the pyrolysis products shown in the last column of Table I.

The partial pressure of each pyrolysis product generated during the decomposition of a 9-mg HMX sample is shown in Figure 1. The main products, shown in the upper graph in Figure 1, are N_2O, H_2CO, and H_2O. The minor products, shown in the lower graph, include HCN, an amide, 1-nitroso-3,5,7-trinitro-1,3,5,7-tetraazacyclooctane,

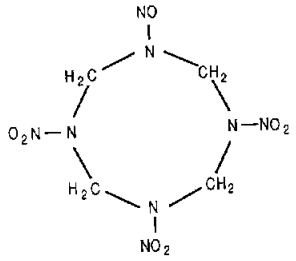

and a species at mass 74 that has a stoichiometry of $H_6C_2N_2O$. Note that although this last product has the same molecular weight as the methylenenitramine monomer ($H_2C = N - NO_2$), the deuterated product shows that it contains six hydrogen atoms and is not the monomer.

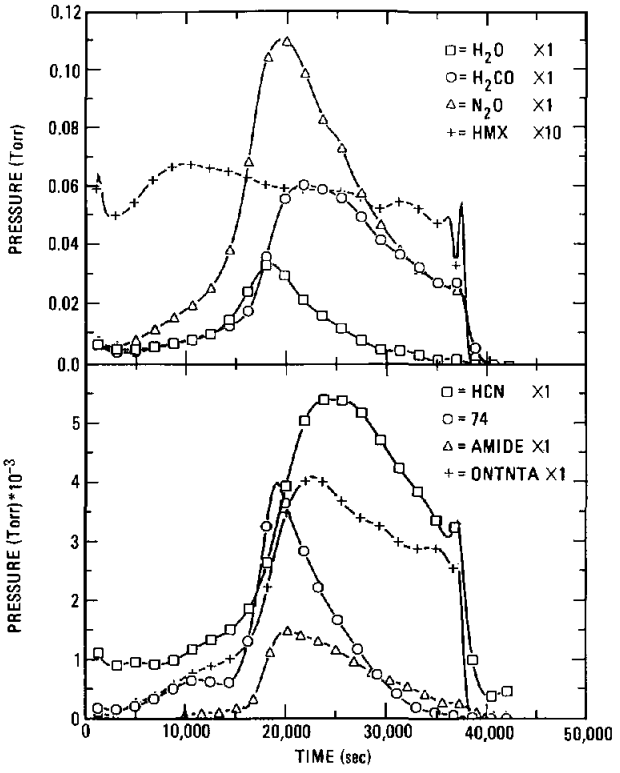

Figure 1. The partial pressures of HMX and its pyrolysis products during an isothermal decomposition at 211°C are shown as a function of time.

†*Proceedings of the 24th JANNAF Combustion Meeting* (CPIA, Baltimore, MD,1987), p. 333.

Table I

HMX and HMX-pyrolysis product molecular formulas, molecular weights, and associated ion signal formulas and molecular weights from protonated, deuterated, and $^{15}NO_2$-labeled HMX

Formula	Ion Properties Molecular Weight of Labeled Compounds			Pyrolysis Product Properties Molecular Weight	Formula
	HMX-h_8	HMX-d_8	HMX-$^{15}NO_2$		
H_2O	18	20	18	18	H_2O
HCN	27	not obs.	27	27	HCN
HCO	29	30	29	30	H_2CO
NO	30	30	31	30	NO
N_2O	44	44	45	44	N_2O
H_4C_2NO	58	62	58	~116	
H_5C_2NO	59	64	59	not meas.	
$H_6C_2N_2O$	74	80	75	74	$H_6C_2N_2O$
$H_3CN_2O_2$	75	78	76	296	HMX
$H_4C_2N_4O_3$	132	136	134	280	$H_8C_4N_8O_7$
$H_4C_2N_4O_4$	148	152	150	296	HMX

After gas evolution ceases, approximately four percent of the sample remains as a nonvolatile residue. Subsequent heating shows that 90% of the residue decomposes to lighter gas products between 280°C and 500°C.

The temporal behavior of the partial pressures of the pyrolysis products during the decomposition is indicative of an autocatalytic decomposition between 200°C and 260°C. The presence of N_2O and H_2CO as major products suggests a mechanism characterized by oxygen-atom transfer to the carbon atom and rupture of the C-N ring bond. However, careful examination of the data in Figure 1 shows that the ratio of the N_2O and H_2CO partial pressure changes during the decomposition, and amides, characterized by the R_2-N-(C=O) -R group, are also observed during the decomposition. This suggests that the N_2O and H_2CO products may not be formed directly from HMX during the decomposition.

Reference:

1. R. Behrens, Jr., Rev. Sci. Instr. **58**, 451 (1987).

Theoretical Studies of the Chemical Reactions Involved in the Ignition of Nitramines

The chemical reactions involved in the ignition and combustion of energetic materials are not well understood, due to the short time scales, high temperature, and pressures involved. Therefore, theoretical modeling techniques have been applied to gain an insight into the various processes involved in the ignition of a nitramine, cyclotrimethylenetrinitramine (RDX).

C. F. Melius

To examine the ignition of RDX, a computational model was solved for various starting temperatures, T_0, ranging from 500 K to 1400 K, and one-to-1000 atmospheres. Figure 1 illustrates a typical result from a computation of RDX ignition with starting conditions of 573 K and one atmosphere. As seen in the figure, two ignition stages are predicted by the model and are consistent with experimental observations. At low temperatures, pressure has little effect on the first-stage-ignition delay time, but significantly decreases the time between the first and second stages of ignition. At higher initial temperatures, increases in pressure significantly decreased both ignition times. Furthermore, higher starting temperatures produce more complex profiles than that shown in Figure 1; specifically, the temperature does not necessarily rise monotonically with time. As an example, the temperature-time profile for T_0 = 850 K shows an initial drop in temperature (due to heat absorbed during RDX thermal decomposition) and reaches a minimum before rising to a maximum of almost 1000 K associated with first-stage ignition. Following this ignition step, the temperature decreases nearly 100 K before abruptly rising at the onset of the second-ignition stage.

The resulting times to first-stage ignition, τ_1, and second-stage ignition, τ_2, are shown in Figure 2 as an inverse function of the starting temperature, T_0. The ignition delay time for the first stage, τ_1, follows predicted behavior, decreasing monotonically with increasing temperature. The effective activation energy for first-stage ignition, estimated from $\tau_1 \approx \exp(-\Delta E/RT)$, is 28 to 34 kcal-mol^{-1} at low starting temperatures ($T_0 < 700$ K), but becomes smaller at higher T_0, due in part to significant temperature drops during the initial RDX decomposition at the higher T_0. The second stage ignition time, τ_2, on the other hand, yields very unusual results. From Figure 2, one can see that τ_2 decreases as T_0 goes from 500 K to 600 K, then increases from 600 K to 850 K, and finally decreases monotonically with T_0 above 850 K. The unexpected behavior of τ_2 is thought to be a result of the temperature going through a minimum following first-stage ignition.

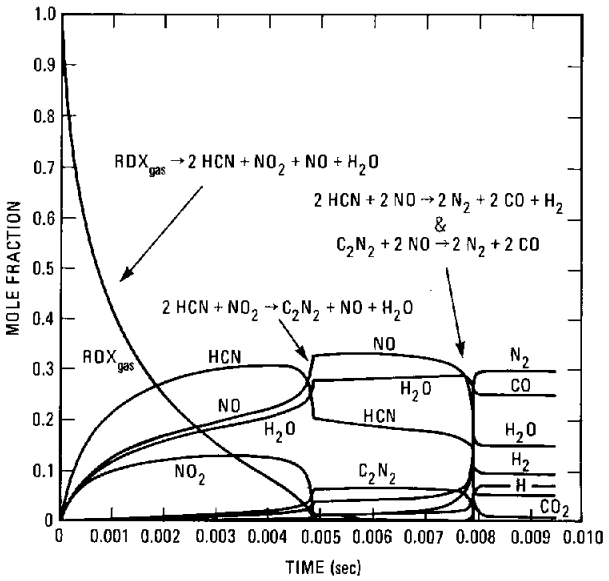

Figure 1. Temperature and major species concentration (mole fraction) profiles as a function of time for the ignition of gaseous RDX at a constant pressure. Starting conditions were T_0 = 573 K and one atm.

The following paragraphs discuss the net chemical reaction occurring during each stage of ignition (see Figure 1). Initially, gaseous RDX undergoes thermal decomposition via two reactions, RDX → 3 CH_2O + N_2O and RDX → 3 HCN + 3 HONO. At low T_0 and early times, the first reaction proceeds, but eventually the second dominates and is responsible for the first-stage ignition. During the first stage ignition, the dominating net chemical reaction is 2 HONO → NO + NO_2 + H_2O followed by CH_2O + NO_2 → H_2O + NO + CO and HNO + HONO → H_2O + 2 NO. The critical step (based on sensitivity analysis) leading to the first-stage ignition is

the thermal decomposition of HONO to form OH and NO. These reactions represent the conversion of weakly bound hydrogen (i.e., all C-H bonds except that in HCN) to water. Between 700 K and 1100 K, CH_2O is initially converted to CO by OH and NO_2. Later, the CH_2O is converted to CO by reacting with NO_2 and NO.

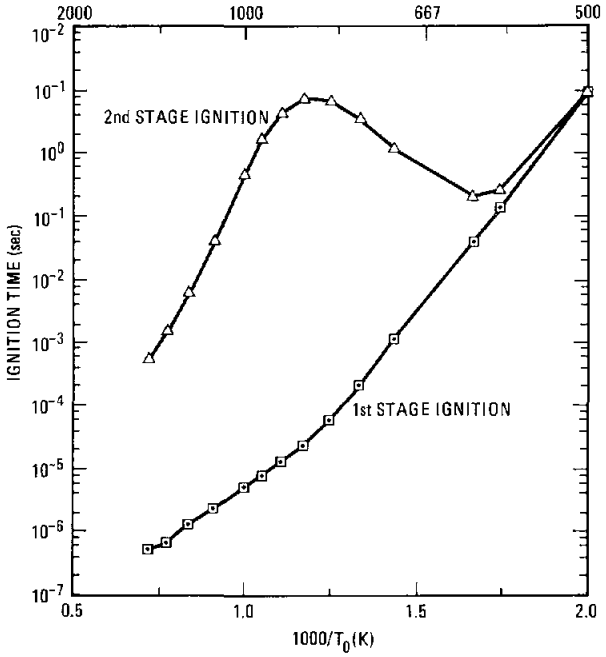

Figure 2. Dependence of gaseous RDX ignition times on the initial starting temperature T_0. The pressure was held fixed at one atmosphere.

During the time leading to the second ignition, the dominating reactions are the conversion of NO_2 to NO, that is, $2\,HCN + NO_2 \rightarrow C_2N_2 + NO + H_2O$, $CO + NO_2 \rightarrow CO_2 + NO$, and $2\,NO_2 \rightarrow 2\,NO + O_2$. At higher temperatures, the reaction $2\,HCN + 3\,NO_2 \rightarrow 2\,CO + 3\,NO + H_2O + N_2$ becomes important.

Having converted the NO_2 to NO, second-stage ignition occurs, with the conversion of NO to N_2 via $C_2N_2 + 2\,NO \rightarrow 2\,CO + 2\,N_2$ and $2\,HCN + 2\,NO \rightarrow 2\,CO + 2\,N_2 + H_2$. In addition, N_2O (which has remained relatively inert until this point) is converted to N_2 via $N_2O + H_2 \rightarrow N_2 + H_2O$, followed by conversion of some CO to CO_2 via $H_2O + CO \rightarrow CO_2 + H_2$.

The critical step (based on sensitivity analysis) leading to the second-stage ignition is the thermal decomposition of N_2O to form N_2 and O. In the second-stage ignition, the conversion of NO to form N_2 and CO is initially by the CN radical via $CN + N_2O \rightarrow NCO + N_2$ and $NCO + NO \rightarrow N_2O + CO$. However, at later times, the N radical becomes dominant.

The results indicate that it is necessary to remove the NO_2 before the second-stage ignition can occur. For instance, it is observed that the temperature drops temporarily in the plateau region while the NO_2 is being consumed. This is consistent with the negative sensitivity of RDX decomposition to form NO_2. Thus, NO_2 acts as an inhibitor to the chemical reactions leading to the second-stage ignition.

The ignition of RDX exhibits multiple stages, with non-monotonic behavior in the temperature rises and ignition delay times. One should expect this behavior to be exhibited for other nitramines such as HMX as well. While much has been learned about the ignition chemistry of nitramines from these calculations, much remains to be done, both with respect to verifying and modifying the elementary chemical reactions used in the model and developing more realistic environments. With respect to this latter point, spatially-independent ignition results presented here are being incorporated into stationary as well as time-dependent flame codes, to treat the effects of heat and mass transport.

Impact of Radical Reactions on Propellant Ignition

Species that participate in low activation bimolecular reactions are found to alter transient characteristics of propellants significantly.

R. C. Armstrong and M. L. Koszykowski

The Denison and Baum (D&B) model, a classical model commonly used in propellant-ignition dynamics, involves a single-step, endothermic solid-to-gas pyrolysis (solid → N·), followed by a single-step, exothermic, gas-phase flame (N· → products). Both of these reactions must have a high-activation energy for the solid to be stable at room temperature and for the customary thin gas-flame to form, standing off the gas/solid surface. Partly because of this high-activation-energy construction, the steady burning solution comes easily and gives a compact and realistic form for the steady burning rate. Unfortunately, also because of this high-activation-energy assumption, the time-dependent behavior of the model is exceedingly stiff (i.e., responsive) so much so that it is difficult to ignite, and once ignited, difficult to maintain. Figure 1 illustrates this for radiant ignition of such a propellant model. At time t = 0, the propellant has been ignited by radiation impinging on the solid surface for a time long enough to establish a steady burning condition—at which time the radiation is suddenly terminated. The result of using the D&B model is that the propellant extinguishes and never reignites. (The phenomenon in question is not new and is usually termed *deradiative extinction*.

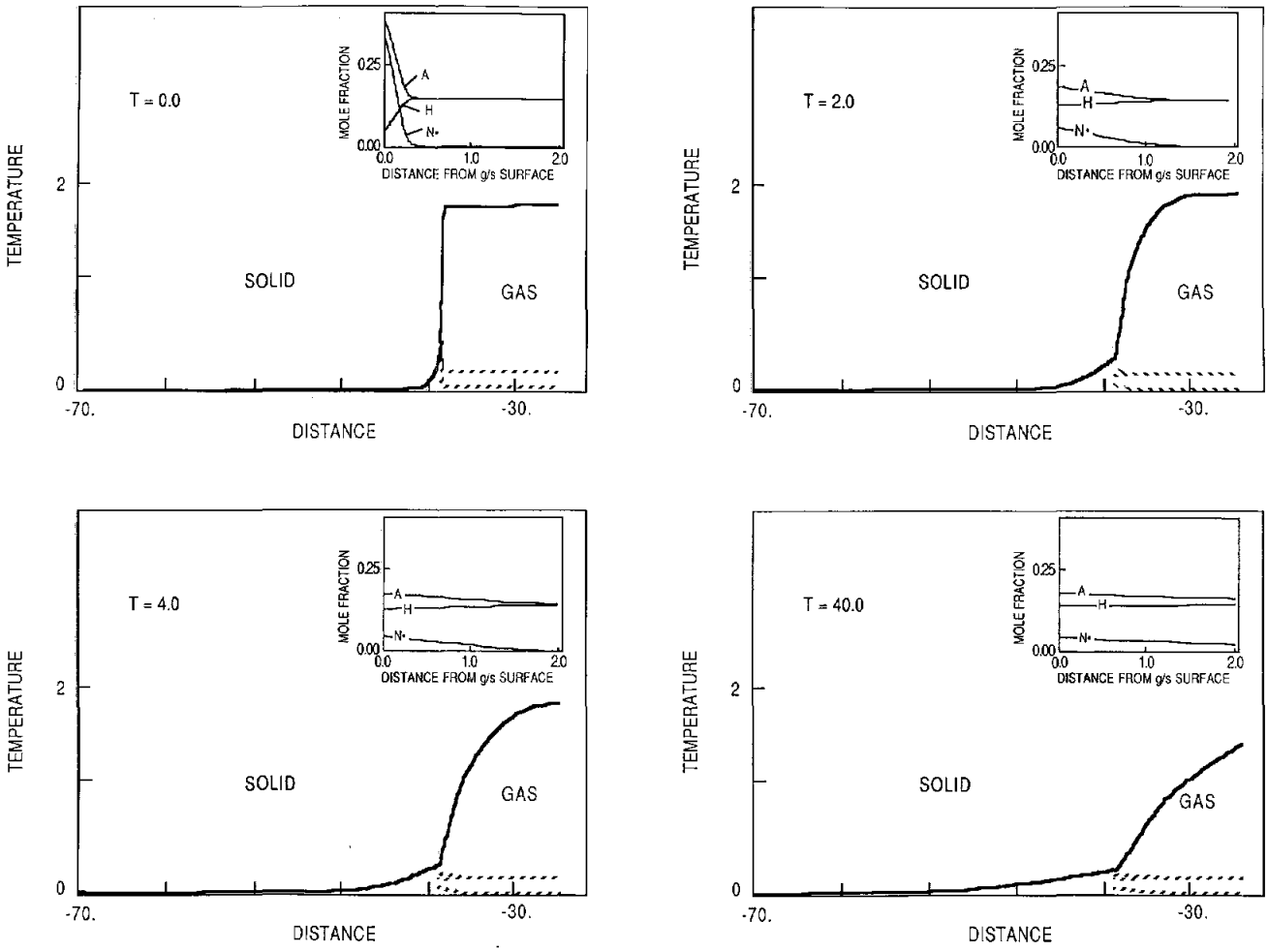

Figure 1. Radiant ignition of a stiff propellant model. This model does not sustain combustion after a transient radiation pulse.

It serves as a useful benchmark tool for investigating the dynamics of energetic materials.) Other transients much less severe than this produce the same result, suggesting that this model is not realistic, at least for time-dependent behavior.

An essential component in the detailed analysis of gas flames is low-molecular-weight, low-activation-energy radical reactions. Shown in Figure 2 is the same transient as in Figure 1 for a proposed reaction scheme involving radical reactions at the surface and in the gas phase. The previous high-activation-energy reactions are still present; however, each reaction produces a radical (A at the surface and H in the gas). The H can diffuse against the flow to react with the surface if it is not first absorbed via recombination (H+A). As in strictly gas-phase combustion, the recombination reaction plays a major role and in this particular case ensures that the chemical routes during steady combustion are dominated by the D&B reactions. Thus, the steady burning rate is little changed from that of the original D&B prediction. Figure 2, however, shows that the unsteady behavior of this system, containing an insignificant quantity of radicals for the original D&B reactions, makes the difference between a propellant that extinguishes and one that attains a steady burn long after the ignition event is over. The explanation for this behavior is as yet unconfirmed. It seems that the inherent gain in stability due to radicals is tied less to an exothermicity in their surface or recombination reactions than to the liberation from the surface of species (N·) that can diffuse to regions of the gas still hot enough to allow them to react.

In any case, it is clear that even models like the D&B model which do a good job of predicting steady behavior in energetic materials, may be incapable of predicting the outcome of simple transients. All propellant models have at least two solutions: one burning, one not. It has been shown here that a change in chemistry insignificant to either the burning or nonburning solution can dramatically effect their response to transients, an important criterion when evaluating the relative merits of different models.

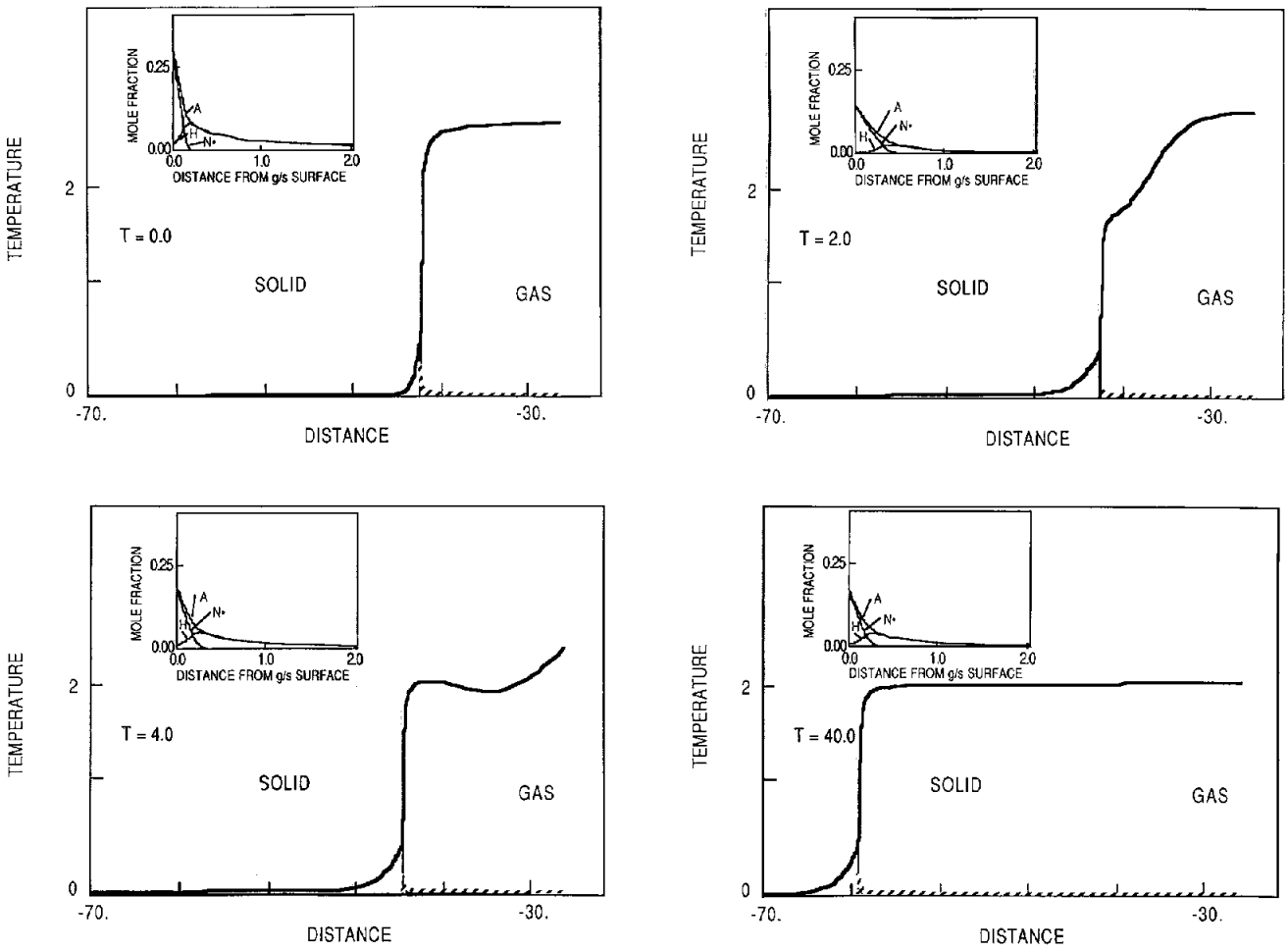

Figure 2. Proposed reaction scheme involving radical reactions at the surface and in the gas phase. This model sustains combustion after a transient radiation pulse.

Diffusional/Thermal Coupling and Intrinsic Instability of Solid Propellant Combustion I. Cellular Instability†

Intrinsic instability in the deflagration of a homogeneous solid propellent is considered through an asymptotic analysis for large, overall activation energies. We relax the usual assumptions of quasi-steadiness and quasi-planarity for the gas phase to show that steady, planar deflagration may be unstable not only to pulsating disturbances, but also to (time-independent, nonplanar) cellular perturbations as well.

S. B. Margolis and F. A. Williams*

Intrinsic instabilities are a well-known feature of solid propellant combustion. That is, the steady, planar burning of the propellant may be unstable even in the absence of any acoustic or velocity disturbances. This phenomenon was first identified by Denison and Baum,[1] who showed that for sufficiently large values of parameters related to the pyrolysis and overall gas-phase activation energies, the steady deflagration of the solid was unstable to small pulsating disturbances. Others have studied these phenomena, but they generally assume a quasi-steady and (quasi-planar) gas phase, whereas other studies which relax this assumption are primarily concerned with the coupled response to external pressure and/or velocity perturbations. Aside from the inability of a quasi-steady, gas-phase model to describe a high-frequency response, or to describe nonsteady deflagrations at very high pressures for which the gas-to-solid density ratio is not necessarily small, there is another limitation which apparently has not been considered; namely, the inability to model the effect of intrinsic gas-flame instability on the stability of the deflagrating solid. In the present work, we wish to incorporate the effects of diffusional/thermal flame instability on the overall intrinsic stability of the propellant.

In a previous study,[2] asymptotic models for homogeneous solid propellant combustion were presented which were valid in the intrusive limit that the gas-phase reaction zone was adjacent to the propellant surface, where a fraction of the propellant is pyrolyzed directly to product gases and the remainder sublimes and burns in the gas phase (Figure 1). Neither a quasi-steady nor a quasi-planar assumption was employed, and the stability of the deflagrating solid, therefore, depended on the properties of the gas phase. In particular, decreasing the gas-to-solid density ratio was shown to be destabilizing in the sense that the stability threshold becomes more accessible for given values of the remaining parameters. When this ratio is unity, the pulsating stability boundary for strictly condensed-phase combustion is recovered. Although this intrusive limit is a well-defined regime in propellant combustion, particularly at high pressures, the more general case in which a gas-phase preheat zone separates the propellant from the gas phase reaction zone is clearly of interest, also. Thus, in the present work, we extend one of these models to include the presence of a gas-phase preheat zone. In this regime, intrinsic gas-flame instability has a qualitatively more significant effect on the overall stability of the burning propellant than was the case in the intrusive limit described above. In particular, in addition to the pulsating instability which exists for both condensed and gaseous combustion, there exists a steady, cellular instability analogous to that which exists only for strictly gaseous combustion. That is, the basic solution corresponding to steady, planar burning may be unstable to either pulsating disturbances or to time-independent, but nonplanar, disturbances. We refer to the corresponding neutral stability boundaries, on which infinitesimal perturbations neither grow nor decay in magnitude as a function of time, as pulsating and cellular stability boundaries, respectively. In the latter case, the propellant surface becomes cellular in appearance as we cross the stability boundary, and the transverse wavelength of the disturbance may be interpreted as a measure of the cell size.

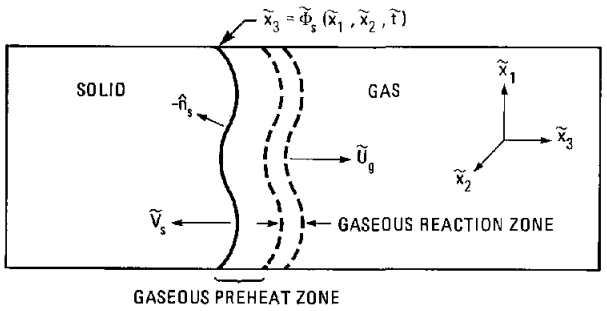

Figure 1. Model geometry.

†Combustion Science and Technology, accepted (1987).
*Princeton University, Princeton, NJ.

This prediction of a cellular-stability boundary, though well-known in strictly gaseous combustion, appears to be the first such theoretical prediction. There is, however, experimental evidence suggesting this phenomenon in the deflagration of ammonium perchlorate, in which a steady, three-dimensional, combustion-zone structure was observed.[4] Since cellular instability apparently does not occur in strictly condensed-phase combustion, for which only a pulsating stability boundary has been obtained, we conclude that the often-used assumption of quasi-steadiness and quasi-planarity for the gas phase filters out this phenomenon. On the other hand, as indicated above, a pulsating stability boundary is already known to exist for solid-propellant deflagration even when these assumptions are employed. We thus conclude that the pulsating instability obtained from models which employ these assumptions is related to the intrinsic instability of the pyrolyzing solid. Since pulsating phenomena occur in both gaseous- and condensed-phase combustion individually, it appears, in general, that intrinsic pulsating instability in solid propellant deflagration can arise from instability in either or both phases. Thus, the present model, which allows the gas flame to be any distance from the deflagrating solid, allows us to study, for the first time, the coupling of these two types of intrinsic pulsating instabilities. Indeed, we find from a linear-stability analysis, that when the gas-phase reaction zone lies far from the propellant surface, the stability boundaries (both pulsating and cellular) resemble those obtained for strictly gaseous flame propagation in appropriate limiting cases. In the limit that the gas-phase reaction zone approaches the propellant surface, the cellular stability boundary disappears, and the pulsating stability boundary is similar to that obtained for strictly condensed-phase combustion.

The general appearance of the cellular stability boundary may be determined analytically and is shown in Figure 2, where we have plotted the product of the deviation in the Lewis number Le from unity and a parameter Δ'_g, which is proportional to the gas-phase activation energy, versus the scaled transverse wavenumber k′ of the disturbance. Here, the scaled distance of the gas flame from the propellant surface is given by (-ln δ), where the parameter δ lies in the range $0 \le \delta < 1$. The dashed curve is the stability boundary which is obtained when the gas flame lies an infinite distance (δ = 0) from the propellant surface. We note, however, that this curve is only continuous at $k' = 0$ when δ = 0 if $\alpha\hat{\beta} = 1$, where α is the fraction of the propellant that sublimes and burns in the gas phase, and $\hat{\beta}$ is a heat-release parameter. Thus, in general, there is a region of nonuniformity for small

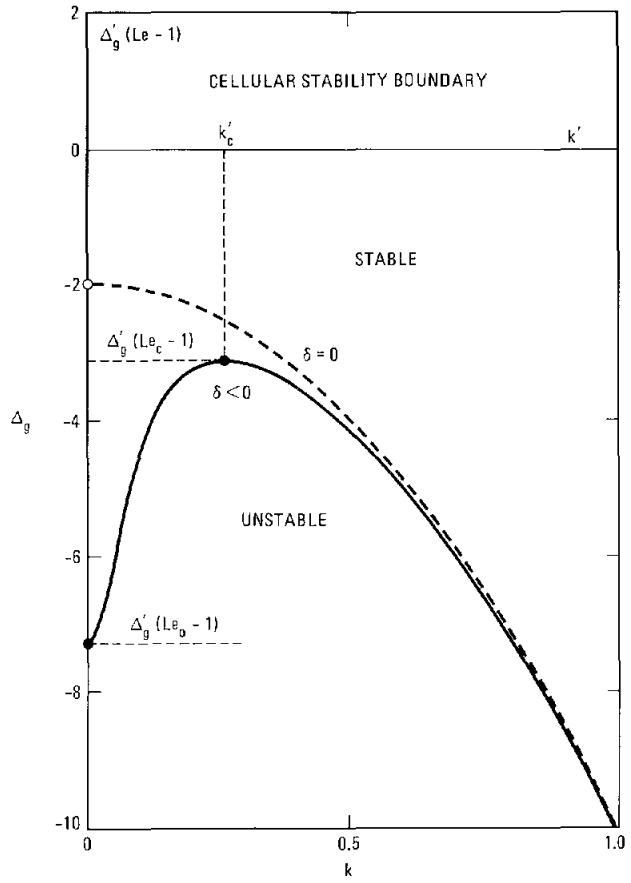

Figure 2. Qualitative appearance of the cellular stability boundary for large values of the flame standoff distance (- ln δ).

wavenumbers, and for large, but finite, values of this standoff distance, the cellular stability boundary has the qualitative appearance shown by the solid curve in that figure.

As the flame standoff distance decreases, the cellular stability boundary shifts downward. That this recession is most pronounced at smaller wavenumbers is consistent with the idea that the finite distance of the solid surface from the gas flame prevents the development of instabilities of long wavelengths and thereby enhances stability with respect to large-scale disturbances. Since the activation-energy parameter Δ'_g is large, we see that this stability boundary is very sensitive to the value of the Lewis number. In particular, as in the case of strictly gaseous combustion, this stability boundary is only encountered if the Lewis number is less than unity.

References:

1. M. R. Denison and E. Baum, ARS J. **31**, 1112 (1961).

2. S. B. Margolis and R. C. Armstrong, Comb. Sci. Tech. **47**, 1 (1986).

3. J. D. Hightower and E. W. Price, *Eleventh Symposium (International) on Combustion* (The Combustion Institute, Pittsburgh, Pa, (1967), p. 463.

Diffusional/Thermal Coupling and Intrinsic Instability of Solid Propellant Combustion. II. Pulsating Instability†

Through the relaxation of the usual assumptions of gas-phase quasi-steadiness and quasi-planarity in the study of intrinsic instability in the deflagration of solid propellants, it is shown that the onset of pulsating instability has a dual character which is related to the intrinsic instabilities of both the deflagrating solid and the gas flame.

S. B. Margolis and F. A. Williams*

Intrinsic instability in the steady, planar deflagration of a homogeneous solid propellant has been considered through an asymptotic analysis for large values of nondimensional overall activation energies for the surface pyrolysis and gas-phase combustion processes.[1] The results show that the previously known pulsating instability[2] is essentially connected with condensed-phase pyrolysis, and that new instability phenomena, which are associated with intrinsic gas-flame instability and which are sensitive to the value of the gas-phase Lewis number and to the distance of the gas flame from the propellant surface, arise. These results are obtained by relaxing the usual assumptions of quasi-steadiness and quasi-planarity for the gas phase, so that the coupling of intrinsic diffusional/thermal instabilities in the gas and solid phases becomes an integral feature of the model. The steady, planar deflagration thus may be unstable not only to pulsating disturbances, but also to (time-independent, nonplanar) cellular perturbations as well. We show that the onset of pulsating instability has a dual character which is related to the intrinsic instabilities of both the deflagrating solid and the gas flame, whereas the onset of cellular instability, apparently not predicted by previous theories for solid propellants, is clearly related to the stability of the gas flame. Appropriate limiting cases of the model retrieve the well-known pulsating and cellular neutral-stability boundaries for strictly gaseous combustion and the pulsating neutral-stability boundary for strictly condensed phase combustion.

Our model, and the cellular instability described above, is discussed in Part I.[3] In this article, we focus on the pulsating instability in solid propellant combustion. In the limit that the gas flame lies far from the propellant surface, there exists a pulsating boundary for Lewis numbers (Le) greater than unity and a cellular stability boundary for Lewis numbers less than unity (the latter recedes as the gas flame moves toward the propellant surface). In the opposite limit in which the gas flame approaches the propellant surface, only a pulsating boundary, which is independent of the Lewis number, is obtained.

Having deduced the behavior of the pulsating stability boundary for both small and large values of the gas-flame standoff distance, we now show how these stability boundaries evolve from one limiting case to the other as δ, the natural logarithm of which is proportional to the gas-flame standoff distance, decreases from unity to zero. In what follows, the neutral stability boundaries are displayed in the form $\Delta_g(k;\ \delta,\ Le,\ ...)$, without the multiplicative factor $(Le - 1)$ that was used in Figure 2 of Part I. The evolution of the neutral stability boundary with δ is qualitatively different for the three cases $Le < 1$, $Le = 1$, and $Le > 1$. In the limit $\delta \to 1$, the pulsating stability boundary is independent of the Lewis number. For Lewis equal to unity, decreasing δ is stabilizing; in the limit that δ becomes small, the pulsating stability boundary is only achieved for very large values of Δ_g. This behavior is consistent with the absence of instability for the gas flame when $Le = 1$.

For Lewis numbers greater than unity, decreasing δ is again stabilizing. However, the pulsating stability boundary does not disappear as $\delta \to 0$; rather, it approaches a limiting form, as shown in Figure 1. The approach to this limiting form is easily seen to be nonmonotonic in nature. The curves in Figure 1 indicate a transition of the stability boundary from one characteristic of condensed-phase pulsations to one characteristic of gas-phase pulsations as k increases past a critical value that increases as δ increases. This is consistent with the observation that the condensed-phase pulsations are the more unstable of the two at large wavelengths, while the gas-phase pulsations are the more unstable at small

†Combustion Science and Technology, accepted (1987).

*Princeton University, Princeton, NJ.

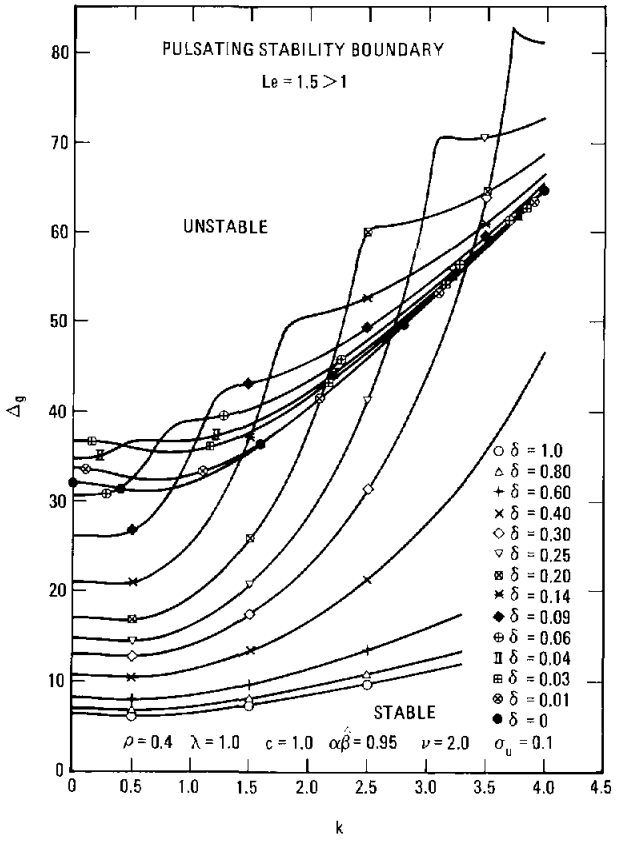

Figure 1. Pulsating stability boundary for $Le > 1$ and various δ.

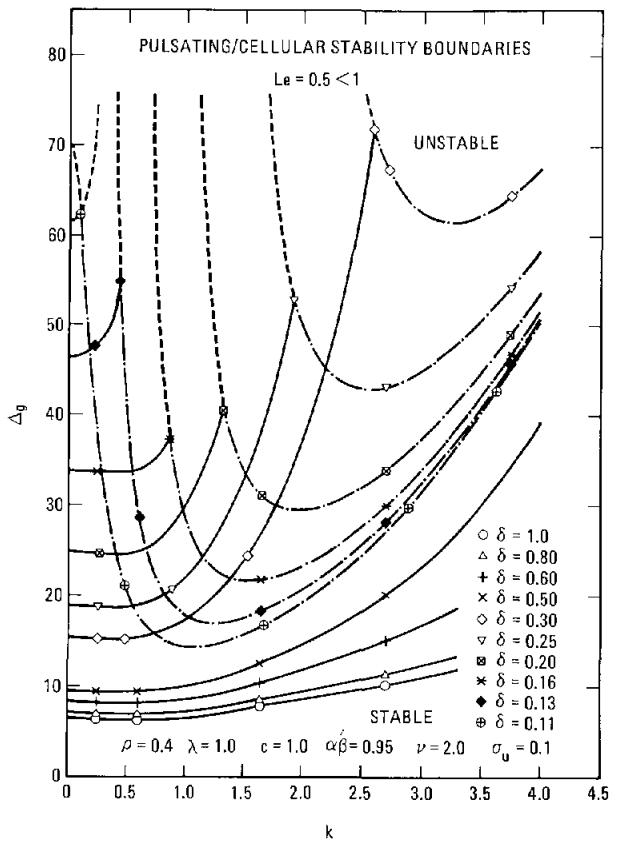

Figure 2. Pulsating stability boundary for $Le < 1$ and various δ.

wavelengths. As the wavelength increases in the range of small wavelengths, the presence of the solid surface exerts a stabilizing influence on the gas-phase pulsations, causing the stability boundary in Figure 1, for example, to rise above that for the limit $\delta = 0$ with decreasing k for k large. When the wavelength becomes comparable with the flame standoff distance, the gas-phase pulsations are suppressed rather abruptly, and at large wavelengths, the stability boundary is that associated with condensed-phase pulsations. Thus, it is understandable that the rather sharp transitions in the curves occur at values of k that increase with increasing δ; it is simply that a decrease in the standoff distance causes a decrease in the transition wavelength. The stabilizing influence of the gas flame on the condensed-phase pulsations is responsible for the increase in stability with increasing k or decreasing δ for small values of k.

Finally, for Lewis numbers less than unity, decreasing δ is again stabilizing with respect to pulsating disturbances, but destabilizing with respect to cellular perturbations. Thus, the pulsating and cellular stability boundaries may intersect for $\delta < 1$, and for sufficiently small values of δ, steady planar burning will always lose stability to the latter type of disturbance first, as shown in Figure 2.

In terms of instability phenomena, Figures 1 and 2 clearly indicate the hybrid nature of solid-propellant deflagration with respect to strictly gaseous flame propagation and strictly condensed-phase combustion. In the limit that the gas flame lies near the propellant surface ($\delta \rightarrow 1$), the basic solution is unstable only to pulsating disturbances and the neutral stability boundary is independent of the Lewis number, as in the case of condensed-phase combustion. On the other hand, in the limit that the gas flame lies far from the propellant surface ($\delta \rightarrow 0$), the stability of the deflagration essentially mimics the results for gaseous combustion, where stability of the basic solution is lost to pulsating disburbances for Lewis numbers greater than unity, and to cellular disturbances for Lewis numbers less than unity. At intermediate values of the gas-flame standoff distance, the stability characteristics of solid propellants incorporate features of both types of single-phase deflagrations.

References:

1. S. B. Margolis and F. A. Williams, Comb. Sci. Tech. (1988).

2. M. R. Denison and E. Baum, ARS J. **31**, 1112 (1961).

3. See article on p. 9-10 this issue.

Measurement of Temperature Transients During the Ignition of Pyrotechnic Materials

A high-speed, two-color-sapphire fiber-optical probe has been developed to measure and characterize the ignition properties of pyrotechnic powders.

K. R. Hencken and R. W. Bickes*

A high-speed, two-color, sapphire fiber optical probe has been developed to monitor the ignition process of pyrotechnic powders. Many explosives and pyrotechnics are ignited by a thermal pulse produced when a current is passed through a metal bridgewire against which the powder is pressed. Although the ignition and burn of these components is understood empirically, a useful quantitative description for the design engineer has not been developed. Data from these measurements will be useful in characterizing the ignition properties of different pyrotechnic powders as a function of the density, total mass, and heat input supplied to the material.

Preparation of the pyrotechnic powder consists of pressing a small amount of the powder into a cup-shaped metal charge holder. In our experiments, as shown in Figure 1, heat input to the pyrotechnic is provided by a Nd:YAG laser focused on the backside of the charge holder. The ignition transient is followed by monitoring the temperature of the surface of the powder directly opposite to the laser-heated surface using the sapphire fiber-optic probe. The high-speed, two-color temperature probe uses a 1-mm-diameter sapphire fiber pressed against the pyrotechnic so that the charge is completely contained.

Following ignition at the laser-heated surface and during the propagation of the ignition wave through the pyrotechnic, the thermal radiation is collected directly by the sapphire fiber and passed to a calcium fluoride lens. Conventional optics attenuate at wavelengths above 2 μm. For this reason sapphire fibers and calcium floride lenses were selected; the sapphire fiber and calcium floride lenses transmit wavelengths up to 4 μm. Collimated radiation from the lens passes to a 2.5-μm dichroic beamsplitter, where radiation at wavelengths greater than 2.5 μm passes through to a liquid nitrogen-cooled, indium-arsenide detector. Radiation at wavelengths below 2.5 μm is reflected by the beamsplitter and is focused onto a second cooled indium-arsenide detector. Additional tuning of each detector is done with bandpass filters placed in the collimated radiation between the dichroic beam-splitter and the detectors. The signals from the two detectors are passed through logarithmic amplifiers before being recorded on a two-channel digitizing oscilloscope. The fiber-optic probe has been optimized for a temperature range of interest from 375 K to 1100 K with rise times less than 1 microsecond. Resolution of waveform-rise times of less than 1 microsecond is required to observe

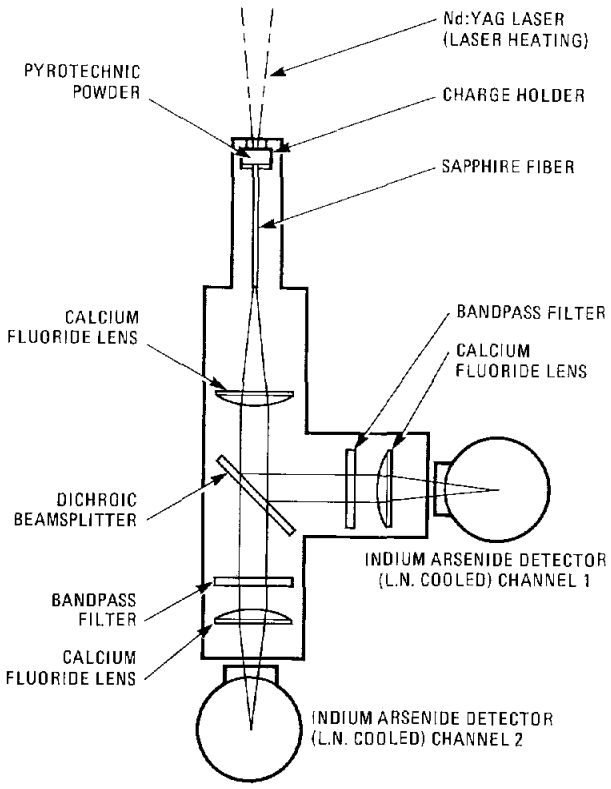

Figure 1. Schematic diagram of the two-color-sapphire fiber-optic probe.

*Sandia National Laboratories, Albuquerque, NM.

the rapid heat-up of pyrotechnic materials during ignition.

In our earlier experiments,[1] a single-color fiber-optic probe was used which required knowledge of the emissivity of the pyrotechnic. Using two different wavelengths to measure temperatures requires only a constant emissivity and calabratic system using a source of known temperature. This calibration was done using a black-body radiation source. The attenuation coefficient of the pyrotechnic was examined experimentally at 3 μm to determine whether radiation from the deflagration wave could penetrate to the opposite surface and thereby invalidate the temperature calibration. Tests of the pyrotechnic PA-29, which is composed of titanium subhydride and potassium perchlorate, and which was used in our experiments, indicated that the material is opaque in thicknesses greater than 20 μm.

In our experiments, small charges of PA-29 were heated by the Nd:YAG laser. Ignition transients were obtained using the two-color-sapphire fiber-optic probe. A typical output from the two logarithmic amplifiers is shown in Figure 2. The transient waveform, due to heating of the monitored surface as the deflagration wave approaches, is resolved. As we observed in earlier experiments at lower heating rates, a brief plateau is evident. This is attributed to melting of potassium perchlorate within the pyrotechnic, an endothermic process which arrests the rate of increase of the surface temperature. This interpretation is consistent with the fact that this event was not observed at heating rates where the pyrotechnic ignites at a temperature below the melting point of its constituents.

Further tests and development of the two-color-sapphire fiber-optical probe are planned. Changes in the band-pass widths and separation in wavelength for the two detectors must be made to improve the sensitivity and accuracy of the system and to reduce the noise in the amplifier data when the signals are ratioed. Also, a higher-speed transient digitizer will be implemented to improve the resolution of significant features of the transient waveforms.

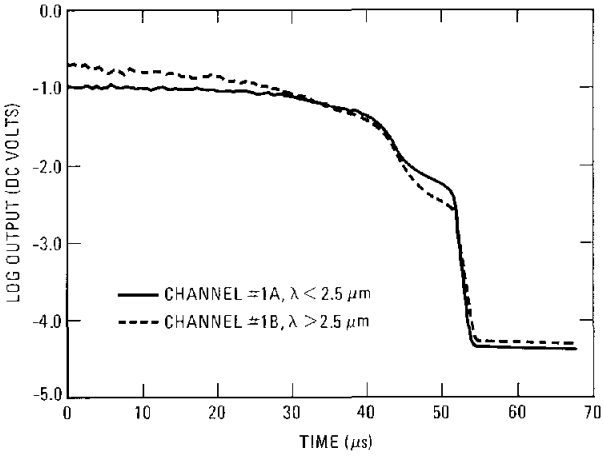

Figure 2. Pyrotechnic PA-29 during ignition as measured by two-color fiber-optic probe.

Reference:

1. D. A. Tichenor, K. R. Hencken, and R. W. Bickes, Jr., *Proceedings of Conference No. 399 on Advanced Instrumentation for Aeroengine Components*, (AGARD, Philadelphia, PA, 1986), p. R3-16.

The Combustion of Hydroxylammonium Nitrate-Based Liquid Propellants†

A strand burner was used to study hydroxylammonium nitrate-based liquid propellant flames. By observing the combustion of liquid propellant in such an arrangement, much has been deduced of the physical processes that occur during ignition and combustion at pressures relevant to liquid propellant gun ignition.

S. R. Vosen

The purpose of this study is to understand the combustion of liquid monopropellants in bulk at high pressure. Of particular interest is an understanding of both the kinetics and the physical processes that occur at the liquid-gas interface during combustion. One would expect chemical reactions from the propellant constituents in the liquid phase and between the propellants and their decomposition products, either dissolved in the liquid phase or in the gas phase. Physical effects that are present in liquid propellant (LP) combustion, such as the stability of the liquid-gas interface, are a function of the reactant and product viscosities, densities, and surface tension. The presence of water in both the reactants and products is expected to greatly affect combustion in the experiments in this study, where the pressure range is one-third to 1.5 times the critical pressure of water.

We will examine the combustion of LP 1846, a hydroxylammonium nitrate (HAN)-based liquid propellant that is a mixture of HAN and triethanolammonium nitrate (TEAN) in water:

$$7(NH_3OH)NO_3 + (CH_2OHCH_2)_3NHNO_3 + 12.3H_2O,$$

and of HAN/water mixtures. In order to obtain information on the combustion of liquid propellant at elevated pressures, experiments for this study were carried out on samples of TEAN/HAN/water mixtures in a strand-type burner which was placed in a large pressure vessel. The strand burner had a cross section of 5 mm square, was 40 mm deep, and was open on top, giving a volume of 1,000 mm^3. The burner was of a sandwich construction, with the central part of the burner machined from a ceramic to give the shape of the liquid "strand" and to allow for the placement of ignition electrodes. The outer parts of the burner were constructed of quartz plates to allow for optical access. The burner was located in the center of a 0.013-m^3 pressure vessel. The pressure vessel windows, in conjunction with the quartz sides on the burner, allowed for the observation of combustion. Backlit photographs were recorded on a video system at 60 frames/second. The burner was filled with propellant, placed in the pressure vessel, and pressurized with an inert gas (either nitrogen or argon). Ignition of the propellant samples was accomplished by an electric discharge through wires mounted flush with the inside surface of the burner.

Results of LP 1846 combustion at pressures of 26.7 to 34 MPa show that the LP flame consists of several regions. As the combustion wave progresses through the liquid, the first step appears to be the decomposition of the liquid. Above the liquid surface is a transparent region in which the motion of a white substance (probably a fog) at times can be seen. Above the transparent region is a highly luminous zone. The regions most likely to be associated with the chemical reactions (the liquid-gas interface and the luminous zone) oscillate over the entire pressure range (both transversely and in the direction of burning), with the luminous zone appearing to be the most unstable.

At pressures below 23 MPa, the combustion of LP appears to be quite different. A liquid-gas interface moves through the liquid at a rate greater than that which occurs at higher pressures, with no visible flame. In addition, the region above the interface is transparent at higher pressures but opaque at lower pressures. At the conclusion of the experiment, a liquid residue remains in the burner. This residue, determined from FTIR analysis, is TEAN. In addition, the pressure rise in the vessel during the experiment is less than 34 kPa, compared to 340 kPa at 30 MPa. The greater pressure rise associated with TEAN combustion at higher pressures is consistent with chemical equilibrium calculations, which predict that the majority of the energy release in LP 1846 results from TEAN decomposition.

†Twenty-Second Symposium (International) on Combustion (The Combustion Institute), accepted (1988).

Apparent linear burning-rate data were obtained from the photographs by determining the displacement of the mean position of the liquid-gas interface. From these data, one can then determine an average apparent linear burning rate by a least-squares fit. Figure 1 summarizes the average apparent linear burning rate results for LP 1846. The apparent burning rate decreases as the pressure increases from 6.7 MPa to 30 MPa. The dependence of the linear burning rate on pressure has been measured for several pure liquid monopropellants, and is found to increase with pressure. It is possible that a decrease in burning rate in LP 1846 might occur as a result of the chemistry of HAN decomposition, as a result of the large concentration of a constituent that will condense (i.e., water), or as a result of increased stability of the liquid-gas interface at high pressures.[1]

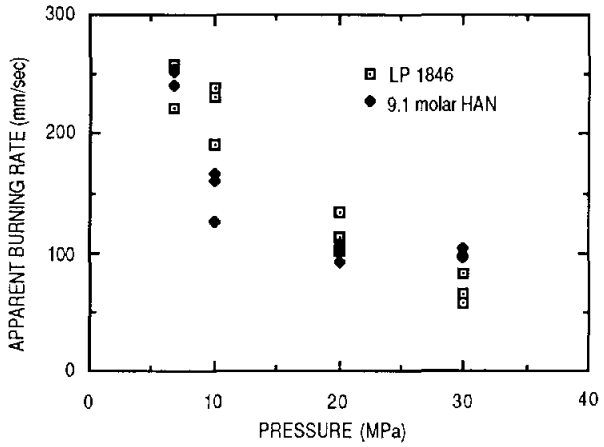

Figure 1. The average apparent linear burning rate for LP 1846 and 9.1 molar HAN.

To simulate HAN decomposition as it occurs in LP 1846, a HAN/water mixture was prepared with a molarity of 9.1, giving the same fraction of HAN per unit volume as the liquid propellant. A series of experiments was conducted to determine the decomposition rate of 9.1 molar HAN as a function of pressure. The interface was found to be corrugated and the region above the interface opaque, similar to the combustion of LP 1846 at 6.7 MPa. At the conclusion of the experiment, a greater quantity of liquid, mainly water, remained in the burner longer than for LP 1846 combustion at the same pressure.

The variation of the apparent overall burning rate with pressure for the HAN/water mixture is shown in Figure 1. As with LP 1846, the burning rate decreases with increased pressure. At the lower pressures (less than 10 MPa), the burning rates of LP 1846 and of 9.1 molar HAN are the same, while at higher pressures the rate for 9.1 molar HAN is nearly twice that of the propellant. While the chemistry and physical properties of the two mixtures are obviously not identical, these experiments show the importance of HAN in determining the overall combustion rate of HAN-based liquid propellants.

Based on the results of HAN/water decomposition and LP 1846 combustion, we propose the flame structure shown schematically in Figure 2. The "flame" region of HAN-based LP combustion is composed of three regions. As the flame approaches the unburnt LP, liquid-phase reactions involving HAN occur near the liquid-gas interface. On the gas side of the interface, a mixture of gaseous HAN decomposition products (mainly nitrogen and oxygen), TEAN, and water exist. Depending on the temperature and pressure on the gas side, this mixture could exist in any state from a water foam to a fine mist. It is not clear at this time whether or not chemical reactions occur in this region. In the last region, which occurs only at higher pressures, reaction of the TEAN occurs, producing a luminous flame and releasing most of the chemical energy of the propellant.

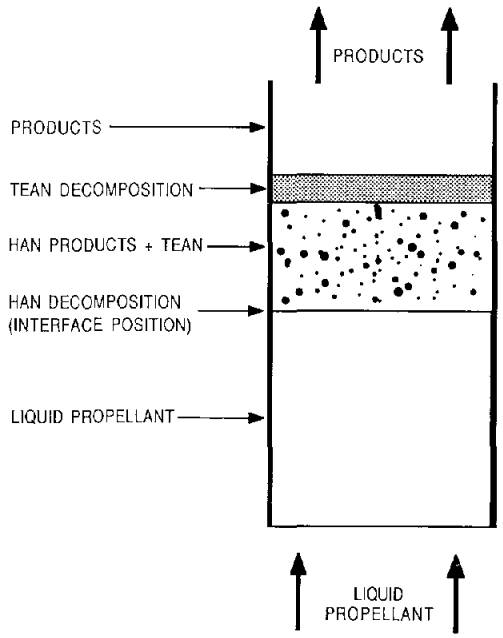

Figure 2. Model of HAN-based LP combustion.

Reference:

1. R. C. Armstrong and S. R. Vosen, "Dynamics of Liquid Propellant Combustion," *Twenty-fourth Combustion Meeting* (CPIA, 1987).

A Dynamic Model of Liquid Propellant Combustion

It is well known that liquid monopropellants do not burn uniformly. This article explains which physical mechanisms enhance or hamper the pulsating and cellular instabilities that result in nonuniform deflagration of these propellants.

R. C. Armstrong and S. B. Margolis

Our purpose in this investigation is to characterize the driving forces behind instabilities in liquid propellant combustion. Instabilities are experimentally observed and we hope to predict the length scales over which the instabilities will be active, and the time scale over which they will be coherent. The analysis we consider centers on the linear stability of the gas/liquid interface and on those forces which discourage or enhance steady, planar burning. A useful inference to be drawn from our analysis is the order-of-magnitude size of droplets that will be formed as a consequence of nonuniform burning. Since the observable burning rate of the propellant is likely to be strongly dependent on the size distribution of these droplets and the mode of burning, the results of an investigation such as this are of keen interest.

Previous investigations have looked at the reactive-diffusive interactions at the expense of realism in fluid mechanics, or have concentrated on inertial-viscous (hydrodynamic) types of interactions at the expense of reaction and heat diffusion. The results for both of these extremes are well known and are summarized in Figure 1. Our purpose here is to merge these two pictures in equal measure to discover any interaction between them and to produce a comprehensive stability diagram, an outcome that simply is not possible when one relies on expansions that are symptotic to one picture or the other.

The combustion model presented here is not significantly different in construction than previous models. We do, however, obtain the exact dispersion relation without resorting to an expansion that yields only a correction to what is already known. Although a relatively large system of equations must be solved to obtain this result, our approach has taken advantage of artificial intelligence techniques. To do this, the problem must be couched in a general form so that all of the equations are treated equally. This means that fortuitous circumstances that the trained mathematical eye can recognize and exploit cannot be taken advantage of *a priori*.

A stability diagram corresponding to typical liquid propellant combustion burning conditions is shown in Figure 2.

The major features of Figure 2 are that both the reactive-diffusive stability boundary and the inertial-viscous stability boundary are present, though much altered in form from Figure 1. The reactive-diffusive curve is still a pulsating stability boundary, but is translated toward higher reaction thermal sensitivity due to the influence of inertia and viscosity. It approaches the solid-propellant

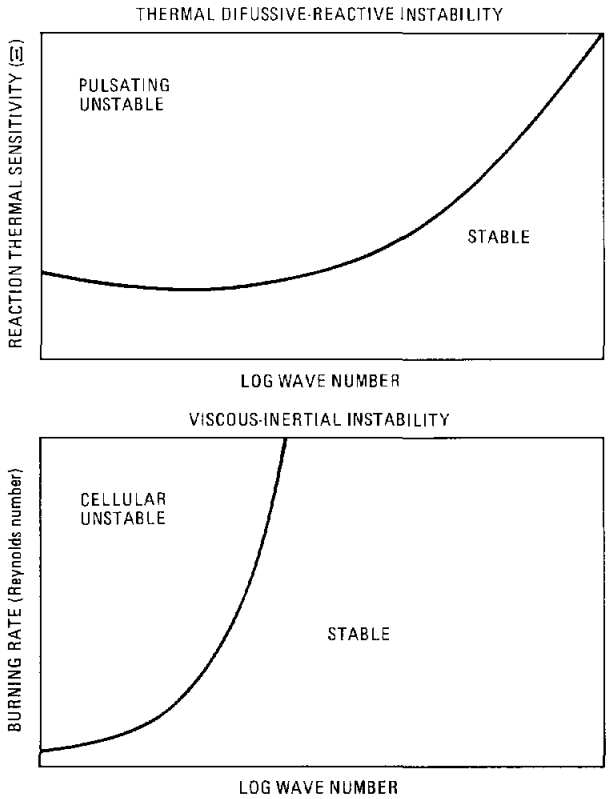

Figure 1. This is a schematic summarizing previous models of liquid propellant combustion. The top curve represents a pulsating reactive-diffusive instability, for a model largely neglecting fluid mechanics, which arises from a sufficiently large reaction thermal sensitivity. The lower diagram denotes a cellular (pulsation frequency is zero) inertial-viscous (hydrodynamic) instability for a model which largely ignores the temperature dependence of the chemical reaction.

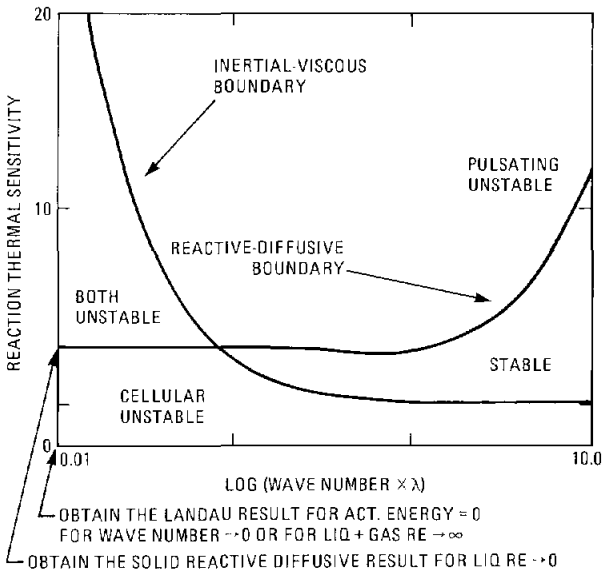

Figure 2. A stability diagram corresponding to typical liquid propellant burning conditions is shown. The inertial-viscous curve is a cellular boundary and is a remnant of previous inertial-viscous (hydrodynamic) models. The reactive-diffusive curve is a remnant of the solid propellant instability of Figure 1 and still demarks a pulsating boundary.

stability limit as the viscosity becomes large (that is, when the liquid propellant behaves as a solid). Similarly, the inertial-viscous curve retains its cellular nature, but there is a singularity at zero wave number. This results in an instability at small wave numbers (large length scales) for finite thermal sensitivity. On the other hand, it is clear that this thermal sensitivity plays a stabilizing role regarding the hydrodynamics in that, at any given wave number, there exists a critical value of the thermal sensitivity that suppresses hydrodynamic instability (previous work found all wave numbers unstable when inertia alone was considered). Increasingly large thermal sensitivity is required to suppress this instability as the wave number approaches zero. In the limit of large burning rate or small wave numbers, the results of previous work are recovered.

At this time, it is difficult to speculate on how such a stability map impacts on the observed burning rate, other than to note that there is experimental evidence that these instabilities control the burning rate, especially at low pressures (ca. 1000 psi). A closer look at these data may provide some guidance in interpreting the experimental observations. Photographic results from these experiments suggest that under certain conditions, an opalescent "fog" of droplets forms between the primary liquid/gas interface flame and a secondary luminous flame. That these droplets (if this is indeed what they are) cannot be individually resolved implies that they are smaller than 100 μm and, therefore, could be explained as the result of a reactive-diffusive instability (length-scale ~ 10 μm).

On the theoretical side, it would be useful to account for the effects of mass diffusion (finite Lewis numbers) in order to further explore the differences between this liquid propellant model and the more well-known gas-phase flame models.

A Dynamic Combustion Model of a Decomposing and Reacting Monopropellant

A two-step decomposition/reaction model of liquid monopropellant combustion has been formulated to study the dynamic behavior of energetic liquids in laboratory and gun environments. A numerical solution of the model equations indicates that the reaction-zone thickness is extremely small, and the overall reaction scheme is limited by the propellant-decomposition step.

H. A. Dwyer* and B. R. Sanders

The purpose of this research is to study the dynamic behavior of a decomposing and reacting monopropellant with the characteristics of HAN- (hydroxylammonium nitrate) and TEAN- (triethanolammonium nitrate) like materials currently being studied for regenerative gun applications. The Navier-Stokes equations have been solved in a time-dependent, one-dimensional form for a chemical model of the monopropellant mixture. The numerical solution was based on the finite-volume formulation of the basic equations and employed the use of adaptive grid methods to resolve the extremely thin flame zones that developed. The results showed that the HAN decomposition reaction is the rate-determining step for the system. It has also been determined that convective effects are large and could play a role in gun system performance.

At present it is difficult to formulate a model of monopropellant burning because of the extreme conditions of the high-pressure and high-temperature surroundings, and the complex chemistry associated with the materials utilized. It is the purpose of this investigation to develop a general numerical model which can be utilized as a tool to parametrically study liquid propellant combustion. A model covering a wide range of pressures and chemical compositions is required to understand experiments that have been carried out on the burning of monopropellants in strand burners and in droplet form. It is hoped from these studies that the correct physics and chemistry can be narrowed down from the many propositions currently being formulated.

The basic starting point for this investigation has been the equations of mass, momentum, and energy in control-volume form. The transport equations in this form allow for the introduction of moving interfaces and the application of moving grids with adaptive methods. It is shown in Reference 1 how these equations are implemented, and in Reference 2 how the numerical algorithms are developed.

The chemical model consists of the following five materials: (1) the oxidizer, HAN ($N_2H_4O_4$); (2) the propellant, TEAN ($C_6H_{16}N_2O_6$); (3) water as a solvent; (4) decomposed HAN'; and (5) products. The compositions of these materials are varied parametrically, and the ignition and burning of the monopropellant studied.

Very little is known about the chemical and physical properties of these materials at conditions of over 500 atms, where they are utilized, and it is necessary to make extensive assumptions to define a model problem. In the present research, the following conditions have been employed.

Two-Step Chemical Reaction

Step I [HAN] → [HAN']

Step II [HAN'] + [TEAN] → [Products]

Transport Properties

Law of Corresponding States - Nitrogen

$= D = 3 \times 10^{7}$ (T=400 K, p=200 atm)

Rate Data

Step I $[\text{rate}]_{HAN} = A_1 Y_{HAN} \exp(-\theta_1/T)$

$A_1 = 1.66 \times 10^{1}$ $\theta_1 = 2000$ K

Step II $[\text{rate}]_{HAN' + TEAN} = A_2 Y_{HAN'} Y_{TEAN} \exp(-\theta_2/T)$

$A_2 = 3.33 \times 10^{6}$ $\theta_2 = 12000$ K

Thermodynamic Properties

Heat release model

$[\Delta T]_1 = 200$ K

$[\Delta T]_2 = 1800$ K

The constants A_1 and A_2 have been chosen so that the results give a burning rate that is comparable with the experimental results of Vosen.[3] One further quantity was chosen for the numerical simulation, and that was a length scale. The length scale chosen was one centimeter, since this size is compar-

*University of California at Davis.

able to Vosen's experimental apparatus. It should also be noted that no interface has been employed in the model, since the pressures are well above the critical pressures of all the species present.

Figure 1 shows the temperature profile for the time evolution of a burning spherical droplet with the properties given above. A study of this figure shows that the flame is quite thin.

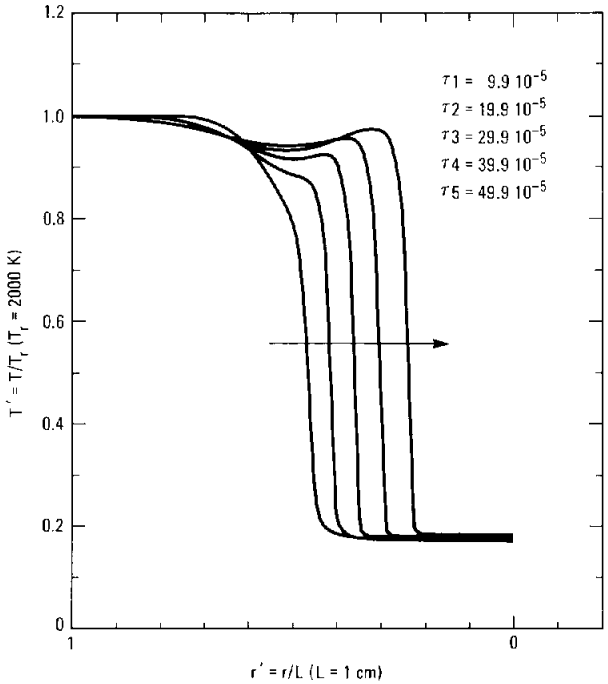

Figure 1. Temperature profiles.

The mass fraction profiles for HAN and TEAN are shown in Figures 2 and 3. It is clearly seen that HAN is decomposing because of the flame propagation and its low activation energy. A careful look at Figure 1 also shows a heat release in the low temperature part of the monopropellant. It is not known at the present time if the exothermic, low-activation energy description is accurate, and this point will be studied in the future.

In summary, a model has now been developed and demonstrated for two-step monopropellant combustion of spherical droplets or planar strand burning. It is recognized that the decomposition reaction chemistry model used in these studies is far too simple and naive to predict actual liquid monopropellant behavior. Therefore, current modeling activities are focused on including detailed nitramine chemistry through use of the CHEMKIN code.

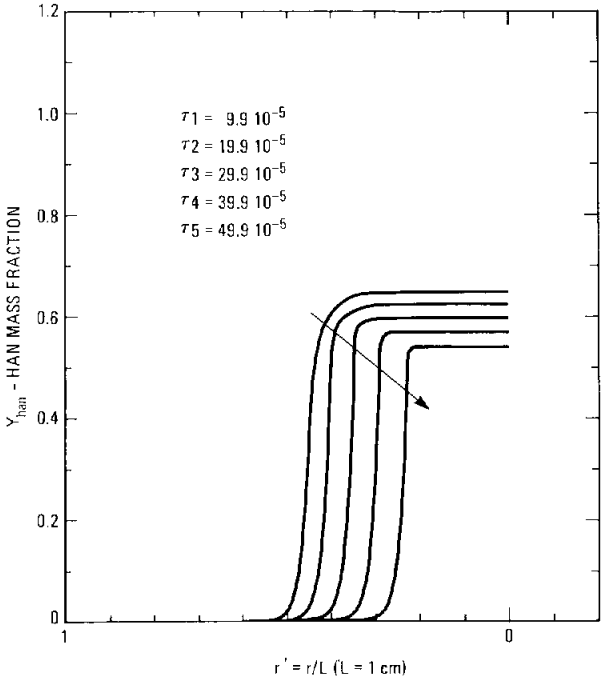

Figure 2. HAN mass fraction profiles.

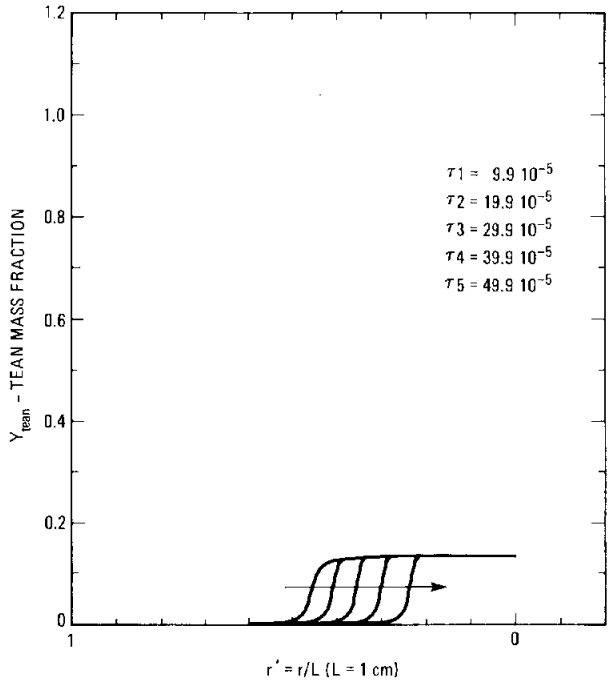

Figure 3. TEAN mass fraction profiles.

References:

1. H. A. Dwyer, "Adaptive Numerical Methods for Reacting Flows," *Lectures for Reacting Flows, Cornell University*, G. Ludford, ed. (North Holland, New York, Ny, 1985).

2. H. A. Dwyer, "Some Uses of Direct Solvers in Computational Fluid Dynamics," AIAA Journal, submitted (1987).

3. S. R. Vosen, private communication.

In-cylinder velocity and turbulence are being measured using laser Doppler velocimetry on a single cylinder NH-series diesel engine in collaboration with Cummins Engine Company. This project is indicative of a new focus for the engine program to develop and apply diagnostics to practical engine configurations under realistic operating conditions.

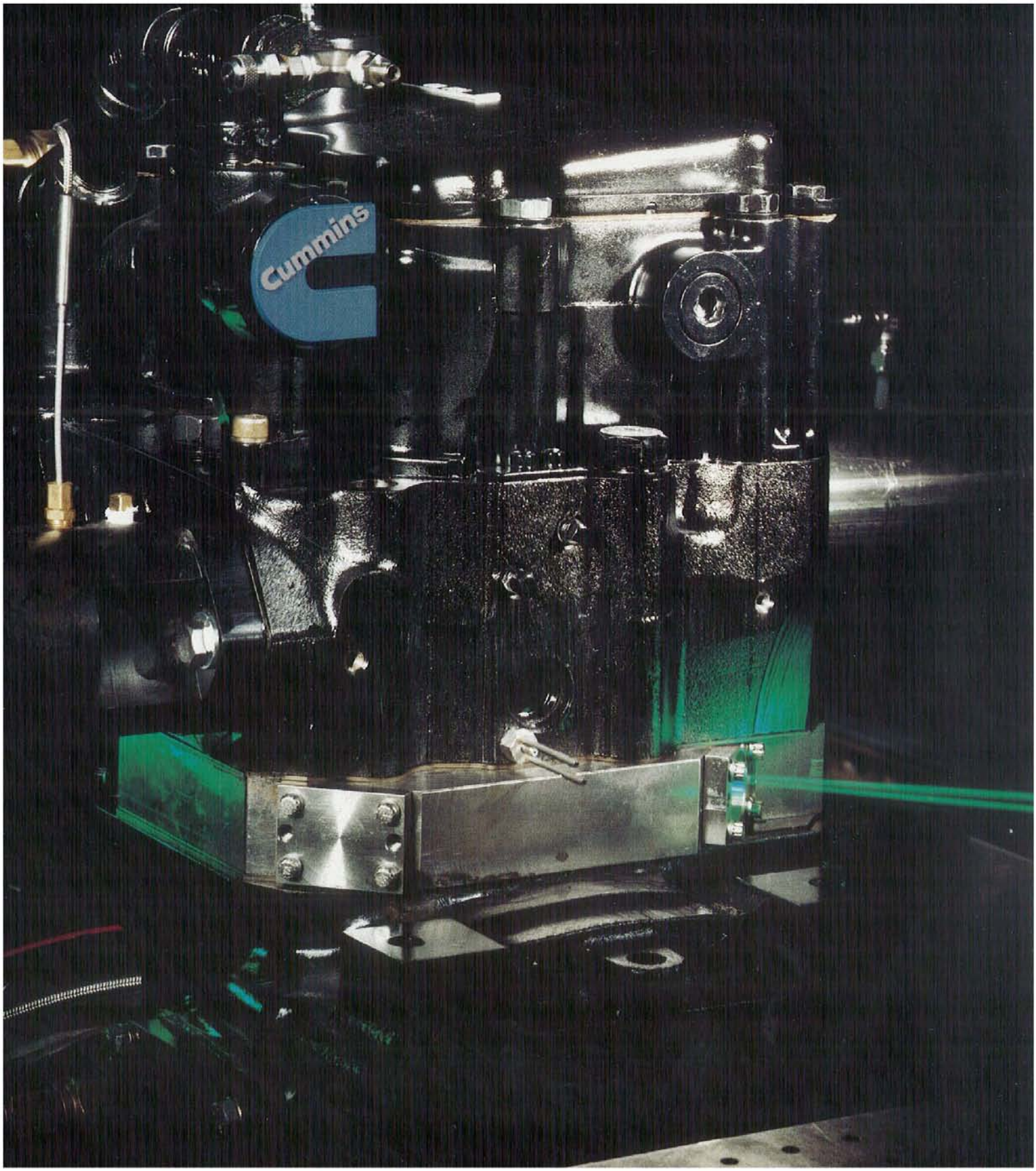
Cummins

Cummins Engine Company and Sandia are collaborating on a program to investigate the processes that control particulate formation in a realistic, heavy-duty diesel engine. This venture is being supported jointly by the Department of Energy's Energy Conversion and Utilization Technologies (ECUT) Program and Cummins. Nominal support for Cummins is also provided through the DOE/ER Industrial Fellow Program.

The objective of this program is to address the regulations to control heavy-duty truck diesel particulate emissions that have now been implemented by the EPA and take effect in 1991. Providing that sulfur is removed from diesel fuel, industry may be able to meet these 1991 standards with refinements in existing engine and injection technology. However, the more stringent regulations effective in 1994 are uniformly felt to be impossible to meet. Industry is experimenting with prototype regenerative catalytic traps to "filter" the exhaust, but this technology has proven unreliable and difficult to engineer for the 200,000 mile useful lifetime of the engine. Thus, the appropriate place to focus is on the fundamental process in the cylinder where these particulates are formed in the first place.

This collaborative program with Sandia will take advantage of the in-cylinder laser imaging diagnostic capability at the CRF and build upon the fundamental soot particulate formation/oxidation. It is in the truest sense a collaborative venture. A Cummins staff member is in residence at Sandia for the two-year duration of the program. Cummins has also developed a complete optically-accessible diesel engine test facility that is currently installed and operating at Sandia as shown. Cummins provides expertise in diesel engine design, development and testing, and knowledge of the NOx/particulate tradeoff that complements the scientific capabilities at Sandia.

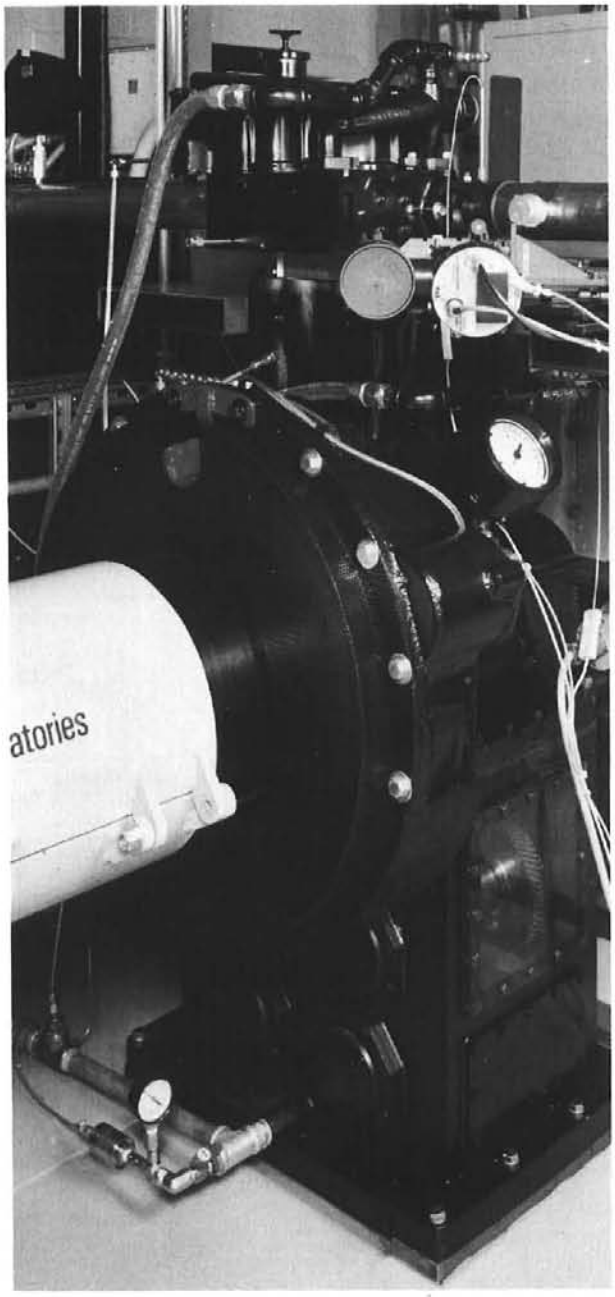

Section 10
Technology Exchange

For more than a decade, researchers at the CRF have sought aggressively to foster the exchange of combustion-related technology with U.S. industries and universities. Our cornerstone activity in this endeavor is the Visiting Scientist Program, bringing representatives from industries and universities to work side-by-side with the in-house research staff. Through 1987, approximately 6000 visitors have come to the facility. Many have stayed for extended periods of up to a year or more, bringing a diverse set of backgrounds, problems, and goals, and taking away CRF-generated technology, research techniques, computer codes, and expertise.

Another important means of fostering technology exchange is through Cooperative Working Groups that bring together industry, university, and national laboratory researchers to address common problems. Traditionally, groups organized by the CRF have focused on automotive industry issues such as combustion in direct injection stratified charge and dilute homogeneous charge engines, emission control in diesel engines, and engine knock. Success has in turn led to the formation of three new groups, focusing on turbulent aerothermochemistry, and spray and pulse combustion.

Perhaps the most direct means of technology exchange is through the formation of new companies and the development of new products. In May 1987, Dr. Robert A. Perry, inventor of RAPRENOx, left Sandia to form Technor, a company intended to commercialize this NOx-control process. In other instances, CRF technology has been incorporated into new products by existing companies. For example, laser injection seeding technology, developed in our diagnostics research effort, is now commercially available through Lightwave Electronics, Inc.

In the final analysis, technology exchange at the CRF is a complex, subtle, and dynamic process that depends critically on individual interactions between in-house researchers and their university and industry counterparts. This section describes some of the activities that have taken place in the past year.

Technology Transfer

The technology developed at the Combustion Research Facility is shared with industry, universities, and other government laboratories through the visiting scientist program and through formal working groups that facilitate the transfer of technology for more applied uses.

G. B. Drummond

An important aspect of the Combustion Research Facility (CRF) program is technology transfer, the movement of research results to the combustion community. Transfer is effected through the visiting scientist program, through the DOE's Industry Technology Program, and by participation in interactive working groups with U. S. industry, universities, and other national Laboratories, and through international collaborations.

Working Groups. Seven joint working groups are now active:

Topic: Direct-Injection Stratified-Charge Combustion

Participants: General Motors, Princeton University, Los Alamos National Laboratory, Sandia National Laboratories.

Topic: Dilute Homogeneous-Charge Combustion

Participants: Ford, Science Applications, Inc., S-Cubed, Massachusetts Institute of Technology, University of California/Berkeley, Imperial College, University of Wisconsin, Integral Technologies, Inc., Pennsylvania State University, Sandia National Laboratories.

Topic: Diesel Combustion

Participants: Cummins, Exxon, Navistar, Physical Sciences, Southwest Research Institute, UTRC, Purdue University, Pennsylvania State University, Yale University, Los Alamos National Laboratory, Sandia National Laboratories.

Topic: Engine Knock

Participants: General Motors, UNOCAL, Princeton University, Drexel University, Lawrence Livermore National Laboratory, Sandia National Laboratories.

Topic: Aerothermochemistry of Turbulent Combustion

Participants: General Electric Company, California Institute of Technology, Cornell University, University of California/San Diego, University of Sydney (Australia), Sandia National Laboratories.

Topic: Spray Combustion

Participants: National Bureau of Standards, Jet Propulsion Laboratories, Los Alamos National Laboratory, Sandia National Laboratories.

Topic: Pulse Combustion

Participants: Lennox Corporation, Ford Energy Engineering, Gas Research Institute, Toshiba Corporation, Battelle Columbus, University of Michigan, Georgia Tech., University of California/Davis, Sandia National Laboratories.

Industrial Interactions. The Industry Technology Fellowship program is funded by the DOE's Office of Basic Energy Sciences, Division of University and Industry Programs. It provides financial support, on a cost-sharing basis, for visits of industrial researchers to the CRF.

Three such interactions have taken place this year. In one, a visitor worked with a CRF researcher to evaluate the feasibility (for possible future industrial applications) of CARS spectroscopy to measure furnace temperatures. In another, the collaborator provided a single cylinder diesel engine, specially modified for optical access, on which to perform engine particulate measurements that will further an understanding of soot formation and oxidation in diesel engines. And in the third interaction, the program participant furnished a 750-horsepower, stratified-charge rotary engine on which laser-Doppler velocimetry measurements of flame fronts are being made under motored conditions.

International Programs. On a global scale, the CRF is active in two programs of the International Energy Agency. In the internal-combustion engine and furnace program, the CRF participates with representatives from Canada, Italy, Japan, Norway, Sweden, the United Kingdom, and West Germany to exchange research progress in the areas of advanced piston-engine technology and in fundamental combustion studies. Some forty-nine research tasks are under way in this program.

The second program, in coal combustion sciences, involves the CRF and other U. S. researchers with representatives of Australia, Canada, and The Netherlands. Both of the programs are conducted as some of the most outstanding research institutions of the world.

Visiting Scientist Program

An extensive visiting scientist program encourages scientists to work side-by-side with the Combustion Research Facility staff and to take advantage of the Facility's unique resources.

G. B. Drummond

The Combustion Research Facility (CRF) is a national facility for studying fundamental problems in energy-related combustion. An important element of the CRF charter provides for promoting the development and application of new combustion research tools (laser diagnostics; computational tools, etc.) with the active involvement of the combustion research community at large. The Visiting Scientist Program enables scientists from universities, industry and other national laboratories to become involved in research at the Combustion Research Facility and to take advantage of the specially designed equipment and resources here. Research support provided to visiting scientists includes technicians and engineering staff dedicated to the project, computer time, shop work and other purchases necessary to support the project. The visitor generally provides his own salary, travel and living expenses. So long as results of a visitor's research are available in the open literature there is no cost imposed for use of the Facility. Support for proprietary research is available, but only on a full cost-recovery basis.

Visitors usually elect to work primarily on collaborative projects or to use some pre-existing experimental setup to do their own research. However, they are free to execute their own research projects.

The Facility opened early in 1981. In six years, we have had over 5200 technical visits. (See Figure 1.) Some 4900 of these visits were brief, typically for one or two days. These short-term visitors were here either to learn something about the technical scope of the CRF program, or to discuss specific combustion research problems of their own with the Facility staff.

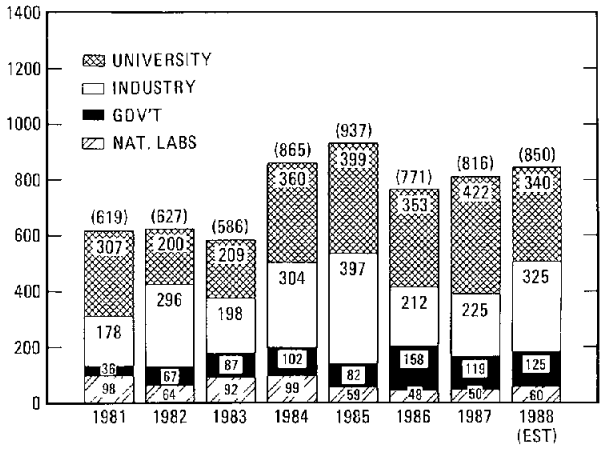

Figure 1. The number of visitors since 1981.

The number of visiting scientists who have spent two weeks or more at the CRF has reached almost 270, as shown in Figure 2. Those visiting in FY87 (listed in Table I) have engaged in a wide variety of research projects, and have included representatives from universities, industry, other national laboratories, and governmental facilities. Fourteen of those on the list are from foreign institutions.

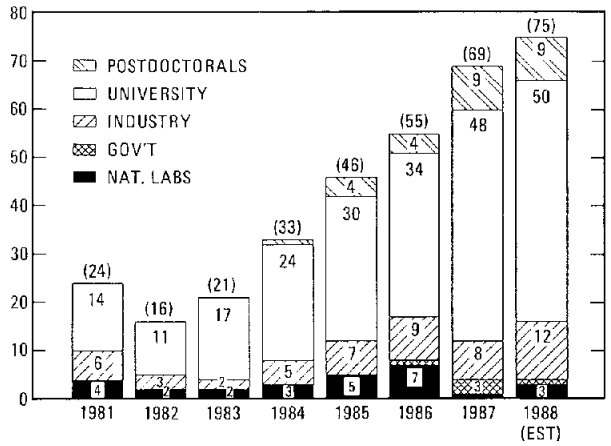

Figure 2. The number of long-term visiting scientists.

Included in the numbers above is another kind of long-term visitor who comes to the CRF through the Sandia Post-Doctoral Program. Sandia Laboratories accepts a small, but growing, number of post-doctoral candidates in its research programs each year for a one-year (renewable to two-year) appointment. The Combustion Research Facility draws physicists, chemists, mathematicians and engineers who wish to work in the field of combustion research. Candidates are expected to move to industry and universities when their term of appointment ends; in this way, the Program provides us another means of transferring CRF technology outside. Graduate students with an interest in combustion science are also in residence at the CRF—many doing thesis work under the guidance of a faculty advisor or a mentor assigned from the Sandia staff.

Table I
CRF Visiting Scientists
October 1, 1986 - September 30, 1987

Name	Affiliation	Term of Stay	Collaborative Project
University			
Allen, Wesley[1]	UC/Berkeley	July 6 - Sept 30	Theoretical chemistry
Arpaci, Vedat	Univ. of Michigan	Sept 4 - Sept 30	Pulse combustion heat transfer analytical studies
Axelbaum, Richard[1]	UC/Davis	Oct 1 - Sept 30	Sooting flame studies
Baxter, Larry[1]	Brigham Young Univ.	Oct 1 - Feb 28	Coal devolatilization studies
Caton, Jerry[2]	Texas A&M	Sept 1 - Sept 30	RAPRENOx studies
Cavolowsky, John	UC/Berkeley	May 1 - Sept 30	Hypersonic diagnostics
Cool, Terry	Cornell Univ.	Jan 12 - Jan 23	REMPI ionization detection
Dec, John	Univ. of Michigan	Oct 1 - Sept 30	Pulse combustion studies
Dixon-Lewis, Graham	Univ. of Leeds	Jan 12 - June 30	Combustion chemistry
Dunn-Rankin, Derek[1]	UC/Berkeley	Oct 1 - July 24 Aug 31 - Sept 30	Coal combustion CARS
Dwyer, Harry	UC/Davis	20% of year	Turbulence modeling
Edwards, Boyd	Univ. of West Virginia	June 8 - June 12	Percolation analysis
Feikema, Douglas[1]	Univ. of Minnesota	May 11 - Aug 30	Hypersonic diagnostics
Fornaciari, Neal[1]	Chabot College	July 1 - Sept 30	Spray combustion lab development
Foster, David[2]	Univ. of Wisconsin	Oct 1 - June 14	LDV engine diagnostics
Gemmen, Ronald[1]	Univ. of Michigan	Sept 8 - Sept 30	Pulse combustion, unsteady droplet dynamics
Glarborg, Peter	Tech. Inst. of Denmark	May 8 - May 22	Combustion chemistry modeling
Grant, David	Univ. of Utah	July 13 - Aug 21	Pulverized coal combustion studies
Hall, Matt[1]	Princeton Univ.	Jan 5 - Sept 30	Natural gas-fueled IC engine studies
Helble, Joe	MIT	Oct 1 - Oct 30	Coal combustion modeling
Houston, Paul	Cornell Univ.	Dec 8 - Dec 19	Imaging ion detector development
Hsu, Steve	MIT	June 9 - Aug 14	Coal devolatilization
Janssen, Maurice	Univ. of Nijmegen	July 20 - Aug 21	Molecular beam experiments
Kennedy, Ian	UC/Davis	Aug 13 - Sept 30	Counterflow diffusion flames
Keck, James	MIT	Feb 15 - Apr 15	Chemical dynamics of autoignition
Kollman, Wolfgang	UC/Davis	20% of year	Turbulence modeling
Komyathy, Phillip[1]	Chabot College	July 1 - Sept 30	Facility laser PC software
Kröger, Hermann	RWTH/Aachen	Oct 1 - Oct 25	Flame detector development
Leung, SiuWang[1]	UC/Berkeley	Jul 1 - Sept 30	Turbulent flame data reduction
Lilleheie, Nils	Norwegian Inst. of Tech.	Oct 1 - Dec 1	Combustion chemistry modeling
Long, Marshall	Yale Univ.	Dec 15 - Dec 24	Turbulent flame imaging
Loui, Dell	UC/Davis	Aug 13 - Sept 30	Counterflow diffusion flames
Mansour, Mohy	Univ. of Sydney	Mar 14 - May 28	Raman scattering in turbulent flames
Masri, Asaad	Univ. of Sydney	Feb 23 - Apr 4	Raman scattering in turbulent flames
Mataga, Thomas[1]	UC/Berkeley	Sept 1 - Sept 30	Optical diagnostics for hypersonic gas dynamics
McKee, Michael[2]	Auburn Univ.	June 1 - Aug 19	Energetic material studies
McMurtry, Patrick[1]	Univ. of Washington	Sept 1- Sept 30	Turbulence simulation
North, Gary[1]	Pennsylvania State	May 18 - Aug 21	Fluid mechanics modeling
Parker, David	UC/Santa Cruz	10% of year	Molecular beam experiments
Peters, Norbert	RWTH/Aachen	Sept 5 - Sept 20	Turbulence modeling
Petropoulos, Peter[1]	UC/Berkeley	June 22 - Aug 30	Turbulence modeling
Prior, Yehiam	Weitzman Institute	Aug 3 - Aug 21	Four-wave mixing experiments
Pugmire, Ronald	Univ. of Utah	July 13 - Aug 21	Pulverized coal combustion studies
Quinn, Terri[1]	Jackson State Univ.	June 1 - Aug 14	Coal combustion studies
Radziemski, Lee	New Mexico State Univ.	Aug 3 - Aug 14	Spark spectroscopy studies
Sheppard, Ian	UC/Berkeley	Aug 13 - Sept 30	Counterflow diffusion flames
Spiglanin, Thomas[1]	Wesleyan Univ.	Oct 1 - Apr 30	HNCO decomposition

Name	Affiliation	Term of Stay	Collaborative Project
Steinhaus, Charles[1]	Cal Poly	June 15 - Aug 30	Diesel experiment buildup
Thoman, John[1]	MIT	Sept 21 - Sept 30	Ion imaging
Tong, Albert[2]	Univ. of Texas	June 1 - Aug 30	Spray modeling
Vorsteveld, Lou[1]	Univ. of Vermont	June 15 - Sept 15	Propellant ignition characteristics studies
Wallace, Jim[2]	Univ. of Toronto	Oct 1 - July 30	Fiber optic instrumentation
Warnatz, Jürgen	Univ. of Heidelberg	May 7 - July 24	Engine knock combustion chemistry
Waters, Bart	Purdue Univ.	April 19 - May 1	Char reactivity measurements
Yip, Brandon	Yale Univ.	Dec 15 - Jan 19	Turbulent flame imaging
Industry			
Dimplefeld, Phil[3]	John Deere Co.	Aug 3 - Sept 30	Laser velocimetry measurements on rotary engine
Evens, Lance	Lennox Corp.	Oct 10 - Oct 24	Pulse combustion modeling
Hongo, Ichiro	Toshiba Corp.	Oct 1 - Sept 30	Unsteady heat transfer studies
Marchant, Rob	Lennox Corp.	Oct 10 - Oct 24	Pulse combustion modeling
Maris, Mark[3]	Computer Genetics	July 22 - Sept 30	CARS code familiarization
Morrison, Cal	SAIC, Inc.	Jan 1 - June 15	Particle/turbulence interaction studies
Namazian, Mehdi	Altex	Oct 1 - Sept 30	2D shear layer studies
Ng, Henry[3]	Cummins Engine Co.	June 1 - Sept 30	Diesel engine installation
Perry, Robert	Technor	May 15 - Sept 30	HNCO oxidation data analysis and RAPRENOx modeling
Potkay, Gene	AT&T Technologies/ERC	Oct 13 - Oct 31	Pyrogenic materials study
zur Loye, Axel[3]	Cummins Engine Co.	Jan 1 - Sept 30	Engine particulate measurements
Government			
Rosasco, Greg	National Bureau of Stds.	Oct 15 - Oct 30	IRS of combustion species
National Laboratories			
Jensen, Peter Arendt	Risø Laboratory	Oct 1 - Apr 10	Optical probes
Marie, Jean Jacques	CNRS/Rouen	Oct 6 - Oct 17	CARS engine temperature measurements

[1] = Post-doctoral or Student Program Participant
[2] = Sandia Faculty Programs Participant
[3] = DOE Industrial Program Participant

Publications 1987

Refereed Journal Articles

R. C. Armstrong and S. B. Margolis, "Nonhomogenous Propellants as Random Media," Comb. Sci. Tech. **52**, 59 (1987).

W. T. Ashurst, "Vortex Simulation of Unsteady Wrinkled Laminar Flames," Comb. Sci. Tech. **52**, 325 (1987).

W. T. Ashurst, J.-Y. Chen, and M. M. Rogers, "Pressure Gradient Alignment with Strain Rate and Scalar Gradient in Simulated Navier-Stokes Turbulence," Phys. Fluids **30**, 3293 (1987).

W. T. Ashurst, A. R. Kerstein, R. M. Kerr, and C. H. Gibson, "Alignment of Vorticity and Scalar Gradient with Strain Rate in Simulated Navier-Stokes Turbulence," Phys. Fluids **30**, 2343 (1987).

W. T. Ashurst and D. I. Merion, "Numerical Study of Vortex Reconnection," Phys. Rev. Lett. **58**, 1632 (1987).

W. T. Ashurst, N. Peters, and M. D. Smooke, "Numerical Simulation of Turbulent Flame Structure with Non-Unity Lewis Number," Comb. Sci. Tech. **53**, 339 (1987).

C. E. Barker, R. Trebino, A. G. Koestenbauder, A. E. Siegman, and G. A. Kenney-Wallace, "Ultrafast Measurements of Nonlinear-Optical Phenomena Using Tunable-Laser-Induced-Grating Methods," J. Opt. Soc. Am. B **4**, 34 (1987).

R. Behrens, Jr.,"New Simultaneous Thermogravimetry and Modulated Molecular Beam Mass Spectrometry Apparatus for Quantitative Thermal Decomposition Studies," Rev. Sci. Instr. **58**, 451 (1987).

M. R. Booty, S. B. Margolis, and B. J. Matkowsky, "Interaction of Pulsating and Spinning Waves in Nonadiabatic Flame Propagation," SIAM J. Appl. Math. **47**, 1241 (1987).

R. W. Bradshaw and R. W. Carling, "A Review of the Chemical and Physical Properties of Molten Alkali Nitrate Salts and Their Effect on Materials for Solar Central Receivers," J. Electrochem. Soc. **134**, 510C (1987).

R. J. Cattolica, "Visualization of Flame Propagation by Laser-Fluorescence Imaging of Nitrogen Dioxide," Comb. Sci. Tech. **54**, 61 (1987).

R. J. Cattolica and N. Klein, "Plasma Ignition of Liquid Propellant," Comb. Sci. Tech. **54**, 139 (1987).

R. J. Cattolica and S. R. Vosen, "Combustion-Torch Ignition: Fluorescence Imaging of OH Concentration," Comb. Flame **68**, 267 (1987).

D. W. Chandler and P. L. Houston, "Two-Dimensional Imaging of State-Selected Photodissociation Products Detected by Multiphoton Ionization," J. Chem. Phys. **87**, 1445 (1987).

J.-Y. Chen, "Second Order Conditional Modeling of Turbulent Nonpremixed Flames with a Composite PDF," Comb. Flame **69**, 1 (1987).

J.-Y. Chen, F. C. Gouldin, and J. L. Lumley, "Second-Order Modeling of a Turbulent Nonpremixed H_2-Air Jet Flame with Intermittency and Conditional Averaging," Comb. Sci. Tech. **53**, 235 (1987).

T. A. Cool and J. E. M. Goldsmith, "Laser-Enhanced Flame Ionization Detector," Appl. Opt. **26**, 3542 (1987).

R. W. Dibble, V. Hartmann, R. W. Schefer, and W. Kollman, "Conditional Sampling of Velocity and Scalars in Turbulent Flames Using Simultaneous LDV-Raman Scattering," J. Exper. Fluids **5**, 103 (1987).

R. W. Dibble, A. R. Masri, and R. W. Bilger, "The Spontaneous Raman Scattering Technique Applied to Nonpremixed Flames of Methane," Comb. Flame **67**, 189 (1987).

A. T. Droege and F. P. Tully, "Hydrogen-Atom Abstraction from Alkanes by OH. 6. Cyclopentane and Cyclohexane," J. Phys. Chem. **91**, 1222 (1987).

D. Dunn-Rankin and A. R. Kerstein, "Numerical Simulation of Particle Size Distribution Evolution During Pulverized Coal Combustion," Comb. Flame **69**, 193 (1987).

D. Dunn-Rankin, J. Hoornstra, F. A. Greulich, and D. J. Holve, "Combustion of Coal-Water Slurries. Evolution of Particle Size Distribution for Coals of Different Rank," Fuel **66**, 1139 (1987).

J. L. Durant and F. Kaufman, "Calculation and Use of Total Collision Rates in Thermal Systems," Chem. Phys. Lett. **142**, 246 (1987).

R. L. Farrow and R. E. Palmer, "Comparison of Motionally Narrowed CARS Lineshapes of H_2 with Hard- and Soft-Collision Models," Opt. Lett. **12**, 984 (1987).

R. L. Farrow, R. Trebino, and R. E. Palmer, "High-Resolution CARS Measurements of Temperature Profiles and Pressure in a Tungsten Lamp," Appl. Opt. **26**, 331 (1987).

R. L. Farrow, R. P. Lucht, and L. A. Rahn, "Measurements of the Nonresonant Third-Order Susceptibilities of Gases Using Coherent Anti-Stokes Raman Spectroscopy," J. Opt. Soc. Am. B **4**, 1241 (1987).

C. R. Ferguson, R. M. Green, and R. P. Lucht, "Unburned Gas Temperatures in an Internal Combustion Engine. II. Heat Release Computations," Comb. Sci. Tech. **55**, 63 (1987).

W. L. Flower and C. T. Bowman, "Observations on the Soot Formation Mechanism in Laminar Ethylene-Air Diffusion Flames at One and Two Atmospheres," Comb. Sci. Tech. **53**, 217 (1987).

W. L. Flower and A. J. Hurd, "*In Situ* Measurement of Flame-Formed Silica Particles Using Dynamic Light Scattering," Appl. Opt. **26**, 2236 (1987).

G. W. Foltz and C. F. Melius, "Studies of Isotopic Exchange Between Gaseous Hydrogen and Palladium Hydride Powder," J. Catal. **108**, 409 (1987).

J. E. M. Goldsmith, "Photochemical Effects in Two-Photon-Excited Fluorescence Detection of Atomic Oxygen in Flames," Appl. Opt. **26**, 3566 (1987).

F. C. Gouldin, R. W. Schefer, S. C. Johnston, and W. Kollmann, "Nonreacting Turbulent Mixing Flows," Prog. Energ. Comb. Sci. **12**, 257 (1987).

T. A. Green, D. R. Jennison, C. F. Melius, and S. J. Binkley, "Hartree-Fock Energies for NaF_6 Cluster Simulations of Na^+ Hole States in the NaF Crystal," Phys. Rev. B **36**, 3469 (1987).

D. R. Hardesty and D. K. Ottesen, "Optical Diagnostics for *In Situ* Measurements in Combustion Environments Containing Coal Particles," Energy **12**, 813 (1987).

D. J. Holve and P. L. Meyer, "Coal/Water Slurries: Fuel Preparation Effects on Atomization and Combustion," Comb. Sci. Tech. **52**, 243 (1987).

D. J. Holve, T. H. Fletcher, and K. Gomi, "Comparative Combustion Studies of Ultrafine Coal/Water Slurries and Pulverized Coal," Comb. Sci. Tech. **52**, 269 (1987).

H. G. Kaper, G. K. Leaf, S. B. Margolis, and B. J. Matkowsky, "On Nonadiabatic Condensed Phase Combustion," Comb. Sci. Tech. **53**, 289 (1987).

J. O. Keller and K. Saito, "Measurements of the Combusting Flows in a Pulse Combustion," Comb. Sci. Tech. **53**, 137 (1987).

A. R. Kerstein, "Percolation Model of Polydisperse Composite Solid Propellant Combustion," Comb. Flame **69**, 95 (1987).

A. R. Kerstein and B. F. Edwards, "Percolation Model for Simulation of Char Oxidation and Fragmentation Time-Histories," Chem. Eng. Sci. **42**, 1629 (1987).

A. R. Kerstein and S. Niksa, "Polymer Scission with Irreversible Reattachment: A Kinetic Model of Pyrolysis with Char Formation," Macromolecules **20**, 1811 (1987).

A. R. Kerstein and R. B. Pandey, "Conductivity Exponent for Stirred Superconductor-Insulator Mixtures," Phys. Rev. A **35**, 3575 (1987).

S. K. Knudson, D. W. Noid, and M. L. Koszykowski, "Semiclassical Determination of Eigenvalues in Nonbending Ozone," J. Phys. Chem. **91**, 2763 (1987).

M. L. Koszykowski, L. A. Rahn, R. E. Palmer, and M. E. Coltrin, "Theoretical and Experimental Studies of High-Resolution Inverse Raman Spectra of N_2 at One-Ten Atmospheres," J. Phys. Chem. **91**, 41 (1987).

M. L. Koszykowski, C. M. Rohlfing, and D. W. Noid, "Semi-Classical Calculation of Vibrational Spectra Using *Ab Initio* Electronic Structure Energies," Chem. Phys. Lett. **142**, 67 (1987).

A. M. F. Lau, D. W. Chandler, M. A. Quesada, and D. H. Parker, "Measurement of Transition Moments Between Molecular Excited Electronic States Using the Autler-Townes Effect," Phys. Rev. A. **35**, 4107 (1987).

A. M. F. Lau, "Double Optical Resonance at High Pressure: Collisional Broadening and Doppler Effects on ac-Stark Splitting," Opt. Commun. **64**, 144 (1987).

A. M. F. Lau, "The Autler-Townes Effect in Hydrogen at Low Pressure," J. Phys. B **20**, L469 (1987).

D. Lucas, D. Dunn-Rankin, K. Hom, and N. J. Brown, "Ignition by Excimer Laser Photolysis of Ozone," Comb. Flame **69**, 171 (1987).

R. P. Lucht, "Three-Laser Coherent Anti-Stokes Raman Scattering Measurements of Two Species," Opt. Lett. **12**, 78 (1987).

R. P. Lucht, R. E. Palmer, and M. A. Maris, "Simultaneous Acquisition of Pure Rotational and Vibrational Nitrogen Spectra Using Three-Laser Coherent Anti-Stokes Raman Spectroscopy," Opt. Lett. **12**, 386 (1987).

R. P. Lucht, R. E. Teets, R. M. Green, R. E. Palmer, and C. R. Ferguson, "Unburned Gas Temperatures in an Internal Combustion Engine. I. CARS Temperature Measurements," Comb. Sci. Tech. **55**, 41 (1987).

S. B. Margolis, F. A. Williams, and R. C. Armstrong, "Influences of Two-Phase Flow in the Deflagration of Homogeneous Solids," Comb. Flame **67**, 249 (1987).

P. Marshall, A. Fontijn, and C. F. Melius, "High-Temperature Photochemistry and BAC-MP4 Studies of the Reaction Between Ground-State H Atoms and N_2O," J. Chem. Phys. **86**, 5540 (1987).

A. R. Masri, R. W. Bilger, and R. W. Dibble, " 'Fluorescence' Interference with Raman Measurements in Nonpremixed Flames of Methane," Comb. Flame **68**, 109 (1987).

K. F. McCarty, "Raman Scattering as a Technique of Measuring Film Thickness: Interference Effects in Thin Growing Films," Appl. Opt. **26**, 4482 (1987).

K. F. McCarty and R. J. Anderson, "Real-Time Measurements of Deposit Formation from Sodium Sulfate-Seeded Flames," Comb. Sci. Tech. **54**, 51 (1987).

J. A. Miller and G. A. Fisk, "Combustion Chemistry," Chem. Eng. News **65**, 22 (1987).

R. E. Mitchell, "Experimentally Determined Overall Burning Rates of Coal Chars," Comb. Sci. Tech. **53**, 165 (1987).

S. Niksa and A. R. Kerstein, "On the Role of Macromolecular Configuration in Rapid Coal Devolatilization," Fuel **66**, 1389 (1987).

S. Niksa, A. R. Kerstein, and T. H. Fletcher, "Predicting Devolatilization at Typical Coal Combustion Conditions with the Distributed-Energy Chain Model," Comb. Flame **69**, 221 (1987).

M. Page, G. F. Adams, J. S. Binkley, and C. F. Melius, "Dimerization Energy of Borane," J. Phys. Chem. **91**, 2675 (1987).

D. H. Parker, J. O. Buck, and D. W. Chandler, "Double-Resonance Laser-Ionization Spectroscopy of Molecular Hydrogen in the Region of the Second Dissociation Limit," J. Phys. Chem. **91**, 2035 (1987).

N. Peters and R. J. Kee, "The Computation of Stretched Laminar Methane-Air Diffusion Flames Using a Reduced Four-Step Mechanism," Comb. Flame **68**, 17 (1987).

R. W. Pitz, C. M. Penney, and M. Lapp, "Acoustically Modulated Optical Transmission for Low-Level Gaseous Species Measurement," Appl. Opt. **26**, 5272 (1987).

M. A. Quesada, A. M. F. Lau, D. H. Parker, and D. W. Chandler, "Observation of Autler-Townes Splitting in the Multiphoton Ionization of H_2: Measurement of Vibronic Transition Moments Between Excited States," Phys. Rev. A **36**, 4107 (1987).

K. Raghavachari and J. S. Binkley, "Structure, Stability, and Fragmentation of Small Carbon Cluster," J. Chem. Phys. **87**, 2191 (1987).

L. A. Rahn, R. E. Palmer, M. L. Koszykowski, and D. A. Greenhalgh, "Comparison of Rotationally Inelastic Collision Models for Q-Branch Raman Spectra of N_2," Chem. Phys. Lett. **133**, 513 (1987).

L. A. Rahn and R. (F. P.) Trebino, "Observation of Collision-Induced Coherences and Ground-State-Spin Gratings in a Flame," J. Opt. Soc. Amer. B **4**, 92 (1987).

M. J. Redmon and J. S. Binkley, "Global Potential Energy Hypersurface for Dynamical Studies of Energy Transfer in HF-HF Collisions," J. Chem. Phys. **87**, 969 (1987).

C. M. Rohlfing and J. S. Binkley, "The Effects of Basis Set and Electron Correlation on the Structure and Stability of Be_4 and Be_{13}," Chem. Phys. Lett. **134**, 110 (1987).

C. M. Rohlfing and P. J. Hay, "The Structure and Bonding of F_2O_2," J. Chem. Phys. **86**, 4518 (1987).

E. A. Rohlfing, D. W. Chandler, and D. H. Parker, "Direct Measurements of Rotational Energy Transfer Rate Constants for $H^{35}Cl$ (v=1)," J. Chem. Phys. **87**, 5229 (1987).

R. W. Schefer, M. Namazian, and J. Kelly, "Velocity Measurements in a Turbulent Nonpremixed Bluff-Body Stabilized Flame," Comb. Sci. Tech. **56**, 101 (1987).

R. W. Schefer, V. Hartmann, and R. W. Dibble, "Conditional Sampling of Velocity in a Turbulent Nonpremixed Propane Jet," AIAA J. **25**, 1318 (1987).

T. A. Spiglanin, D. W. Chandler, and D. H. Parker, "Mass-Resolved Laser Ionization Spectroscopy of HCl," Chem. Phys. Lett. **137**, 414 (1987).

T. A. Spiglanin, R. A. Perry, and D. W. Chandler, "Internal State Distribution of CO from HNCO Photolysis," J. Chem. Phys. **87**, 1568 (1987).

T. A. Spiglanin and D. W. Chandler, "Rotational State Distributions of NH(a $^1\Delta$) from HNCO Photodissociation," J. Chem. Phys. **87**, 1577 (1987).

T. A. Spiglanin and D. W. Chandler, "Translational Spectroscopy of HNCO Photodissociation," Chem. Phys. Lett. **141**, 428 (1987).

R. (F. P.) Trebino and L. A. Rahn, "Higher-Order Collision-Enhanced Wave Mixing in a Sodium-Seeded Flame," Opt. Lett. **12**, 912 (1987).

R. (F. P.) Trebino and L. A. Rahn, "Collision-Induced Six-Wave Mixing and Subharmonic Resonances: Experiments in a Sodium-Seeded Flame," J. Opt. Soc. Am. B **4**, 200 (1987).

R. (F. P.) Trebino and L. A. Rahn, "Subharmonic Resonances in Higher-Order Collision-Enhanced Wave-Mixing in a Sodium-Seeded Flame," Opt. Lett. **12**, 912 (1987). Also, *Laser Spectroscopy VIII*, W. Persson and S. Svanberg, eds. (Springer-Verlag, New York, NY, 1987), p. 335.

F. P. Tully and A. T. Droege, "Kinetics of the Reactions of the Hydroxyl Radical with Dimethylether and Diethylether," Int. J. Chem. Kinet. **19**, 251 (1987).

F. P. Tully, "Hydrogen-Atom Abstraction from Alkenes by OH. Ethene and 1-Butene," Chem. Phys. Lett. **143**, 510 (1987).

R. A. Whiteside, J. S. Binkley, M. E. Colvin, and H. F. Schaefer, III, "Parallel Algorithms for Quantum Chemistry. I. Integral Transformations on a Hypercube Multiprocessor," J. Chem. Phys. **86**, 2185 (1987).

Other Publications

W. D. Allen and H. F. Schaefer,III, "Reaction Paths for the Dissociation $\tilde{a}^3A''CH_2CO \rightarrow \tilde{X}^3B_1CH_2 + \tilde{X}\,^1\Sigma^+CO$," J. Chem. Phys., submitted (1987).

R. J. Anderson and J. C. Hamilton, "Azimuthally Resolved Optical Second-Harmonic Generation From Hydrogen on Nickel (111)," Phys. Rev. Lett., submitted (1987).

R. J. Anderson, J. C. Hamilton, and G. W. Foltz, "Optical Second Harmonic Generation Studies of Surface Adsorption and Segregation of Fe-18, Cr-3, Mo(110)," Opt. Soc. Amer., accepted (1987).

R. L. Axelbaum, W. L. Flower, and C. K. Law, "Dilution and Temperature Effects of Inert Addition on Soot Formation in a Counterflow Diffusion Flame," Comb. Sci. Tech., submitted (1987).

R. S. Barlow and J. P. Johnston, "Structure of a Turbulent Boundary Layer on a Concave Surface," J. Fluid Mech., submitted (1987).

R. S. Barlow and J. P. Johnston, "Local Effects of Large-Scale Eddies in a Concave Boundary Layer," J. Fluid Mech., submitted (1987).

R. S. Barlow and C. Q. Morrison, "Velocity Discrimination Technique for Two-Phase Measurements in Dense Particle-Laden Flows," Experiments in Fluids, submitted (1987).

P. K. Barr, H. A. Dwyer, and T. T. Bramlette, "A One-Dimensional Model of a Pulse Combustor," *Proceedings of the Joint ASME/JSME Thermal Engineering Conference*, Vol. 1, P. J. Marto and I. Tanasawa, eds. (ASME, New York, NY, 1987), p. 283.

T. T. Bramlette and J. O. Keller, "Theoretical and Experimental Investigation of a New Pulse Combustor," Sandia Report *SAND86-8050* (Sandia National Laboratories, Livermore, CA, 1987).

T. T. Bramlette, "The Role of Fluid Dynamic Mixing in Pulse Combustors," Comb. Sci. Tech., submitted (1987). Also, Sandia Report *SAND87-8622* (Sandia National Laboratories, Livermore, CA, 1987).

R. J. Cattolica, P. K. Barr, and N. N. Mansour, "Propagation of a Premixed Flame in a Divided-Chamber Combustor," Comb. Flame, accepted (1987).

J.-Y. Chen, W. Kollmann, and R. W. Dibble, "Numerical Computation of Turbulent Free-Shear Flows Using a Block-Tridiagonal Solver for a Staggered-Grid System," *Proceedings of the Eighteenth Annual Conference on Modeling and Simulation* (Instrument Society of America, Pittsburgh, PA, 1987), p. 1833.

J.-Y. Chen, "A General Procedure for Constructing Reduced Reaction Mechanisms with Given Independent Relations," Comb. Sci. Tech., submitted (1987).

D. A. Clabo, Jr., W. D. Allen, R. B. Remington, Y. Yamaguchi, and H. F. Schaefer, III, "A Systematic Study of Molecular Vibrational Anharmonicity and Vibration-Rotation Interaction by Self-Consistent-Field Higher Derivative Methods," J. Chem. Phys., submitted (1987).

M. E. Coltrin, R. J. Kee, G. H. Evans, and J. A. Miller, "Theoretical Modeling of the Fluid Mechanics and Gas-Phase Chemistry in a Rotating-Disk Chemical Vapor Deposition Reactor," *Proceedings of the Tenth International Conference on Chemical Vapor Deposition*, Vol. 87-8, G. W. Cullen, ed. (Electrochemical Society, Pennington, NJ, 1987), p. 33.

D. S. Dandy and L. G. Leal, "Buoyancy-Driven Motion of a Deformable Drop Through a Quiescent Liquid at Intermediate Reynolds Numbers," J. Fluid Mech., submitted (1987).

R. W. Dibble, P. Magre, R. W. Schefer, J.-Y. Chen, V. Hartmann, and W. Kollmann, "Simultaneous Mixture Fraction and Velocity Measurements in a Turbulent Nonpremixed Flame," Comb. Sci. Tech., submitted (1987).

R. W. Dibble, P. Magre, R. W. Schefer, J.-Y. Chen, V. Hartmann, and W. Kollman, "Measurement of Joint Probability of Velocity and Concentrations of a Turbulent Nonpremixed Flame," Comb. Flame, submitted (1987).

D. R. Dudek and T. H. Fletcher, "Numerical Calculations of the Drag Force Induced by Natural Convection of Spheres at Low Grashof Numbers," Sandia Report *SAND87-8201* (Sandia National Laboratories, Livermore, CA, 1987).

D. R. Dudek, T. H. Fletcher, J. P. Longwell, and A. F. Sarofim, "Natural Convection-Induced Drag Forces on Spheres at Low Grashof Numbers: Comparison of Theory with Experiment," Int. J. Heat and Mass Transfer, accepted (1987).

D. Dunn-Rankin, "Kinetic Model for Simulating the Evolution of Particle Size Distributions During Char Combustion," Sandia Report *SAND87-8615* (Sandia National Laboratories, Livermore, CA, 1987).

D. Dunn-Rankin, R. R. Steeper, and P. A. Jensen, "Using Mie Scattering for Measuring Size Changes of Individual Combustion Particles," Opt. Eng., submitted (1987).

D. Dunn-Rankin and D. R. Hardesty, "The Role of Dispersant in Coal/Water Slurry Agglomerate Formation," Fuel, submitted (1987).

D. Dunn-Rankin and A. R. Kerstein, "The Influence of Ash on Particle Size Distribution Evolution During Coal Combustion," Comb. Flame, submitted (1987).

H. A. Dwyer, "Some Uses of Direct Solvers in Computational Fluid Dynamics," AIAA J., submitted (1987).

H. A. Dwyer and B. R. Sanders, "Unsteady Influences in Droplet Dynamics and Combustions," *Calculation of Turbulent Reactive Flows*, AMD-Vol. **81**, Book No. H00350, (ASME, New York, NY, 1987).

H. A. Dwyer and B. R. Sanders, "A Study of the Ignition Characteristics of Droplet Fuels and Monopropellants," *Proceedings of the Joint ASME-JSME Thermal Engineering Conference*, Vol. 1, P. J. Marto and I. Tanasawa, eds., (ASME, New York, NY, 1987), p. 511.

R. L. Farrow and D. W. Chandler, "Raman Pump/Probe Measurements of State-to-State Energy Transfer Rates in the v=1 State of H_2," J. Chem. Phys., submitted (1987).

T. H. Fletcher, L. L. Baxter, and D. K. Ottesen, "Spectral Emissivities of Size-Graded Coal Particles: Implications for Pyrometry," *Coal Science and Technology*, Vol. 11, J. A. Moulijn, K. A. Nater, and H. A. G. Chermin, eds. (Elsevier, New York, NY, 1987), p. 945.

J. E. M. Goldsmith, "Photochemical Effects in Two-Photon-Excited Fluorescence Detection of Atomic Oxygen in Flames," *Technical Digest*, Vol. 5 (Optical Society of America, Washington, DC, 1987), p. 39.

J. E. M. Goldsmith, "Recent Advances in Flame Diagnostics Using Fluorescence and Ionization Techniques," *Laser Spectroscopy VIII*, W. Persson and S. Svanberg, eds. (Springer-Verlag, New York, NY, 1987), p. 337.

F. C. Gouldin, K. N. C. Bray, and J.-Y. Chen, "Chemical Closure Model for Fractal Flamelets," Comb. Sci. Tech., submitted (1987).

G. E. Hall, R. O. Loo, H.-P. Harri, N. Svakumar, G. K. Chawla, P. L. Houston, D. W. Chandler, J. W. Hepburn, and I. Burak, "Vector Correlations in the Photodissociation of Ch_3I, OCS, and Glyoxal," Ber. Bunsenges. Phys. Chem., submitted (1987).

J. C. Hamilton, R. J. Anderson, and G. W. Foltz, "Optical Second-Harmonic Generation from Surface Segregants and Adsorbed Oxygen on an Fe-18Cr-3Mo(110) Surface," Materials Research Society Symposia Proceedings **83**, 251 (1987).

J. Hoornstra and D. Dunn-Rankin, "Size Distribution Characteristics of Size-Graded Pulverized Coal," *Proceedings of International Conference on Coal Science* (Elsevier, New York, NY, 1987), p. 949.

J. O. Keller, J. E. Dec, C. K. Westbrook, and T. T. Bramlette, "Pulse Combustion: The Importance of Characteristic Times," Comb. Flame, submitted (1987). Also, Sandia Report *SAND 87-8783* (Sandia National Laboratories, Livermore, CA, 1987).

M. L. Koszykowski, G. A. Pfeffer, and D. W. Noid, "Application of the Spectral Analysis Method to Atomic, Molecular, Nuclear, and Polymeric Systems," *Chaotic Phenomena in Physics and Astrophysics* (Academy of Science, New York, NY, 1987), p. 173.

N. M. Laurendeau and J. E. M. Goldsmith, "Comparison of Laser-Induced Fluorescence Methods for Measurement of Hydroxyl Concentration in Flames," Appl. Opt., submitted (1987).

T. J. Lee, J. E. Rice, R. B. Remington, W. D. Allen, and H. F. Schaefer, III, "How Bent Can a Benzene Be? The Molecular Structure, Infrared Spectrum, and Energetics of [6] Paracyclophane," Chem. Phys., submitted (1987).

R. P. Lucht, "Applications of Laser-Induced Fluorescence Spectroscopy," *Laser Spectroscopy and its Applications*, L. J. Radziemski, R. W. Solarz, and J. A. Paisner, eds. (Marcel Dekker, New York, NY, 1987), p. 623.

R. P. Lucht and R. L. Farrow, "Calculation of Saturation Line Shapes and Intensities in Coherent Anti-Stokes Raman Scattering Spectra of Nitrogen," J. Opt. Soc. Am. B, submitted (1987).

R. P. Lucht and M. A. Maris, "CARS Measurements of Temperature Profiles Near a Wall in an Internal Combustion Engine," SAE Trans., accepted (1987).

A. E. Lutz, R. J. Kee, and J. A. Miller, "SENKIN: A Fortran Program for Predicting Homogeneous Gas-Phase Chemical Kinetics with Sensitivity Analysis," Sandia Report *SAND87-8248* (Sandia National Laboratories, Livermore, CA, 1987).

P. Magre and R. W. Dibble, "Finite Chemical Kinetics Effects in a Subsonic Turbulent Hydrogen Flame," Comb. Flame, submitted (1987).

S. B. Margolis and B. J. Matkowsky, "New Modes of Quasi-Periodic Combustion," SIAM J. Appl. Math., submitted (1987).

S. B. Margolis and F. A. Williams, "Diffusional/Thermal Coupling and Intrinsic Instability of Solid Propellant Combustion I. Cellular Instability," Comb. Sci. Tech., submitted (1987).

S. B. Margolis and F. A. Williams, "Diffusional/Thermal Coupling and Intrinsic Instability of Solid Propellant Combustion II. Pulsating Instability," Comb. Sci. Tech., submitted (1987).

K. D. Marx, "Development and Application of a Computer Model for Large-Scale Flame Acceleration Experiments," Sandia NR Report *NUREG/CR-4855* (Sandia National Laboratories, Livermore, CA, 1987).

K. D. Marx, "Generation of Confined Ring Vortices by Falling Sprays," Phys. Fluids, submitted (1987).

M. Namazian, R. W. Schefer, and J. Kelly, "Scalar Dissipation Measurements in the Developing Region of a Jet," Comb. Flame, accepted (1987). Also, Sandia Report *SAND87-8652* (Sandia National Laboratories, Livermore, CA, 1987).

M. Namazian, R. L. Schmitt, and M. B. Long, "Two-Wavelength Single Laser CH and CH_4 Imaging in a Turbulent Diffusion Flame," Appl. Opt., submitted (1987).

M. Namazian, J. Kelly, R. W. Schefer, S. C. Johnston, and M. B. Long, "Nonpremixed Bluff-Body Flow and Flame-Imaging Study," J. Exper. Fluids, submitted (1987).

D. K. Ottesen, "*In Situ* Real-Time Analysis of Particulates," *Quarterly Project Report* (Sandia National Laboratories, Livermore, CA, 1/1/87-3/1/87). Also, *Proceedings of International Conference on Coal Science* (Elsevier, New York, NY, 1987), p. 777.

E. A. Rohlfing, D. W. Chandler, and G. A. Fisk, "Laser-Based Techniques for the Detection of Chlorinated Aromatic Hydrocarbons," Sandia Report *SAND 87-8787* (Sandia National Laboratories, Livermore, CA, 1987).

E. A. Rohlfing and D. W. Chandler, "Laser Spectroscopy of Jet-Cooled Chlorinated Aromatic Hydrocarbons," *Advances in Laser Science II*, M. Lapp, W. C. Stwalley, and G. A. Kenney-Wallace, eds. (American Institute of Physics, New York, NY, 1987), p. 618.

G. J. Rosasco, L. A. Rahn, W. S. Hurst, R. E. Palmer, J. P. Looney, and J. W. Hahn, "High Resolution Inverse Raman Spectroscopy of the CO *Q*-Branch," Proc. SPIE, accepted (1987).

B. R. Sanders and H. A. Dwyer, "Unsteady Influences in Droplet Dynamics and Combustion," Comb. Sci. Tech., submitted (1987).

R. W. Schefer, M. Namazian, J. Kelly, and M. B. Long, "CH_4 Concentration Imaging in Simple Jet and Bluff-Body Flames," Comb. Flame, submitted (1987).

I. R. Slagle, D. Sarzynski, D. Gutman, J. A. Miller, and C. F. Melius, "Kinetics of the Reaction Between Oxygen Atoms and Ethyl Radicals," J. Chem. Soc. Faraday Trans. II, submitted (1987).

R. (F. P.) Trebino, "A New Nonlinear-Optical Expansion and Diagrammatic Approach: N^{th}-Order Dephasing-Induced Effects," Phys. Rev. A, submitted (1987).

R. (F. P.) Trebino and L. A. Rahn, "Observation of Long-Lived Collision-Induced Coherences and Ground-State-Spin Gratings in a Flame," *Advances in Laser Science II*, M. Lapp, W. C. Stwalley, and G. A. Kenney-Wallace, eds. (American Institute of Physics, New York, NY, 1987), p. 217.

S. R. Vosen, R. J. Cattolica, and F. J. Weinberg, "Chemical Effects of Plasma Gases on Flame Kernel Development," Pro. Royal Soc. London, submitted (1987).

S. P. Walch, C. M. Rohlfing, C. F. Melius, and C. W. Bauschlicher, Jr., "Theoretical Characterization of the Minimum Energy Path for the Reaction $H + O_2 \rightarrow HO_2^* \rightarrow HO + O$," J. Chem. Phys., submitted (1987).

B. J. Waters, R. E. Mitchell, R. G. Squires, and N. M. Laurendeau, "Evidence for Formation of CO_2 in the Vicinity of Burning Pulverized Carbon Particles," Comb. Flame, accepted (1987).

Presentations

R. J. Anderson, J. C. Hamilton, and G. W. Foltz, "Optical Second Harmonic Generation Studies of Surface Adsorption and Segregation on Fe-18Cr-3Mo (110)," Topical Meeting on Microphysics of Surfaces, Beams, and Adsorbates Technical Digest Series 9, 96 (Opt. Soc. Amer., Washington, DC, 1987).

R. C. Armstrong and S. R. Vosen, "Dynamic Model of Liquid Propellant Combustion," Twenty-fourth JANNAF Combustion Meeting, Monterey, CA (CPIA, 1987).

R. S. Barlow and C. Q. Morrison, "LDV Measurements of Gas Velocities in a Dense Particle-Laden Jet Using Velocity PDF Discrimination," Fortieth Anniversary Meeting of the Division of Fluid Dynamics, Eugene OR (American Physical Society, 1987).

R. Behrens, "Thermal Decomposition Mechanisms of RDX," Twenty-fourth JANNAF Combustion Meeting, Monterey, CA (CPIA, 1987).

R. Behrens, "Thermal Decomposition Mechanisms of HMX," Twenty-fourth JANNAF Combustion Meeting, Monterey, CA (CPIA, 1987).

R. W. Bilger and R. J. Kee, "Simplified Kinetics for Diffusion Flames of Methane in Air," Western States Section/ Japanese Section Joint Technical Meeting, Honolulu, HI (The Combustion Institute, 1987).

R. W. Bradshaw and R. W. Carling, "A Review of the Chemical and Physical Properties of Molten Alkali Nitrate Salts and Their Effect on Materials for Solar Central Receivers," Electrochemical Society 172nd Meeting, Honolulu, HI (The Electrochemical Society, 1987), Paper No. 1505.

J.-Y. Chen, "A General Procedure for Constructing Reduced Reaction Mechanisms with Given Independent Relations," Western States Section/Japanese Section Joint Technical Meeting, Honolulu, HI (The Combustion Institute, 1987).

D. E. Foster and P. O. Witze, "Velocity Measurements in the Wall Boundary Layer of a Spark-Ignition Research Engine," International Fuels and Lubricants Meeting, Toronto, Ontario, Canada (SAE, 1987), Paper No. 872105.

R. M. Green, N. P. Cernansky, W. J. Pitz, and C. K. Westbrook, "The Role of Low Temperature Chemistry in the Autoignition of N-Butane," International Fuels and Lubricants Meeting, Toronto, Ontario, Canada (SAE, 1987), Paper No. 872108.

R. M. Green, C. D. Parker, W. J. Pitz, and C. K. Westbrook, "The Autoignition of Isobutane in a Knocking Spark-Ignition Engine," International Fuels and Lubricants Meeting, Toronto, Ontario, Canada (SAE, 1987), Paper No. 870169.

V. P. Heiskanen and R. E. Mitchell, "Temperature, Size and Overall Burning Rates of Pulverized Peat from Finland," Western States Section Spring Meeting, Provo, UT (The Combustion Institute, 1987), Paper No. 87-9.

R. J. Kee and J. A. Miller, "A Structured Approach to the Computational Modeling of Chemical Kinetics and Molecular Transport in Flowing Systems," Invited Paper, Symposium on Chemistry on Minisupercomputer and Supercomputers at ACS 193rd National Meeting, Denver, CO (Division of Physical Chemistry, 1987).

J. O. Keller, T. T. Bramlette, C. K. Westbrook, and J. E. Dec, "Pulse Combustion: The Quantification of Characteristic Times," Western States Section/Japanese Section Joint Technical Meeting, Honolulu, HI (The Combustion Institute, 1987).

W. E. King, J.-H. Park, K. F. McCarty, and J. C. Hamilton, "Characterization of the Oxidation of Undoped and Y-Doped Fe-Cr Alloys by SIMS and Rutherford Backscattering," Electrochemical Society 172nd Meeting, Honolulu, HI (The Electrochemical Society, 1987), Paper No. 936.

R. P. Lucht and M. A. Maris, "CARS Measurements of Temperature Profiles Near a Wall in an Internal Combustion Engine," Soc. Automotive Eng. Trans. Meeting, Detroit, MI (1987), Paper No. 870459.

A. E. Lutz, R. J. Kee, and J. A. Miller, "The Influence of Pressure Disturbances on Spontaneous Ignition," Western States Section/Japanese Section Joint Technical Meeting, Honolulu, HI (The Combustion Institute, 1987).

P. Magre and R. W. Dibble, "Effects of Finite Chemical Kinetics in Subsonic, Nonpremixed, Turbulent Flames of Hydrogen," AIAA Twenty-fifth Aerospace Sciences Meeting, Reno, NV (1987), Paper No. AIAA87-0378.

S. B. Margolis and F. A. Williams, "Diffusional/Thermal Coupling and Intrinsic Instability of Solid Propellant Combustion I. Cellular Instability," Western States Section/Japanese Section Joint Technical Meeting, Honolulu, HI (The Combustion Institute, 1987).

S. B. Margolis and F. A. Williams, "Diffusional/Thermal Coupling and Intrinsic Instability of Solid Propellant Combustion II. Pulsating Instability," Western States Section/Japanese Section Joint Technical Meeting, Honolulu, HI (The Combustion Institute, 1987).

A. R. Masri, R. W. Bilger, and R. W. Dibble, "The Local Structure of Turbulent Nonpremixed Flames of Methane Near Extinction," Western States Section/Japanese Section Joint Technical Meeting, Honolulu, HI (The Combustion Institute, 1987).

K. F. McCarty, J. C. Hamilton, and W. E. King, "Real-Time Studies of the Oxidation of Undoped and Y-Doped Fe-Cr Alloys," Electrochemical Society 172nd Meeting, Honolulu, HI (The Electrochemical Society, 1987), Paper No. 920.

W. J. McLean, C. A. Amann, C. T. Bowman, P. A. Libby, R. E. Palmer, L. D. Smoot, and R. A. Strehlow, "Soviet Combustion Research," Foreign Applied Sciences Assessment Center Meeting, McLean, VA (Science Applications Intl. Corp., 1987), Paper No. FASAC-TAR-3120.

C. F. Melius, "Theoretical Studies of the Chemical Reactions Involved in the Ignition of Nitramines," Western States Section/Japanese Section Joint Technical Meeting, Honolulu, HI (The Combustion Institute, 1987). Also, Twenty-fourth JANNAF Combustion Meeting, Monterey, CA (CPIA, 1987).

J. A. Miller, "Chemical Kinetics and Flame Modeling," Invited Paper, Conference on Numerical Combustion, San Francisco, CA (SIAM, 1987).

J. A. Miller, "Mechanism and Modeling of Nitrogen Chemistry in Flames," Symposium of the Formation and Control of NOx Emissions from Combustion Sources; ACS Award Symposium on the Chemistry of Contemporary Technological Problems (William Bartok); Invited Paper, ACS 193rd National Meeting, Denver, CO (Division of Environmental Chemistry, 1987).

R. E. Mitchell, "High-Temperature Burning Rates of Pulverized Coal Chars," Fourteenth Annual NOBCChE National Conference, San Francisco, CA (1987).

D. A. Nissen and F. A. Greulich, "Automated Image Analysis of Coal Minerals," Electrochemical Society 172nd Meeting, Honolulu, HI (The Electrochemical Society, 1987), Paper No. 965.

R. A. Perry and D. L. Siebers, "Rapid Reduction of Nitrogen Oxides in Exhaust Gas Streams," Health Effects Institute Annual Meeting, Seabrook Island, SC (1987).

R. A. Perry, F. P. Tully, and M. D. Allendorf, "Free-Radical Oxidation of Isocyanic Acid," Western States Section/ Japanese Section Joint Technical Meeting, Honolulu, HI (The Combustion Institute, 1987).

D. L. Siebers and C. F. Edwards, "Autoignition of Methanol and Ethanol Fuel Sprays Under Diesel Engine Conditions," International Congress and Exposition, Detroit, MI (SAE, 1987), Paper No. 870588.

R. R. Steeper, N. W. Sorbo, D. P. Y. Chang, and C. K. Law, "Incineration of Liquid Hazardous Wastes: Vaporization and Combustion of Droplets of Chlorinated Hydrocarbons," AFRC International Symposium on the Incineration of Hazardous, Municipal, and Other Wastes, Palm Springs, CA (1987).

S. R. Vosen, "The Combustion of Hydroxylammonium Nitrate Based Liquid Propellants," Twenty-fourth JANNAF Combustion Meeting, Monterey, CA (CPIA, 1987).

Issued by Sandia National Laboratories, operated for the United States Department of Energy by Sandia Corporation.